Effects of spatial resolution on radar-based precipitation estimation using sub-kilometer X-band radar measurements

Zur Erlangung des akademischen Grades eines
DOKTORS DER NATURWISSENSCHAFTEN
von der KIT-Fakultät für Physik des
Karlsruher Instituts für Technologie (KIT)

genehmigte

DISSERTATION

von

Yaoyao Zheng
aus Wenzhou (China)

Tag der mündlichen Prüfung:	02.07.2021
Referent:	Prof. Dr. Christoph Kottmeier
Korreferent:	Prof. Dr. Michael Kunz

Abstract

Known for the ability to observe precipitation at spatial resolution higher than rain gauge networks and satellite products, weather radars allow us to measure precipitation at spatial resolutions of 1 kilometer (typical resolution for operational radars) and a few hundred meters (often used in research activities). In principle, we can operate a weather radar at resolution higher than 100 m and the expectation is that radar data at higher spatial resolution can provide more information. However, there is no systematic research about whether the additional information is noise or useful data contributing to the quantitative precipitation estimation. In order to quantitatively investigate the changes, as either benefits or drawbacks, caused by increasing the spatial resolution of radar measurements, we set up an X-band radar field experiment from May to October in 2017 in the Stuttgart metropolitan region. The scan strategy consists of two quasi-simultaneous scans with a 75-m and a 250-m radial resolution respectively. They are named as the fine scan and the coarse scan, respectively. Both scans are compared to each other in terms of the radar data quality and their radar-based precipitation estimates. The primary results from these comparisons between the radar data of these two scans show that, in contrast to the coarse scan, the fine scan data are characterized with losses of weak echoes, are more subjected to external signals and second-trip echoes (drawback), are more effective in removing non-meteorological echoes (benefit), are more skillful in delineating convective storms (benefit), and show a better agreement with the external reference data (benefit).

Contents

1. Introduction

Precipitation information is of interest to both the meteorology and hydrology communities. Meteorologists deal with hydrometeors either in the atmosphere or reaching the ground surface, whereas hydrologists are concerned with the water after it reaches the ground surface. This difference determines the different roles of precipitation data in meteorological or hydrological applications. For instance, regarding numerical modeling, precipitation data are often among final output of many Numerical Weather Prediction (NWP) models, whereas they serve as fundamental input for the majority of hydrological models.

Demand for spatiotemporal resolution of precipitation data varies among these different applications. In terms of meteorological applications, observational rainfall data are used for various purposes: to assess whether an NWP model is robust or reliable, to calibrate or validate satellite observations, and to capture fine features of severe weather systems. Each purpose is associated with its own demand on the spatiotemporal resolution. Grid resolutions of the majority of NWP models are on the 1-kilometer scale (Vannitsem et al., 2021). For inter-comparisons between areal and point measurements of precipitation, spatial resolution of the areal measurements should be as high as possible. To investigate severe weather systems characterized by large gradients in rainfall intensity, spatial resolution of precipitation data should be about tens to hundreds of meters, and temporal resolution should be shorter than 5 minutes (Ochoa-Rodriguez et al., 2015) especially if these weather systems move and evolve rapidly.

When it comes to hydrological modeling, unlike lumped and semi-distributed models, physics-based fully distributed models are capable of providing a detailed description of hydrological processes (infiltration, runoff, etc.) at almost any location within a single catchment. They perform calculations for each grid cell, and thus require precipitation input to be high-resolution (Salvadore et al., 2015). The demand for the spatiotemporal resolution depends on the size of a catchment (Rossa et al., 2011; Schellart et al., 2014). This demand is stronger for small-sized catchments, particularly those in urban environments where small-sized features of intense precipitation can exert a considerable impact.

Such strong demand for the resolution is attributed to unique characteristics of urban catchments. First, unlike a rural environment, an urbanized area is characterized by diminished natural retention and vast expanses of impervious surfaces. This speeds up the reaction of a catchment to precipitation, such as surface or subsurface flows, and increases the likelihood of urban floods. Second, the majority of urban catchments are relatively small. This small size accelerates the flood reaction speed, and also

implies less physical space for flood control structural facilities. Third, the conventional design for the existing drainage systems for many developed metropolitan regions is imperfect, and these systems are unable to respond promptly to the more frequent precipitation extremes against the background of climate change (Seneviratne et al., 2012; Arnbjerg-Nielsen et al., 2013; Prein et al., 2017). Fourth, urban environments are extremely spatially heterogeneous, which implies non-linear interactions among different hydrological components, and adds complexity to the hydrological modeling. Fifth, in case of a hilly orography such as the Stuttgart metropolitan area to be investigated in this thesis, the flow of water downstream can be further accelerated, thus inducing rapid peak flows. These characteristics lead to more rapid hydrological responses in urban catchments with durations of less than a few hours, thereby rendering the aftermath of urban floods more devastating, requiring a shorter lead time for flood alert systems, making urban flood management more challenging. In Europe, the flood-related economic losses have been a few billion euros per year, together with numerous causalities (Sénési et al., 1996; Douben, 2006; Barredo, 2007; Kron et al., 2012; Jongman et al., 2014). As urbanization is still expanding all over the world (Nations, 2019), growing attention is being paid to floods in urban catchments. The relevant applications are forecasting, real-time management and risk assessment of urban floods.

Precipitation input should be high-resolution in these applications concerning urban floods. A theoretical analysis recommended the desirable spatiotemporal resolution to be 1-minute and 1-km^2 (Schilling, 1991). Other applied studies adjusted the resolution depending on sizes of urban catchments. Berne et al. (2004) proposed a resolution of 3 km and 5 minutes for a 10-km^2 catchment, and 2 km and 3 minutes for a 1-km^2 urban catchment. A 2.5-km resolution is for a 6-km^2 catchment (Emmanuel et al., 2012), and a 1-km^2 resolution for a 10-km^2 catchment (Schellart et al., 2012). It turns out that the 1-km spatial resolution should be sufficient for precipitation data in urban hydrology.

If we need precipitation information at such a resolution of 1 km and 5–10 minutes, what can be the source? Rain gauges, satellites and ground-based weather radars all provide precipitation measurements, but each of them has its pros and cons. Owing to the effective area less than 1 m^2, a rain gauge provides point measurements at its local measuring site, which implies a lack of spatial information between rain gauges. Germany has the world's densest rain gauge network, but the average distance between rain gauges is on the order of 10 km (Kidd et al., 2017). In fact, rain gauge densities are much lower in the majority of countries and regions except Germany. Given the sparse rain gauge networks in reality, these point measurements from rain gauges are insufficient to describe the spatial variability of precipitation on small scales whose rainfall characteristic lengths are shorter than the distance between any two rain gauges (Sharif et al., 2006; Villarini et al., 2008; Maier et al., 2020). For satellite products, one datum represents the mean value over a footprint or pixel, but the spatiotemporal resolution of the majority of satellite observation is too coarse, on the order of several kilometers and hourly to daily. It means, neither rain gauge measurements nor satellite precipitation products are able to resolve precipitation's great spatial variability. Thus, we focus on the ground-based weather radar which is able to

measure precipitation at a spatial resolution higher than the 2-km resolution, and at a temporal resolution shorter than the 15-minute time interval, over geographic coverage on the order of $4 \times 10^4\,\mathrm{km}^2$. A large amount of research on urban hydrological modeling has utilized weather radar measurements to reconstruct or predict urban floods (Niemczynowicz, 1991; Schilling, 1991; Yuan et al., 1994; Han et al., 2000; Tilford et al., 2002; Einfalt et al., 2004; Sharif et al., 2006; Smith et al., 2007; Wright et al., 2014; Rico-Ramirez et al., 2015; Niemi et al., 2017; PC et al., 2019).

Radar measurements are sampled in a polar coordinate system. A radar datum represents the averaged information of atmospheric particles within a radar sampling volume. In terms of operational applications, these data are often converted to the Cartesian coordinate, in which a radar datum represents the averaged information of targets within a grid. Despite the radar's ability to provide measurements at the 1-km spatial resolution, chances are that precipitation can be spatially heterogeneous under this 1-km spatial scale, which is often the case for convective precipitation (Bornstein and Lin, 2000; Dabberdt et al., 2000; Bentley et al., 2010; Davini et al., 2012). An extreme example showed that precipitation measurements from nine rain gauges within a single radar pixel ($500 \times 500\,\mathrm{m}^2$) for a 4-day period showed discrepancies up to twice in terms of precipitation amounts measured by these nine rain gauges (Jensen and Pedersen, 2005). High gradients of rainfall accumulation amounting up to $15\,\mathrm{mm\,km}^{-1}$ were found from precipitation measurements of 13 rain gauges at a $1 \times 5\,\mathrm{km}^2$ test site (Fiener and Auerswald, 2009). Convective storms exhibited very small-scale rainfall variability on the basis of precipitation measurements of 27 rain gauges within a $2 \times 2\,\mathrm{km}^2$ domain (Peleg et al., 2013). The radar measurements at the 1-km resolution are unable to resolve these sub-kilometer spatial variability demonstrated by these studies.

To investigate this sub-kilometer variability, Paschalis et al. (2013) used a stochastic space-time model which generated artificial high-resolution precipitation data, and Gires et al. (2012) downscaled the original resolution of $1\,\mathrm{km}^2$ and 5 min by using multifractal cascades models. Although both methods produced 'extra' datasets at other resolutions higher than the original measurements, these extra datasets were essentially based on radar measurements at the original resolution and contain no new information beyond the original resolution. Whether these statistically manipulated data reflect the true physics of changing sampling resolutions is in doubt. The most reasonable way to deepen into this sub-kilometer precipitation variability is to measure precipitation directly at spatial resolutions higher than the 1-km resolution. However, a few studies about radar sampling suggested that errors increased with higher spatial resolutions (Fabry et al., 1994; Jordan et al., 2000; Piccolo and Chirico, 2005; Shucksmith et al., 2011). Thus, we are interested in whether radar measurements sampled at the sub-kilometer resolution contain more errors compared to those sampled at spatial resolutions coarser than the 1-km resolution, and also interested in how large these errors can be. Besides, each aforementioned study involves measurements sampled with one spatial resolution only, and we are curious about whether their conclusions are still valid in case of two direct measuring resolutions. Moreover, these studies quantify

sampling errors using statistics calculated on the basis of precipitation accumulation, but we are also concerned with errors in the directly measured radar variables. Since errors indicate bad data quality, we are essentially interested in quality of information from radar measurements, and this information can be in terms of both radar variables and precipitation quantities. However, within the author's knowledge, few studies involved such radar datasets with various sampling resolutions, and no research has ever used such radar datasets to investigate effects or outcome of changing spatial resolutions in a systematic and quantitative manner. The aim of this thesis is to fill in this gap.

The most prevalent and crucial application of radar measurements is to estimate precipitation in terms of either instantaneous precipitation intensity or precipitation accumulation amount over a period. That is also the reason for these measurement errors expressed in terms of precipitation accumulation amount in the aforesaid research. Thus, besides the radar variables, we analyze radar-derived precipitation estimates. In accord with definitions of the level II and III data in the common data recording systems for weather radars, for the remaining thesis, radar data are defined as the output directly from radar signal processors, and they are the level II data; the level III data are derivatives of the level II data, such as these radar-derived precipitation estimates. Quality of any data depends on the intended uses of the data. Since we focus on using radar measurements for precipitation estimation only, quality of both the level II and III data depends on their ability to help us quantify precipitation in the real world.

The important attributes of data quality are accuracy and reliability. The accuracy refers to the exactness of the data, and the reliability is about whether the data contradict other trusted resources. Since precipitation data are also available from other instruments, to evaluate quality of the level III data, we can check whether these level III data are commensurate with other sources of precipitation measurements. However, we do not have direct measurements for the variable of the level II data, so assessment of the quality of the level II and III data should be separated. As is well-known, radar observation is subject to lots of factors, and radar data contain various sources of noise which severely affects the accuracy of radar measurements. Thus, regarding the quality of the level II data, we can inspect whether and how much the data are contaminated by noise. Noise is unwanted, irrelevant or meaningless data. In this research, noise is the data which bring misleading information about precipitation; for instance, an indication of rain in case of a dry condition, or an indication of heavy rain intensity in case of light rain, or vice versa. The existence of noise makes it difficult for the 'true' precipitation information to be seen clearly. The more noise exists, the worse the data quality is. Thus, the quality of the level II data can be assessed by a measure of how much noise—'fake' or 'wrong'precipitation information—a radar collects compared to the 'true' precipitation information.

The radar-derived precipitation estimates are calculated from radar data via empirical relations which are also subject to their own errors and uncertainties. It means, besides the errors and uncertainties of the radar data which propagate into the radar-derived precipitation estimates, these empirical relations also bring errors and uncertainties to these precipitation estimates. Unlike some radar

variables, precipitation quantities obtained by means of arithmetic calculations are all in the linear scales and have their own physical meaning, which implies the quality of radar-derived precipitation estimates is not identical to the quality of radar data. This is an additional reason why we assess the quality of radar data and radar-derived precipitation estimates separately, which is not addressed by other previous studies.

The foregoing assessment of noise in radar data brings us a good knowledge of characteristics of noise in radar data. This assessment facilitates developments of radar data quality control (QC) procedures which improve radar data quality by filtering out various types of noise. We plan to develop individual procedures responsible for each type of noise, and expect some of these procedures are identical but some of them are different between the radar data with different resolutions. Through these procedures we can examine how these data QC procedures impact the effects of the spatial resolution on radar data quality. After applying data QC procedures to the radar data, the data quality of precipitation estimates based on the radar data should be altered. Thus, we can also compare the sensitivity of radar-based precipitation estimates to the data QC procedures in case of different spatial resolutions. No similar study has existed.

Similar to the aforementioned literature, we plan to employ a scientific control, in which the experimental group will use radar data or precipitation quantities with relatively higher resolutions and the control group will use relatively lower spatial resolutions. This scientific control enables comparisons between the experimental and control groups, and we hypothesize that both groups should be different. Then, differences deduced from these comparisons can serve as indications of the effects of spatial resolutions on radar data and radar-based precipitation estimation. However, unlike these aforementioned literature, this research aims at radar measurements with different sampling resolutions. We expect results of this research to reflect the physics caused by using different resolutions that are truly and physically sampled. The previous studies using only the statistically generated 'artificial' resolutions were unable to demonstrate such physics.

Because of a lack of the relevant research, the aim of this research is to investigate the effects of changing spatial resolutions of radar sampling in two aspects—radar data quality and radar-based precipitation estimation—using radar datasets measured using two sampling resolutions, at least one of which is at the sub-kilometer resolution. Since radar measurements sampled at two radial resolutions are available, we can investigate these effects through comparisons of radar data quality and radar-based precipitation estimation between two spatial resolutions. To fulfill the aim, the following objectives should be addressed through the thesis

- 1) to determine the differences between two spatial resolutions in terms of radar data quality by assessing and comparing radar data quality between the radar data at different spatial resolutions through characteristics of noise in radar data;

- 2) to determine the differences between two spatial resolutions in terms of radar-based precipitation quantities by assessing and comparing radar-based precipitation quantities at different spatial resolutions by evaluating their consistency with references;
- 3) to inspect the sensitivity of these two categories of differences to the data QC procedures.

The field experiment's design is constrained by practical technical limitations, so sampling at two sampling resolutions is sufficient. In addition, considering the strongest demand for the spatial resolution of precipitation measurements in urban hydrology, our radar experiment site was chosen in an urban environment. The portability of the X-band radar renders itself as the optimal instrument to observe precipitation customized for a specific location within a relatively small coverage (on the order of $1 \times 10^4 \text{km}^2$).

The thesis is structured as follows. Chapter 2 provides an introduction to theories of radar meteorology. It involves basic concepts of the weather radar system and its working principles, explains definitions of dual-polarization and physical meanings of polarimetric variables, and elucidates the radar-based quantitative precipitation estimation based on both single-polarization and polarimetric variables. Chapter 3 describes the X-band radar field campaign, with an emphasis on the scan strategy and the resultant two radar datasets in two different spatial resolutions, referred as the fine scan data and the coarse scan data, respectively. Chapter 3 also describes supplementary datasets which contributes to the subsequent analyses, and presents statistical concepts to be used later on.

The data analyses, results and relevant discussions are presented in Chapter 4 and 5. Chapter 4 discusses the effects of the spatial resolution on radar data quality by comparing the two X-band radar datasets which are at two different spatial resolutions. The comparisons are performed on the various aspects: i) existence of one part of 'extra' data which are only available in one dataset and absent in the other dataset, ii) characteristics of these extra data quantitatively described by the single-polarization or polarimetric radar variables, iii) procedures of identification and removal of these extra data if they are identified as noise, iv) spatiotemporal variations of these extra data over the entire measuring period and the whole radar coverage, v) statistical errors of polarimetric variables, vi) range dependences of radar variables, either single-polarization or polarimetric. Through these comparisons, we simultaneously process the data QC procedures for both fine and coarse scan datasets to improve the radar data quality for the precipitation estimation in Chapter 5. It compares two sets of precipitation estimates derived from these two radar datasets at two different spatial resolutions. The comparisons between the fine and coarse scans are done in terms of: i) their ability to resolve structures of convective systems through case studies of convective storms, ii) their agreement with other precipitation measurements at various temporal scales, iii) spatial distributions of radar-derived precipitation quantities. The sensitivity of differences shown by the comparisons regarding radar data quality to the radar data QC procedures is also presented at the end of Chapter 4, and the sensitivity of differences shown by the comparisons

concerning precipitation quantities to the radar data QC procedures are in the last part of Chapter 5. Chapter 6 summarizes the main conclusions of these results.

2. Basic Theory of Radar Meteorology, Dual-polarization and Radar-based Precipitation Estimation

Basic knowledge of radar meteorology is a prerequisite for designing a radar experiment (Section 3.1) and performing data analysis procedures in the following sections. This chapter gives concepts of both single-polarization and polarimetric variables and their characteristics. These concepts are associated with the radar data QC procedures (Chapter 4), visualization of convective storm inner structures (Section 5.1) and quantitative precipitation estimation (QPE) (Section 5.2 and Section 5.3).

2.1. Weather radar system and principles

Scattering, absorption and refraction are the processes which occur when the electromagnetic (EM) waves interact with atmospheric particles. The Rayleigh scattering approximation that is valid for the majority of atmospheric hydrometeors is used to define the radar equation and radar reflectivity that is the most important radar variable in QPE (Section 5.3). A radar system transmits EM signals whose propagation path is controlled by the refraction process, and the trajectory of this path should be known for the radar-gauge match-up procedure (Section 5.2). The pulse-to-pulse sampling of a weather radar fits its hardware design. The sampling parameters affect radars' performance and their ability to observe precipitation. Knowledge of physical constraints between these sampling parameters is a prerequisite for designing the scan strategy for a radar experiment (Section 3.1). Doppler dilemma is closely related to second-trip echoes—a type of noise discussed in Section 4.3. Weather radars can be categorized according to its microwave frequency, and the S-, C- and X-band radars exhibit different characteristics in terms of radar measurements. Discussions on these different characteristics correspond to the selection of instruments (Section 3.1).

Electromagnetic waves' interaction with atmospheric particles

Radar is an acronym for "RAdio Detecting And Ranging". As active remote sensors emitting EM waves, radars have been used for military, civil navigation, automobile, agriculture and geophysics. For a meteorological radar, its EM waves propagate through the atmosphere filled with hydrometeors (cloud droplet, raindrop, ice crystal, graupel, snowflake, etc.) (Fig. 2.1) and non-meteorological scatterers.

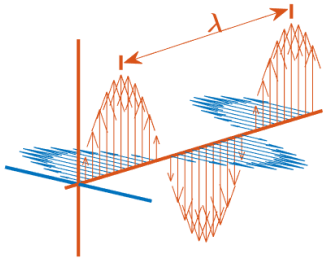

Fig. 2.1.: Sketch of single-polarized (horizontally) EM wave propagation, where the red color indicates the electric field, and the blue color represents the magnetic field

The EM wave, a traverse wave whose oscillation direction is perpendicular to the direction of wave propagation, can be characterized by *wavelength* (λ), *frequency* (f), *phase*, *amplitude*, and *polarization* (direction of electric field oscillation). When the EM wave irradiates a single particle, several processes occur. A proportion of the EM energy is absorbed in the process named *absorption*, but a fraction of the absorbed energy is immediately re-radiated in the same frequency in all directions out of the particle; this re-radiation process, in which the propagation direction of the EM wave deviates from its original straight forward direction, is called *scattering*, and the term *backscattering* refers to that part of the scattered radiation returning back to the radar (180° angle to the incident waves). For particles in the atmosphere, scattering and absorption are two crucial processes.

For a spheric scatterer whose diameter is D, the backscattered power flux density (power per unit area) at the radiation receiving point at range r (S_r) is related to the power flux density intercepted by the particle S_inc through a parameter named as *radar backscattering cross section* (σ_b) as

$$S_\mathrm{r} = \frac{\sigma_\mathrm{b}}{4\pi r^2} S_\mathrm{inc}. \tag{2.1}$$

In order to better understand σ_b, we can assume a spheric particle which is capable of scattering radiation isotropically (uniformly in all directions) and is also located at range r. With the complex refractive index of this scatterer (n) and the dielectric constant (also called relative permittivity) (ε_r), if the size of a spheric particle is much smaller than λ ($\pi n D \ll \lambda$), the radar cross section (σ_b) approximates to the sixth power of D following (Hulst and van de Hulst, 1981)

$$\sigma_\mathrm{b} = \frac{\pi^5 |K|^2 D^6}{\lambda^4}, \tag{2.2}$$

where K is named as dielectric factor, associated with n, or the dielectric constant (also called relative permittivity) ε_r through

$$K = \frac{n^2 - 1}{n^2 + 2} = \frac{\varepsilon_\mathrm{r} - 1}{\varepsilon_\mathrm{r} + 2}. \tag{2.3}$$

This is the *Rayleigh scattering* approximation for a small spherical particle, which forms the basis of the weather radar equation in terms of power measurement (to be discussed in the next subsection). For a

unit volume (V_c) filled with spherical particles whose radii are all small enough to satisfy the Rayleigh scattering approximation criterion, the ensemble radar cross section is given as

$$\sum_j \sigma_j = \frac{\pi^5 |K|^2}{\lambda^4} \sum_j D_j^6, \tag{2.4}$$

where j represents each particle within this unit volume. This ensemble radar cross section per unit volume leads to the concept of *radar reflectivity* (η)

$$\eta = \frac{\sum_j \sigma_j}{V_c} = \frac{\pi^5 |K|^2}{\lambda^4} \frac{\sum_j D_j^6}{V_c} = \frac{\pi^5 |K|^2}{\lambda^4} Z, \tag{2.5}$$

where

$$Z = \frac{\sum_j D_j^6}{V_c}. \tag{2.6}$$

Z is the *radar reflectivity factor* per unit volume in units of $\mathrm{mm^6\,m^{-3}}$. It is the most important quantity in radar meteorology. The magnitude of Z on the linear scale varies over several orders of magnitude from 0.01 $\mathrm{mm^6\,m^{-3}}$ to $10^6\,\mathrm{mm^6\,m^{-3}}$. For convenience, $10 \log_{10} Z$ is calculated for each Z, with the unit of decibels (dB) of $\mathrm{mm^6\,m^{-3}}$ (written as dBZ), and then the magnitude of Z on the logarithmic scale becomes between -20 dBZ and 60 dBZ.

If the circumference (πD) of this scatter becomes comparable with or larger than λ, Rayleigh scattering approximation becomes invalid. The σ_b magnitude is no longer proportional to the 6th power law, but oscillates (decreases or increases alternatively) as the particles size increases. This oscillation of σ_b is named as *resonance*. This scattering is termed as *Mie scattering*, for particles whose sizes are comparable with the wavelength ($\pi D \approx \lambda$). Beyond the Mie scattering regime, for particles whose dimensions are much larger than λ, the scattering is not longer dependent on λ but instead is proportional to the 2nd power of the diameter; this is termed as *optical or non-selective scattering*. The variations in scattering amplitude with size of scatterers over the complete scattering regime, including Rayleigh, Mie and optical scattering, can be found in Fig. 2.2 in Fabry (2015) and Fig. 3.10 in Zhang (2016)

The above definition of Z is based on the Rayleigh scattering approximation which is only valid if $\pi nD \ll \lambda$, or specifically $\pi nD/\lambda$ is less than 0.3 for hydrometeors (Ryzhkov et al., 2011). This criterion depends on λ, which means the shorter-wavelength radar has a stricter requirement on the sizes of particles. Thus, meteorologists are in favor of using radars in longer wavelengths to ensure the Rayleigh scattering approximation is valid. For the non-spherical particles, such as hailstones, ice crystals or snowflakes and the majority of non-meteorological targets (such as insects, birds, ground clutters), the σ_b magnitude is not yet theoretically defined. Under both circumstances, the term *equivalent radar reflectivity factor* per unit volume (Z_e) is used to approximate the magnitude of backscattering. It means that the radar reflectivity factor actually refers to Z_e. Conventionally we name Z and Z_e as radar reflectivity (not η).

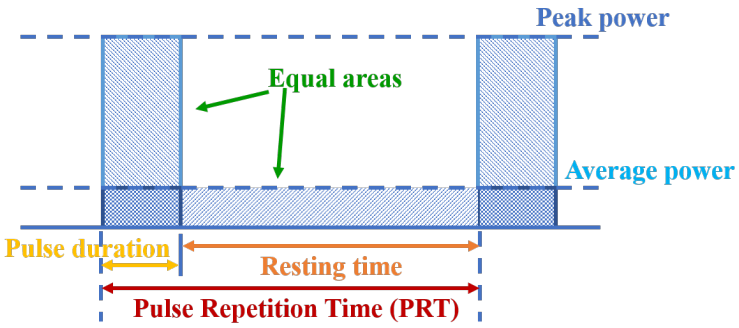

Fig. 2.2.: Schematic diagram to show the concept of duty cycle, and its relation to pulse duration and pulse repetition time, peak power and average power, and this plot is not drawn to scales (adjusted from https://msi.nga.mil/Publications)

Besides the dimension criterion, Eq. 2.4 is valid for uniformly filled homogeneous spheroids only, and invalid for mixed-phase, or oblate or prolate spheroids. The equation for the Rayleigh scattering for non-spheric particles is beyond the scope.

As mentioned, in addition to the scattering, EM waves also interact with hydrometeors through *absorption* in which the absorbed EM energy is converted into thermal energy and then dissipates. The energy loss due to the absorption becomes more significant for the short wavelengths, which limits the usage of short-wavelength weather radars for precipitation observation.

Weather radar sampling parameters and system hardware

The majority of weather radars are pulsed radars. A radar transmits EM waves in a form of sequential short-duration high-power pulses at a single frequency. One pulse lasts on the order of $1\mu s$ with power varying from a few hundreds of watts (W) up to a few megawatts (MW). Given that the majority of weather radars are monostatic with one antenna for the collocated transmitter and receiver, after one pulse is fired, the transmitter turns silent and waits over a relatively long duration for the weak signals to be scattered back to the receiver, before transmitting the next pulse. The short duration when the transmitter is sending out EM waves is termed as pulse duration (τ), and the silent time is termed as reseting time (Fig. 2.2). Summation of τ and reseting time is the pulse repetition time (PRT or T_s), which is usually on the order of 1 ms. The pulse repetition frequency (PRF), which is inversely proportional to PRT, defines how many pulses are transmitted during a unit of time (one second conventionally), varying from a few hundreds to a few thousand Hz for weather radars. The duty cycle, defined as the ratio of τ to PRT, is also the ratio of average power to peak power (the power transmitted into the atmosphere from antenna) (Fig. 2.2). For weather radars, the duty cycle is roughly on the order of 0.1%.

A single radar beam is regarded as being in the shape of an elongated cone, and the shape of a unit volume V_c along one radar beam is analogous to a truncated cone (Fig. 2.3(a)). Such a unit volume

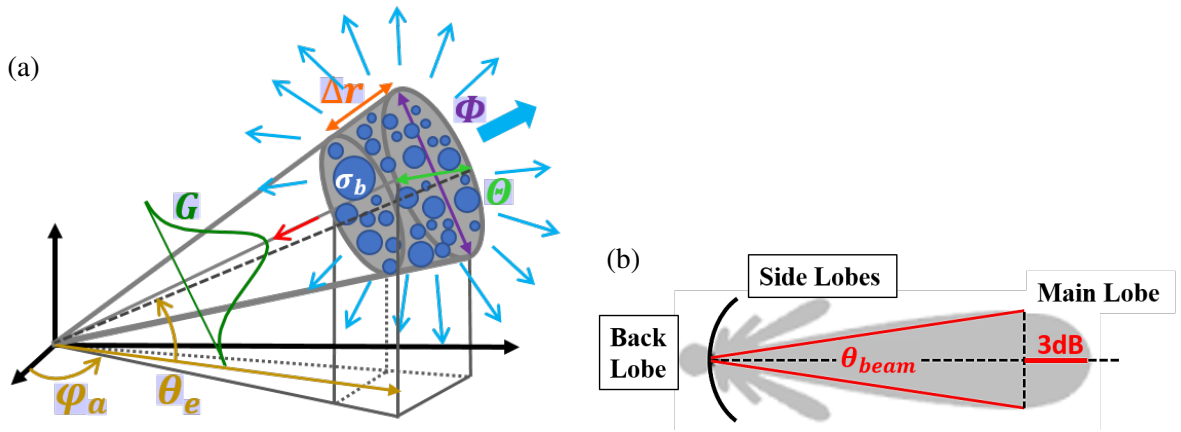

Fig. 2.3.: (a) A sketch of a sampling volume within a conical radar beam with scattering (blue arrows) and backscattering (the single red arrow opposing the direction of wave propagation) (adapted from Montopoli and Marzano (2011)). The sampling volume is defined by range spacing Δr, horizontal beamwidth Θ and the vertical beamwidth Φ, located at a point (θ_e, ϕ_a, r) in the spherical coordinate whose origin is collocated with the antenna, where θ_e is the elevation angle (with respect to the horizon), ϕ_a is the azimuth angle (with respect to the north), G is antenna gain function, and r is the radial distance; (b) the antenna gain function with mainlobe, sidelobes and backlobe with the definition of θ_{beam} (adapted from a figure of https://msi.nga.mil/Publications)

can be named as *sampling volume*, or *resolution volume* or *contributing volume* or *pulse volume* or *radar gate*. Each sampling volume corresponds to one radar measurement, and each radar measurement of a sampling volume is a reflection of the averaged information about hydrometeors within that unit volume. Ideally, the size of a sampling volume can be expressed as

$$V_c \equiv \pi \frac{r\Theta}{2} \frac{r\Phi}{2} \Delta r, \tag{2.7}$$

where r is the *range*, Δr is the *range spacing* or *radial resolution*, Θ is the horizontal (azimuthal) beamwidth and Φ is vertical (elevation) beamwidth of a radar beam. r is the distance between the radar and the center of V_c; Δr is the interval between the centers of two successive V_c along the radar beam; $r\Theta$ or $r\Phi$ describes the angular or cross-range distance between the centers of two adjoint V_c along the azimuthal direction.

The dimension of the sampling volume is associated with the radar pulse. The maximum distance an EM wave travels forth and back within a pulse cycle also defines the possible maximum distance of a sampling volume to the radar. This maximum unambiguous range $r_{\max}$ is defined via

$$r_{\max} \equiv \frac{c}{2(PRF)}, \tag{2.8}$$

and varies from tens to hundreds of kilometers for weather radars. The centers of consecutive V_c are spaced at an interval of Δr, and the length of Δr is determined by τ following

$$\Delta r = \frac{\tau c}{2}. \tag{2.9}$$

Recall that τ usually lasts a few microseconds, the range spacing Δr varies from the order of 100 m to the order of 1 km. Δr is independent of the range and can be adjusted by changing τ (Section 3.1.4). In contrast, the cross-range distance between two sampling volumes along angular directions, either $r\Theta$ or $r\Phi$, increases with the increasing range. It leads to the gradual enlarging of sampling volumes and deteriorating spatial resolution, which brings about the *range dependency* effect inherent in the radar measurements (Section 4.9). For the power measurements such as Z, extreme values tend to be smoothed out within a larger sampling volume, which constrains the radar's detectability in the far range. The range dependency or*range degradation* is a source of errors in radar data applications. In brief, the dimension of V_c represents the spatial resolution of radar measurements and the spatial resolution is defined by Δr and azimuth (angular) resolution ($r\Theta$ or $r\Phi$). Δr is typically smaller than the azimuth resolution. For a common beamwidth of 1°, the maximum size of the sampling volume, determined by τ and PRF, can be up to a few cube kilometers. The majority of meteorological radar beams are designed to be in circular symmetry with equal horizontal and vertical beamwidths ($\Theta = \Phi$), symboled as θ_{beam} (Rauber and Nesbitt, 2018).

The hardware design of weather radars is congruent with the aforementioned radar pulse sampling strategy. The monostatic pulsed weather radar, which transmits and receives EM waves, requires at least four fundamental parts: transmitters, receiver, antenna and Transmitter-Receiver (T-R) switch (Fig. 2.4), in spite of its sophisticated mechanical and electronic configuration in reality. The transmitter (Magnetron or Klystron or solid-state) sends out the high-power pulsed microwave signals on the orders of 10^5–$10^6\,W$ through a waveguide (an energy-efficient conductor connecting transmitter and antenna) to the antenna—a combination of a feed horn and a reflector—regulating how the EM waves are radiated into the space. A circular parabolic reflector is quite typical for weather radars, and its diameter D_a is associated with θ_{beam} through (Fabry, 2015)

$$\theta_{\text{beam}} \approx 1.22\frac{\lambda}{D_a}. \tag{2.10}$$

For instance, for a 1°-θ_{beam}, the antenna size of a 5-cm wavelength weather radar should be no less than 3 m. The backscattered signal, which is on the order of $10^{-10}\,W$ and usually much weaker than the transmitted signal, should be amplified in the T-R switch before entering the very sensitive receiver. Then, the receiver amplifies the received signals, and the signal processor processes these signals to retrieve radar variables which can be shown in the real-time display such as the Plain Position Indicator (PPI), if the antenna rotates in a full circle, or Range-height Indicator (RHI) if the antenna performs vertical

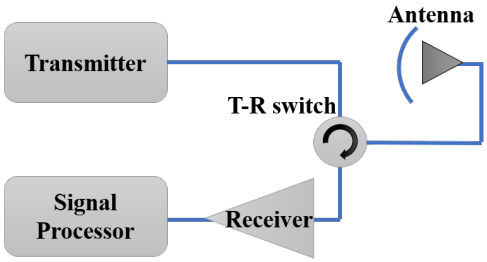

Fig. 2.4.: The block diagram for a pulsed weather radar hardware, where T-R is the acronyms for transmitter-receiver

cross section scanning. We talk about only four main components in the radar hardware (Fig. 2.4), but in reality the modern radar hardware is far more complicated (Fig.13.1 of Fabry (2015), Fig.13 of Kumjian (2018) and Fig.2.1 of Ryzhkov and Zrnić (2019)).

In accordance with the conical radar beam (Fig.2.3(a)), an antenna should radiate energy into a narrow angular range. Such an antenna is called a non-isotropic or directive antenna, unlike an isotropic antenna which radiates the EM energy equally in all directions. For the fixed amount of EM energy into the antenna, the non-isotropic antenna is able to transmit stronger signals into a certain direction. However, for this non-isotropic antenna, in reality, a portion of energy still goes to other directions beyond this narrow angular range. It means, the *antenna beam pattern*, which describes the radiation distribution around the radar, ideally should be a single envelop along the main axis of the radar beam named as *mainlobe*, but in reality consists of many smaller peaks named as *sidelobe* (Fig. 2.3(b)). The mainlobe usually occupies the majority of energy, but the occasional presence of sidelobes may still induces erroneous measurements. Associated with the mainlobe, θ_{beam} is more precisely defined as the angular width of the mainlobe, and is conventionally defined as the width across the antenna beam pattern between the two points where the power is reduced to half of the most intense power along the beam axis (or 3 dB less than the maximum value).

An antenna gain function ($G_{\Theta,\Phi}$) is defined to describe how efficiently the antenna radiates energy relative to the desired direction. It is defined as the ratio of the actual power received at a point of the angular coordinate (Θ, Φ) to the assumed power that impinging on the same point if the antenna is perfectly isotropic. Particularly, $G_{\Theta,\Phi}$ along the beam axis ($\Theta = 0$, $\Phi = 0$), is the ratio of the actual power (P_1) received along the beam axis to the supposed power (P_0) that would have been received at the same location if the radiator is perfectly isotropic

$$G = 10 \log\left(\frac{P_1}{P_0}\right). \tag{2.11}$$

The antenna gain can be related to the antenna beamwidth through

$$g = \frac{\pi^2 k_g^2}{\Theta\Phi}, \tag{2.12}$$

where g is G on the linear scale, and $k_g^2 = 1$ for the circular antenna.

Radar antenna can be manipulated in two modes. First, the antenna rotates over 360° full circle and so a radar beam also rotates over 360° following the radar antenna. Such a 360° sweeping is termed as a radar sweep. A radar scan strategy, also called Volume Coverage Pattern (VCP), consists of at least one sweep. Usually the rotation speed is fixed, and the time for a scan strategy is predetermined. This scan strategy is repeated continuously over the entire measuring period. Then we obtain a circular radar coverage, which can be displayed via PPI—a top view of the coverage with a radar situated in the exact center of the radar coverage, with the longitude as the x-axis and the latitude as the y-axis. The second mode is vertical sweeps of a radar antenna, which can be visually displayed by RHI—a vertical cross section with the range as the x-axis and the altitude as the y-axis.

Radar equation for disturbed targets

The size of a radar sampling volume varies from approximately 0.1 to 10 km^3 (Eq. 2.7). The concentration of raindrops varies from 10 to $10^4 \mathrm{m}^{-3}$, which means a radar sampling volume roughly contains 1–10^5 billion raindrops whose sizes are on the order of 1 mm. Thus, one measurement from a sampling volume actually represents the average status contributed by all the particles within this single sampling volume, and we name it as a *distributed target* (or beam-filling targets) (its antonym is *solitary target* or *point target*). For distributed targets, in terms of the power measurement, the classical weather radar equation (Probert-Jones, 1962) with additional three explicit loss factors (Smith, 1986) is expressed as

$$\overline{P}_\mathrm{r} = [\frac{10^{-18}\pi^3 c}{1024\ln(2)}][\frac{P_\mathrm{t}\tau g^2 \Theta_\mathrm{b}\Phi_\mathrm{b} L_\mathrm{m} L_\mathrm{r}}{\lambda^2}][\frac{L_\mathrm{a}}{r^2}][|K|^2 Z_\mathrm{e}], \tag{2.13}$$

where

$\overline{P}_\mathrm{r}$	received power at the receiver, in W
P_t	peak power of the transmitter, in W
Z_e	equivalent radar reflectivity factor, in $\mathrm{mm^6 m^{-3}}$
c	microwave propagation speed in this medium,$\mathrm{m\,s^{-1}}$
τ	pulse duration of the transmitted pulse, in s
g	antenna gain, dimensionless
Θ_b	azimuth beamwidth of the antenna, in radian
Φ_b	elevation beamwidth of the antenna, in radian
λ	radar wavelength, in m
$\lvert K\rvert^2$	2nd power of dielectric factor, dimensionless (0.93 for liquid water and 0.176 for ice)
r	range to the target, in m
L_m	microwave loss due to transmission through the radar hardware system (waveguide, antenna, radome, etc.), dimensionless
L_r	receiver loss, dimensionless
L_a	atmospheric loss due to attenuation by gases or particles along the propagation path, or is regarded as transmittance of the atmosphere along the path (Fabry, 2015), dimensionless

All the quantities in Fig. 2.13 are in SI units except Z_e which is in $\mathrm{mm^6 m^{-3}}$. We skip the derivation of Eq. 2.13 which is available in most of textbooks on radar meteorology. The first bracket is a constant value; the second bracket is about the radar parameters characterizing the radar system; the third bracket represents properties of the intervening atmosphere along the propagation path between the radar and targets; and the fourth bracket represents characteristics of targets.

For a given radar (fixed λ, g, Θ_b and Φ_b) operated in a predetermined scan strategy (fixed P_t and τ), excluding three loss factors, the first and second brackets in Eq. 2.13 can be grouped as a *radar constant* C_r. Given that $|K|^2$ depends whether scatterers are water or ice along with additional slight dependence on the temperature and λ, if we assume liquid hydrometeors only, the $|K|^2$ is also kept constant. Then, Eq. 2.13 can be reformatted as

$$\overline{P_\mathrm{r}} = \frac{C_\mathrm{r}|K|^2 Z_\mathrm{e}}{r^2}. \tag{2.14}$$

which means that the power received by radar reflected from a sampling volume of atmosphere at range r is inversely proportional to r^2. It implies that, the received power degrades rapidly with the increasing range of the sampling volume or the target to the radar. Such a feature is named as range dependence.

As mentioned, a distributed target, such as a single sampling volume along the radar beam (V_c), contains a huge quantity of scatterers. Each scatter contributes its portion to the power of the total returned signal. In other words, the received EM signal from one sampling volume is an aggregative rep-

resentation of all the scatterers within that single sampling volume (Fig. 2.3(a)). We assume a rectangular waveform with τ and T_s illuminating two particles; one is at range r_1 at time t_1; the other is at range r_2 and at time t_2. r_1 can be any point within r_{max}, and r_2 depends on r_1. In the range-time diagram with the time as the abscissa and the radial range as the ordinate (Fig. 2.7), the propagation of the front and rear points of a pulse is shown as the lines $r = ct$ and $r = c(t - \tau)$. The received signal at t' is a combination of the scattered signals from the closer particle at r_1 whose amplitude is evaluated at t_1 (the yellow dot in Fig. 2.7), and the farther particle at r_2 whose amplitude is evaluated at t_2 (the green dot in Fig. 2.7). In reality, more than two particles coexist in the atmosphere. More precisely, the received signal at t', aggregates the signals scattered by all the particles located between r_1 and r_2 evaluated between t_1 and t_2 satisfying the relation of $\frac{r}{r_2} = \frac{t-t'}{t_2-t_1}$ along the line with slope of $-c$ (horizontally flip of the characteristics line $r = ct$).

Within a unit volume, each scatterer, depending on its relative movement and position, may interfere constructively or destructively with the other scatterers, which leads to random fluctuations in the returned signals at the reception point; this refers to Rayleigh fading model (Goodman, 2015). This stochastic property of radar echoes implies that a measurement from a single pulse might be absolutely different from the statistically averaged status, thus the radar usually needs to illuminate a sampling volume multiple times. Another extreme situation is that, the measurements of two successive pulses are identical if the in-between time gap of these two successive pulses is too short. To address this duplication, *decorrelation time* or *the time to independence* (τ_{decorr}) defines the time which should be long enough to allow scatterers within a sampling volume to reshuffle (to move around relative to other scatterers), to generate measurements statistically independent from measurements of the previous pulse (mathematically below the correlation of 0.01). In this way, averaging over these multiple independent samples can provide a true representation of the mean status and can cancel out the constructive or destructive interferences. The decorrelation time increases with a longer λ and a narrower distribution of the scatter velocity represented by the spectral width (σ_v) following (Fabry, 2015; Zhang, 2016)

$$\tau_{decorr} = \frac{\lambda}{4\pi^{1/2}\sigma_v}. \tag{2.15}$$

The dependence of τ_{decorr} on λ is clear, because the decorrelation requires hydrometeors to reshuffle over a distance of appreciable fraction of λ. For a moderate stratiform precipitation, $\sigma_v = 1.5\,\mathrm{m\,s^{-1}}$ for instance (Sauvageot, 1992), τ_{decorr} is on the order of 3 ms for X-band (3.5-cm λ). Although a sampling volume is illuminated multiple times, not all the measurements are independent. Thus, we introduce another term—number of equivalent independent samples M_I, defined as

$$M_I = M/\mu_M, \tag{2.16}$$

where M is *hit per scan* or the theoretical maximum number of transmitted pulses received by a target per azimuth resolution or can be interpreted as the number of samples for one estimate, and M is regulated by the PRF and antenna rotation speed (N_a) in unit of rpm (revolutions per minute) (Wolf, 2021)

$$M = PRF \times \frac{\theta_{beam}}{6 \times N_a} = \frac{T_D}{PRT}, \tag{2.17}$$

where the dwell time (T_d) defines the duration a radar beam dwelling on a target,

$$T_d = \frac{\theta_{beam}}{6 \times N_a}, \tag{2.18}$$

and

$$\mu_M = \sum_{m=-(M-1)}^{M-1} (1 - \frac{|m|}{M})|r(m)|^2, \tag{2.19}$$

where

$$r(m) = exp(j\,2\,k\,v_D\,T_s\,m)\,exp(-(2\,\pi\,m\,\sigma_{vn})^2) \tag{2.20}$$

is the autocorrelation coefficient (Ryzhkov and Zrnic, 1998b),

$$\sigma_{vn} = \sigma_v/(2v_a) = 2\sigma_v\,T_s/\lambda \tag{2.21}$$

is the normalized spectrum width (Doviak et al., 1993), $v_a = \lambda/(4\,T_s)$ is the unambiguous velocity, $k = 2\pi/\lambda$ is the radar wave number, v_D is the mean Doppler Velocity, σ_v is the Doppler velocity spectrum width (Doviak et al., 1993), and j is the imaginary one. Obviously, M_I, an indicator of the correlation of samples from successive transmitted pulses, depends on radar parameters (λ, τ, PRF and θ_{beam}) and the spread of radial velocity (σ_{vn}) in the sampling volume (Doviak et al., 1993). M_I should be large enough to guarantee the reasonable accuracy of radar measurements.

Ray propagation path

In the *refraction* process, the propagation direction of the EM wave deviates from the straight line when the wave travels from one medium to another medium, if both mediums are characterized by different refractive indexes, and the *refractive index* (n) is the ratio of the EM wave velocity in the vacuum (c) to that in a non-vacuum medium (v_c),

$$n = \frac{c}{v_c}. \tag{2.22}$$

The magnitude of n depends on pressure, temperature, and humidity. Given that pressure, temperature, and humidity vary everywhere in the atmosphere, the geometry of a radar beam never follows a straight

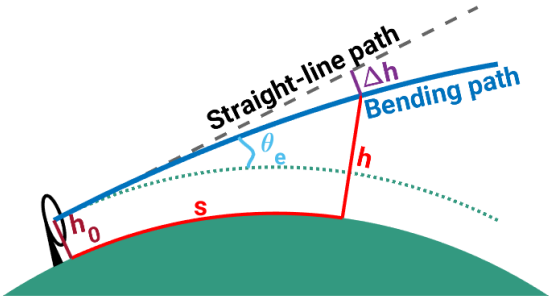

Fig. 2.5.: Illustration of a propagation path of a radar beam in the assumed standard atmosphere (curvatures are exaggerated for illustrative purpose) (adapted from Fig. 4.4 in Rauber and Nesbitt (2018)), where the solid dark blue line is the propagation path of the radar ray which bends due to the atmospheric refraction, the dashed gray line is the path of the ray under the circumstance of no refraction, the dot green line is the curvature of the earth lifted to the same altitude as the height of radar antenna, Δh is the relative displacement of the sampling volume caused by the refraction in the air

line but a curve instead. Because n of the near surface atmosphere is about 1.0003, for convenience, *refractivity* (N) is defined as

$$N = (n-1) \times 10^6. \tag{2.23}$$

The N, as a function of atmospheric temperature, pressure and vapor pressure, normally decreases with the increasing altitude (varying from ∼400 m near the surface to ∼200 m in the middle troposphere in the warm season), which makes the ray bend downward towards the earth's surface (Fig. 2.5). To calculate the actual path of a radar ray, for convenience, the *standard refraction* of the *International Standard Atmosphere* is assumed via its vertical gradient $\frac{\mathrm{d}n}{\mathrm{d}h} = -39^{-6}\mathrm{km}^{-1}$ or equivalently $\frac{\mathrm{d}n}{\mathrm{d}\Xi h} = 39N \cdot units\,\mathrm{km}^{-1}$ (Rauber and Nesbitt, 2018).

With the assumed refractive index, the height of a sampling volume along the radar beam (h) can be calculated as

$$h = \sqrt{r^2 + (ka_\mathrm{e})^2 + 2ra_\mathrm{e}\sin(\theta_\mathrm{e})} - ka_\mathrm{e} + h_0, \tag{2.24}$$

where h_0 is the above mean sea level (AMSL) height of radar antenna, and a_e is the radius of the earth, θ_e is the elevation angle of the radar beam, and

$$k = \frac{1}{1 + a_\mathrm{e}(\frac{\mathrm{d}n}{\mathrm{d}h})}, \tag{2.25}$$

and meanwhile the distance of the projected point of that sampling volume on the ground surface to the radar (s) approximates to

$$s = ka_\mathrm{e}\,\sin^{-1}(\frac{r\cos(\theta_\mathrm{e})}{ka_\mathrm{e} + h}). \tag{2.26}$$

The derivation of Eqs. 2.24 and 2.26 can be find in Rauber and Nesbitt (2018) and these equations will be used to determine radar gates geographically collocated with external instruments (Section 5.2).

This standard atmosphere is a conventional approximation of the low-level atmosphere, but it is not always valid. A phenomenon named as *anomalous propagation (AP)*, also abbreviated to *anaprop*, occurs when non-standard refractive indexes prevail through the atmosphere. It includes the scenarios of *sub-refraction* (less bending with $\frac{\mathrm{d}n}{\mathrm{d}h} < -39^{-6}\mathrm{km}^{-1}$), and *super-refraction with* $\frac{\mathrm{d}n}{\mathrm{d}h} > -39^{-6}\mathrm{km}^{-1}$ (more bending). A special case of the super-refraction is *ducting* or *trapping*, in which the refractivity declines much faster than the normal situation. In other words, the vertical gradient of the refractivity $\frac{\mathrm{d}n}{\mathrm{d}h}$ is even more negative than minus the curvature of the earth around $-157^{-6}\mathrm{km}^{-1}$ so that the downward-bending radar ray is trapped in a layer of atmosphere and strikes to the ground surface. The ducting usually occurs when the upper air is extremely warm and dry compared to the lower air, in case of nocturnal temperature inversion, thunderstorm outflows and fronts. It enables radar beams to scan immobile obstacle reflectors (Section 4.5) at the farther ranges which are normally well below the ray, and these resultant unwanted AP echoes bring uncertainties into radar measurements (Section 4.5).If the vertical gradient of the refractivity deviates much from the standard values, the propagation path should be recalculated by using real-time refractivity estimated from atmospheric soundings from nearby radiosondes.

Due to the curvature of the earth, as the radar beam goes farther from the radar, the sampling volume along that radar beam rises with the increasing altitude. Such an increase in altitude is more apparent for long-range radars. Owing to the combination of the earth's curvature and the refraction process, the height of the sampling volume can be indicated by the displacement ($\Delta h = h - h_0$) in Fig. 2.5. For instance, in case of the foregoing assumed standard atmosphere, for a radar beam with a tilted elevation angle of 1.5°, the altitudes of sampling volumes at the ranges of 50 km, 100 km and 150 km are 1.5 km, 3.2 km and 5.2 km above the height of the radar antenna, respectively.

During the warm season, the altitude of the freezing level (or the 0°C isotherm level) fluctuates around 3–4 km in altitude in the southern Germany (Fig.B.19). Then, the radar beam at the far range penetrates into solid phase precipitation. Given the large discrepancy of dielectric factor between water and ice (Eq. 2.13), Z value in the solid phase precipitation is much different from that of liquid phase, which brings errors to Z measurements. The situation can be more complicated if mixed phase hydrometeors prevail. This effect is named as *overshoot*. Clearly, the proportion of sampling volumes affected by this overshooting effect depends on θ_e and air temperature.

In order to mitigate the overshooting effect, especially for those who are primarily interested in liquid precipitation at the ground surface, it is better to use θ_e closer to the horizon. However, in most of the time, obstacles dwell at least somewhere within the radar observational coverage, blocking fully or partially the radiation, making the radar "blind" or "half-blind" to the precipitation behind these obstacles (Fig. 2.6). This is named as *beam blockage*, or *beam shielding*, or *beam occultation*. For a propagation path free from blockage, when the path is calculated using the standard refraction, the partial blockage might occur for this radar beam, in case of the actual refraction different from the standard refraction. What is even worse, the departures from the standard refraction often occur when meteorological systems

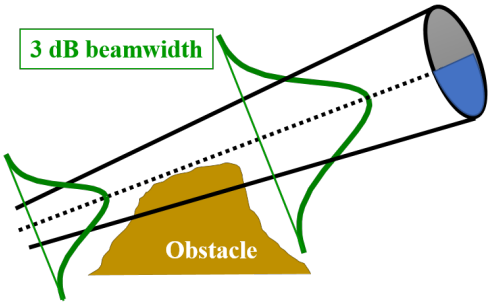

Fig. 2.6.: Two-dimensional schematic diagram to show radar beam partial blockage, where 50% of the transmitted power is shielded by an obstacle, indicated by the blue shaded area, and the antenna pattern follows the typical Gaussian-shaped distribution

of our interest are present. For the partial blockage, the assumed Gaussian-shaped antenna pattern for the weather radar is distorted, for instance, missing the peak value along the beam axis if the blockage exceeds 50%. This modifies the receiver power in Eq. 2.13. Therefore, in order to determining proper θ_e in the radar experiment or selecting the suitable measuring site, it is necessary to consider seriously about the local topographic features (Section 3.1).

Doppler radial velocity and Doppler dilemma

Besides amplitude, the received EM wave also contains information about another property—phase. *Doppler effect* describes a phase change (equivalently frequency change) at the receiver when an objective is approaching or is leaving away from the radar. Utilizing the Doppler effect, a Doppler radar measures the phase of each returned EM pulse, and according to the phase change between two successive pulses, we can measure the *radial velocity*–the reflectivity-weighted velocity along the radar beam – through

$$v_r = \pm \frac{\lambda}{2T_s}\left(\frac{\Delta\Phi}{2\pi}\right), \tag{2.27}$$

where $\Delta\Phi$ is the phase shift (in radians) during a pulse period between two successive pulses, and we regulate positive (negative) velocity if the target is moving away from (towards) the radar. The solution to Eq. 2.27 is not unique. For instance, the radial velocities are identical for the phase change of π and the phase change of $-\pi$. To address this *velocity ambiguity*, for the Doppler radar, all the phase increments should be less than π

$$|\Delta\Phi| = \left|\frac{4\pi v_r T_s}{\lambda}\right| < \pi, \tag{2.28}$$

which leads to the definition of *maximum unambiguous velocity* or *Nyquist velocity* as

$$|v_r| < \frac{\lambda\,\mathrm{PRF}}{4} \equiv v_{\max}. \tag{2.29}$$

This Nyquist velocity sets the two-end threshold for the available Doppler velocity values, and any velocity higher than $v_{\max}$ or lower than $-v_{\max}$ is folded into the Nyquist interval, which is referred as *velocity aliasing*.

As shown by the range-time diagram with the time as the abscissa and the radial range as the ordinate (Fig. 2.7), the propagation of front edges of two successive pulses in a rectangular shape is represented by the characteristics lines $r = ct$ and $r = c(t - T_s)$. The signal received at t'' at the antenna port is contributed from both scatterers at r'' and r_2. The range r'' exceeds $r_{\max}$, and the velocity aliasing occurs. The signal scattered by the scatterer at range r'' is termed as *second-trip echo* (Section 4.3).

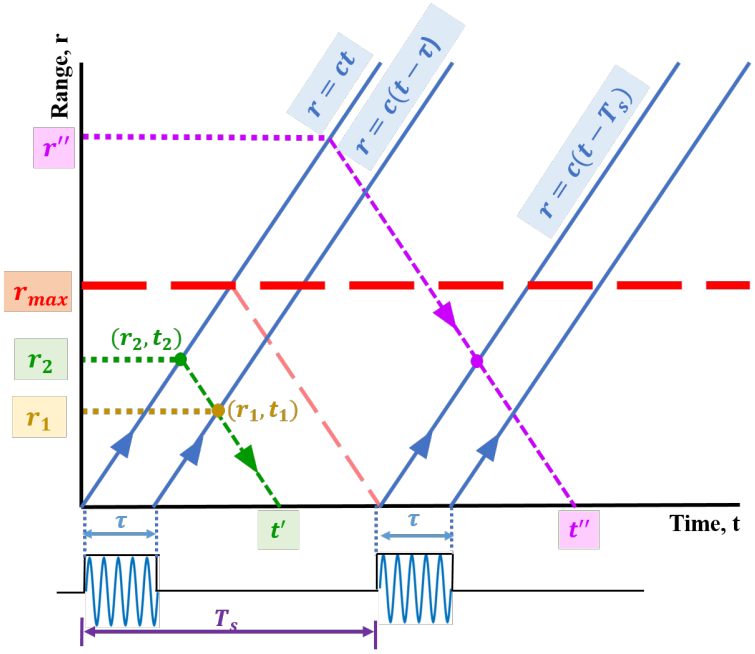

Fig. 2.7.: Illustration of concepts about range aliasing (adjusted from Figs. 5.6 and 5.11 in Bringi and Chandrasekar (2001)), where the x-axis is time, the y-axis is range, τ is the pulse duration, T_s is pulse repetition time, the blue solid slanted lines are characteristic lines, $r = ct$ represents the leading edge of the first pulse, $r = c(t - \tau)$ represents the rear edge of the first pulse, and $r = c(t - T_s)$ represents the leading edge of the second pulse, the horizontal red dashed line represents the maximum unambiguous range, the pixel (r_1, t_1) and pixel (r_2, t_2) represents two point scatterers within the maximum unambiguous range and both point scatterers contribute to the received signal at the antenna at time of t', and the received signal at time $t''$is a superposition of scattered signals from the scatterers beyond $r_{\max}$, and also the scatterers within $r_{\max}$

Implied by Eq 2.29, more frequent pulses or a larger λ allows more tolerance on measuring radial velocity unambiguously. Combing Eqs. 2.29 and 2.8, we obtain

$$r_{\max}\, v_{\max} = \frac{c\lambda}{8} \tag{2.30}$$

Eq. 2.30 describes the Doppler dilemma, one of the major compromises we need to balance carefully when it comes to choosing the radar frequency or designing the scan strategy. For instance, for a

given λ, widening Nyquist interval leads to very high PRF, increasing chances of contaminations caused by multi-trip echoes (Section 4.3.1). Furthermore, the radial velocity is only one component of a three-dimensional wind field, and the Doppler radar is unable to provide any information about the motions perpendicular to radar beams. In other words, retrieving a wind field requires additional approximations or assumptions.

Despite these foregoing limitations, research has shown that the measured Doppler velocity provides plenty of information to decipher storm motions. Doppler velocity has become a standard initial dataset assimilated into NWP models for short-term forecast or nowcasting, and the Doppler capacity has been a necessity for operational radars.

Given that within a sampling volume each particle has its distinct radial velocity, Doppler spectrum of the ensemble of these particles represents the reflectivity-weighted distribution of particle radial velocity (Rauber and Nesbitt, 2018). Regarding Doppler spectrum, Z and (Z-weighted) mean Doppler velocity (V_{Do}) are usually regarded as the zeroth and first moment of the scattered signal, and the second moment is regarded as the spectrum width (σ_{v})—the variance of V_{Do} (Rauber and Nesbitt, 2018). It is a measure of degree of dispersion of V_{Do} (or variability of wind) within a sampling volume, and the σ_{v} of hydrometeors is attributed to several different causes as

$$\sigma_{\mathrm{v}}^2 = \sigma_{\mathrm{shear}}^2 + \sigma_{\mathrm{dv}}^2 + \sigma_{\alpha}^2 + \sigma_{\mathrm{t}}^2, \tag{2.31}$$

where the right side equation consists of the wind shear term, terminal velocity term, the antenna scan rate term and turbulence term (Doviak et al., 1993). A graphical illustration for these causes can be found in Figure 5.2 in Fabry (2015). Since σ_{v} is affected by several different factors, its usage is not that straightforward. In operation, σ_{v} is used to estimate turbulence and check the quality of radial velocity, and occasionally is used to locate the significant wind shear (Klazura and Imy, 1993).

Weather radar types: S-, C- and X-band radars

With respect to the purpose of precipitation observation, the weather radars mainly function in three microwave frequencies: S-band (3.0 GHz), C-band (5.5 GHz), X-band (10 GHz). The wavelength affects radars' technical characteristics (Tab. 2.1), such as the spatial resolution of radar sampling, which is of the most concern in this research. From the foregoing Eq. 2.7, the spatial resolution of radar sampling is subject to θ_{beam}, whereas there is a physical constrain between the antenna aperture size, θ_{beam} and λ (Eq. 2.10). For instance, the beamwidths of the 1-m antenna for S- and X-band radars are 5.7° and 1.8° respectively, corresponding to 3-km and 1-km $r\Theta$ at the 30-km range respectively. Thus, a high spatial resolution with a small size aperture is practically possible at the short λ; this is an advantage of using X-band radar. Meanwhile, Eq. 2.10 implies this cross-range resolution, constrained by the antenna

aperture size and λ, cannot be adjusted after radar design or construction. As a consequence, changing spatial resolution for radar measurements refers to changing Δr, which can be manipulated by modifying τ because Δr is linearly proportional to τ (Eq. 2.9).

Tab. 2.1.: Typical characteristics for S-, C- and X-band weather radars

Parameter	X-band	C-band	S-band
Frequency (GHz)	8–12 (9.3)	4–8 (5.6)	2–4 (2.9)
Wavelength (cm)	2.5–4 (3.2)	4–8 (5.3)	8–16 (10.3)
Peak power (kW)	50–200	250–500	500–1000
Antenna diameter (m)	2.5	4.2	<7.5
Typical Range (km)	30–60	100–130	100–200
Radial resolution (km)	0.05–1	0.25–2	1–4

Regarding the precipitation estimation, the major differences among these three frequencies lie in the following two aspects: i) attenuation and ii) validity of the Rayleigh scattering approximation. First, the amplitude of EM wave is attenuated (reduced) due to presence of particles in the atmosphere. In most cases except some extreme precipitation events (Ryzhkov and Zrnic, 1995), the attenuation is negligible in S-band, moderate in C-band and severe in X-band radars, respectively. Second, as mentioned, the Rayleigh scattering approximation used in Eq. 2.13 is only valid if the particle size is much shorter than λ ($\pi nD/\lambda$<0.3). It means that, for a particle whose diameter is more than 2.3 mm for C-band or 1.4 mm for X-band, the Rayleigh approximation becomes invalid and Z is not longer proportional to the 6th power of the particles size (Tab. 2.1). In short, selecting radar frequency depends on not only the technical aspects such as cost, weight and size of hardware, but also on the practical requirements of an application. For instance, we need to consider the aimed sensitivity of radar data to weak echoes, the desired ability to resolve small or rapidly evolving features (spatial and temporal resolutions), and the impact of intervening atmosphere exerted by attenuation.

For the pulse radar, one more drawback of the shorter-wavelength radar is due to the Doppler dilemma. For the X-band frequency, to achieve the ability to measure $\pm 50\,\mathrm{ms}^{-1}$ radial velocity, the maximum range is less than 23 km (Eq. 2.30). It confirms that the trade-off between range and velocity aliasing is particularly severe for radars in the short wavelengths (Joe and May, 2003). Thus, the dual PRF mode with two different pulse repetition frequencies can be a solution (Doviak et al., 1977; Sirmans et al., 1976).

In European continent, the majority of operational weather radars operated by the local weather service agencies are in the C-band frequency, except some S-band radars in the southern Europe where heavy and convective precipitation is more frequent. In general, the X-band radar takes up a small portion in the operation radar network. In contrast, owing to its portability and mobility relative to

Fig. 2.8.: Mapping distribution of the S-, C- and X-band country-level weather radar network by countries, screen shot from the World Meteorological Organization (WMO) radar database website (wrd.mgm.gov.tr)

S- or C-band radars, the X-band radar is primarily used as a research radar being deployed specifically in proximity to small-sized catchments or urban environments of specific investigations.

2.2. Polarimetry, polarimetric quantities and their characteristics

The polarization is a fundamental property of an EM wave besides the other two properties—frequency and amplitude. Despite the fact that polarization was explained by Young and Fresnel in the 1800s and documented in the Maxwell equation in 1861, polarization did not attract much attention from radar engineers until the 1950s (Giuli, 1986). Calculating wave scattering of non-spherical raindrops (Atlas et al., 1953; Waterman, 1965) provided the theoretical basis for polarization diversity. A summary of the relevant research around the 1950s was presented in Atlas (1964). In spite of the theoretical analyses (Atlas et al., 1953; Shupiatskii, 1959) and a few measurement activities on radar polarimetry after World War II (Browne and Robinson, 1952; Hunter, 1954; Shupiatskii and Morgunov, 1968), it was the progress in the research on radiowave (3 KHz–1 GHz) attenuation in the 1970s that prompted the research on polarimetry in the microwave frequency (1 GHz–1000 GHz). The period before the 1980s was the early stage when the radar instrumentation and the radar theory were the main focus. After that, the golden period for the research on radar meteorology began until 1995 followed by the period when the relevant operational activities flourished. The change of the research focus was well reflected by different names of two radar polarimetry workshops in 1981 and 1995, named as Polarization Techniques in Radar Meteorology (Metcalf and Humphries, 1981), and Weather Radar Polarimetry for Research and Operational Applications (Illingworth and Zrnic, 1995), respectively.

The advantages of radar polarimetry have been justified by a vast number of scientific research and operational applications in terms of interpreting and quantifying precipitation, especially its capability to estimate precipitation quantitatively, to decipher internal structures of convective storms, to

assess the bulk property of hydrometeors quantitatively, and to assist the NWP and hydrological modeling (Thorndahl et al., 2017; Ryzhkov and Zrnić, 2019). In order to better understand these advantages, the concept of dual-polarization, definitions and characteristics of polarimetric variables, as well as the polarimetric radar hardware system are presented as follows.

Concept of polarization and dual-polarization

For a homogeneous sphere, the backscattering from horizontally and vertically polarized waves exhibits no difference in polarization. Instead, it is the non-spherical nature of raindrops that motivates the development of weather radar polarimetry to improve radar-based precipitation estimation. However, the meaning of the dual-polarization is distinct from polarization.

The *state of polarization* is a property of a monochromatic (i.e., time-harmonic) EM wave besides its amplitude, frequency and phase. According to the Maxwell equations, the electric polarization $\mathbf{P}$ is the average electric dipole moment or the vector sum of all the dipole moments within a unit volume of the medium (Bohren and Huffman, 1983),

$$\mathbf{P} = \varepsilon_0 \chi \mathbf{E}, \tag{2.32}$$

where ε_0 is the *permittivity*, χ is the *electric susceptibility*, and $\mathbf{E}$ is the electric field. After putting a piece of the unpolarized matter ($\mathbf{P} = 0$) into an external electric field, the electric field induces a net dipole moment, and this matter becomes *polarized* ($\mathbf{P} \neq 0$).

Since an EM wave is a time-harmonic wave, a certain point of its electric field vibrates sinusoidally with time if this point is far enough away from the sources. The electric vectors $\vec{\mathbf{E}}$ lie in a plane perpendicular to the direction of wave propagation. The polarization can be described by a curve connecting all the end points (the tip) of the instantaneous electric vectors within a single plane over time. We call this curve the locus of the tip of electric vectors (Zhang, 2016) or the vibration ellipse (Bohren and Huffman, 1983), and this plane the polarization plane (Ryzhkov and Zrnić, 2019). Within a three-dimensional Cartesian coordinate system, consider an EM wave propagating along the x-axis direction with its angular frequency $\omega = 2\pi f$ and wave number k, the electric vectors lie within the y-z plane,

$$\vec{E}(x,t) = E_y(x,t)\hat{y} + E_z(x,t)\hat{z}, \tag{2.33}$$

$$E_y(x,t) = A_y \cos(\omega t - kx + \phi_{01}), \tag{2.34}$$

$$E_z(x,t) = A_z \cos(\omega t - kx + \phi_{02}), \tag{2.35}$$

where, the orthogonal axes $\hat{y}$ and $\hat{z}$ define the polarization plane, A_y and A_z are the amplitudes of y- and z-components of the wave, ϕ_{01} and ϕ_{02} are their initial phases. When the initial phase difference is an integer multiple of π,

$$\delta = \phi_{02} - \phi_{01} = 0 \ \ or \ \ \pi, \tag{2.36}$$

the electric vectors satisfy the criterion as

$$\vec{E}(x,t) = (A_y \hat{y} + A_z \hat{z}) \cos(\omega t - kx + \phi_1) \tag{2.37}$$

The term $\mathbf{A} = A_y \hat{y} + A_z \hat{z}$, which describes the electric vectors as a function of time and the location, represents a straight line. In other words, if the locus of the tips of the electric field $\vec{E}(x,t)$ becomes a straight line, the wave is termed as *linearly polarized*. Waves can also be in circular and elliptical polarizations, but nowadays they are not commonly used in the modern weather radars. Our discussion is constrained to the linear polarization only.

Conventionally, given that the x-axis of the three-dimensional Cartesian coordinate is set as parallel to the local flat surface of the ground, the wave propagating along the x-axis oscillating with the x-y plane is named as a horizontally-polarized wave, whereas the wave propagating along the x-axis oscillating with the x-z plane is named as a vertically-polarized wave. Clearly, the axis $\hat{y}$ ($\hat{z}$) corresponds to horizontal (vertical) polarization. For the linearly polarized wave, the horizontally and vertically polarized components of the electric field E_y and E_z are kept in phase or out of phase (Ryzhkov and Zrnić (2019); Eq. 1.9).

In brief, the polarization, as a property of a wave, describes the time-varying direction and relative magnitude of the electric vector (Balanis, 2016). When it comes to an isotropic sphere, the scattered wave is independent of the directions of the electric field. It means that the amplitude and phase of the horizontally-polarized wave is identical to that of the vertically-polarized wave. It implies that the polarization has no special implication and seems a "boring" property.

All the aforementioned concepts in Section 2.1 deal with a conventional Doppler single-polarization radar, which only transmits horizontally-polarized waves which propagate horizontally (perpendicular to the x-z plane)) with the electric field oscillating in a horizontal plane (x-y plane), in the standard 3D Cartesian coordinate. Illuminated by these horizontally-polarized waves, a hydrometeor behaves as a horizontal dipole antenna.

It is also possible for a radar to transmit vertically-polarized waves which propagate also horizontally but with electric field oscillating in a vertical plane (x-z plane). A raindrop, if in equilibrium, can be regarded as a sphere as far as it is small enough, and becomes oblate (the major axis of the spheroid oriented horizontally) as its size increases. This change in shape is owing to aerodynamic force, and this oblateness becomes greater as raindrops become larger (Beard and Chuang, 1987; Pruppacher and Klett,

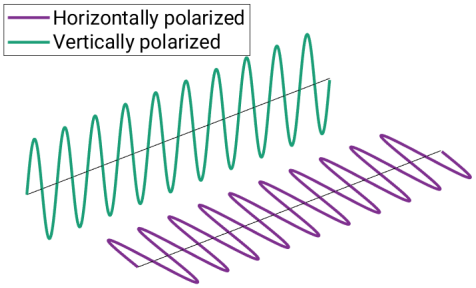

Fig. 2.9.: Three-dimensional illustration of concept of dual-propagation (adjusted from Fig. 7.1 in Rauber and Nesbitt (2018))

2011). Owing to the difference between the horizontal and vertical dimensions of the oblate drops, the interaction between the EM wave and this non-spheric particle differs depending on whether the particle is illuminated by a horizontally or vertically polarized wave. Then, the different interactions lead to differences in the amplitude and phase of the scattered waves or the received signals by radars.

To give insights into how different polarizations of the incident radiation affect the particles' scattering response, consider a highly non-spheric ice crystal composed of a large number of tiny spheres with its major axis oriented horizontally (Kumjian, 2018). Once illuminated by the external EM waves, each sphere is activated, inducing its own electric field which is immediately exerted on its neighboring spheres. In this way, each sphere is affected by the electric field from both the external incident EM waves (indicated by the blue arrows in Figs. 2.10(c) and 2.10(d)) and from their neighboring spheres (indicated by the black arrows in Figs. 2.10(c) and 2.10(d)). Both electric fields are in the same direction if the external incident EM wave is horizontally polarized, and in the reverse direction if the external incident EM wave is vertically polarized (Figs. 2.10(a) and 2.10(b)). Summation of two electric fields of the identical direction results in constructive inference (indicated by the orange arrow in Fig. 2.10(c)), while the electric fields of the reverse directions cancel out, leading to destructive inferences (indicated by the orange arrow in Fig. 2.10(d)). As a consequence, for this oblate spheroid, the total scattered EM energy under the horizontally-polarized wave is more than that under the vertically-polarized wave. This explains the principle of the dual-polarization for the non-spheric particle.

Besides the amplitude of the scattered wave, the nonsphericity of hydrometers is also illustrated in terms of phase shifts. An EM wave traveling into a non-vacuum medium becomes slower compared to the same EM wave traveling into a vacuum, and the refractive index is a measure of how slowly EM waves propagate in a homogeneous medium relative to the vacuum (Eq. 2.22). As mentioned, the majority of hydrometeors in the atmosphere are oblate with the major axis oriented horizontally longer than that of the minor axis oriented vertically, with exceptions of very tiny raindrops whose size is on the order of 0.1 mm. For the atmosphere filled with these oblate hydrometeors, the horizontally polarized wave propagates through more matters (water) than the vertically polarized waves (Rauber and Nesbitt,

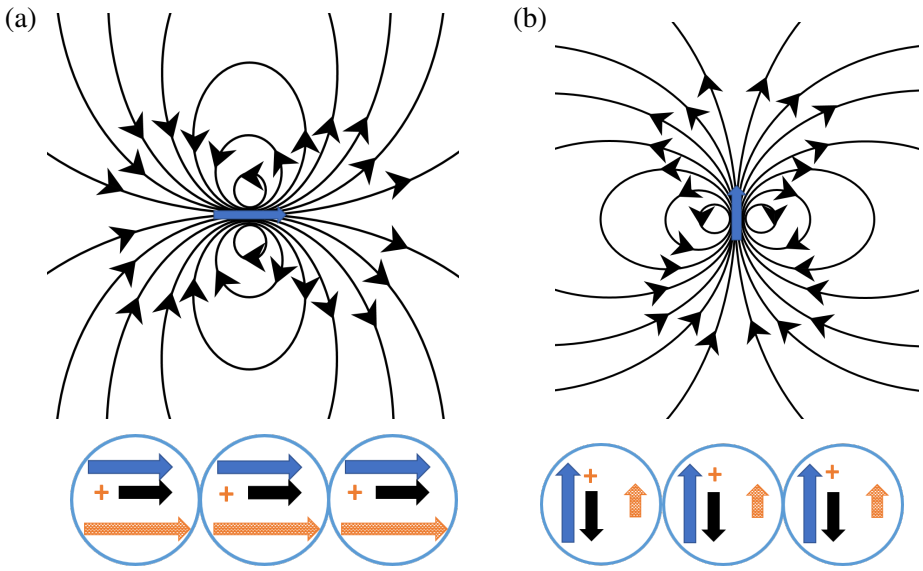

Fig. 2.10.: Illustration of the concept of dual-polarization taking a highly non-spheric homogeneous particle as an example (adapted from Figs. 4 and 5 in Kumjian (2018)), where (a) is the electric field pattern for a tiny sphere of the particle illuminated by a horizontally incident wave and the associated enhancement of the internal electric field by summing external electric field (blue arrows) and the electric filed induced by the nearby tiny sphere (black arrows), (b) is the same as (a) but for a vertically incident wave and the associated reduction of total electric field

2018), and n for the horizontally polarized waves is larger than that for the vertically polarized waves (Ryzhkov and Zrnić, 2019). It accounts for a more significant slowdown in the propagation speed for the horizontally polarized wave than the vertically polarized one,

$$c_{\mathrm{h}} < c_{\mathrm{v}}, \tag{2.38}$$

where $c_{\mathrm{h}} = c/n_{\mathrm{h}}$, $c_{\mathrm{v}} = c/n_{\mathrm{v}}$, c_{h} is the propagation speed of the horizontally polarized waves, and c_{v} is the propagation speed of the vertically polarized waves. Then, τ of the horizontally polarized wave is also shorter than that of vertically polarized one, $c_{\mathrm{h}}\,\tau < c_{\mathrm{v}}\,\tau$. For a pair of horizontally and vertically polarized waves which are transmitted simultaneously, the front ends of the reflected signals return from a scatterer at range r_1 to the radar receiver at time $t = 2r_1/c_{\mathrm{h}}$ and $t = 2r_1/c_{\mathrm{h}}$; for the next pair of waves and a scatterer at range r_2, the returning time points are $t = T_{\mathrm{s}} + 2r_2/c_{\mathrm{h}}$ and $t = T_{\mathrm{s}} + 2r_2/c_{\mathrm{h}}$. As a result, at any time point, the scattered wave in the vertical polarization has undergone more vibrations, equivalently a larger amount of phase shifts relative to the wave in the horizontal polarization (Fig. 2.11). This difference in phase shift for the coincident horizontally and vertically polarized waves is named as differential phase (Φ_{DP}). Note that there is also a phase shift between the two successive pulses of

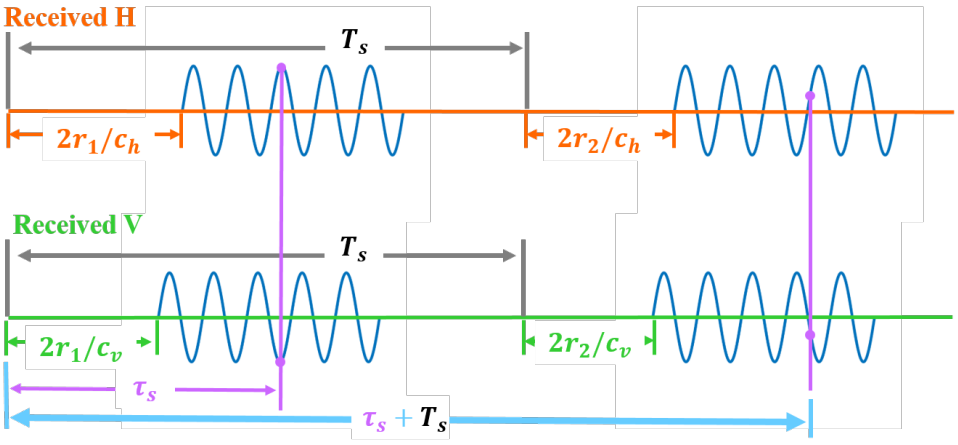

Fig. 2.11.: Illustration of the concept of propagation differential phase (adapted from Fig. 2.10. in Ryzhkov and Zrnić (2019)), where c_h is the propagation speed for the horizontally polarized waves, and c_v is the propagation speed for the vertically polarized waves, T_s is pulse repetition time, r_1 is the range of a scatterer for the first pair of horizontally and vertically polarized waves, r_2 is the range of a scatterer for the second pair of horizontally and vertically polarized waves, τ_s and $\tau_\mathrm{s} + T_\mathrm{s}$ are the time points when the radar receiver samples received signals

the same polarization caused by the relative motions of scatterers to the radar due to the Doppler effect (Eq. 2.27), illustrated as

$$\frac{2r_1}{c_\mathrm{h}} + T_\mathrm{s} \neq \frac{2r_2}{c_\mathrm{h}} + T_\mathrm{s}, \tag{2.39}$$

$$\frac{2r_1}{c_\mathrm{v}} + T_s \neq \frac{2r_2}{c_\mathrm{v}} + T_\mathrm{s}, \tag{2.40}$$

and this Doppler phase shift is absolutely distinct from Φ_{DP} regarding the dual-polarization.

In terms of the differences between horizontally and vertically polarization in either amplitude or phase shift, the non-spherical nature of hydrometers is the prerequisite to utilize the radar polarimetry in precipitation observation and quantification. Historically, this nonsphericity accounted for the early-stage research on the radar polarimetry.

Utilizing these differences in the interaction between waves and particles brings us additional measurables which hold further information (except Z_H, V_Do and σ_v) about bulk properties of the precipitation such as size, shape, orientation and phase (solid or liquid). This feature is termed as *dual-polarization*. The radar which is able to utilize the information from both horizontal and vertical polarized waves is called a polarimetric radar, and the radar variables on the basis of the dual-polarization are polarimetric variables. The dual-polarization can be interpreted quantitatively by means of the scattering model from an electromagnetic perspective (Bringi and Chandrasekar, 2001; Zhang, 2016; Ryzhkov and Zrnić, 2019)).

Polarimetric radar system

Compared to the single-polarization radar system, the polarimetric radar system needs to further take into consideration appropriate types of a polarization base and a transmission/receive mode.

At the early exploratory period (1950s–1970s), radars in circular polarization, originally intended for clutter suppression (White, 1954; Offutt, 1955; Beasley, 1966), were modified to explore some meteorologically interesting phenomena (McCormick and Hendry, 1979a). Notable works were from National Research Council of Canada in the early 1970s (Hendry and McCormick, 1971; McCormick and Hendry, 1979b; Barge and Isaac, 1973). Nevertheless, the introduction of differential reflectivity (Z_{DR}) by Seliga and Bringi (1976) and differential phase (Seliga and Bringi, 1978) brought popularity to the linear polarization, which led to the early version of the modern weather radar. The linear orthogonal polarization coherent pulse Doppler radar emerged around the late 1970s–1980s in the United States (Seliga and Bringi, 1976). Retrievals of Z_{DR} and K_{DP} from the linear polarization were found to be more reliable compared to the circular polarization which became obsolete later on. Currently most of weather surveillance polarimetric radars are configured in the linear polarization, and it is easier to remove the propagation effect than other orthogonal polarization bases (Zrnić, 1996). So are the radars in German weather service radar network and the weather radars in this research.

In addition to the polarization base, there are three options for the transmission/receiver mode of a polarimetric radar in principle: alternate transmission and alternate reception (ATAR) mode, alternate transmission and simultaneous reception (ATSR) mode, and simultaneous transmission and simultaneous reception (STSR) (Zhang, 2016). The polarimetry can be implemented in either dual-polarization (STSR) mode or full-polarization (ATSR) mode, where the ATAR mode can obtain either dual-polarization or full-polarization (Zhang et al., 2019). Dual-polarization implies the capacity to obtain polarimetric information from two copolar channels, while full polarization involves the information switched from a co-polar and a cross-polar channel.

The ATAR mode still involves one transmitter and one receiver, but sequentially changes its polarization state. It was used at the early stage and is obsolete. Its limitation is its poor capability in estimating the copolar component that is related to calculations of the copolar correlation coefficient. Only with some specific assumptions is the radar with a single receiver able to estimate the cross-polar component (Zrnić, 1991). The hydrometeors are assumed as "frozen" during the time gap between two alternate pulses, but it is not the case in reality due to the reshuffling of hydrometeors. Thus, it requires the inter-pulse time interval to be much shorter than the decorrelation time. Obviously, the ATSR and STSR mode is not subject to this constrain.

The ATSR mode has one more receiver compared to the ATAR mode. It allows estimations of cross-polar components. Both alternate transmission (ATAR and ATSR) modes require a fast and high-power switch which is less economically feasible.

The STSR mode involves one more transmitter compared to the ATSR mode and has been adopted widely currently. An advantage of the STSR mode is that the radar's technical configurations don't need to be modified too much when upgrading from single-polarization to dual-polarization for an existing radar (Doviak et al., 2000). The second merit is that the expensive and sensitive switch is not mandatory in the STSR mode. However, one well-recognized drawback of the STSR mode is the potential cross-polar contamination caused by canted particles in the ice phase of convective storms (Ryzhkov and Zrnić, 2007; Hubbert et al., 2010; Wang et al., 2006). Thus, the STSR mode usually assumes an absence of cross coupling between H and V electric fields, or equivalently zero mean canting angle for all the hydrometeors within the sampling volumes, and negligible antenna errors (Hubbert et al., 2010). Note that a radar with the STSR mode is unable to measure the Linear Depolarization Ratio L_{DR} (to be defined in the next section).

The weather radar polarimetry in Germany started from a German Aerospace Research Establishment (DLR) C-band polarimetric radar in the late 1980s. Its design was the most advanced at that time. It included the elliptical polarization, double receivers for simultaneous reception of orthogonally polarized waves, and the flexibility to change transmission polarization from pulse to pulse. For more details about this radar system design, see Schroth et al. (1988)); for its polarimetric measurements of a convective storm and the accompanying interpretation of precipitation physics, see Bringi et al. (1991) and Meischner et al. (1991).

The first measurement of Z_{DR} in Europe dates back to 1980s (Hall et al., 1980). Besides Germany, France and Italy also built their own radar systems which were different from the current modern mode (Cordesses et al., 1983; Husson and Pointin, 1989; Leonardi et al., 1984; Ryzhkov et al., 1994). Generally the radar polarimetry for research in Europe started around the 1990s (Meischner et al., 1991), and for operational purpose around 2005 (Saltikoff and Nevvonen, 2011). The currently available operational radar products include Radar-Online-Aneichung (RADOLAN) in Germany (Bartels et al., 2004b), Nimrod in UK (Moore et al., 2004), and the OPEAR programme which incorporates the radar data sharing through several countries (Holleman et al., 2008; Huuskonen et al., 2012).

A historical account of the evolution of radar polarimetry technology (Bringi and Hendry, 1990; Bringi and Zrnic, 2019) discussed in detail different radar systems developed in various configurations in different key research institutes over the world. The current popular configuration selected by manufacturers and radar meteorologists should be the best compromise with practical considerations of cost and maintenance. The technical configurations on polarimetry, such as polarization base and implementation mode, strongly affect estimations of polarimetric variables and their interpretation. Thus, a standard configuration for the radar system can avoid the non-standard measurements and reduce confusions.

Defining polarimetric variables

The polarimetric variables are defined on the basis of scattering matrix. Thus, we first talk briefly about the scattering matrix, to facilitate the following definition of polarimetric variables. When an EM wave propagates through a medium filled with scatterers, in addition to the part of EM energy lost due to absorption, a portion of energy is scattered in a form of secondary radiations in all directions. The scattering matrix describes the relation between the electric field of the scattered radiation $\vec{E}^{\mathrm{s}}$ and the electric field of the incident radiation $\vec{E}^{j}$ through

$$\vec{E}^{\mathrm{s}} = \frac{e^{-jkr}}{r}\vec{S}\vec{E}^{\mathrm{i}}, \tag{2.41}$$

where the superscript i is related to the incident EM field, the superscript j is about scattered fields, r is the distance between the particle and observing point in the $\vec{E}^{\mathrm{s}}$ which is far from the particle ($r > 2D^2/\lambda$), $\vec{S}$ is the scattering matrix, and e^{-jkr} is the propagation term. This scattering equation (Eq. 2.41) in the matrix form can be expressed as

$$\begin{bmatrix} E_{\mathrm{h}}^{\mathrm{s}} \\ E_{\mathrm{v}}^{\mathrm{s}} \end{bmatrix} = \frac{e^{-jkr}}{r} \begin{bmatrix} s_{\mathrm{hh}}(\hat{k}_{\mathrm{s}}, \hat{k}_{\mathrm{i}}) & s_{\mathrm{hv}}(\hat{k}_{\mathrm{s}}, \hat{k}_{\mathrm{i}}) \\ s_{\mathrm{vh}}(\hat{k}_{\mathrm{s}}, \hat{k}_{\mathrm{i}}) & s_{\mathrm{vv}}(\hat{k}_{\mathrm{s}}, \hat{k}_{\mathrm{i}}) \end{bmatrix} \begin{bmatrix} E_{\mathrm{h}}^{\mathrm{i}} \\ E_{\mathrm{v}}^{\mathrm{i}} \end{bmatrix}, \tag{2.42}$$

where $E_{\mathrm{h}}^{\mathrm{i,s}}$ and $E_{\mathrm{v}}^{\mathrm{i,s}}$ are the horizontally and vertically polarized components of the incident and scattered field, $\hat{k}_{\mathrm{i}}$ is the unit vector of the incident wave, $\hat{k}_{\mathrm{s}}$ is the unit vector of the scattered wave, and the backscattering matrix is given as

$$\vec{S} = \begin{bmatrix} s_{\mathrm{hh}} & s_{\mathrm{hv}} \\ s_{\mathrm{vh}} & s_{\mathrm{vv}} \end{bmatrix}, \tag{2.43}$$

where the terms s_{hh}, s_{hv} and s_{vv} are backscatter coefficients, the second subscript refers to the polarization of the incident waves transmitted by a radar, and the first subscript indicates the polarization of the backscattered waves, and $s_{\mathrm{vh}} = s_{\mathrm{hv}}$. The power returned in the same polarization state as the transmitted power is termed as the *co-polar* power, such as s_{hh} and s_{vv}, whereas the *cross-polar* power refers to the power returned in the state orthogonal to the transmitted power such as s_{hv} and s_{vh}.

For the backscattering $\vec{k}_{\mathrm{s}} = -\vec{k}_{\mathrm{i}}$, then we have $|s(-\vec{k}_{\mathrm{i}}, \vec{k}_{\mathrm{i}})|^2 = |s(-\vec{k}_{\mathrm{i}}, \vec{k}_{\mathrm{i}})|^2 = |s(\pi)|^2$.

Thus, the radar reflectivity of the horizontal polarization transmission (Eq. 2.5) is expressed in another form (Battan, 1973) as

$$Z_{\mathrm{hh}} = \frac{4\lambda^4}{\pi^4 |K_{\mathrm{w}}|^2} \langle n | s_{\mathrm{hh}}(\pi)|^2 \rangle, \tag{2.44}$$

where the operator $\langle\cdot\rangle$ is the ensemble average of a distribution of hydrometeors with various physical properties including size, shape, canting angle, density, composition, dielectric constant and falling velocity. Similarly Z of the vertical polarization transmission is expressed as

$$Z_{\mathrm{vv}} = \frac{4\lambda^4}{\pi^4 |K_{\mathrm{w}}|^2} \langle n | s_{\mathrm{vv}}(\pi)|^2 \rangle. \tag{2.45}$$

The differential reflectivity (Seliga and Bringi, 1976) is the ratio of Z measured at the horizontal polarization from a horizontally polarized incident wave to Z measured at the vertical polarization from a vertically polarized incident wave, with the expression as

$$Z_{\mathrm{DR}} = 10 \log\left(\frac{Z_{\mathrm{hh}}}{Z_{\mathrm{vv}}}\right) = 10 \log\left(\frac{\langle n | s_{\mathrm{hh}}(\pi)|^2 \rangle}{\langle n | s_{\mathrm{vv}}(\pi)|^2 \rangle}\right). \tag{2.46}$$

The linear depolarization ratio is the ratio of the cross-polar signal power to copolar power with the same polarization at the receiver, given as

$$LDR = 10 \log\left(\frac{Z_{\mathrm{vh}}}{Z_{\mathrm{hh}}}\right) = 10 \log\left(\frac{\langle n | s_{\mathrm{vh}}(\pi)|^2 \rangle}{\langle n | s_{\mathrm{hh}}(\pi)|^2 \rangle}\right). \tag{2.47}$$

The cross-correlation coefficient (Sachidananda and Zrnic', 1985) is the pulse-by-pulse correlation between the returned power of the horizontally and vertically polarized transmissions, and is calculated as

$$\rho_{\mathrm{hv}} = \frac{|\langle n\, s^*_{\mathrm{hh}}(\pi)\, s_{\mathrm{vv}}(\pi)\rangle|}{\left(\langle n | s_{\mathrm{hh}}(\pi)|^2\rangle \langle n | s_{\mathrm{vv}}(\pi)|^2\rangle\right)^{1/2}}. \tag{2.48}$$

When it comes to the variables associated with the wave propagation, the differential phase shift Ψ_{DP} is the difference between the phase of the horizontally polarized wave (ϕ_{hh}) and the phase of the vertically polarized wave (ϕ_{vv})

$$\Psi_{\mathrm{DP}} = \varphi_{\mathrm{hh}} - \varphi_{\mathrm{vv}} = \delta + \phi_{\mathrm{DP}} + \phi_0, \tag{2.49}$$

and Ψ_{DP} is also the sum of the backscatter differential phase (δ_0), the propagation differential phase (ϕ_{DP}) and the system offset phase (ϕ_0). These three terms on the right side of Eq. 2.49 have different meanings: i) δ_0 is a local term caused by the electromagnetically large non-spheric particles at the range r, ii) ϕ_{DP} is caused by the two-way propagation between the particle and the radar, and iii) ϕ_0 is the phase shift between two transmit signals at the antenna controlled by the radar system.

The reason for the naming of ϕ_{DP} as the propagation differential phase is as follows. As mentioned before, when interacting with hydrometers in the atmosphere, the propagation speed of an EM wave is reduced and thus the EM wave acquires an additional phase shift (Fig. 2.11), and the amount of this phase shift caused by the wave propagation is proportional to n. The aggregative effective refrac-

tive index for a unit volume containing a large number of scatterers is related to the forward-scattering amplitude of each scatter. In fact, atmosphere gases contribute the majority part to ϕ_{hh} and ϕ_{vv}, but the difference $\phi_{hh} - \phi_{vv}$ is caused by the non-spheric and preferentially orientated hydrometeors. Thus, we are not concerned about the absolute value of the ϕ_{hh} and ϕ_{vv} but their differences only. The specific differential phase, the range derivative of ϕ_{DP} is given as

$$K_{DP} = \frac{1}{2}\frac{\mathrm{d}(\phi_{DP})}{\mathrm{d}r} = \frac{\phi_{DP}(r_2) - \phi_{DP}(r_1)}{2(r_2 - r_1)}. \tag{2.50}$$

The number 2 in the denominator is introduced because it represents the two-way propagation of the radar signals—the first time from the radar to the scatterers and the second time from the scatterers back to the radar.

Note that the variables defined by the above equations ignore the propagation effect and are referred as the *intrinsic* radar variables.

Besides, for the rest of this thesis, the subscripts in capitalized letter means logarithmic scale and in lower-case means linear scale, such as the pair of Z_H and Z_h, another pair of Z_{DR} and Z_{dr}. This lower-case/capital-letter convection is also for other parameters. Specifically, z also represents the linear-scale radar reflectivity in linear scale with unit of $\mathrm{mm}^6\mathrm{m}^{-3}$.

Characteristics of polarimetric variables

Besides backscattering, hydrometeors along the radar beam also cause attenuation, phase delay and depolarization. Strictly, the characteristics of polarimetric weather radar measurements are dependent on the physical (size, shape, and orientation), statistical (the distribution of sizes and orientations), and EM properties (dielectric constant and conductivity) of hydrometeors (raindrops, snowflakes, hailstones, cloud droplets, ice crystals, etc.), as well as other scatterers (aerosols, insects, birds, etc.) that might be also in the radar resolution volume. Clearly, characteristics of polarimetric variables vary among different types of hydrometeors. Chapter 5 of the book Ryzhkov and Zrnić (2019) discusses characteristics of each polarimetric variables for raindrops, frozen particles and mixed-phase hydrometeors respectively. We discuss in brief one or two most interesting characteristics for each polarimetric variable regarding the size dependence or the frequency dependence primarily for pure liquid precipitation. A more exhaustive discussion about the characteristics and for other types of precipitation is available in radar meteorology textbooks (Fabry, 2015; Zhang, 2016; Rauber and Nesbitt, 2018; Ryzhkov and Zrnić, 2019).

The axis ratio of a hydrometeor is the ratio of the horizontal axis radius to the vertical axis radius. Z_{DR} (Eq. 2.46) is a measure of the Z-weighted mean axis ratio of the hydrometeors in a unit volume. Z_{DR} is independent of total concentration of hydrometeors, and is subject to the calibration issue owing to the potential difference in the polarization port of the radar hardware. Z_{DR} is a good measure

of median drop diameter (D_m) (Maki et al., 2005), that is, Z_{DR} can serve as an additional constrain to drop size distribution (DSD). Thus, incorporating Z_{DR} into precipitation estimation should help mitigate rainfall estimation uncertainties caused by DSD variability.

From definition, we know K_{DP} depends on the EM waves' forward propagation, but it is estimated through backscattered echoes (Mueller, 1984; Jameson and Mueller, 1985; Sachidananda and Zrnić, 1986). K_{DP} is not affected by the calibration and attenuation, immune to partial beam blockage, and less sensitive to the variation of DSD compared to Z (Sachidananda and Zrnić, 1986; Ryzhkov and Zrnić, 1996; Zrnić and Ryzhkov, 1996). Besides, K_{DP} is directly proportional to the concentration of particles, and monotonically increases with D if the concentration is fixed. Its magnitude increases with oblateness and dielectric constants. These features render K_{DP} as a useful variable for precipitation estimation (Section 4.6). One drawback is that its data quality is affected by Z gradient owing to the non-uniform beam-filling (NBF) (Ryzhkov and Zrnic, 1998a; Ryzhkov, 2007).

Negative K_{DP} values occasionally appear on the presence of large wet aggregates in melting layers or of large hailstones which are characterized by noticeable backscatter differential phase (δ). Negative K_{DP} values also occasionally appear on the rear side of intense convective storms, such as squall lines or isolated hail-bearing convective cells at the far distance away from the radar, owing to the large gradient of Z_H along the azimuth direction within the radar beam or non-uniformity of measurements (Ryzhkov and Zrnić, 1996). K_{DP} is a measure of the mean of the mass-weighted axis ratio of the drops (Jameson, 1985).

The copolar correlation coefficient (ρ_{HV}) is a measure of degree of decorrelation caused by variability of the size, shapes, orientation and phase composition of hydrometeors within a unit volume. The presence of backscatter differential phase reduces ρ_{HV} and its dependence on phase composition is more remarkable than that on the shape and orientation. Besides, ρ_{HV} is a good indicator of the data quality of polarimetric measurements, and ρ_{HV} in high data quality should be not less than 0.995. Its magnitude is independent from hydrometeor concentration, unaffected by propagation and free of calibration issue. ρ_{HV} is a measure of shape variations and irregularities in individual resolution volumes (Balakrishnan and Zrnic, 1990)

Tab. 2.2 summarizes the typical sources of noise for polarimetric variables. The variables subject to miscalibration require calibration before usage, and the variables affected by attenuation require attenuation correction before usage. Tab. 2.3 summarizes the factors which affect the magnitude of polarimetric variables.

Tab. 2.2.: Effects of sources of noises on polarimetric variables adopted from Tab. 6.1 of (Ryzhkov and Zrnić, 2019) and (Kumjian, 2013), where NBF is the acronyms for non-uniform filling effect

–	Miscalibration	Attenuation	Resonance scattering	Beam block	NBF	Depolarization	Noise
Z_{H}	Y	Y	Y	Y	Y		Y
Z_{DR}	Y	Y	Y	Y	Y	Y	Y
$\phi_{\mathrm{DP}}(K_{\mathrm{DP}})$			Y		Y	Y	
ρ_{HV}			Y		Y		Y

Tab. 2.3.: Characteristics of polarimetric variables adopted from (Kumjian, 2013)

–	dependent of particle concentration	dependent on particle density	dependent on DSDvariability	dependent on wavelength	used for quantitative estimation
Z_{H}	Y	Y	Y	Y	
Z_{DR}		Y	Y	Y	Y
$\phi_{\mathrm{DP}}(K_{\mathrm{DP}})$	Y	Y		Y	Y
ρ_{HV}		Y		Y	

The typical values of polarimetric values determined via either theoretical simulation, radar measurements, disdrometer measurements or subjective experience are available (Tab. 2.4). Polarimetric variables are used collectively to develop the hydrometeor classification to improve precipitation estimation, and to assist hail and tornado detection.

Despite the invariable definitions, these polarimetric variables exhibit different features depending on the radar frequency. One prominent feature is that K_{DP} is inversely proportional to λ, and precipitation estimation using K_{DP} is more reliable for X-band radar measurements. For the shorter λ, the Rayleigh scattering approximation becomes more easily violated and consequently the chance of the resonance effect increases, particularly affecting power measurements. T-matrix simulations shows, for pure rain, Z_{DR} increases approximately monotonically with the equivalent D for the S-band frequency, but for the C- band X-band frequency, the monotonic dependence of Z_{DR} on the D is interrupted by occasional bumps because of the resonance effect. Although the resonance criteria is less stringent for the C-band frequency, its impact is more remarkable than that at X-band frequency. Also the shorter λ correspond to a wider numerical range for ρ_{HV} measurements. For instance, ρ_{HV} values below 0.97 in the rain medium is more frequent in the C-band radar data with remarkable sensitivity to hail and melting snow.

Tab. 2.4.: Typical values for polarimetric variables for different types of hydrometeors (from Tab. 8.1 in (Doviak et al., 1993)), similar tables with slightly different thresholds can be found in Straka et al. (2000)

–	Z_H(dBZ)	Z_{DR}(dB)	ρ_{HV}	$K_{DP}(^\circ\,km^{-1})$	L_{DR}(dB)
Drizzle	<25	0	>0.99	0	<-34
Rain	25–60	0.5–4	>0.97	0–10	-27– -34
Snow (dry, low density)	<35	0–0.5	>0.99	0–0.5	<-34
Crystal (dry, high density)	<25	0–5	>0.95	0–1	-25– -34
Snow (wet, melting)	<45	0–3	0.8–0.95	0–2	-13– -18
Graupel (dry)	40–50	-0.5–1	>0.99	-0.5–0.5	<-30
Graupel (wet)	40–50	-0.5–3	>0.99	-0.5–2	-20– -25
Hail (< 2 cm, wet)	50–60	-0.5–0.5	>0.95	-0.5–0.5	<-20
Hail (> 2 cm, wet)	55–70	<-0.5	>0.96	-1– 1	-10– -15
Mixture of rain and hail	50–60	-1–1	>0.9	0–10	-20– -10

The foregoing discussion of characteristics of polarimetric variables is just a brief. Detailed descriptions and interpretations about the polarimetric variables are available in radar meteorology textbooks (Doviak et al., 1993; Bringi and Chandrasekar, 2001; Zhang, 2016; Kumjian, 2018; Ryzhkov and Zrnić, 2019).

2.3. Radar-based precipitation observation and estimation

As an integral part of the atmospheric observing system, the weather radar can observe many aspects of the atmosphere. The applications of weather radar data usually fall into two main categories. First, in terms of wind, the applications include the wind field retrieval from the Doppler velocity used for mesoscale weather prediction and data assimilation, and the studies on turbulence and atmospheric structure from the clear-air echoes from wind profilers which is a type of Doppler radar. Second, in terms of precipitation, the applications include precipitation observation for a concrete understanding of precipitation physics (such as determining the thermodynamic phase of hydrometeors and delineating melting layers, and discerning the presence of hails), precipitation estimation for hydrological floods prediction, and the non-meteorological derivatives such as tracking bird immigration routines.

Our focus of radar measurements is the second category—QPE. The conventional single-polarization radar provides information about spatiotemporal variability of precipitation via Z, while the weather radar polarimetry is intended to mitigate the ambiguities inherent in the single-polarization radar data to obtain more accurate QPE through improving radar data quality, distinguishing precipitation from other non-meteorological scatterers, and mitigating the impact of DSD variability on QPE.

Drop size distribution and polarimetric variables

The same precipitation intensity may occur in case of either a large number of small drops or a small number of big raindrops. Obviously, R is insufficient to describe the precipitation microphyiscs. Usually a comprehensive understanding of precipitation microphysics can be obtained from DSD (equivalently particle size distribution (PSD))(Maki et al., 2005; Zhang, 2016). The DSD model is given as

$$N_{\mathrm{t}} = \int_0^{D_{\max}} N(D)\mathrm{d}D \quad [\#\,\mathrm{m}^{-3}], \tag{2.51}$$

where N_{t} is the total number concentration, $N(D)$ is the number of drops whose diameter is equal to a certain value of D. The n th moment of the DSD is given as

$$M_n = \int_0^{D_{\max}} D^n N(D)\mathrm{d}D \quad [m^n]. \tag{2.52}$$

The mean volume diameter is the volume-weighted size distribution of raindrops

$$D_{\mathrm{m}} = \frac{M_4}{M_3} \quad [m], \tag{2.53}$$

and is related to Z_{DR} directly. It is one of the motivations for developing radar polarimetry because the the information about D_{m} provided by Z_{DR} can add one more constrain to reduce the DSD variability. Then, the rain rate (rainfall rate, precipitation rate) is given as

$$R = 6\pi \times 10^{-4} \int_0^{D_{\max}} D^3 w_{\mathrm{t}}(D) N(D)\mathrm{d}D \quad [\mathrm{mm\,hr}^{-1}], \tag{2.54}$$

and the liquid water content (LWC) is given as

$$LWC = \frac{\rho_{\mathrm{w}}\pi}{6} \int_0^{D_{\max}} D^3 w_{\mathrm{t}}(D) N(D)\mathrm{d}D \quad [\mathrm{kg\,m}^{-3}], \tag{2.55}$$

where w_{t} is the terminal or falling velocity of raindrops. The rainfall rate is proportional to the 3.67th moment of raindrop size distribution. The gamma model (Ulbrich, 1983) is used to describe DSD, and is given as

$$N(D) = N_0 D^{\mu} exp(\Lambda D) \quad [\#\,\mathrm{m}^{-3}\mathrm{mm}^{-1}], \tag{2.56}$$

where N_0 ($\mathrm{mm}^{-\mu-1}\,\mathrm{m}^{-3}$), μ and Λ (mm^{-1}) are concentration, shape and size parameters, respectively. When $\mu = 0$, the gamma model is simplified to an exponential model. The well-known and simple Marshall-Palmer DSD model (Marshall and Palmer, 1948) is a special version of the exponential model if N_0 is suggested to be $8 \times 10^{-6}\mathrm{m}^{-4}$

$$N(D) = 8000 exp(\Lambda D). \tag{2.57}$$

If the scattering amplitude of each hydrometeor and DSD are known, polarimetric radar variables can be calculated by integrating all the scattering amplitudes over all the sizes. Consequently, radar variables can be defined in the form of DSD as

$$Z_{\mathrm{h}} = \frac{\lambda^5}{\pi^5 |K|^2} \int_0^{D_{\max}} \sigma_{\mathrm{h}} N(D) \mathrm{d}D \quad (\mathrm{mm}^6 \mathrm{m}^{-3}), \tag{2.58}$$

$$Z_{\mathrm{v}} = \frac{\lambda^5}{\pi^5 |K|^2} \int_0^{D_{\max}} \sigma_{\mathrm{v}} N(D) \mathrm{d}D \quad (\mathrm{mm}^6 \mathrm{m}^{-3}), \tag{2.59}$$

where σ_{H} or σ_{V} is the backscattering cross section of raindrops for horizontal or vertical polarization,

$$\rho_{\mathrm{HV}} = \frac{\int_0^{D_{\max}} s_{\mathrm{hh}}(D) s_{\mathrm{vv}}(D) N(D) \mathrm{d}D}{[\int_0^{D_{\max}} |s_{\mathrm{hh}}|^2 N(D) \mathrm{d}D]^{1/2} [\int_0^{D_{\max}} |s_{\mathrm{vv}}|^2 N(D) \mathrm{d}D]^{1/2}}, \tag{2.60}$$

where $\rho_{\mathrm{HV}} = \rho_{\mathrm{HV}}(0)/e^{i\delta}$, and δ is the backscatter differential phase shift

$$K_{\mathrm{DP}} = \frac{180\lambda}{\pi} Re \int_0^{D_{\max}} [f_{\mathrm{HH}} - f_{\mathrm{VV}}] N(D) \mathrm{d}D \quad (^\circ \mathrm{km}^{-1}), \tag{2.61}$$

where f_{HH} and f_{VV} are the forward-scatter amplitude at horizontal and vertical polarization respectively, and *Re* indicates the real part,

$$\Phi_{\mathrm{DP}} = 2 \int_{r_1}^{r_2} K_{\mathrm{DP}}(r) \mathrm{d}r \quad (\mathrm{deg}). \tag{2.62}$$

The T-matrix, a numerical simulation of the scattering amplitudes, is commonly used to retrieve theoretical values for the polarimetric values once the DSD is available with supplementary assumptions of the axis-shape ratio. It is widely used to provide theoretical estimates of polarimetric variables with conditions of varying temperature, particle canting angle and mixed phase.

In addition to this normal procedure about deriving the polarimetric variables from DSD, the polarimetric variable measurements can be reversely used to reconstruct DSD (Gorgucci et al., 2002). Incorporating polarimetric variables into numerical weather prediction is currently one of the hottest topics in the radar meteorology community.

Single-polarization and polarimetric rainfall estimators

Eqs. 2.58 and 2.54 imply a relation between Z and R. However, this relation is indefinite and is subject to a great variability, as first pointed out by Twomey (1953), and substantiated by 69 Z-R relations published even before the 1970s (Battan, 1973), and a complete summary by Rosenfeld and Ulbrich (2003) which reported more 200 published Z-R relations. Such a great variability of these Z-R relations is attributed to either DSD variability caused by evaporation, air vertical motion, phase change, wind drift, or measuring methodology such as data selection, sampling volume discrepancy, measurement

errors, and fitting procedures (Tab. 2.5). The second term in Tab. 2.5 refers to presences of hails, bright bands, and non-meteorological targets such as ground clutters.

Tab. 2.5.: Sources of errors in radar-based precipitation estimation, adopted from Tab. 10.1 (Ryzhkov and Zrnić, 2019)

Factors	Addressed using radar polarimetry ?
Variability of drop size distribution	Yes
Contamination from mixed-phase and frozen hydrometeors	Yes
Radar miscalibration	Yes
Attenuation	Yes
Partial beam blockage	Yes
Nonuniform beam filling	Not
Sampling errors	Not
Overshooting precipitation	Not
Evaporation	Yes
Vertical air motion	Not

For the classic Marshall-Palmer Z-R relation $Z = 200R^{1.6}$, the single-polarization rainfall estimator for Z_h in unit of $\mathrm{mm^6 m^{-3}}$ is given as

$$R(Z_\mathrm{h}) = 3.65 \times 10^{-2} Z_\mathrm{h}^{0.625} \qquad [\mathrm{mm\,h^{-1}}]. \tag{2.63}$$

Eq. 2.63 is used frequently to estimate precipitation rate and calculate precipitation accumulation (AR) used in Chapter 5 .

In addition to Z_H, polarimetric variables are believed to improve QPE, but the role of each polarimetric variable in precipitation estimation differs from the others. Correspondingly, analogous to the general form of the Z-R relation ($R(Z_\mathrm{h}) = aZ_\mathrm{h}^b$), the polarimetric rainfall estimators also describe quantitative relations between R and polarimetric variables in power-law forms as well. They are $R(K_\mathrm{DP}) = aK_\mathrm{DP}^b$, $R(Z_\mathrm{h}, Z_\mathrm{dr}) = aZ_\mathrm{h}^b Z_\mathrm{dr}^c$, $R(K_\mathrm{dp}, Z_\mathrm{dr}) = aK_\mathrm{DP}^a Z_\mathrm{dr}^c$, $R(A) = aA^b$. Be cautious that the coefficients a and b in an estimator differ from another estimator. These coefficients can be estimated based on the simulated dataset with the assumed drop shape-size axis ratio relations (Brandes et al., 2002), and DSD from the disdrometers. Similar to coefficients in the Z_H rainfall estimator, these coefficients are subject to DSD variability. For the estimators involving K_DP, the coefficients also depend on the radar frequency. For instance, for $R(K_\mathrm{DP}) = aK_\mathrm{DP}^b$, the value of a falls between 15 and 20, and of b varies between 0.7 and 0.85 (Matrosov, 2010; Maki et al., 2005; Matrosov et al., 2006; Giangrande et al., 2014; Borowska et al., 2011; Anagnostou et al., 2009; Koffi et al., 2014; Park et al., 2005; Martner et al., 2008).

K_{DP} has been suggested as a measure of R starting from 1970s (Humphries, 1974; Seliga and Bringi, 1976, 1978; Sachidananda and Zrnić, 1986, 1987; Jameson, 1985, 1991). Using K_{DP} in rainfall estimation (Zrnić and Ryzhkov, 1996) is less sensitive to DSD and unaffected by the absolute calibration. The non-spheric shape of a raindrop causes the difference in phase shift between two polarization states (Fig. 2.11). The magnitude of this difference depends on the accumulative oblateness of all the non-spheric raindrops; the larger a raindrop is, the more oblate it appears (Green, 1975; Pruppacher and Pitter, 1971), and the more non-spheric raindrops are within the propagation path, the greater the differential phase shift (ϕ_{DP}) is. Accordingly, K_{DP} quantifies the amount of ϕ_{DP} per unit interval of propagation path and indicates R. Since R is the 3.67th moment of the DSD, and K_{DP} is found to be the 4.24th and 5.6th moment at the large drops and small drops respectively (Sachidananda and Zrnić, 1987). Thus, K_{DP} is less affected by the DSD variability compared to Z_H. Unlike Z_H and Z_{DR} are subject to the melting hydrometeors, $R(K_{DP})$ is immune to the bright band contamination.

Humphries (1974) first proposed a linear relationship between K_{DP} and R, although the linear relationship is not true in fact. The K_{DP}-based rain rate estimator with a frequency-scaling is expressed as (Bringi and Chandrasekar, 2001)

$$R(K_{DP}) = 129(\frac{K_{DP}}{f})^b \qquad \mathrm{mm\,h^{-1}}, \tag{2.64}$$

where $b = 0.85$. For the Beard-Chuang equilibrium shape model (Beard and Chuang, 1987), a equals to 50.7, 30.3 and 18.2 for the S-, C- and X-band frequencies, respectively; for the Pruppacher-beard equilibrium shape model (Pruppacher and Beard, 1970), a equals to 40.5, 24.4 and 14.5 for the S-, C- and X-band frequencies, respectively. The difference in coefficients a and b in $R(K_{DP})$ is attributed to the DSD variability and the non-uniformity across the radar beams.

$R(K_{DP})$, especially in the S-band frequency, often also includes negative K_{DP} values because the magnitude of ϕ_{DP} is low and the negative K_{DP} is often caused by the noise resulting from the K_{DP} retrieving procedure rather than the physical presence of negative K_{DP} as mentioned in the previous section. In contrast, in the X-band frequency, the magnitude of ϕ_{DP} is three times higher than that in the S-band frequency, and thus, the retrieval of K_{DP} is more reliable and Eq. 2.64 is also used in Section 4.6.

Besides the foregoing relation to R, K_{DP} is more closely related to LWC

$$K_{DP} = a(\mathrm{LWC})^b, \tag{2.65}$$

where $b = 1.4$ and the value of a is 0.3, 0.65 and 0.89 for the S-, C- and X-band frequencies (Ryzhkov and Zrnić, 2019).

Z_{DR} alone cannot support the precipitation estimation, but Z_{DR} plays its role in QPE via its combination with Z_H or K_{DP} in the rainfall estimators. The function of Z_H is to add one more constraint

to reduce the DSD variability (Jameson, 1991). However, in practice, the K_{DP}-Z_{DR} joint estimator will be affected by additional errors regarding Z_{DR} measurements when Z_{DR} is close to 0 dB, and by differential attenuation (Ryzhkov and Zrnić, 1996) and resonance effect especially at the shorter wavelengths.

In contrast, the role of ρ_{HV} in improving QPE is less straightforward. In general, ρ_{HV} can help distinguish the echoes from non-precipitating echoes and reduce the potential contamination from these non-precipitating scatterers.

Besides the frequent usage of Z_H, Z_{DR} and K_{DP}, specific attenuation (A) was shown their great potential to estimate R (Ryzhkov et al., 2014; Diederich et al., 2015). A is defined as the attenuation a wave experiences during its propagation in a unit distance, typically 1-kilometer. The dependence of A on the DSD resembles the dependence of R on the DSD most among other parameters. However, A is not directly measured in most current operational radars.

The multi-parameter estimation of polarimetric data provides more quantities to constrain the DSD, thereby reducing the degree of freedom of variability. Despite the theoretical superiority of polarimetric rainfall estimators, their practical applications are negatively affected by the errors, and their performance might be subject to precipitation types as well (convective or stratiform). Nevertheless, research has shown improved precipitation accuracy benefiting from the utilization of polarimetric variables (Zrnic and Ryzhkov, 1999; Matrosov et al., 2002). The synthetic algorithm in the current Next-Generation Radar (NEXRAD) network in the United States, in which $R(Z)$ estimators are used for light rain and $R(K_{DP})$ is used for heavy rain, was proven to bring a better performance than the conventional Z-R relation (Ryzhkov et al., 2005).

A comprehensive utilization of polarimetric radar variables is present in Fig. 2.12. The polarimetric measurement can be directly used to estimate R via the aforementioned polarimetric rain estimators (the brown arrow in Fig. 2.12). Characterizing the error structures inherent in the polarimetric measurements can bring us a quantitative representation of the errors which assists in incorporating polarimetric data into NWP models by means of either improving microphysical parameterization scheme or data assimilation (the blue arrows in Fig. 2.12). Besides the precipitation estimation, other applications of radar data include wind retrievals using Doppler velocity, and using refractivity as the initial field for driving NWP models since refractivity is a function of moisture, temperature and pressure.

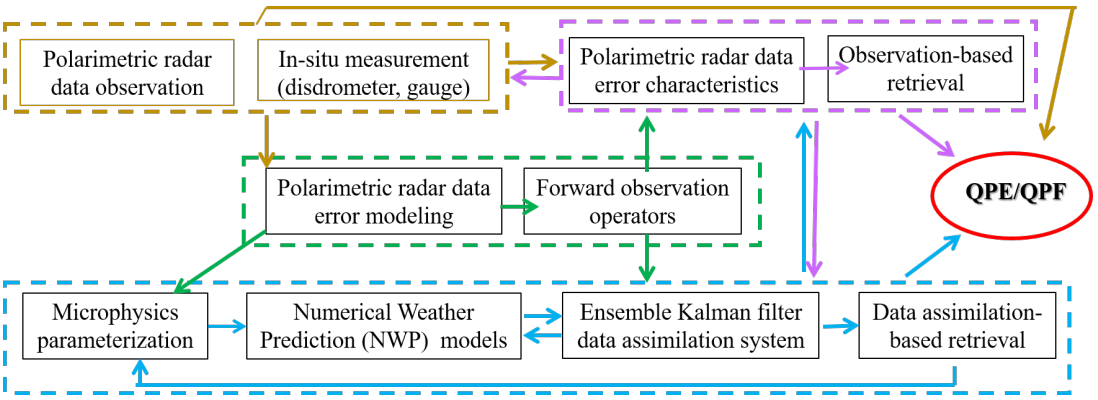

Fig. 2.12.: A schematic summary of the role of dual-polarization in the QPE and QPF (adjusted from Fig. 7.14 in Zhang (2016))

3. Experiment, Data and Methods

Observational data used for this research primarily come from an X-band radar field experiment (Section 3.1) in Stuttgart, with supplementary datasets from a C-band radar (Section 3.2.1), the local rain gauge network (Section 3.2.3), as well as a micro rain radar (MRR) (Section 3.2.2). The X-band radar scan strategy comprises two types of volume scans (Section 3.1.4), serving as the experimental fundamental for this research. Besides the radar scan strategy, we go over the selections of instruments and the measuring site, and present information on the measured datasets from our field campaign as well as the supplementary datasets from other sources. Some general statistical concepts and methods are mentioned in Section 3.3.

3.1. Stuttgart 2017 field experiment and X-band radar datasets

A field experiment was established and implemented in order to obtain the radar data that serve our research objectives (Chapter 1). For this field experiment, we discuss selections of its main instrument and its measuring site, design of its scan strategy, the radar variables obtained from measurements and the derivatives of radar data as follows.

3.1.1. Instrument: X-band radar

An X-band radar was selected as the main instrument in the field experiment for the following two reasons. First, according to the aim (Section 1), this research needs high-resolution radar data. Based on the comparison of weather radars in different frequencies (Section 2.1), the radial resolution on the scale of less than 300 m is used more frequently at the X-band frequency, and the X-band radar used in my research is able to provide measurements at a resolution as high as 50 m. Second, the X-band radar is relatively small and portable. Given our research interest in an urban environment, it is convenient to transport and set up an X-band radar in or close to an urban environment. The X-band radar used in our field experiment is the Meteor 50DX (Selex Systems Integration GmbH) dual-polarized radar contributed by Karlsruhe Institute of Technology (Fig. 3.1(a)). The technical information is given in Tab. 3.1.

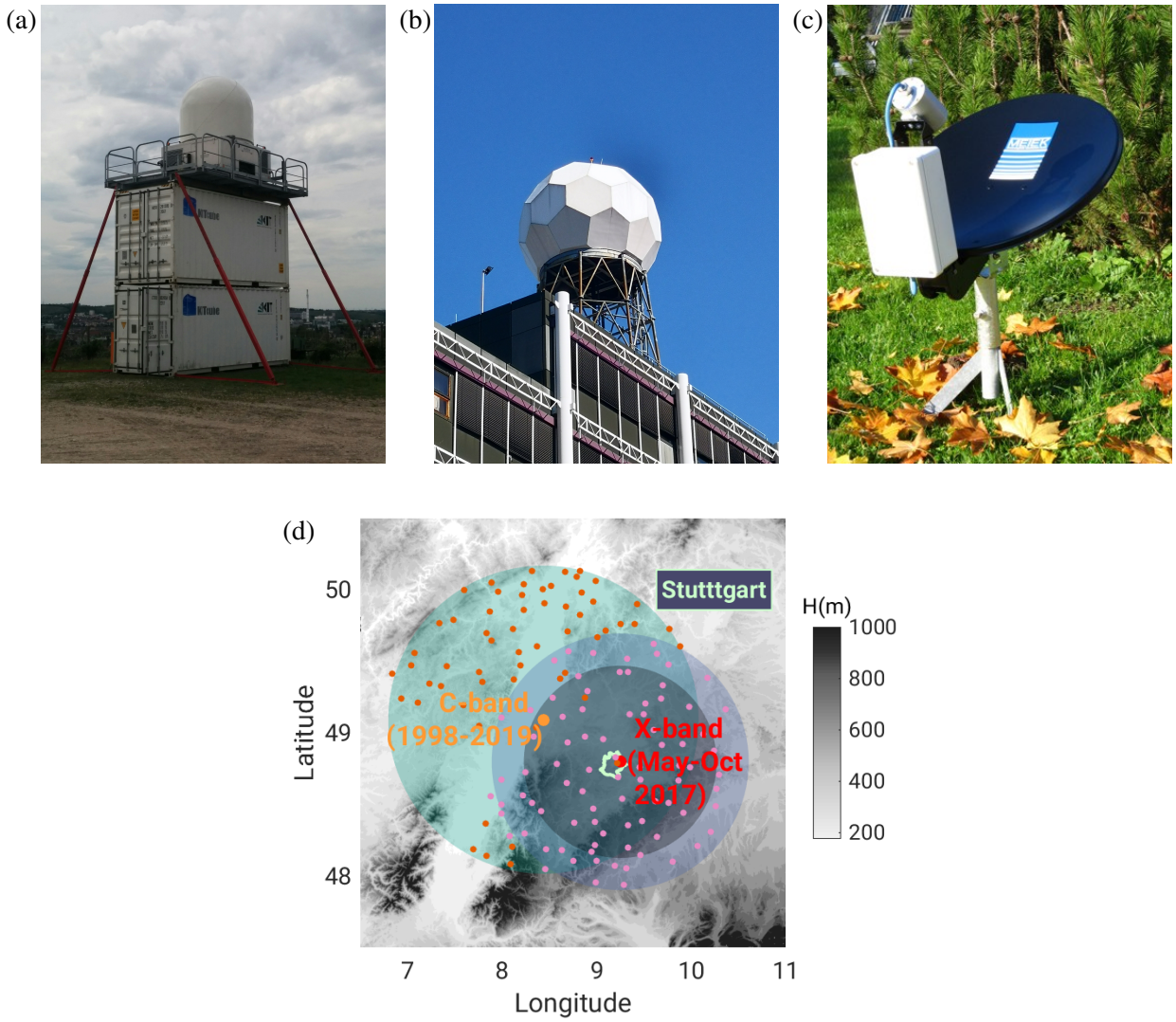

Fig. 3.1.: (a) The X-band radar, (b) the C-band radar, (c) the MRR, and (d) the X-band and C-band radar location and range coverage with the underlying terrain height in gray shading. The light green curve around the X-band radar is the boundary of the city of Stuttgart; the dots either in orange or pink colors represent DWD rain gauge network

3.1.2. Radar measuring site

Since urban environments show the strongest demand for high-resolution radar measurements (Section 1), the field experiment site should be in proximity to an urban environment. We select Stuttgart for the following four reasons. First, the Stuttgart metropolitan area is one of the most populated and urbanized areas in Germany with ample industrial activities. Second, the Stuttgart region has ample precipitation. Climatologically, it is characterized by annual rainfall amount of 650–700 mm and summer rainfall amount of 250–350 mm from May to September (Zheng et al., 2019). Severe convective storm events occur quite frequently during summers, often resulting in severe flash floods affecting traffic and

Tab. 3.1.: Technical details of X- and C-band radars, where SHV is the acronym for simultaneous transmission/reception

–	X-band	C-band
Transmitter type	Magnetron	Magnetron
Transmission mode	SHV	SHV
Antenna type	Central feed	Central feed
Antenna reflector Diameter (m)	1.8	4.2
Antenna gain (dB)	42.5	45.7
Radome diameter (m)	2.55	—
Wavelength (cm)	3.2	5.3
Frequency (MHz)	9400	5610
Peak Power (kW)	75	250
Beam Width (°)	1.3	1.0
Location	48.8° N, 9.25° E	49.09° N, 8.44° E,
Height above sea level (m)	315	148
Period	May–Oct 2017	1997–present

city dwellers' properties. This is also the reason why our field experiment period was done in summertime. Third, the Stuttgart region is well-known for its complex topography; the city nestles in the Neckar Valley Basin, enclosed by the hills at heights of 300–400 meters and vineyards. Specifically, the city is shielded by the Black Forest in the west, the Swabian Alb in the South, the Schurwald in the East and the Stromberg and Heuchelberg regions in the Northwest. Such a topography is likely to make aftereffects of flooding events more terrible, further warranting the hydrometeorological research in Stuttgart. Fourth, the current operational radar measurements in Stuttgart are insufficient. Within the DWD radar network, two radars closest to Stuttgart are located 45 km and 135 km away from Stuttgart's city center, respectively. Given the current spatial resolutions of DWD radars, the Stuttgart's downtown area lacks high-resolution radar measurements, hence the reason that X-band radar measurements from our field experiment can offset this deficiency. Fifth, a project "three-dimensional observations of atmospheric processes in cities", a module in the German research programme "Urban Climate Under Change" ($[UC]^2$) was also conducted in summer 2017 in Stuttgart (Scherer et al., 2019). Our X-band radar field experiment provided supplementary precipitation observation to this project as well.

For selecting a measuring site within the Stuttgart metropolitan area, we considered the land use right, availability of electricity, surrounding obstructions and microwave emission regulation. Eventually we selected the measuring site in a vineyard in the town called Bad Cannstatt, northeast of Stuttgart city in Germany, at a latitude of 48.8° N, a longitude of 9.25° E and at a height above seal level of 315 m (Fig. 3.1(d)). It is around 5 km away from the Stuttgart city center (using Stuttgart Schlossplatz as the reference point), 15 km away from University of Stuttgart where the MRR is located (Section 3.2.2),

and 68 km away from the C-band radar (Section 3.2.1). In spite of our initial intention to avoid nearby obstacles, a few terrain structures reside less than 5 km away from the X-band radar (Fig. 3.2(a)). The measuring period lasted from May 23 to October 16 in 2017, which corresponds to our research focus on the summer or warm season precipitation.

3.1.3. Radar beam shielding

In order to maximize radar visibility and data availability, an ideal experiment site for a ground-based weather radar is a flat terrain without obstructions in the 360° all azimuthal directions, especially for a radar performing a full-circle volume scan. However, it is hard to find an absolutely clutter-free location in the hilly Stuttgart region. Thus, the beam blockage was inevitable in the field experiment we conducted in Stuttgart in 2017.

For a sampling volume along a radar beam with an elevation angle of θ_e, we project it to the ground. Assuming the standard atmosphere condition, there should be a radar propagation path which connects this projected point to the radar site, and we can determine an elevation angle (θ_{sfc}) for this path (Fig. 2.5). Similarly, for each sampling volume, we can determine its θ_{sfc}. This elevation follows the terrain and its meaning is analogous to the terrain-following vertical coordinate in numerical weather modeling. Basically, θ_{sfc} is a function of θ_e, r and Θ, and can be positive or negative depending on terrain height. Then, consider a scenario that θ_{sfc} for a sampling volume located at the 30-km range reaches a maximum value compared to all the other sampling volumes along the same radar beam. In other words, θ_{sfc} of all the sampling volumes farther than 30 km away from the radar are no more than this maximum value, which means the radar beam along that azimuthal direction is intercepted by a high terrain structure at the 30-km range. Then, for all the sampling volumes farther than 30 km away from the radar, we adjust their θ_{sfc} to the peak value. After adjustment, we name these elevations as *terrain-following minimum elevation* (θ_{min}). The θ_{min} is able to quantify the beam blockage effect or the radar visibility. It is analogous to *beam blockage fraction* which has been used frequently to show the degree of beam blockage effect from another perspective (Delrieu et al., 1995; Bech et al., 2003; Zhang et al., 2011)

Recall that the mechanical θ_{beam} of our X-band radar is 1.3° (Tab. 3.1), for the lowest-elevation sweep at 1.5°(Tab. 3.2), the radar beam should fall between an angular width from 0.85° to 2.15°from the horizon along the vertical direction. It means that, with the assumed standard atmosphere, the sample volume whose θ_{min} below 0.85° is free of the beam blockage, whose θ_{min} between 0.85°and 2.15° are affected by the partial beam blockage, and whose θ_{min} over 2.15° are affected by the total beam blockage. For our X-band radar field experiment, at the 1.5°-elevation, θ_{min} over half of the radar coverage is below 0.85, and nearly 1/6 of the radar coverage in the southwest directions is affected by the partial blockage effect (Fig. 3.2(b)).

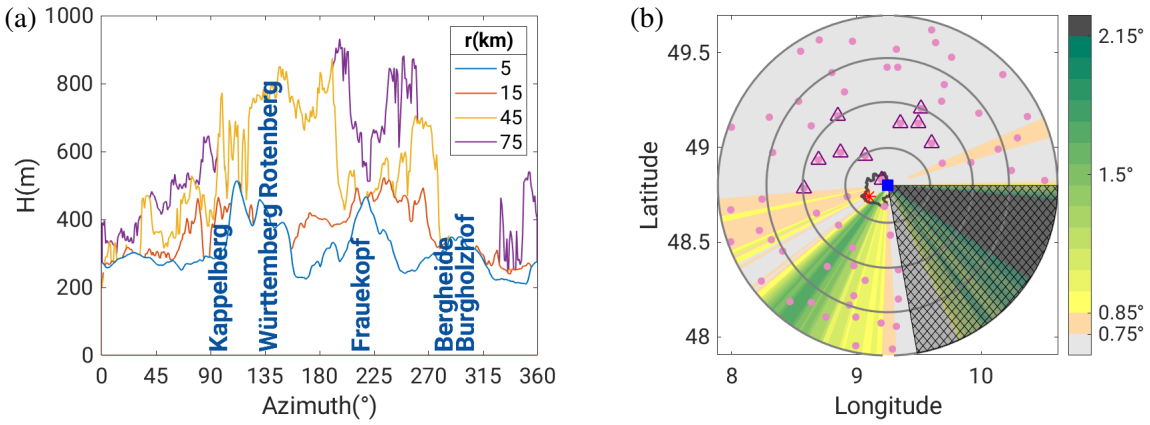

Fig. 3.2.: (a) Terrain heights along the range rings of 5 km, 15 km, 45 km and 75 km away from the X-band radar with the names of terrain structures within the 5-km range. (b) Terrain-following minimum elevation over the X-band radar coverage. The blue dot in (b) is the location of X-band radar and the red dot is MRR location; the hatch-filled sector in (b) is the area without radar radiation; the black curve around the center of (b) is the boundary of the city of Stuttgart; the pink dots in (b) are the locations of rain gauges from DWD rain gauge network; the triangles in (b) highlight the rain gauges which are close to the radar and free of the partial blockage; the gray concentric circles in (b) show the 25-km, 50-km, 75-km and 100-km range rings

Besides the beam blockage caused by the local topography, the radar's radiation was off in the sector between the azimuth of 91° and 170° below the fourth elevation of coarse scan because of the local administration of microwave radiation,(Fig. 3.2(b)).

3.1.4. Scan strategy design

The scan strategy defines how a radar is operated, by regulating 1) its radial resolution Δr, 2) scanning time interval, 3) antenna tilted elevation angle (θ_e), 4) antenna rotation speed (N_a), 5) PRF and the associated r_{max}. The scan strategy is crucial to the radar performance and the data quality (Helmert et al., 2014). Designing a scan strategy requires careful considerations, and is always a matter of compromises. For instance, we considered the constraint between the spatial and temporal resolution (Villarini et al., 2008; Cristiano et al., 2017) when determining the scanning time interval, and we considered the Doppler dilemma when determining the radial resolution and PRFs. As follows, we discuss in order 1) Δr, 2) temporal resolution and scanning time, 3) θ_e, 4) N_a, 5) PRF and r_{max} for the X-band radar field experiment in Stuttgart.

Corresponding to our aim of this thesis (Chapter 1), the X-band radar in this field experiment was operated with two types of scans whose technical details are given in Tab. 3.2. The most important difference between these two scans is their radial resolution; one is 75 m and the other one is 250 m. We refer the scan with the 75-m radial resolution as the fine scan, and the scan with the 250-m resolution as the coarse scan. Recall the definition of a radar sampling volume (Eq. 2.7), given the identical Θ for both

Tab. 3.2.: Performance parameters for X- and C-band radar measurements

Radar	X-band fine	X-band coarse	C-band
Radial resolution (m)	75	250	500
Pulse duration (μs)	0.5	1.67	3.33
Pulse Repetition Frequency (Hz)	2000	500	1180
Duty cycle (max) (dimensionless)	0.001	0.00083	0.0039
Averaged power (W)	75	62.5	980
Operation range (km)	75	100	120
Doppler range (km)	75	300	127
Nyquist velocity ($\mathrm{m\,s^{-1}}$)	32	4	15.6
Antenna speed ($^\circ\,\mathrm{s^{-1}}$)	13.5	18	20
Antenna speed (rpm)	2.25	3.0	3.5
Scan duration (second)	100	255	300
Number of elevations	3	10	14
Elevations ($^\circ$)	1.5, 3.2, 5.0 (before 13:30 UTC 6 June 2017); 1.5, 3.6, 6.2	1.5, 3.6, 6.2, 9.4, 13.3, 18, 23.8, 30.8, 39.5, 90	0.4, 1.1, 2, 3, 4.5, 6, 7.5, 9, 11, 13, 16, 20, 24, 30
Data amount (Giga)	250	101	1070

scans, the difference in Δr determines the different spatial resolutions for both scans. This difference in the spatial resolution is the basis for our investigation about the effect of spatial resolutions on the radar data. From here on, the subscripts f and c are used to represent the fine and coarse scans, respectively.

In a scientific control design, control and experimental groups should be identical in every respect except one difference merely. In order to investigate effects of the radial resolution on the radar data, we can regard radar data measured by coarse scans as the control group, and the radar data measured by fine scans as the experimental group. In a standard scientific control, the radial resolution should be the only difference between fine and coarse scans, and all other technical parameters should be identical for both scans. Nevertheless, it is hard to implement such a procedure in reality. In practice, the fine and coarse scans also differ in other technical parameters and we point them out as follows.

The second difference is scanning time interval. In the scanning procedure, for each 10-minute interval, a 100-second fine scan was repeated three times, followed by a 255-second coarse scan (Fig. 3.3). The coarse scan repeats each 10 minutes and its temporal interval is even, but the temporal interval for the fine scan is uneven. In other words, the fine and coarse scans have different temporal resolutions. However, if we consider only the third fine scan with each 10-minute interval, its temporal resolution is also in 10 minutes.

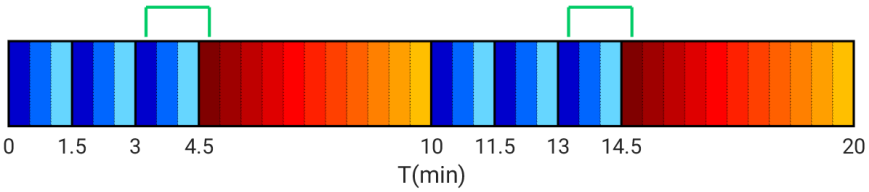

Fig. 3.3.: The X-band radar scan strategy over a 20-minute period with each 10-minute interval as a unit, including three fine scans in cold colors and one coarse scan in warm colors. Each fine scan contains three sweeps whereas each coarse scan contains 10 sweeps; the green lines indicate a time gap (roughly 100 seconds) between the first sweep in the third fine scan and the first sweep in the coarse volume scan

The third difference is the number of sweeps in volume scans. Both fine and coarse scans are volume scans comprising full 360° radar sweeps with different elevation angles, but a fine scan contains three sweeps and a coarse scan contains 10 sweeps (Tab. 3.2). This is one reason why the scanning time of coarse scans is much longer than that of fine scans. Using only three sweeps in fine scans shortens the time gap between a fine volume scan and a subsequent coarse volume scan. Within each 10-minute interval, the coarse scan lags only 100 seconds behind the third (temporally adjacent) fine scan. We assume that the majority of precipitation does not change too much within a 100-second period, and so the third fine scan and coarse scan with each 10-minute time span are deemed as quasi-simultaneous, which serves as a basis for our following comparison between fine and coarse scans in Chapter 4 and Chapter 5.

The fourth difference is N_a, which also partially accounts for the second difference about scanning time interval. Theoretically, N_a is associated with number of independent sample (Section 2.1). A small N_a (such as 1 rpm or $6^\circ\,s^{-1}$) can be dictated to reduce and isolate statistical measurement errors (Ryzhkov et al., 2005). Hence, the difference in terms of N_a adds another freedom of variability to our comparison between the fine and coarse scan data besides Δr.

The fifth difference is PRF and its associated r_{max}. Recall Eqs. 2.2 and 2.9, the duty cycle is the ratio of τ to PRT which is inversely proportional to PRF, and the Δr is linearly proportional to τ. Normally, for a specific radar, the duty cycle is steady, which means changing radial resolutions changes PRFs simultaneously. The fine and coarse scan use different PRFs (Tab. 3.2). Recall Eq. 2.8, determined by the PRF, the r_{max} is 75 km and 300 km for the fine and coarse scans, respectively. The r_{max} defines the distance within which a radar is able to observe the targets without ambiguity. This short r_{max} in fine scans implies a larger chance of second-trip echoes, whereas because of the large r_{max}, the coarse scan data are not affected by the second-trip echoes.

The discussion above illustrates that these foregoing differences between the fine and coarse scans, except Δr, are essentially associated with Δr. Thus, it is unrealistic to change Δr only but keep all other aspects identical for both scans. Although the fine and coarse scans aren't strictly perfect

experimental and control groups, this alternating scan strategy is the best option compared to other possible alternatives to be discussed below.

One alternative is to operate two or multiple radars simultaneously and each of them uses its own Δr. For instance, a radar network consisted of four X-band radars separated over 30 km from each other (Chandrasekar et al., 2012), one study involved two X-band radars only 3.7 km away from each other (i Ventura et al., 2015), and another study used two S-band radars placed 2 km away from each other (Brandes et al., 1999). However, these radars were not co-located and they observed precipitation systems from different viewing angles. It contradicts the principle of the scientific control. For instance, one radar may be under the front side of a squall line, with another radar under the rear part of that squall line. To avoid this situation, we can place two radars at exactly the same location. However, the interference may occur between two co-located radar systems which operate simultaneously. Another drawback of using two radars is that both the hardware and technical configurations of both radars must be identical and remain constant during the entire measuring period, which requires lots of additional efforts. A more realistic reason not to use two radars is that we had access to only one X-band radar in 2017. Therefore, instead of involving two radars, we designed this alternating scan strategy which gave us radar datasets characterized by different radial resolutions.

The feasibility of this alternating scan strategy lies in the assumption that precipitation systems remain unchanged during the 100-second time gap between both scans. However, to which degree this assumption is valid depends on characteristics of precipitation systems. For the fast-developing and short-lived convective storms, this assumption is invalid. One way to increase the credibility of this assumption is to shorten the time gap between the fine and coarse scans, which can be done by reducing number of sweeps, if the antenna rotation speed is unchanged. For example, if each fine or coarse scan contains only one sweep, then the time gap can shrink to a duration on the order of 30 seconds. However, we did not adopt this idea, but instead insisted on volume scans with multiple radar sweeps, for the following three reasons. First, this study mainly addresses summer precipitation and a large proportion of the summer precipitation systems are convective storms with substantial vertical extends and structures. In order to observe upper structures of convective storms, high-elevation sweeps are necessary. The second reason is that, using volume scans containing different elevation angles allows us to access valid radar measurements when the radar data from the lowest elevation sweep are affected by ground clutters or beam blockage. The third reason is due to the vertical incident scan required for Z_{DR} calibrations (Section 4.7),

Given that both fine and coarse scans are volume scans, a proper selection of elevation angles is also crucial to the scan strategy (Fabry et al., 1992). According to the radiosonde data, the mean freezing level of the Stuttgart region during the X-band radar's measuring period is 3.3 km AMSL (Fig. B.19). Within the 75-km range, nearly all the sampling volumes along the 1.5° elevation sweeps are below 3.3 km (Fig. 3.4), which implies the radar beam at the 1.5° elevation observes liquid precipitation during

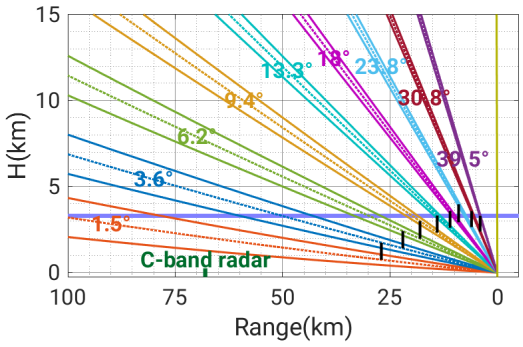

Fig. 3.4.: The VCP of the coarse scan in the X-band radar experiment. The slanted dashed lines represent centerlines of radar beams and every two slanted solid lines near each dashed line in the same color represent the radar azimuthal interval for that radar beam; the horizontal solid blue line at the roughly 3 km height indicates the mean freezing level averaged from May to October 2017 in Stuttgart based on Fig. B.19, the short black vertical line is the vertical interval between two adjacent elevations

the majority of time. The bright band phenomenon—an enhancement of radar reflectivity Z_H resulting from phase transition of solid hydrometeors to liquid hydrometeors aloft—is less likely to occur in the 1.5° elevation sweep, and thus bright-band correction will be excluded in this study. The vertical interval between two elevations (Fig. 3.4) increases with the farther range. It is a reflection of range dependence (Section 2.1). For instance, to achieve the 1-km vertical resolution, we should focus on convective storms within the 30-km range.

The second and third lowest elevations of fine scans were slightly different from their counterparts of the coarse scans before 13:30 UTC on 6 July 2017 (Tab. 3.2). Thus, when we compare the radar measurements from the second and third elevations between fine and coarse scans, we only use the radar data measured after 13:30 UTC on 6 July 2017. When we deal with surface precipitation estimation on the basis of radar data at the lowest elevation, we use the radar data over the whole measuring period.

Given that the terms “fine scan” and “coarse scan” are used throughout the remaining thesis, to clarify, we specify the *fine scan* as the volume scan using the 75-m radial resolution while the *coarse scan* refers to the volume scan using the 250-m radial resolution. Correspondingly, the term *fine scan data* refers to the radar data obtained from fine scans, while the term *coarse scan data* refers to the radar data obtained from the coarse scan.

3.1.5. X-band radar measureables and derived datasets

Radar variables are classified into three levels in our radar data recording system similar to the one employed in the WSR-88D (Crum et al., 1993) and DWD radar network (Helmert et al., 2014). The level I data are EM signal outputs from a radar receiver. They are mainly used for engineering purposes, and are not involved in this thesis. The level II data are outputs obtained after EM signals have been

processed by the default data QC procedure within the built-in radar processor, and are named as *base data*. The level III data are the products derived from the base data or outputs produced by customized algorithms, and are named as *base product*. The precipitation estimate calculated on the basis of radar reflectivity in the base data is the example of the level III data. Corresponding to the research questions (Chapter 1), the level II data are used for the first part of data analyses concerning radar data quality (Chapter 4), and the level III data are involved in the second part of data analyses regarding the radar-based precipitation estimates (Chapter 5).

During the Stuttgart experiment, 12 radar variables were collected (Tab. 3.3). The first seven variables in Tab. 3.3 are from single-polarization, whereas the rest were obtained through the dual-polarization capability. A default clutter removal procedure within the radar processor converts the *uncorrected radar reflectivity* (u-Z_H) into the *(corrected) radar reflectivity* (Z_{H}), while the built-in phase filtering procedure converts the *uncorrected differential phase shift* (u-ϕ_{DP}) to the *corrected differential phase shift* (ϕ_{DP}) (Tab. 3.3). A variable named as *clutter correction* (CCOR) defines the difference between the u-Z_H and Z_{H}. We use (corrected) radar reflectivity for the rest of the thesis, but this default correction is not perfect and we need additional data QC procedures (Chapter 4). The difference between u-ϕ_{DP} and ϕ_{DP} is that the ϕ_{DP} is the filtered and smoothed differential phase after applying the phase filtering procedure which removes the fluctuating noisy components of the directly measured u-ϕ_{DP}. The majority of discussions on differential phase in this thesis is about u-ϕ_{DP}, including spike signal (Section 4.2), second-trip echoes (Section 4.3) and non-meteorological echo removal (Section 4.5), whereas the K_{DP} retrieval and attenuation correction (Section 4.6) uses the filtered ϕ_{DP}. Because Z_{H}, ϕ_{DP} and K_{DP} are calculated using the built-in procedures from the radar signal processor, these variables are also regarded as the level II base radar data in this thesis. Unlike the base radar data, the *processed radar data* refer to the radar data after being applied with external radar data processing procedures (discussed in Chapter 4).

Numerical ranges and accuracies of all these 12 variables given in Tab. 3.3, are customized by the radar signal processor of our X-band radar, and can be different from radar datasets from other experiment. A large portion of data have no numerical value within their corresponding numerical ranges, and we regard that the data is invalid or cannot be retrieved. The radar data reading algorithm assigns -32 dBZ to both u-Z_H and Z_{H}, -0.5 dB to SNR, -0.0039 to SQI and ρ_{HV}, 0° to u-ϕ_{DP} and ϕ_{DP}, and NaN value to V_{Do}, K_{DP}, and Z_{DR} for such situations. The retrievability and validity of K_{DP} and V_{Do} is used in non-meteorological echo removal (Section 4.5) and second-trip echo removal (Section 4.3), respectively.

For Z_{H}, besides the data at their original resolutions, we interpolated Z_{H} of fine scans into a new dataset at the same Δr as the coarse scan, named as *f2c* data, and we also obtained the coarse scan data as the same Δr as the fine scan data, named as *c2f* data. Both linear interpolations are performed on the rainfall rate scale (Section 3.3.1). We deal with f2c and c2f data mainly in Section 5.3. As mentioned

Tab. 3.3.: Measurables from the Stuttgart X-band radar field experiment. For Doppler velocity, the values in before round brackets are for the fine scan data, the value within round brackets are for the coarse scan data

Measurable	Unit	Numerical Range	Accuracy
Uncorrected radar reflectivity (u-Z_H)	dBZ	-31.5 – 95	0.5
Radar reflectivity (Z_{H})	dBZ	-31.5 – 95	0.5
Signal-to-noise ratio (SNR)	dB	0 – 72	0.5
Signal quality index (SQI)	dimensionless	0 – 1	0.0039
Doppler velocity (V_{Do})	$\mathrm{m\,s^{-1}}$	$\pm32(\pm4)$	0.252(0.0315)
Spectrum width (σ_{v})	$\mathrm{m\,s^{-1}}$	0 – 12	0.0625
Clutter correction ratio (CCOR)	dB	0 – 70	0.315
Differential radar reflectivity (Z_{DR})	dB	-8 – 12	0.0787
Uncorrected differential phase (u-ϕ_{DP})	°	0 – 360	0.0055
Filtered differential phase (ϕ_{DP})	°	-180 – 180	0.0055
Specific differential phase (K_{DP})	$^\circ\,\mathrm{km^{-1}}$	-32 – 32	not applicable
Copolar cross-correlation coefficient (ρ_{HV})	dimensionless	0 – 1	0.0039

in Section 2.2, the term *intrinsic* variables refer to the radar variables without considering propagation effect, that is, without attenuation correction.

When it comes to V_{Do}, the Doppler dilemma (Eq. 2.30) constrains the unambiguous velocity between -32 m/s and +32 m/s for the fine scan data and between -4 m/s and +4 m/s for the coarse scan data (Fig. 3.5). This narrow range of Doppler velocity for the coarse scan limits the reliability of using Doppler velocity.

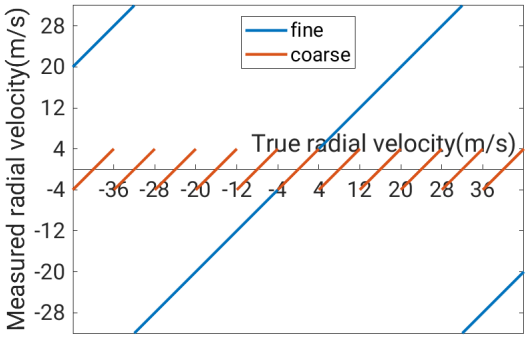

Fig. 3.5.: Doppler velocity ambiguity of the X-band radar fine and coarse scans

In addition to the single-polarization variable (Z, V_{Do} and σ_{v} defined in Section 2.1) and polarimetric variables defined in Section 2.2, another three variables in Tab. 3.3 are defined as

$$\mathrm{SQI} = \frac{|R_1|}{R_0} \tag{3.1}$$

$$\mathrm{SNR} = 10log(\frac{R_0}{P_N}) \tag{3.2}$$

$$\mathrm{CCOR} = 10log(\frac{T_0 - P_N}{R_0 - P_N}) \tag{3.3}$$

where R_0 is signal autocorrection at lag 0, R_1 is signal autocorrection at lag 1, P_{N} is noise power level, and T_0 is signal autocorrelation at lag 0 from uncorrected data. SQI varies from 0 (completely uncorrected data) to 1 (completely corrected data) (SELEX, System Integration GmbH, 2015). SQI is related to σ_{v}, and low SQI corresponds to high σ_{v}, and the erratically high σ_{v},implies weak signal near the noise level (Klazura and Imy, 1993). The relation between SNR and SQI is given as

$$\mathrm{SQI} = \frac{\mathrm{SNR}}{\mathrm{SNR}+1} exp(-\frac{\pi^2 \sigma_{\mathrm{v}}^2}{2}) \tag{3.4}$$

Various algorithms exist for retrieving K_{DP} (Wang and Chandrasekar, 2009; Otto and Russchenberg, 2011; Maesaka et al., 2012; Giangrande et al., 2013; Huang et al., 2016). Given that K_{DP} is the range derivative of ϕ_{DP} (Eq. 2.50), the intuitive equation for computing K_{DP} is

$$\hat{K}_{\mathrm{DP}}^i = \frac{\phi_{\mathrm{DP}}^{i+1} - \phi_{\mathrm{DP}}^i}{2\Delta r} \tag{3.5}$$

where ϕ_{DP}^i is ϕ_{DP} at the i th gate. However, because of the random gate-to-gate fluctuations, calculating K_{DP} using the adjoint gates often generates erratic K_{DP} values. A simple solution is to calculate K_{DP} as the slope of ϕ_{DP} profile over N radar gates via the least square fitting as

$$\hat{K}_{\mathrm{DP}}^i = \frac{\sum_{i=1}^{N} (\phi_{\mathrm{DP}}^i - \bar{\phi}_{\mathrm{DP}})(i - \frac{N+1}{2})\Delta r}{2\sum_{i=1}^{N} [(i - \frac{N+1}{2})\Delta r]^2} \tag{3.6}$$

where $\overline{\phi}_{\mathrm{DP}}$ is the average of ϕ_{DP} over the N-gate interval. A series of such N consecutive gates is named as a calculating window. Obviously, the number of radar gates or the length of the calculating window affects the accuracy of K_{DP} retrievals (Ryzhkov and Zrnić, 1996). For instance, a longer calculating interval might cause excessive smoothing, thereby leading to underestimations of K_{DP}. In principle, the spatial resolution of K_{DP} is usually not consistent with the radar variables, but instead depends on both the number of gates used in the K_{DP} retrieval and Δr. The standard K_{DP} retrieval algorithm normally uses range derivatives over a number of radar gates, so the spatial resolution of K_{DP} is coarser than that of the original radar data. In the signal processor of our X-band radar, the number of radar gates for calculating K_{DP} is conditioned by the magnitude of Z_{H} (SELEX, System Integration GmbH, 2015). If N gates are

used for Z_H above 45 dBZ, $2 \times$ N gates are needed for Z_H between 35 and 45 dBZ and $3 \times$ N gates for Z_H less than 35 dBZ. A typical value of N is 6, but basically the signal processor determines N depending on the range resolution.

In our Rainbow signal processor, the built-in procedure for retrieving K_{DP} of the Rainbow processor sequentially includes selecting "good data", smoothing the u-ϕ_{DP}, determining and subtracting the system offset, unwrapping, and finally deriving K_{DP} along radial directions (Selex-SI, 2012; M.Thurai, 2007). KDP is a range derivative and is subject to statistical fluctuations. Thus, the K_{DP} retrieval requires a filter which is able to smooth the peak and introduce biases (Chandrasekar et al., 2012). The "good data" selection uses criteria in terms of SNR, ρ_{HV} and texture of u-ϕ_{DP} (see definitions of the texture parameter in Section 3.3.1). A phase filtering procedure is necessary to suppress the fluctuations in the range profiles of the u-ϕ_{DP} measurements. The signal processor of our X-band radar provides two options for filtering ϕ_{DP} in the K_{DP} retrieval procedure—finite impulse response (FIR) filter (Proakis and Manolakis, 1988) and simple smoothing based on linear regression (M.Thurai, 2007). FIR is more advanced since it was deliberately designed to tackle the non-monotonic features in the ϕ_{DP} range profile induced by backscatter of the raindrops which are large enough to violate the Rayleigh scattering approximation (Section 2.1), and to simultaneously preserve the physically meaningful trends of ϕ_{DP} (Hubbert and Bringi, 1995). However, the FIR filter is much more computationally intensive. For the real-time K_{DP} retrieval output, the signal processor automatically chooses the simple smoothing filtering other than the FIR. We did not process the ϕ_{DP} data manually once more to calculate the K_{DP} filtered by the FIR, which implies that K_{DP} data in this research are affected by the backscatter effect.

3.2. Supplementary instruments and datasets

In addition to the X-band radar, this study also involves the data from a C-band radar, an MRR and DWD rain gauge network. For qualitative analyses, the radar images in terms of Z_H measured by the C-band radar are compared to the radar image of the X-band radar data (Section 5.1). For quantitative analyses, the Z_H and associated precipitation estimates derived from the C-band radar and MRR datasets are compared to Z_H of the X-band radar data, and precipitation measurements from rain gauges are also compared to precipitation estimates of the X-band radar data (Section 5.2).

3.2.1. 23-year C-band radar and its measurables

A C-band radar has been situated on the roof of a seven-floor high building on the north campus of Karlsruhe Institute of Technology (KIT) since 1997, at a latitude of 49.09° N, a longitude of 8.44° E and at a height above sea level of 148 m. The radar was single-polarized until June 2013 when the dual-polarization capability was added. However, this study mainly uses Z_H from this C-band radar, and the

only exception is Section 4.6 which uses the C-band Z_{DR}. The VCP of C-band radar data comprises 14 elevations, starting from 0.4°, followed by 1.1° and 2.0° (Tab. 3.2). However, we leave out the data from the 0.4°-elevation sweep owing to the overwhelming beam blockage and ground clutter contaminations in the 0.4° elevation sweeps, and only use the radar data starting from the 1.1° elevation sweep. Given that our X-band radar field experiment lasted from 23 May to 16 October 2017, we address the C-band radar data measured during 21 summer seasons (five months from 1 May to 30 September every year) from 1998 to 2019 except 1997 (due to bad data quality in May and June) and 2013 (due to the change of radar hardware). It means we have roughly 462,000 volume scans in the total 105 months. The spatiotemporal resolution of the C-band radar dataset is 500 m and is different from those of the fine and coarse scans (Tab. 3.2), which provides the foundation to compare radar measurements at three different spatial resolutions (Section 5.1)

Effort has been made to maintain the radar hardware's stability and data consistency since 1997. The radar engineer technicians from DWD calibrate this C-band radar every half a year using power curves of the receiver, and the radar meteorology group in KIT continuously compares the radar-derived precipitation estimates with local rain gauge measurements. The evolution of the minimum detectable signal (MDS) averaged over each month shows the stability of the radar hardware over the past two decades (Appendix B.2.1) .

3.2.2. Micro rain radar and its measureables

We also use a vertical-pointing K-band (24 GHz) MRR manufactured by METEK GmbH and operated by the University of Stuttgart. The MRR is located at a latitude of 48.73° N, a longitude of 9.1° E at the 453-m height above sea level, around 13 km away southwest of the X-band radar (Fig.5.23(a)). Unlike pulsed weather radars, the MRR utilizes frequency modulated continuous waves. Other technical specifications of the MRR are available from METEK GmbH (2014). The MRR retrieves Doppler spectra of hydrometeors on the basis of the received spectral power (Peters et al., 2002). The MRR directly measures Doppler frequency (f_D), the frequency shift between the transmitted and received signals of the MRR. If we know the Doppler frequency (f_D), DSD and terminal fall velocities of falling raindrops (w_t), the measured spectral volume reflectivity $\eta(f_D)$ can be related to the volume reflectivity $\eta(D)$ through

$$\eta(D) = \eta(f_D)\frac{\partial f_D}{\partial w_t}\frac{\partial w_t}{\partial D} \tag{3.7}$$

and then $N(D)$ is calculated according to

$$N(D) = \frac{\eta(D)}{\sigma(D)} \tag{3.8}$$

where $\sigma(D)$ is single particle scattering cross section and can be calculated by the Mie theory. Once $n(D)$ is available, Z, LWC and R can be calculated with aid of empirical relations about terminal velocity of hydrometeors. It means R data from the MRR is not directly derived from Z from the MRR (Peters et al., 2002).

This MRR provides us datasets of Z_H and R with a 1-minute temporal resolution and a 100-m vertical resolution between 0.1 km to 3 km above the ground surface of the measuring site. A weighing Pluvios rain gauge situated a few meters away from the MRR provides simultaneous 5-minute rainfall measurements which serve as coincident and co-located reference to the MRR dataset. Precipitation measurements from the MRR and the Pluvios rain gauge are well correlated, at least during the measuring period of our X-band radar campaign (Appendix B.3.2).

3.2.3. Rain gauge network and its precipitation measurements

This study utilizes the 1-minute rain gauge rainfall measurements downloaded from Climate Data Center (CDC) of DWD (DWD Climate Data Center (CDC), 2019) over the X- and C-band radar coverage (Fig. 3.1(d)). The minimum measure accuracy for the 1-minute gauge measurement is 0.01 mm. The DWD regularly changes the suppliers of rain gauges over certain years (personal communication), and the current rain gauge employed is the rain[e]H3 weighting tipping bucket precipitation senor from Lambrecht Meteo GmbH (LAMBRECHT, 2021), with an automatic self-empty capability against freezing. The spatial distribution of the rain gauge network is presented in Fig. 3.1(d). During the summer 2017, there were 86 rain gauges within a 100-km radius of the X-band radar, 125 rain gauges within a 120-km radius of the C-band radar, and 67 rain gauges in the area overlapped by both the X-band and C-band radar coverages. Actually, the number of rain gauges changes with time over two decades (Fig.B.9).

Rain gauges are always subject to measurement errors (Upton and Rahimi, 2003; Vasiloff et al., 2009; Habib et al., 2010), such as timing and transmission errors, risk being clogged with water trickling in over time, random mechanical errors, non-shielded tipping-bucket, strong wind (reduce gauge collection efficiency), and undercatch in case of heavy rain. The rain gauge network is operated by DWD, so we have no control over rain gauge data quality. For the remaining thesis, we assume these rain gauge measurements are on-time and trustworthy.

3.3. Statistical methods in this study

The radar datasets used in this study are large, such as 84,000 X-band radar volume scans and 460,000 C-band radar volume scans. In order to extract useful information from such a large amount of data, we need to orderly organize, efficiently analyze, graphically present and physically interpret information behind these datasets. The following statistical concepts and methods serve as useful tools.

3.3.1. Univariate descriptive statistics

A *population* is defined as the entire group of an element or variable of interest. For the hourly precipitation rate in the Stuttgart metropolitan region, one seldom obtains its total population, but instead what an instrument can provide is a *sample*—a subset of the population. There may exist several different samples for a specific population.

A quantity which describes or characterizes a population is called a *parameter*, and an estimate of a population parameter through samples is called a *statistic* (Zar, 2007). The descriptive statistics, such as mean, median and standard deviation, summarize the dataset and draw clear-cut conclusions about the variable of interest. The descriptive statistics measure the central tendency (arithmetic mean, median and mode, etc.), and also variability/dispersion (standard deviation, etc.). We acknowledge that mean and standard deviation are statistically neither robust nor resistant (Wilks, 2006), but they are still utilized in the following analyses because of their wide use and also for the purpose of comparison with others' research.

As Z_{H} is expressed on the logarithmic scale (Section 2.1), its arithmetic operations such as averaging or subtracting conflict with the physical meaning of variables in the logarithmic scale, and thus should not be done directly on the logarithmic scale (Fabry, 2015). In contrast, precipitation amount and precipitation intensity are on linear scales. Thus, for calculating the arithmetic mean of Z_{H}, we can convert Z_{H} into R using Z-R relation (Section 2.1), calculate the arithmetic mean of R, and then convert the mean rainfall rate back Z_{H} using the inverse Z-R relation. An exception is to keep Z_{H} in logarithmic scale for calculating correlation coefficients (Fabry, 2015).

A variable in the circular scale has no true zero points but arbitrary designations of high or low values, such as wind direction (θ_{V}). In meteorology, for θ_{V}, we conventionally assign the direction of east as 90° and the direction of west as 270°, but it doesn't imply that the wind direction in the west is "larger" than that in the east. Therefore, calculating descriptive statistics of circular variables should be different from statistics of linear variables. We adopt the circular descriptive statistics from Zar (2007) and utilize the tools from Berens et al. (2009) to calculate the descriptive statistics of circular variables, such as differential phase ϕ_{DP} and u-ϕ_{DP}.

For a radar variable x, its texture parameter $\sigma(x)$ defines its localized spatial variability. The texture parameter at a radar gate $\sigma(x_r)$ calculates standard deviation or root mean square difference of that radar datum (x_r) across a certain number of adjacent radar gates, either within a box whose dimensions are along both radial and azimuthal directions, or within a moving window containing radar gates along one radial direction merely. $\sigma(x_r)$ can be calculated using several different techniques (Giuli et al., 1991;

Schuur et al., 2003; Chandrasekar et al., 2013). Similar to Dufton and Collier (2015), the one we used is calculated as

$$\sigma(x_r) = \sqrt{\frac{1}{N-1}\sum_{i=-(N-1)/2}^{(N-1)/2}(x_{r+i}-\bar{x})^2} \tag{3.9}$$

where N is the number of radar gates within the calculating window of which the target radar gate is in the center, and thus normally N is an odd number. Obviously, the magnitude of a texture parameter changes with N, so we should be cautious about N. Given that Δr is 75 m for fine scans and 250 m for coarse scans, when calculating $\sigma(x)$ for both fine and coarse scan data, we have two options—using either equivalent window length or equal number of radar gates. Note that the texture parameters for ϕ_{DP} ($\sigma_{\phi_{\mathrm{DP}}}$) and u-ϕ_{DP} ($\sigma_{\phi_{\mathrm{DP}}}$) use the circular scale standard deviations. This thesis also involves the texture parameter for Z_{DR} ($\sigma_{Z_{\mathrm{DR}}}$), and the texture parameter for ρ_{HV} ($\sigma_{\rho_{\mathrm{HV}}}$). Be cautious about distinguishing $\sigma(x)$ from the standard deviation of a sample of data ($SD(x_r)$). The former represents a spatially localized variation, while the latter is used to represent the variation with a sample.

3.3.2. Frequency, probability and probability density

A variable can be discrete (discontinuous) or continuous; a discrete variable can take on only certain values, whereas a continuous variable can be any conceivable value within a specific observed range. The majority of meteorological variables are conceptually continuous but reported discretely owing to accuracies of instruments. For instance, air temperature and precipitation amount can be any real number in principle but are conventionally reported as discrete multiples of 0.1°C and 0.01 mm. The situation is similar for all the radar variables except K_{DP} (Tab. 3.3). For instance, the Z_{H} value outputted from our radar processor is linearly spaced between -32 dBZ and 95 dBZ with an even interval of 0.5 dB. It means that, the value 14.76 dBZ might exist in nature, but is rounded to 15 dBZ in our radar dataset.

Given the large amount of the radar dataset (Tab. 3.2), in order to quantitatively summarize such a big dataset, we use frequency, relative frequency, frequency distribution, probability and probability density. The *frequency* (or *absolute frequency*) presents a list of all the observed values of a variable and counts how many times each value is observed in a sample. The *relative frequency* is the proportion of the total frequency. The summation of all the absolute frequencies in a sample should equal to the total sample size and the relative frequency varies between 0 and 1 (0% to 100%).

A *frequency distribution* is the distribution of the total number of observations among various categories (groups or range intervals). A *bar graph* presents the frequency distribution for a discrete variable. In contrast, for a continuous variable, its frequency distribution is tabulated by categories or groups, which can be graphically presented by a *histogram* whose adjacent bars are normally touching each other. The vertical axis of a histogram can be absolute or relative frequency. If the number of categories or groups are too many, we often use a *frequency polygon* which connects the midpoint of

each adjacent bar by straight lines. If the width of bars is small enough, these connected straight lines look like in the shape of smooth curves.

A phenomenon occurs in any one of different ways, but in only one of those ways at a time, and each possible output is referred to as an *event*, such as a Z_{H} datum being 15.0 dBZ or 15.5 dBZ. To obtain a frequency distribution, the sample range of data is divided into several intervals or bins, typically with equal bin width (Δx_i), and then the number of samples (c_i) whose values fall into each interval is counted. Then the absolute frequency of an event is c_i, and the relative frequency of an event is the ratio of the occurrence frequency of an event to the total number of all the events $c_i / \sum c_i$. If a sample is large enough, the probability of an event can be expressed in the long-run relative frequency. This interpretation of probability essentially follows *frequency interpretation* (Wilks, 2006). Regarding the event of hourly *AR* exceeding 5 mm, if a rain gauge located within Stuttgart city reported 66 times of 1-minute *R* over 5 mm h^{-1} in 2017, the relative frequency is 0.15% and thus we regard the probability of precipitation hourly *AR* over 5 mm h^{-1} as 0.15%.

Analogous to the frequency distribution, we are also interested in the probability distribution of a variable over its whole range, using probability density function (PDF, or $f(x_i)$) defined as

$$f(x_i) = \frac{c_i}{N_{\mathrm{t}} \cdot \Delta x_i} \tag{3.10}$$

where $N_{\mathrm{t}} = \sum c_i$ is the total number of the sample. PDFs can efficiently summarize information from a large dataset. Plotting the PDFs into a frequency polygon leads to the total area under the frequency curve being 1 ($\int_a^b f(x)\mathrm{d}x = 1$), which facilitates a direct comparison between different PDFs or different datasets. When visualizing a PDF, the height of PDF is density rather than probability; instead a probability is the area under the PDF curve.

As mentioned, radar variables are continuous, but outputs of the radar processor are discrete values. According to Tab. 3.3, we use the minimum interval as the bin width for plotting PDFs to avoid unnatural distortions of the PDFs caused by inappropriate bin widths, such as 0.5 dB for Z_{H}. If the data amount is sufficiently big, then frequency polygons are semi-smooth curves. Any irregular troughs or ridges along these frequency polygons curve imply hidden noise or distortions of data, and demand a cautious inspection of the dataset (Section 4.9). Besides this intuitive judgment, we can also calculate the expectation ($E(X)$) and variance or standard deviation ($\sigma(X)$) from the PDFs through the following equations

$$E(X) = \int_a^b x f(x)\mathrm{d}x \tag{3.11}$$

$$\sigma(X) = \sqrt{\int_a^b (x-\mu)^2 f(x)\mathrm{d}x} \tag{3.12}$$

$$E(X) \approx x_k f(x_i)\Delta x \tag{3.13}$$

$$\sigma(X) \approx (x_i - E(X))^2 f(x_i)\Delta x \tag{3.14}$$

where Eqs. 3.11 and 3.12 are for continuous variables, while Eqs. 3.13 and 3.14 are for discrete variables. This calculation is valid for variables which do not follow the Gaussian distribution, such as precipitation intensity whose small or near-zero values dominate the whole dataset. The Z_{H} data from all the volume scans at a specific radar gate are used to calculate a PDF which can be used to calculate the mean precipitation rate over that radar gate. PDFs for multivariate are in Section 3.3.3.

The cumulative frequency distribution (CFD) provides information about sample quantiles or percentiles. As the median is the value above and below which lies half the set of data, a quantile can be defined as below which lies other fractional portion of the data. Quartiles divides one complete dataset into four equal parts and are actually special cases of quantiles. We reserve Q for quantile or quartile, such as the symbol $Q_{0.1}$ for the 0.1 quantile, the symbol $Q_{0.25}$ for the lower quartile, and the symbol $Q_{0.75}$ for the upper quartile.

3.3.3. Bivariate analysis

The *paired data* (X,Y) refers to two variables (X and Y) linked together. A bivariate sample consists of paired data and can be expressed as

$$(X_1, Y_1), (X_2, Y_2), ..., (X_i, Y_i), ..., (X_n, Y_n)$$

In other words, within a bivariate sample, each datum X_i is paired with a corresponding datum Y_i, and thus the total numbers of the X sample and the Y sample are equal.

The concept of paired data will appear frequently in the next chapters. Paired data can be a pair of data from two individual samples—Z_{H} data from a coarse scan and a fine scan within each 10-minute interval, if both are spatially interpolated into the same spatial resolution; paired data can also be data obtained using different observational techniques —precipitation measurements from rain gauges and precipitation estimates derived from the coincident and concurrent radar data.

For a dataset consisting of paired data, we are interested in the statistics to describe the relationship between these two variables (X and Y). Correlation and regression are used to illustrate and quantify such a relationship. The linear regression illustrates the linear dependence of one variable on the other variable, whereas the linear correlation illustrates the association between two variables neither of which is assumed to be functionally dependent upon the other. Non-linear correlations illustrated as a monotonic increasing trend is also another possibility.

Scatterplot and joint histogram

The scatterplot or scatter diagram is a typical graphical summary of bivariate data; one coordinate axis represents one quantity of the paired data (X) while the other coordinate axis represents the other quantity of the paired data (Y). The scatterplot presents an association between X and Y, and this association is not causality. If this association is strong enough, it can be explained in the following three ways: a) X causes Y to change, b) Y causes X to change, c) a third unknown or unquantified variable causes both X and Y to change. For instance, no causality exists between two samples because both are measured individually from two instruments/methods, such as radar measurements from fine and coarse scans, and so only the situation c) is reasonable.

In spite of the prevalence of scatterplots in bivariate analyses, the scatterplot for the instantaneous R or hourly AR is usually visually unfriendly. Rain in measurable intensity is a rare case; dry periods or light rain dominate the entire measuring period, which means a huge amount of precipitation measurements are below the minimum measurable threshold of rain gauges. This feature is reflected in the scatterplot where the majority of scatterers cluster around the origin of the scatterplot. Many scatterers are overlapped at one location and indistinguishable. Graphically, we cannot know the frequency of scatterers at a location. For instance, the scatterplot with the paired values of $1.1\,\mathrm{mm\,h^{-1}}$ and $0.9\,\mathrm{mm\,h^{-1}}$ occurring 10 times, and the paired values of $1.1\,\mathrm{mm\,h^{-1}}$ and $0.1\,\mathrm{mm\,h^{-1}}$ occurring once, is graphically equivalent to another scatterplot with the paired values of $1.1\,\mathrm{mm\,h^{-1}}$ and $0.9\,\mathrm{mm\,h^{-1}}$ occurring once, and the paired values of $1.1\,\mathrm{mm\,h^{-1}}$ and $0.1\,\mathrm{mm\,h^{-1}}$ occurring 10 times, given the size and color of dots is kept the same (Fig. 3.6(a) and Fig. 3.6(b)). Although the first scenario shows stronger agreement than the second scenario, such stronger agreement is graphically hidden in the scatterplot. This is a drawback of the scatterplot, especially for the dataset with a large data amount.

In contrast, the joint histogram, also named as the two-dimensional bivariate histogram or heatmap, serves an alternative way to tackle the overploting of scatterplots (Figs. 3.6(c) and 3.6(d)). The color of dots indicates the occurrence frequency of the sample with each two-dimensional bin. Fig. 3.6(d) shows the majority of the paired data close to the diagonal line, indicating a better concordance between the X and Y sample sets. The two-dimensional probability density function (2D-PDF) is a form of the joint histogram, if the data in both the X and Y sample sets are normalized to the probability density function.

Statistics for correlation and concordance

Three types of correlation coefficient (CC) statistics are used to describe the correlation between two variables: Pearson correlation coefficient (CC_{PS}), Spearman rank correlation coefficient (CC_{SP}) (Spearman, 2010; Spiegelman, 2010), and concordance correlation coefficient (CCC)(Steichen and Cox, 2002;

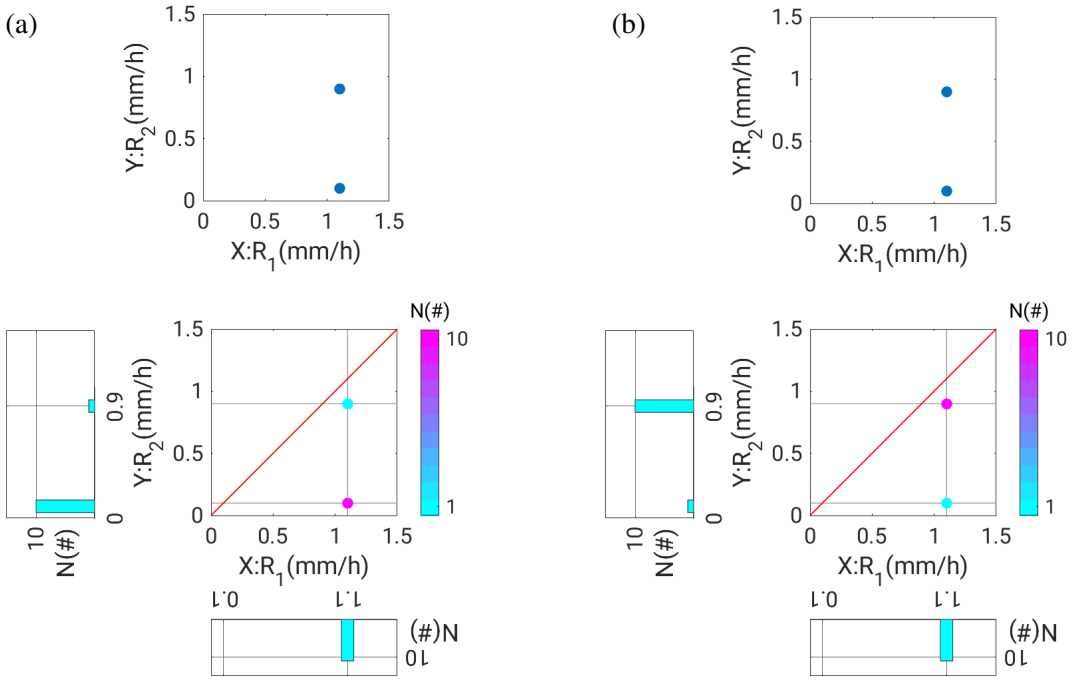

Fig. 3.6.: Illustration of drawbacks of scatterplot and advantages of joint histogram: (a) bad concordance, and (b) good concordance

Lin, 1989; McBride, 2005). A "good" statistic should be unbiased, efficient, reliable and consistent (Zar, 2007).

CC_{PS} refers to "Pearson product-moment coefficient of linear correlation", which is the most common statistic to measure the strength of the association between two variables or two samples.

$$CC_{PS}(X,Y) = \frac{1}{N-1}\sum_{i=1}^{N}\left(\frac{\overline{X_i-\mu_X}}{\sigma_X}\right)\left(\frac{\overline{Y_i-\mu_Y}}{\sigma_Y}\right) \tag{3.15}$$

CC_{PS} is statistically neither robust nor resistant and it is sensitive to outliers. However, due to its common use and its application in regression analyses, CC_{PS} is frequently used in the next chapters.

In contrast, CC_{SP} is statistically more robust and resistant, and its equation is

$$CC_{SP}(X,Y) = 1 - \frac{6\sum_{i=1}^{N} d_i^2}{N^3 - N} \tag{3.16}$$

where d_i is a difference between X and Y ranks: d_i = rank of X_i - rank of Y_i. CC_{SP} indicates the strength of monotonic relations, rather than the linear relationship reflected by the foregoing CC_{PS}.

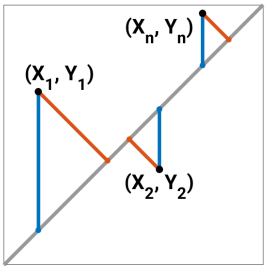

Fig. 3.7.: Schematic comparison of the linear and orthogonal regression. The blue lines show the vertical distance whose sum of squares is minimized in the simple linear regression; the red lines show the shortest distances perpendicular to the fitting lines and orthogonal regression minimizes the length of red lines

CCC (Lin, 1989) is also used to evaluate the relationship between two variables, and is calculated as

$$\rho_c = \frac{2\sigma_{XY}}{\sigma_{XX} + \sigma_{YY} + (\mu_X - \mu_Y)^2} \tag{3.17}$$

CCC was supposed to be superior than other procedures such as CC_{PS}, least square for slope and intercept (Zar, 2007). CCC less than 0.9 indicates the poor strength-of-agreement; CCC between 0.9 and 0.95 is moderate; CCC between 0.95 and 0.99 is substantial; CCC larger than 0.999 is almost perfect (McBride, 2005).

Besides these foregoing *CC*s in different definitions, when it comes to the paired data of two variables with the identical physical meaning, if the orthogonal regression brings about straight fitting lines characterized by the 45°-slope and a zero intercept, $Y = X$, these two variables are perfectly correlated and also in a perfect concordance.

Specifically, in order to assess the relation between rain gauge precipitation measurements (AR_G) and radar-based precipitation estimates (AR_R), we define $\Delta = AR_R - AR_G$, and the following statistics: bias $B = \langle\Delta\rangle$, averaged absolute deviation (AAD) $= \langle|\Delta|\rangle$, root mean square error $RMSE = (\langle|\Delta|^2\rangle)^{1/2}$, relative root mean square error $rRMSE =$ normalized by the mean rain gauge precipitation accumulation ($\overline{AR_G}$), and normalized bias nB divided by ($\overline{AR_G}$) as well (Jaidan et al., 2018).

Orthogonal regression

The linear least-square fitting is used to perform a linear regression between two variables, one termed as predictor (X) and the other termed as response (Y). The linear least-square fitting minimizes the sum of squares of predictor errors.

Unlike the linear regression which implicitly assumes that measurement errors exist only in the response variable (Y), the Deming regression assumes the measurement errors of X and Y to be in Gaussian distribution and independent. The Orthogonal Regression (OR) is a special case of the Deming

regression if the variances of two measurement errors of X and Y are identical. It minimizes the distance of the response values perpendicular to the fitting line (red lines in Fig. 3.7), which implies the fitting coefficients keep constant if the X-axis and Y-axis is exchanged.

A classical use of OR is to test the consistency of one quantity which is measured by two instruments or two experimental methods, referred to X_1 and X_2. No causality or dependence exists between X_1 and X_2, so the terms "response" and "predictor" are inappropriate. In the paired datasets of our study, we eliminate the concept of "response" and "predictor", and then both variables X and Y refer to two independent samples which observe the same thing but resulted from different instruments or measuring methods. If $X_1 = X_2$, we can conclude both the measurements from the instruments are perfectly correlated and also comparable in magnitude, which implies both instruments are able to observe that variable accurately. However, in reality, two instruments have different measurement errors, conflicting the assumption of the equal measurement error variance, and casting doubt on the use of OR . For example, the variances of measurement errors from radar and rain gauge measurements are quite likely to be different. Therefore, the results of orthogonal regression should be interpreted with caution.

4. Effects of Spatial Resolution on Radar Data Quality

Data, regardless of their sources, always include both useful and irrelevant information, and must be processed to obtain the meaning information, which can be done by data quality management. We usually access radar data after they were produced (such as after a field campaign), so the data quality management for the radar data lies in data QC—the reactive and corrective procedures—other than data quality assurance.

The Data QC is a crucial step before using observational data into applications (Friedrich et al., 2006). The objective of this chapter is to investigate the effects of spatial resolution of radar measurements on the data quality of the radar "base" data by comparing the differences between two radar datasets at two different spatial resolutions—the fine and coarse scan data. The following data analyses include: i) deciphering the sources of errors and uncertainties which affect the radar data quality, ii) developing the automatic algorithms to identify and filter out the less qualified data or noises, iii) characterizing the spatiotemporal distribution of various types of noises.

4.1. Visual inspections of differences between fine and coarse scans

Looking through radar images is always the first step for the majority of the radar data users when they obtain a new set of radar data, and nowadays the radar images have become common for the public as well. Similarly, at the first step, we also conduct qualitative visual inspections over a small sample of radar images. Such "quick" looks before any data processing or calculation are supposed to provide us a preliminary overview about the similarities and differences between the fine and coarse scan datasets.

4.1.1. Loss of weak echoes in fine scans

Since the peak power of a radar transmitter is relatively unvaried (Section 3.1), a short pulse duration means shortening the time in which the transmitter is sending out EM waves, weakening the total transmitted power and correspondingly reducing the returned echoes. In other words, in case of a shorter pulse duration, the radar signal processor tends to overlook the weak returned signals and subsequently a diminished percentage of measurable radar reflectivity (Z_{H}) above a certain threshold—approximately 12 dBZ for our fine scan shown in Fig. 4.1(e).

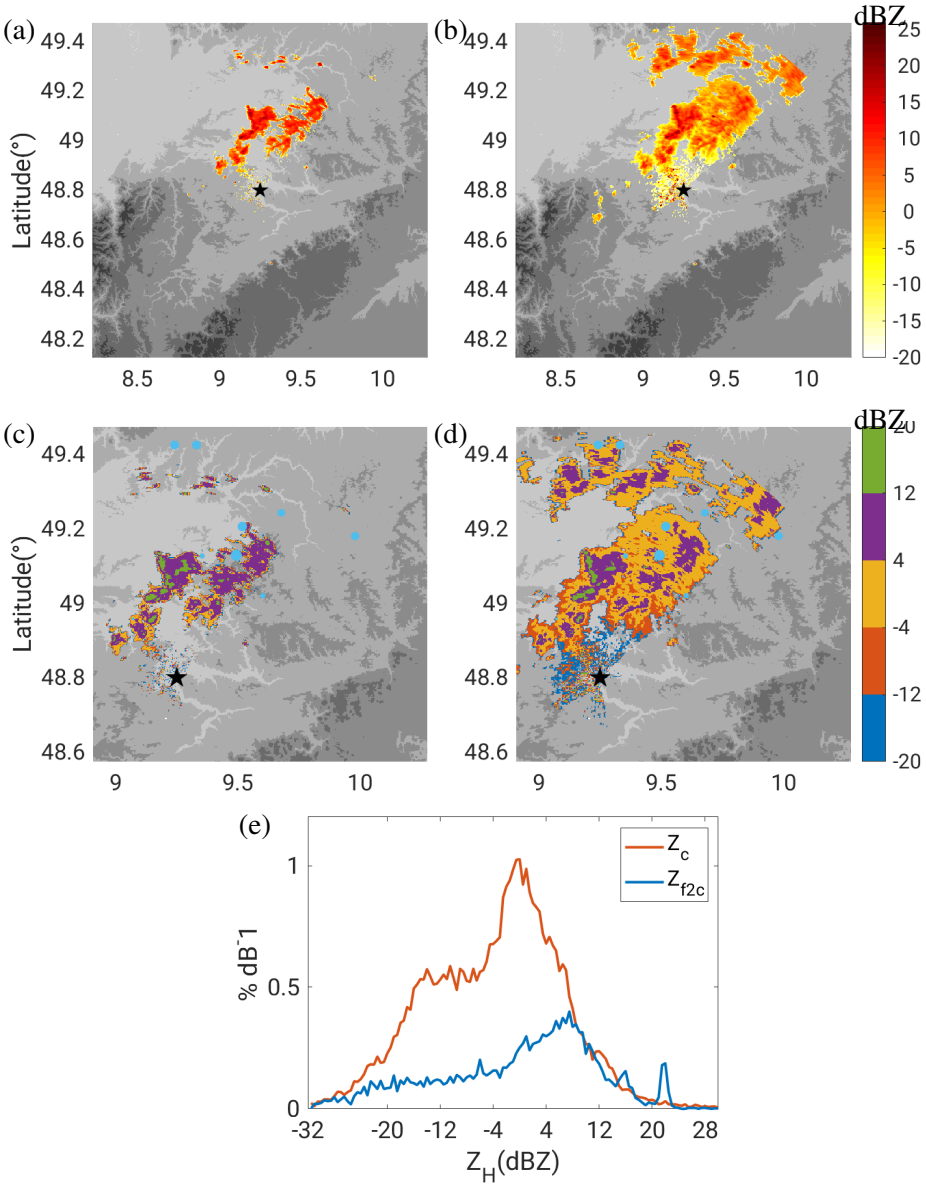

Fig. 4.1.: PPI displays of Z_H at the 1.5° elevation at 01:23(01:24) UTC on 11 October 2017 to show a lack of weak echoes in fine scan data, where the Z_H of the fine scan (a) is interpolated into the same spatial resolution as the coarse scan, (b) only includes Z_H of the coarse scan within the 75-km range, in order to present both PPI displays at the same dimension, (c) uses the same data as (a), but in a discrete color scheme and zoomed in the northeast quarter (the same for (d)), the black stars indicate the location of radar, and the size of light blue dots in (c) and (d) represents the magnitude of 10-minute rainfall accumulation during 01:10–01:19 UTC from DWD rain gauge measurements, and (e) is PDF of Z_H for the original coarse scan data at 01:24 UTC, and the fine scan at 01:23 UTC interpolated into the same spatial resolution as the coarse scan referred as f2c

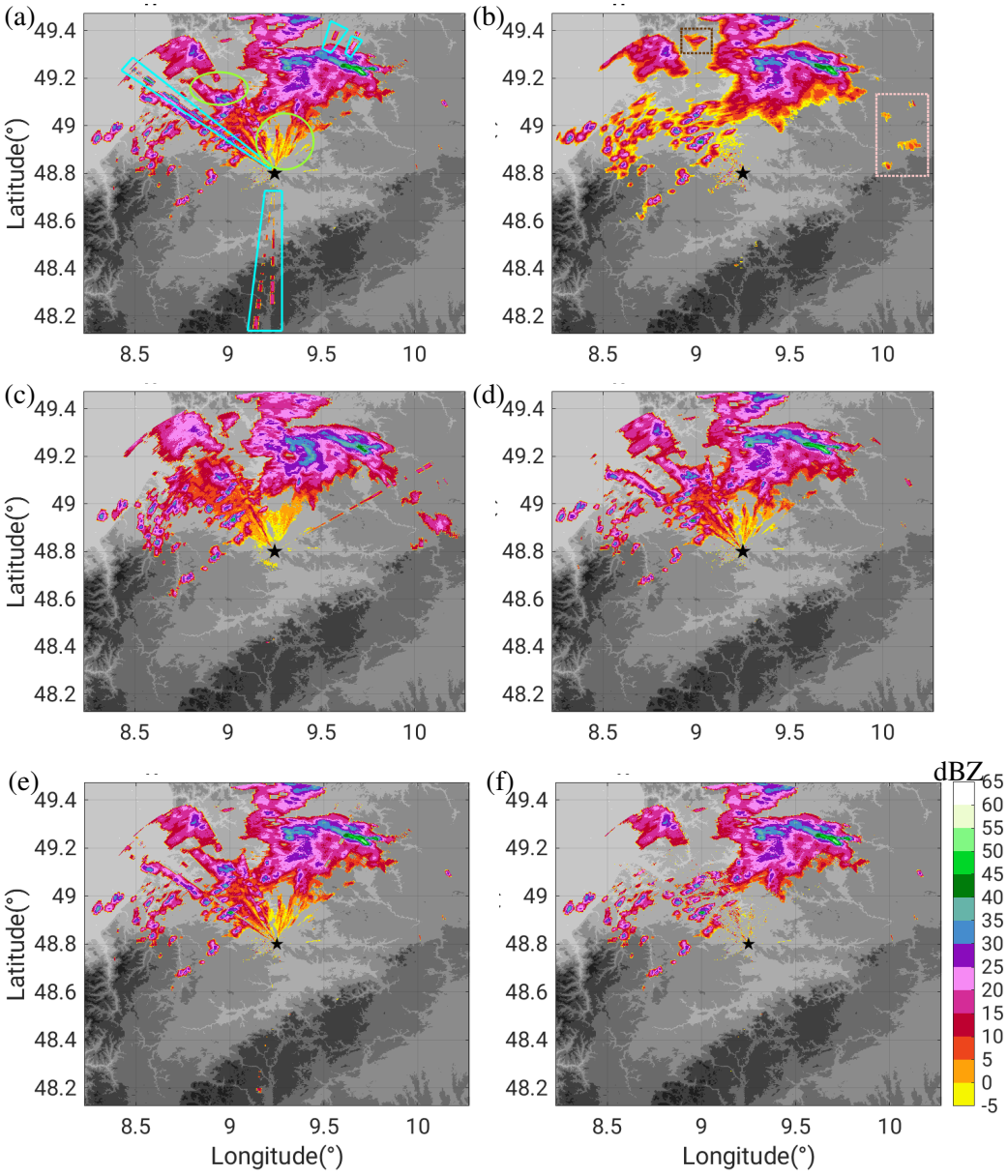

Fig. 4.2.: PPI displays of Z_H around 04:30-04:39 UTC on 7 July 2017 to show the additional suspicious echoes in fine scan data, where (a), (e) and (f) are the fine scans of 1.5° elevation at 04:33 UTC, (b) is the coarse scan of 1.5° elevation at 04:34 UTC, (c) is the fine scan of 3.6° elevation at 04:33 UTC, and (d) is the fine scan of 1.5 ° elevation at 04:31 UTC. In (a), the unfilled trapezoids in cyan refer to the suspicious echoes caused by external EM sources, and the unfilled ellipses in green-yellow color refer to the second-trip echoes; the unfilled squares in (b) show the weak echoes present in the coarse scan but absent in the fine scan; in (e) the suspicious echo caused by external transmission is removed (Section 4.2); in (f) both types of suspicious echoes are removed (Section 4.3); the black stars indicate the location of the X-band radar site

At the first glance at PPI displays in Fig. 4.1, we notice the area with measurable Z_H(above -32 dBZ) in the fine scan (Fig. 4.1(a)) is much smaller than that of the coarse scan (Fig. 4.1(b)). Besides, the areas which can be only seen in the radar images of the coarse scan are characterized by Z_H mainly between -12 and 12 dBZ, corresponding to the areas in red, yellow and purple in both Figs. 4.1(c) and 4.1(d).

Radar reflectivity below 12 dBZ, which is equivalent to rainfall rate less than 0.2 mm h^{-1} and corresponds to drizzle or light rain with very small drops, is usually referred as weak echoes and has a minimal contribution to flash floods. Light rain was reported by rain gauges, as indicated by these blue dots in both Figs. 4.1(c) and 4.1(d). For the coarse scan (Fig. 4.1(d)), all the blue dots overlap with the measurable Z_H, but for the fine scan (Fig. 4.1(c)), there is no measurable radar signal near the rain gauges which report precipitation. In short, the fine scans miss weak precipitation.

In contrast, the area with Z_H over 12 dBZ resides in both scans with nearly identical shapes and locations, corresponding to the green area in both Figs. 4.1(c) and. 4.1(d), which means the fine scan has comparable capability as the coarse scans in observing moderate-to-heavy precipitation that is of most interest to hydro-meteorological applications. The difference in PDF (Fig. 4.1(e)) further quantitatively confirms a diminished presence of weak echoes along with these remaining strong echoes for fine scans.

This deficiency of weak radar reflectivity is ubiquitous through the entire radar data, which means plenty of cases to illustrate this reduction of weak radar echoes. However, we deliberately choose the example case in Fig. 4.1—light rain to minimize the effect of attenuation correction (Section 4.6), no precipitation at 75–150 km radar range to avoid the possible contamination from the second-trip echoes (Section 4.3), and no calibration (Section 5.2.1). These strict criteria attempt to eliminate other possible reasons accounting for the difference in Z_H value between the fine and coarse scans, and to illustrate merely the lack of weak radar echoes in fine scans in a rigorous manner.

Regarding radar detection, radar sensitivity refers to detectability of weak echoes against the background of the radar receiver's noise (Smith, 1986). The background noise may also include interference signals (natural or man-made), or even ground clutters. The background noise usually tends to fluctuate rapidly, so the matter of the radar sensitivity is a statistical problem. The system sensitivity is greater at the expense of a loss in effective spatial resolution, which fits much clearly with losses of weak echoes in the fine scan data we discussed above.

4.1.2. Additional suspicious echoes in fine scans

Despite the reduced presence of weak echoes, the radar images of fine scans often show additional echoes which are absent in the coarse scan. For instance, comparing the radar images between the fine and coarse scans in Figs. 4.2(a) and 4.2(b), we can find that, contrary to the weak echoes present in the coarse scan but absent in the fine scan (within the dashed square in Fig. 4.2(b)), some radar echoes only exist in the fine scan, such as these within the trapezoids or ellipses in Fig. 4.2(a). We classify these radar echoes seen only in this fine scan into two types based on their patterns and intensity. Within the trapezoids, the suspicious echoes reside along the radar beams interrupted with random short breaks, narrow in the azimuth directions (only spreading over one to three azimuths) but elongated in the radial

directions, either with moderate (the trapezoid to the south of the radar) or strong (the trapezoid in the northwest of the radar coverage) intensity. For two trapezoids in the north-northeast (NNE) directions in Fig. 4.2(a), the suspicious signals may also radiate from the radar site, but they are overlapped with the precipitation targets and it is not easy to distinguish them from the precipitation body. These suspicious echoes disappear or relocate to absolutely different azimuthal directions in the sweeps of 3.6° elevation within the same volume scan, and of 1.5° elevation of the volume scan performed 90 seconds earlier, thus suspicious echoes are random both in time or space. The second type of suspicious signals is quite different from the first type. The "extra" radar reflectivity (Z_{H}) within the ellipses remains steady in the temporally adjacent radar scan or the radar sweeps of adjacent elevations, usually with a weak-to-moderate intensity. The different characteristics of suspicious echoes in the trapezoids and ellipses imply different causes behind both.

The meteorologically meaningful radar echoes appear in similar shapes with comparable intensity in both fine and coarse scans and their spatially or temporally adjacent scans, no matter how tiny they might be in size, such as these sparely scattered convective storms in the western part of the radar coverage in all the four PPI displays in Fig. 4.2. We trust the radar's reliable ability to observe, and believe that no arbitrary radar echo exists in a radar image without a reason, and thus there must be reasons for both suspicious echoes.

To recap, our glances over radar images gives us a quick overview on similarities or dissimilarities between the fine and coarse scans before meticulous examinations. It not only confirms the loss of weak echoes in the fine scan which is in accord with the radar theory, but also unfolds two types of suspicious echoes that add "extra" Z_{H} into the fine scan solely. We discuss extensively about these two types of suspicious echoes respectively in the following two sections to assess their roles in radar data quality.

4.2. Spike signals from an unknown source

The radar reflectivity (Z_{H}) patterns within the trapezoids in Fig. 4.2 along the azimuthal directions vary in intensity, and are random in space and time; they don't recur in the adjacent elevations and are also absent in the preceding and following volumetric scans. We name these "spike-shaped" patterns briefly as spike signals; we deliberately use the term "signal" rather than "echo", because their EM energy may not be from our X-band radar but other external EM sources.

4.2.1. Characteristics of spike signal

In addition to the varying Z_{H} (Figs. 4.2 and 4.3(a)), the spike signals are characterized by unreasonably high u-ϕ_{DP} above 200° (Fig. 4.3(b)), and these u-ϕ_{DP} values keep nearly constant over consecutive radar

gates (Fig.4.3(c)), which is equivalent to a low $\sigma_{u\text{-}\phi_{DP}}$. Such features are quite distinct from other kinds of echoes, as we know that radar gates contaminated by ground clutters have both high u-ϕ_{DP} values and large $\sigma_{u\text{-}\phi_{DP}}$ values while the precipitation echoes are usually characterized by low u-ϕ_{DP}. Thus, we can distinguish the spike signals from ground clutters and precipitation via a combined use of u-ϕ_{DP} and its texture, automatically for the entire radar data. For instance, in Fig. 4.3, despite different Z_H intensity, spike signals within both the trapezoid 1 and 3 exhibit u-ϕ_{DP} higher than 210° and low $\sigma_{u\text{-}\phi_{DP}}$ lower than 10°, both satisfying the criteria of high u-ϕ_{DP} and low $\sigma_{u\text{-}\phi_{DP}}$, thereby being identified as a flag for the spike signal (marked as the green lines in Figs. 4.3(d) and 4.3(e)). By the way, we select this case in Fig. 4.3 deliberately in which spike signals don't penetrate through the precipitation to avoid the misleading overlapping with precipitation echoes, and these three trapezoids from 1 to 3 represent three scenarios respectively—spike signal with moderate Z_H, spike signal within the azimuths where the radar radiation was off, and spike signals with high Z_H.

Given that microwave radiation of radar was deliberately switched off for the azimuths between 91° to 170° (Section 3.1) during the entire measure period, the existence of spike signals within this azimuthal range (the trapezoid number 2 in Fig. 4.3) leads to our argument that the energy of spike signals comes from an external source—probably a transmitter operating in exactly the same frequency as our X-band radar. A candidate is the navigation radar for the inland vessels traveling along the Neckar River as shown in Fig. 4.4(a). The traffic regulations (minimum safety standards) of the European Union for inland waterways requires all the vessels to have a 9-GHz radar as the secondary navigation radar in addition to a S-band radar as the primary one for the purpose of navigating and avoiding collisions (ETSI, 2016). Although technical details of the 9-GHz X-band navigation radars vary among different design modes and manufacturers, the spatial resolution of these pulsed X-band navigation radars can be as high as 5 meters (note that these X-band navigation radars are absolutely different from our X-band weather radar).

After identifying the spike signals in the entire X-band radar dataset by applying the aforementioned criteria relying on the u-ϕ_{DP} dataset, we find the identified spike signals exhibit diurnal variations and spatial patterns which might be associated to the navigation radars (Fig. 4.4). The occurrence frequency of spike signals was much lower during the nighttime especially from 23 UTC to 04 UTC (01 am to 06 am local time in summer daylight saving time), which may be explained by the reduced transportation activity of inland vessels during the nights. Moreover, for both fine and coarse scans, the spike signals are spatially distributed more frequently in the azimuthal range between 310°and 60° (Figs. 4.4(c) and 4.4(d)), which corresponds to a twist in the inland waterway of the Neckar River near our X-band radar site within the highlight shaded dark blue area in Fig. 4.4(b).

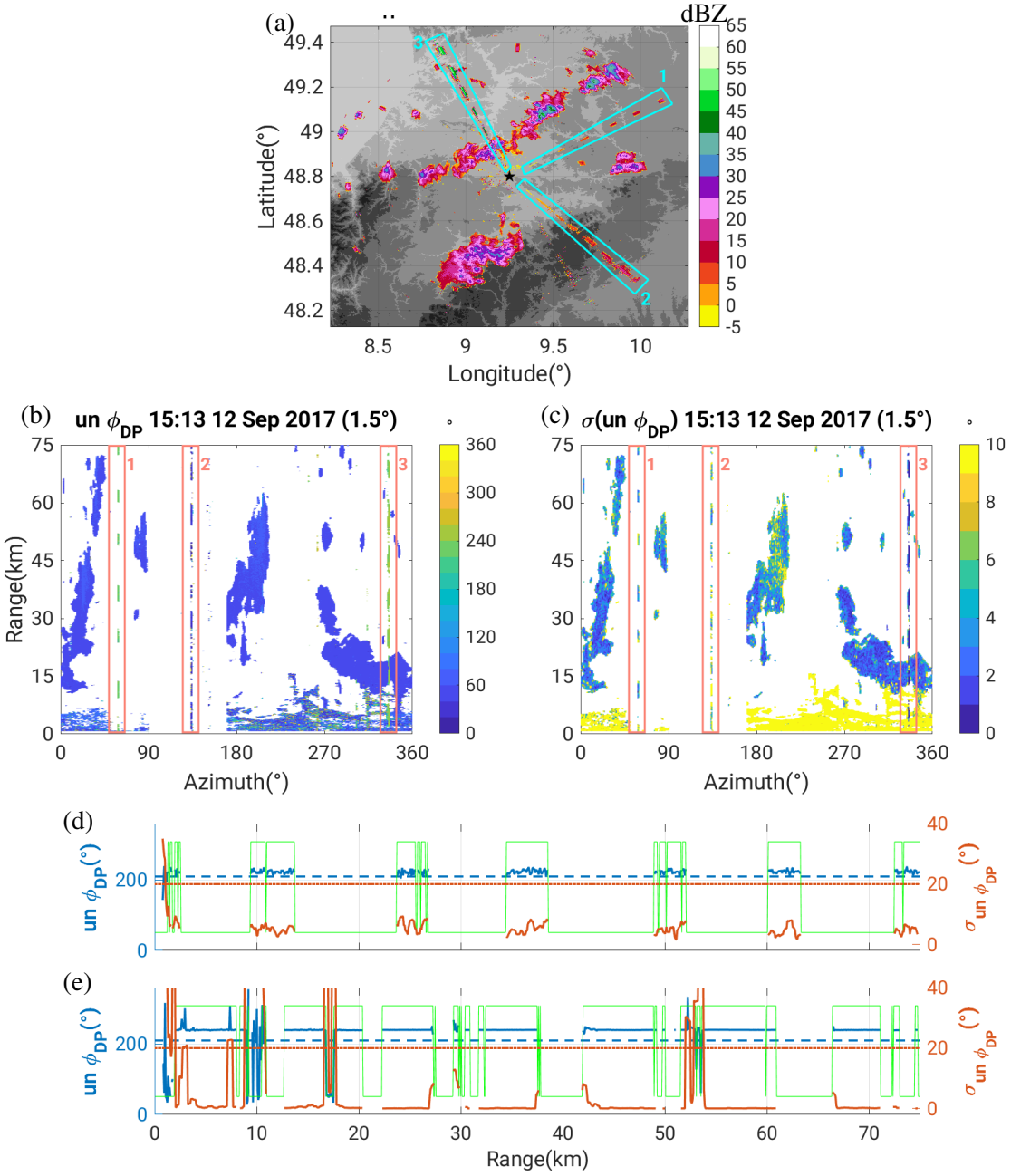

Fig. 4.3.: A case of spike signal at 15:13 UTC on 13 September 2017 to characterize and identify the spike signals using u-ϕ_{DP} and $\sigma_{u\text{-}\phi_{DP}}$, where (a) is a PPI display of Z_H at the 1.5° elevation (with the black star as the X-band radar site location), (b) is u-ϕ_{DP} in azimuth-range section, (c) is $\sigma_{u\text{-}\phi_{DP}}$ in azimuth-range section, (d) is the 60° azimuth ray section of u-ϕ_{DP} (in blue lines) and $\sigma_{u\text{-}\phi_{DP}}$ (in red lines), as well as flags for spike signals (in green lines), and (e) is the same as (d) but for the 335° azimuth

Clearly, it seems impossible to find another type of the EMtransmitter that is able to continuously send signals following such duration variations. These above characteristics of the spike signals help us narrow down the possibility for the source, which supports our assumption that these spike signals are from external shipborne navigation X-band radars along the Neckar River inland waterway in proximity to our X-band radar site. Besides, other X-band radar field experiments near waterways also

reveal the similar suspicious signals in their radar datasets. Note that this type of spike signal caused by shipborne radars is absolutely different from the echoes from ships' corner reflectors for C-band radars (Rico-Ramirez et al., 2007; Werner, 2014).

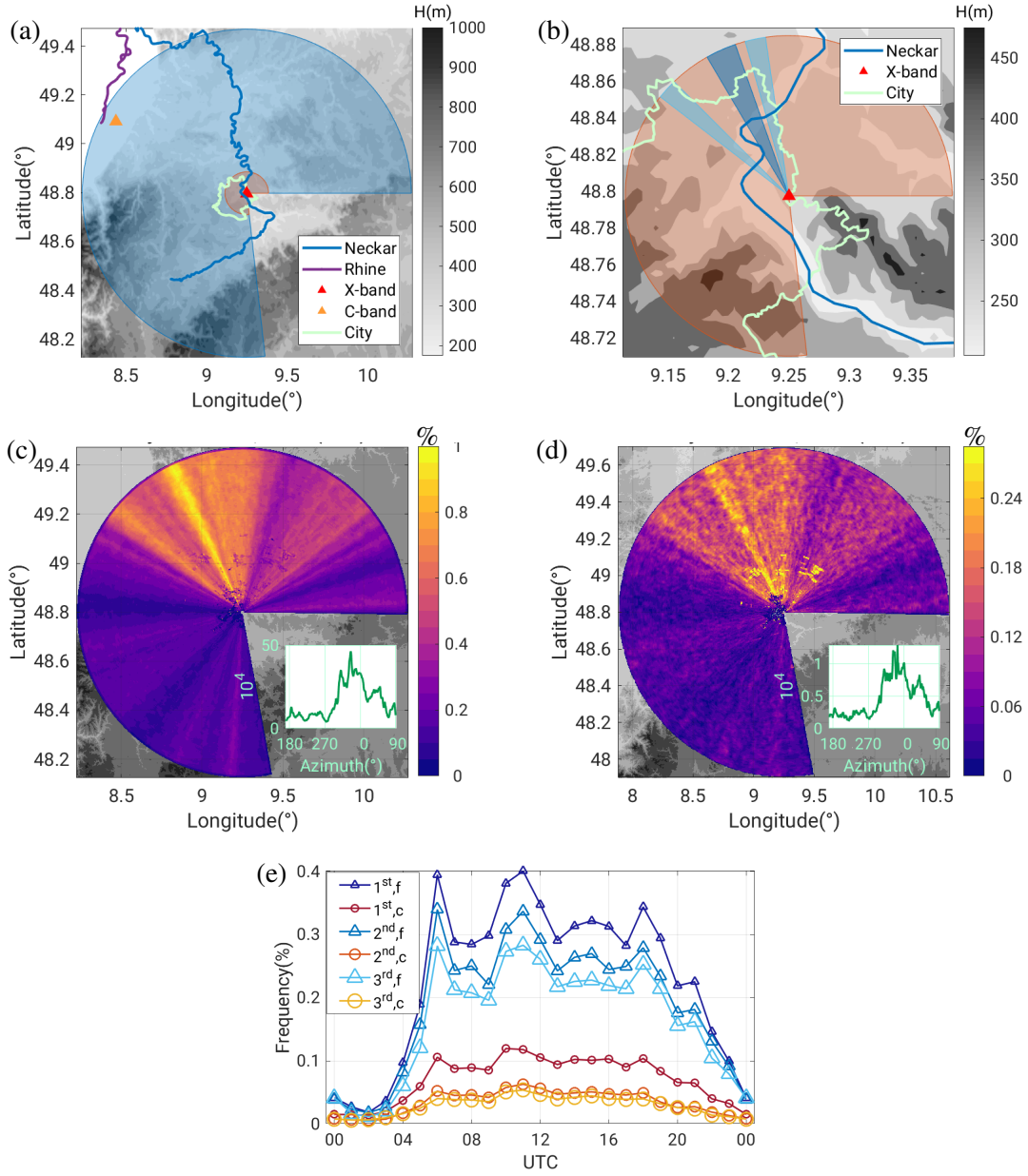

Fig. 4.4.: Spatiotemporal statistics of spike signals for the whole measuring period and its association with inland waterways, (a) the Neckar waterway within the 75-km range of the X-band radar, (b) the Neckar waterway within the 10-km range, (c) spatial distribution of relative frequency of spike signals over each radar gate for fine scan data, (d) the same as (c) but for coarse scan data, the small inserted plots in (c) and (d) are absolute frequency of spike signal along the azimuthal directions (the data within the 15-km range are excluded to mitigate the contamination of ground clutters), and (e) diurnal variation of the relative frequency of spike signals over radar sweeps of three elevations and all the radar gates

This type of spike signals becomes less frequent with the increasing elevations for both fine and coarse scans (Fig. 4.4(e)); higher altitudes can mitigate the impact from the waterway. Moreover, spike signals are much less frequent in coarse scans, which means the radar measurements with a higher spatial resolution are more subject to external emissions.

4.2.2. Spike signal identification and filtering

Filtering unwanted data (noise) usually has two steps—removing the suspicious data and fill in empty areas with the right values. Based on the characteristics of the polarimetric variables discussed above, we can identify spike signals on the basis of the u-ϕ_{DP} and its texture ($\sigma_{u\text{-}\phi_{DP}}$). These identified spike signals exhibit statically spatial distributions over some certain azimuthal directions and clear diurnal variations, arbitrary intensity and random azimuth directions from-scan-to-scan. Obviously, these spike signals were from a steady source during the entire measuring period. The X-band radars on the transporting ships near the Neckar waterway are the only sources within our X-band radar coverage accounting for the suspicious spike-shaped signals. To clarify, this spike signal we talk about should be distinguished from the echoes for C-band radars in the form of a trail along coasts, which are also caused by the ships(Werner, 2014; Rico-Ramirez et al., 2007).

After identification, the majority of the spike signals occur in the non-precipitating gates, and we treat them as not a valid measurement. However, the spike signals occasionally spear into precipitation (Fig. 4.2(a)), which means that these gates should have provided precipitation echoes had they not been contaminated by the spike signals. After removing the erroneous data over these gates, we interpolated the radar measurements from the adjacent azimuthal directions to fill in the removed data (the dark blue curve in Fig. 4.5). For example, we used the $Z_H$from azimuths of 311° and 314° to calculate the Z_H for the azimuth of 312° whose data are contaminated by spike signals.

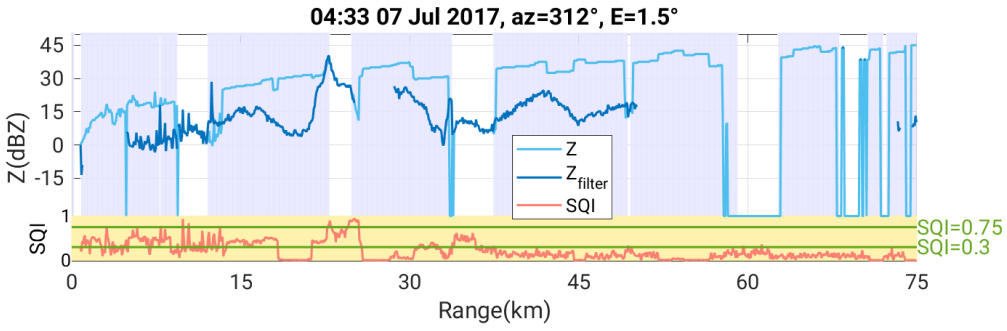

Fig. 4.5.: Ray cross-section at 312° azimuth of Z_H before (in light blue) and after (in dark blue) spike signal filtering, where the shaded areas are flagged as spike signals, and the red curve in the bottom part is SQI with two thresholds values of 0.3 and 0.75 in green horizontal lines

We also found that the spike signals correspond to SQI lower than a certain threshold (the red curve in the bottom part of Fig. 4.5), which is approximately 0.3 in our fine scan dataset. We might treat these radar gates with low SQI values but measurable radar reflectivity ($Z_H > 0\,\mathrm{dBZ}$) as spike signals; this is another criterion to filter out the spike signals.

4.3. Second-trip echo removal for fine scans

As discussed in Section 4.1.2, another type of extra echoes in the fine scan exhibits different characteristics from the spike signals above (Section 4.2). As follows, we present a brief theory of the second-trip echo (STE), show their existences in our dataset, seek for the criteria to remove them, and assess their effect on the specific differential phase (K_{DP}) retrieval and attenuation correction.

4.3.1. General concept of second-trip echo

A transmitter for the pulsed weather radar sends out EM signals, waits a while with the switched off radiation for the reflected signals, and then sends out the second series of signals. Ideally we assume the first series of signals has already returned to the radar before the second series of signals is emitted.

The PRF controls how often the transmission repeats or how long the transmitter is off between the first and second series of transmission. For instance, the PRF for fine scans is $2000\,Hz$ (Tab. 3.2), which means the transmission repeats each $0.666\,\mu$s. Such a 0.666-μs duration allows the signal to travel forth and back totally $c \times 2 \times 0.666\,\mu\mathrm{s} = 75$ km at the speed of light ($c \approx 3 \times 10^8\,\mathrm{m\,s^{-1}}$). Given this 75-km round-trip distance, all the signals reflected by the targets within r_{max} =75 km are able to return to the radar before the next series of transmission is sent out. For the signal reflected by the target located at $75 + \Delta r_0$ km away from the radar, it takes $\Delta t + 2\mu s$ to travel (note that $\Delta r_0 = c \times \Delta t$), but the radar wrongly supposes that this returned signal travels Δt only and is reflected from the target located at Δr_0 km away from the radar. This is the cause of the second-trip echo. According to the radar equation (Eq. 2.13), the intensity of the radar signal over a certain radar gate is proportional to the square of its distance to the radar (r). Given a certain total received power P_r regardless of the first-trip or second-trip echo, Z_H is corrected with a range factor of $1/r^2$. The second-trip echo is wrongly applied with a range factor of $1/(\Delta r_0)^2$ rather than the true $1/(75 + \Delta r_0)^2$, and thus its linear-scale radar reflectivity z_{ste} (with the uppercase letter) is expressed as

$$z_{ste} = \frac{(\Delta r_0)^2}{(\Delta r_0 + r_{max})^2} z_0 = \left(\frac{1}{1 + \frac{r_{max}}{\Delta r_0}}\right)^2 z_0 \tag{4.1}$$

where z_0 is the supposed linear-scale radar reflectivity if r_0 exceeds r_{max}, or if the range ambiguity occurs.

Eq. 4.1 tells us three points: i) z_{ste} is usually less than the supposed z_0, since the term $r_{max}/\Delta r_0$ is always positive (Eq. 4.1); ii) the larger Δr_0 is, the greater z_{ste} is; iii) the larger r_{max} is, the smaller z_{ste} is. Regarding the second point, for a convective system with Z_H of 55 dBZ (roughly 100 mm h^{-1} in rainfall rate if following Marshall-Palmer Z-R relation) located at 305 km away from the X-band radar ($\Delta r_0 = 5$ km), it is reported by the coarse scan as 19.3 dBZ (0.6 mm h^{-1}) at a fake location 5 km away from the radar. If this convective system moves to a location 310 km away from X-band radar ($\Delta r_0 = 10$ km), the second-trip echo is regarded as 25 dBZ (1.3 mm h^{-1}) at 10 km away from the radar. Thus, z_{ste} increases with an increasing Δr_0.

Regarding the third point, because r_{max} of the coarse scan is much longer than that of the fine scan (r_{max} =75 km), the effect of second-trip echoes is usually much less severe for the coarse scans. For fine scans, if a second-trip echo of 19.3 dBZ occurs at 5 km away from the radar, it requires a convective storm with Z_H of 43.5 dBZ at 80 km away from the radar, in contrast to Z_H of 55 dBZ in the coarse scan at 305 km away from the radar. We know Z_H of 43.5 dBZ (18.5 mm h^{-1}) is more likely to occur than Z_H of 55 dBZ, assuming the rainfall intensity probability distribution is spatially homogeneous in our area of study. It means the second-trip echoes in the fine scan data are more likely to reach moderate (or even heavy) intensity.

Moreover, for the coarse scan, the second-trip echo won't occur until the convective storm is located 300 km away from the radar, while the second-trip echoes occur in fine scans as far as any targets are situated beyond 75 km away from the radar. It means that the second-trip echo is more frequent in the fine scan data. Therefore, although the second-trip or multi-trip echoes may occur for both fine and coarse scans, the impact is far more severe in fine scans along with intenser and more frequent second-trip echoes.

We consider two scenarios to illustrate the causes of second-trip echoes in our X-band radar experiment. When the precipitation is located between 75 km to 100 km away from the X-band radar, both the C-band radar and the X-band radar coarse scan can observe this precipitation at its origin location (Figs.4.6(a) and (b)), but it appears between 0 km to 25 km away from the X-band radar with reduced intensity for the fine scan (Fig4.6(c)). When the precipitation is located between 100 km to 150 km away from the X-band radar in the northwestern azimuthal directions, it is visible to the C-band radar (Fig4.6(d)) but invisible to the coarse scan (Fig4.6(e)), and for the fine scan it appears between 25 km and 75 km away from the X-band radar (Fig4.6(f)).

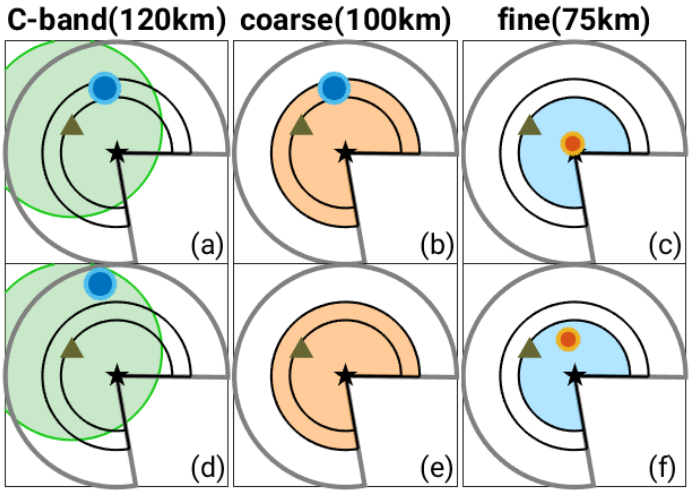

Fig. 4.6.: Configuration of second-trip echoes, where panels in the upper row are for precipitation in the range of 25–75 km, panels in the bottom row are for precipitation in the range of 100–150 km, the black stars/upward-pointing triangles indicate the location of the X-band/C-band radar, the blue filled circles are the location of the precipitation echoes, the red filled circles are the location of the second-trip echoes corresponding to the blue filled circles, the black unfilled circles are 75-,100- and 150-km range rings for the X-band radar, the green unfilled circles are 120-km range rings for the C-band radar, the light blue, light red and light green shaded areas correspond to the radar coverages for the X-band fine scan, coarse scan and C-band radar, respectively

In both scenarios, the second-trip echoes in fine scans represent the targets in wrong locations with incorrect Z_H intensity. In the second scenario, some radar echoes are present in the fine scan but absent in the coarse scan. Under the circumstance of no precipitation, if an echo only appears in a fine scan and not in the simultanous coarse scan, we can infer it is the second-trip echo; under the circumstance of second-trip echoes overlapped existing precipitation within the radar coverage, Z_H intensity of the existing precipitation in the fine scan is larger than that in the coarse scan without second-trip echoes. Therefore, the second-trip echo accounts for one of the major differences between the fine and coarse scans. Since the second-trip echo introduces "extra" measurement at the wrong locations with false intensity, we regard it as another type of noise and aim to filter it out.

To recap, we talked about the cause of second-trip echoes and their severe impact on the fine scan data. As follows, we verify the existence of second-trip echoes in our fine scan data via other concurrent measurements—coarse scan, rain gauge network and the nearly C-band radar—in terms of both power and phase measurements.

4.3.2. Characteristics of second-trip echoes in terms of radar reflectivity

According to the external Z_H measurement from the C-band radar (Section 3.2.1), only one large convective system was located between 60 and 110 km away from the X-band radar in the northwestern

direction, and the rest of the radar coverage was free of precipitation targets (Fig. 4.7(c)). The majority of this precipitation system was beyond 75 or even out of the observational coverage for the fine scan. Nevertheless, echoes with moderate intensity around 10–20 dBZ lay along the radar beams from the radar site to the radar coverage edge in the northwestern azimuthal direction of the fine scan (Fig. 4.7(a)); these echoes are present in neither the coarse scan data (Fig. 4.7(b)) nor C-band radar measurements. Associating to Fig. 4.6, we know these "extra" echoes that are merely present in the fine scan are the second-trip echoes of the large convective precipitation system beyond 75 km from the X-band radar.

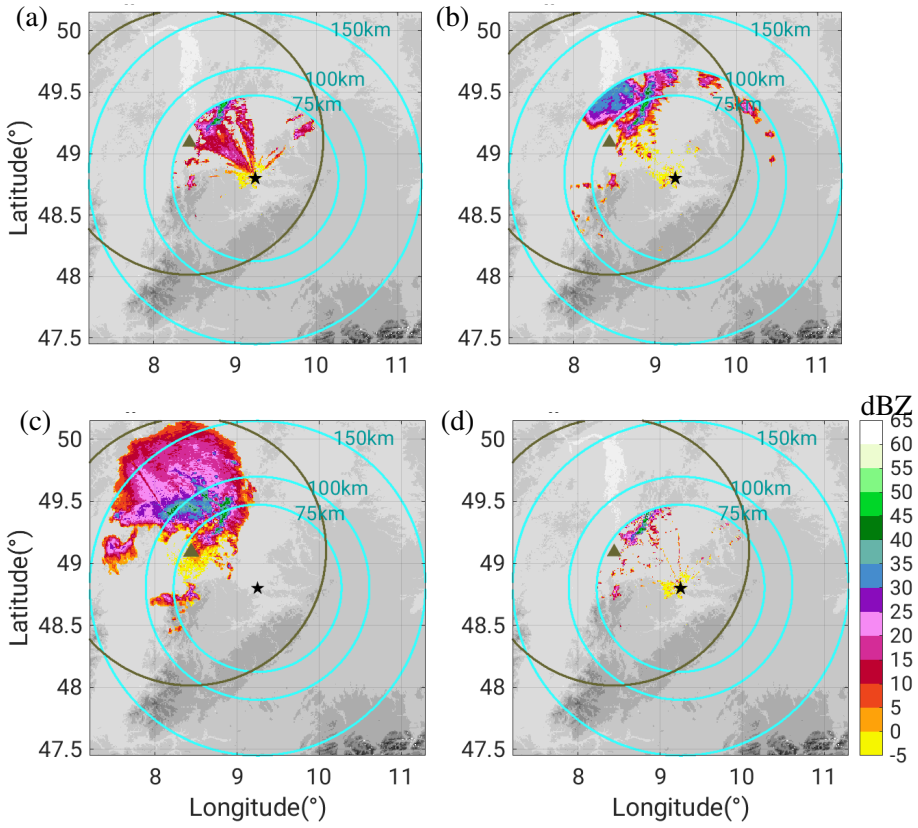

Fig. 4.7.: PPI displays of Z_H showing presences of the second-trip echoes in terms of Z_H on 7 July 2017, where (a) is for the fine scan at 00:03 UTC at the 1.5° elevation sweep, (b) is for the coarse scan at 00:04 UTC at the 1.5° elevation sweep, (c) is for the C-band radar at 00:05 UTC at the 4.5° elevation sweep, where the black star (or the upward-pointing triangle) indicates the location of the X-band (or C-band) radar site, the concentric circles in cyan indicate the 75-km, 100-km, 150-km range rings of the X-band radar, and the circles in bronze indicate the 120-km range rings of the C-band radar, and (d) is nearly the same as (a), but after filtering the second-trip echoes

Given that there was no precipitation within the 50-km range (Fig. 4.8(b)), we can infer all the additional echoes within the 50-km range of the fine scan are second-trip echoes. Using the Z_H measurements in the range of 75–100 km from the coarse scans and according to Eq. 4.1, we calculate the theoretical second-trip echoes (Fig. 4.8(d)). They reveal similar shapes as the measured second-trip echoes in the fine scan (Fig. 4.8(c)), and slightly less intensity owing to the radar reflectivity attenuation. This example clearly demonstrates the existence of second-trip echoes in terms of Z_H.

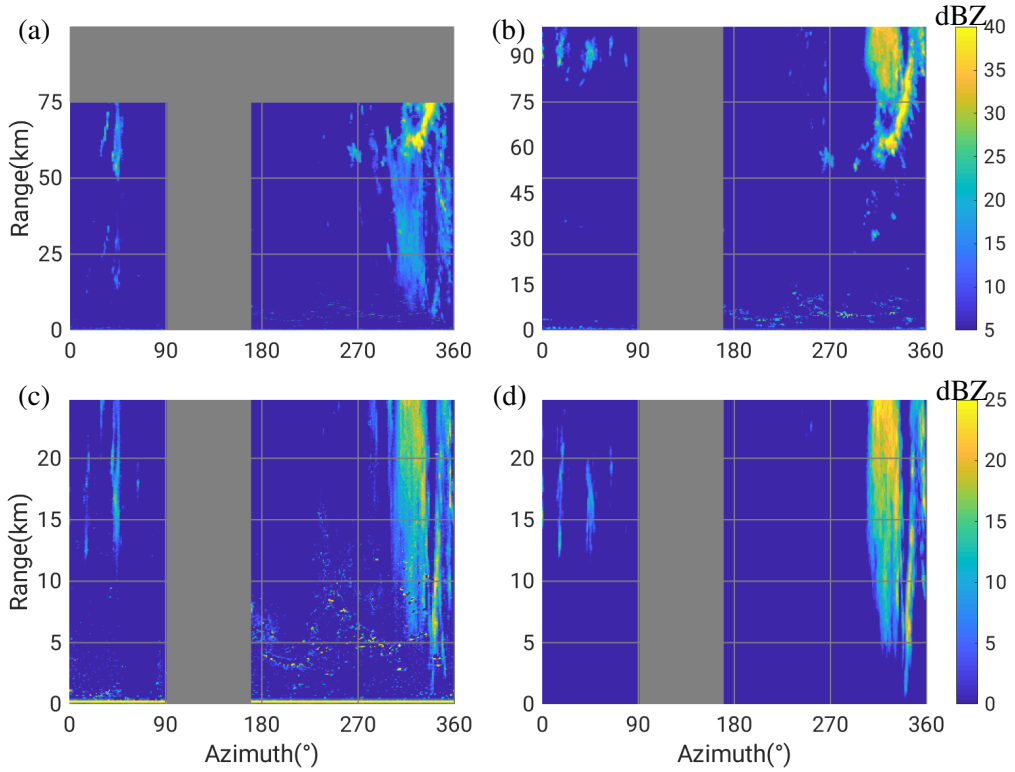

Fig. 4.8.: Illustration of the second-trip echo in terms of radar reflectivity Z_H for the case in Fig. 4.7, where (a) is $Z_H$of the fine scan at 00:03 UTC, (b) is Z_H of the coarse scan at 00:04 UTC, (c) is Z_H within 0–25 km radar coverage at 00:03 UTC, and (d) is the artificial Z_H in the 0–25 km range generated from the coarse scan in the 75–100 km radar coverage at 00:04 UTC

4.3.3. Characteristics of second-trip echoes in terms of differential phase

Second-trip echoes also exist in the form of the "extra" uncorrected differential phase u-ϕ_{DP} measurements, which is rarely discussed in literature. The u-ϕ_{DP} values of the second-trip echoes are quite different between the fine and coarse scans (Figs. 4.9(a) and 4.9(b)). Lack of u-ϕ_{DP} measurements within the 50-km range in the coarse scan (Fig. 4.9(b)) is in a good accord with the absence of precipitation within the 50-km range illustrated already in Figs. 4.7(c) and 4.8(b), which is in contrast to the presence of u-ϕ_{DP} within the 50-km range in the fine scan. However, by comparing Fig. 4.9(c) to Fig. 4.9(d), we find that u-ϕ_{DP} in the 0–25 km range of the fine scan is similar to that in 75–100 km range of the coarse scan, although part of radar gates lack the valid u-ϕ_{DP} in the 0–25 km range of the fine scan owing to the radar processor built-in ground clutter removal procedure.

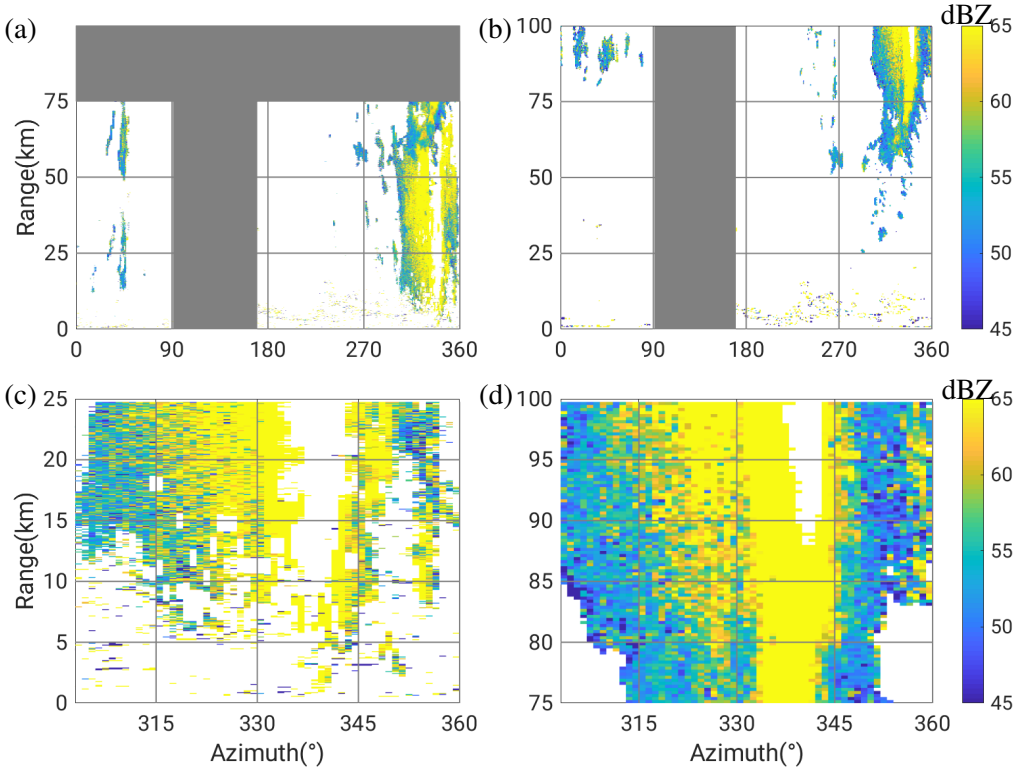

Fig. 4.9.: Illustration of the second-trip echoes in terms of u-ϕ_{DP} for the case in Fig. 4.7, where (a) is for the fine scan at 00:03 UTC, (b) is for the coarse scan at 00:04 UTC, (c) is for the fine scan within the 0–25 km radar coverage at 00:03 UTC, and (d) is for the coarse scan within the 75–100 km radar coverage at 00:04 UTC

Theoretically, unlike radar reflectivity, the differential phase has no range factor correction to reduce the magnitude of second-trip echoes. The second-trip echoes in terms of u-ϕ_{DP} remain the same magnitudes as the origin measurements, and are simply relocated from a farther range r km to a closer range $r - r_{max}$ km away from the radar. For instance, if we simply move u-ϕ_{DP} at the 75–100 km range measured by the coarse scan (the red curve in the upper plot Fig. 4.10(a)) to the 0–25 km range (the yellow curve in the upper plot Fig. 4.10(a)), despite the turbulent u-ϕ_{DP} measurements in the fine scan, both curves match well with each other. To mitigate the effect of the turbulent nature of u-ϕ_{DP}, we averaged u-ϕ_{DP} arithmetically over a few azimuths along the azimuthal directions, and ended up with a high linear correlation between the coarse scan in the 75–100km range (within the light yellow shading area in Fig. 4.10(b)) and the fine scan in the 15–25 km range (within the light yellow shade area in Fig. 4.10(b)). This close linear correlation in u-ϕ_{DP} measurements between the fine scan and the "relocated" coarse scan substantiates that the extra u-ϕ_{DP} measurements are due to the second-trip echoes.

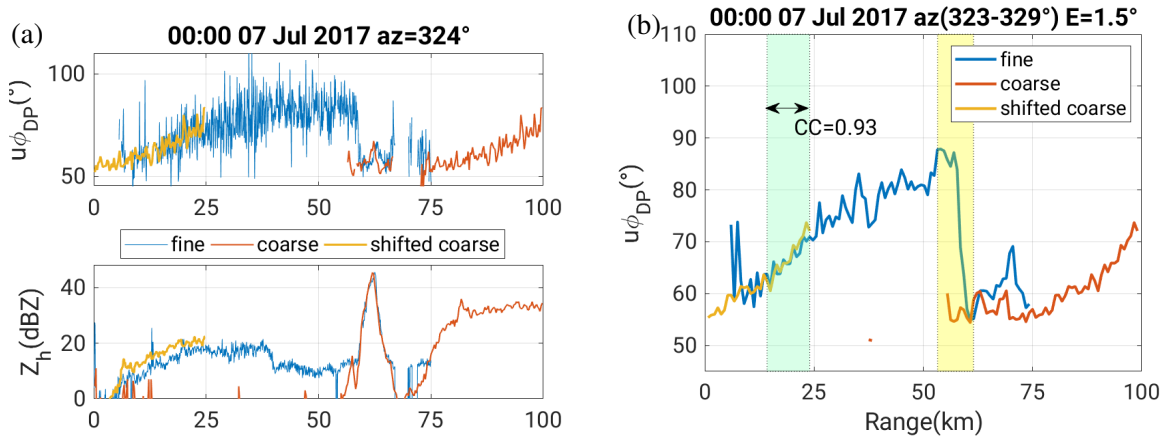

Fig. 4.10.: Ray cross-section to show second-trip echoes in terms of ϕ_{DP} at 00:00 UTC on 7 July 2017 for the case in Fig. 4.7, (a) u-ϕ_{DP} and Z_H for a single azimuth of 324° for the fine scan (in blue), the coarse scan (in red) and manipulated shifted coarse scan (in yellow), (b) u-ϕ_{DP} interpolated into 750-m Δr and averaged over azimuths from 323° to 329°. *CC* is the Pearson correction coefficient calculated in terms of u-ϕ_{DP} between the fine scan and the shifted coarse scan for the radar gates within the light green shaded area (roughly between 5 and 25 km range)

Despite a lack of the reference u-ϕ_{DP} in the coarse scan beyond the 100-km range, it is reasonable to infer that the extra u-ϕ_{DP} measurements in the range of 25–75 km in the fine scan (Fig. 4.9(a)) are also the second-trip echoes of the precipitation system in the 100–120 km range seen by the C-band radar (Fig. 4.7(c)). At the location roughly 60 km away from the radar, the second-trip echo diminishes and u-ϕ_{DP} returns back to the low value, resulting in a dramatic drop in u-ϕ_{DP} along the radar beam (Fig. 4.10(b)). Recall that K_{DP} is a derivative of differential phase relative to the distance to the radar, we thus expect large negative K_{DP} values at the edge of the second-trip echoes with dramatic drops in u-ϕ_{DP}. These negative K_{DP} values are caused by second-trip echo, have no physical implication for precipitation or cloud physics, and should be excluded. However, their removal is tricky, because these gates, although very close to the second-trip echoes, are not subject to the second-trip echoes and thus won't be filtered out by the second-trip echo filtering. Thus, we inevitably end up with some erroneous negative K_{DP} estimates due to the second-trip echo in format of u-ϕ_{DP}.

Comparing the upper and lower plots in Fig. 4.10(a), we easily see the second-trip echoes exist in the form of both power and phase measurements, indicated by the "extra" Z_H and u-ϕ_{DP} measurements solely in fine scans and not in coarse scans. The difference between the power and phase measurements is the reduced magnitude for second-trip echoes in the form of Z_H — the yellow curve in the lower part in Fig. 4.10(a) with Z_H much less than the red curve in the range of 75–100 km— and the unchanged magnitude for the second-trip echo in terms of u-ϕ_{DP}. Besides, the second-trip echo distorts the monotonic increasing trend of u-ϕ_{DP} (Fig. 4.10), which may induce errors for K_{DP} retrievals and associated rainfall estimation using K_{DP}.

If the probability of precipitation is assumed to be homogeneous and the probability of precipitation within the 75-km range is P, then the probability of second-trip or tripe-trip echoes within the 75-km range is $8 \times P$. Therefore, it is crucial to filter out second-trip echoes for fine scan data.

4.3.4. Second-trip echo removal procedure

In the operational application, the second-trip echoes can be prevented by using two pulse durations in the scan strategy or, is filtered during the radar signal processing (Zrinc and Mahapatra, 1985; Torres et al., 2004; Cao et al., 2011). However, our research investigates both the fine and coarse scans individually. Using the information from coarse scans to process the fine scan data conflicts with our initial purpose for this research. Therefore we need to seek other methods to filter out the second-trip echoes in our fine scans.

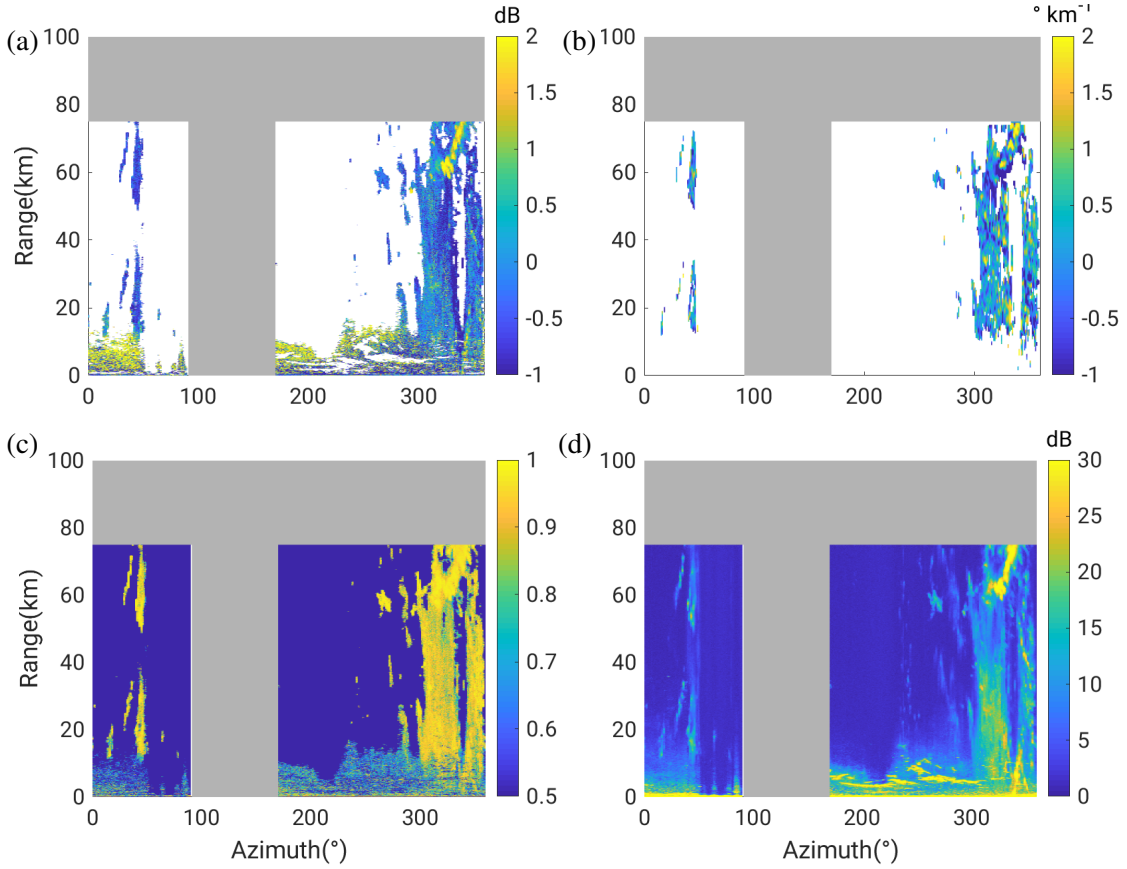

Fig. 4.11.: Azimuth-range sections of radar variables which are unable to detect second-trip echoes in the fine scan from the same case as Fig. 4.7, (a) Z_{DR}, (b) K_{DP}, (c) ρ_{HV}, and (d) SNR

In our X-band radar data, besides Z_H and u-ϕ_{DP}, the second-trip echoes also reside in the form of Z_{DR}, K_{DP}, ρ_{HV} and SNR (Fig. 4.11) and the magnitude of these variables over the second-trip echoes are comparable to that of weak precipitation; thus, it is inappropriate to distinguish the second-trip echoes

from weak precipitation by using these variables. For instance, although SNR is relatively low for the second-trip echoes, but its magnitude is comparable with SQI of the weak precipitation situated at the 270° and around 55 km (Fig. 4.11(d)). On the other hand, it implies that, utilization of these variables for other applications (non-meteorological echoes removal or precipitation estimation) should exclude second-trip echoes.

In contrast, the signal quality index SQI and Doppler velocity V_{Do} can serve as effective discriminators to detect second-trip echoes in fine scans (Fig. 4.12). Locations of precipitation determined according to the radar reflectivity exceeding 5 dBZ (Fig. 4.7(b)) tally well with the radar gates whose SQI values are over 0.4 in Fig. 4.12(a), and the SQI value for the second-trip echoes is at the comparable magnitude as these non-precipitation radar gates. According to this feature, we may identify a radar gate being contaminated by the second-trip echo if its Z_{H} exceeds 5dBZ but with very low SQI values (second-trip echoes may also occur over the gates with Z_{H} less than 5dBZ, but they are of little interest for precipitation estimation and so we excluded them in the following second-trip echo removal procedure). Similarly, there is no valid Doppler velocity V_{Do} over the radar gates affected by second-trip echoes, but these precipitation gates have valid V_{Do} measurements regardless of the intensity of V_{Do} or Z_{H}. Therefore, using the magnitude of SQI or the retrievability of Doppler Velocity can help us identify and filter out the second-trip echoes. In practice, we identified these radar gates with both Z_{H} over 5 dBZ and SQI less than 0.3 as the gates affected by the second-trip echoes. Because the SQI values fluctuate (Fig. 4.13), the SQI threshold of 0.3 is not fixed, and we added some tolerances to this threshold. The SQI value is well above 0.3 for the radar gates with precipitation (the shaded blue area), so this SQI filter can remove the unwanted noises, and simultaneously reserve the precipitation information—the overlap of the blue and red curves in the range between 35 and 67 km in Fig. 4.13(b). The SQI value in the coarse scan is irrelevant to the second-trip echo (the red curve in Fig. 4.13(a)).

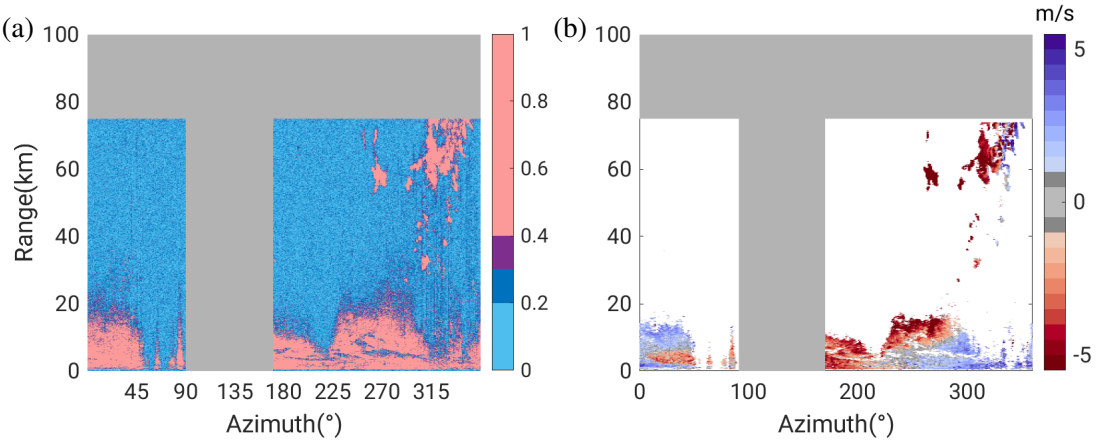

Fig. 4.12.: Azimuth-range sections of effective discriminators to detect second-trip echoes from the same case as Fig. 4.7, (a) SQI and (b) V_{Do}

The theoretical basis for using SQI is presented herein. SQI is also named as *normalized coherent power* (NCP). NCP is ratio of the power used to calculate the Doppler velocity to the total power used to calculate radar reflectivity. It means that, SQI or NCP is highly relevant to the Doppler velocity V_{Do}. Specifically, NCP is approximately inversely proportional to the Spectrum Width (Bell et al., 2013). SQI or NCP is very efficient in removing noise, with its value near one indicating strong coherence of the velocity, and with its value near zero indicating noise. In other words, the lower the SQI values are, the more likely that given radar return is noise (Lim and Chandrasekar, 2011). Although NCP indicates the probability of weather echoes, this single parameter alone is unable to define an optimal threshold to delineate weather echoes in all situations.

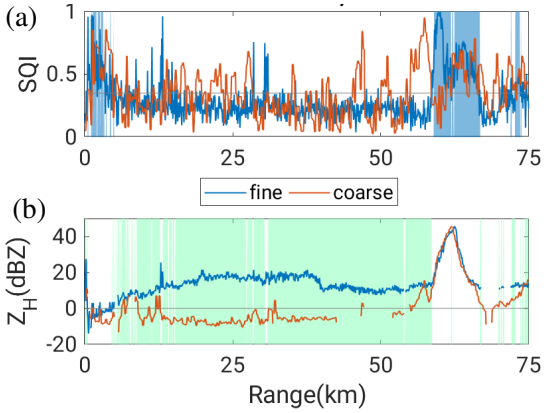

Fig. 4.13.: An example ray to show second-trip echo removal process using the SQI from the fine scan in the same case at 00:03 UTC 7th July 2017 as Fig. 4.7. (a) includes SQI for the fine and coarse scans respectively (in blue and red lines respectively), and the light blue areas are the radar gates with valid Doppler velocity values; (b) includes Z_{H} for the fine and coarse scans respectively (in blue and red lines respectively), and the light green areas flag the radar gates as being contaminated by second-trip echoes for the fine scan

The spatial distribution and diurnal variation of the identified second-trip echoes (Fig. 4.14) are quite different from those of spike signals (Fig. 4.4). First, the frequency of second-trip echoes decreases with the increasing distance away from the radar starting from roughly 15 km away from the radar, while there is no range degradation for spike signals. Within the 15-km range, the second-trip echoes are less frequent, probably due to the built-in clutter removal procedure which has already removed part of the suspicious second-trip echoes in the near range. Second, the second-trip echo is distributed more evenly across the azimuth directions except those suffering from partial blockage, while the majority of spike signals reside along the azimuths between 315° and 45°and is even more concentrated along the azimuth of 325°. Third, the identified second-trip echoes occur more frequently during the convective active period (13 UTC to 20 UTC, afternoon in the local time) (Figs. 4.14(c) and 4.14(d)), while the spike signals are frequent during the entire daytime including the mornings. This is because, according to Eq. 4.1, Z_{H} of second-trip echoes is usually weaker than the true Z_{H} magnitude of precipitation echoes, and so the diurnal variation of the second-trip echoes is essentially associated with the

diurnal variation of summer precipitation that is in moderate-to-heavy intensity. In additional to the forgoing three differences between the spike signals and the identified second-trip echoes, both are more prevalent in the lower elevations (Fig. 4.14(c)) since the radar beams are slanted. The precipitation echoes at altitudes between 2.0 and 3.9 km are responsible for the second-trip echoes in the 1.5° elevation, between 4.7 and 9.0 km are responsible for the second-trip echoes in the 3.6° elevation. Most stratiform precipitation is below 5 km in altitude, and only convective precipitation system can contribute to the second-trip echoes at the second elevation. Thus, we find a decrease of second-trip echoes with the increasing elevations.

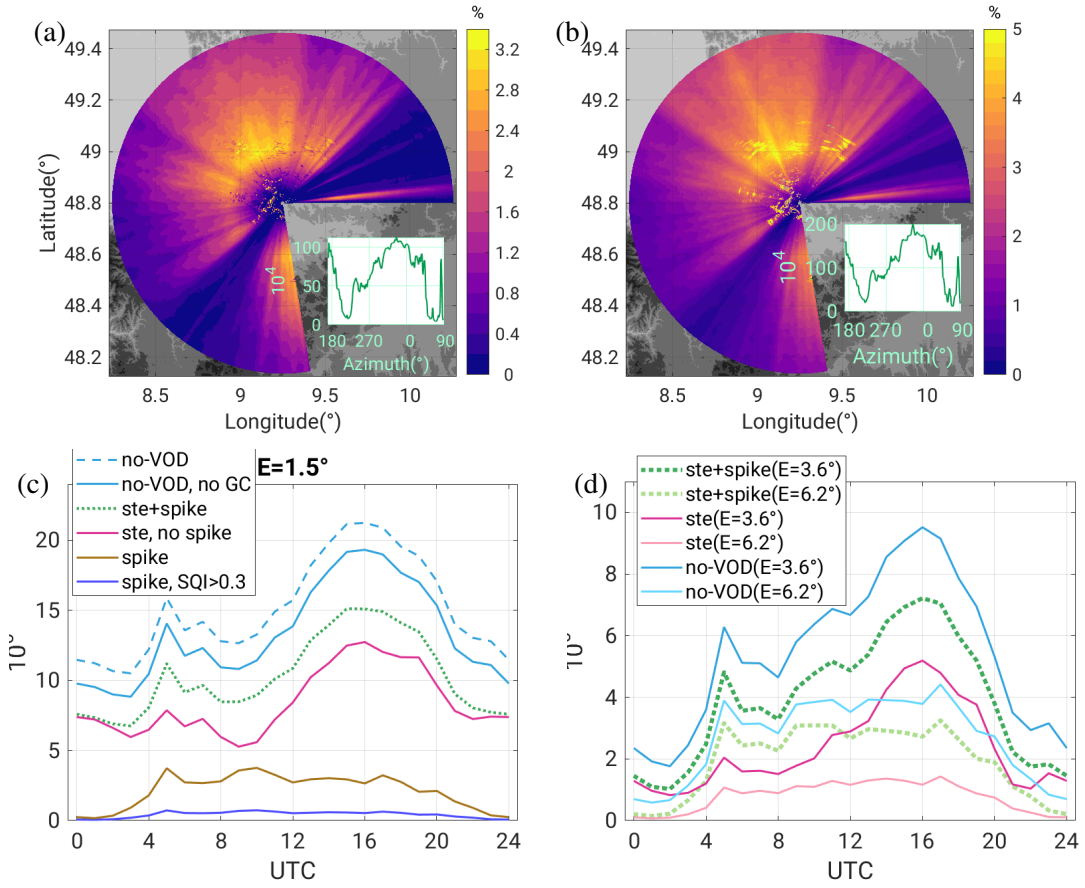

Fig. 4.14.: Spatiotemporal statistics of identified second-trip echoes (a) using the filter based on SQI, (b) using the filter based on Doppler Velocity V_{Do}, diurnal variation of the absolute occurrence frequency of identified radar gates by different filters for the radar data (c) at the first elevation and (d) at the second and third elevations. The small inserted plots in (a) and (b) are summations of the absolute frequency of identified second-trip echoes along the azimuth distribution (data in the first 15-km range are excluded to mitigate the impact of ground clutters); in (c), the curve from the upper to the bottom represent the number of second-trip echoes identified by the V_{Do}-based filter (dashed blue line), the number of second-trip echoes identified by the V_{Do}-based filter excluding ground clutter gates (solid blue line), the number of second-trip echoes identified by the SQI-based filter (dotted green line), the number of second-trip echoes identified by the SQI-based filter (dotted green) excluding the gates identified as spike signals based on the spike filters (magenta solid line), the number of spike signals identified by the spike filters (Section 4.2.2) (brown solid line), the number of spike signals identified by the spike filters but unable to satisfy the SQIfilters (violent solid line), respectively; in (d) the lines have similar meaning as those in (c), but for the second and third elevations of 3.6° and 6.2°

The second-trip echo filter based on the retrievability of Doppler velocity V_{Do} tends to identify more second-trip echoes than the filter based on SQI (Figs. 4.14(a) and 4.14(b)). Specifically, some radar gates clustered in several small irregularly shaped groups within the 30-km range (Fig. 4.14(b)) are characterized by very high frequency of invalid Doppler velocity V_{Do} measurements, and these gates tally with ground clutters (Section 4.4). It implies that V_{Do}-based filter also tends to leave out the radar gates contaminated by the ground clutters. However, even if we exclude these gates frequently contaminated by ground clutters (the blue solid curves in Fig. 4.14(c)), the number of second-trip echoes identified by the V_{Do}-based filter still surpasses those identified by SQI. The remaining excess is partially owing to lack of invalid V_{Do} measurements for radar gates along the edges of precipitation systems. It implies that the V_{Do}-based filter also tends to leave out a portion of radar data but that portion in fact is not affected by second-trip echoes, in additional to the excess associated with the ground clutters. Therefore, it is inappropriate to use the V_{Do}-based filters, and instead we prefer to use the SQI-based filters, corresponding to our intention to keep as much useful information as possible rather than an exhaustive filtering.

Since the majority of spike signals have low SQI values (Section 4.3.4), the filter was originally intended to remove second-trip echoes according to the low SQI values but also inevitably filters out spike signals (the green dotted curves in Fig. 4.14(c)). If we exclude the spike signals which are also filtered out by the SQI-based filters, we can exclusively obtain the number of second-trip echoes identified by the filters based on the low SQI values (the magenta solid curve in Fig. 4.14(c)). For instance, at 05 UTC in the first elevation, the number of second-trip echoes identified by SQI values is around 7.5 million, and the number of a combination of second-trip echoes and spike signals is around 11 million. Analogous to the difference between the dashed blue curve and solid blue curve for the V_{Do}-based filters, the actual number of second-trip echoes filtered out by SQI is relatively 15%–30% less than the inclusive number before separating the spike signals and second-trip echoes. Then we compared the real number of second-trip echoes filtered out by second-trip echo filters based on both V_{Do} and SQI —the number of radar gates filtered by the V_{Do}-based filters excluding the radar gates contaminated by ground clutters (the blue solid curve) and the number of radar gates filtered by SQI-based filters (the magenta solid curve in Fig. 4.14(c)). It turns out a nearly constant spacing between them, which again illustrates the surplus of radar gates filtered out depending on the retrievabililty of V_{Do}.

Although the filter based on the low SQI values also removes the spike signals, it is not complete. Not all the SQI values of spike signals are below the predetermined SQI threshold for which we use value 0.3 here. Roughly 20% of spike signals will be omitted if we identify the spike signal by merely using the SQI values, when comparing the portion of the lowest line relative to the second lowest line in Fig. 4.14(c)). It implies that using SQI-based filters is unable to remove both second-trip echoes and spike signals simultaneously and it is necessary to keep an independent spike signal filter aside from considering the SQIvalues.

Given the characteristics of the above three types of filters, the SQI-based filter identifies the second-trip echoes and majority of the spike signals, while the V_{Do}-based filter identifies second-trip echoes but also other gates contaminated by ground clutter or along the edge of precipitation systems. Acknowledgedly, there is a gap between the identified second-trip echoes and intrinsic second-trip echoes, the same for the identified spike signal and the intrinsic spike signals. For instance, ideally we assume the spike filter used in Section 4.2.2 identifies all the existing spike signals, but in fact it still omits a small number of intrinsic spike signals. Similarly, the filter based on a fixed predetermined SQI value might ignore a small portion of second-trip echoes. However, it is more or less useless to separate the spike signals and second-trip echoes when we tend to filter out these suspicious data within our radar dataset in practice. Thus the most efficient option is to apply both the spike filter and the SQI-based second-trip echo filter, and then we can remove nearly all the spike signals and most of second-trip echoes. Otherwise, if we aim to identify merely the second-trip echoes, we can use the SQI-based filter and then exclude the spike signals already identified by the spike filter (the magenta solid curve in Fig. 4.14(c)).

4.4. Z-based ground clutter identification

Radar images often contain radar gates with very high radar reflectivity Z_{H} distributed in irregular shapes in the region without precipitation. Such high Z_{H} values are caused by physical structures whose surfaces are able to reflect the EM signals such as buildings, trees, wind farms, and communication towers. These structures are referred as Ground Clutter (GC) targets, and these radar gates with high Z_{H} are referred as GC gates. Although physical locations of these targets are normally geographically stationary over a certain period (such as the five-month measuring period for our X-band radar experiment), these GCs are in slightly changeable locations in proximity to the GC targets, and vary in Z_{H} intensity. This change is due to the fact that the propagation path of radar beams through the atmosphere is governed by the continuously varying atmospheric temperature and humidity.

The refractive index (Eq. 2.22), which quantitatively represents the variations of air temperature and humidity, is used to calculate the propagation path of radar beam using vertical variations of refractive index. For simplicity, we assume the standard atmosphere scenario (Section 2.1), and determine the radar beam propagation path using the assumed refractive index for the "standard atmosphere". If the real-time refractive index differs much from the assumed value, then the propagation path of radar beam will deviate much from the assumed path, causing AP (Section 2.1). In some extreme circumstances, the curvature of the radar beam is so large that it bends to the ground at an intersect point much closer than the supposed location, or is so small that the radar beam never reaches the ground. The former scenario occurs often when a shallow layer of moist cool air lays at the ground surface after intense

convective storms' departure. The changeable nature of GCs increases the difficulty to delineate them sharply from precipitation targets.

One feature which assists us in delineating GCs is that high Z_H magnitudes occur much more frequently over these GC gates than normal levels. Acknowledgedly, the complex topography is characterized with enhanced precipitation. For example, in the Black Forest region, the occurrence frequency of precipitation (from light to heavy rain) is less than 15% and of the heavy precipitation only is less than 2% (Zheng et al., 2019). However, the occurrence frequency of moderate-to-high Z_H over these GC gates is even much higher than these regions with enhanced precipitation. In general, if a radar gate continuously reports radar reflectivity with measurable intensity (at least greater than 5 dBZ) and quite often with moderate intensity (greater than 35dBZ), this gate should be identified as a GC gate. Based on the probability frequency of Z_H reaching measurable and moderate intensity for each radar gate, we establish a map to show geographic distribution of the frequent GCs within the radar coverage.

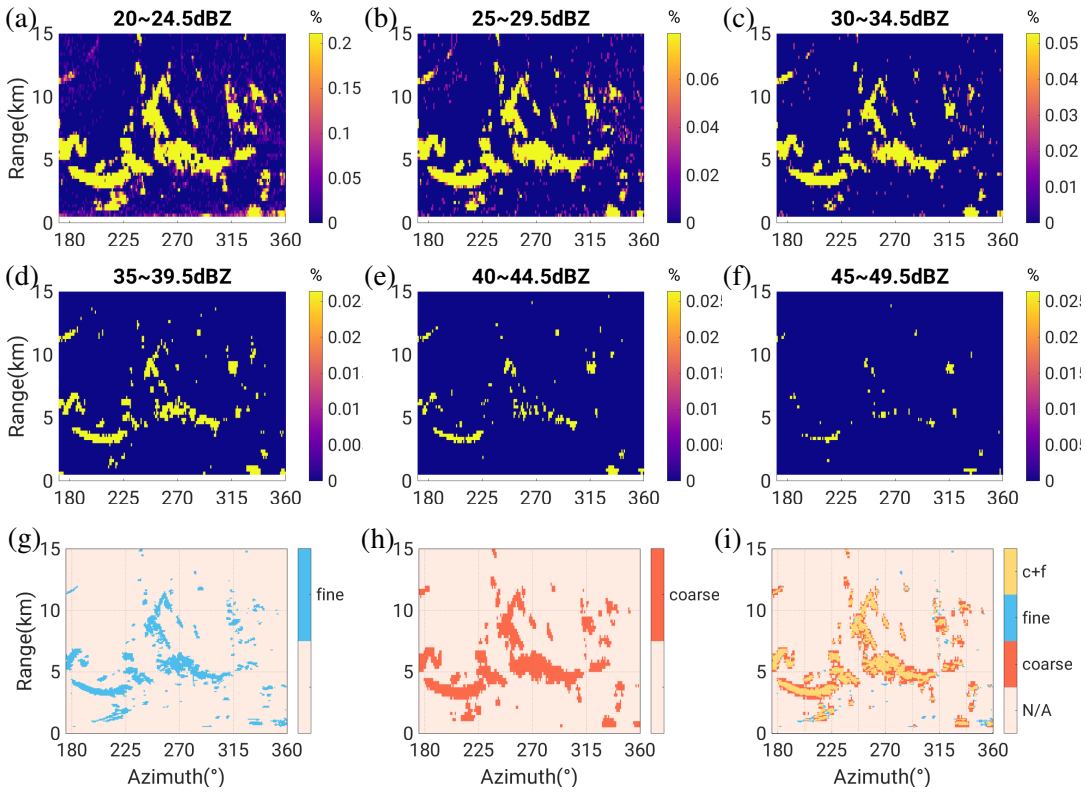

Fig. 4.15.: Mapping of occurrence frequencies of Z_H within different intensity ranges in azimuth-range coordinate (across the 0-15km range and the 180-360° azimuths) during the predetermined non-rainy period (totally 25 whole days), (a) between 20 and 25 *dBZ*, (b) between 25 and 30 dBZ, (c) between 30 and 35 dBZ, (d) between 35 and 40 dBZ, (e) between 40 and 45 dBZ, (f) between 45 and 50 dBZ, the "static" GC gates based on (g) the fine scan only, (h) the coarse only, and (i) both fine and coarse scans

The Z_H intensity of signals reflected by the GC targets varies, depending on the wetness or materials of the surface of those targets. To address this large variation of echo intensity, we stratify the

radar reflectivity measurements into six different intensity ranges: 20–25 dBZ, 25–30 dBZ, 30–35 dBZ, 35–40 dBZ, 40–45 dBZ and 45–50 dBZ). Only Z_H measurements from 25 non-rainy days are involved to avoid misleading echoes from precipitation and insects, and the spike signal should be also filtered in advance. A radar gate is identified as a GC gate if it has "unrealistically" high frequency of radar reflectivity in one of the intensity ranges. For instance, if a radar gate has more than 0.2% relative frequency of Z_H falling between 20 and 25 dBZ, it is deemed as a GC gate (Fig. 4.15(a)). Similarly for other intensity ranges but with different thresholds for the relative frequency, we obtain six sets of GCs gates and then combine them. Such multiple thresholding helps us detect GCs regardless of its changing intensity, and thus reduces missed detections. This procedure is the same for both fine and coarse scans.

Although the lowest elevation of our volume scan in this X-band experiment was set to be 1.5° in order to avoid "seeing" the GCs, GCs still exist within the radar coverage, especially along the southwestern directions where the Stuttgart downtown is situated. The GC gates identified by either the fine or coarse scan data both align well with the topographic features such as ridges (Fig. 4.16), but the GC gates in either fine or coarse scans exhibit different characteristics in terms of effective area and Z_H intensity. First, the GCs identified by the coarse scans have a larger areal extent (the greater area in color red in Fig. 4.16). If we interpolate both the blue and red areas into a polar coordinate with 25-m radial resolution, then proportion of GC gates identified by the coarse scans takes up 2.1%, larger than that of 1.3% by the fine scans. The smaller areal extent of the GCs in fine scans implies a high efficiency in data usage. Second, the GCs identified by coarse scans are characterized by higher Z_H (comparing between Figs. 4.17(a) and 4.17(b)). For the GCs identified by both fine and coarse scans, their mean Z_H values in coarse scans are much larger than that of fine scans (Fig. 4.17(c)), in sharp contrast to these radar gates identified neither by fine nor coarse scans whose mean Z_H values in fine scans are reversely slightly greater than those of coarse scans.

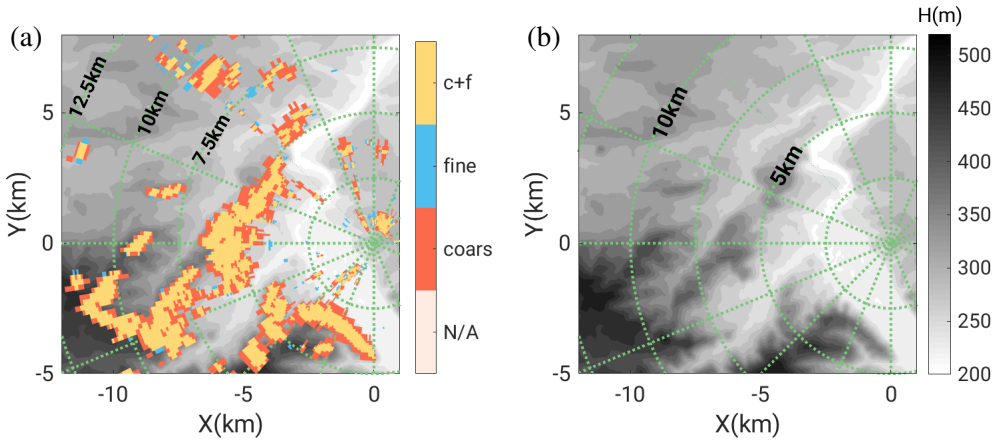

Fig. 4.16.: (a) Mapping of static GC gates in polar coordinate with underlying topography, where the blue (red) shaded area corresponds to GCs identified by fine (coarse) scans and the yellow area corresponds to GCs identified by both fine and coarse scans, (b) the corresponding topography

Both differences indicate that the GC contaminations are less in fine scan data whereas coarse scans end up with a larger positive bias in terms of radar reflectivity due to the presence of GCs. As mentioned that we have set the lowest elevation as 1.5° to avoid the GCs as much as possible, the advantage of fine scans, or the benefit of using this shorter radial resolutions, could be more pronounced if the radar is situated in the center of a region that is scattered with a number of artifacts such as wind farms.

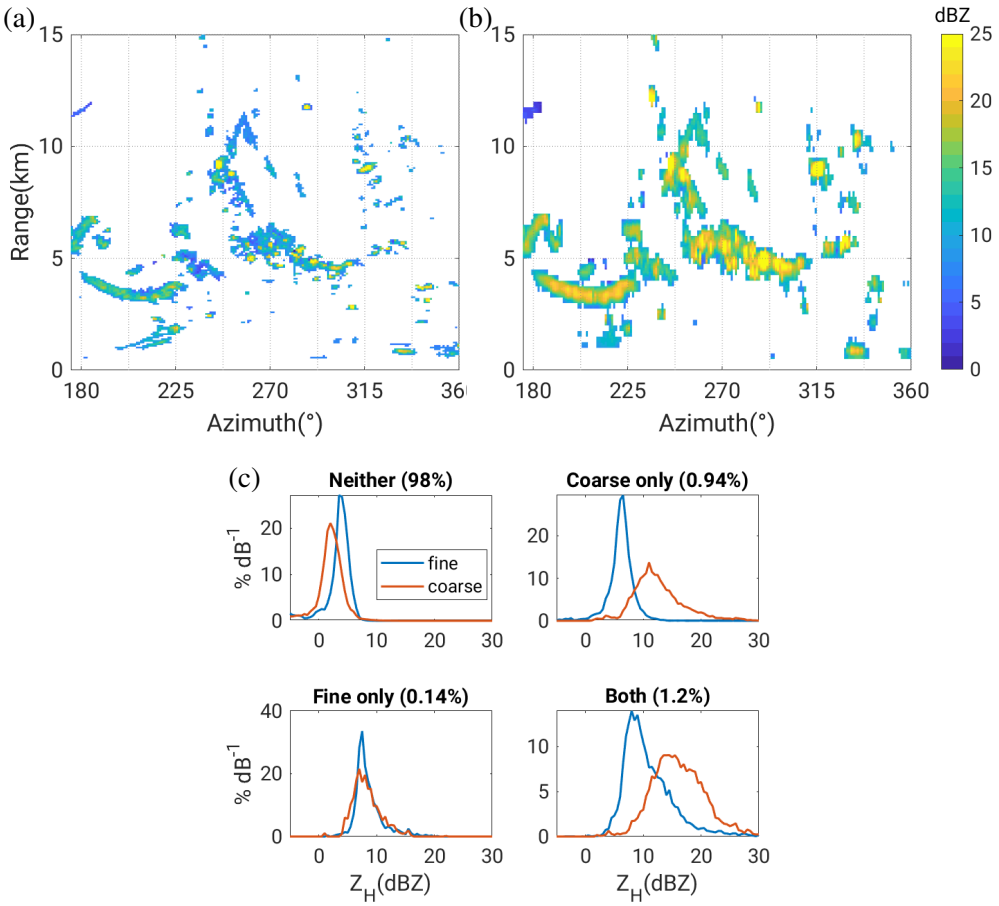

Fig. 4.17.: Comparison of echo intensity between fine and coarse scans in terms of Z_H over GC gates determined using the multiple-thresholding procedure, mapping the Z_H averaged over the entire measuring period of the GC gates determined from (a) fine scan data, and (b) coarse scan data, (c) PDFs of Z_H between fine and coarse scans over deliberately interpolated 25-m resolution radar gates, identified neither by fine nor coarse scans (the left upper panel), by coarse scans only (the right upper panel), by fine scans only (the left bottom panel), by both fine nor coarse scans (the right bottom panel), respectively

In brief, the characteristics of GCs differ between the fine and coarse scans in terms of the occurrence frequency and Z_H intensity of the GCs. The identified GCs are less prevalent in fine scans, implying that the high spatial resolution can help mitigate the negative impact of GCs. Regardless the difference, we apply the same procedure for both fine and coarse scans to identify GCs on the basis of abnormally high frequencies of Z_H measurement, obtaining the static GC maps for fine and coarse scans respectively. For simplicity, we discard all the measurements over these fixed GCs, by assuming that these GCs are spatially steady. However, the assumption is invalid because GCs are changeable; it is

the drawback of this static mapping method. Thus, we need another method that is able to identify GCs dynamically.

4.5. Non-meteorological echo removal

One application of the polarimetric information is non-meteorological echo removal (NMER). It was one of the motivations for weather radar polarimetry. The reason is, in case of radar dataset with single-polarization variable but without polarimetric variables, the echoes returned from non-meteorological scatters are always mixed with precipitation echoes, making the radar dataset unreliable and even questionable.

One important part of this section is to develop a NMER procedure by virtue of the polarimetric variables from our X-band radar measurements. The NMER is a common procedure for distinguishing between the non-meteorological echoes and precipitation echoes, but the algorithm depends on the radar instruments and the radar data. Thus, for our X-band radar dataset, we need to develop our own FLC algorithm.

We also aim to compare characteristics and performances of this NMER applied over between fine and coarse scans to see whether the higher spatial resolution in radar measurement can facilitate the NMER procedure. As follows, we first inspect the characteristics of different echo types, then use a quantitative fuzzy logic classification (FLC) procedure to identify automatically these echoes types, and then assess the results of identification.

4.5.1. Polarimetric characterization of echo classes

A radar receives returned signals regardless of the types of targets. It means, although precipitation is of our interest, the radar measurements unavoidably include the echoes reflected by other non-meteorological targets. The traditional ρ_{HV} thresholding is an easy method to identify and remove the non-meteorological echoes, especially in the operation sectors. However, in a strict sense, ρ_{HV} thresholding has a few limitations related to non-uniform beam filling and its dependence on the radar system performance (Section 2.2).

Besides the GCs (Section 4.4), biological scatterers, such as insects, were also prevalent in our radar coverage (recall that our experiment was conducted in a vineyard during the summertime when insects were ubiquitous). Another type of echoes, which is absolutely distinct from either insect echoes or GCs (Appendix B.1.3), also occurred during the non-rainy period, but it was rare so we don't discuss it separately here. Thus, our radar dataset mainly consists of three types of echoes: GC including AP (Section 2.1), biological scatterers primarily from insects—Insect echo (IC), and precipitation echo (PR)

Correspondingly, we will classify the radar echoes into these three categories. Each type of echo has its distinctive characteristics. For example, ρ_{HV} values are low for the GCs but high and more uniform for precipitation. However, a single radar variable is not sufficient to separate the classes decisively, because there are usually a few exceptions. For instance, the ρ_{HV} values are also low for the tumbling hails within the intense convective storm. Combing variables can help resolve this insufficiency. For instance, high radar reflectivity Z_H cannot distinguish between heavy rain and hail, but a combination of high Z_H and near-zero Z_{DR} indicates a strong probability of dry hails, and a combination of high Z_H and near-zero Z_{DR} with collocated ρ_{HV} depression implies the presence of wet hailstones.

Several techniques have been investigated to classify the echoes (Straka et al., 2000; Marzano et al., 2007; Dolan and Rutledge, 2009; Schuur et al., 2012; Chandrasekar et al., 2013; Grazioli et al., 2015; Bechini and Chandrasekar, 2015; Wen et al., 2015; Besic et al., 2016). Among these techniques, several studies have proved the capacity of FLC method in identifying echo types (Zrnic and Ryzhkov, 1999; Liu and Chandrasekar, 2000; Gourley et al., 2007; Park et al., 2009; Al-Sakka et al., 2013; Dufton and Collier, 2015; Krämer and Verworn, 2008; Dufton and Collier, 2015). We will present the procedure of constructing our own FLC and its application into our X-band radar data as follows. Basically, our method is adjusted on a combined basis of Krause (2016) and Dufton and Collier (2015).

The basic principle of the FLC is to combine and utilize the characteristics of several radar variables to achieve a more definite separation among echoes. The practice of this FLC procedure might vary among different studies. First, they vary in terms of the suspected targets. Park et al. (2009) and Marzano et al. (2006) further classified the precipitation targets into big drops, snow, light rain, heavy rain, graupel and so on. Thompson et al. (2014) aimed to distinguish mainly the solid precipitation such as dry snow or wet snow, graupel, and deliberately excluded the data below 3 km. For the radar situated onshore, the sea clutters should be taken into account. Second, the radar data are different. The polarimetric variables such as ϕ_{DP} are frequency-dependent, so its representation in the FLC should be adjusted quantitatively if shifting from S-band to X-band radar data. For the radar data in which the variable Linear Depolarization Ratio (L_{DR}) is available, hailstones are much easily detected (Straka et al., 2000). Third, these algorithms are different. Dufton and Collier (2015) added the range correction in their FLC. Liu and Chandrasekar (2000) used beta functions. Someone applied artificial intelligence to train their dataset. Someone relied on the polarimetric variables from the theoretical simulation such as T-matrix (Al-Sakka et al., 2013) for establish the training dataset. Temperature information was incorporated often (Al-Sakka et al., 2013; Schuur et al., 2012; Kouketsu and Uyeda, 2010).

In addition, the discriminators (variables that help us discriminate classes of echoes) involved in numerous versions of the FLC are different, although intuitively it is better to involve more variables available to include more comprehensive information. For instance, GCs are usually characterized by low Doppler velocity V_{Do} (-1 – 1 $m\,s^{-1}$) so V_{Do} is often used to detect GCs (Krause, 2016). Nevertheless, the unambiguous velocity in our coarse scan dataset is so low that the measured V_{Do} of 0 $m\,s^{-1}$

might be intrinsically $4\,\mathrm{m\,s^{-1}}$ and other multiples of $4\,\mathrm{m\,s^{-1}}$, hence the reason we cannot trust V_{Do} in our echo classification. In addition, Z_{H} is also often used in identifying echoes, because Z_{H} less than 0 dBZ corresponds to $0\,\mathrm{mm\,h^{-1}}$ rainfall rate or equivalently absence of rain, and insects usually correspond to Z_{H} between 0 and 20 dBZ. However, in our dataset, Z_{H} at the far range (beyond 50 km away from the radar) deteriorates faster than the range degradation for C-band or S-band radars, due to the strong signal attenuation (Section 4.6). The variation of Z_{H} along the radial direction might be even greater than differences of Z_{H} between different types of echoes in our investigation. The case study below also confirms that Z_{H} is poor in distinguishing between targets. As a result, our FLC procedure mainly relies on the following five discriminators: Z_{DR} and its texture parameter $\sigma_{Z_{\mathrm{DR}}}$, ρ_{HV} and its texture parameter $\sigma_{\rho_{\mathrm{HV}}}$, and it texture parameter of u-ϕ_{DP} $\sigma_{\mathrm{u}\text{-}\phi_{\mathrm{DP}}}$.

A complete FLC procedure theoretically consists of four components: i) fuzzification and membership functions, ii) inference, iii) aggregation, iv) defuzzification (Liu and Chandrasekar, 2000; Dufton and Collier, 2015). The main step in our FLC procedure is to determine the membership function (MF) for each echo and for each radar variable, which requires a training dataset comprised of the volumetric scans clearly containing GCs, insects or precipitation. We selected the volume scans by inspecting radar images by eye. To guarantee that the training dataset is representative enough, these volume scans for studying the GCs and ICs are not only from the long dry period but also shortly before or right after either stratiform or convective precipitation. Moreover, our measuring period lasting from May to October precludes the possibility of solid precipitation (except occasional hails), hence the reason we only discuss liquid precipitation. However, the liquid precipitation may be diverse. For instance, a rain event dominated with a large number of small raindrops might exhibit different polarimetric characteristics from a rain event containing a small number of large raindrops. To ensure representativeness, our discussion includes a large variety of rain events—scattered isolated convective storms, large-scale stratiform precipitation, small-sized light rain, a cluster of convective storms embedded or followed by stratiform precipitation. Eventually, this training dataset involves a large number of volume scans and is supposed to be sufficiently large (Table 4.1), and representative enough as well. We try to avoid the presence of second-trip echoes in the cases selected herein, although in principle the second-trip echoes should show characteristics identical to the meteorologic returns.

Tab. 4.1.: The fuzzy logic classification training dataset for three classes of echoes: ground clutter (GC), insect echo (IC) and precipitation echo (PR). Note that an episode includes an unfixed number of volume scans

Echo type	GC	IC	PR
Number of episodes	14	20	21
Duration of time (hour)	55	97	74.5
Number of radar gates for fine scans (10^6)	13	44	22.5
Number of radar gates for coarse scans (10^6)	3.6	11	3.3

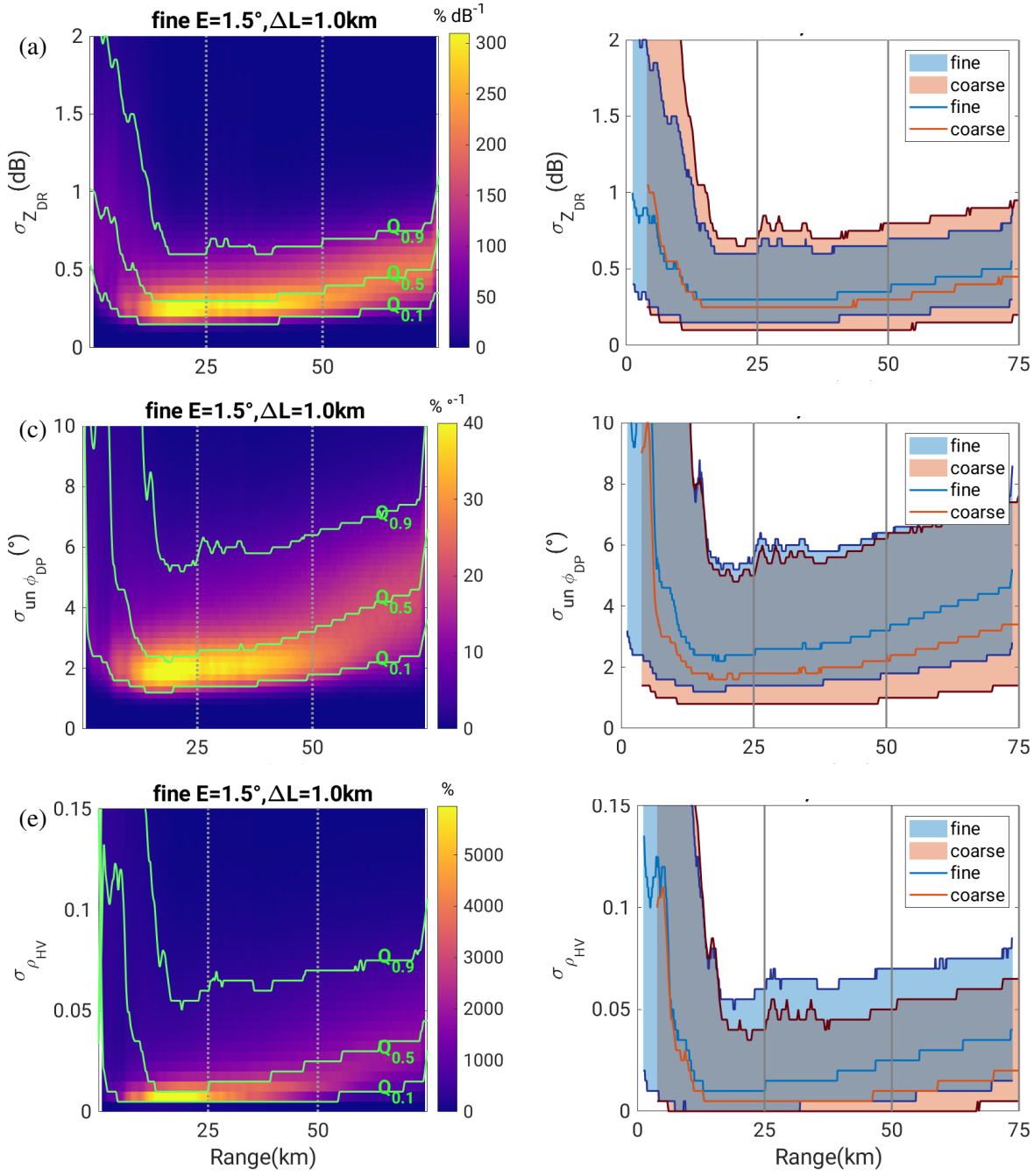

Fig. 4.18.: Range variation in terms of PDF for texture parameters (a) $\sigma_{Z_{DR}}$, (c) $\sigma_{u\text{-}\phi_{DP}}$ and (e) $\sigma_{\rho_{HV}}$ for fine scans, comparisons between fine and coarse scans in (b), (d), and (f) for over 20 widespread stratiform precipitation episodes (250 volume scans together), where the green curves from the bottom to up in (a) or (c) or (e) are 0.1, 0.5 and 0.9 quantiles ($Q_{0.1}$, $Q_{0.5}$ and $Q_{0.9}$) , the shaded areas in (b) or (d) or (f) are between the 0.1 quantile ($Q_{0.1}$) and 0.9 quantile ($Q_{0.9}$), and the curves (b) or (d) or (f) are the 0.5 quantile ($Q_{0.5}$)

After obtaining the training dataset with three subsets (GC, IC, and PR), we characterize the echoes of either GC, ICs or PRs using radar data from its corresponding subset. For instance, to study characteristics of GCs, we use the volume scans purely from the GC subset. Nevertheless, quite often,

one volume scan contains more than one class of echoes. To mitigate this ambiguity, we use the radar gates within the 25-km range for GCs, within the 50-km range for ICs, and in the 25–50 km range for PRs. We exclude the PRs within the 25 km range to avoid overlap with these frequent ICs and GCs in the close range (less than 25 km away from the radar). The reason to also exclude the PRs beyond the 50 km range lies in the range dependence of texture parameters. The texture parameters, which are calculated based on 250 volume scans of wide-spread stratiform precipitation, increase slowly within the 50-km range, and more abruptly beyond the 50-km range (Fig. 4.18). We expect the range dependence of measurements during the convective precipitation might be even more pronounced. The radar beam beyond 50 km away from the radar reaches the vertical height exceeding 1.3 km, where the GCs and ICs are rare in principle. Since the GCs and insects dominate within the 50-km range, there is no need to apply the FLC for the radar gates beyond 50 km away from the radar. Thus, our training dataset focuses on the PRs in the 25–50 km range where the range dependence of texture parameters is quite small (Fig. 4.18). Besides, within the IC subset, due to the persistence of GC targets, a portion of the radar received signals which are supposed to be reflected from insects might actually be from GCs. It brings misleading information for characterizing the ICs. To tackle this ambiguity between the GCs and insects, we exclude some gates in the IC subset which are frequently affected by GCs determined by the static GC maps from Section 4.4.

The differences between these three classes of echoes are easily visually perceptible from radar images. Basically, the GCs, mainly at weak intensities and occasionally at moderate intensity, are scattered throughout the near range within 25 km (Figs. 4.19(a) and 4.19(b)). In contrast, the ICs are clustered much densely along with weak intensity mostly (Figs. 4.19(c) and 4.19(d)). Since IC are mainly weak echoes in term of Z_{H}, the area with measurable Z_{H} in the fine scan is much smaller than that of the coarse scan, in accord with the conclusion in Section 4.1.1 that the fine scan data tend to overlook the weak echoes. In other words, if we are interested in precipitation, then disturbances of GCs and ICs are seemingly much suppressed in the fine scan data, and we have less demand for removing the non-meteorological echoes for fine scans. Unlike the GC and IC, the PRs are characterized by a vast variety of intensity in terms of Z_{H} (Figs. 4.19(e) and 4.19(f)). Several convective storms exist within the radar coverage, and the center of each storm has higher Z_{H} surrounded by the weaker intensity. Note the volume scans presented in Fig. 4.19 are randomly selected but they are representative of the entire dataset.

Besides the foregoing visual inspection, we quantitatively characterize the differences between GC, ICs and precipitation (PR) echoes through the PDFs of the polarimetric discriminators. According to Eq. 3.9, the magnitude of texture parameters depends on the number of radar gates involved in the calculation or the length of calculating window. To assess the effect of the calculating length on the magnitude of textures, we compute the texture parameters in three different lengths: 1.0 km, 1.5 km and 2.0 km—equivalently 17, 23 and 29 radar gates along radar beams for fine scan data, and of 5, 7 and

9 radar gates for coarse scan data. Although the textures in larger lengths are supposed to be slightly greater than those in shorter lengths, textures calculated in three different lengths are in general quite comparable regardless of the type of echoes (Figs. 4.20, 4.21 and 4.22). The following analyses only involve the textures in the 1-km length.

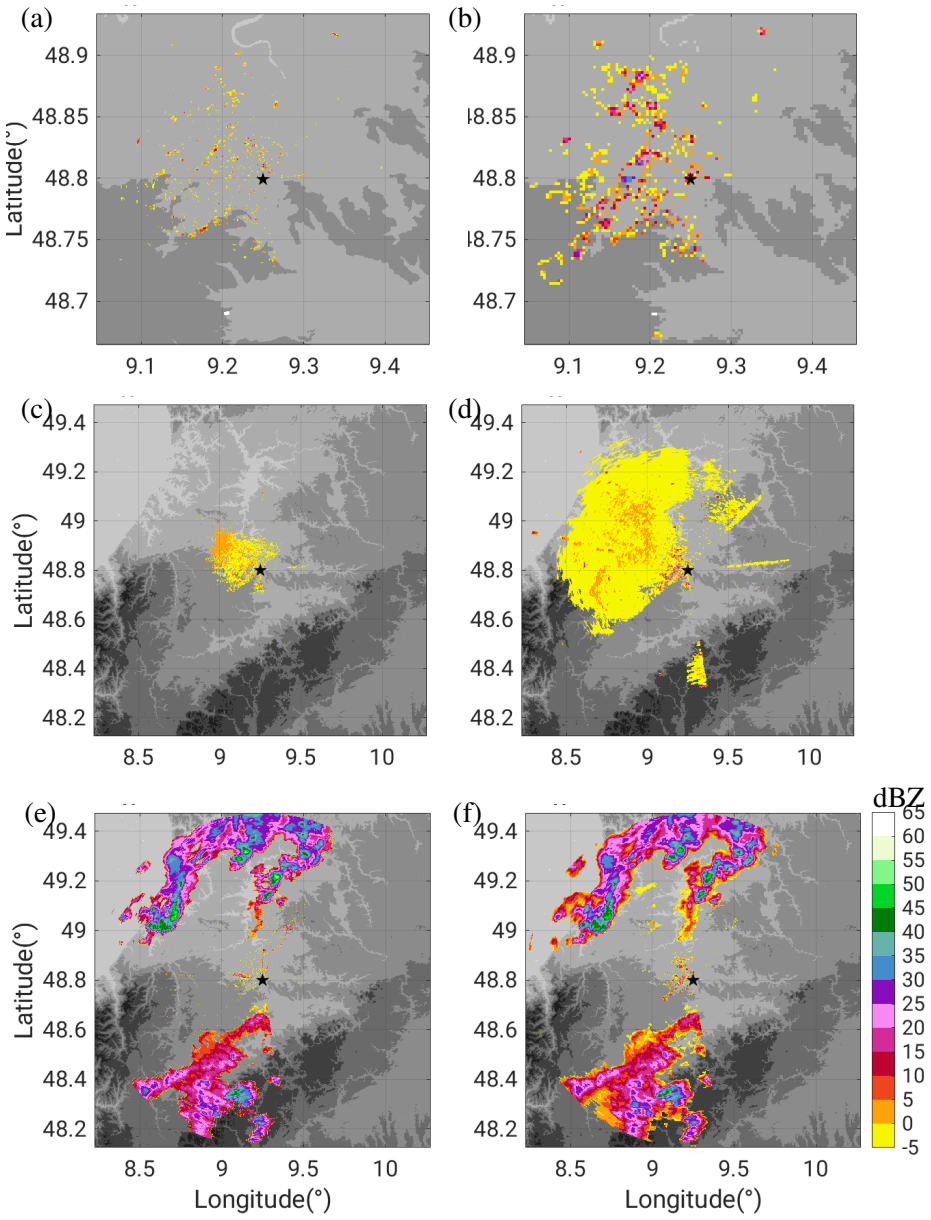

Fig. 4.19.: PPI displays of six selected volume scans to show the Z_H characteristics of GC for (a) a fine scan at 04:03 UTC on 11 June 2017, and (b) a coarse scan at 04:04 UTC on 11 June 2017, of IC for (c) a fine scan at 10:13 UTC on 15 June 2017, and (d) a coarse scan at 10:15 UTC on 15 June 2017, of PR for (e) a fine scan at 18:03 UTC on 9 June 2017, and (f) a coarse scan at 18:04 UTC on 9 June 2017, where the black star represents the location of our X-band radar, the areal dimension of (a) and (b) is 15 km$\times$15 km, and of the other panels is 75 km$\times$ 75 km

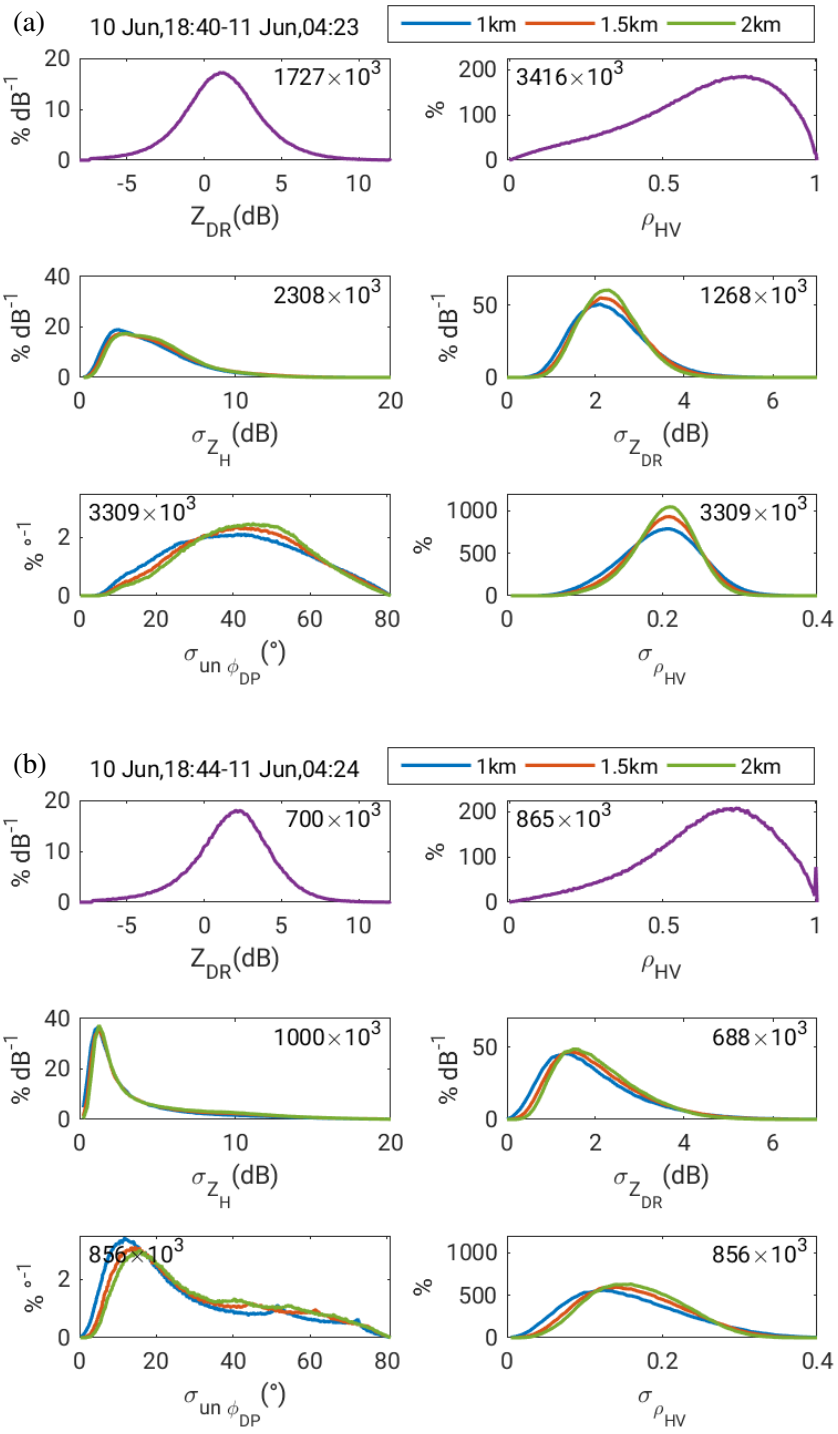

Fig. 4.20.: Characteristics of discriminators—polarimetric variables (Z_{DR}, ρ_{HV}) and their texture parameters (σ_{Z_H}, $\sigma_{Z_{DR}}$, $\sigma_{\phi_{DP}}$ and $\sigma_{\rho_{HV}}$)—in terms of PDFs for GCs within the 25-km range radar coverage in an example episode from 18:40 UTC on 10 June 2017 to 04:29 UTC on 11 June 2017, (a) is for the fine scan data and (b) is for the coarse scan data, where the blue, red and green curves represent the texture parameters calculated with window lengths of 1.0 km, 1.5 km and 2.0 km respectively

For the GCs, the frequencies of either $\sigma_{Z_{DR}}$ above 2 dB, or $\sigma_{\phi_{DP}}$ above 40° or $\sigma_{\rho_{HV}}$ above 0.2 are higher in the fine scan data rather than that in the coarse scan data (Fig. 4.20). Similarly, as illustrated by the location of peaks in these PDFs, ICs exhibit a higher frequency of larger texture parameters calculated using the fine scan data than the coarse scan data (Fig. 4.21). In contrast, the PDFs of texture parameters for PRs are quite comparable between the fine and coarse scans (Fig. 4.22).

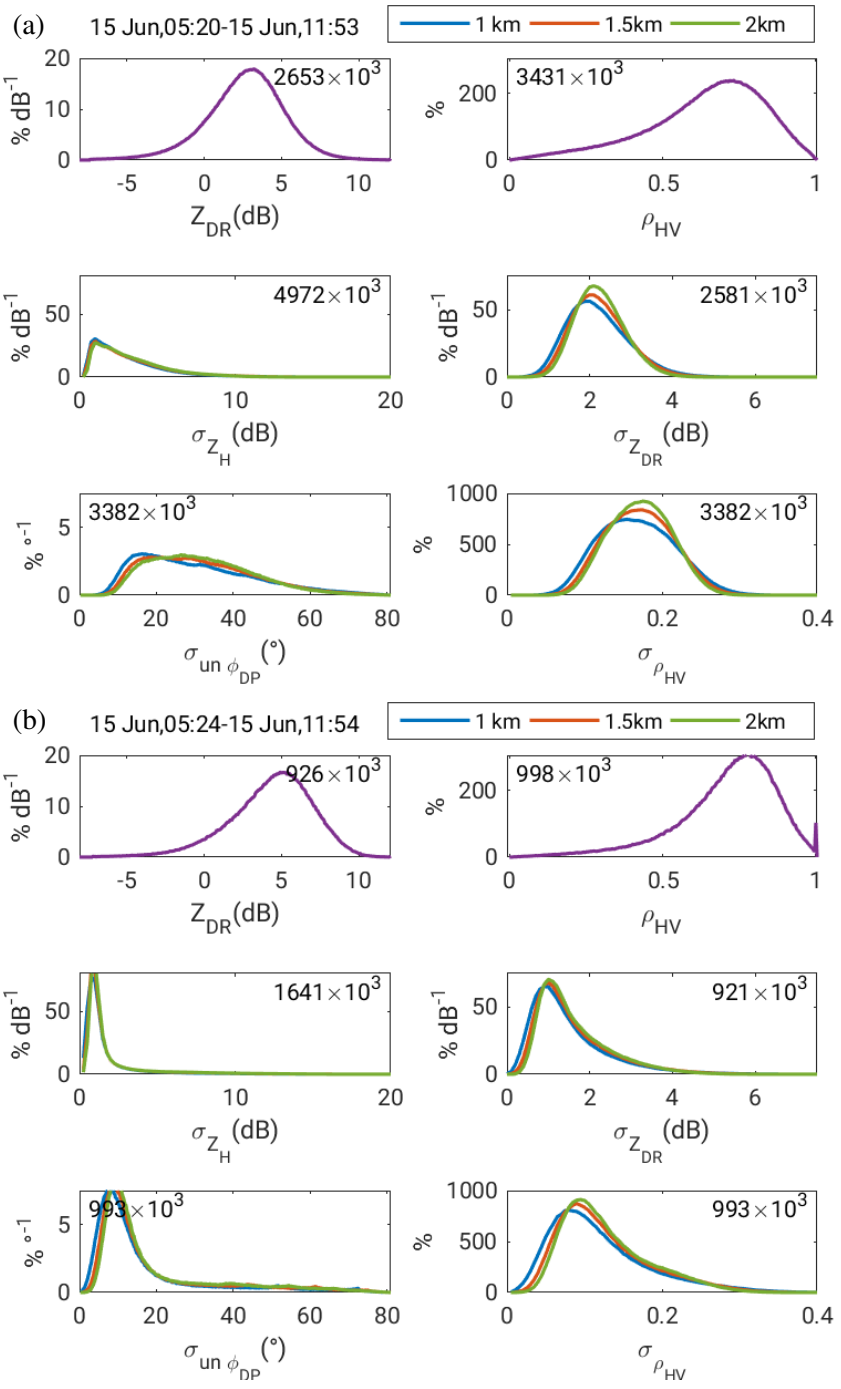

Fig. 4.21.: Similar to Fig. 4.20, but for ICs from 05:20 to 11:59 UTC on 15 June 2017 within the 50-km range of the radar coverage

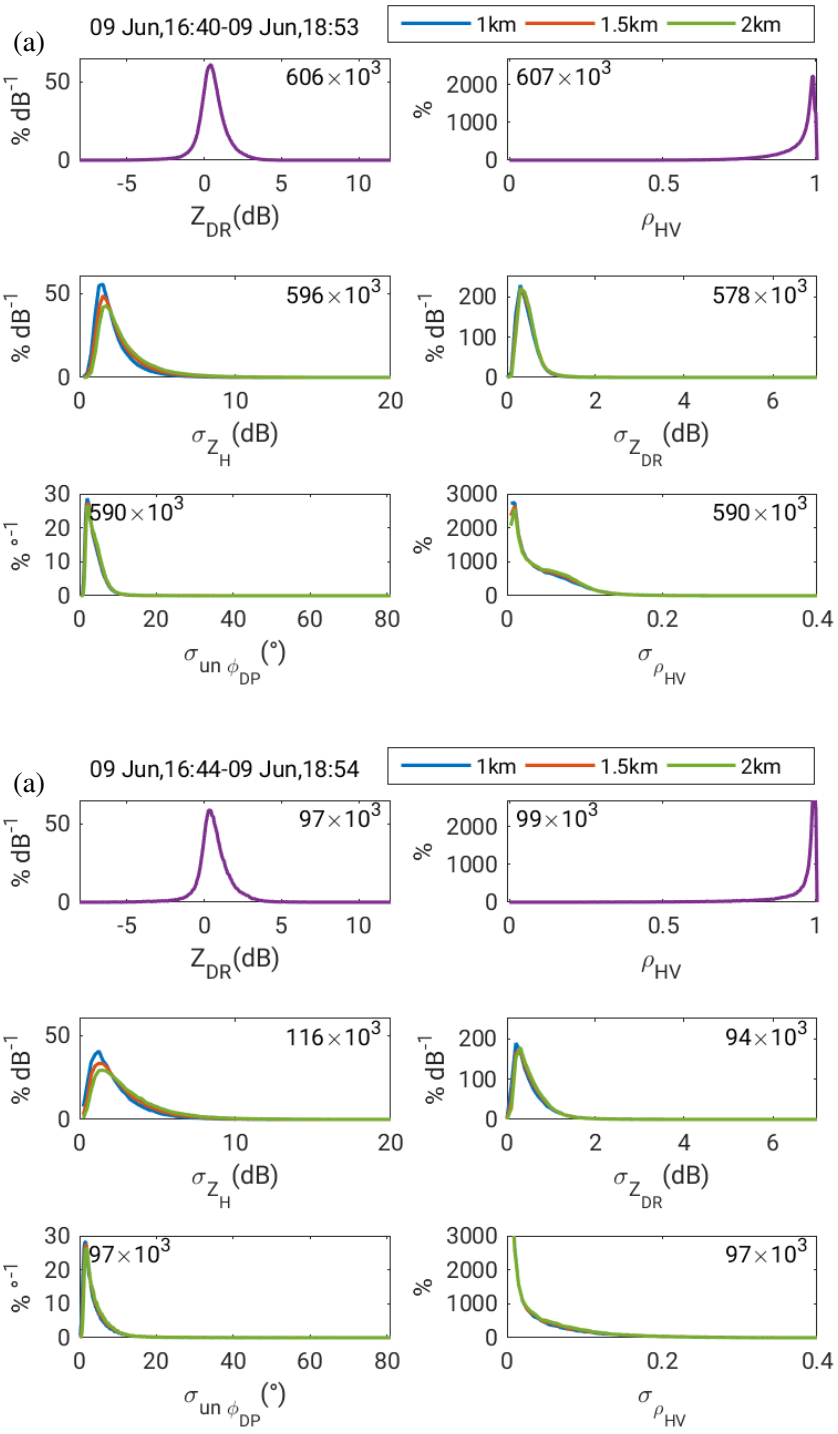

Fig. 4.22.: Similar to Fig. 4.20, but for PRs from 16:40 to 18:59 UTC on 9 June 2017 in the radar coverage in the 25–50 km range

Recall that Fig. 4.22 is for PRs in the 25–50 km range. We also calculated PDFs using the PRs within the radar coverage in the 50–75 km range (not shown). The PDFs of texture parameters calculated using the radar data at this farther range (with 50–75 km range) slightly differ from those

texture parameters based on the radar data in the near range (25–50 km). The major difference lies in ρ_{HV} which is an indicator of data quality, and $\sigma_{\rho_{HV}}$. Farther than 50 km away from the radar, the low value of ρ_{HV} is much more frequent within the precipitation targets, which often leads to large $\sigma_{\rho_{HV}}$, and consequently we end up with flatter or wider MFs for both ρ_{HV} and $\sigma_{\rho_{HV}}$. The non-uniform beam filling (NBF) effect in the farther range further reduces the magnitude of ρ_{HV} (Ryzhkov, 2007).

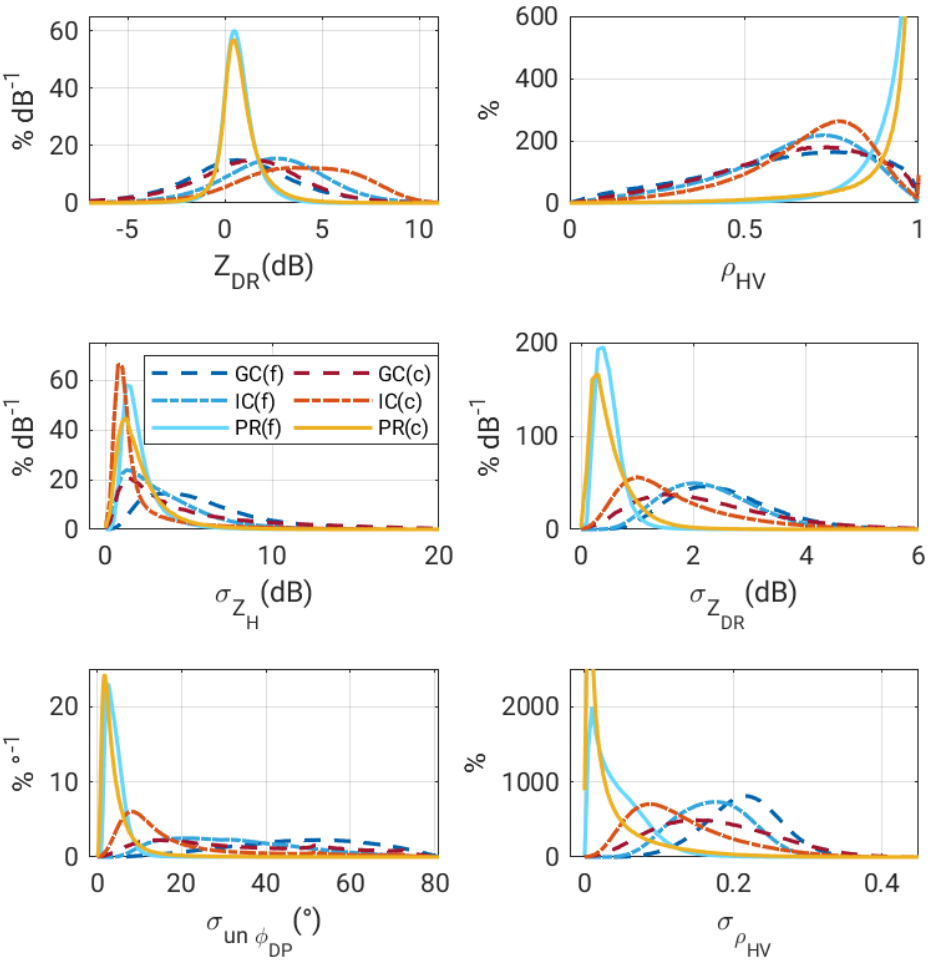

Fig. 4.23.: Comparison of PDFs of discriminators—polarimetric variables (Z_{DR}, ρ_{HV}) and their texture parameters (σ_{Z_H}, $\sigma_{Z_{DR}}$, $\sigma_{\phi_{DP}}$ and $\sigma_{\rho_{HV}}$)—for all three classes: GC (in dashed lines), IC (in dash-dotted lines) and PR (in solid lines), and also between fine (in red colors) and coarse scans (in blue colors) using all the episodes in the entire training dataset as shown in Table.4.1

The polarimetric discriminators for three classes of echoes exhibit quite different characteristics, especially between the precipitation class and the other two non-meteorological classes, as seen from their PDFs (Fig. 4.23). First, the PDFs for the precipitation class (PR) are remarkably more concentrated or slimmer, in contrast to the wide/flat distribution for the GC and ICs. This difference suggests great

potential to distinguish precipitation echoes from the other two non-meteorological echoes. Second, for precipitation class, PDFs for the coarse scans of all the discriminators except Z_{DR} are even slightly slimmer than those for the fine scans. This difference between the fine and coarse scans suggests the effect of spatial resolution on the characteristics of radar echoes. Third, the differences between GCs and ICs are mainly seen in terms of Z_{DR}, $\sigma_{\phi_{DP}}$ and $\sigma_{\rho_{HV}}$. For instance, ICs have higher frequencies in Z_{DR} around 2–5 dB for the fine scans, and around 3–7 dB for the coarse scans, while Z_{DR} values for GCs are smaller either for the fine scans or coarse scans. These differences suggest that discriminators have different contributions to classifying echoes.

4.5.2. Fuzzy logic memberships calculation

The noticeable differences in the characteristics among these three classes serve as the foundation for our FLC. On the basis of the PDFs in Fig. 4.23, we construct the piecewise MFs which allow us to calculate the membership $(M_{i,j})$ individually for each class of echo (represented by the first subscript index i) and each polarimetric discriminator (represented by the second subscript index j) (Fig. 4.24). A membership numerically varies from 0 to 1, and a larger value indicates a higher probability being a certain type of echo. Rather than a trapezoid shape (Zrnić et al., 2001) or beta function (Liu and Chandrasekar, 2000), the MFs here are in the form of multi-apex shapes. The apexes-confining shapes of MFs are determined quantitatively based on the curvature of the PDFs; the method to determine the apexes is objective and quantitative, and the criteria for fine and coarse scans are identical.

In our FLC procedure, these five discriminators contribute to various extent to distinguishing one class of echoes from the other two, and the three discriminators in the form of texture parameters exhibit different distinguishing abilities between the fine and coarse scan data (Fig.4.24). Z_{DR} contributes little to distinguishing between precipitation classes from others, but high Z_{DR} values are much likely to indicate ICs. ρ_{HV} plays a more pronounced role in distinguishing between the PRs and non-meteorological echoes (GC and IC), but not between the GCs and ICs shown by the similar MFs for these two non-meteorological echoes. For precipitation targets, unlike MFs for ρ_{HV} in other radar frequencies from others' studies, the X-band radar data provide ρ_{HV} values less than 0.9 more frequently. Three texture parameters are supposed to effectively distinguish precipitation echoes from the other two non-meteorological echoes. Unlike Z_{DR} and ρ_{HV} that are relatively similar between fine and coarse scans, the MFs in terms of these texture parameters differ between fine and coarse scans. For either GCs or ICs, the overall $\sigma_{Z_{DR}}$ of the coarse scans is smaller than its counterpart of the fine scans. However, for the PRs, $\sigma_{Z_{DR}}$ has a higher frequency of being above 1 dB, which results in a larger overlap with the other two non-meteorological echoes. In comparison to the fine scans, this larger overlap of MFs of the coarse scan data might imply a lower efficiency to distinguish precipitation classes from either GCs or ICs. $\sigma_{u\text{-}\phi_{DP}}$, particularly for the fine scans, exhibits obvious discrepancies among all three classes of echoes, implying

the usefulness of $\sigma_{\phi_{DP}}$ in identifying echo classes. Besides, similar to $\sigma_{Z_{DR}}$, $\sigma_{\phi_{DP}}$ also differs between fine and coarse scans. This difference is, for either GCs or ICs, large values in $\sigma_{\phi_{DP}}$ for fine scans are clearly more frequent than those of coarse scans. This difference suggests a higher efficiency of fine scan data in identifying echoes rather than coarse scan data. In parallel, the distinctive separation of the MFs of these three classes demonstrated by $\sigma_{\rho_{HV}}$ substantiates a good capacity of $\sigma_{\rho_{HV}}$ to distinguish among these three classes of echoes. Besides, regardless of the echo types, $\sigma_{\rho_{HV}}$ also show higher frequencies of greater magnitudes for fine scans rather than coarse scans, which again implies that the polarimetric data of fine scans has a greater distinguishing efficiency than those of coarse scans.

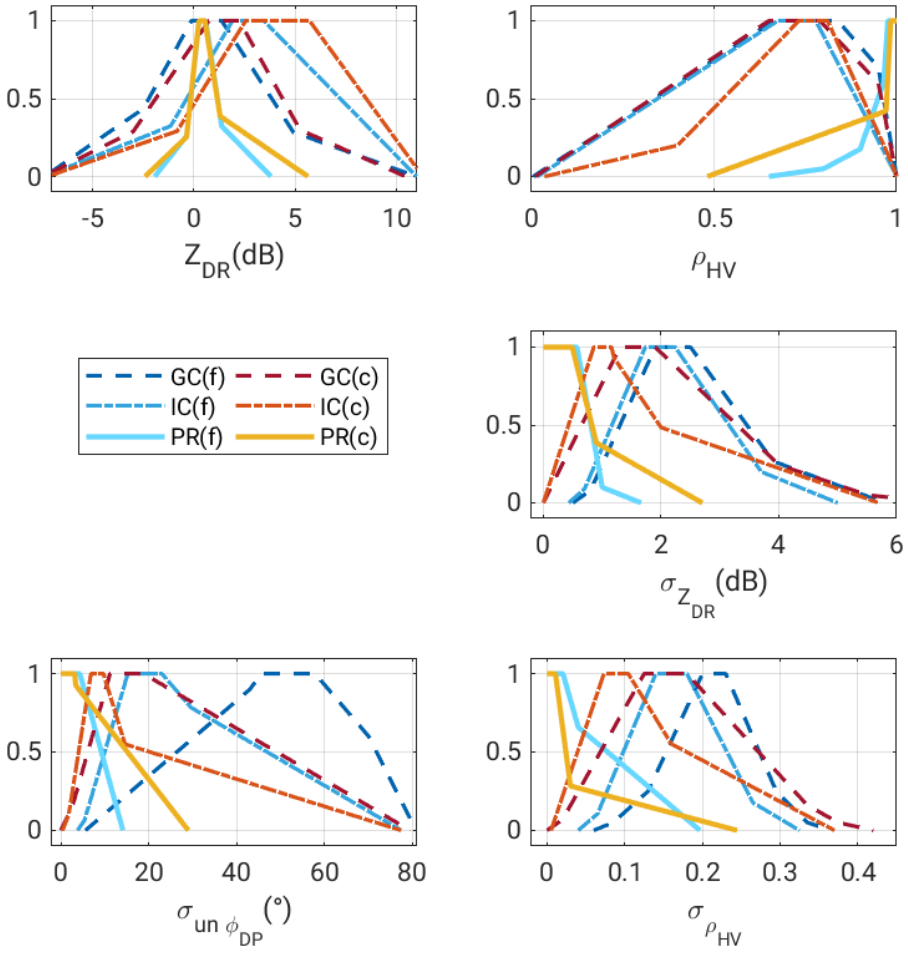

Fig. 4.24.: MFs for five discriminators (Z_{DR}, ρ_{HV}, $\sigma_{Z_{DR}}$, $\sigma_{\phi_{DP}}$ and $\sigma_{\rho_{HV}}$) for three classes of echoes and for both fine and coarse scans, and the meaning of the lines are the same as those in Fig. 4.23

After calculating membership ($M_{i,j}$) for each echo class and for each discriminator utilizing the above MFs, the next step is to obtain an aggregative membership function for each class (M_i) by aggregating memberships of these five individual discriminators

$$M_i = \frac{\sum w_{i,j} M_{i,j}}{\sum w_{i,j}} \tag{4.2}$$

where the first index means the echo type, i=1 for GC, i=2 for IC, and i=3 for PR, and then the second index means which discriminator is used, j=1 for Z_{DR}, j=2 for ρ_{HV}, j=3 for $\sigma_{Z_{\mathrm{DR}}}$, j=4 for $\sigma_{\phi_{\mathrm{DP}}}$ and j=5 for $\sigma_{\rho_{\mathrm{HV}}}$, M is the membership, w represents the weights in the aggregation. For each target, we can calculate the aggregative memberships in terms of ground clutters (M_{GC}), of insect echoes (M_{IC}) and of precipitation echoes (M_{PR}), regardless of echo classes.

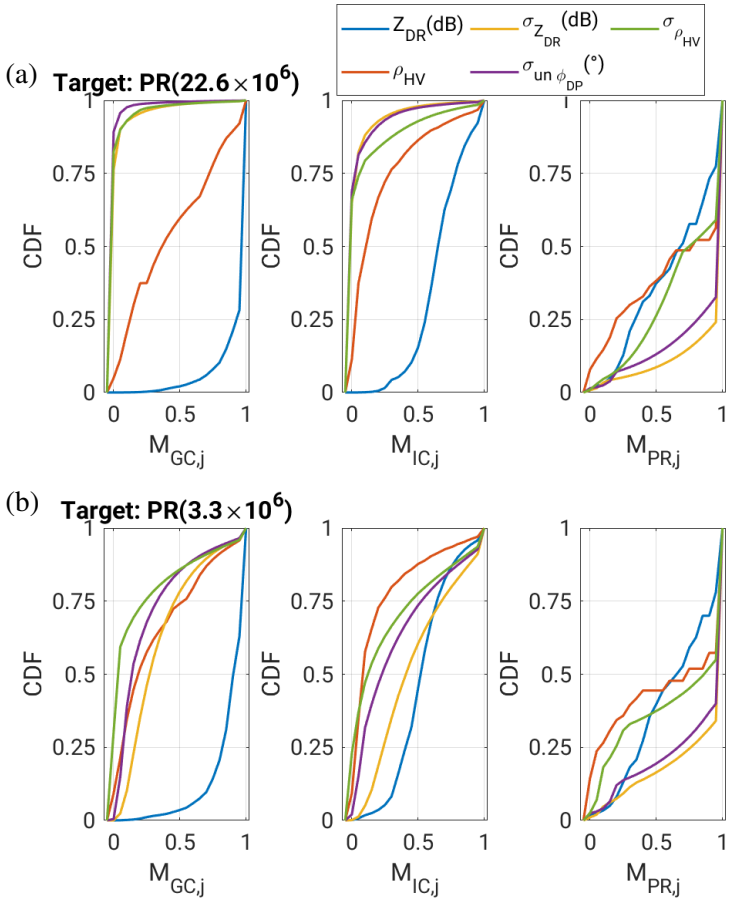

Fig. 4.25.: CDFs of memberships in terms of ground clutters, insect echoes and precipitation echoes for each discriminator ($M_{i,j}$) for the precipitation (PR) subset of the training dataset for (a) fine scan data and (b) coarse scan data, where the second subscript j in $M_{\mathrm{GC},j}$, $M_{\mathrm{IC},j}$ and $M_{\mathrm{PR},j}$ indicates which discriminator is. The curves in colors of blue, red, yellow, purple and green are for Z_{DR} ($j=1$), ρ_{HV} ($j=2$), $\sigma_{Z_{\mathrm{DR}}}$ ($j=3$), $\sigma_{\phi_{\mathrm{DP}}}$ ($j=4$) and $\sigma_{\rho_{\mathrm{HV}}}$ ($j=5$), respectively

Take the precipitation target as an example (Fig. 4.25). In order to identify a radar echo as the precipitation echo, its M_{GC} and M_{IC} should be much smaller than its M_{PR}, that is to say, all the $M_{\mathrm{GC},j}$ and

$M_{\mathrm{IC},j}$ should be as low as possible while all the $M_{\mathrm{PR},j}$ are as high as possible. We calculate these three aggregative memberships ($M_{\mathrm{GC},j}$, $M_{\mathrm{IC},j}$ and M_{PR}) for the entire PR subset of the training dataset. It turns out that the majority of the memberships ($M_{i,j}$) fit our anticipation with a few exceptions. For instance, over 25% of memberships in terms of ground clutter based on Z_{DR} ($M_{\mathrm{GC},1}$) surpass 0.9 (Fig. 4.25). This large magnitude of $M_{\mathrm{GC},1}$ magnifies (M_{GC}), which opposes our expectation. Similarly, the memberships in terms of insect echoes based on Z_{DR} ($M_{\mathrm{IC},1}$) contribute to a high M_{IC} which should be low for the precipitation target (Fig. 4.25). The large magnitude of both $M_{\mathrm{GC},1}$ and $M_{\mathrm{IC},1}$ corresponds to the MFs based on Z_{DR} in Fig. 4.24, where the MF for precipitation echoes are entirely overlapped within the MFs of ground clutters and insect echoes.

Furthermore, the relative contributions of each discriminator to the aggregative membership differ between the fine and coarse scans. For instance, in the fine scan data (Fig. 4.25(a)), nearly 75% of the memberships in terms of insect echoes based on $\sigma_{Z_{\mathrm{DR}}}$, $\sigma_{\phi_{\mathrm{DP}}}$ and $\sigma_{\rho_{\mathrm{HV}}}$ are nearly 0, in contrast to their counterparts in the coarse scans that are characterized by much higher magnitudes (Fig. 4.25(b). The cumulative probability function (CDF) of the memberships for each discriminator for each echo type quantitatively reflects the degree of overlapping or separation of the MFs.

In Eq. 4.2, the weight of each variable $w_{i,j}$ indicates the expectation of that variable's importance. Given that these discriminators contribute to various extent to the aggregative membership function M_i, we can adjust weighting coefficients to balance the different contributions from these five discriminators. For example, more advanced methods such as the neural network method (Jang, 1993) and iterative testing (Krause, 2016) have been used to train the weights in their fuzzy logic procedure (Jang, 1993; Krause, 2016), in which the variable exhibiting a larger overlap with other variables indicates less trust, and then is given less weight. In the iterative method, the FLC procedure is repeated iteratively until achieving the best results (Krause, 2016). Lakshmanan et al. (2015) emphasized the better discriminating ability of $\sigma_{Z_{\mathrm{DR}}}$ and gave more weight to Z_{DR} while Z_{DR} is excluded due to the calibration issue. Krause (2016) assigned $w = 2$ to $\sigma_{Z_{\mathrm{DR}}}$ and $\sigma_{\phi_{\mathrm{DP}}}$, respectively, and $w = 1$ to $\rho_{\mathrm{HV}}$and $\sigma_{\rho_{\mathrm{HV}}}$, respectively because Krause (2016) thought $\sigma_{\rho_{\mathrm{HV}}}$ was highly correlated with ρ_{HV}values. However, we are not sure about whether their ideas work for our algorithm.

Obviously, appropriate weighting coefficients can further improve the efficiency of our FLC. However, due to the time constraint, I had no time to seek for the optimal weighting coefficients, but for simplicity assume equal weight for each discriminator in the following calculation. Besides the simplicity, the assumed equal weights further guarantee the equivalence between the fine scan and the coarse scan in terms of the aggregative membership calculations, in order to aid the following comparison of the FLC procedure between fine and coarse scans.

Besides the weights, the availability of discriminators calls for our attention. A texture parameter is calculated over a number of consecutive radar gates along the radial direction, which is named

as a calculating window. Quite often, some radar gates within the calculating window have no valid measurements. For instance, for calculating a texture parameter in the 1-km length for a radar gate (G_0) located outside the precipitation system, a few gates at the one-side end of the calculating window may be located along the margin of the precipitation system. If this non-rainy radar gate is neither GC nor insect echo, it has no valid measurements, and likewise the majority of remaining radar gates within this calculating window have no valid measurements except a few gates along the edge of PRs. The texture parameter for that non-rainy radar gate (G_0) can be still calculated based on the rainy radar gates within its calculating window, and thus we obtain a "rainy" texture for this non-rainy radar gate (G_0). It gives us a false impression that this radar gate itself (G_0) contains PRs. To avoid this mistake, a texture parameter is only calculated if more than half of the radar gates have valid measurements. This criterion is crucial for the radar gates in proximity to the margin of precipitation system. With this criterion, a radar gate near the edge of precipitation is very likely to lack valid values for texture parameters, and therefore no membership. Another less frequent situation is that the majority of the radar gates within the calculating window have valid measurements but the center radar gate does not has a valid value. In other words, the availability of Z_{DR} is not equivalent to the availability of $\sigma_{Z_{\mathrm{DR}}}$, and the unavailability of Z_{DR} also does not imply the availability of $\sigma_{Z_{\mathrm{DR}}}$. Thus, the number of discriminators available over a single radar gate can vary from 0 to 5 given that we use five discriminators in our FLC procedure. According to our sensitivity study (not shown here), for a radar gate with only four valid discriminators, its membership in terms of either ground clutters or insect echoes (M_{GC} or M_{IC}) is high if this radar gate contains GCs or insect echoes, but its membership in terms of precipitation echoes (M_{PR}) are low even if we suppose this radar gates contains PRs. It means that M_{PR} is only possible if all the five discriminators are available. However, for M_{GC} or M_{IC}, there is no such requirement for availability of valid values for discriminators. This finding is reasonable since the PRs should have valid polarimetric measurements.

Then, for each radar gate, we calculate three memberships in terms of ground clutters (M_{GC}), insect (M_{IC}) and precipitation echoes (M_{PR}). Understandably, for a radar gate contaminated by ground clutter, its membership in terms of ground clutters (M_{GC}) should be larger than the other two memberships (M_{IC} and M_{PR}); similarly for a radar gate with ICs, its M_{IC} should be greater than M_{GC} and M_{PR}; within the precipitation targets, we expect M_{PR} to be larger than M_{GC} and M_{IC}. Conversely, for a radar gate, we may identify it: 1) as ground clutter if its membership in terms of ground clutter (M_{GC}) is the highest among all the three memberships, 2) as insect echo if its membership in terms of insect echo (M_{IC}) is the largest, 3) as precipitation echo if its membership in terms of precipitation echo (M_{PR}) is the greatest. In other words, the final identification depends on the relative magnitude of the memberships for these three types of echoes.

To verify these criteria of assigning echo types, we calculate the three memberships (M_{GC}, M_{IC} and M_{PR}) individually for each radar gate in the training dataset, in which we have already determined the echo types for each volume scan according to the previous visual inspections (Fig. 4.26). For

radar measurements within the PR subset, the majority of memberships in terms of precipitation echoes (M_{PR}) are larger than the other two memberships (M_{GC}) and (M_{IC}). For the fine scan data, less than 8% of M_{PR} is below 0.4, while 90% of M_{GC} and M_{IC} are less than 0.4; the median of M_{PR} about 0.8 is much larger than the medians of M_{GC} and M_{IC}, which are both less than 0.35. Besides, radar gates in the PR subset of the training data correspond to M_{PR} above 0.8, whereas the majority of M_{IC} over the same radar gates are below 0.2 (Figs. 4.27(e) and 4.27(f)). The highest magnitude for (M_{PR}) meets our expectation. In contrast, the memberships in terms of precipitation echoes (M_{PR}) are quite low for the ground clutters (Fig. 4.26(a)) and insect echoes (Fig. 4.26(b)). For instance, most of M_{PR} are less than 0.4 within the ground clutters, and less than 0.45 within the insect echoes. It implies that we may identify a radar gate as non-meteorological echo as far as its M_{PR} is less than 0.45. Furthermore, in accordance with our previous discussion that MFs of texture parameters are different between fine and coarse scans (Fig. 4.24), the aggregative memberships (M_{GC}, M_{IC} and M_{PR}) differ much between fine and coarse scans. For instance, the separation between the memberships in terms of precipitation M_{PR} and other two non-meteorological classes M_{GC} and M_{IC} is remarkably wider in the fine scan data rather than that in the coarse scan data, illustrated by the larger spacing between the CDF curves of M_{PR} and the other two (M_{GC} and M_{IC}).

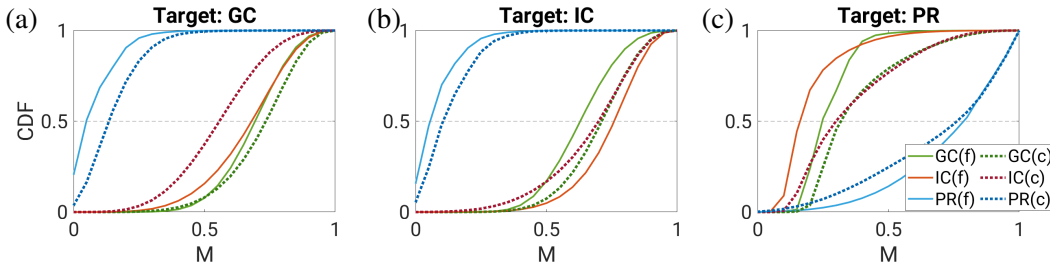

Fig. 4.26.: CDFs of memberships for ground clutter class, insect class and precipitation class (M_{GC}, M_{IC} and M_{PR}) for both fine and coarse scans in the training dataset (a) with the known class of ground clutters, (b) with the known class of insect echoes and (c) with the known class of precipitation, where green lines are for M_{GC}, and red lines for M_{IC}, blue lines for M_{PR}, solid lines for fine scan data, and dashed lines for coarse scan data

However, the memberships in terms of ground clutters (M_{GC}) and insect echoes (M_{IC}) are not distinct from each other but instead quite comparable in magnitude for all the three types of targets. For instance, within the ground clutters, the median of M_{GC} nearly equals the median of M_{GC} for fine scans; similarly, the ICs within the coarse scan data also provide their medians nearly equivalent for two memberships M_{GC} and M_{IC}. This comparability is further substantiated by the two-dimensional bivariate histogram of M_{GC} and M_{IC} (Figs. 4.27(c) and 4.27(d)), especially by the symmetric 2D histogram for the coarse scan data in which both M_{IC} and M_{GC} are very likely to fall between 0.65 and 0.9. For fine scans, the majority of M_{IC} falling between 0.7 and 0.9 are also close to the majority of M_{GC} between 0.45 and 0.75. This comparability between M_{GC} and M_{IC} points to the potential difficulty of assigning the radar gates whether with GCs or with ICs in the next step of our FLC procedure.

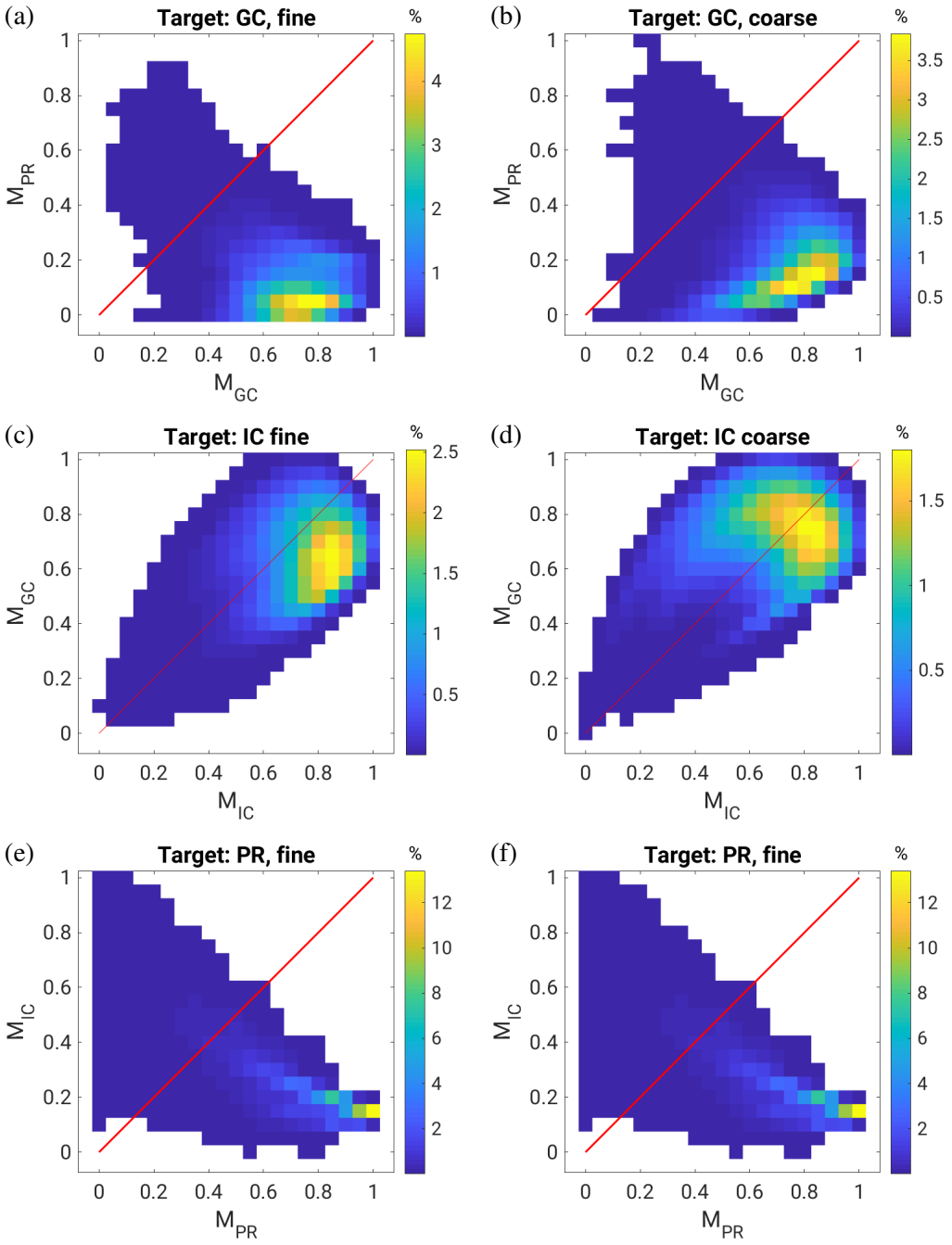

Fig. 4.27.: Two-dimensional bivariate histograms of the relative frequency of the memberships in terms of, between ground clutters (M_{GC}) and precipitation echoes (M_{PR}) (a) for fine scans and (b) for coarse scans in the GC subset of training dataset; between insect echoes (M_{IC}) and ground clutters (M_{GC}) (c) for fine scans and (d) for coarse scans in the IC subset of training dataset; between precipitation echoes (M_{PR}) and insect echoes (M_{IC}) (e) for fine scans and (f) for coarse scans in the PR subset of training dataset

4.5.3. Echo class assignment

After obtaining the memberships (M_{GC}, M_{IC} and M_{PR}) for each radar gate, it is time to assign the echo type to each radar gate. We may assign the type of class according to the relative magnitude of memberships, and it should bring about a satisfying performance in distinguishing the PRs from the other two non-meteorological echoes, since M_{PR} is clearly much high in precipitation echo and quite low in non-meteorological echoes as mentioned before. However, we also see a challenge in identifying between GC and insects because both memberships are of comparable magnitude. Although our main objective to distinguish the non-meteorological echoes and PRs can be fulfilled, for the sake of the completeness of this FLC, we still hope to also distinguish between GCs and ICs.

Instead of using the relative magnitude of memberships (M_{GC}, M_{IC} and M_{PR}) we compare the magnitudes of quantiles of each calculated membership according to the CDF in Fig. 4.26. More specifically, for a radar gate, we may identify it as GC if the quantile of its membership in terms of ground clutter $Q(M_{GC})$ is the highest, as insect echo if the quantile of its membership in terms of insect echo $Q(M_{IC})$ is the largest, and as precipitation echo if the quantile of its membership in terms of precipitation echo $Q(M_{PR})$ is the greatest. In other words, the final identification depends on the relative magnitude of quantiles of their memberships. This step provides us another method to explore how to better distinguish between the GCs and ICs. The entire flow for our FLC procedure is shown as follows (Fig. 4.28).

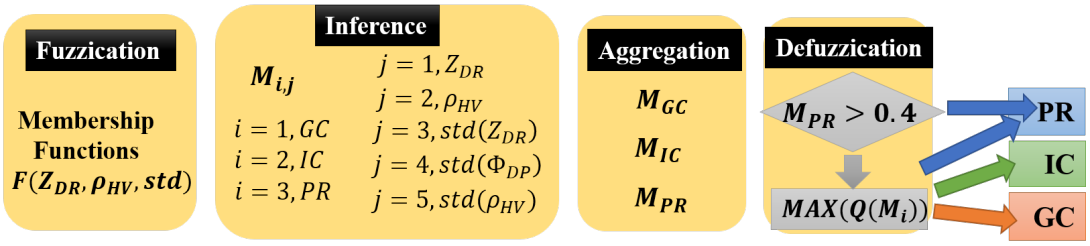

Fig. 4.28.: The block diagram of the FLC algorithm developed specifically for the X-band radar data in this research, where GC, IC and PR are abbreviations of ground clutters, insect echoes, and precipitation echoes

The echo class types identified by our FLC procedure fit our expectation to a large extent (Fig. 4.29). For the volume scans at 04 UTC on 11 June 2017, before applying FLC, we assumed both the fine and coarse scans containing only GCs in the range less than 25 km away from the radar (Figs. 4.19(a) and 4.19(b)), and our FLC procedure identifies most of the radar gates of both scans as GCs with occasional ICs, which meets our expectation (Fig. 4.29(a) and 4.29(b)). The occasional presence of ICs is reasonable; though we hope all the volume scans only contain the GCs, ICs are very common and unavoidably appear in the GC subset.

For another pair of volume scans at 10 UTC on 15 June 2017, we initially assumed that both the fine and coarse scans exclusively contained the ICs within 50 km away from the radar (Figs. 4.19(c)

and 4.19(d)). Then, our FLC result shows the majority of echoes are ICs with intermittent underlying GCs, and most of these GCs are located within the close range (25 km away from the radar) (Figs. 4.29(c) and 4.29(d)). This result, albeit slightly different from our initial assumption, is also quite reasonable because GCs should be naturally persistent in space and in time, contaminating at least a portion of the radar gates at the closer range.

In parallel, for the third pair of volume scans at 18 UTC on 9 June 2017, according to our previous visual inspections through radar images, we assumed precipitation prevailed in the range beyond 25 km away from the radar (Figs. 4.19(e) and 4.19(f)). It turns out that the echo types identified by means of our FLC procedure are again in good accord with the initial visual inspection (Figs. 4.29(e) and 4.29(f)). Especially for the fine scan, most radar gates beyond 25 km are identified as PRs with a few exceptions, and the majority of the exception gates, if within 50 km away from the radar, lie along the edge of the precipitation system. Beyond the 50 km away, more radar gates are identified as insect or GCs even inside the precipitation system. This false identification is caused by the misuse of MFs. Recall that the MF in terms of PRs is based on the radar gates exclusively within the near range (25 to 50 km away from the radar) (Section 4.5.1). If we use these MFs intend for the range between 25 to 50 km to calculate the membership (M_{PR})) for the radar gates beyond 50 km away from radar, we are much likely to obtain inappropriate magnitudes of memberships and subsequent misidentification, as a result of the range dependence of texture parameters (Fig. 4.18). Additionally, this misidentification is more apparent in the coarse scan than that of the fine scan. A possible explanation is that coarse scans tend to keep more weak echoes especially along its edge and the ICs usually belongs to the weak echoes. Another potential explanation is that, despite the same length for texture parameters for fine and coarse scans, the number of radar gates involved in calculating these texture parameters differs between fine and coarse scans. For instance, the texture in the 1-km length involves 15 radar gates for the fine scan data and five radar gates for the coarse scan data in their calculating windows. Using fine scan data, equivalently involving more radar gates, is more successful in identifying the echo types accurately in our FLC procedure which in fact was constructed following the same principle and criteria for both fine and coarse scans.

In fact, we particularly inspected three memberships (M_{GC}, M_{IC} and M_{PR}) for the coarse scan at 18 UTC on 9 June 2017 associated with Fig. 4.29(f). $\sigma_{\rho_{\mathrm{HV}}}$ accounts for lower values of M_{PR} for the radar gate at the far range (beyond 50 km). It might be a corollary of the low ρ_{HV} radial streak caused by the non-uniform beam-filling (Ryzhkov, 2007), or the deteriorating radar performance and worsening data quality with the increasing range. Thus, for a proper classification, we should develop another set of MFs specifically to characterize the foregoing given polarimetric discriminators at the far range. However, such an set of MFs is not included because non-meteorological echoes are not common at the far range of our radar coverage thanks to the 1.5° elevation for the lowest scan.

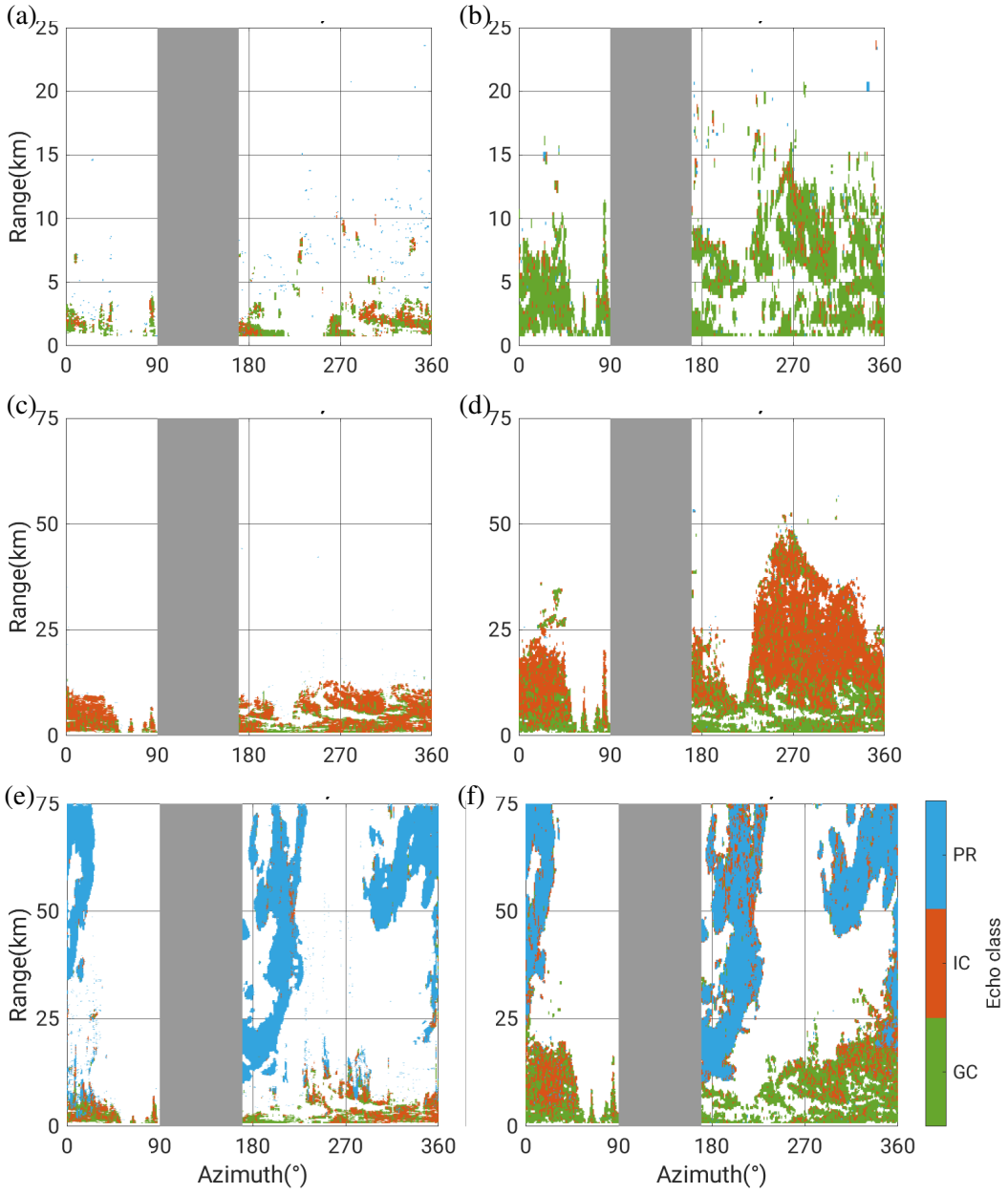

Fig. 4.29.: Azimuth-range section of identified echo classes using the FLC procedure for the same volume scans in Fig. 4.19, where the green/red/blue colors are for GC, IC and PR, respectively

To make this FLC algorithm even simpler, we can treat the radar measurements with radar reflectivity Z_H less than -5 dBZ as very weak echoes irrelevant to precipitation or other issues associated with low SNR, and thus there is no need to identify echo types for them (most of them are GCs or insects or noise). In this way, we separate the type of echoes into four classes with this additional fourth class of very weak echoes (Fig. 4.30). Referring to radar images in terms of radar reflectivity Z_H (Fig. 4.19), the spatial distribution of these identified echo classes shown in the polar coordinates is reasonable, with a majority of GCs in Figs. 4.30(a) and 4.30(b), with a majority of ICs in Figs. 4.30(c) and 4.30(d), and with a majority of PRs between 25-50 km away from the radar in Figs. 4.30(e) and 4.30(f).

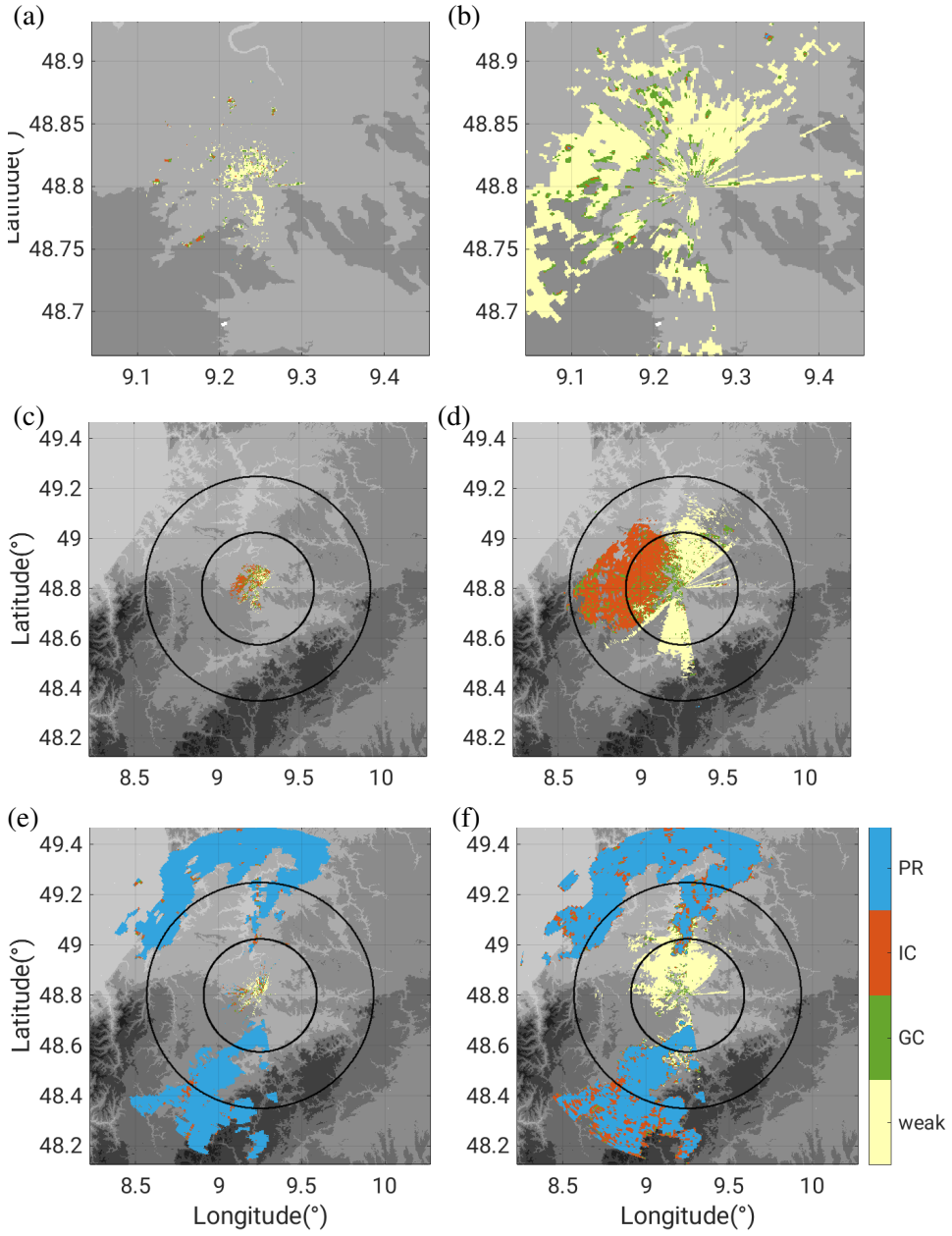

Fig. 4.30.: PPI displays of identified echo classes using the FLC procedure for the same volume scans in Fig. 4.19, where the green color is for GCs, the red color for insect, and the blue color for precipitation, and the smaller (bigger) black circles represent the 25-km (50-km) range rings

After testing our FLC procedure for the training dataset with the predetermined echo classes, we apply our FLC procedure to volume scans outside the training dataset, to further evaluate the performance of our FLC procedure. For the volume scans at 21 UTC on 26 June 2017, visually from the radar images, we thought the non-meteorological echoes prevailed in the close range (within the 0-25 km range) of the volume scans in a combination of the majority of ICs and a smaller portion of GCs, and one additional convective cell located at the 20-25 km range in the southwestern direction; several convective storms in different sizes and shapes were in the near range (within the 25–50 km range); stratiform

precipitation with a few embedded convective storms dominated in the far range (within the 50-75 km range) (Figs. 4.31(a) and 4.31(b)).

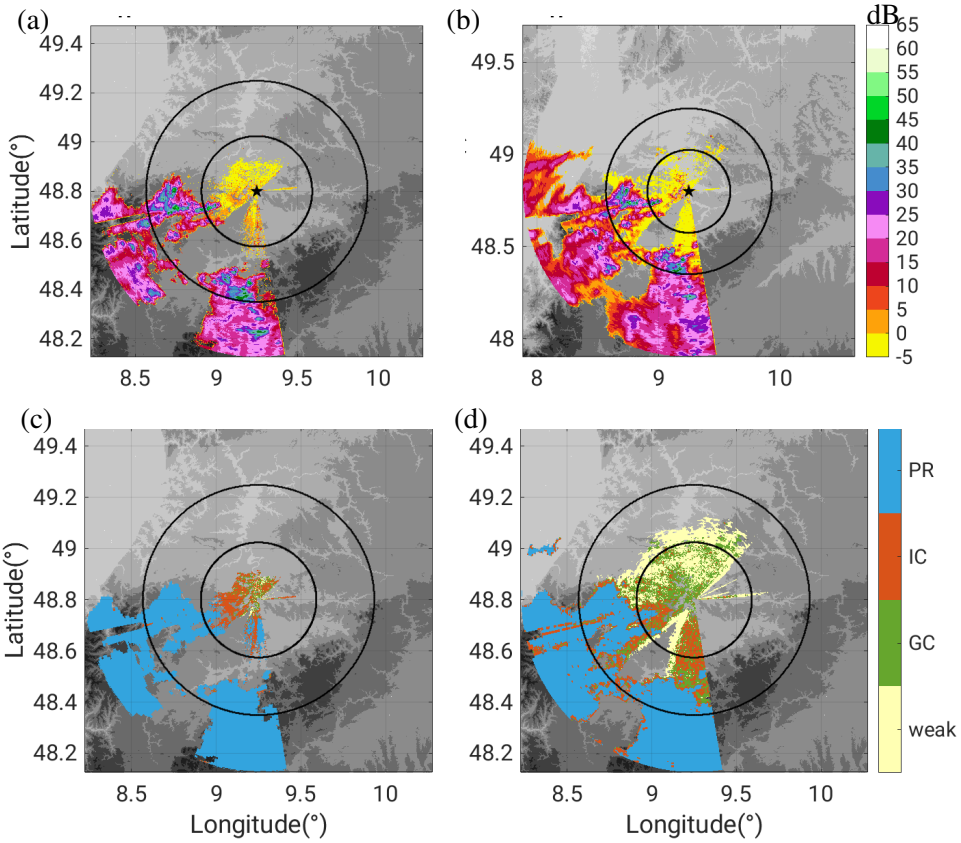

Fig. 4.31.: PPI displays for a case mixed with GCs, ICs, convective and stratiform precipitation at 21:33 (21:34) UTC on 26 June 2017, of Z_H for (a) the fine scan and (b) the coarse scan, of the identified echo classes for (c) the fine scan, and (d) the coarse scan

With the 25-km range, our FLC procedure based on fine scans can successfully identify GCs ICs and PRs at the locations which are in good accord with the intensity of radar reflectivity Z_H. Starting from the radar site, the GCs are scattered closest to the radar, and surrounded by the densely clustered ICs. In this case, both GCs and ICs are below 10 dBZ. Beyond 25 km away from the radar, our FLC procedure identifies most of radar gates as PRs, and very few gates as ICs (Figs. 4.31(c) and 4.31(d)). In contrast, the FLC based on the coarse scans tends to identify a larger portion of radar measurements beyond 50 km away from the radar as ICs, which should be unlikely in reality. However, we notice most of these identified ICs beyond 50 km away from the radar are located near the edge of the precipitation system with Z_H below 15 dBZ, similar to the situation in Fig. 4.30(f) in our aforementioned discussion. As we know, a large proportion of weak echoes are absent in fine scans but are kept in coarse scans (Section 4.1.1), hence the reason these falsely identified ICs in the far range are much less in the fine scan but more frequent in the coarse scan.

We also notice that the FLC based on the coarse scan identifies a large number of radar gates within the close range (0–15 km) as GCs, but at the same locations these radar gates are identified as ICs by the fine scan. Based on my subjective visual inspection, these radar gates are much likely to be ICs. It implies that our FLC procedure based on the coarse scans exhibit a weaker capacity to correctly distinguish between GCs and ICs. However, these radar gates identified as different classes by the fine and coarse scans correspond to the radar reflectivity less than 0 dBZ, and our FLC procedure still correctly identifies them as non-meteorological echoes, which means we already achieved our main objective – to distinguish between PR and non-meteorological echoes. On the other hand, the different performances of FLC in the fine and coarse scan data suggest one more benefit of using radar measurements in a higher spatial resolution.

As we mentioned, changing the weights in calculating the aggregative memberships can promote the capacity of our FLC. There is still great potential to improve the accuracy of the results of the preceding FLC procedure by adjusting the weights in aggregating the memberships in terms of each echo class instead of assuming equal weights (Eq. 4.2). For instance, for ϕ_{DP}, we only use its texture, whereas for Z_{DR} and ρ_{HV}, we use both their own value and their textures. It means that we gave two units of weight to Z_{DR} and ρ_{HV}, but only one unit of weight to ϕ_{DP}. However, we do not have evidence to prove that ϕ_{DP} is less important than the other two variables in terms of their roles in echo classification. Thus, one reasonable solution is to increase the weight of ϕ_{DP} from one to two, and then we have equal weights for all three polarimetric variables (Z_{DR}, ϕ_{DP} and ρ_{HV}) used in our FLC procedure.

4.5.4. Spatiotemporal variations of identified echo classes

After applying this above FLC procedure to the entire fine and coarse scan datasets respectively, we obtain the spatial distribution of identified echo classes (Fig. 4.32), which is undoubtedly significantly distinct from the spatial distribution of spike signals (Fig. 4.4) and second-trip echoes (Fig. 4.14). For both fine and coarse scan, the relative frequency of non-meteorological echoes (GCs and ICs) exceeds 90% for these radar gates very close to the radar, and these echoes are clustered in several irregular shapes, These radar gates are constantly impacted by the non-meteorological echoes consisting of GCs and ICs, but in fact primarily affected by the persistent and stable GCs. Despite this similarity, the area of these GC gates in the coarse scan data extends more that in the fine scan data, in accord with our findings in Section 4.4 that the coarse scan data are more susceptible to the GCs. Another difference is the deceasing gradient in the relative frequency along the radar beams as the radar gates become farther away from the radar. This gradient is very clear in the coarse scan data but invisible in the fine scan data. The reason is that weak echoes such as the ICs are preserved more in the coarse scans than in the fine scans. On the other hand, the fine scan data have a seemingly less frequency of precipitation echoes in comparison with the coarse scan data (Fig. 4.32(c)). However, the frequency does not directly equal the

intensity or the precipitation amount. The miss part in the fine scan mainly consists of the weak echoes above -5 dBZ but below 5 or 10 dBZ, and it barely contributes to the precipitation amount. Thus, the identified precipitation echoes from our fuzzy logic classification are less frequent in fine scans, but it won't lead to differences in the precipitation estimation between fine and coarse scans.

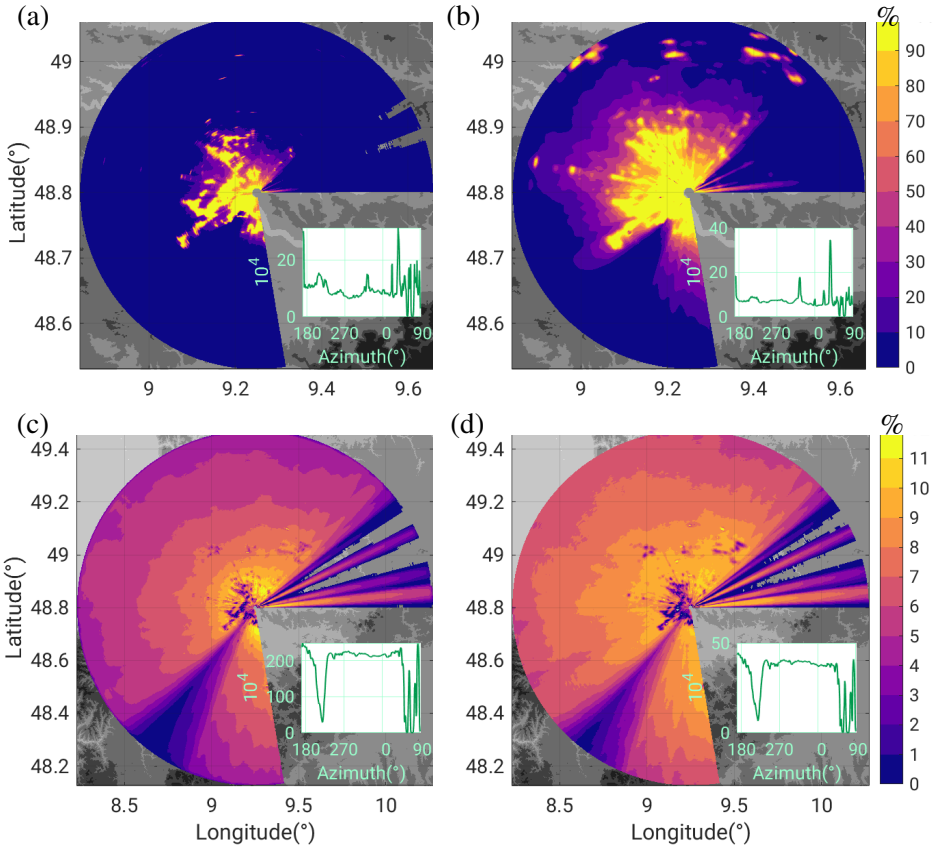

Fig. 4.32.: PPI displays of the relative frequency of identified echo classes for the entire measuring period, being identified as GCs and ICs within the 30-km range for (a) fine scans and (b) coarse scans, or being identified as precipitation echoes within the 75-km range for (c) fine scans and (d) coarse scans

4.6. Attenuation correction

The shorter wavelength of the X-band radar renders its power measurements vulnerable to the attenuation (reductions in magnitude of Z_H and Z_{DR}), which is the major reason impeding the wide use of the X-band frequency in precipitation observation until the availability of attenuation correction procedures. As shown in the following case study, the erroneous Z_H /Z_{DR} measurements caused by the presence of attenuation /differential attenuation are in contrast to the attenuation-corrected Z_H /Z_{DR} measurements, which emphasizes the necessity of effective attenuation correction algorithms. Then, we process Z_H /Z_{DR} measurements with two attenuation correction procedures, and verify these attenuation-corrected measurements by K_{DP} measurements. We also discuss differences between fine and coarse scans regarding attenuation correction to illustrate the effect of radial resolution on the attenuation correction.

4.6.1. Incorrect measurements caused by attenuation and differential attenuation

Absorption of EM waves or scattering of EM waves out of the beam is collectively referred as attenuation. It is caused by atmospheric gases invariably and ubiquitously, by hydrometeors when raining, and by liquid water residing on the radar radome occasionally. Since the magnitude of attenuation caused by gas is negligible compared to that by hydrometeors, attenuation by hydrometeors is our target within this thesis. The attenuation of weather radar signals by atmospheric hydrometeors has been long recognized (Ryde, 1946; Atlas and Banks, 1951; Hitschfeld and Bordan, 1954; Gunn and East, 1954).

The magnitude of attenuation depends on the frequency/wavelength of the EM waves and becomes greater for the shorter-wavelength radars (Bringi et al., 1990). Thus, the attenuation issue is significantly less for the S-band (10-cm λ) radars and is conventionally neglected except in rare cases (Ryzhkov and Zrnic, 1995). This accounts for a typical use of the S-band radars over broad areas or in the region where heavy rain events are frequent. For the C-band (5.5-cm λ) radars widely used in European continent, the attenuation becomes moderate and should not be neglected. Attenuation correction for the C-band radar data is strongly recommended before using radar data in the QPE (Krämer and Verworn, 2008; Jacobi and Heistermann, 2016; Vulpiani et al., 2008; Gu et al., 2011). When it comes to the X-band radar (10-cm λ), the attenuation becomes far more severe. Thus, in the X-band frequency, the attenuation correction is a prerequisite or a must, (Delrieu et al., 2000; Matrosov et al., 2002; Anagnostou et al., 2004; Matrosov et al., 2005; Park et al., 2005; Gorgucci et al., 2006; Snyder et al., 2010), otherwise Z_{H} and Z_{DR} measurements are inaccurate.

Attenuation occurs no matter in which polarization direction. Recall the definition of Z_{DR} (Eq. 2.46), the magnitude of Z_{DR} also changes due to the fact that attenuation in the horizontally polarized direction is normally severer than that in the vertically polarized direction. This inconsistency of attenuation between two polarization directions leads to a change in the magnitude of Z_{DR}. Such a change, mostly in the form of a reduction, is referred as *differential attenuation*.

To show how the attenuation (differential attenuation) affects Z_{H} (Z_{DR}) measurements, we conduct visual inspections for the following two cases: one for convective storms, and the other for stratiform precipitation. As mentioned, the C-band radar signals are less attenuated. In the first case, according to the C-band radar measurements (Fig. 4.33(e)), a convective storm present roughly 30–40 km west to the radar exhibits Z_{H} around 45–60 dBZ, but Z_{H} from the X-band radar measurements of either the fine or coarse scans barely reaches 35 dBZ (Figs. 4.33(a) and 4.33(c)). Moderate precipitation prevails between the X-band radar and this intense convective storm. It means that the radar echoes returning from that the convective storms have to propagate forth and back through the intermediate precipitation. The hydrometeors along the propagation paths weaken the radar signals through the attenuation, thereby reducing Z_{H}. Situations are the same for other convective storms scattered within the entire radar cover-

age. Although the morphologies of these convective systems are alike between the X-band and C-band radar measurements, the overall intensity of Z_H for the X-band radar is appreciably lower.

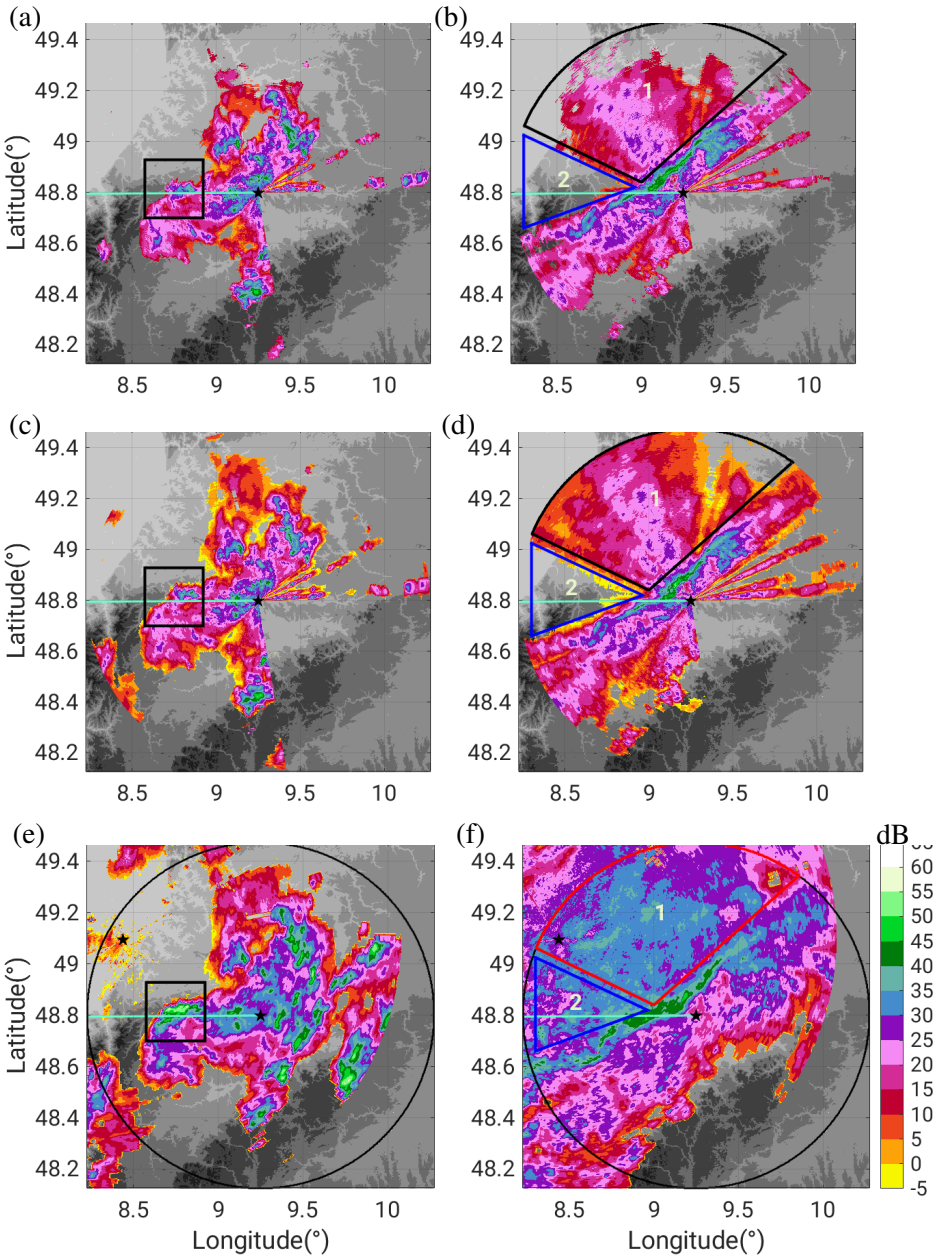

Fig. 4.33.: PPI displays of Z_H where (a), (c) and (e) are based on Z_H from the fine scan, coarse scan and C-band radar data respectively for a case at 15:53–15:55 UTC on 18 August 2017, (b), (d) and (f) are for another case at 10:05 UTC on 3 October 2017. The black stars represent the location of the X-band radar site, the green straight horizontal lines are the azimuth of 270°, the black squares in (a), (c) and (e) confine a convective storm in the western direction (at the 270° azimuth) in the radar coverage for the case on 18 August 2017, and the larger unfilled sectors in black or red numbered as 1 in (b), (d), and (f) indicate the location of widespread stratiform precipitation whose Z_H intensity is considerably weakened by attenuation, and the smaller unfilled blue sectors numbered as 2 indicate the area with a lack of radar measurements caused by severe attenuation

In the other case, according to the C-band radar measurements, a squall line in roughly 50-km length with Z_H intensity around 40–50 dBZ was approaching the X-band radar, leaving behind widespread stratiform precipitation with Z_H intensity around 25–40 dBZ (Fig. 4.33(f)). In contrast, for the X-band radar measurements, a part of radar coverage west to the radar has no measurable Z_H at all (the blue unfilled triangle numbered as 2 in Figs. 4.33(b) and 4.33(d)), while precipitation in the remaining radar coverage is characterized by considerably less Z_H intensity from 5 to 25 dBZ, owing to the attenuation. It is worth noting that, beyond the 55-km range, the weak Z_H still expands in the radar coverage of the coarse scan, but almost vanishes in the fine scan. Keep in mind that this difference between the fine and coarse scans matters in the following discussion on correcting attenuation (Fig. 4.37).

When it comes to Z_{DR}, according to the C-band radar measurements (4.34(e), the strong convective in the first case exhibits Z_{DR} up to 4 dB, but Z_{DR} from the X-band radar measurements is less than 2.5 dB along with a large part of negative Z_{DR}. Analogous to the above Z_H attenuation, this reduction in the magnitude of Z_{DR} reflects the impact of differential attenuation. Similarly, the differential attenuation also occurs for other convective storms within the radar coverage. In the second case, the C-band radar provides Z_{DR} measurements varying between 0.5 and 2.5 dB across the radar coverage (Fig. 4.34(b)). In contrast, for the X-band radar measurements, Z_{DR} measurements are absent in the western part of radar coverage (the blue triangle numbered as 2 in Fig. 4.34(d)), along with the remaining Z_{DR} in a much smaller magnitude or negative values (the black sector numbered as 1 in Fig. 4.34(d)). Similar to the situation in Z_H, we also see a deficiency of low or negative Z_{DR} (Park et al., 2005) beyond the 55-km range in the fine scan, while for the coarse scan, the negative Z_{DR} measurements still persist within the entire radar coverage.

The first case shows that the attenuation weakens Z_H intensity of convective systems, whereas the second case exhibits the weakened Z_H in stratiform precipitation and even an absolute loss of radar echoes behind a squall line. The absolute loss occurs once the returned echo power is below the noise level, as illustrated by the reduction in ρ_{HV} and SNR(not shown). We here use the C-band radar measurement as a reference to demonstrate the reduction or loss in the X-band radar measurements, however, the attenuation occurs for C-band radars as mentioned (Aydin et al., 1989), in the overall moderate magnitudes. It means the magnitude of the X-band radar attenuation shown here might be even more severe. In other words, if an S-band radar is nearby, it might help give us a more accurate feeling about how strong the attenuation in the X-band frequencies could be. In principle, despite the varying magnitude, the attenuation is omnipresent throughout our X-band radar measurements during the rainy period. Even for the radar beams propagating through into drizzle, the attenuation also occurs, but with weak and probably unnoticed magnitudes.

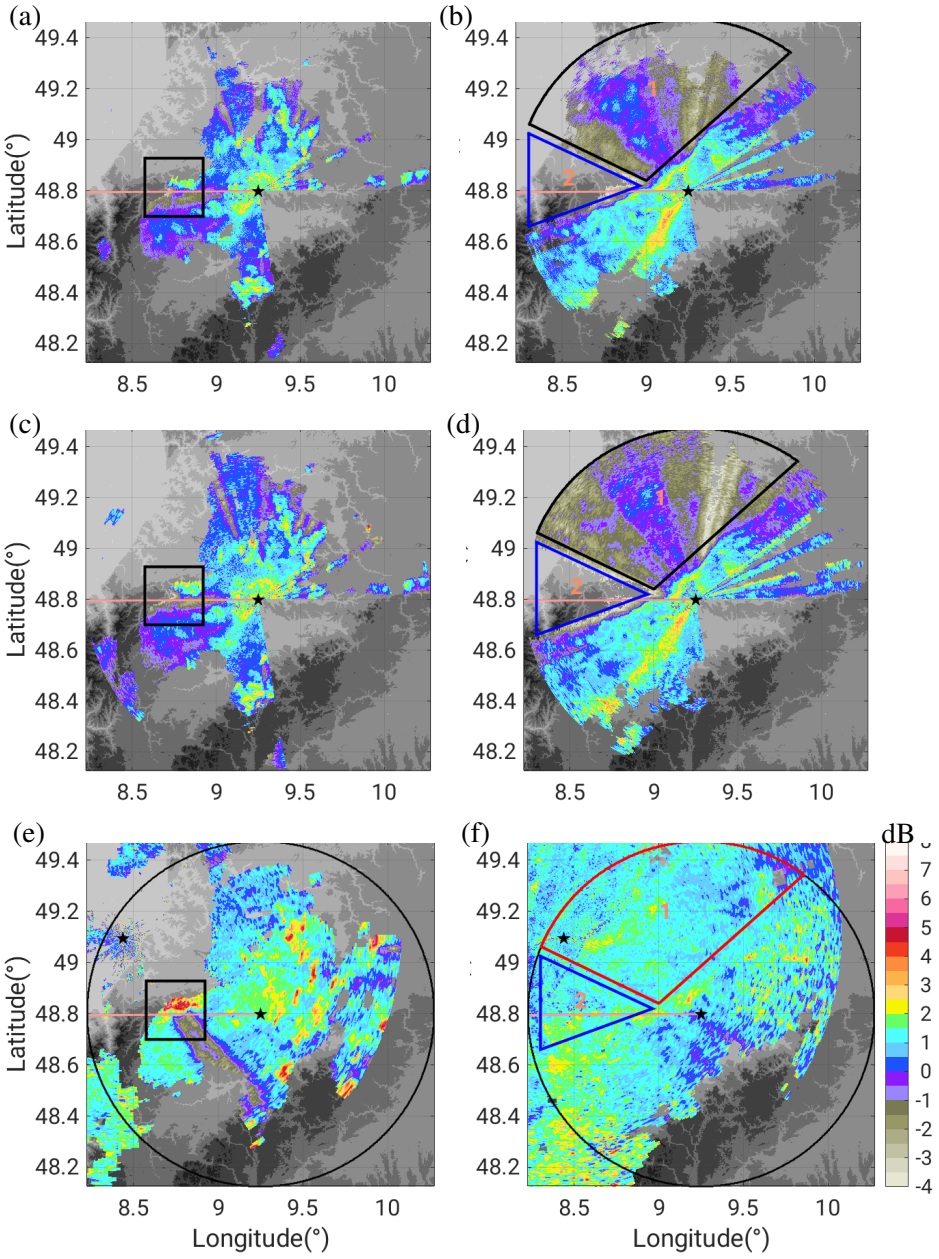

Fig. 4.34.: PPI displays of differential reflectivity Z_{DR} to show the effect of differential attenuation on diminishing the radar measurements of Z_{DR}, where (a), (c) and (e) are based on Z_{DR} from the fine scan, coarse scan and C-band radar data for the case at 15:53-15:55 UTC on 18 August 2017, (b), (d) and (f) are for another case at 10:05 UTC on 3 October 2017, and the meaning of the geometry are identical to Fig. 4.33. The Z_{DR} calibration (Section 4.7) has been already applied

Via the foregoing two distinct cases, we show how the attenuation and differential attenuation modify the radar data and bring about incorrect Z_H and Z_{DR} measurements. Given that attenuation and differential attenuation occur all the time and ubiquitously in our X-band radar dataset, we need to correct the attenuation and differential attenuation, and the correction should be applied with a procedure that can work automatically for the entire dataset.

4.6.2. Differential phase-based attenuation correction

The radar reflectivity and differential reflectivity measured from our X-band radar are propagation-included radar variables (Z'_{H} and Z'_{DR}), which can be linked to the unattenuated (intrinsic) Z_{H} and Z_{DR} through two terms: two-way path-integrated attenuation (PIA) and Two-way path-integrated differential attenuation ($\mathrm{PIA_{DP}}$) (Meneghini and Nakamura, 1990)

$$\mathrm{PIA_H} = Z_{\mathrm{H}} - Z'_{\mathrm{H}} \tag{4.3}$$

$$\mathrm{PIA_{DP}} = Z_{\mathrm{DR}} - Z'_{\mathrm{DR}} \tag{4.4}$$

The attenuation correction is to obtain the unattenuated (intrinsic) Z_{H} and Z_{DR}, that is, to calculate the PIA and $\mathrm{PIA_{DP}}$, and then add PIA and $\mathrm{PIA_{DP}}$ to the measured Z'_H and Z'_{DR}. Thus, the key of attenuation correction is to determine PIA and $\mathrm{PIA_{DP}}$. We introduce specific attenuation (A) and accompanied specific differential attenuation (A_{DP}) as follows

$$\mathrm{PIA} \equiv 2\int_0^r A(s)\mathrm{d}s \tag{4.5}$$

$$\mathrm{PIA_{DP}} \equiv 2\int_0^r A_{\mathrm{DP}}(s)\mathrm{d}s \tag{4.6}$$

where s is the length of the propagation path along which the attenuation occurs, A is the amount of attenuation for a wave propagating through a unit distance, and A_{DP} is the difference of specific attenuation between the horizontally and vertically polarized waves:

$$A_{\mathrm{DP}} = A_{\mathrm{H}} - A_{\mathrm{V}} \tag{4.7}$$

The larger A (A_{DP}) is, the more severe attenuation (differential attenuation) is.

Similar to differential phase shift that is the range interval of K_{DP} (Eq. 2.62), the PIA and $\mathrm{PIA_{DP}}$ are the range integral of A and A_{DP} (Eqs. 4.5 and 4.6). A basic assumption was proposed that A and A_{DP} are linearly proportional to K_{DP} (Bringi et al., 1990), and the coefficients for this linear proportionality are written as α and β in unit of $dB/^\circ$,

$$\alpha = A_{\mathrm{H}}/K_{\mathrm{DP}} \tag{4.8}$$

$$\alpha = A_{\mathrm{DP}}/K_{\mathrm{DP}} \tag{4.9}$$

Accordingly, we obtain two approximations as follows,

$$\mathrm{PIA} = -\alpha\,\phi_{\mathrm{DP}} \tag{4.10}$$

$$\mathrm{PIA_{DP}} = -\beta\,\phi_{\mathrm{DP}} \tag{4.11}$$

In other words, the amount of Z_{H} or Z_{DR} attenuated during the path propagation is assumed to increase linearly with the increasing magnitude of u-ϕ_{DP} measurement.

The magnitudes of the coefficients α and β vary widely with the radar frequency (Table 4.2) and show dependence on temperatures well (Jameson, 1992; Carey et al., 2000; Ryzhkov et al., 2014; Bringi et al., 1990).

Tab. 4.2.: Numerical range of linearity coefficient α and β (from Table 6.4 in Ryzhkov and Zrnić (2019))

Frequency	$\alpha(\mathrm{dB}/^\circ)$	$\beta(\mathrm{dB}/^\circ)$
S-band	0.015 – 0.04	0.0025 – 0.009
C-band	0.05 – 0.18	0.008 – 0.1
X-band	0.14 – 0.35	0.03 – 0.06

We examine the linearity between two pairs of variables—u-ϕ_{DP} and Z_{H}, as well as u-ϕ_{DP} and Z_{DR} in a heavy rain event with both convective and stratiform precipitation (Fig. 4.35(e)). We only involve the radar measurements whose K_{DP} value is between 2 and $3\,^\circ\mathrm{km}^{-1}$, to avoid the negative K_{DP} values, weak echoes from light precipitation or other disturbances on the Z_{H} data, analogous to the criterion used by Ryzhkov and Zrnic (1995) who chose K_{DP} of 1–2 $^\circ\mathrm{km}^{-1}$. It turns out both pairs of variables exhibit clear linearities, and the linearity between u-ϕ_{DP} and Z_{DR} is stronger than that between the other pair (Fig. 4.35). The linearity coefficients (α and β) estimated from this rainy episode are similar to the theoretical values in literature (Tab. 4.2), and their magnitudes are comparable in the fine and coarse scan data.

We further calculate coefficients of linearity (α and β) individually within each volume for all together 646 volume scans during rainy periods for both fine and coarse scans (Fig. 4.36). Either α or β is comparable between fine and coarse scans. The most frequent value for α is between -0.25 and -0.15 $\mathrm{dB}/^\circ$, and is between -0.045 to -0.055 $\mathrm{dB}/^\circ$ for β, which exactly matches up with the values in literature (Tab. 4.2).

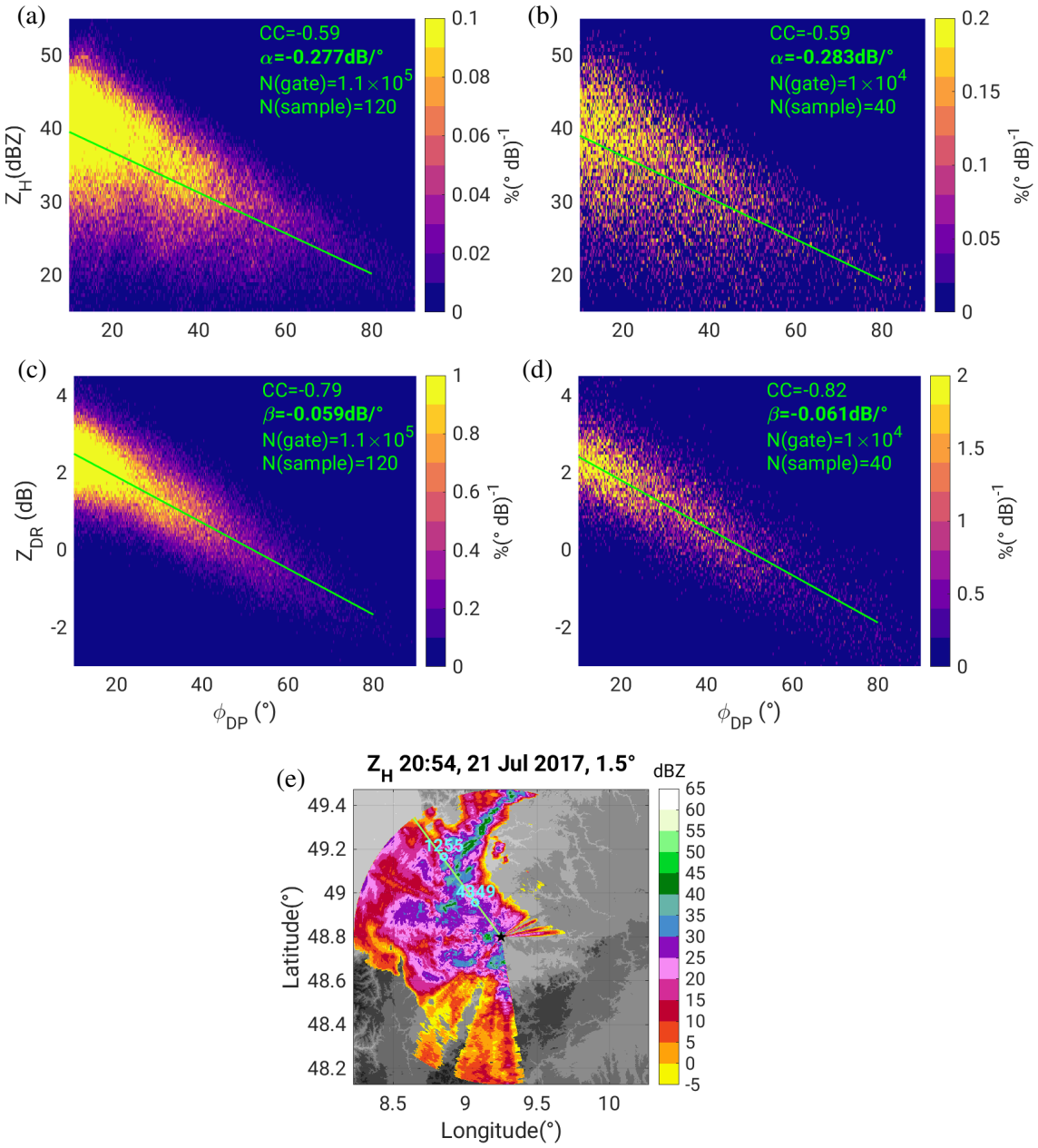

Fig. 4.35.: Relationships between ϕ_{DP} and Z_H measurements, or between ϕ_{DP} and Z_{DR} measurements for a rainy episode characterized by intense convective systems embedded in widespread stratiform precipitation during 16:10-22:49 UTC on 21 July 2017, (a) and (c) are for fine scans, (b) and (d) are for coarse scans, and (e) is a PPI display. In (a-d), the green lines are the linear least square fitting lines, "CC" represents the Pearson correlation coefficient, α represents the linearity coefficient between u-ϕ_{DP} and Z_H, and β represents the linearity coefficient between u-ϕ_{DP} and Z_{DR}. The black star in (e) represents the location of the X-band radar, with two marks representing locations of two DWD rain gauges indexed as 1255 and 4349. A sample defined here refers to a fine scan or a coarse scan excluding the 75–100 km range

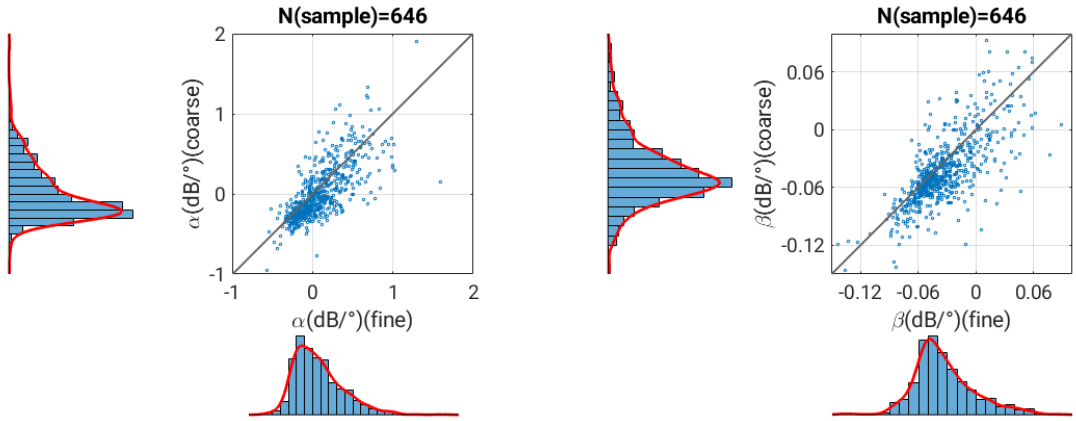

Fig. 4.36.: The scatter diagram with PDFs to compare the linearity coefficients between fine and coarse scans from the selected 646 volume scans during the rainy periods, (a) for coefficient between u-ϕ_{DP} and Z_{H} –α, and (b) for coefficient between u-ϕ_{DP} and Z_{DR} —β

However, there is a vast variety of the two linearity coefficients: α varies between -0.4 and 0.5 °km^{-1}, and β varies between -0.08 and 0.02 °km^{-1}. This high variability in magnitudes means that we may need to adjust the α and β values scan-by-scan for attenuation correction in practice. Moreover, the previous calculation implicitly assumes that α and β are constant with each volume scan. Nevertheless, in reality, the coefficients can even vary between radar beams or even within a single radar beam. For instance, when the center of a rapidly developed convective cell in the near range coexists along one radar beam with the decaying flank of the mature convective system in the far range, α and β can be different between sections along the radar beam. Given that the α and β values vary greatly in space and in time, assuming universally constant values for α and β is questionable. In order to tackle the spatiotemporal variability, α and β values should be allowed to change over each segment and each radar beam. Thus, for every range gate at range r

$$Z_{\mathrm{H}}(r) = Z'_{\mathrm{H}}(r) + \alpha\,\phi_{\mathrm{DP}}(r) \tag{4.12}$$

$$Z_{\mathrm{DR}}(r) = Z'_{\mathrm{DR}}(r) + \beta\,\phi_{\mathrm{DP}}(r) \tag{4.13}$$

The differential phase at the first radar gate $\phi_{\mathrm{DP}}(r_0)$ is normally azimuth-dependent and should be subtracted from all the ϕ_{DP} measurements along the ray.

Rather than estimating PIA (PIA$_{\mathrm{DP}}$) at each range gate, the ZPHI method (Hitschfeld and Bordan, 1954; Marzoug and Amayenc, 1994; Testud et al., 2000; Le Bouar et al., 2001; Tabary et al., 2011) estimates PIA for the last radar gate (r_N) across the range interval along a propagation path, and then distribute the total attenuation to each gate based on the reflectivity Z_{h} in linear scale (mm^{6}m^{-3}), assuming

$$A = a Z_{\mathrm{h}}^{b} \tag{4.14}$$

where the parameter b is almost constant for a given frequency, and the parameter a varies with temperature. The attenuation-corrected Z_{H} is expressed as

$$Z_{\mathrm{h}}(r) = \frac{Z'_{\mathrm{h}}(r)}{[1 - 0.46\,b\,a \int_{r_0}^{r} Z'^{b}_{\mathrm{h}}(s)\mathrm{d}s]^{1/b}} \tag{4.15}$$

$$a = \frac{1 - exp[0.23\,b\,\mathrm{PIA_H}\,(r_N)]}{0.46\,b \int_{r_0}^{r_N} Z'^{b}_{\mathrm{h}}(s)\mathrm{d}s} \tag{4.16}$$

as a function of the change in differential propagation phase $\Delta\phi_{\mathrm{DP}}$ across the range interval (from r_0 to r_{N}), the measured Z_{h} in the linear scale, the coefficient a and parameter b. The attenuation correction in ZPHI is constrained by $\Delta\phi_{\mathrm{DP}}$. The complete derivation of Eqs. 4.15 and 4.16 can be found in Bringi and Chandrasekar (2001), or a simplified version (Zhang, 2016), along a detailed implementation (Testud et al., 2000).

Given the variety of α and β values, assuming a constant coefficient α is a big limitation of the ZPHI algorithm. In contrast, in the iterative ZPHI (Bringi et al., 2001), also called as Self-consistent with Constraint Method (SCWC), the optimal value for the coefficients (α_{opt} and β_{opt}) are determined dynamically within a predetermined range through optimizations to achieve a minimal difference between the constructed and measured differential phase profile,

$$\chi = \sum |\phi^{(e)}_{\mathrm{DP}}(r_{n,\alpha}) - \phi^{(m)}_{\mathrm{DP}}(r_n)|; \alpha_{min} \leq \alpha \leq \alpha_{max} \tag{4.17}$$

where $\phi^{(\mathrm{m})}_{\mathrm{DP}}(r_n)$ is the measured ϕ_{DP} at the radar gate n, and $\phi^{(\mathrm{e})}_{\mathrm{DP}}(r_n, \alpha)$ is the constructed ϕ_{DP} with assumed coefficient α. Once the attenuated-corrected Z_{H} is obtained, there are two ways to obtain the attenuated-corrected Z_{DR}—processing the same optimization procedure to seek the best value for coefficient β, or assuming a linear relation as follows

$$\beta_{\mathrm{opt}} = \frac{Z_{\mathrm{DR}}(r_N) - Z'_{\mathrm{DR}}(r_{\mathrm{N}})}{\phi^{(m)}_{\mathrm{DP}}(r_{\mathrm{N}}) - \phi^{(m)}_{\mathrm{DP}}(0)} \tag{4.18}$$

As an extension to ZPHI, the idea of the iterative ZPHI is closer to the physics and more reasonable. Unlike the ZPHI method assuming a constant coefficient α, the iterative ZPHI algorithm seeks for the optimal coefficients to tailor the constructed ϕ_{DP} with the ϕ_{DP} measurements. It means that this iterative ZPHI method utilizes the ϕ_{DP} measurements along the entire propagation path, in contrast to that ZPHI algorithm which only uses ϕ_{DP} at the farthest radar gate as a constraint.

For this study, we applied both the ZPHI and iterative ZPHI attenuation correction procedures built-in in the Rainbow5 radar signal processor with the default setting for the X-band radar (M.Thurai, 2007; Selex-SI, 2012). More detailed aspects of the attenuation correction procedure algorithms are available in the user manual of the radar data processor (SELEX, System Integration GmbH, 2015).

The effect of attenuation correction is shown in Figs. 4.37 and 4.38, corresponding to the aforementioned two cases (Figs. 4.33 and 4.34). Applying either the ZPHI or iterative ZPHI attenuation correction procedure, the Z_H measurements regain high intensity. For the first case of convective storms, either for the fine or coarse scans, the attenuation-corrected Z_H of the storm west of the radar reaches above 55 dBZ, agreeing with Z_H from the C-band radar (the black squares in Figs. 4.37(a) and 4.37(c)). In the second case, for the coarse scan, over the northern part of the radar coverage (the sector numbered as 1 in Fig. 4.37(d)), the majority of Z_H in the stratiform precipitation returns to a magnitude comparable to the C-band radar measurements. Nevertheless, no Z_H is corrected over the western sector of the radar coverage (the sector numbered as 2 in Fig. 4.37(d)), which is due to the total loss of radar signals. For the fine scan, the total loss of radar signals also occurs in the sector 2, and no Z_H is corrected (Fig. 4.37(b)). However, in the north part of the radar coverage (the sector 1), for the fine scan, nearly a third of stratiform precipitation, most of which is beyond 50 km away from the radar, is still missing, although the remaining two thirds of stratiform precipitation mostly within the 50-km range magnify their Z_H intensity to a magnitude comparable to the C-band radar measurements (Fig. 4.37(b)). It means that these attenuation-corrected Z_H are different between the fine and coarse scans in the stratiform precipitation area (the Sector 1). The attenuation correction is able to recover the majority of Z_H for the coarse scan but still miss a large portion of Z_H for the fine scan.

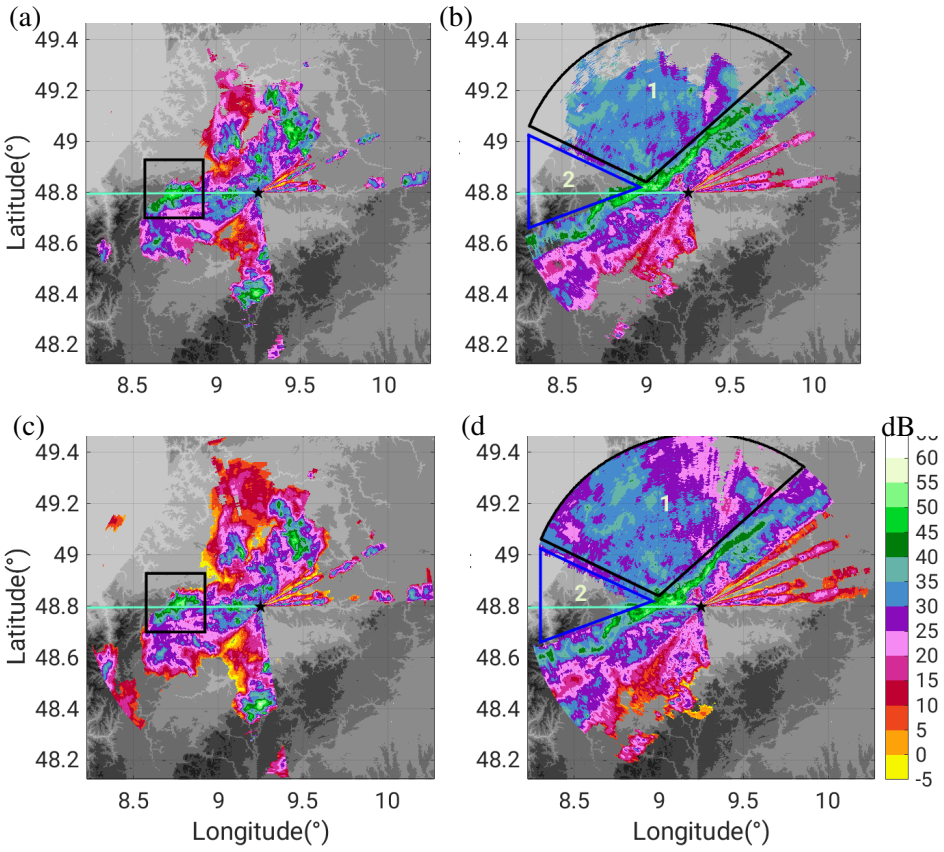

Fig. 4.37.: PPI displays of attenuation-corrected Z_H as the same case as Fig. 4.33

This difference in attenuation-corrected Z_H between fine and coarse scans is essentially associated with the fine scans' tendency to lose weak echoes. Although the weak echoes with Z_H below 20 dB have minimal impact on the radar-based precipitation quantities (Section 4.1.1), the impact of weak echoes can be more problematic in case of severe attenuation (differential attenuation), For instance, if the attenuation lessens the Z_H intensity from moderate to weak, then these weak echoes vanish in the fine scan, and we end up with an absolute lack of Z_H of the fine scan over the area where severe attenuations occur. In other words, attenuation correction is unable to retrieve any Z_H measurement if the radar signals totally vanish, which is the situation occurring in the northern part of the radar coverage for the fine scan (Fig. 4.37(b)). In contrast, the weak echoes remain in the coarse scan, so the Z_H correction still functions for the coarse scan data as far as the Z_H measurements are available, albeit in weak intensity (Fig. 4.37(c)). In this way, the loss of weak echoes combined with severe attenuation leads to another form of difference between fine and coarse scans—recurrent losses of radar echoes when attenuation occurs.

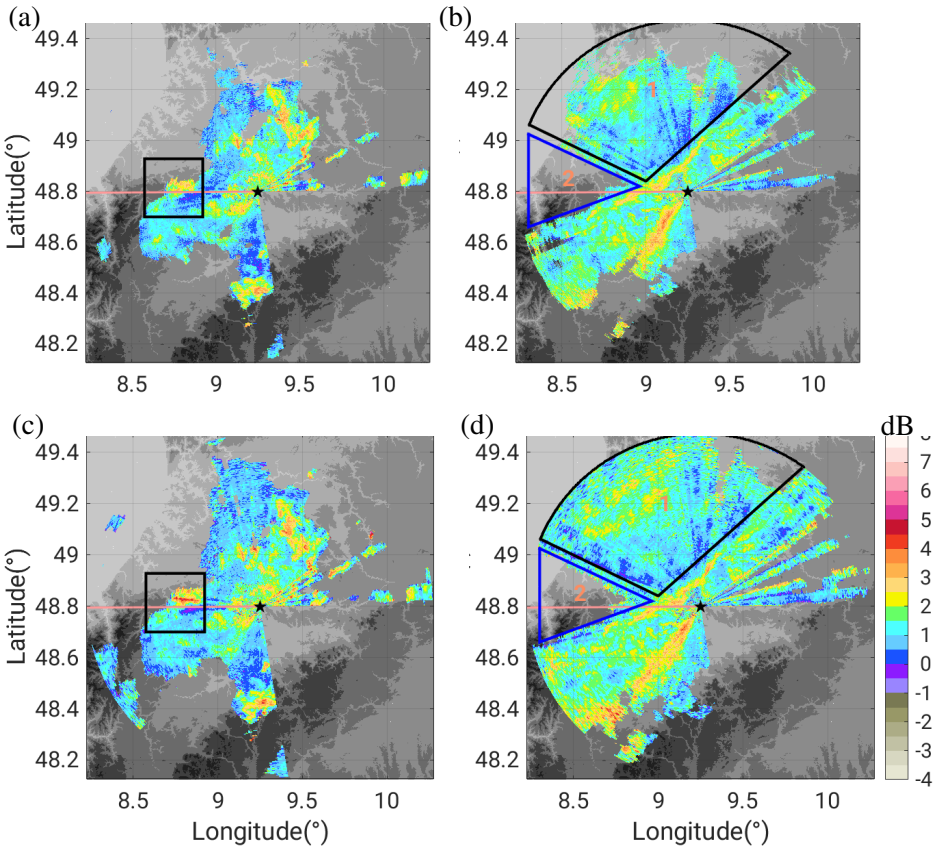

Fig. 4.38.: PPI displays for attenuation-corrected Z_{DR} as the same case as Fig. 4.34

As regards differential attenuation correction, in the first case of convective storms, either for the fine or coarse scans, the attenuation-corrected Z_{DR} in the center of the convective storm west of the radar increases considerably, reaching a magnitude only slightly less than Z_{DR} of the C-band radar

(Fig. 4.38(c)). Recall the concept of resonance (Section 2.1), and its dependence on radar λ. The resonance only occurs, if the raindrops are large enough and the threshold size of the raindrops increase with λ. Because λin the C-band frequency is longer than that of the X-band frequency, within the same precipitation, the resonance should less frequent in C-band radar measurement than that of X-band radar. However, the resonance effect is more significant in C-band rather than X-band. For instance, the resonance effect adds 1 dB or 1.5 dB to the X-band Z_{DR} but 3 dB or 4 dB to the C-band Z_{DR}. Thus, the resonance effect is the reason why Z_{DR} from the X-band radar measurement, even after correcting attenuation, is less than that of the C-band radar. Outside this convective storm, the overall Z_{DR} after differential attenuation noticeably increase, approaching the Z_{DR} magnitude of the C-band radar measurements.

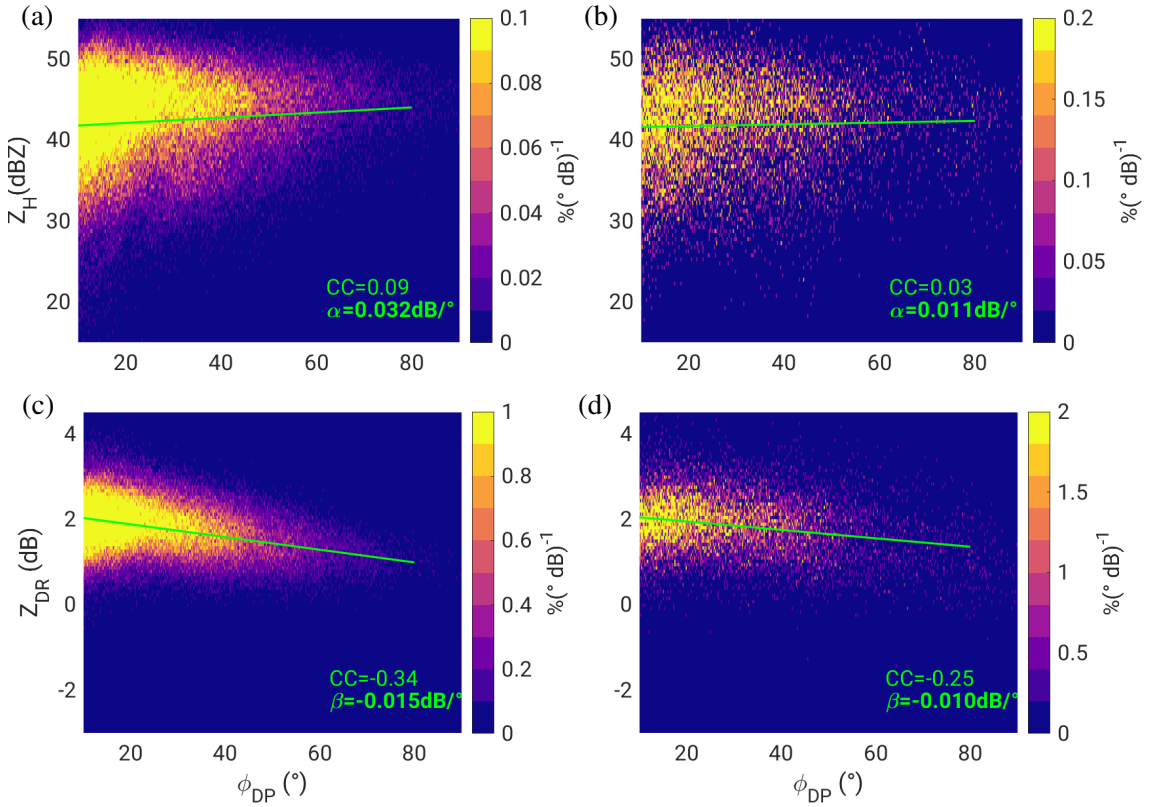

Fig. 4.39.: Diminished linear relationships between u-ϕ_{DP} and Z_H, or between u-ϕ_{DP} and Z_{DR} after attenuation correction or differential attenuation correction using the iterative ZPHI method, for the same case as Fig. 4.35, (a) and (c) are for the fine scans, and (b) and (d) are for the coarse scans

Similar to the part of unsuccessful attenuation for Z_H, differential attenuation also fails to recover Z_{DR} in the areas devoid of radar echoes (the unfilled triangles west of the radar in Figs. 4.38(b) and 4.38(d)). Besides, the abnormal linear pattern along the radar beams in the attenuated-corrected Z_{DR} is obvious in both fine and coarse scans, reflecting somehow the insufficiency/inability of this differential attenuation correction.

The linearity between u-ϕ_{DP} and Z_H or Z_{DR} should diminish or vanish after attenuation correction. The linear correlation between u-ϕ_{DP} and the attenuation-corrected Z_H barely exists, but the linear correlation between u-ϕ_{DP} and the attenuation-corrected Z_{DR} is kept to some extent (Fig. 4.39). The remaining linearity between u-ϕ_{DP} and the attenuation-corrected Z_{DR} may be another explanation corresponding to the discrepancy between the attenuation-corrected Z_{DR} and Z_{DR} of the C-band measurements.

Several factors influence the accuracy of the foregoing attenuation correction using ϕ_{DP}—DSD variability, temperature dependency, drop shape-size relationship, existence of backscatter differential phase, and statistical error in ϕ_{DP} measurements (Carey et al., 2000).

4.6.3. Comparing two attenuation correction methods

The iterative ZPHI attenuation correction procedures allows flexibility for coefficients α and β and thus should be more advanced. However, in the implementation, the values of α and β tend to reach the extreme values—two ends of the allowed range—after one or two iterations (through personal communication). Here we quantify the relative performance of ZPHI and the iterative ZPHI according to the AR over a certain time interval, which is calculated using Z_H corrected by means of ZPHI and iterative ZPHI algorithms $AR_{ZPHI,f}, and AR_{iterative,f}$ for fine scans, and $AR_{ZPHI,c}$ and $AR_{iterative,c}$ for coarse scans, respectively. $AR_{0,f}$ and $AR_{0,c}$ are for the AR without attenuation correction. Note that Z_H involved here is base data, not processed by the external QC procedures. To compare between ZPHI and iterative ZPHI algorithms, we calculate $\Delta_f = AR_{ZPHI,f} - AR_{iterative,f}$ for the fine scans, and $\Delta_c = AR_{ZPHI,c} - AR_{iterative,c}$ for coarse scans, respectively. To show the difference between the fine and coarse scans, we also calculate, $\Delta_{fc,0} = (AR_{ZPHI,c} - AR_{ZPHI,f})$, $\Delta_{fc,ZPHI} = (AR_{ZPHI,c} - AR_{ZPHI,f})$ and $\Delta_{fc,iterative} = (AR_{iterative,c} - AR_{iterative,f})$; the positive values for these three terms means the precipitation quantities of the coarse scan data is greater than its counterpart in the fine scan data. Besides, we define $\Delta_{fc} = \Delta_c - \Delta_f = (AR_{ZPHI,c} - AR_{ZPHI,f}) - (AR_{iterative,c} - AR_{iterative,f})$, to show whether the differences between ZPHI and iterative ZPHI algorithms are larger for the fine or coarse scans; the positive values of Δ_{fc} mean a greater difference between the fine and coarse scans if the ZPHI algorithm rather than the iterative ZPHI algorithm is used.

For this heavy rain event lasting for 4 hours (Fig. 4.35), attenuation correction can regain the AR exceeding 30 mm (Figs. 4.40(a) and 4.40(c)) especially over the intense convective cells, while the difference between two attenuation correction algorithms (Δ_f) is merely around 2 mm (Fig. 4.40(e)). It means that the difference caused by different attenuation correction procedures is significantly smaller than difference in AR between without and with attenuation correction. The larger portion of positive values in Δ_f means that the ZPHI algorithm is able to recover more precipitation than the iterative one.

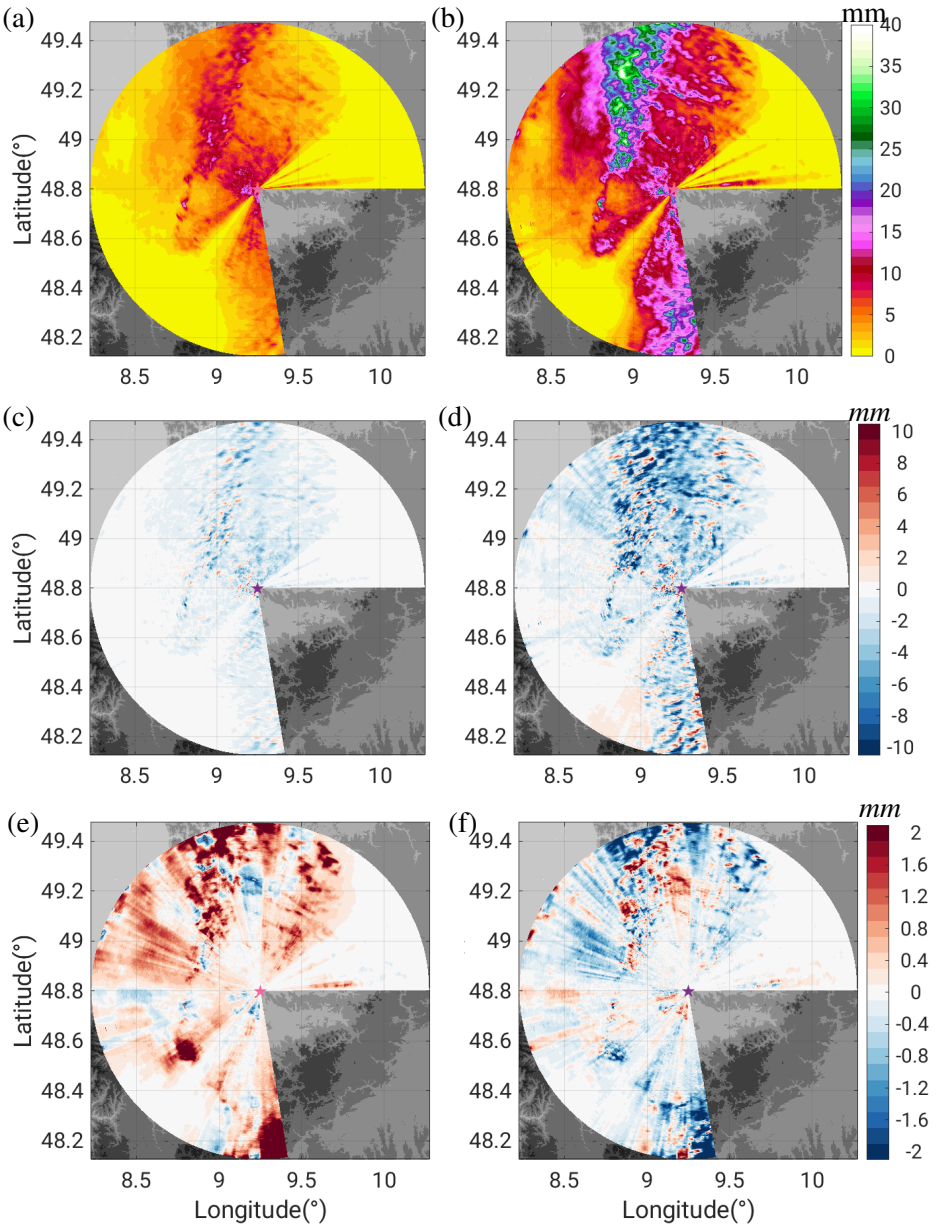

Fig. 4.40.: PPI displays showing the effect of attenuation correction on the rainfall accumulation for a 4-hour rainy episode from 20:00 to 23:00 UTC on 21 July 2017, (a) AR_{f} the total AR estimated from the fine scans without attenuation correction, (b) $AR_{\mathrm{ZPHI,f}}$ with Z_{H} corrected by ZPHI attenuation correction, (c) $\Delta = AR_{\mathrm{c}} - AR_{\mathrm{f}}$ difference between the fine and coarse scans before attenuation correction, (d) $\Delta = AR_{\mathrm{c}} - AR_{\mathrm{f}}$ after attenuation correction (e) $\Delta_{\mathrm{f}} = AR_{\mathrm{ZPHI}} - AR_{\mathrm{iterative}}$ the difference in rainfall accumulation corrected by ZPHI and iterative ZPHI for fine scan, and (f) $\Delta_{\mathrm{c}} - \Delta_{\mathrm{f}}$

The attenuation correction modifies the difference in AR between the fine and coarse scans. Before attenuation, this difference is relatively small (Fig. 4.40(c)), and becomes remarkably larger after attenuation correction (Fig. 4.40(d)). Either before or after attenuation correction, the negative values dominate the radar coverage, which means AR estimated from coarse scans is smaller than that of fine scans. In other words, although Z_{H} of both fine and coarse scans increases after attenuation correction,

the fine scans regain a greater *AR*. Given Z_H is not processed by the data QC procedures, one possible explanation for the greater amount of Z_H correction for the fine scan data is that, in this 4-hour precipitation event, the widespread precipitation also persisted beyond the 75-km range of the radar coverage, resulting in the second-trip echoes. These second-trip echoes, although in the moderate intensity, bring about the "extra" amount of "fake" precipitation into the total amount of *AR*. It again reflects the necessity of the second-trip echo removal (Section 4.3). The relationship between the second-trip echo and attenuation correction procedures is presented in Appendix B.1.2.

In addition to the foregoing comparisons over a large area, we also examine the effect of attenuation correction over time. The reference data are the rain gauge measurements of two selected DWD rain gauge situated in the adjacent azimuthal directions. The 5-minute *AR* is calculated from the 1-minute rainfall amount measured by the rain gauges, and then divided by the 5-minute time span to obtain the 5-minute averaged *R* for each 5-minute interval. This *R* is then converted into the equivalent radar reflectivity Z_e using the Marshall-Palmer Z-R relation. We compare three types of Z_H —without, with ZPHI and with iterative ZPHI attenuation correction—to the Z_e from rain gauges. Within each 10-minute interval, Z_e of the first 5-minute interval is compared to Z_H of fine scans, and the of Z_e the second 5-minute interval is compared to Z_H of coarse scans.

The majority of Z_H increases, after being applied with attenuation corrections, and gets closer to the rain gauge measurements (Fig. 4.41). The increase is far more remarkable for the rain gauge (numbered 1255) farther from the radar than the other one located closer to the radar site, and this larger correction of Z_H in the farther range tallies with the physics of attenuation. The radar signals arriving at the farther rain gauge need to propagate a longer distance through the atmosphere filled with more liquid water and therefore is subject to a severer attenuation. Besides, the attenuation-corrected Z_H from the ZPHI and iterative ZPHI procedures are nearly identical except a small difference from 20:00 UTC to 20:59 UTC for the rain gauge numbered as 1255. However, unlike the comparison over a large area (Fig. 4.40), there is no clear tendency that the difference between fine and coarse scans becomes greater after rather than before correction over these two particular rain gauges. Instead, after attenuation correction using either ZPHI or the iterative ZPHI procedure, Z_H of both fine and coarse scans exhibits good agreements with Z_e of the rain gauge measurements. Overall, the difference between the uncorrected and corrected Z_H is far more pronounced than the difference between the fine and coarse scans, and also than the difference between two attenuation correction algorithms. Keep in mind that the rain gauge measurements allow us to verify Z_H only. There is no suitable reference for Z_{DR} to enable a quantitative evaluation of the attenuation-corrected Z_{DR}.

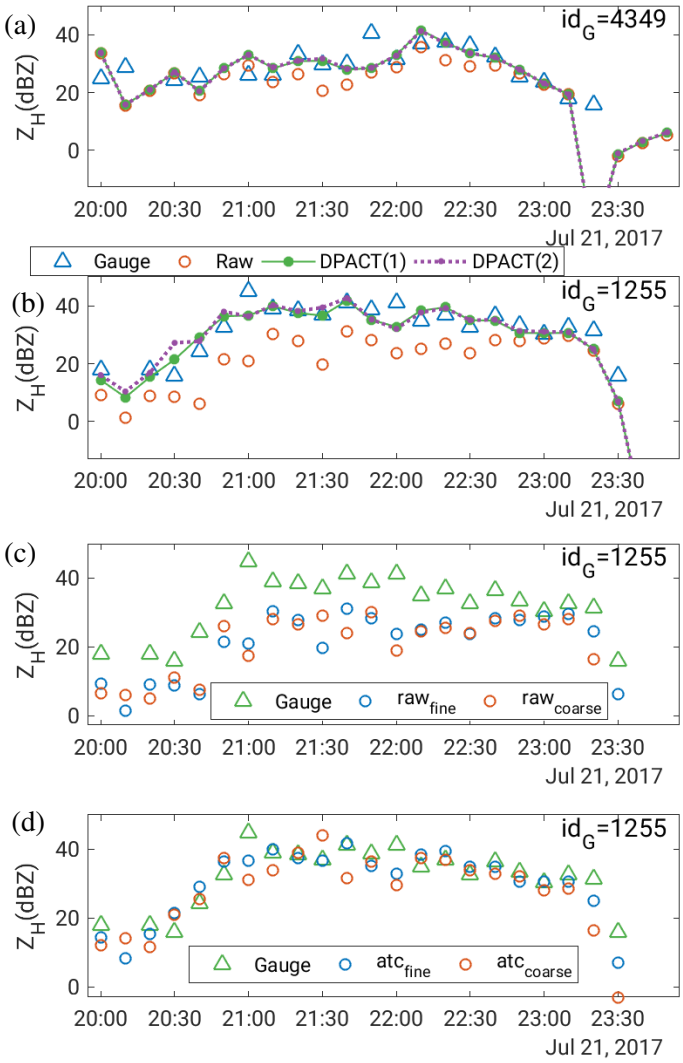

Fig. 4.41.: Time series of Z_H from different datasets during the same rain event as Fig. 4.40. (a) and (b) are for two rain gauges with ID numbers of 4349 and 1255 respectively, with Z_e converted from DWD rain gauge measurements (denoted as *Gauge*), the attenuated and uncorrected Z_H (denoted as *raw*), the attenuation-corrected Z_H using the ZPHI algorithm (denoted as DPACT(1)), the attenuation-corrected Z_H using the ZPHI algorithm (denoted as DPACT(2)). (c) and (d) are for the rain gauge with ID number 1255 with and without attenuation correction, where "atc" means the attenuation-corrected Z_H using the ZPHI algorithm

After comparing *AR* retrieved from Z_H corrected by ZPHI and iterative ZPHI algorithms respectively in the preceding case study, we find the differences between ZPHI and iterative ZPHI attenuation correction are moderate but exist. However, the algorithms of the built-in attenuation correction procedures provided from the signal processor are not open-source, and it is not easy to investigate the reason for these differences. The further analyses in Section 5.2.1 show the iterative ZPHI procedure outperforms. Since then, without special statements, the iterative ZPHI procedure is the default attenuation correction for the remaining of this thesis.

4.6.4. Verifying attenuation correction with K_{DP}

Given that K_{DP} is immune to attenuation (as far as the echo power is above the noise level) (Section 2.2), the rainfall estimate on the basis of K_{DP} ($R(K_{DP}) = aK_{DP}^{b}$) is not affected by attenuation. Thus, we can assess the performance of the attenuation correction by comparing K_{DP}-based rainfall estimates to the attenuation-corrected Z_H-based rainfall estimates.

As shown in Section 2.3, the coefficients a and b in the K_{DP}-based rainfall estimator vary much depending on the radar frequency and drop size distribution. However, within this section, we only aim to prove that the rainfall estimates from the attenuation-corrected Z_H are comparable to the rainfall estimates using K_{DP}, so the exact values of a and b are not that important. We use 17 for a and 0.73 for b.

Return to the first example where an intense convective appears in moderate intensity due to the severe attenuation (Fig. 4.33(a)). Along the 270° azimuth, according to K_{DP} data, a convective storm centered at 35 km away from the radar is more intense than another convective storm centered at 10 km away from the radar, and moderate stratiform precipitation prevails between the two convective storms. it is in accord with the C-band radar measurements (Fig. 4.33(e)). The only difference between the K_{DP} data and C-band radar Z_H measurements is, as a result of the total loss of echoes, the K_{DP} data end within 40 km away from the radar, at a shorter range than the C-band radar data. As discussed before, the attenuated and uncorrected Z_H intensity of the farther convective storm is much less than that of the closer one because of the severe attenuation, in contrast to what are presented by K_{DP} data or C-band radar data. In terms of precipitation estimation, R estimated based on the attenuated Z_H for the farther convective storm hardly exceeds 3 mm h^{-1}, in contrast to R estimated using the K_{DP} data in magnitude of over 45 mm h^{-1} (upper in Fig. 4.42(b)).

After attenuation correction has been applied, R estimated using Z_H around 30–40 km away from the radar increases dramatically for the farther storm and moderately for the closer storm, and thus reaches similar magnitudes as R calculated from the $R(K_{DP})$ estimator, for the coarse scan (Fig. 4.42(b)) and the fine scan (Fig. 4.43(b)). Owing to the fast movement of this storm within the 100-second time interval between the coarse scan and the fine scan, the precipitation presented by this cross-section along the ray differ slightly between fine and coarse scans. However, in general, R from the K_{DP}-based rain estimator resembles the corresponding R from the Z_H-based rain estimator.

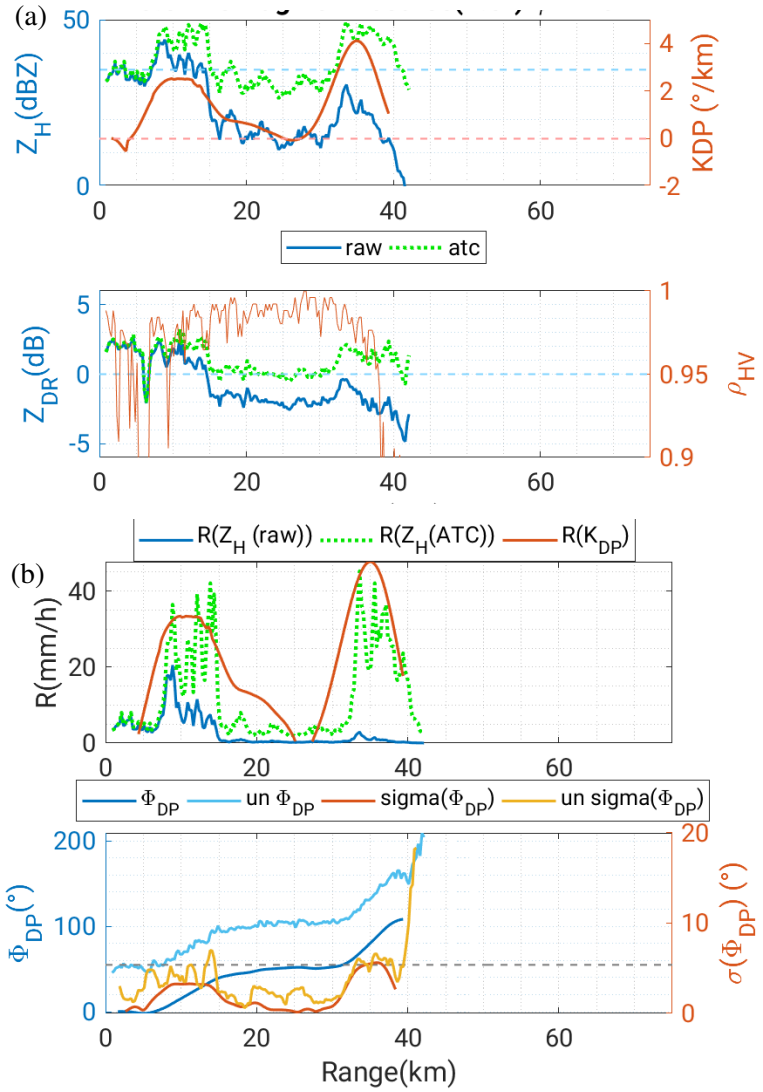

Fig. 4.42.: Ray cross-sections to show the effect of attenuation correction, of the following variables: uncorrected and attenuation-corrected Z_H, uncorrected and attenuation-corrected Z_{DR}, K_{DP}, ρ_{HV}, the rainfall rate based on the uncorrected Z_H and attenuation-corrected Z_H—$R(Z_H)$, rainfall rate based on K_{DP} — $R(K_{DP})$, uncorrected and corrected differential phase ϕ_{DP}, and texture of corrected ϕ_{DP} ($\sigma_{\phi_{DP}}$)for the azimuth at 270° for the coarse scan at 15:44UTC on 18 August 2017, along the green horizontal line in Fig. 4.33(c), where the blue solid lines in (a) represent the uncorrected Z_H (or Z_{DR}), the green dot lines represent the attenuation-corrected Z_H (or Z_{DR}), the red solid line in upper (bottom) of (a) is K_{DP} (ρ_{HV}), the blue solid line/green dot line/red solid line in the upper panel of (b) represents the R estimated based on uncorrected Z_H, based on corrected Z_H, and base on K_{DP}, respectively, the dark (light) blue solid lines in the bottom of (b) represent ϕ_{DP} (u-ϕ_{DP}), the red (yellow) solid lines in the bottom of (b) represent the texture of corrected (uncorrected) ϕ_{DP} ($\sigma_{u\text{-}\phi_{DP}}$), the light blue horizontal dashed line in the upper (bottom) of (a) is Z_H at 35 dBZ (Z_{DR} at 0 dB), and the light red horizontal dashed line in the upper of (a) is K_{DP} of 0 ° km^{-1}. Z_H are from the coarse scan exclusively. The blank areas beyond the 45-km range are kept to emphasize the absolute loss of radar signals

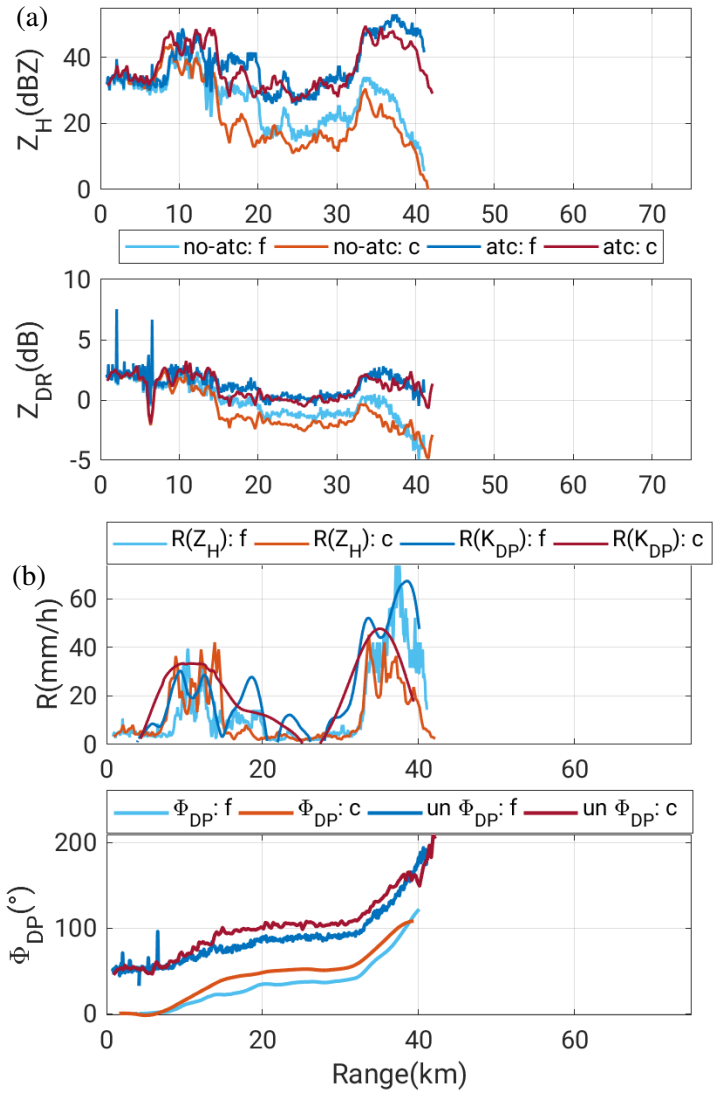

Fig. 4.43.: Ray cross sections to compare between fine and coarse scans in terms of uncorrected and attenuation-corrected Z_H or Z_{DR}, the R estimated based on uncorrected and attenuation-corrected $Z_H - R(Z_H)$ and based on $K_{DP} - R(K_{DP})$, and u-ϕ_{DP} and ϕ_{DP} along the same radar beam as Fig. 4.42. The blank areas beyond the 45-km range are kept to emphasize the absolute loss of radar signals

In addition to Z_H, the negative Z_{DR} data become positive after differential attenuation correction (Fig. 4.42(a)). ρ_{HV}keeps being above 0.95 until 5 km before the total loss of signal occurs. The constant difference (around 50°) between uncorrected and processed ϕ_{DP} gives a value for the system phase shift (Fig. 4.42(b)), and the processed ϕ_{DP} retrievals of both fine and coarse scans follow the monotonically increasing trend, despite slight differences in magnitude. The profile of $\sigma_{\phi_{DP}}$ is smooth and thus $\sigma_{\phi_{DP}}$ has no specific usage.

The case is deliberately selected to show attenuation and the corresponding attenuation correction for three different scenarios—for stratiform precipitation (in the range of 15–30 km), a intense convective storm (between 10–42 km, and for total losses of signal (beyond 42.5 km away from the

radar)). R estimated using attenuation-corrected Z_{H} can reach the same order of magnitude with$R$ estimated using K_{DP}. In contrast, lack of attenuation correction leads to an appreciable negative Z_{H} bias and its corresponding precipitation estimates. Such contrast verifies the necessity of attenuation correction in QPE. The attenuation correction process recovers the reduced signals and provides a more exact estimation of rainfall rate, especially for the precipitation behind strong convective. It further proves that, at the X-band frequency, the precipitation estimation based on Z_{H} can only be trustful if the attenuation correction is applied in advance.

In addition to the necessity of attenuation correction, the above example also illustrates the advantage of using K_{DP} in rainfall estimating at the X-band frequency—free of the negative affect caused by Z_{H} attenuation. However, K_{DP} in essence is calculated using ϕ_{DP} over calculation window—an interval consisting of several successive radar gates, so the spatial resolution of K_{DP}-based rainfall estimation is much coarser than that of Z_{H} measurements. This difference in the radial resolution between K_{DP} and Z_{H} is clearly reflected in difference between $R(K_{\mathrm{DP}})$ and $R(Z_{\mathrm{corrected}})$. The fluctuating curve of rainfall estimates based on Z_{H}, regardless before or after attenuation correction, is in sharp contrast to the spatially smooth curve with large widths along the radial direction for $R(K_{\mathrm{DP}})$ (Fig. 4.43(b)). Such difference attributes to the fact that Z_{H} is measured at each radar sampling volume, whereas K_{DP} is estimated using the ϕ_{DP} measurements that has been smoothed (Park et al., 2005) by removing fluctuations in the u-ϕ_{DP} measurements. More precisely, the spatial resolution of K_{DP} retrievals deteriorates and it depends on the length of calculation window. It implies, $R(K_{\mathrm{DP}})$ is not high-resolution, and the ratio of the spatial resolution of $R(K_{\mathrm{DP}})$ of fine to coarse scans is no longer 10 to 3.

As mentioned in Section 3.1.5, K_{DP} in our X-band radar dataset was retrieved automatically through the built-in K_{DP} retrieval procedure (Selex-SI, 2012) which uses a Z_{H} dependent window length according to the handbook (M.Thurai, 2007). This flexible window length changes the number of radar gates within the calculating window depending on the Z_{H} intensity in the center of calculating windows. This flexible calculation window for the K_{DP} retrieval fits the physics because the change in difference phase through the light rain is small and can be noisy, and it is more reliable to involve more gates to achieve a substantial change in ϕ_{DP}. However, the built-in K_{DP} retrieval procedure states that the choice of the window length depends not only on the Z_{H} intensity but also on the range spacing and radar frequency (wavelength). The built-in K_{DP} retrieval procedure does not explicit state the exact number of radar gates used for retrieving K_{DP}. Chances are that, in order to achieve a sufficient change in ϕ_{DP}, the calculating window lengths of fine and coarse scans are adjusted to be comparable, which means no difference in spatial resolution for K_{DP} data between the fine and coarse scans, and so are its associated rainfall estimates. In order to figure out the length of calculating window for calculating K_{DP}, we particularly count the frequency of retrievable K_{DP}. The spatial distribution of the retrievable K_{DP} (not shown) shows K_{DP} at the first 20 gates and the last 13 gates are inaccessible for fine scans, and at the first 6 gates and

the last 7 gates are inaccessible for coarse scans. Thus, we suspect the number of radar gates used to retrieve K_{DP} are 13 and 7 gates respectively for fine and coarse scans.

Moreover, it is worth noting that the attenuation correction was not applied before K_{DP} retrieval. It indicates, although the "true"K_{DP} value are unaffected by attenuation, the retrieving procedure utilizes the attenuated Z_H for dynamically adjusting K_{DP} calculation lengths, and thus is implicitly influenced by attenuation.

As mentioned in Section 3.1.5, the first step in the K_{DP} retrieval—"good" data masking—selects radar data which satisfy the criteria of small $\sigma_{u\text{-}\phi_{DP}}$, high ρ_{HV}, and SNR above a threshold (M.Thurai, 2007), and K_{DP} is only retrieved over these good data. This criterion could be different between fine and coarse scan data especially in terms of the texture parameter, illustrated by the different PDFs of $\sigma_{u\text{-}\phi_{DP}}$ (Section 4.5.1). Even if the criteria are identical for fine and coarse scans, the ability of the mask to filter out the bad data could differ between fine and coarse scans, and then we end up with a situation that K_{DP} retrievals are available in the fine scans but not in the coarse scans. Besides, with the same precipitation, the "true" value of K_{DP} may be the same or comparable for both fine and coarse scan, but the K_{DP} values retrieved in practice are quite often not equal to the theoretical values. As a consequence, we may expect the retrieved K_{DP} values to be different between the fine and coarse scans.

Despite the advantage of immunity to attenuation, K_{DP}-based rainfall estimation also demonstrates undesirable characteristics such as smearing and speckling, and unphysical behaviors such as negative rainfall rate. The reason for these abnormal characteristics is the resonance effect (backscatter effect of large raindrops) which is more common at the X-band frequency rather than at the S- and C-band frequencies (Giangrande et al., 2013; Huang et al., 2016), and the non-uniform beam filling (NBF) effect (Ryzhkov, 2007).

The coefficients a and b depend on the drop shape model assumed for the $R(K_{DP})$ estimator. A rigorous method to determine an appropriate drop shape model requires a large dataset of raindrops collected from the local disdrometers data and theoretical simulations, which is beyond the scope of this thesis. It means the $R(K_{DP})$ estimator with $a = 17$ and $b = 0.73$ used previously may not be quantitatively accurate.

To sum up, when it comes to the K_{DP} -based rainfall estimate, we need to keep the following four points in mind. First, we only know the spatial resolution of K_{DP} retrieval should be coarser than Z_H, but we don't know the exact values, and are not sure whether the radial resolution of K_{DP} retrieval of fine scans is comparable or still three times higher than coarse scans. Second, the retrieval of K_{DP} for both coarse and fine scans are implicitly affected by the Z_H attenuation. Third, as mentioned in Section 4.3.3, a portion of K_{DP} retrievals in the fine scan data are contaminated by second-trip echoes and thus are not reliable. Fourth, the differences in data quality between fine and coarse scans might lead to the discrepancy in the good data masking process between fine and coarse scans, and subsequent discrepancies

in the availability of K_{DP} retrievals and associated K_{DP}-based rainfall estimates between fine and coarse scans. Another limitation of K_{DP} in rainfall estimation is the backscatter effect (Trömel et al., 2013)

4.6.5. Effect of radial resolution on attenuation correction

Attenuation correction algorithms utilize u-ϕ_{DP}, which is a variable integrating over the range and whose magnitude theoretically should not be influenced by the radial resolution. Thus, it should be reasonable to suppose that the attenuation correction procedure functions in the same manner for fine and coarse scans, except the cases of the total loss of radar signals (more precisely, the returned echo power below the noise level) which are much more frequent in fine scans as already discussed in Fig. 4.37(b). However, Feng et al. (2016) showed that X-band radar data with 450-m sampling resolution is slightly closer to attenuation-corrected intrinsic measurements than the radar data with 750-m radial resolution.

As mentioned, the ZPHI algorithm is constrained by the valid ϕ_{DP} measurements at the last gate of the propagation path—more precisely, an average of the last few radar gates—within the rainy medium since the attenuation through water vapor is normally small and thus negligible. As mentioned, the maximum range for fine and coarse scans are 75 km and 100 km respectively (Section 3.1). For the precipitation prevailing beyond the 75-km range but within the 100-km range, the attenuation correction for fine scans uses ϕ_{DP} at the radar gates within the 75-km range (more preciously within 73.5 km roughly) as the constraints, whereas the attenuation correction for coarse scans uses ϕ_{DP} over the radar gates at the farther periphery of precipitation system (between 75 and 100 km) as the constraints. The different ϕ_{DP} constraints for fine and coarse scans respectively might lead to differences propagating into the attenuation-corrected fine and coarse scan data. Another scenario is, for precipitation whose entire body is within the 75 km, if the extremely severe attenuation occurs and weakens radar signals below the noise level (Fig. 4.37), the measurable signals of fine scans may cease at a range closer to the radar than that of the coarse scan. It means, the ϕ_{DP} constraints used in the attenuation correction are from radar data at different ranges for the fine and coarse scans, and the ϕ_{DP} constraints are much likely to be different from each other.

One more scenario which may also cause differences in ϕ_{DP} measurement and the resultant difference in the constraints for attenuation correction, is with regard to second-trip echoes in the fine scans (Fig. 4.44(a)). Between azimuths of 180°and 200°, the processed ϕ_{DP} measurements of the fine scan surpass much that of the coarse scan, corresponding to the prevalence of second-trip echoes between 30 and 70 km away from the radar in the fine scan. This excess of ϕ_{DP} in the fine scan is in accord with our previous discussion on the sensitivity of attenuation to second-trip echoes (Fig. B.2 or Section4.3). For the remaining azimuths of this case or another pair of volume scans without the presence of second-trip echoes, the processed ϕ_{DP} measurements of fine and coarse scans agree quite well with each other (Fig. 4.44(b)).

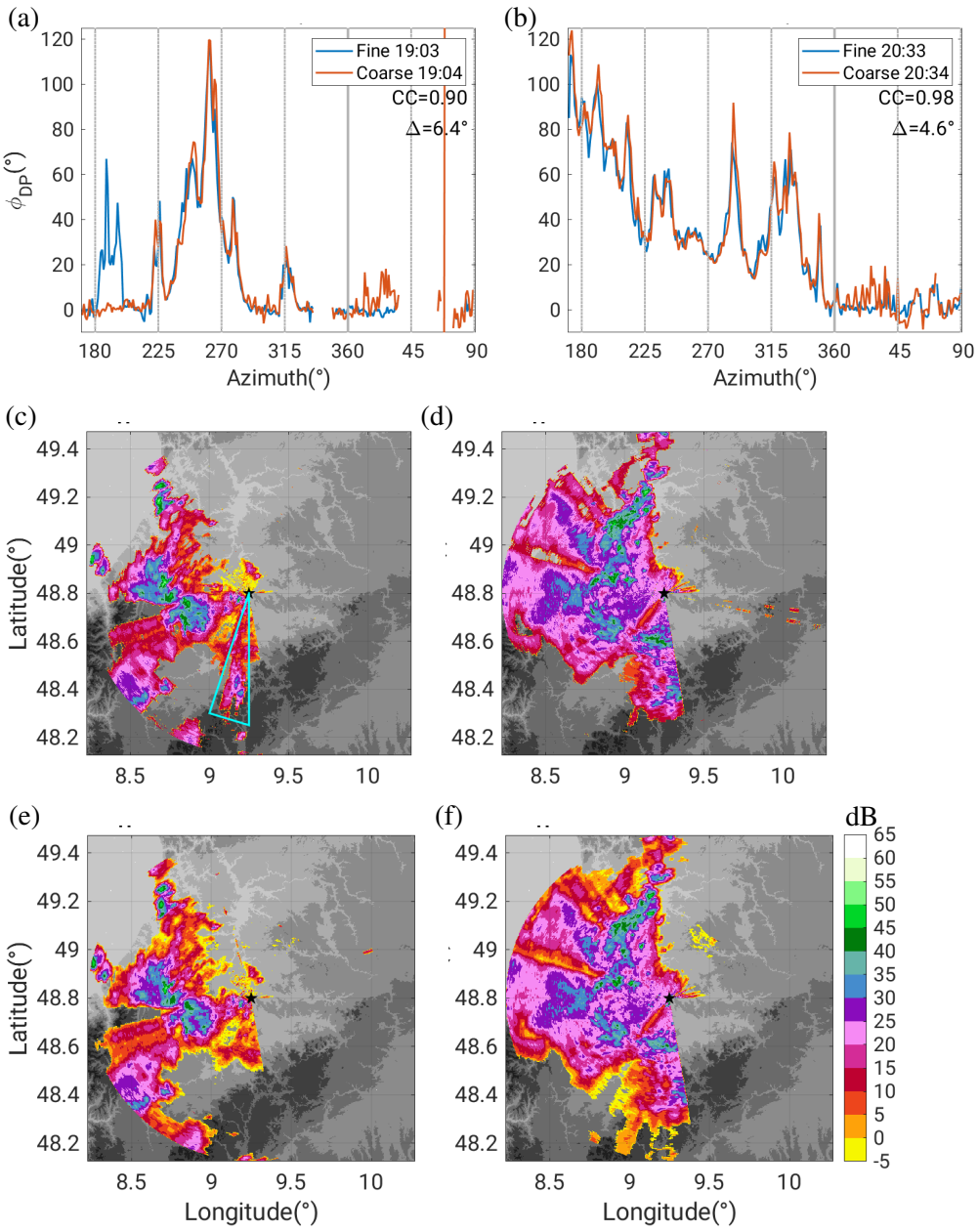

Fig. 4.44.: Two pairs of volumes scans at 19:03(19:04) UTC and at 20:33(20:34) UTC on 21 July 2017) to evaluate the agreements between fine and coarse scans in terms of the ϕ_{DP} constraints at ends of rays used for attenuation correction. (a), (c) and (e)) are for the case with apparent second-trip echoes, (b), (d) and (f) are for the case 1.5 hour later without second-trip echoes, and the unfilled triangle in (c) points out the location of second-trip echoes

Briefly, the processed ϕ_{DP} data used in the attenuation correction procedure exhibit a good accordance between fine and coarse scans over the areas free from second-trip echoes contamination or extremely severe attenuation, although we admit they may differ between fine and coarse scans in the foregoing special scenarios.

The iterative ZPHI does not requires the initial and terminal ϕ_{DP} values, so we don't discuss the effect of resolution on the iterative ZPHI.

4.7. Differential reflectivity calibration

As a ratio between the horizontally-polarized and vertically-polarized power, Z_{DR} might be miscalibrated in practice (Frech, 2013). Our X-band radar employs the SHV mode (Section 2.2) with two separate orthogonal channels. Chances are these two channels differ from each other regarding the transmission power, receiver gains and other engineer aspects. For instance, despite using the same antenna for horizontal and vertical polarization, the antenna beam pattern might still differ between both polarizations. Such difference yields the system bias for Z_{DR} measurements—ΔZ_{DR}. In order to address this Z_{DR} miscalibration, the solar radiation in H- and V-polarizations should be checked continuously during the experiment to monitor ΔZ_{DR} the reception component, but this procedure is not for the transmission part. Alternatively, Z_{DR} measurements from the vertical incidence (or birdbath scan, or vertical-pointing scan, or 90°-elevation sweep) are a widely accepted and reliable method to estimate ΔZ_{DR}, as far as the vertical-pointing scan is included in the scanning strategy. For the radar which is unable or does not plan to perform the birdbath scan, alternative solutions might include cross-power techniques (Hubbert et al., 2008).

Besides the routine of checking on the solar radiation, our X-band experiment in Stuttgart deliberately included a birdbath scan for the coarse scan for the Z_{DR} calibration purpose. Thus, we focus on using the birdbath scan to calibrate Z_{DR} directly for coarse scans, and then using inter-comparison of Z_{DR} data between the fine and the coarse scans to indirectly estimate the Z_{DR} system bias for fine scans.

4.7.1. Calibrating coarse scans

Raindrops falling in still air are mostly oblate with their symmetry axes oriented in vertical direction normal to the flat surface of the ground (Pruppacher and Beard, 1970; Beard and Chuang, 1987; Andsager et al., 1999; Pruppacher and Klett, 2011); when projected into the x-y plane (or the horizontal plane), the shape of raindrops are spheric and symmetric, leading to a lack of polarimetry in the radar beams of vertical incidences. It means, Z_H should be identical to Z_V and correspondingly the intrinsic differential reflectivity Z_{DR} should be zero (Gorgucci et al., 1999a). For the spherical raindrops, a deviation of Z_{DR} from zero can be used to determine the Z_{DR} offset—ΔZ_{DR}. Similar to others, we use the feature to calibrate Z_{DR} via the vertical incidences available in coarse scans.

Nevertheless, in real scenario especially when it rains, the air vertical motion is not zero, tilting the symmetric axes of the falling raindrops away from the vertical direction. In other words, raindrops were tilted with canting angles—deviations of the long axes of raindrops from the horizontal

plane (Rauber and Nesbitt, 2018). From a viewpoint of polarimetry, the canting angle can be defined as the angle between the normal to the polarization plane and the projection of the raindrops' symmetry axis on the same polarization plane (Huang et al., 2008). Past literature has showed that the mean canting angle $\hat{\beta}$ is close to 0° with a standard deviation around 7° for drops larger than 2 mm (Huang et al., 2008). Besides canting angle, drops oscillation and shape deformation due to break-up further complicate the orientation of falling raindrops. In order to mitigate the fluctuation, we take the Z_{DR} measurement of all the vertical scans into account.

The results turn out that Z_{DR} is negatively biased throughout our measurements (Fig. 4.45(a)). This negative bias remains in a relatively constant magnitude, regardless of the vertical heights (except the lowest 500m layer) (Fig. 4.45(b)), the rainfall intensity (Fig. 4.45(d)), and the time (Fig. 4.45(c)). Since the accuracy required for Z_{DR} is 0.1 dB, the Z_{DR} offset is determined as +0.78 dB, and we calibrate the Z_{DR} measurements with +0.78 dB for all the elevations, assuming that the miscalibration is fixed for sweeps at different elevations within the coarse scan.

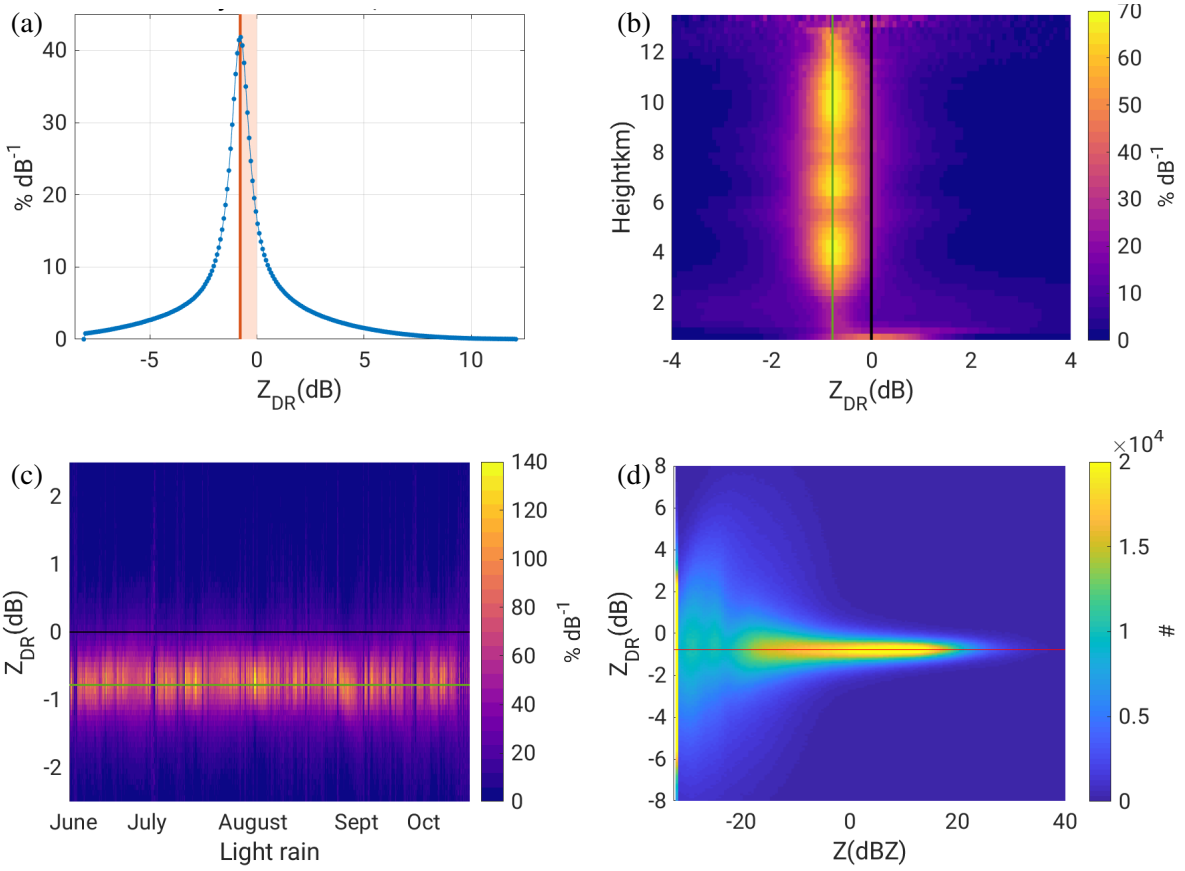

Fig. 4.45.: Z_{DR} calibration for the coarse scan using the radar sweeps of vertical incidence (θ_{beam} = 90°) for the entire measuring period, where (a) is the coarse scan PDF, (b) is the PDFs at different vertical altitudes, (c) is the PDFs for the light rain period only, (d) is the two-dimensional bivariate histogram of the absolute occurrence frequency between Z_H and Z_{DR}, and the red/green lines indicate the magnitude of Z_{DR} miscalibration for the coarse scan

We consider all the Z_{DR} measurements over all the altitudes without any criteria, unavoidably including Z_{DR} measurements, which are from other scatters such as hail or ground clutters, or which are of poor quality. Besides, quite a number of convective or heavy precipitation events occurred within our experiment in Stuttgart, and the aforementioned raindrop canting and oscillation contribute to anisotropy of falling raindrops. Additionally, the ice aggregates in the bright band will also exhibit non-zero intrinsic Z_{DR}. Despite the factors contributing to fluctuations in Z_{DR} offset, the PDF based on 20 thousands of birdbath scans should be sufficient, and the single peak clearly seen in PDFs should be close to the true Z_{DR} offset.

4.7.2. Calibrating fine scans

Given that the vertical incidence scan is not included in fine scans, theZ_{DR} measurement from birdbath scans are not available. Alternatively, we compare PDFs of Z_{DR} between fine and coarse scans for their corresponding elevations to see whether a "relative" miscalibration of Z_{DR} exists between fine and coarse scans. Since small raindrops are can be fairly assumed as spherical, we consider light rain events exclusively in order to minimize other factors responsible for changing Z_{DR} values.

The Z_{DR} data in our dataset are negatively biased of 0.44 dB for fine scan and of 0.60 dB for coarse (Fig. 4.46(a) and Figure 4.46(b)). Given that the Z_{DR} calibration factor for coarse scans is +0.78 dB Z_{DR} the calibration factor for fine scans can be determined as +0.62 dB.

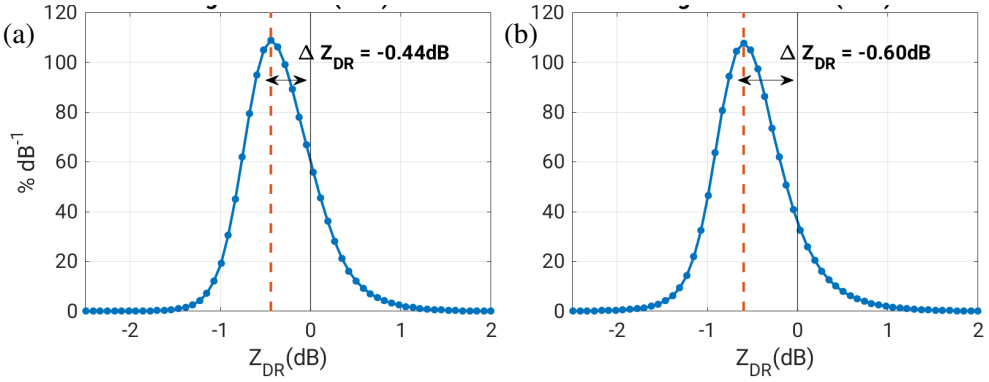

Fig. 4.46.: Z_{DR} calibration in light rain ($Z_H < 20$ dBZ) for fine scans by comparing difference in Z_{DR} between fine and coarse scans for the non-vertical elevations taking the 1.5° elevation sweeps as an example, where (a) and (b) are PDF for the fine and coarse scans respectively

4.8. Polarimetric radar data quality

Polarimetric data have been used in removing spike signal, second-trip echoes, non-meteorological echoes and correcting attenuation in the previous sections. However, we have not yet evaluated the data quality of these polarimetric measurements. To evaluate Z, we can compare R calculated from Z_H via the

assumed Marshall-Palmer Z-R relation (Section 2.3) to the external reference such as rain gauge measurements. Unlike Z_{H}, there is no direct reliable reference for polarimetric measurements. Alternatively, we assess statistical errors of the polarimetric variable estimates.

As mentioned in Section 2.1, an estimate of a certain polarimetric variable is calculated on the basis of a pulse train consisting several successive transmitted pulses, and its variance can be regarded as the statistical accuracy or statistical error of polarimetric variables. Understandably, the more equivalent independent samples M_{I} are used to estimate polarimetric variable, the smaller the statistical errors will be (Eq. 2.16). Besides, the radar polarimetry involves comparisons of two polarization states, so the correlation between horizontally and vertically polarized signals is also crucial to the data quality. For weather signals, the horizontally polarized signals are well correlated with the vertically polarized one, and this absolutely differs from noise which has correlation between the horizontally and vertically polarized signals. This correlation can be quantitatively represented by ρ_{HV}, hence the reason that ρ_{HV} is a measure of quality of polarimetric measurements (Section 2.2).

Based on theory of weather signal processing (Doviak et al., 1993), the analytical standard deviations of estimates for the polarimetric variables depend on M_{I} (Section 2.1) and ρ_{HV}, and are expressed as

$$SD(\hat{Z}_{\mathrm{H}}) \approx 10\log[1+\frac{1}{\sqrt{M_{\mathrm{I}}}}] \tag{4.19}$$

$$SD(\hat{Z}_{\mathrm{DR}}) \approx 4.343\sqrt{\frac{2}{M_{\mathrm{I}}}(1-\rho_{\mathrm{HV}}^2)} \tag{4.20}$$

$$SD(\hat{\rho}_{\mathrm{HV}}) \approx \sqrt{\frac{1-\rho_{\mathrm{hv}}^2}{2M_{\mathrm{I}}}} \tag{4.21}$$

$$SD(\hat{\phi}_{\mathrm{DP}}) \approx \frac{180}{\pi\rho_{\mathrm{hv}}}\sqrt{\frac{1-\rho_{\mathrm{hv}}^2}{2M_{\mathrm{I}}}} \tag{4.22}$$

The hats over variables' names indicates they are *estimates* of polarimetric variables. As mentioned in Section 3.3.1, we reserve the symbol σ for texture parameters, and desingate the symbol *SD* for standard deviation of polarimetric variables.

Determined by N_{a} and PRF (Table 3.2), the total numbers of transmitted pulses within each azimuth resolution (M) are 148 and 28 for our fine and coarse scans respectively (Eq. 2.17). Then, M_{I} is calculated using Eqs. 2.16, 2.19, 2.20 and 2.21. σ_{v} varies depending on the degree of perturbation in a flow, being $1\,\mathrm{m\,s^{-1}}$ for rain, up to $5\,\mathrm{m\,s^{-1}}$ for convective storms (Sauvageot, 1992). Here we consider the typical range from $1\,\mathrm{m\,s^{-1}}$ to $4\,\mathrm{m\,s^{-1}}$. Take the analytical standard deviation of ϕ_{DP} for instance. With Eq. 2.16, Eq. 4.22 can be reformed into

$$\sqrt{M}\cdot SD(\hat{\rho}_{\mathrm{HV}}) = \frac{180}{\sqrt{2}\pi}(|\rho_{\mathrm{hv}}|^{-2}-1)^{1/2}\sqrt{\mu} \tag{4.23}$$

The term $\sqrt{M} \cdot SD(\hat{\rho}_{\mathrm{HV}})$ decreases with more variability in V_{Do} and higher ρ_{HV}, and this decreasing tendency depends on ρ_{HV} (Fig. 4.47). For instance, if reducing ρ_{HV} from 0.99 to 0.9, the standard deviation of ϕ_{DP} triples, and if further reducing ρ_{HV} from 0.9 to 0.7, the standard deviation of ϕ_{DP} doubles (Fig. 4.47). These curves tally with their counterparts of the S-band frequency in Fig.1A in Ryzhkov and Zrnic (1998b).

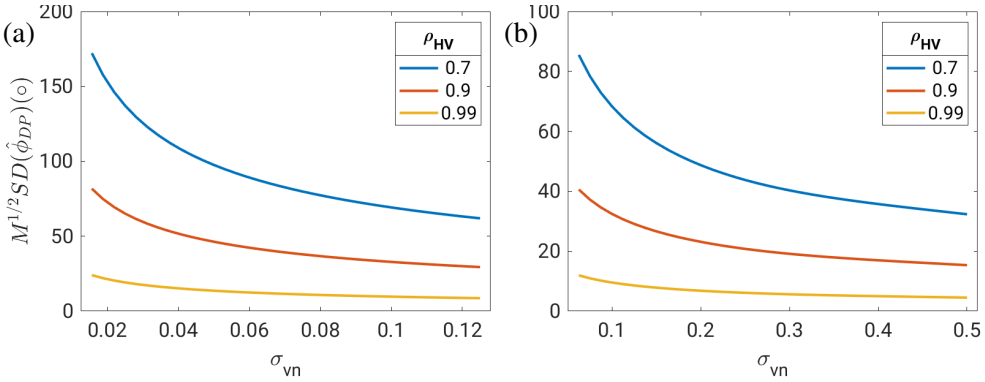

Fig. 4.47.: $\sqrt{(M)} \cdot SD(\hat{\phi}_{\mathrm{DP}})$ as a function of the normalized spectrum width $\sigma_{\mathrm{vn}} = 2\sigma_{\mathrm{v}}T/\lambda$ under the condition of ρ_{HV} =0.7, 0.9 and 0.99, for the fine (a) and coarse (b) scan

For the S-band radar polarimetric variables, the desired statistical errors should be less than 0.2 dB for Z_{DR}, 2° for ϕ_{DP} and 0.01 for ρ_{HV}, respectively (black lines in Fig. 4.48) (Melnikov and Zrnic, 2004; Melnikov and Zrnić, 2007). For the C-band frequency, $SD(\hat{\phi_{\mathrm{DP}}})$ is around 3–4° (Keenan et al., 1998). Given that the phase shift is inversely proportional to λ, we adjust the threshold of $SD(\phi_{\mathrm{DP}})$ to 5° for the X-band frequency.

In order to compare the standard deviations directly between the fine and coarse scans, we adjust the x- and y-axes (since M and σ_{vn} differ between the fine and coarse scans) as shown in Fig. 4.48. Standard deviations of polarimetric variables for both fine and coarse scans decrease with the increasing T_{d}, but the decreasing tendencies differ between the fine and coarse scan. For a specific ρ_{HV}, the standard deviations of estimates of ϕ_{DP} ($SD(\hat{\phi}_{\mathrm{DP}})$) of fine scans are much larger than those of coarse scans (Fig. 4.48(b)), whereas the standard deviations of estimates of ρ_{HV} or Z_{DR} ($SD(\hat{\rho}_{\mathrm{HV}})$ or $SD(\hat{Z}_{\mathrm{DR}})$) of fine scans are slightly smaller than those of coarse scans (Figs. 4.48(a) and 4.48(c)). In particular, $SD(\hat{\phi}_{\mathrm{DP}})$ of coarse scans with ρ_{HV}= 0.7 is nearly identical to $SD(\hat{\phi}_{\mathrm{DP}})$ of fine scans with ρ_{HV}= 0.9 (Fig. 4.48(b)). Besides, the higher ρ_{HV} leads to smaller differences in these standard deviations between fine and coarse scans.

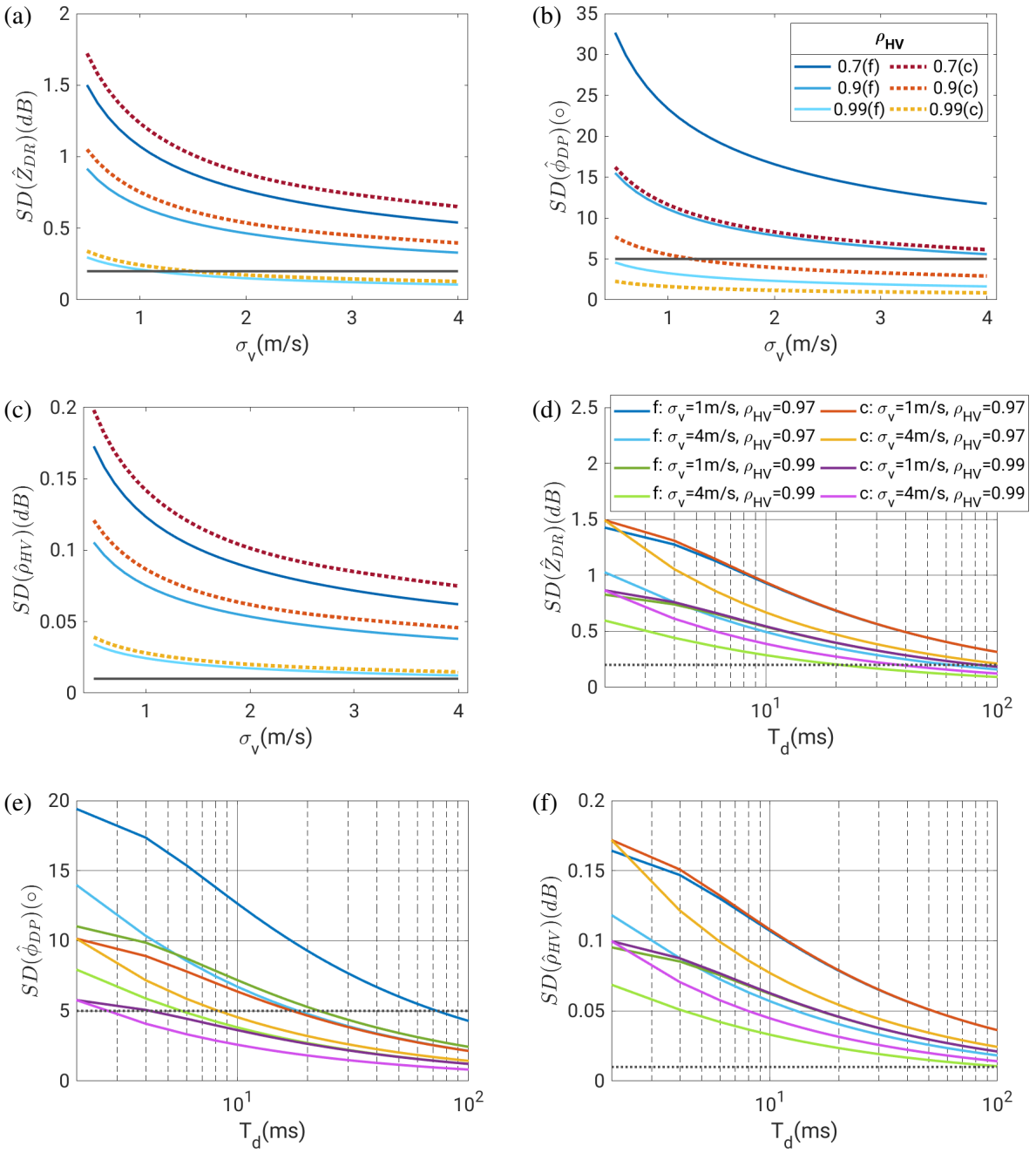

Fig. 4.48.: Theoretical standard deviations of polarimetric variables for fine and coarse scans, where (a), (b) and (c) are $SD(\hat{\phi}_{\mathrm{DP}})$, $SD(\hat{Z}_{\mathrm{DR}})$ and $SD(\hat{\rho}_{\mathrm{HV}})$ as a function of σ_{v} for fine and coarse scans with conditions of $\rho_{\mathrm{HV}} = 0.7$, $\rho_{\mathrm{HV}} = 0.9$ and $\rho_{\mathrm{HV}} = 0.99$, and (d), (e) and (f) are $SD(\hat{\phi}_{\mathrm{DP}})$, $SD(\hat{Z}_{\mathrm{DR}})$ and $SD(\hat{\rho}_{\mathrm{HV}})$ as a function of T_{d}, with conditions of $\rho_{\mathrm{HV}} = 0.97$, $\rho_{\mathrm{HV}} = 0.99$, $\sigma_{\mathrm{v}} = 1\,\mathrm{m\,s^{-1}}$ and $\sigma_{\mathrm{v}} = 4\,\mathrm{m\,s^{-1}}$, the black horizontal lines are $SD(Z_{\mathrm{DR}}) = 0.2\,\mathrm{dB}$, $SD(\phi_{\mathrm{DP}}) = 2^{\circ}$ and $SD(\rho_{\mathrm{HV}}) = 0.01$

On the other hand, standard deviations of polarimetric variables also vary with T_{d} (Sachidananda and Zrnić, 1986; Kostinski, 1994; Zhang, 2016). T_{d} for fine and coarse scans are fixed as 74 ms and 55 ms (Eq. 2.18 and Tab. 3.2). Instead of the fixed values, here we assume T_{d} is changeable and keep other technical specifications unchanged. It turns out that the standard deviations of polarimetric vari-

ables decrease with the increasing T_d (slower antenna rotation rate) (Fig. 4.48(d), 4.48(e) and 4.48(f)). $SD(\hat{Z}_{DR})$ can be below 0.2 dB only if T_d is longer than 22 ms for the fine scan and exceeds 38 ms for the coarse scan, when $\sigma_v = 4\,m\,s^{-1}$ and ρ_{HV}= 0.99 (Fig. 4.48(d)). $SD(\hat{\phi}_{DP})$ can be below 5° only if T_d is more than 6 ms for the fine scan and exceeds 3 ms for the coarse scan, when $\sigma_v = 4\,m\,s^{-1}$ and ρ_{HV}= 0.99 (Fig. 4.48(e)). $SD(\hat{\rho}_{HV})$ can be below 0.01 only if T_d is over 100 ms for the fine scan and exceeds 150 ms for the coarse scan when $\sigma_v = 4\,m\,s^{-1}$ and ρ_{HV}= 0.99 (Fig. 4.48(f)). The differences between $\rho_{HV} = 0.99$ and $\rho_{HV} = 0.97$ ((d), (e) and (f) in Fig. 4.48) also indicate that a small difference in ρ_{HV} also changes significantly the level of fluctuation of estimates of all the polarimetric variables.

After discussing the theoretical standard deviations of estimates of polarimetric variables (Fig. 4.48), we pay attention to the real measurements, in particular from light rain events in which the raindrops are assumed to be spherical and nearly uniform in shape and scattering properties (Marks et al., 2011). In addition, the small size of raindrops in light rain can avoid the potential certainties caused by resonance effect. Following the method in Marks et al. (2011), polarimetric measurements from this light rain are used as indicators of data quality.

We calculate the following statistics for each selected volume scan containing light rain: standard deviations for measurements of Z_{DR}, ρ_{HV}, K_{DP}, ϕ_{DP} and $\sigma_{u\text{-}\phi_{DP}}$ ($SD(Z_{DR})$, ($SD(\rho_{HV})$, ($SD(K_{DP})$, ($SD(\phi_{DP})$, $SD(\sigma_{\phi_{DP}})$), median for Z_H, ρ_{HV}, K_{DP} and ϕ_{DP}, mean Z_{DR}, and AAD for Z_{DR}. Note that each volume scan includes the same amount of radar pixels which are identified as being light rain regardless of fine or coarse scans to guarantee identical sample sizes for calculating standard deviations (19.6×10^3 radar gates for the cases presented in Fig. 4.49). The medians of Z_H measurements vary between 10 and 20 dBZ, and the medians of Z_{DR} measurements fall below 0.3 dB, which confirms the selection of light rain medium. Note that $SD(Z_{DR})$ is distinct from $SD(\hat{Z}_{DR})$. $SD(Z_{DR})$ is calculated on the basis of polarimetric measurements of light rain with a volume scan, while $SD(\hat{Z}_{DR})$ represents the theoretical variability of Z_{DR} as a function of ρ_{HV} or other radar parameters.

Recall that ρ_{HV} is a measure of data quality, the standard deviation $SD(\rho_{HV})$ larger than 0.01 in light rain is used as a warning for the radar system (Doviak et al., 1993; Marks et al., 2011). Our ρ_{HV} data of all these light rain episodes exhibit the median values above 0.99 with $SD(\rho_{HV})$ around 0.005, which substantiates the good data quality for polarimetric moments in our measurements for both fine and coarse scans (Fig. 4.49). In addition, $SD(Z_{DR})$ is around 0.2 dB, and $SD(\phi_{DP})$ is less than 5°, both of which are congruent with the theoretical thresholds in Fig. 4.48. For Z_{DR}, ϕ_{DP} and K_{DP}, fine scans have slightly greater standard deviations than those of coarse scans.

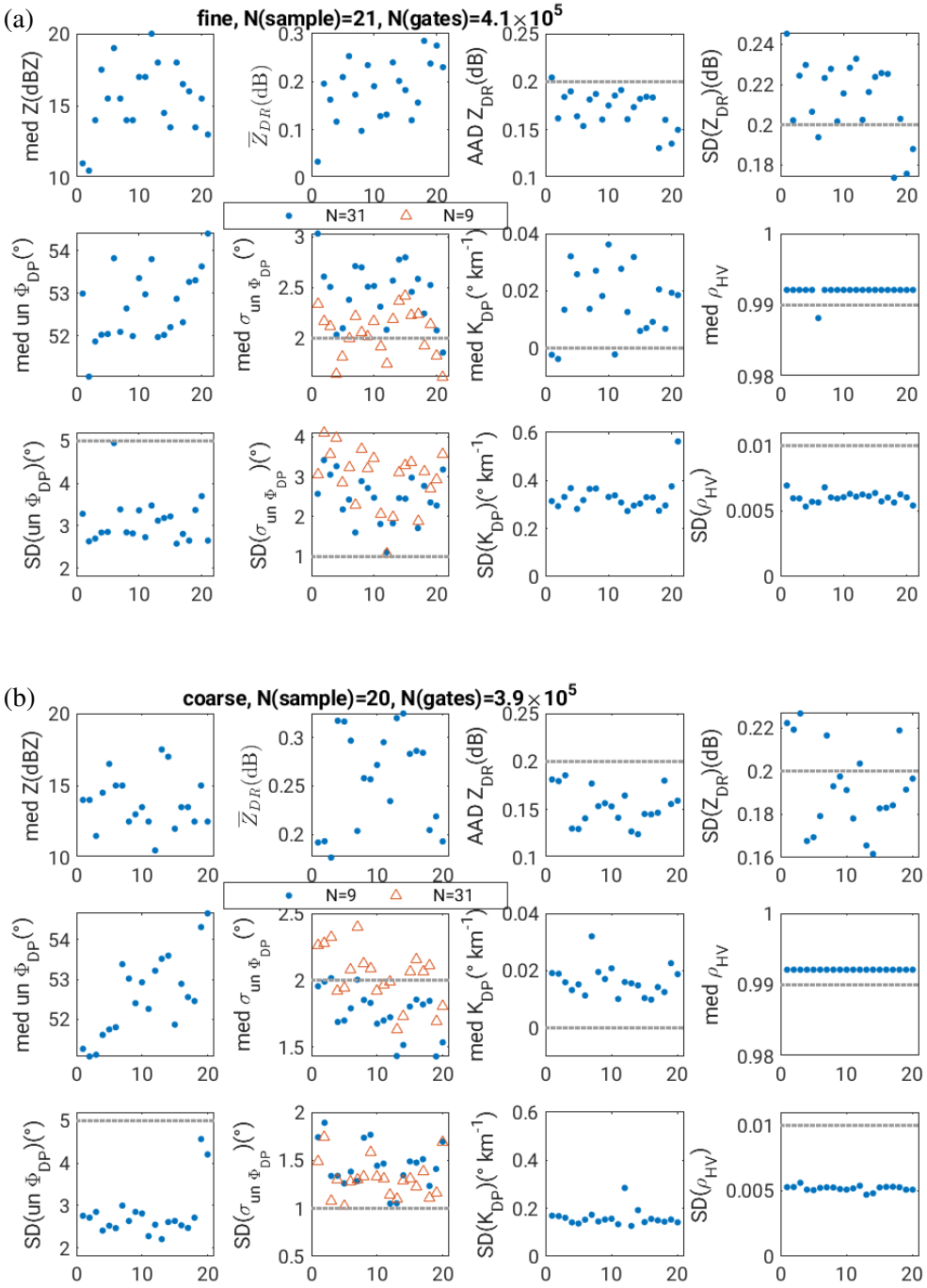

Fig. 4.49.: Statistics of polarimetric variables in light rain for (a) fine scans, (b) coarse scans, including median of Z_H, mean Z_{DR}, AAD of Z_{DR}, standard deviation of Z_{DR} ($SD(Z_{DR})$), median of u-ϕ_{DP}, median of $\sigma_{u\text{-}\phi_{DP}}$, median of K_{DP}, median of ρ_{HV}, standard deviation of u-ϕ_{DP} ($SD(\phi_{DP})$), standard deviation of $\sigma_{u\text{-}\phi_{DP}}$ ($SD(\sigma_{\phi_{DP}})$), standard deviation of K_{DP}, and standard deviation of ρ_{HV} over selected 21 light raiy events for the fine scans and 20 light rain volume scans for the coarse scans (each volume scan is calculated from roughly 20×10^3 radar gates with light rain signature)

In addition to these foregoing standard deviations, the absolute deviations of Z_{DR} are less than 0.2 dB, in agreement with the 0.2 dB thresholds of Marks et al. (2011). When it comes to K_{DP}, its medians surpass $0.2^\circ\,km^{-1}$ for the fine scans and $0.1^\circ\,km^{-1}$ for the coarse scans, instead of the theoretically expected value of $0^\circ\,km^{-1}$. Its standard deviations ($SD(K_{DP})$) are around 0.3–$0.4^\circ\,km^{-1}$ for fine scans and around $0.2^\circ\,km^{-1}$ for coarse scans, respectively, greater than 0.1–$0.2^\circ\,km^{-1}$ in Marks et al. (2011).

Besides, we also calculate $\sigma_{\phi_{DP}}$ since it is associated with $SD(K_{DP})$ (Eq. 4.25). Be cautious that the texture of ϕ_{DP} ($\sigma_{\phi_{DP}}$) is different from the aforementioned standard deviation of ϕ_{DP} ($SD(\sigma_{\phi_{DP}})$). We calculate $\sigma_{\phi_{DP}}$ using 31 and 9 gates, since the range interval of 31 consecutive radar gates in the fine scan equals to that of 9 consecutive radar gates in the coarse scan. Comparing $\sigma_{\phi_{DP}}$ in the 31-gate length from the fine scan with $\sigma_{\phi_{DP}}$ in 9-gate length from the coarse scan means comparing $\sigma_{\phi_{DP}}$ of the same calculating window length between the fine and coarse scans. Comparing $\sigma_{\phi_{DP}}$ in 9-gate length from the fine scan with $\sigma_{\phi_{DP}}$ in 9-gate length from the coarse scan means comparing $\sigma_{\phi_{DP}}$ of the same radar gates. Comparison in the same window length emphasizes the spatial variability of the variables, whereas comparison in the same number of radar gates underlines the statistical consistency.

If we compare $\sigma_{\phi_{DP}}$ of the same calculating window length, then the fine scans exhibit obviously higher medians (around 2–$2.7^\circ\,km^{-1}$) than those of the coarse scans (around 1.5–$2^\circ\,km^{-1}$) (Fig. 4.49). If we compare $\sigma_{\phi_{DP}}$ of the same number of radar gates, then the fine scans exhibit slightly higher medians (around 1.5–$2.5^\circ\,km^{-1}$) than those of the coarse scans (around 1.5–$2^\circ\,km^{-1}$). Standard deviations of $\sigma_{\phi_{DP}}$ ($SD(\sigma_{\phi_{DP}})$) of fine scans vary between 1 and $4^\circ\,km^{-1}$, in contrast to values between 1 and $2^\circ\,km^{-1}$ for the coarse scan, regardless of the number of radar gates.

The foregoing comparisons lead to two conclusions. First, an increase in the number of radar gates for calculating the texture magnifies the median of $\sigma_{\phi_{DP}}$, but exerts nearly no effect on $SD(\sigma_{\phi_{DP}})$. Second, the most noticeable difference between the fine and coarse scans lies in $\sigma_{\phi_{DP}}$, and the fine scans have larger median and wider standard deviation of $\sigma_{\phi_{DP}}$ compared to that of the coarse scans. In comparison to $\sigma_{\phi_{DP}}$ in 25-gates length which was characterized by its median of 2.5° and its standard deviation of 0.6°(Marks et al., 2011), both fine and coarse scans exhibit larger standard deviations and comparable medians.

The foregoing statistics are for the light rain medium (Fig. 4.49), but when it comes to K_{DP}, we are more interested in moderate-to-heavy precipitation because of the advantage of using K_{DP} in rainfall estimation since K_{DP} is not affected by attenuation.

Interpretation of statistical errors in K_{DP} estimation depends on the retrieving method. If K_{DP} is estimated using two neighboring gates (Eq. 3.5), then the fluctuations at the two gates are uncorrected, so their variances add together. If ρ_{HV} are equal at the two gates, then the standard deviations of ϕ_{DP} are also equal, and then the corresponding standard deviation of K_{DP} is $\sqrt{2}$ larger than the standard

deviation of ϕ_{DP}. On the other hand, if K_{DP} is retrieved using the least square fit of ϕ_{DP} (Eq. 3.6), the variance of estimates of K_{DP} over the interval of N radar gates is given as

$$var(\hat{K}_{DP}) = \frac{var(\Phi_{DP})}{\frac{N(N+1)(N-1)}{3}(\Delta r)^2} \tag{4.24}$$

where $var(\Phi_{DP})$ is the variance of Φ_{DP} with the N-gate interval. According to Eq. 4.24, the accuracy or standard deviation of estimates of K_{DP} is independent of K_{DP} but depends on the texture of ϕ_{DP} over the N-gate interval, and the theoretical formula is as follows (Gorgucci et al., 1999b)

$$SD(\hat{K}_{DP}) = \frac{\sqrt{3}\,\sigma_{\phi_{DP}}}{N^{3/2}\Delta r} \tag{4.25}$$

where N is the number of range gates for retrieving each K_{DP}. As mentioned, in our radar signal processor, the calculating interval for K_{DP} is adjusted according to the intensity of Z_H (Section 3.1.5), so we also adjust the interval for calculating $\sigma_{\phi_{DP}}$ using 31 (9) gates for Z_H below 30 dBZ, 21 (7) gates for Z_H between 30 and 45 dB, and 11 (5) gates for Z_H above 45 dB for fine (coarse) scans. Note that Eq. 4.25 in principle assumes the uniform precipitation within its each calculating interval, which might not be valid if the calculating interval is too long.

Then we calculate $SD(\hat{K}_{DP})$ using ϕ_{DP} from real measurements as follows. For the 6-hour precipitation episode consisting of stratiform and convective precipitation discussed in Section 4.6, following the method in Marks et al. (2011), based on Z_H intensity, we stratify the radar measurements into 0.5-dB increment from 30 dBZ to 55 dBZ. For instance, there are 306 157 radar gates whose Z_H equal 30 dBZ, and the average K_{DP} of those radar gates is $0.213\,^{\circ}\,km^{-1}$. The maximum allowed K_{DP}, defined as 20% of this average K_{DP}, is $0.0425\,^{\circ}\,km^{-1}$. Their textures of ϕ_{DP} vary from 0.56° to 38.2°, and according to Eq. 4.25, $SD(\hat{K}_{DP})$ vary from $0.134\,^{\circ}\,km^{-1}$ to $9.16\,^{\circ}\,km^{-1}$. For Z_H of 30 dBZ, 21 gates are used to calculate $\sigma_{\phi_{DP}}$, so the number of independent samples are 14579 (306157/21). Then, the reduction factor which is defined as the square root of the number of independent samples is 121 ($\sqrt{14579}$). The observed range of K_{DP} is 0.001 (0.134/121)–0.0759 (9.16/121) $^{\circ}\,km^{-1}$. The same procedure for other Z_H increments. The results show that the observed ranges of K_{DP} are well below the maximum allowed K_{DP} values, supporting the reliability of K_{DP} retrievals (Figs. 4.50(a) and 4.50(b)).

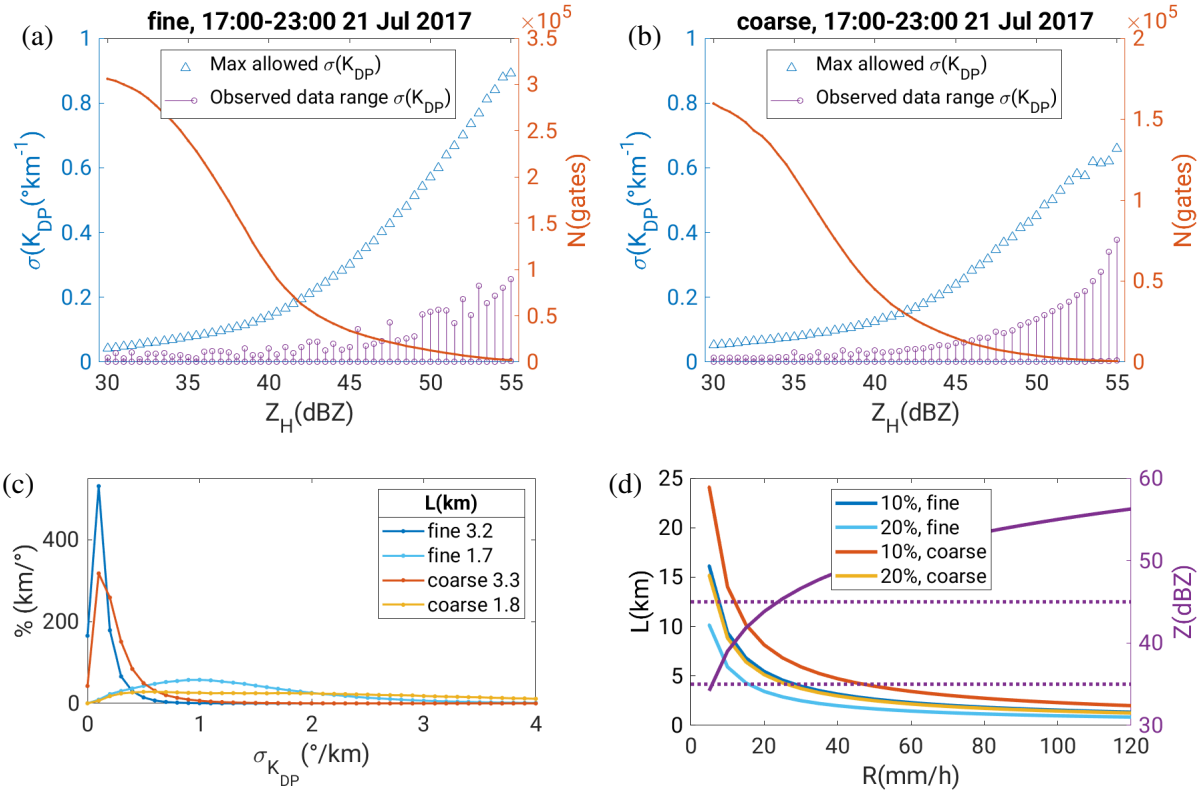

Fig. 4.50.: Accuracy or standard deviation of K_{DP} for a heavy rain event from 18 UTC to 23 UTC on 21 July 2017, (a) and (b) are for fine and coarse scans, respectively.

The length of the calculating path for K_{DP} is crucial to the statistical accuracy of K_{DP} (Fig. 4.50(c)). Following Gorgucci et al. (1999b), after combining Eqs. 2.64 and 4.25, we can obtain the pathlength required to estimate K_{DP} below a given fractional standard error (FSE) for the X-band frequency, which is given as

$$L = [\sqrt{3}\Delta r \frac{18.2}{(K_{DP})^{0.85}} \frac{\sigma(\phi_{DP})}{\text{FSE}}]^{2/3} \tag{4.26}$$

To estimate K_{DP} with 20% accuracy for a precipitation rate of 24 mm h^{-1} or equivalently radar reflectivity of 45 dBZ, the path for K_{DP} retrieval should be at least 3 km or 4 km for the fine and coarse scans respectively (Fig. 4.50(d)).

4.9. Probability density function (PDF)

Our Stuttgart field experiment collected the single-polarization radar variables—uncorrected Z_H corrected Z_H, SNR, SQI, V_{Do}, σ_v and CCOR—and the polarimetric variables—Z_{DR}, u-ϕ_{DP}, filtered ϕ_{DP}, K_{DP} and ρ_{HV} (Section 3.1.5). As we will show soon, the majority of radar variables do not follow the normal distribution so the typical statistics (median, mean, .etc.) cannot fully describe characteristics of each variable. Instead, we use the distribution of absolute (relative) occurrence frequency, or PDFs

of radar variables to characterize general features of each radar measurable. From the PDFs, we can easily extract information such as data availability and the frequent values, and also analyze the range dependency of these radar variables.

We have two categories of data; one is the radar data retrieved directly from the radar built-in signal processor without external data QC procedures, and the other one is the radar data processed with the external data QC procedures discussed in the previous sections (Section 4.2, Section 4.3, Section 4.5, Section 4.6 and Section 4.7). The PDFs are calculated from both categories. Although the default data processing chain in the Rainbow signal processor automatically rejects some bad data (SELEX, System Integration GmbH, 2015), the default data QC is incomplete and calls for further steps; this is the reason why these external data QC procedures (Section 4.2, Section 4.3, Section 4.5, Section 4.6 and Section 4.7) are needed to identify and to filter out bad data before applying the radar data for precipitation estimation in Chapter 5.

4.9.1. PDF for base data

A radar cannot distinguish the sources of echoes but instead treats the non-meteorological echoes or other types of noise equally with precipitation echoes. However, only precipitation echoes are of interest to us. Before applying data QC procedures, the non-meteorological echoes or other kinds of noise appear in forms of some weird features within the base data.

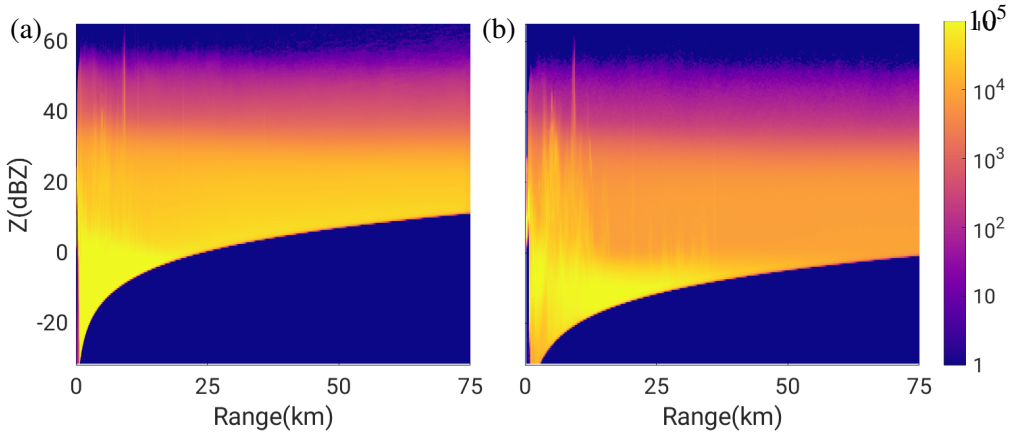

Fig. 4.51.: Range variation of absolute occurrence frequency of the X-band radar polarimetric measurements at the 1.5° elevation for the entire measuring period for radar reflectivity (Z_H) for the fine (a) and coarse (b) scans respectively

One of the deficiencies in the radar measurements is the range dependence owing to the broadening θ_{beam} as the range increases. For instance, the minimum detectable radar reflectivity (Z_{min}) increases with r. For instance, Z_{min} at $r = 20$ km, $r = 40$ km and $r = 60$ km are around -1.5 dBZ, 5 dBZ and 9 dBZ for the fine scans, and around 14 dBZ, -7 dBZ and -3 dBZ for the coarse scans (Fig. 4.51).

Obviously, Z_{min} in the fine scan is much larger than that in the coarse scan, corresponding to the lack of weak echoes in the fine scan as discussed in Section 4.1. In brief, the range dependence differs between the fine and coarse scans. Besides, several vertical lines reaching above 50 dBZ are present within the 10-km range, but such lines are much less obvious in the fine scan. The vertical lines are caused by the abnormally high Z_H from the GCs, which is more prevalent in the coarse scan.

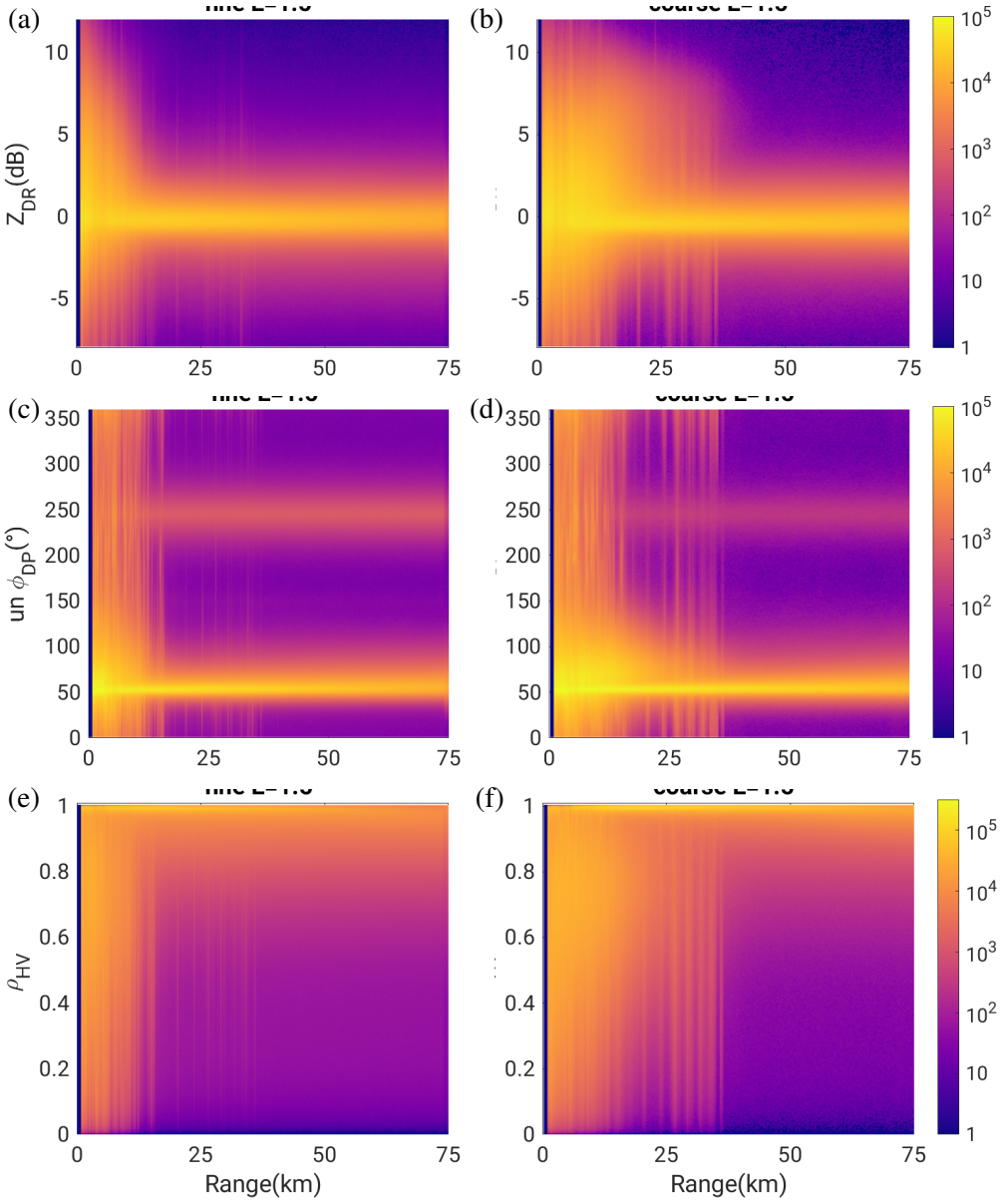

Fig. 4.52.: Range variation of absolute occurrence frequency of the X-band radar polarimetric measurements at the 1.5° elevation for the entire measuring period, specifically, Z_{DR} (a) and (b), u-ϕ_{DP} (c) and (d), ρ_{HV} (e) and (f), panels on the left/right column are for the fine/coarse scan data respectively

For the fine scan, Z_{DR} within the 15-km range has a wider distribution across the -8 dB and 10 dB than Z_{DR} beyond the 15-km range (Fig. 4.52(a)), while such a wide distribution extends to 35 km for the coarse scan, along with particularly high frequencies of large positive Z_{DR} for the range between

15 km and 35 km (Fig. 4.52(b)). Large Z_{DR} is caused by the non-meteorological echoes, and is most likely by GCs. It implies that the coarse scan data are more subject to the GCs, in accord with our discussion in Section 4.4. Beyond 15 km for the fine scan and beyond 35 km for the coarse scan, we can see the majority of Z_{DR} data fall between -3 dBZ and 3 dBZ with the peak around 0 dBZ.

The frequency distributions of u-ϕ_{DP}, either the fine and coarse scans, show two ridges, a major one around 50° and a minor one around 240° (Figs. 4.52(c) and 4.52(d)). The major one is due to the system differential phase (Eq. 2.49) and the minor one is caused by the spike signals which are characterized by abnormally high differential phase (Section 4.2). In accord with our conclusion in Section 4.2 that spike signals occur much more frequently in the fine scans, the minor peak in the fine scan data is more apparent than its counterpart in the coarse scan data. Besides, similar to Z_{DR}, u-ϕ_{DP} in the coarse scan data is also affected by GCs to a greater extent than that of the fine scan.

Within the 15-km range for the fine scans and within the 35-km range for the coarse scans, ρ_{HV} has comparable occurrence frequencies across the value 0–0.99 (Figs. 4.53(e) and 4.53(f)). Besides this large proportion of low ρ_{HV} primarily caused by GCs, the frequency distributions for the fine and coarse scan data are quite similar. This similarity between fine and coarse scans can be also seen from Z_{DR} and u-ϕ_{DP} if the noise echoes or these weird features are absent (such as the data beyond 40 km away from the radar). It implies that the fine and coarse scan data (at least for Z_{DR}, ϕ_{DP} and ρ_{HV}) should be in good accord with each other if the noises are successfully removed.

In contrast, the frequency distributions of K_{DP}, SNR and SQI show discrepancies between the fine and coarse scans (Fig. 4.53). For the fine scan data, K_{DP} retrievals are distributed more broadly and are less concentrated around the $0\,^{\circ}\mathrm{km}^{-1}$, while for the coarse scan data, the majority of K_{DP} data are more concentrated between -2 and $2\,^{\circ}\mathrm{km}^{-1}$ (Figs. 4.53(a) and 4.53(b)). Given that K_{DP} is retrieved over the radar data which must satisfy the "good" data criteria (Section 3.1.5), no K_{DP} is retrieved over the data contaminated by GCs within the 30-km range. No major differences exist between the fine and coarse scan data in terms of u-ϕ_{DP}, which implies the difference in K_{DP} between the fine and coarse scans is very likely due to the K_{DP} retrieval algorithm. The number of radar gates and the interval of calculating windows in the K_{DP} retrieval are associated with Δr. Thus, it is reasonable to infer differences in K_{DP} retrievals between the fine and coarse scans result from the difference in spatial resolutions of the radar data.

The frequency distributions of SNR of the coarse scan data are wider through the entire range than those of the fine scan data (Figs. 4.53(c) and 4.53(d)). For instance, at the 50-km range, the chance of SNR being larger than 40 dB in the coarse scan is nearly 10 times more than that of the fine scan. At the 75-km range, SNR greater than 50 dB is quite rare in the fine scans but frequent in the coarse scans. SNR data are also subject to GCs, illustrated by the strange vertical structures within the 15-km (35-km) range for the fine (coarse) scan data. The large magnitude of SNR in the coarse scans be associated with

loss of weak echoes in the fine scans, and the related worsening capacity in attenuation correction for the fine scan data. It pinpoints the sacrifice we made if we set our radar measurements at a higher spatial resolution.

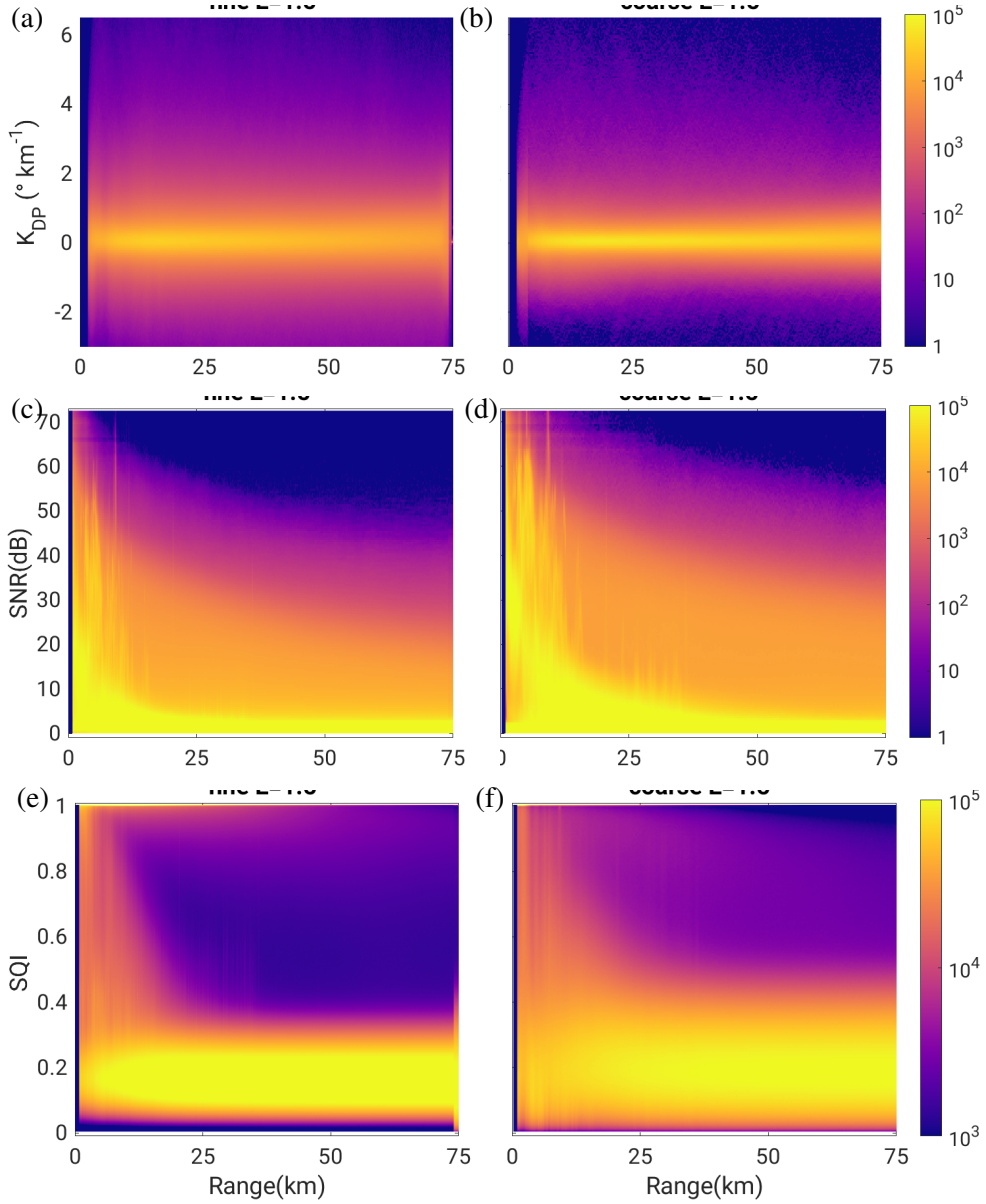

Fig. 4.53.: The same as Fig. 4.52, but the upper row is for K_{DP}, the middle row is for SNR, and the bottom row is for SQI

When it comes to SQI, the frequency distribution of the fine scan data is quite different from that of the coarse scan data (Figs. 4.53(e) and 4.53(f)). The most impressive difference is that for the fine scan beyond 25 km, the majority of SQI dat are constrained below 0.25, with very little SQI data between 0.4 and 0.7, and the minority of SQI more than 0.8. For the coarse scans, the majority of SQI data are roughly below 0.45. Unlike the fine scans, there is no lack of SQI and the frequency of

SQI decrease gradually as SQI increases from 0.45 to 0.55 (illustrated by the gradually changing color), and remains in a relative small magnitude. With the range increases from 25 km to 75 km, SQI can be as high as 1 in the fine scan data, but the upper maximum SQI in the coarse scan data becomes lower than 1. As we know, SQI above 0.8 corresponds to precipitation echoes, and the low SQI values represent the non-meteorological echoes or noises. Thus, in the fine scans, this deficiency of SQI between 0.4 and 0.7 can be used to distinguish the non-meteorological and precipitation echoes efficiently. However, such a criterion is not applicable in the coarse scan data. This contrast is exactly associated with the second-trip echo removal in Section 4.3. Within the 20-km range, except SQI above 0.8 corresponding to the precipitation echoes, there is a certain amount of SQI between 0.4 and 0.8. For the fine scan data, within this range, this upper threshold within 0.4 and 0.8 declines gradually as the range increases, and then converges to 0.4 at the 25-km range approximately. In contrast, for the coarse scan, the change in SQI with the increasing range is gradual and smooth without clear-cut delineations. Besides, we also notice separated artificial vertical lines around 25–30km range for the fine scans.

Given that precipitation is a rare event in nature, if without data QC, the majority of radar data are not precipitation echoes. It implies that the differences or similarities we pinpoint from the above frequency distributions of polarimetric variables mostly reflect characteristics of clear-sky echoes and non-meteorological echoes. This base radar dataset without data QC procedures definitely contains the precipitation echoes, but their proportion is quite tiny. Thus, the polarimetric characteristics of precipitation echoes are hidden in the general feature of the non-meteorological echoes. In order to inspect polarimetric variables of precipitation echoes and keep consistent with the previous discussion about the range dependence of polarimetric texture parameters (Fig. 4.18), we also calculate the quantiles and PDFs for these polarimetric variables using the same dataset of stratiform precipitation events.

More quantitatively by means of quantiles and PDFs, for the range beyond 15 km, 80% percent of Z_{DR} falls between -1 dB and 1 dB for the fine scans (Fig. 4.54(a)). The PDFs of the coarse scan data have similar shapes to those of the fine scan data and are slightly shifted downward, which is in good agreement with the different Z_{DR} calibration factors for the fine and coarse scan data discussed in Section 4.7. The PDFs of u-ϕ_{DP} of the fine scan are nearly identical to that of the coarse scans, except the first 15-km range in which the GC contamination in the coarse scan introduces a higher frequency of abnormally high ϕ_{DP} (Figs. 4.54(c) and 4.54(d)). When it comes to ρ_{HV}, for the fine scan, the existence of GCs brings about a large portion of low ρ_{HV} values within the 15-km range, and the medians of ρ_{HV} reach the maximum values around the 15-km range and then gradually decrease due to the enlarging sampling volume and resultant non-uniform beam filling effect (Fig. 4.54(e)). Within the 15-km range, the coarse scan has a wider distribution extending downward to the lower values, illustrated by the slight downward shift of the 0.1 quantile ($Q_{0.1}$) and 0.5 quantile ($Q_{0.5}$) (Fig. 4.54(f)). In contrast, beyond 15 km away from the radar, the coarse scan data are characterized by a slightly upward 0.1 quantile ($Q_{0.1}$) and an apparently upward 0.5 quantile ($Q_{0.5}$) compared to the fine scan. This difference exactly tallies with

our discussion in Section 4.5 that the fine scan has a more obvious decreasing trend in $\rho_{HV}$and a clearly high frequency of low ρ_{HV} values with the increasing range. It reconfirms a very important difference between the fine and coarse scan, that is, the higher radial resolution may bring about a severer non-uniform beaming filling effect and thus reduce ρ_{HV}.

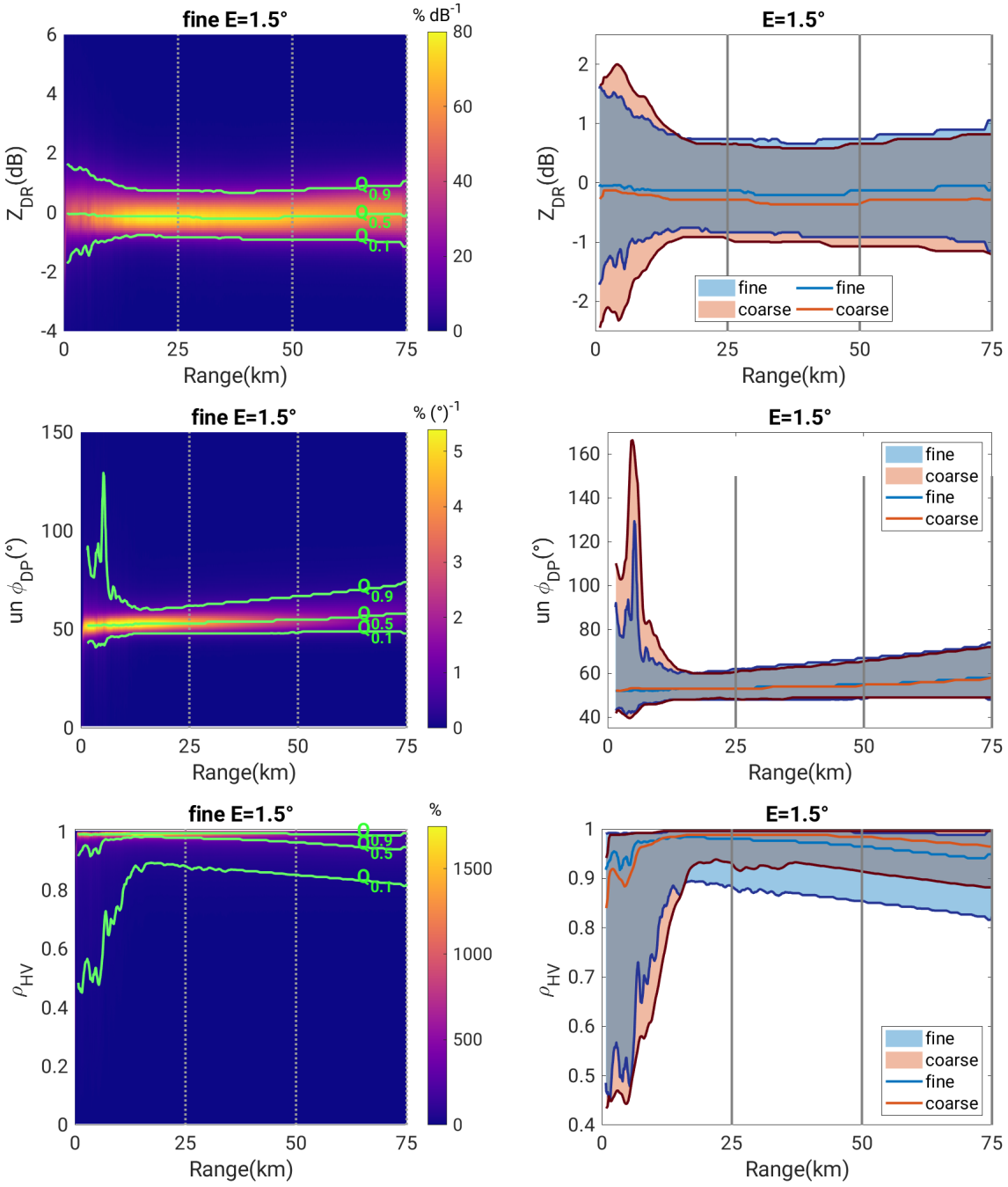

Fig. 4.54.: The same as Fig. 4.18 (merely stratiform precipitation), but for Z_{DR}, u-ϕ_{DP} and ρ_{HV}

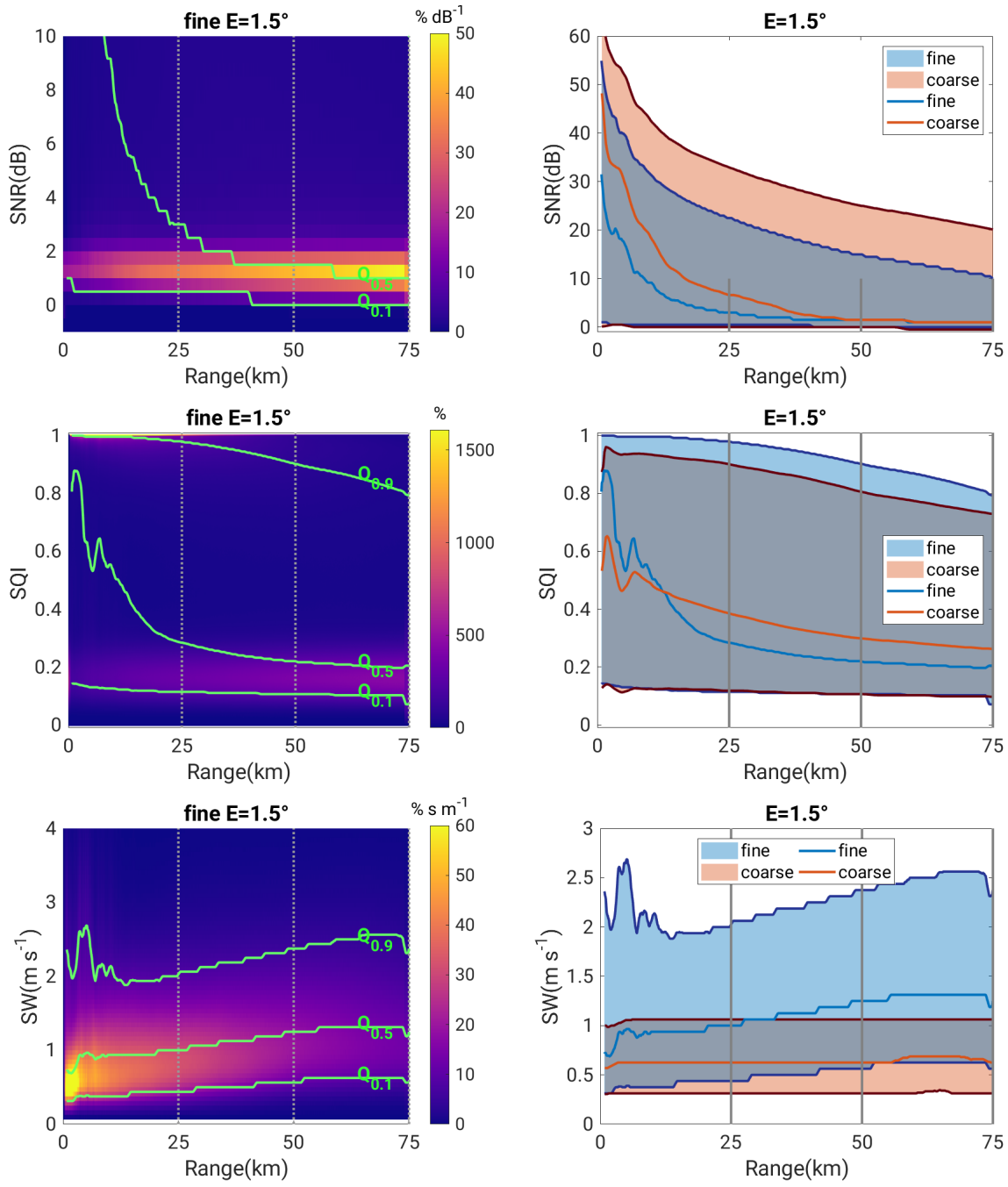

Fig. 4.55.: Same as Fig. 4.54, but for SNR, SQI and σ_v

With respect to SNR, the median values in the fine scan data decrease rapidly within the 35-km range, and keep consistent around 1 dB beyond 35 km. The median value ($Q_{0.5}$) and the 0.9 quantile ($Q_{0.9}$) of the coarse scan are clearly larger than those of the fine scan data, which tallies with the differences between the fine and coarse scan data we just discussed in Figs. 4.53(c) and 4.53(d). For SQI in the fine scan data, with the increasing range, the lower thresholds remain invariable, the medians decrease rapidly and the upper thresholds decline gradually (Fig. 4.55(c)). The coarse scan has similar

shapes in terms of the decreasing tendency of these three quantiles. Through the entire range, the 0.9 quantile ($Q_{0.9}$) of the coarse scans is always 0.1 lower than that of the fine scan, but the quantile 0.5 ($Q_{0.5}$) is always 0.1 higher than that of the fine scans except the first 15-km range (Fig. 4.55(d)). It agrees with our previous discussion that the fine scan data have a more definite ability to discriminate between precipitation echoes and all the other types of echoes according to their SQI values. In the fine scan data, σ_v increases slightly with the increasing range, whereas σ_v of the coarse scan are limited to the $1\,\mathrm{m\,s^{-1}}$ due to the Doppler dilemma. The reason to mention σ_v is that SQI is closely linked to σ_v. The Doppler dilemma in the coarse scans accounts for the reason why SQI values in the coarse scans cannot distinguish between the precipitation echoes and other, but SQI values in the fine scans can.

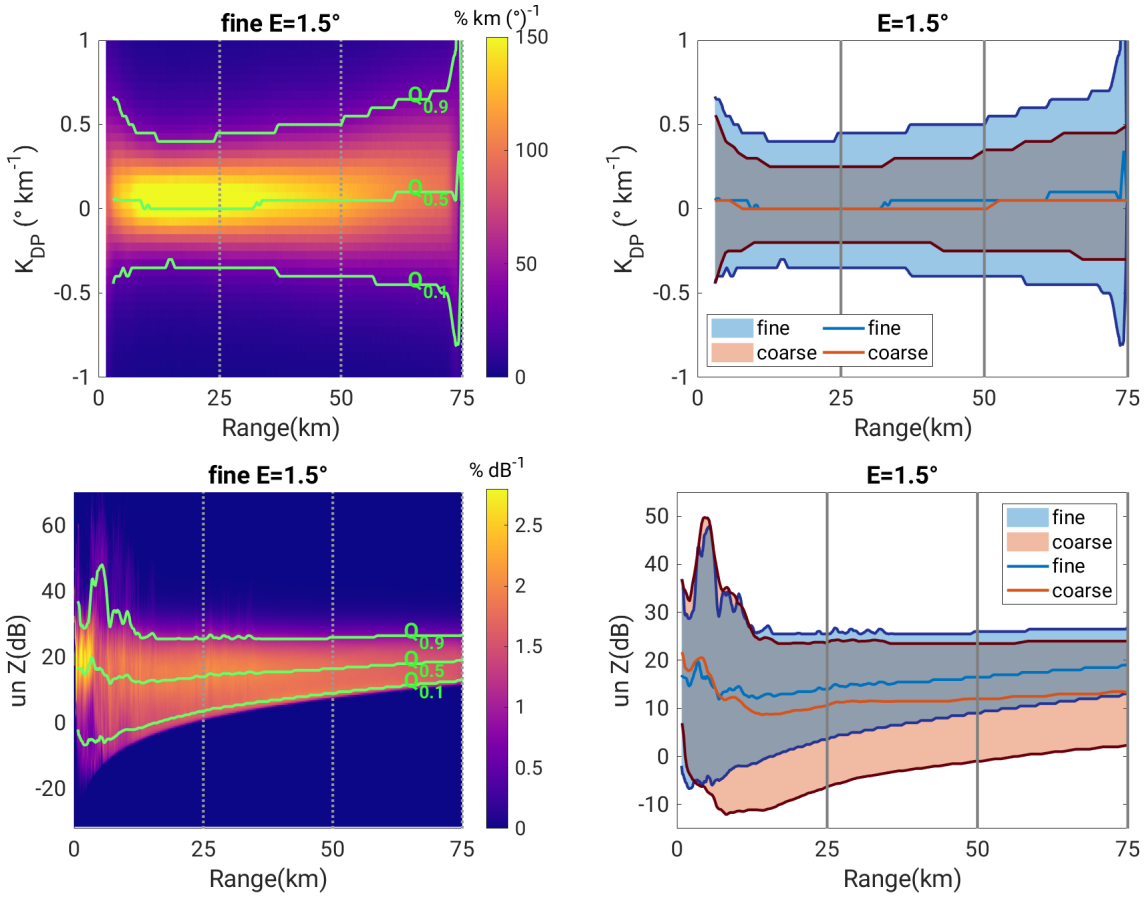

Fig. 4.56.: The same as Fig. 4.54, but for K_{DP} and uncorrected Z_H

For K_{DP}, the 0.1 quantile ($Q_{0.5}$) and 0.9 quantile ($Q_{0.9}$) are approximately symmetric around the $0\,^{\circ}\mathrm{km^{-1}}$, and the widths of the frequency distributions of the coarse scan data are slimmer than those of the fine scan, concurring with the contrast between Figs. 4.53(a) and 4.53(b). For the uncorrected Z_H, except the first 15-km range with some abnormally high Z_H values caused by GCs, as the range increases, the 0.9 quantile ($Q_{0.9}$) keeps consistent, the median values ($Q_{0.5}$) increase slightly and the increasing trend of the 0.1 quantile ($Q_{0.1}$) is more obvious than that of $Q_{0.9}$. The dramatic difference

between the fine and coarse scan data is that lower thresholds of the coarse scan data are mostly about 8–10 dB lower than those of the fine scan. It is another illustration that the fine scan data tend to overlook the weak echoes which are kept in the coarse scan data. Note that this uncorrected Z_H is without the clutter correction procedure default in the radar signal processor, and should be distinguished from the (corrected) Z_H in the base data (Section 3.1.5).

However, the PDFs (Figs. 4.54, 4.55 and 4.56) are only based on the selected stratiform precipitation episodes. For the overall precipitation, in order to decipher its characteristics in terms of polarimetric radar variables, it is necessary to apply data QC procedures to distinguish the precipitation echoes from others, which is the topic as follows.

4.9.2. PDF for processed data and range dependence

Although the radar was operating continuously for 24 hours every day, the moderate-to-heavy precipitation occurred even less 1% of the operating time. If we calculate PDFs using all the measurements from the entire measuring period, then the resultant PDFs represent primarily the characteristics of non-meteorological or clear-sky echoes that are not of interest to us. Since we are concerned mostly with precipitation, the PDFs of our interest should be based purely on the radar echoes from precipitation targets. To achieve this, we specifically select over 2000 volume scans from precipitating periods in which we collected a large amount of the radar data reporting valid K_{DP} (roughly four times the radar data reporting invalid K_{DP}). K_{DP} is only retrievable if it is a good data satisfying the low texture of differential phase, high ρ_{HV}, and high SNR (see "good data masking" in Section 3.1.5). Thus, a valid K_{DP} retrieval is associated with precipitation except that it is contaminated by noise. Accordingly, we classified the radar measurements into two categories depending on whether the valid K_{DP} retrieval was available or not. To clarify, since we have already applied the spike signal and second-trip echoes removal, the radar data with valid K_{DP} retrieval can be regarded as precipitation echoes, whereas the radar data without K_{DP} retrieval indicate the non-meteorological echoes or the radar data along edges of precipitation systems. The latter situation is because K_{DP} is usually retrieved over a calculating window consisting of several radar gates.

PDFs are calculated using Eq. 3.10, in which Δx_i for Z_H, Z_{DR}, ϕ_{DP}, ρ_{HV}, SNR, SQI, V_{Do}, K_{DP} are 0.5 dB, 0.079 dB, 1°, 0.003937, 0.5 dB, 0.003937, 0.252 $m\,s^{-1}$ and 0.05° km^{-1}, respectively. The total data include 57.5 and 17.2 million radar gates for fine and coarse scans respectively.

For the precipitation echoes, the PDFs of Z_H for either fine or coarse scans regardless of the range have unimodal shapes free of apparent skewness, resembling the normal distribution (Fig. 4.57). The PDFs for Z_H from the 0 –7.5 km range interval are much different from others, although we have already remove data from the first 750 m range. This abnormality implies cautions to use the radar data very close to the radar. For other range intervals, both the centers and left flanks of PDFs shift noticeably to the right sides as the ranges increase, while the right flanks of PDFs slightly shift to the left sides as

the range increases (Figs. 4.57(a) and 4.57(b)). The much narrower shifts of the right flanks than the left flanks of PDFs imply a gradually slimmer PDFs of Z_H with the increasing range.

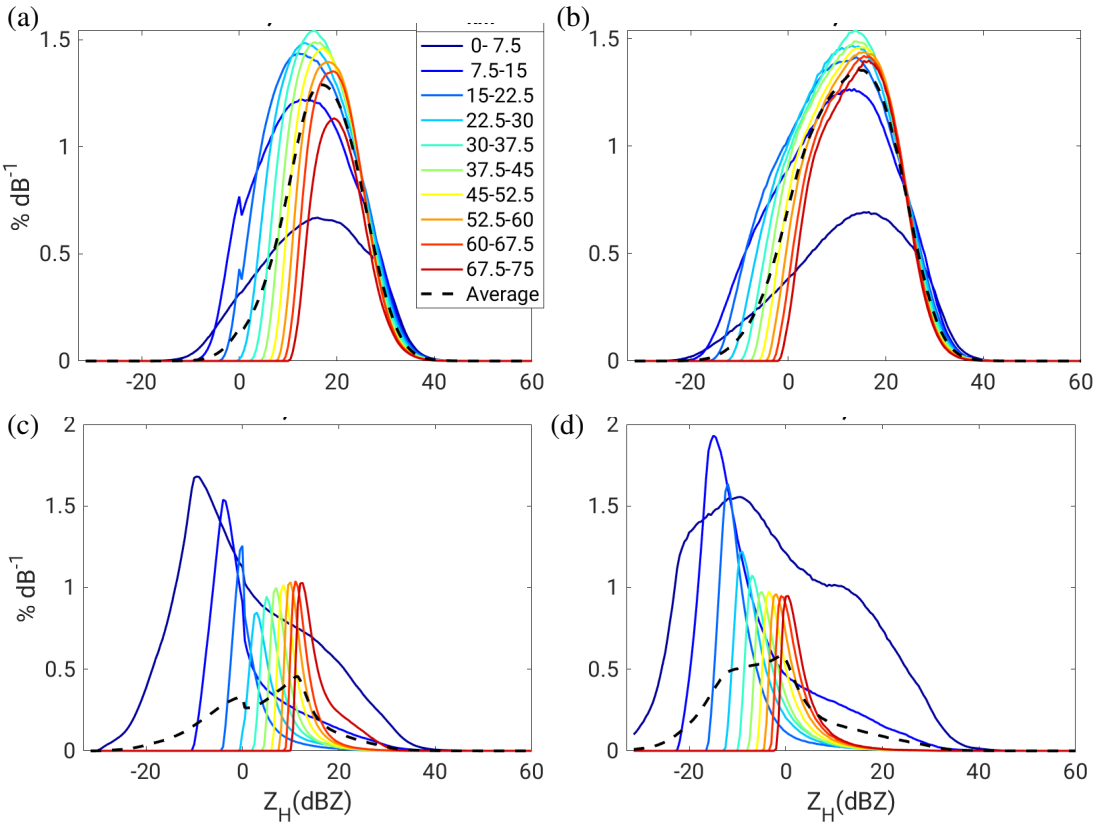

Fig. 4.57.: PDFs of Z_H within each 7.5-km interval of the radar range from the first elevation during stratiform precipitation events to illustrate the range dependence of Z_H, where (a) and (b) are for the data with valid K_{DP} but (c) and (d) are for the data without valid K_{DP} retrievals

The rightward shift of the left flanks of PDFs corresponds to an increase in the lower threshold of the available Z_H values. For instance, for the fine scan data, 0 dBZ, which is available within the 15-km range, becomes barely inaccessible beyond 15 km away from the radar. Besides, this shift of the left flanks slows down with the increasing range—wider gaps between the bluish lines and narrower gaps between the red lines in Figs. 4.57(a) and 4.57(b) respectively. This rightward shift shows a large discrepancy between fine and coarse scans. For precipitation echoes, within each range interval except the first 7.5 km, the left flanks of PDFs of coarse scans are on the left side of those of fine scans (Fig. 4.58). It implies, the lower Z_H values can be measurable in the coarse scan but not in the fine scan, which exactly corresponds to the loss of weak echoes in fine scans (Section 4.1). The explanation is that the noise level of fine scans is higher than that of coarse scans. Since the signal weaker than the noise level is removed in the signal processing procedure, more weak echoes are absent in the fine scans.

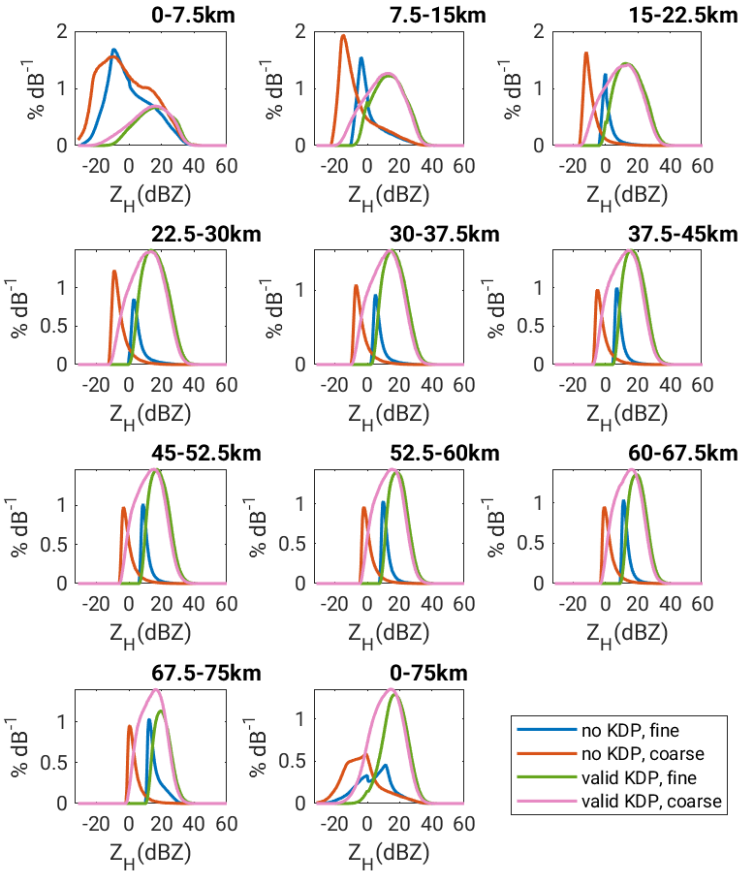

Fig. 4.58.: Comparing PDFs of radar reflectivity (Z_H) between the fine and coarse scans, between precipitation echoes and non-meteorological echoes, within each 7.5-km interval of the radar range

For a quantitative illustration, we regard the intersection of each left flank with the abscissa as Z_{min}. Z_{min} increases with the increasing range but this increase shrinks (Tab. 4.3). For instance, for the fine scan, Z_{min} of the 22.5–30 km range is 3.5 dB larger than its closer range interval (15–22.5 km), but is only 2.5 dB less than its farther range interval (30-37.5 km). Clearly, Z_{min} measurements of fine scans are much (at least 10 dB) larger than those of coarse scans.

Tab. 4.3.: Range dependence of Z_{min} for both fine and coarse scans

Range (km)	0–7.5	7.5–15	15–22.5	22.5–30	30–37.5	37.5–45	45–52.5	52.5–60	60–67.5	67.5–75
Fine (dBZ)	-30	-10.5	-4	-0.5	2.0	4.5	6.0	7.5	9	10
Coarse (dBZ)	-31.5	-22.5	-16.5	-12.5	-10	-8	-6	-4.5	-3	-2

In contrast, the leftward shift of the right flanks of PDFs corresponds to a decrease in the upper threshold of the available Z_H values, and the shift is much smaller than the rightward shift of the left flanks, as illustrated by the closely cluster left flanks in Figs. 4.57(a) and 4.57(b). This subtle right-to-left shift of these right flanks is attributed to either the smoothing effect of the range dependence or attenuation. As the sampling volume becomes larger with the increasing range, the intense Z_H values tend to be averaged over this larger volume, and the extreme values are smoothed out. Moreover, attenuation becomes more frequent and severer with the increasing range since the radar signals have to propagate through more water to reach the targets farther away from the radar. Unlike large gaps among the left flanks, there is almost no gap between fine and coarse scans in terms of right flanks, illustrated by the nearly overlapped green and pink lines of the right sides of the peaks in Fig. 4.58. It also corresponds to our discussion in Section 4.1 that despite loss of a large number of weak signals in fine scans, the capability to observe intense echoes is not affected by the smaller Δr.

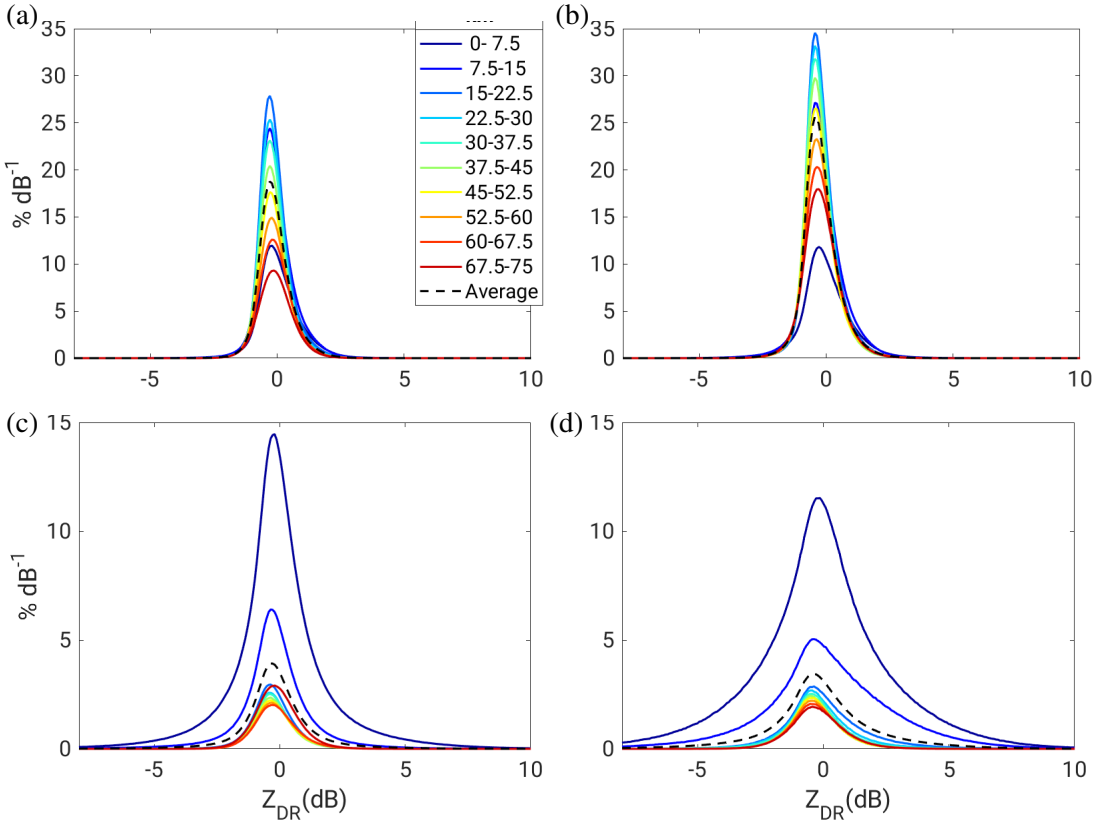

Fig. 4.59.: The same as Fig. 4.57, but for Z_{DR}

The PDFs of radar data without valid K_{DP} retrievals are slimmer than those of precipitation echoes, and they are located on left side of those of precipitation echoes, which is as expected (Figs. 4.57(c) and 4.57(d)). Unlike precipitation echoes whose PDFs are close to symmetry, the PDFs of the non-meteorological echoes are left skewed with longer tailors on the right sides of the PDFs. This skewness implies that the majority of the non-meteorological echoes are weak in intensity and only a

small portion can reach 10 dBZ. Despite these differences in PDFs, either for fine and coarse scans, Z_{min} are identical for both precipitation echoes or the non-meteorological echoes—the overlapped red and pink intersection points, or the collocated blue and green intersection points in Fig. 4.58. It implies the ability to observe weak echoes—the detectability of radar—does not change with the targets.

Regarding comparisons between fine and coarse scans, while the precipitation echoes share the overlapped peaks between fine and coarse scans, the peaks of PDFs for the non-meteorological echoes of fine scans are always located roughly 15 dB left the peaks of coarse scans (Fig. 4.58). For the range intervals 37.5–45 km until 60–67.5 km, the heights of peaks are quite comparable between fine and coarse scans.

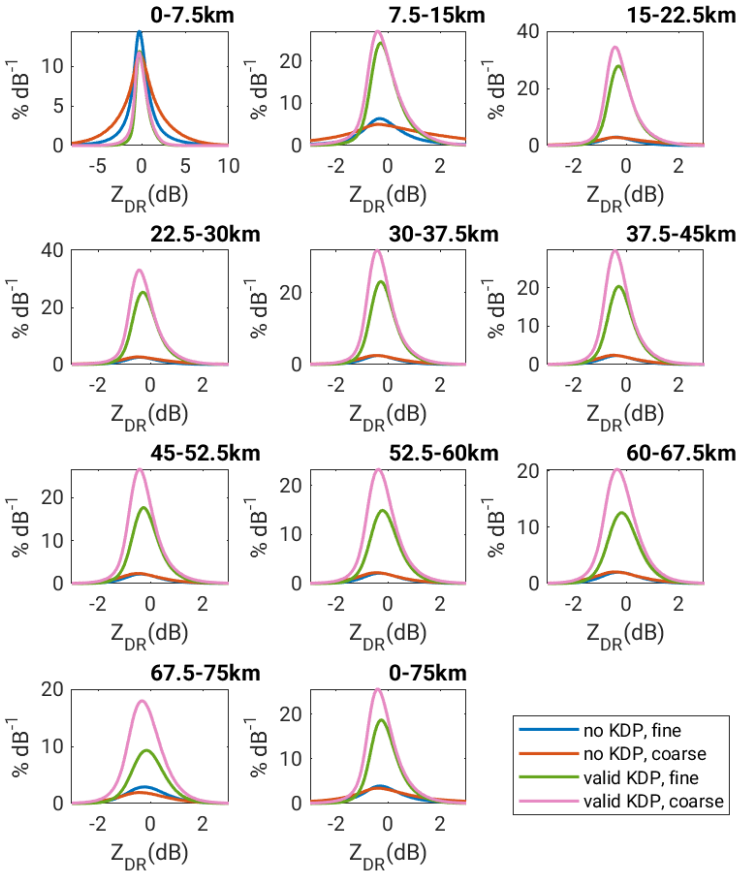

Fig. 4.60.: The same as Fig. 4.58, but for Z_{DR}

The PDFs of Z_{DR} from precipitation echoes are narrower than those of non-meteorological echoes (Figs. 4.59 and 4.23. The PDFs of Z_{DR} become flatter and the heights of peaks get lower with the increasing ranges, either for fine and coarse scans, either for precipitation or non-meteorological echoes. For precipitation echoes, the right flanks of fine scans nearly overlap those of coarse scan, while the left

flanks of coarse scans are always on the left sides of the left flanks of fine scans with roughly 0.1 dB spacing (Fig. 4.60). This contrast corresponds to the slight different ΔZ_{DR} between fine and coarse scans (Section 4.7).

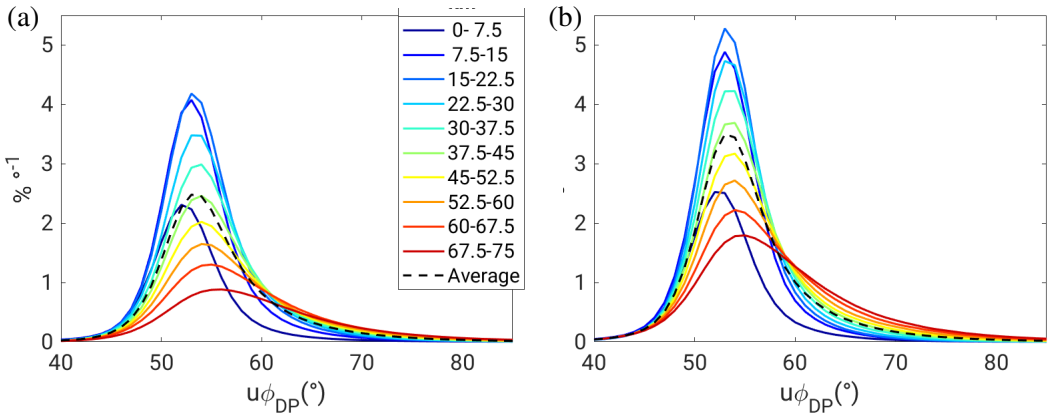

Fig. 4.61.: The same as (a) and (b) in Fig. 4.57, but for u-ϕ_{DP}

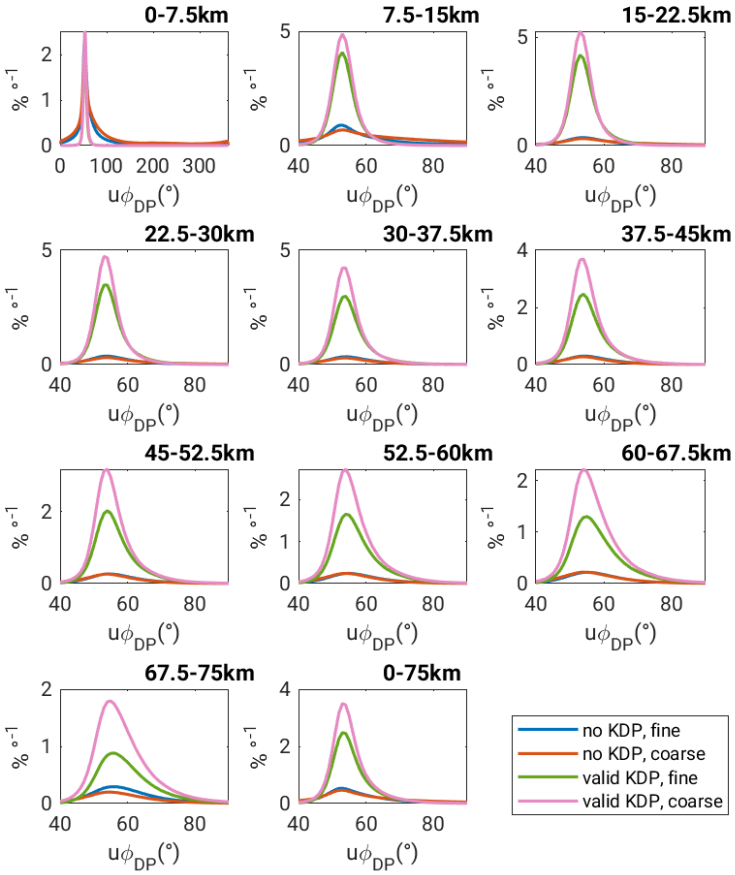

Fig. 4.62.: The same as Fig. 4.58, but for u-ϕ_{DP}

With the increasing range, the PDFs of u-ϕ_{DP} become flatter with the peaks moving from around 53° to 55°, and become left-skewed (Fig. 4.61). This increased skewness with noticeable tailors on the right sides of the peaks is as expected, because the differential phase is an accumulative variable ideally monotonically increasing with the range (Section 2.2). When it comes to the differences between fine and coarse scans, the PDFs in fine scans are lower than those of coarse scans, indicating that the fine scan data have less valid u-ϕ_{DP} measurements (Fig. 4.62).

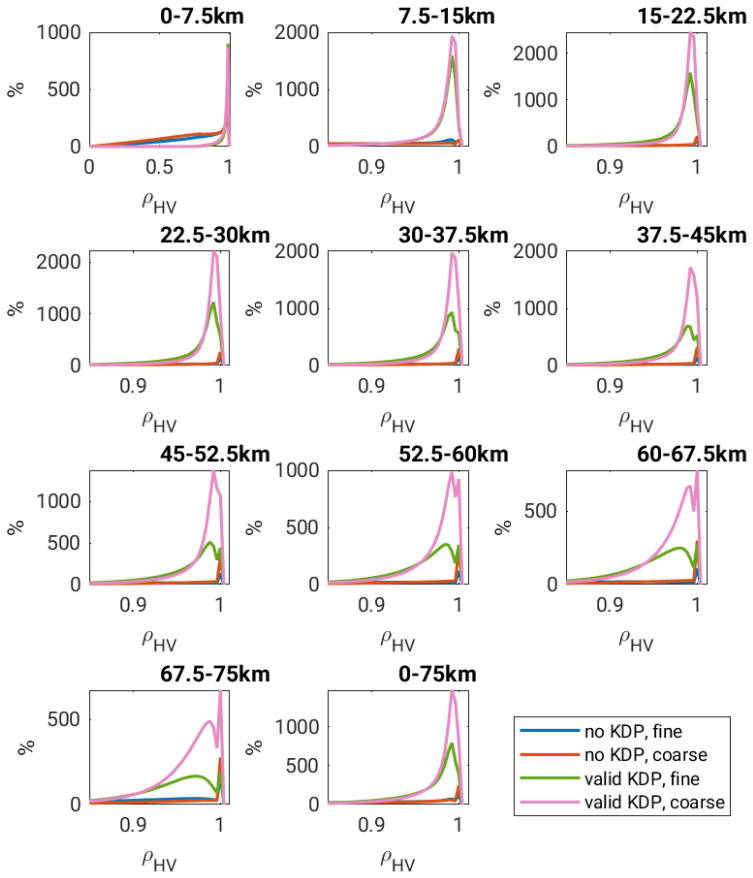

Fig. 4.63.: The same as Fig. 4.58, but for ρ_{HV}

Similar to Z_{DR} and ϕ_{DP}, the farther the radar measurements are away from the radar, the flatter the PDFs of ρ_{HV} become (Fig. 4.63). The discrepancy between fine and coarse scans also becomes more pronounced with the increasing range, since the PDFs of the fine scan shrink much faster. NBF partially accounts for these much shorter PDFs of ρ_{HV} for the fine scans than the coarse scans. It implies NBF is more evident in the fine scans. Since Θ is kept the same for both fine and coarse scans and Δr of the fine scans is more than three times less than that of the coarse scans, a possible explanation is that the ratio of the azimuthal resolution to the radial resolution becomes extremely large for the fine scan especially for

the radar gates at the far range. For instance, at the 60-km range, the ratios are 14 and 4.2 for the fine and coarse scans respectively. This larger ratio of the fine scan renders NBF more severe for the fine scan, associated with the worsen data quality for the polarimetric variable for fine scans as well. Besides, a single dent appears around $\rho_{HV} = 0.99$ for each PDF, for fine scans starting from 37 km and for coarse scans starting from 52.5 km away from the radar.

Opposing to Z_{DR}, u-ϕ_{DP} and ρ_{HV}, the PDFs of SNR become narrower with the increasing range (Figs. 4.64(a) and 4.64(b)), along with the leftward-moving peaks to the smaller SNR values (Tab. 4.4). This decrease in SNR corresponds to the increase of noise in the radar signals, another manifestation of the range dependence of radar measurements. Besides, the PDFs of fine and coarse scans are also in sharp contrast. The PDFs of SNR for the fine scans are much narrower than that of the coarse scan. The PDFs of fine scans are more left skewed while the PDFs of coarse scans are close to symmetry. In general, the peak values of the fine scan data are roughly 10 dB less than those of the coarse scan data (Tab. 4.4). The upper thresholds fall between 25 and 50 dB for the fine scans and between 35 and 60 dB for the coarse scans. For the non-precipitation echoes, SNR values are below 10 dB for both fine and coarse scans (Figs. 4.64(c) and 4.64(d)).

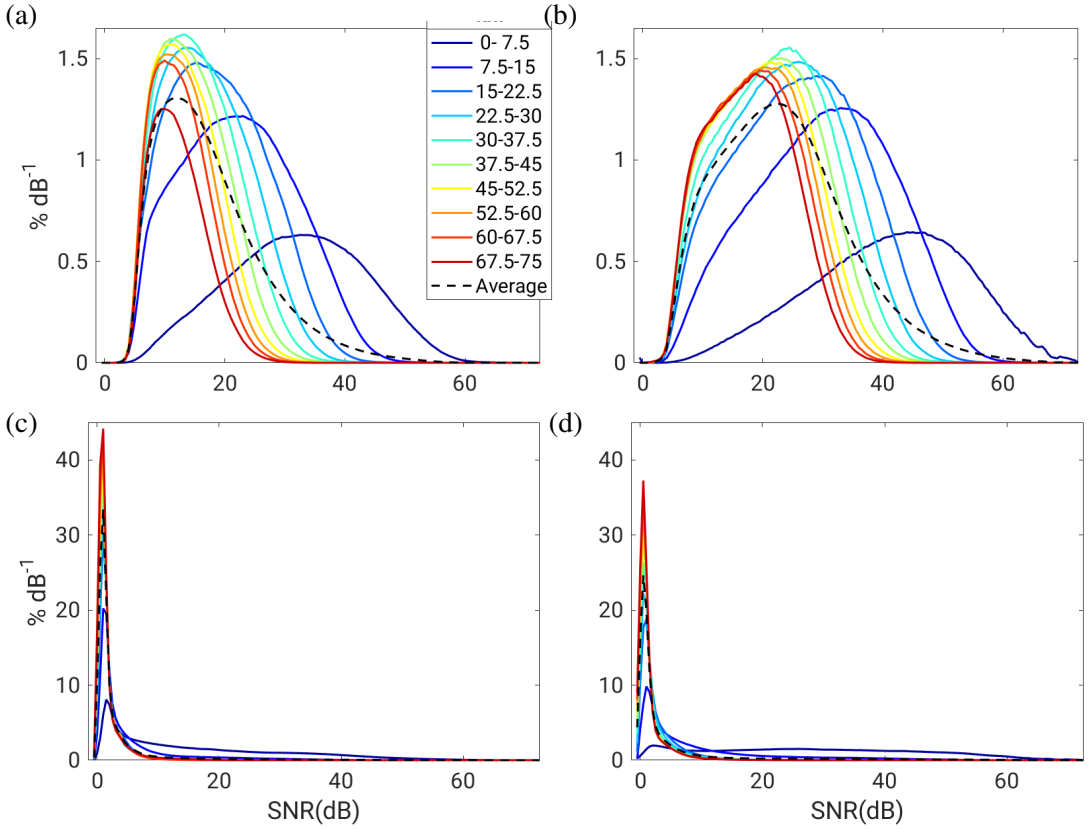

Fig. 4.64.: The same as Fig. 4.57, but for SNR

Tab. 4.4.: Range dependence of SNR_{peak} for both fine and coarse scans for precipitation echoes

Range (km)	0–7.5	7.5–15	15–22.5	22.5–30	30–37.5	37.5–45	45–52.5	52.5–60	60–67.5	67.5–75
Fine (dB)	32.5	23	15.5	13.5	13	11	11	10.5	10	9.5
Coarse (dB)	44	33	30	26	24.5	23	21.5	20	19.5	19

When it comes to SQI, for the precipitation echoes, the PDFs become flatter and more right-skewed with the larger tailors extending to lower values, with the increasing range (Figs. 4.65(a) and 4.65(b)). For instance, the PDFs of the SQI for the range less than 45 km exhibit peaks above 0.8, but such peaks disappear for the range farther than 45 km (Fig. 4.65(b)). This gradual change in shapes of PDFs is reasonable since it exactly corresponds to the severer deterioration of data quality for the radar measurements farther away from the radar. Besides, the PDFs of SQI of the coarse scan are much flatter than those of the fine scans, and the chance of SQI smaller than 0.8 is much larger for SQI of the coarse scan data. The reason why SQI below 0.4 is rare for the fine scan data is that the second-trip echo removal has been applied to get rid of the data affected by the second-trip echo contamination.

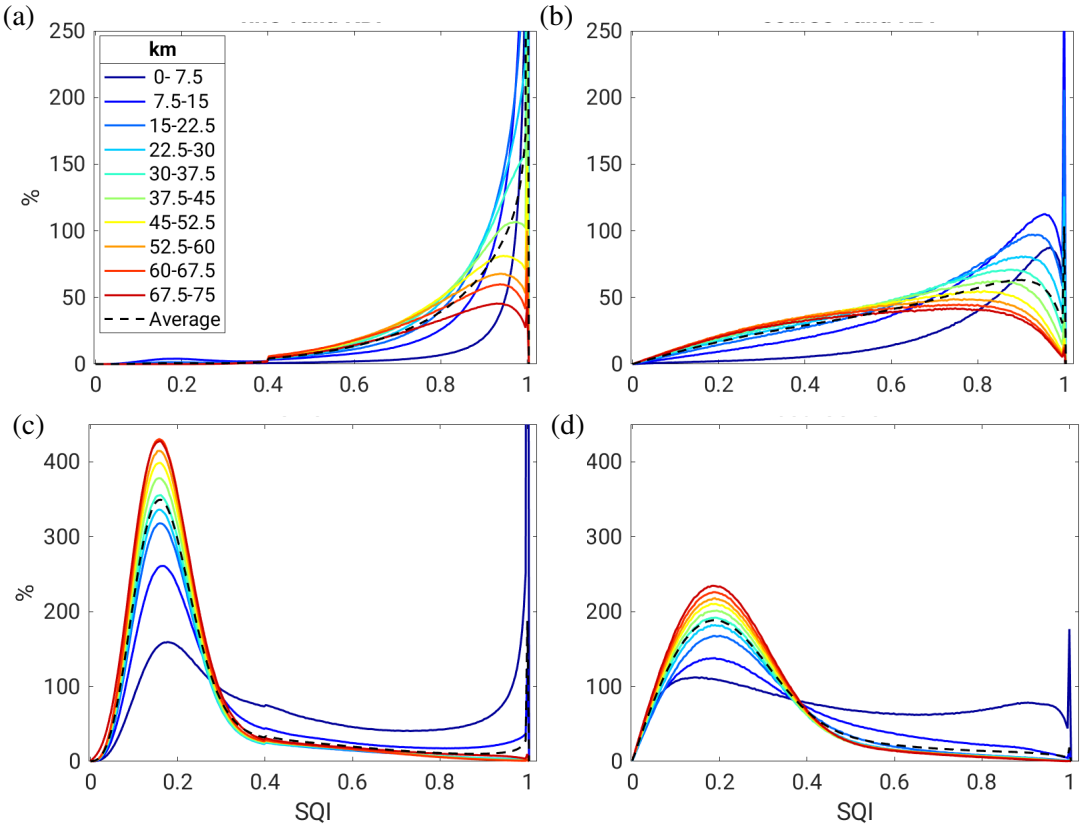

Fig. 4.65.: The same as Fig. 4.57, but for SQI

For the radar data without valid K_{DP} retrievals, the PDFs of SQI for either fine and coarse scans become narrower with the increasing range, and the PDFs of fine scans are narrower than those of coarse scans, along with the stationary peaks around 0.16 for the fine scan and 0.19 for the coarse scan regardless of the range intervals except the first 7.5 km (Figs. 4.65(c) and 4.65(d)). The tailors of PDFs for the coarse scans extend to the magnitude over 0.6, while the tailors in PDFs for the fine scan are normally less than 0.4. It implies, SQI of the coarse scan for the non-meteorological echoes can often reach higher values.

The fine scan data are characterized by larger SQI for precipitation echoes and smaller SQI for non-meteorological echoes, whereas the coarse scan data are characterized by smaller SQI for precipitation echoes and larger SQI for non-meteorological echoes (Fig. 4.66). It means SQI of fine scans is more capable of distinguishing precipitation echoes from non-meteorological echoes, compared to coarse scans, which corresponds to our SQI-based second-trip echo removal for fine scan data.

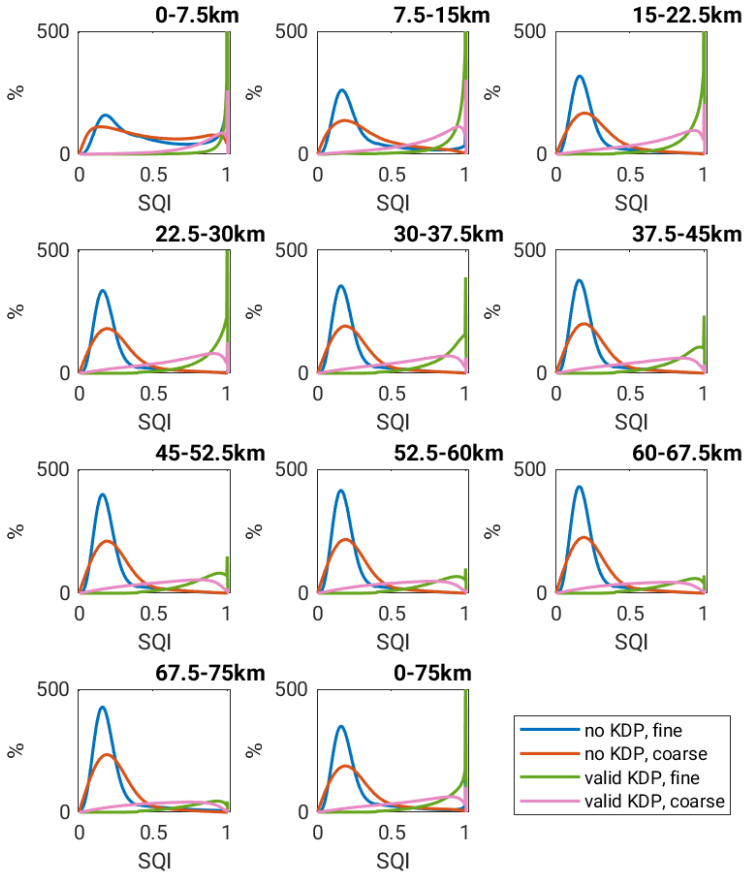

Fig. 4.66.: The same as Fig. 4.58, but for SQI

The Doppler dilemma limits the reliability of V_{Do} measurements in the coarse scans, but the symmetry of V_{Do} either for precipitation echoes or non-meteorological echoes is evident (Figs. 4.67(b) and 4.67(d)). In contrast, the PDFs of V_{Do} for the fine scan are not symmetric, and the negative V_{Do} values are more frequent than the positive values. Besides, for the fine scans, the PDFs of V_{Do} become flatter with the increasing range. The peaks in PDFs of V_{Do} around 0 m s^{-1} for the range less than 30 km away from the radar reflect the relative stationary feature of GCs.

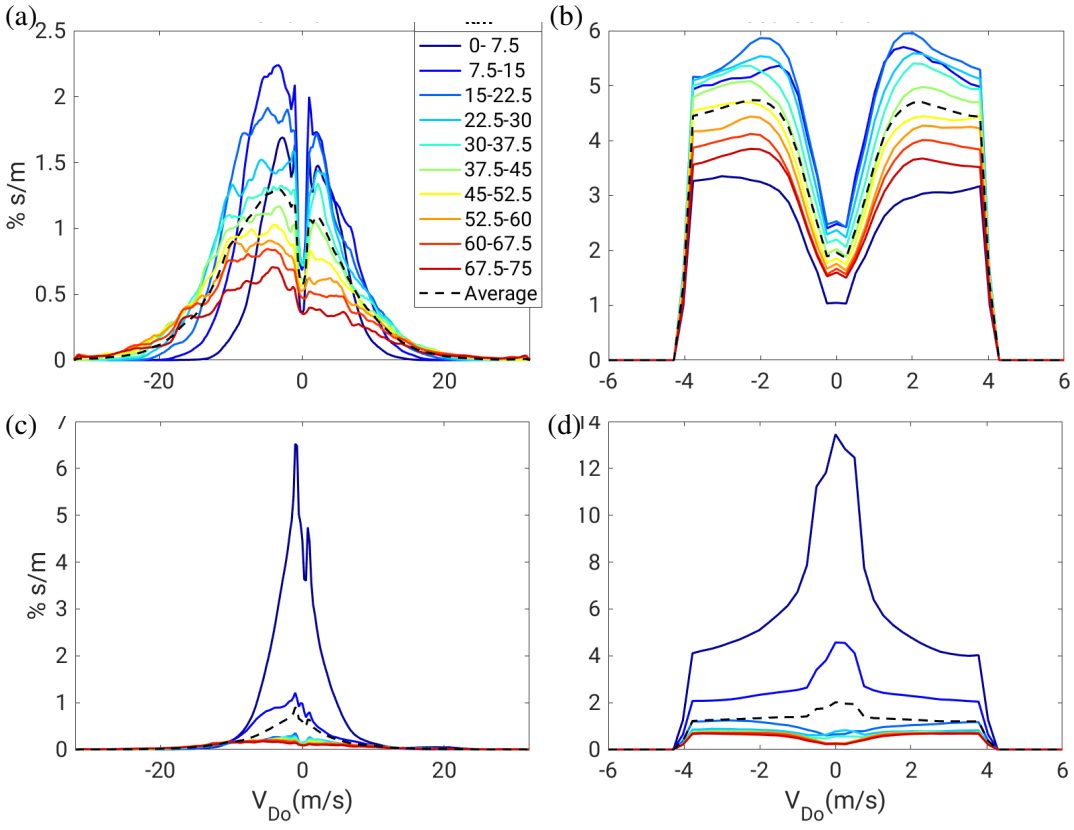

Fig. 4.67.: The same as Fig. 4.57, but for V_{Do}

PDFs of K_{DP} either for the fine and coarse scans get flatter as the increasing range, but the heights of peaks of fine scans are much shorter than those of coarse scans, regardless of the range interval (Figs. 4.68(a) and 4.68(b)). It means K_{DP} is less retrievable in the fine scans rather than the coarse scans. K_{DP} is only retrieved for the good data (Section 3.1.5), so it is tempting to consider the less availability of valid K_{DP} retrievals in fine scans implies a worsening data quality in the fine scan data than the coarse scan data. However, for K_{DP} larger than 0.25 $^{\circ}$ km^{-1} which corresponds to R over 5 mm h^{-1}), between the 7.5-km and 15-km range, the PDFs of K_{DP} of the fine scan are nearly overlapped with those of the coarse scan. The same overlap can be seen at other range interval as well. It means that the large K_{DP} has the nearly equal chance to be retrieved in the fine and coarse scans. This absence of small K_{DP} retrievals in fine scan is much likely attributed to loss of weak echoes below the noise level. Besides, the peaks in

PDFs of K_{DP} of the fine scans are around 0.15 and 0.2° km^{-1}, and those of of the coarse scans are 0.1 and 0.15° km^{-1}.

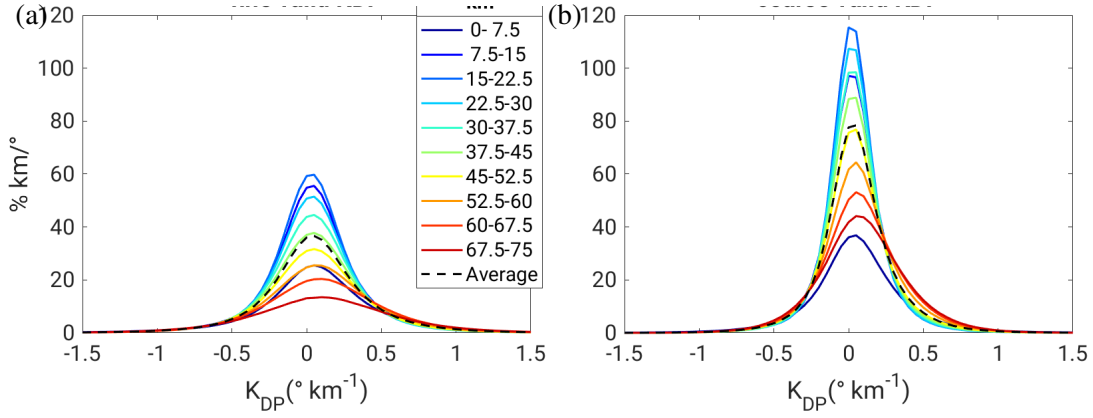

Fig. 4.68.: The same as (a) and (b) in Fig. 4.57, but for K_{DP}

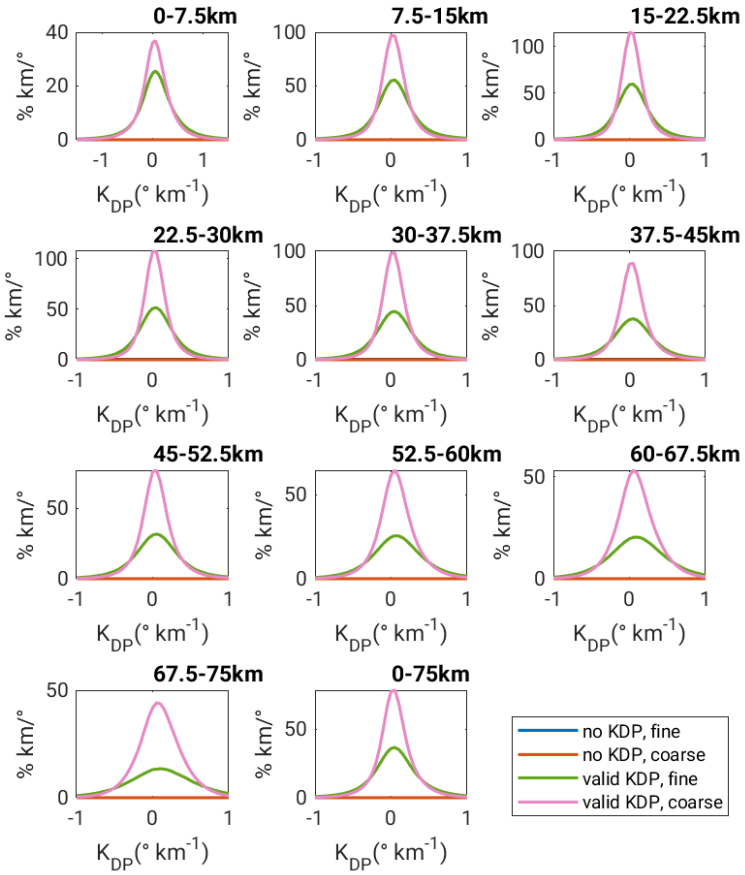

Fig. 4.69.: The same as Fig. 4.58, but for K_{DP}

4.9.3. Effect of data quality procedure on PDF

The radar echoes during the rainy days are a mixture of non-meteorological and precipitation echoes, whereas the non-rainy days should only contain the non-meteorological echoes. During the entire measuring period lasting over 147 days from 23 May to 16 October 2017, 23 full days (24 hours from 00:00 UTC to 23:59 UTC as one unit) had absolutely no precipitation over the whole X-band radar coverage, and these days are defined as clear-sky days. The rest of these days are named as rainy days regardless of the rainy duration, rain intensity or rain's areal extent. Accordingly, we divide the radar measurements into two datasets, one dataset from these clear-sky days and the other one from these rainy days. The former is referred as the "csky" dataset and the latter as the "rain" dataset. Keep in mind that before applying the NMER, the non-meteorological echoes prevail in the "rain" dataset where the "csky" dataset only contains the non-meteorological echoes.

For the "csky" dataset, the PDFs of the fine scans are much lower than that of the coarse scans for Z_H less than 0 dBZ, and PDFs of both scans nearly overlap for Z_H greater than 0 dBZ (Fig. 4.70(a)). It implies that weak echoes still exist in the fine scan and the majority of these lost echoes are weaker than 0 dBZ in magnitude. It also implies that, the non-precipitation echoes greater than 0 dBZ are persistent during the absolutely non-rainy days. For the "rain" dataset, for Z_H below 0 dBZ, similar to the situation in the "csky" dataset, the PDF of the fine scan is much lower than that of the coarse scan. However, for Z_H above 0 dB, in contrast to the situation in the "csky" dataset, there are noticeable discrepancies in PDFs between the fine and coarse scans. For instance, the PDF of the fine scan exhibit a peak around 12 dBZ, which is not seen in the PDF of the coarse scan. For Z_H above 20 dB, both PDFs get closer to each other and share the similar tendency, but along with a narrow gap (around 1–2 dB in width). This gap indicates that Z_H in fine scan is always 1–2 dB greater than that of the coarse scan. This gap attributes to the difference in the Z_H absolute calibration (to be discussed in Section 5.2 and Section 5.3).

After obtaining the general feature for the PDFs of the "rain" and "csky" datasets, we analyze the effect of data QC procedures on these PDFs. We start with the attenuation correction, then spike signal filtering and second-trip echo removal, and followed by NMER.

The effect of attenuation correction is to increase Z_H magnitudes, leading to higher PDFs for the higher Z_H, and meanwhile lower PDFs for the relatively low Z_H. For the fine scan, the reduction in PDF starts around -2 dBZ, while such reduction starts at 1 dBZ for the coarse scan data, and attenuation correction makes no difference on PDFS below 1 dBZ (-2 dBZ) for the fine (coarse) scan (Fig. 4.70(b)). In other words, the weak echoes present in the fine and coarse scans could be also precipitation echoes, and the attenuation can reduce the Z_H intensity of precipitation echoes as low as 1 dBZ (-2 dBZ) for the fine (coarse) scan. The Z_H magnitude of 1 dBZ (-2 dBZ) corresponds to R less than 0.05 mm h^{-1}, which is closer to the minimum accuracy of a rain gauge. Besides, after correcting attenuation, for Z_H greater than 40 dBZ, the discrepancy in terms of the PDF still exists between the fine and coarse scans. In brief,

attenuation removes the precipitation that should be observed by radar if attenuation does not take effect, so correcting attenuation is one of the necessary data QC procedures (Section 4.6).

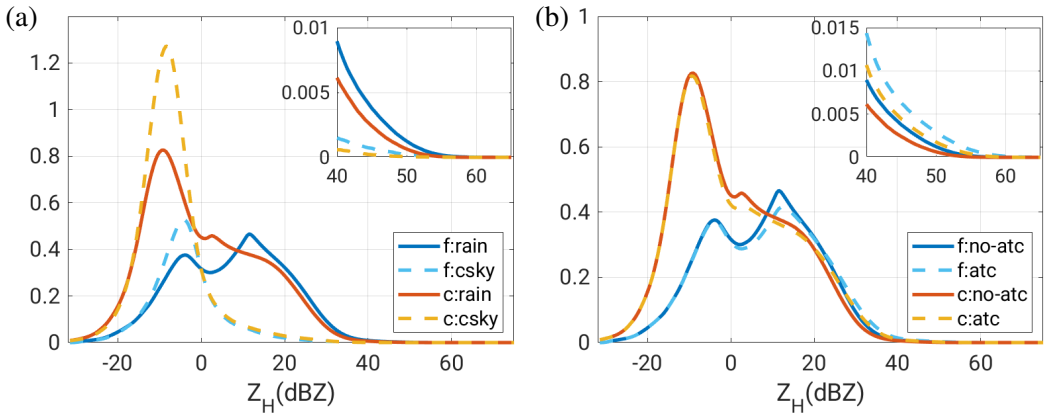

Fig. 4.70.: PDFs of Z_H for the fine and coarse scan respectively, where (a) compares the "rain" and "csky" datasets, and (b) compares the data with and without attenuation correction for the "rain" dataset

Given the fraction of echoes affected the spike signals is quite small (Section 4.2), the spike signal removal procedure does not modify the PDFs much as other data QC procedures (Fig. 4.71(b)). However, for Z_H between 40 dB and 60 dB in the "rain" dataset, we can still see the PDFs for the data after spike signal filtering are on the left side of the PDFs for the data without spike signal filtering. Besides, for the "csky" dataset, we notice a more apparent leftward shift of PDFs for Z_H between 5 dB and 25 dB. Given that spike signals are quite often characterized by high Z_H (Section 4.2), the existence of precipitation echoes in the "rain" dataset reduces the relative portion of these spike signals characterized by high Z_H, so removing spike signals only makes a small difference on the PDFs. However, the high Z_H in the "csky" dataset have a larger chance being caused by spike signals, so the modification of PDFs after removing spike signals is much clear.

Compared to the spike signals, the amount of the second-trip echoes is much larger (Section 4.3). Thus, removing the second-trip echoes leads to the obvious reductions of PDFs in both the "rain" and "csky" datasets (Fig. 4.71(b)). The reduction starts from Z_H as low as -10 dBZ, and the reduction is more obvious in the "rain" dataset.

The most striking modification to the PDFs comes from NMER, which removes nearly all the Z_H measurements for the "csky" dataset, and converts the bio-mode PDFs of the fine scan data and the irregularly-shaped PDFs of coarse scan data into the singe-peak PDFs which resemble the normal distribution (Figs. 4.71(c) and 4.71(d)). Besides, after applying the NMER procedure, the PDFs of both fine and coarse scans becomes similar to each other, for instance, both peaks reaching around 0.3 $\%dB^{-1}$.

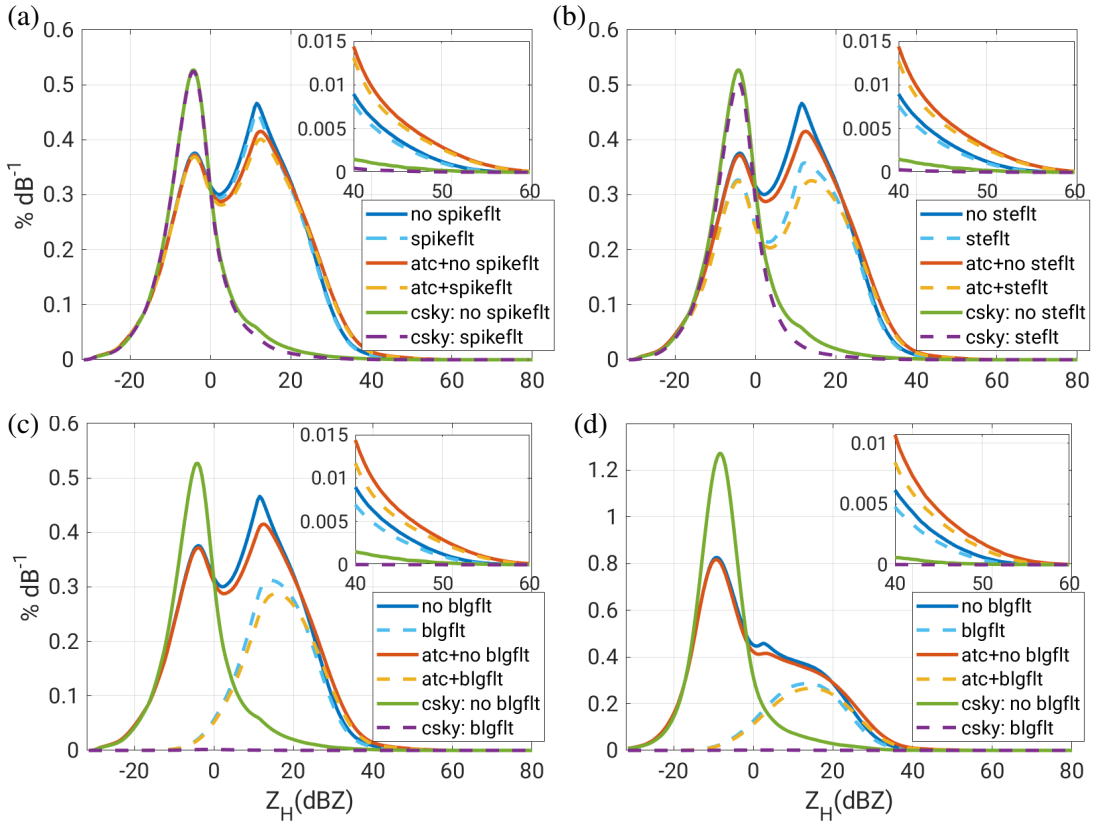

Fig. 4.71.: PDFs of $Z_H$where (a) is for the effect of spike signal filtering for the "rain" or "csky" fine scan datasets with or without attenuation correction, (b) is for the effect of second-trip echo filtering for the "rain" or "csky" fine scan datasets with or without attenuation correction, (c) is for the effect of non-meteorological echo filtering for the "rain" or "csky" fine scan datasets with or without attenuation correction, and (d) is the same as (c), but for the coarse scan data

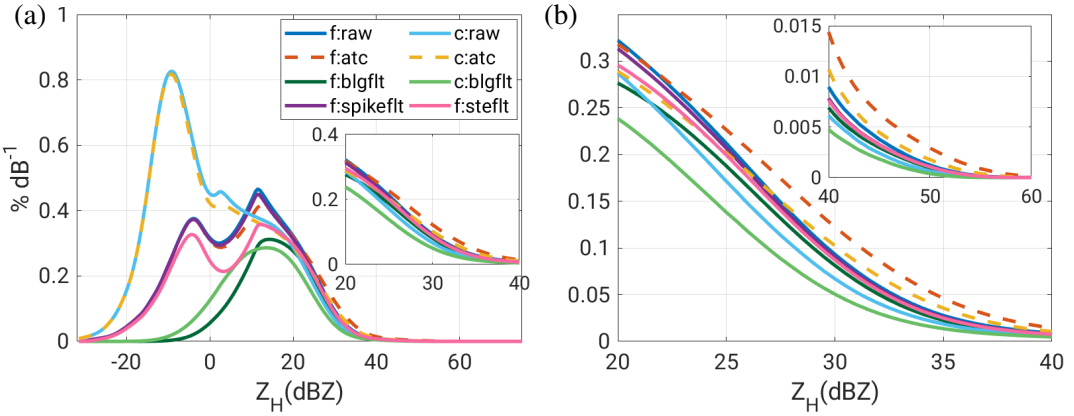

Fig. 4.72.: PDFs of Z_H to directly compare the effect of attenuation correction, NMER, spike signal and non-meteorological echo filtering on the fine and coarse scan respectively, where (a) is for Z_H below 40 dBZ, and (b) is for Z_H above 40 dBZ

In general, these data QC procedures gradually render the PDFs of both scans similar to each other, especially for Z_H below 40 dBZ (Fig. 4.72). For the large Z_H of our particular interest, the

attenuation correction increase the Z_H magnitude, but the NMER reduces the Z_H magnitude, and the discrepancy between the fine and coarse scans persists.

4.10. Sub-summary

The differences between the fine and coarse scans in terms of radar data quality are discussed extensively from various perspectives within this chapter. Starting from radar images for Z_H, we find that the fine scan data tend to overlook weak echoes but exhibit two additional types of suspicious noise which is not present in the coarse scan data. Further analyses identify the causes for both types of suspicious noise, and they are referred as spike signals and second-trip echoes. The spike signals are also present in the coarse scans but in a much less frequency than those of the fine scans, while the second-trip echoes are absent in the coarse scans. Despite these two extra sources of noise in the fine scans, the GC contamination is less severe for the fine scan. The polarimetric characteristics differ among three echoes types—GCs, ICs and PRs. These differences also differ between the fine and coarse scans. Despite the same algorithm, the non-meteorological echo removal procedure using the fine scan data is more efficient in filtering out non-meteorological echoes than that using the coarse scan data. Besides, the attenuation correction procedure is based on u-ϕ_{DP} and theoretically should not be affected by the difference in Δr. However, associating to the loss of weak echoes in the fine scan, the comparison in the attenuated-corrected Z_H between fine and coarse scan data pinpoints that the attenuation correction is slightly less effective in the fine scan.

The characteristics of polarimetric variables provides us the rationale to remove spike signals, non-meteorological echoes, and correct the attenuation, while the second-trip echoes removal is based on single-polarization variable (SQI). For each source of noise, the nose identification is treated separately from the noise filtering procedure, although both steps are associated with each other. In addition to the identification and removal of noises, the spatiotemporal distribution, the general statistics, such as PDF, of the noise are compared between different sources of noise, and also are compared between the fine and coarse scan data, providing us a more extensive understanding of effects of the spatial resolution on the X-band radar data quality.

Going through several data QC procedures including removing spike signals, second-trip and non-meteorological echoes, correcting attenuation and calibrating Z_{DR}, we obtain the radar data which are characterized by less noise and better data quality. Afterwards, we also discuss the range dependence on the characteristics of Z_H and other polarimetric variables for precipitation echoes, and also compare the range dependence between the fine and coarse scans.

5. Effects of Spatial Resolution on Radar-based Precipitation Estimation

Precipitation tity can be calculated based on either the single polarization or polarimetric radar variables (Section 2.3). These radar variables are the level II data (Section 3.1.5), and these precipitation quantities—the derivatives of these level II data—are the level III data (Section 3.1.5). Since the quality of the level II data is affected by the spatial resolution (Chapter 4), these radar-based precipitation quantities should be also affected by the spatial resolution. Thus, we need to investigate effects of the spatial resolution on the radar-based precipitation estimation.

With the fine scans as the experimental group and the coarse scans as the control group, effects of the spatial resolution can be illustrated by comparing the fine scan data with the coarse scan data. The comparisons can be done in three aspects: i) the ability to present details of convective storm inner structures (Section 5.1), ii) the agreement with external precipitation references (Section 5.2), iii) the spatial distribution of total precipitation accumulations (Section 5.3). Comparisons of the first aspect involve radar data at three radial resolutions—the fine and coarse scan data and the C-band radar data (Fig. 5.1). Comparisons of the second aspect includes i) comparisons between the X-band radar data and measurements from rain gauges (Section 5.2.1), i) comparisons between the X-band radar data and the MRR measurements (Section 5.2.2), i) comparisons between the C-and X-band radar data (Section 5.2.3) (Fig. 5.1). Comparisons of the third aspect only involve the X-band radar data. The comparison of the first aspect is qualitative, and of the other two aspects are quantitative and can be used to derive Z calibration factor in the absolute calibration procedures.

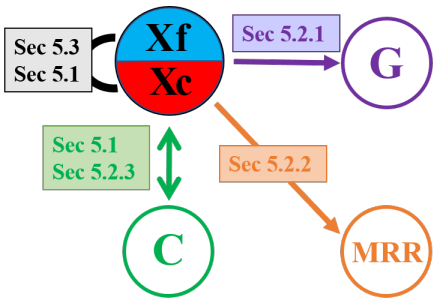

Fig. 5.1.: Block diagram of different precipitation datasets and their uses in Chapter 5, X_f denotes the X-band radar fine scan data (in blue), X_c denotes the X-band radar coarse scan data (in red), C stands for the C-band radar data (in green), G stands for the rain gauge measurements (in purple), MRR means the Micro-Rain-Radar (MRR) (in orange)

5.1. Convective storm case study

One of the most important applications of radar measurements lies in convective precipitation—either delineating its structure (Houze Jr et al., 1989; Pazmany et al., 2013; Wurman and Kosiba, 2013; French et al., 2015), or interpreting storm microphysical features (Ryzhkov and Zrnić, 1994; Cao et al., 2008; Kumjian et al., 2014; Homeyer and Kumjian, 2015), or tracking and nowcasting convective storms (Asai et al., 1977; Rosenfeld, 1987; Handwerker, 2002; Kyznarová and Novák, 2009; Hu et al., 2019; Fridlind et al., 2019), detecting the potential presence of hailstones (Hubbert et al., 1998; Kennedy et al., 2001; Matrosov et al., 2013; Vulpiani et al., 2015; Capozzi et al., 2018).

In general, convective precipitation is more variable in space than stratiform precipitation. The precipitation data, if their spatial resolution is too coarse, are unable to depict inner structures of the convective storms, or miss the intensity maximums, whereas the high-resolution precipitation data are able to present the large spatial variability of precipitation fields (Thorndahl et al., 2014). It implies that observing convective storms requires high-resolution precipitation measurements. In contrast, stratiform precipitation is relatively homogeneous, and its demand for spatial resolution is less. In other words, the benefits of the high-resolution precipitation can be seen most clearly when it comes to convective precipitation. To align with the aim of this research, the high resolution refers to the sub-kilometer resolution.

In order to illustrate such benefits, we focus on small-size and intense convective storms which are characterized with highly heterogeneous spatial distributions. Similar to Section 4.1, we also conduct visual inspections over radar images to examine the differences between fine and coarse scans in terms their presentation of convective storms in radar images of either single-polarization or polarimetric variables. Regarding Z_{H}, the C-band radar data at the 500-m radial resolution are also available. Thus, Z_{H} of the fine and coarse scan (250-m radial resolution) data, together with the C-band Z_{H} allow us to compare Z_{H} in three different spatial resolutions. For other radar variables, the comparisons are only done between fine and coarse scans. Utilizing the coincident and col-located radar measurements of different spatial resolutions, we discuss the differences in precipitation patterns from radar images, and the reasons accounting for these differences, to pinpoint the merits of using high-resolution radar measurements.

Three criteria for selecting convective storms for this case study are as follows. The C-band radar is about 65 km away from the X-band radar, a convective storm which is present in proximity to the C-band radar should be far away from the X-band radar. Given that radar measurements in the polar coordinate are highly range-dependent (Sections 2.1 and 4.9.2), for a single convective storm closer to either the X- or the C-band radar, the precipitation patterns described by C-band or X-band radar measurements should be quite different from each other. Thus, the first criterion is regarding the range of convective storms. To minimize the range effect on comparisons of radar datasets, we only consider the convective storms which are at the same distances to both C- and X-band radars.

The radar images we discuss here are in the form of PPI displays, and the second criterion is about elevation angles for the PPI displays. A PPI display of one radar sweep samples hydrometeors at a certain height above the ground rather than across the entire vertical extent. In order to minimize uncertainties caused by the vertical variability of convective storms, we should select the elevations of PPI displays to ensure that radar beams of both radars penetrate into the convective storm at the same altitude.

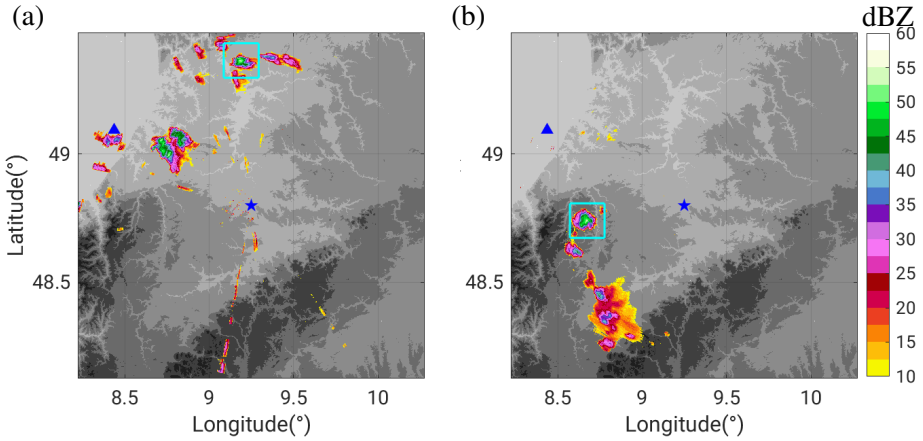

Fig. 5.2.: PPI displays at the 1.5° elevation using fine scans, where (a) is for a storm at 13:50–13:59 UTC on 7 July 2017, (b) is for a storm at 12:20–12:29 UTC on 9 July 2017, the dark blue triangle/star represents the location of the C- or X-band radar site, the unfilled square indicates the storm to be discussed in Section 5.1

Tab. 5.1.: Azimuthal direction of convective storms in Fig. 5.2 to the X-band radar (ϕ_a), distances of these convective storms to the X- and C-band radars (s_X and s_C), and heights of the selected radar beams of X- and C-band radars intersecting the centers of these convective storms ($H_{ASL,X}$ and $H_{ASL,C}$)

Storm	ϕ_a (°)	s_X (km)	s_C (km)	$H_{ASL,X}$ (km)	$H_{ASL,C}$ (km)
"N"	357	63	63	2.2	2.5
"W"	261	43	43	5	4.8

The third criterion is regarding the QC procedure. No attenuation correction is applied to the C-band radar data, and the attenuation at the C-band frequency is less severe than that of the X-band frequency due to different λs. In order to eliminate the effect of attenuation, we only consider the convective storms between which and both radars there was no precipitation (Fig. 5.2). Besides, in order to focus on the precipitation echoes from the convective storms, we also only consider convective storm free of the contaminations from either spike signals, second-trip echoes or non-meteorological echoes.

Among all these convective storms which satisfy all these three criteria, we select two storms at different azimuthal directions and ranges to both radars but in nearly the same size (Tab. 5.1). In the polar coordinate, the orientation of a radar gate depends on its azimuthal directions and the size of a radar

gate is affected by its range, so we expect patterns of the Z_H intensity and the Z_H-derived R change with the azimuthal direction and the range of the precipitation echoes to a radar. The first storm is 63 km away from and to the north of the X-band radar, while the second storm is 43 km away from and to the west of the X-band radar. Such different azimuthal directions and distances to the radar allow us to assess how ϕ_a and r affect the Z_H-derived R pattern, and the comparable size is to mitigate the potential impact of the storm size on this dependence of the Z_H-derived R pattern on ϕ_a and r. According to their azimuthal direction to the X-band radar, we designate the first and second storms as the storm "N" and the storm "W" respectively.

The storm "W" is only two days later than the storm "N", so the large-scale atmospheric circulation patterns did not change too much. During that 2-day period, two low pressure systems dominated the arctic region. For both storms, the relative humidity at the 700 hPa pressure level reached above 90%, and the air temperatures at 850 hPa were more than 16°C, with the prevailing westward and southwestward winds respectively, which provided the warm moist air to trigger the convective systems.

Regarding the PPI displays, because the PPI displays are made after converting the polar coordinate into the Cartesian coordinate, we see rectangular pixels in these PPI displays if we zoom in these radar images. Grid lines of the polar coordinate are added to demonstrate the sizes of single radar gates in the original polar coordinate for the fine and coarse scan datasets and the C-band radar dataset. Be aware that the size and shape of a radar gate in the polar coordinate are different from the rectangular pixel in the Cartesian coordinate. Due to small sizes of convective storms, the PPI displays presented below focus on the area of 15 km$\times$15 km around the convective storms instead of the entire radar coverage. We present the PPIs in terms of R calculated from Z after attenuation correction and Z_H calibration (a data QC procedure to be discussed in Section 5.2), and polarimetric radar variables.

For storm "N" (Fig. 5.2(a)), the fine scan provides us with the smoothest contours of Z_H-derived R in comparison to those of the other two radar datasets (Fig. 5.3(a)). These smooth contours in the fine scan data present a clear-cut Z_H-derived R gradient, a distinct indicator of a complete internal structure of the convective storm, along with a clear illustration of localized heterogeneity within very small areas. In contrast, the coarse scan presents the slightly rugged contours which indicate a choppy structure of this storm, and is unable to present the very tiny areal heterogeneity (Fig. 5.3(c)) as the fine scan. From the C-band radar data, we can only infer the approximate location of the storm center according to these much more rugged contours, and the shape or the structure of the storm is even more ambiguous (Fig. 5.3(e)). Thus, via the comparison of the radar images from these three radar datasets, this example clearly illustrates three different levels of clarity in terms of presenting inner structures of convective storms on the basis of the Z_H-derived R at three different resolutions. Obviously, the fine scan data which at the highest spatial resolution is able to present precipitation pattern most clearly, which is the benefit of high-resolution radar data.

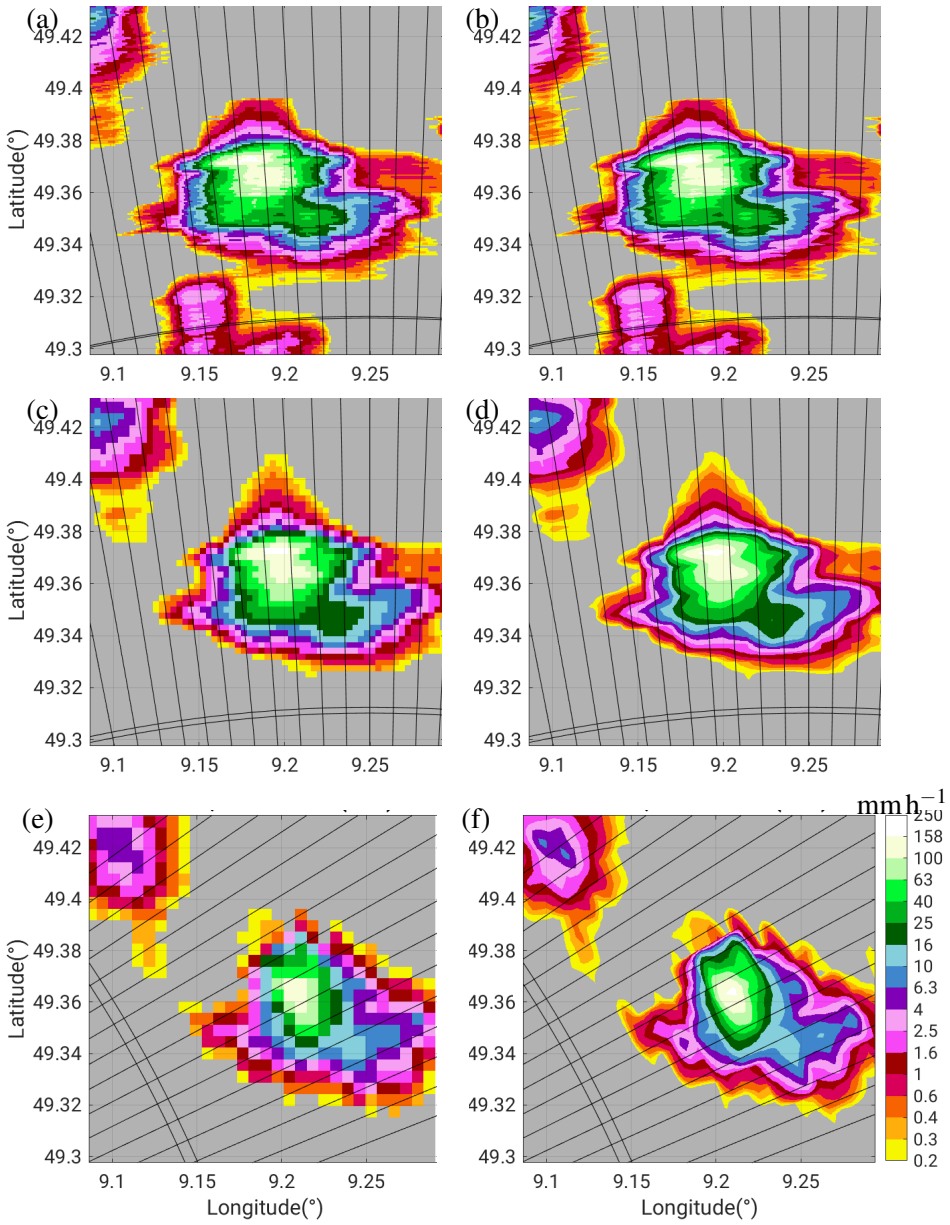

Fig. 5.3.: Zoomed-in parts of PPI displays of the convective storm "N" marked in Fig. 5.2(a) to compare the Z_H-derived R between the X- and C-band radar data, where (a) is for the 75-m resolution fine scan, (b) for the 25-m interpolation of the 75-m resolution fine scan, (c) for the 250-m resolution coarse scan, (d) for the 25-m interpolation on the 250-m resolution coarse scan, (e) for the 500-m resolution C-band radar and (f) for the 25-m interpolation on the 500-m resolution C-band radar data, (a)–(d) are at 1.5° elevation for the X-band radar volume scan, (f) and (e) are at the 1.1° elevation for the C-band radar volume scan, the black straight lines and curves are the grid lines of the polar coordinate (including only two azimuthal grid lines for a neat visualization and also to show the sizes of single radar gates for the 75-m, 250-m and 500-m radial resolution radar data)

The smoothness in the fine scan data (Fig. 5.3(a)) is unnaturally oriented along the azimuthal direction. This unnatural feature is attributed to the intrinsic feature of the polar coordinate of the original radar measurements. Θ for all three radar datasets is 1°, so $r\Theta$ is roughly 1.1 km at the 63-km range, which is much larger than Δr of the fine scan. The ratios of $r\Theta$ to Δr, symbolled as κ, are 0.07, 0.25

and 0.5 for the fine or coarse scans or the C-band radar data respectively. The shape of a radar gate is a line oriented along the concentric circles for fine scans, an elongated rectangle for coarse scans, and a short rectangle for C-band radar data (the intersecting black lines in Figs. 5.3(a), 5.3(c) and 5.3(e)). The different κ reflects a limitation of achieving high spatial resolution by increasing Δr only but keeping Θ unchanged. This imbalance in $r\Theta$ and Δr of radar gates lessens the benefits of using radar data at high-spatial resolutions.

To study the effect of spatial resolutions, other research interpolated their radar datasets which are measured at a single spatial resolution into the interpolated radar datasets at various spatial resolutions (Chapter 1). In contrast, this research uses the radar datasets which are already measured at spatial resolutions and do not need interpolations. Thus, our results emphasize the pure characteristics of increasing the 'measured' spatial resolution rather than the 'interpolated artificial' spatial resolution. However, we are curious about the effect of the interpolation, and interpolate all the three radar datasets into the 25-m spatial resolution (the right column in Fig. 5.3). Then we compare the radar datasets of the same spatial resolution—the fine scan data, the interpolated coarse scan and the interpolated C-band radar data. The Z_{H}-derived R contours of the interpolated coarse scan data and C-band radar data become smooth (Figs. 5.3(d) and 5.3(f)). When comparing the interpolated fine and coarse scans (Figs. 5.3(b) and 5.3(d)), we notice R in the southeastern corner of the storm center is lower in the coarse scan ($10\,\mathrm{mm\,h^{-1}}$ or equivalent to roughly 40 dBZ) than that in the fine scan ($25\,\mathrm{mm\,h^{-1}}$ or equivalent to roughly 45 dBZ). According to the subsequent PPI displays (not shown), this storm moves eastward and decays rapidly. It seems that the less intense Z_{H}-derived R in the southeastern corner of the storm center is due to the evolution of the storm during the 100-second time gap between 13:53 UTC and 13:54 UTC. For the C-band radar, this interpolation smooths the Z_{H}-derived R contours considerably, as illustrated by the contrast between Figs. 5.3(e) and 5.3(f). The shape of the storm center in the interpolated C-band radar data appears as an oval, which differs from the irregular shapes of storms shown in the X-band radar data either fine and coarse scans. This discrepancy may attribute to the coarse resolution of the original C-band radar measurements. The difference in R intensity between the C- and X-band radars might be due to the miscalibration of either or both C-band and X-band radar data, or the attenuation caused by weak precipitation lying in the southern direction of this convective storm. Above all, we may conclude that, in spite of the interpolation in the same 25-m spatial resolution, the effect of the high 'measured' spatial resolution on the visualization is still obvious, interpolation (downscaling) can render the Z_{H}-derived R contour smooth but the small spatial heterogeneity cannot be created or reproduced.

Despite the same range, this storm is to the north of the X-band radar but to the northeast of the C-band radar, so the relative positions of this storm to the C- and X-band radars are different. In order to assess the effect of this relative location on comparisons of radar images, we inspect the storm "W" which was situated 42 km away to the west of the X-band radar and to the southeast of the C-band radar (Fig. 5.2(b)). As mentioned, the storm "W" is in the same size as the storm "N"; the encircled areas of

the 16 mm h^{-1} R contours of both storms are comparable. In comparison to the storm "N", the storm "W" gets closer to both radars (only 43 km away), along with κ of the individual radar gates to be 1/10, 1/3, 2/3 for the fine scan, the coarse scan and the C-band radar data; these ratios are less contrasting than those of the storm "N".

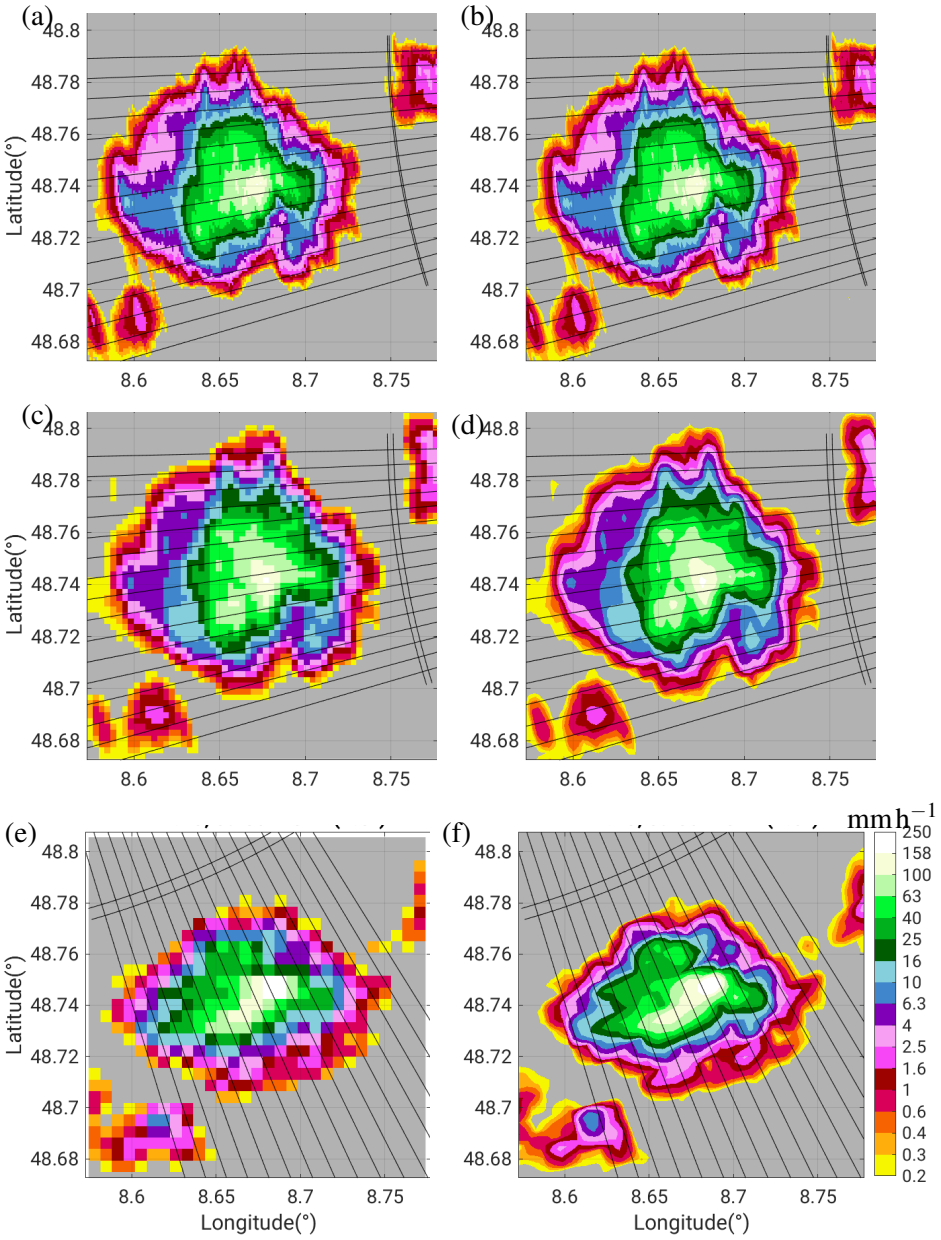

Fig. 5.4.: The same as Fig. 5.3, but for the storm "W" shown in Fig. 5.2(b), (a) to (d) are at 6.2° elevation for the X-band radar volume scan, (f) and (e) are at the 4.5° elevation for the C-band radar volume scan

Similar to the storm "N", before interpolation, the contours of the Z_H-derived R pattern become more wrinkled as the radial resolution decreases from 75 m to 500 m (the left column in Fig. 5.4). The 25-m interpolation makes the structure of the storm center in the interpolated coarse scan data resemble much that in the fine scan data (Figs. 5.4(b) and 5.4(d)). Accordingly, we may state that the necessity

of increasing the measured spatial resolution may be reduced, since the benefits of higher measured spatial resolution might be partially achieved through interpolation. However, there is a clear discrepancy in the shapes of the storm internal structure presented by the X- and C-band radar data. In the C-band radar data, the distance of storm's north-and-south side is shorter while the distance of storm's east-and-west side is wider (Figs. 5.4(e) and 5.4(f)). This discrepancy may be caused by the relative direction of the storm to both radars.

Then we discuss the polarimetric data. For both storms, the area with measurable Z_{DR} is larger in the coarse scan, with a portion of measurable Z_{DR} outside of the 20-dB contours (Fig. 5.5), in accord with the discussion in Section 4.1.1 that the weak echoes are lost in fine scans but remain in coarse scans. Similar to the Z_H-derived R contours, the contours of the measured Z_{DR} in the fine scan data consist of the short lines orienting along the azimuthal direction, bringing the azimuth-oriented higher spatial variability of Z_{DR}. For the storm "N", one difference between the fine and coarse scan is the presence of Z_{DR} over 8 dB at the farther side of the storm presented by the coarse scan and the absence of such a region in the fine scan data (Figs. 5.5(a) and 5.5(b)). This discrepancy may be due to the combination effect of the severe attenuation and losses of weak echoes in the fine scan (Section 4.6 and Fig. 4.37). For both storms, the square or rectangular pixels are easily seen in the coarse scans, but not in the fine scans; instead, the single radar gate in the fine scans is a shape of a narrow line (Figs. 5.5(c) and 5.5(d)).

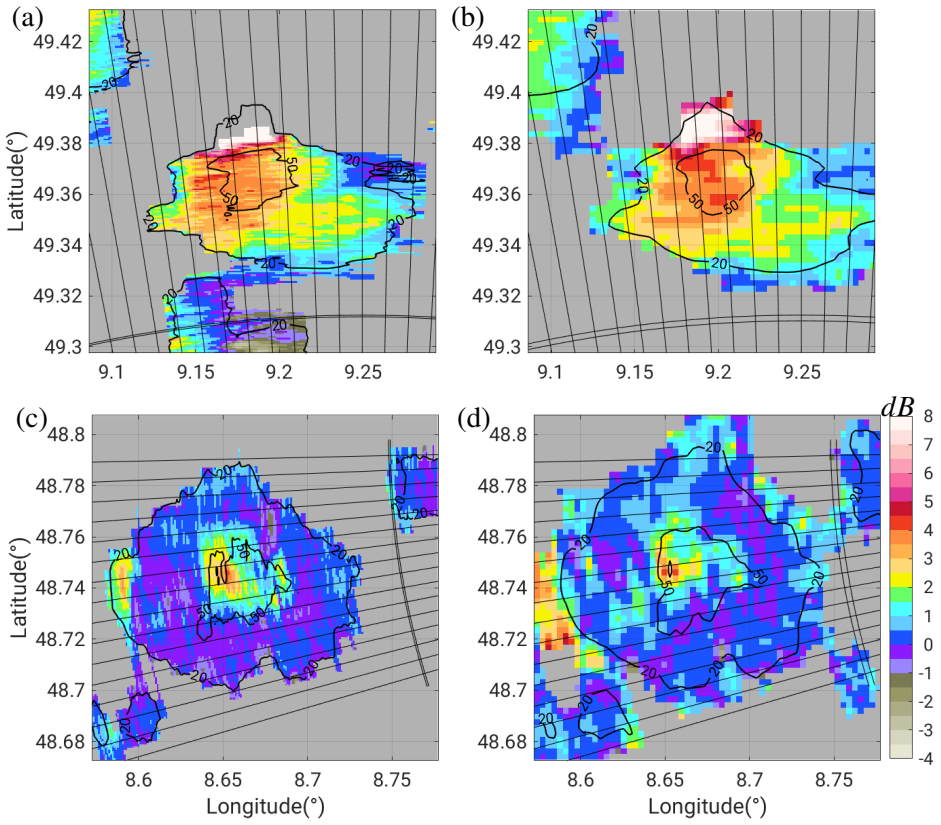

Fig. 5.5.: Zoomed-in parts of PPI displays of Z_{DR} ((a) and (b)) for the storm "N" in Fig. 5.2(a), ((c) and (d)) for the storm "W" in Fig. 5.2(b), (a) and (c) for the fine scan data, (b) and (d) for the coarse scan data, where the black contours represent the Z_H contours in 20 and 50 dBZ

Although the Z_H-derived R patterns of both storms resemble each other well (Figs. 5.3(a) and 5.4(a)), it is not the case for the Z_{DR} patterns (Fig.5.5). The majority of the storm "N" is characterized by positive Z_{DR} exceeding up to 5 dB, while the center of the storm "W" presents Z_{DR} over 4 dB and is surrounded by an extensive area of the near zero Z_{DR}. The vertical heights may explain such a discrepancy, given that the center of the storm "N" intercepted by the 1.5° elevation radar beams is at an altitude of 2.5 km above the sea level in contrast to the 5-km altitude for the storm "W". We can infer that, the raindrops at lower levels are big oblate drops which are characterized by large positive Z_{DR}, while the hydrometeors at higher altitudes may be smaller in size and also tumble around with quite random canting angles, because of the existence of the strong updraft within the storm center.

For u-ϕ_{DP}, the difference between fine and coarse scans is not that apparent (Fig. 5.6) since the differential phase is a parameter, integrating over the radar range, increasing with the range and should not be subject to the radial resolution.

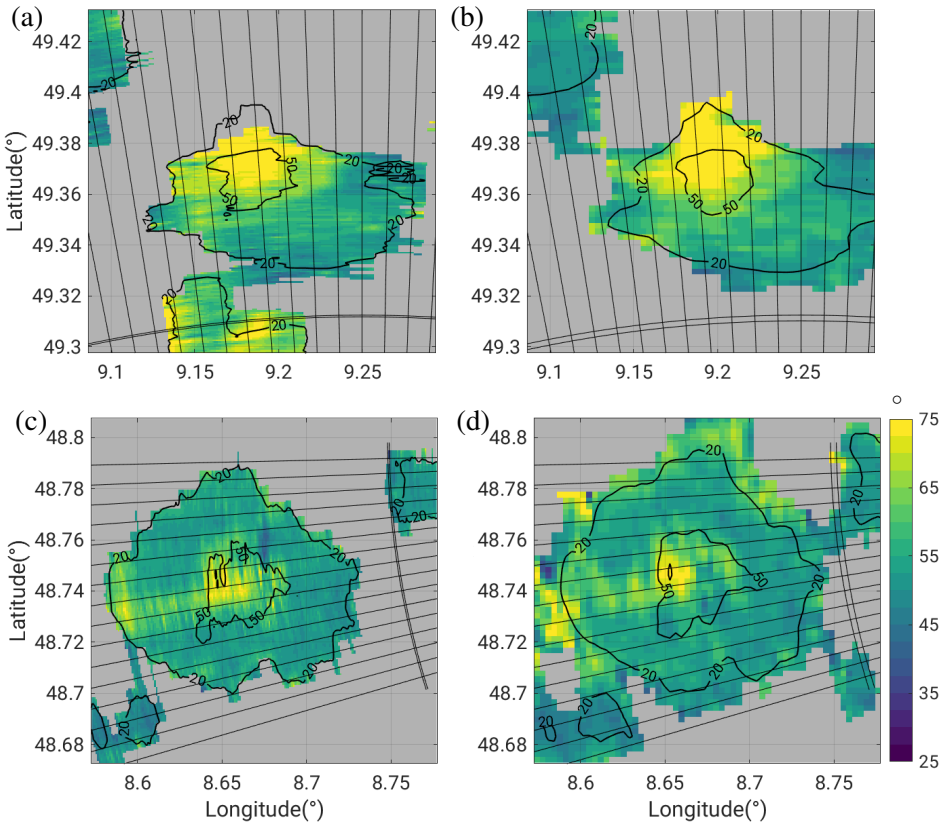

Fig. 5.6.: The same as Fig. 5.5, but for u-ϕ_{DP}

Besides Z_H-derived R, K_{DP} is also quantitatively related to R (Section 2.3). For the storm "N", the precipitation patterns delineated by K_{DP} of the fine and coarse scan data are different (Figs. 5.7(a) and 5.7(b)), although their spatial distribution of the Z_H-derived R is quite comparable (Figs. 5.3(a) and 5.3(c)). The area with K_{DP} larger than $2^\circ\,\mathrm{km}^{-1}$ is an oval oriented in west-east direction for the fine scan, but in the north-south direction for the coarse scan. The area with K_{DP} greater than $3.5^\circ\,\mathrm{km}^{-1}$ in the fine scan is more extensive than that of the coarse scan, but K_{DP} of the coarse scan exceeds $4^\circ\,\mathrm{km}^{-1}$. It seems that the high K_{DP} values in the fine scan 'dilute' into a larger area in the coarse scan.

For the storm "W", the storm center is surrounded by negative or near-zero K_{DP} either from the fine or coarse scan data, and the negative K_{DP} is more apparent and extensive in the fine scan data (Figs. 5.7(c) and 5.7(d)). K_{DP} in the storm center is less than $2^\circ\,km^{-1}$ for the coarse scan, but surpasses $4^\circ\,km^{-1}$ for the fine scan. Besides, in the farther end of the storm (western of the storm), the fine scan data exhibits a secondary weak maximum which is absent in the coarse scan. In general, the spatial distribution of K_{DP} magnitude presented by the fine scan is more heterogeneous. These noticeable differences between fine and coarse scans contradicts the resemblance in the Z_H-derived R patterns for fine and coarse scan data (Figs. 5.4(a) and 5.4(c)).

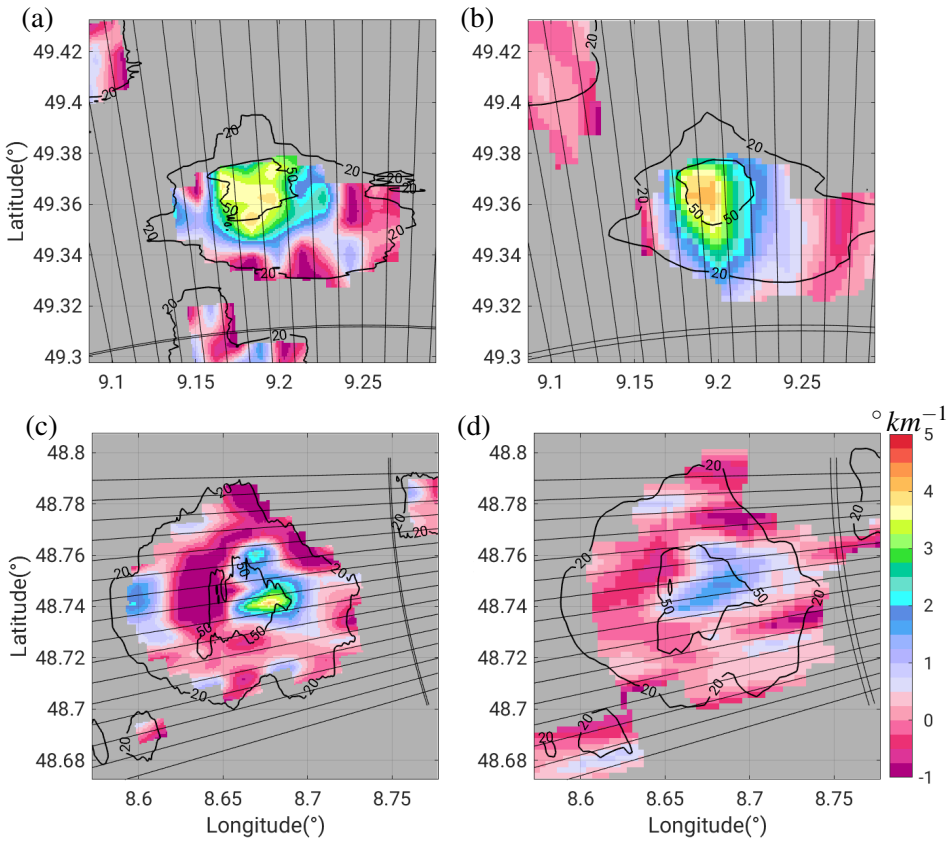

Fig. 5.7.: The same as Fig. 5.5, but for K_{DP}

These differences in K_{DP} values may be attributable to the K_{DP} retrieval algorithm. As we mentioned, the K_{DP} data we use in this research do not undergo the iterative FIR filtering, and thus are frequently contaminated by the backscatter phase. Especially in the convective storms, the existence of large raindrops leads to substantial backscatter phases, and neglecting these large backscatter phases brings about the uncorrected K_{DP} retrievals. We infer the contamination of backscatter is more pronounced for the fine scan data. This comparison in terms of K_{DP} between fine and coarse scan data proves that the difference at the radial resolution of radar measurements can propagate into the K_{DP} retrieval procedure, and we need recommended to adjust the K_{DP} retrieval algorithm setting according to the radial resolutions.

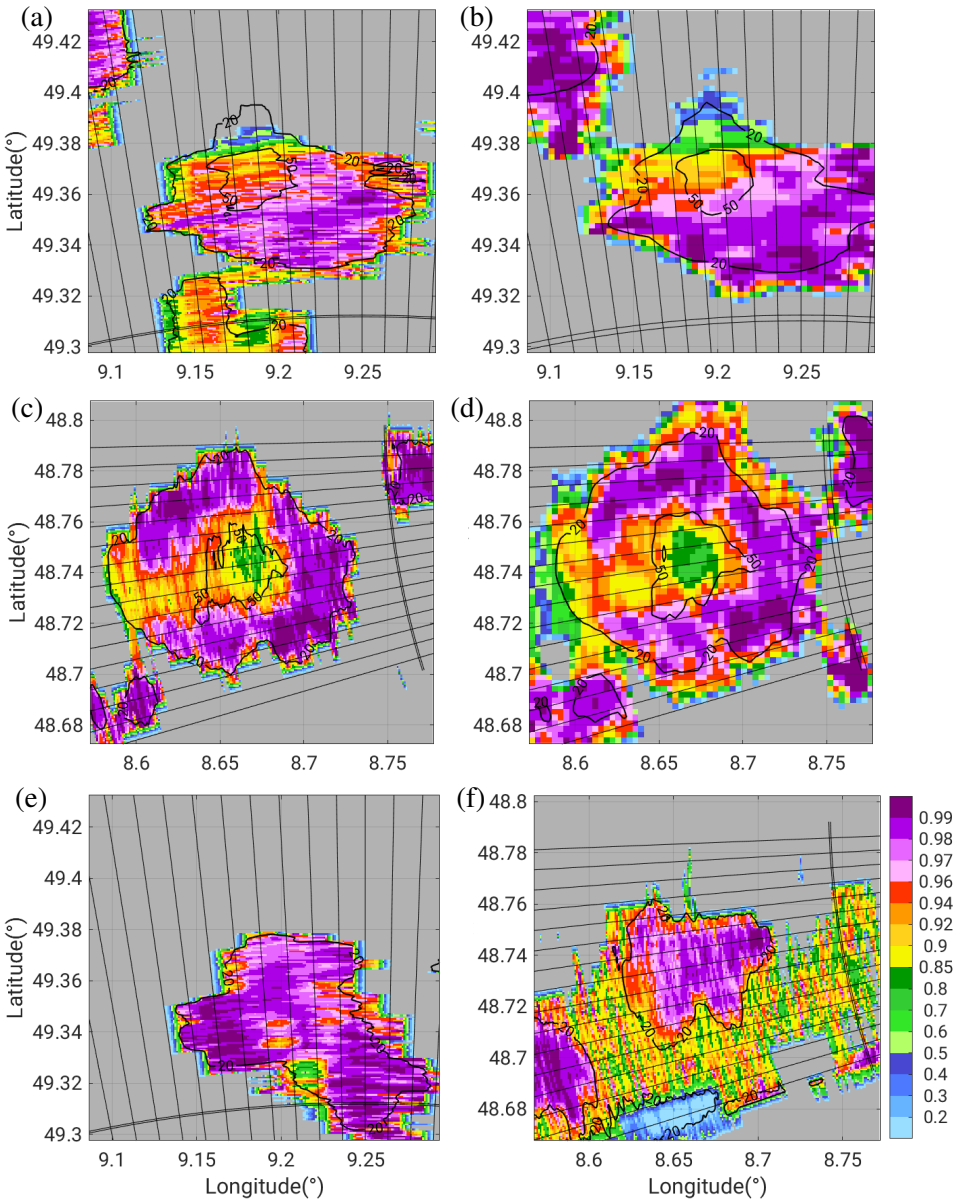

Fig. 5.8.: The first four panels are the same as Fig. 5.5, but for ρ_{HV}, and (e) is for the PPI display at 6.2° elevation at 13:53 UTC on 7 July 2017, and (f) is for the PPI display at 1.5° elevation at 12:53 UTC on 9 July 2017

In accord with the Z_H-derived R pattern, the spatial distribution of ρ_{HV} in the fine scan is characterized by short lines owing to the large contrast between the widths and lengths of radar gates, whereas the coarse scan presents ρ_{HV} in a more uniform spatial distribution due to its smaller κ (Fig. 5.8). Similar to the Z_{DR} pattern, the area with valid ρ_{HV} values expands wider in the coarse scans than that of the fine scans, since the fine scans tend to lose weak echoes which are kept in the coarse scans. Besides, for either the storm "N" or the storm "W", either the fine or coarse scan, the edge of the storm is characterized by a thin outer skin (a few pixels wide) characterized by very low SQI values (less than 0.5). It attributes to the decaying of precipitation echoes between the non-rainy space and precipitation systems. For the storm "N", as the range of the radar gates increases, the magnitude of ρ_{HV} decreases

from above 0.98 in the front side of the storm to less than 0.8 in the rear side of the storm (Figs. 5.8(a) and 5.8(b)).

For the storm "W", the ρ_{HV} valley with ρ_{HV} values as low as 0.7, is surrounded by a hook-shaped area of high ρ_{HV} with a dent in the farther side (in the western) of the storm. Since the vertical heights of the centers of both storms are different, we also inspect the PPI display at the 6.2° elevation for the storm "N" (Fig. 5.8(e)), and the PPI display at 1.5° elevation for the storm "W" (Fig. 5.8(f)). For the storm "N", the altitude of sampling volumes at the 6.2° elevation is around 7.3 km ; for the storm "W", the altitude of sampling volumes at the 6.2° elevation is around 1.5 km. The upper part of the storm "N" does exhibit a very small ρ_{HV} valley, but the hook-shape structure is absent. The low-level structure of the storm "W" is characterized by a high ρ_{HV} uniform center surrounded with relatively lower ρ_{HV} values. In brief, the difference between the fine and coarse scan is not noticeable in terms of ρ_{HV}, and interpolation can be easily implemented since ρ_{HV} is on a linear scale.

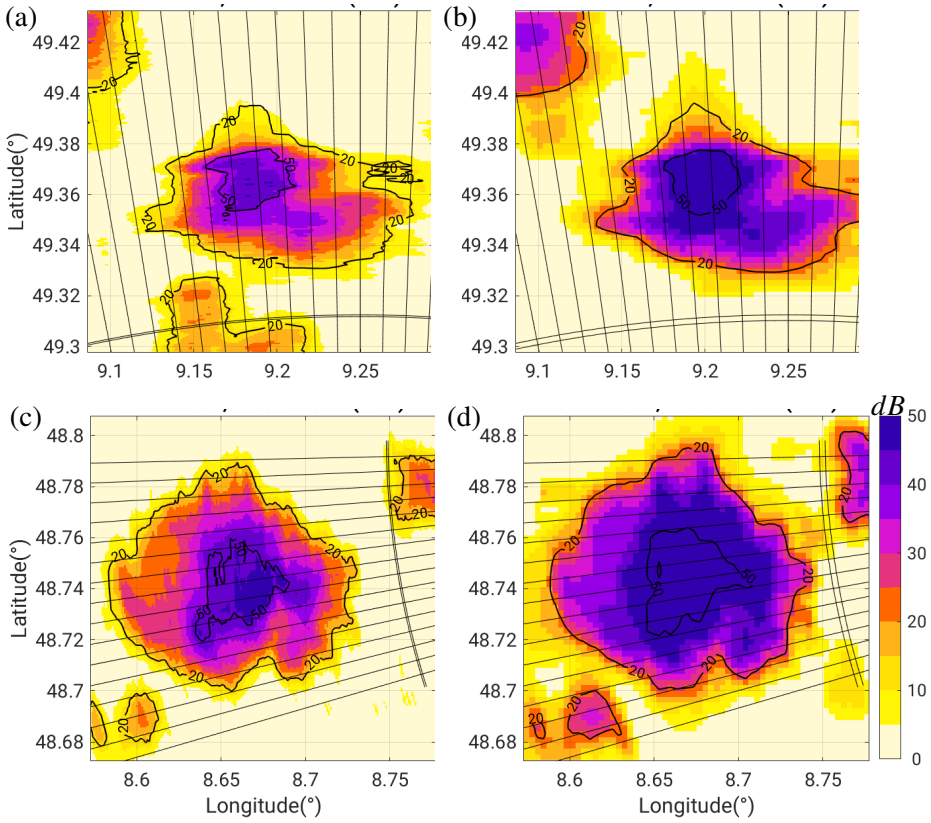

Fig. 5.9.: The same as Fig. 5.5, but for SNR

The SNR contours of the fine and coarse scans are quite similar in terms of shapes but not intensity. Indicated by the shrunk contours, the storm in the fine scan data exhibits smaller SNR than its counterparts in the coarse scan (Fig. 5.9). This difference corresponds to the reduction of weak echoes in fine scans, as we discussed in Section 4.1.

The SQI data exhibit a remarkable discrepancy between the fine and coarse scans (Fig. 5.10). The fine scan data demonstrate a distinct separation of rainy and non-rainy areas indicated by the SQI values; the storm is clearly delineated by SQI larger than 0.65, and the area without precipitation is characterized by SQI between 0.0 and 0.4. In contrast, SQI of precipitation echoes is as low as SQI of the non-precipitation echoes. This vagueness in magnitude of SQI in the coarse scan is associated with the extremely small maximum Nyquist velocity, and it substantiates our use of SQI for the fine scan data but neglect of SQI for the coarse scan data in the previous data QC procedure (Sections 4.2 and 4.3).

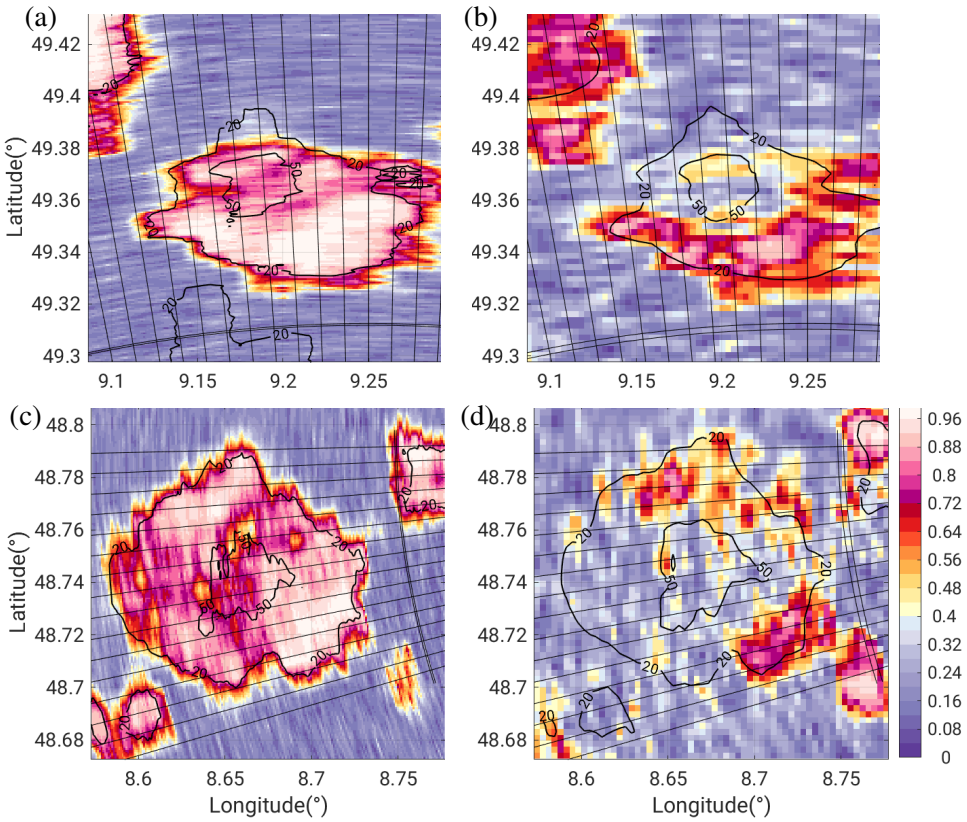

Fig. 5.10.: The same as Fig. 5.5, but for SQI

By means of the foregoing radar images, we compare the radar datasets at different spatial resolutions for two selected convective storms. Both storms are at the comparable distances to both C- and X-band radars, and have similar sizes, although measured during different rainy episodes. Similar comparisons have been conducted for a number of convective storms (not shown), the results are also similar to the case study of these two storms.

Our aforementioned discussion deciphers the differences between radar data at different spatial resolutions. However, these differences might be caused by other reasons, not only the effect of radial resolutions on radar measurements. For each comparision, the fine scan is 100 seconds ahead of the coarse scan, and the C-band radar is 1 minute later than the coarse scan (2.5 minutes later than the

fine scan). The time gaps at such lengths are short and can be ignored for the majority of stratiform precipitation, but could be long and cannot be ignored for convective storms. The lifetime of convective storm varies from half of an hour to 1-2 hours, and can be even as short as 20 minutes for small-size and intense convective storms, such as the two convective storms in our foregoing case study. Convective storms evolves and moves continuously. During the time gaps between the measuring time of these radar datasets, the intensity and morphology of the convective storms are much likely to change, and such changes should be more apparent for the small convective storms which usually develop more rapidly and move faster than other large convective storms. Therefore, in our previous case study, precipitation patterns measured by a fine scan and its successive coarse scan should be different in terms of magnitude of these radar variables, which is reflected as the altered shape of contours of the radar variables. To determine which factor takes the main role is on the case-by-case basis.

In other words, the different storm intensity between the fine and coarse scans illustrated by these radar images can be caused either by using different radial resolutions for radar measurements, or by the dynamic evolution of convective storms during the time gap between measuring time of different radar datasets, or a combination of both factors. Although we are only interested in the effect of radial resolution, we are unable to separate the effect of storm evolution, especially if we are to interpret the different shapes of contours of radar variables between the fine and coarse scans. Fortunately, the different smoothness presented by the fine and coarse scans are not affected by the factor of storm evolution. Thus, the difference we can confirm from our foregoing comparison is that the fine scan data can present clearer structures with smooth contours and sharp gradients, and are able to pick up a few rainfall extremes that were smoothed out by the coarser radar measurement (Paz et al., 2018).

Regarding the difference between the storms presented by the C- and X-band radars, the heights of the storm center sampled by the C- and X-band radar beams are also not identical. Although we try to select the radar elevations in order to minimize this difference in altitude, the intersection points of the X-band radar beams can still be 300 to 400 m higher or lower than that of the C-band radar beams (Table 5.1). Given the larger vertical variability of convective precipitation, this displacement in the vertical direction serves as another factor contributing to differences in the foregoing comparison of convective storms presented by C- and X-band radars.

Each convective storm in nature evolves and moves continuously, and no two storms are the same. Case studies of individual convective storms via the fine /coarse scan and C-band radar datasets are not an easy job. This large temporal and vertical variability of convective storms adds difficulty or introduces disturbances when we compare these three radar datasets. The time gaps of the measuring time points and different heights inhibits the direct comparisons across these datasets. The reason to mention the unfavorable factors in our comparison is to render our discussion critical. We acknowledge such uncertainties are unavoidable, but the foregoing comparison of two convective storms at three

spatial resolutions still shows the characteristics and merits of using the higher-resolution radar data in improving our understanding of convective precipitation.

5.2. Evaluation of radar data using independent references

Until now the data analyses are constrained to the X-band radar data. For a comprehensive assessment of the accuracy and reliability of our radar measurements, the external precipitation information is needed. Besides, the absolute calibration of radar measurements also requires the external data as references. In fact, precipitation measurements from other instruments are available; a number of DWD rain gauges (Section 3.2.3) and an MRR (Section 3.2.2) were also operated simultaneously during our X-band radar measuring period and within the X-band radar coverage. Both can be the alternative sources of precipitation information serving as a reference to evaluate the X-band radar data and perform the absolute calibration.

Rain gauges and the MRR measure precipitation from different perspectives. Both types of instruments are necessary, and their individual comparisons to the X-band radar data are not duplicate tasks. Rain gauges, located near the ground surface and spatially distributed within the radar coverage, are used for areal comparisons, whereas the vertical-looking MRR is used for comparing the data along vertical directions. A rain gauge measures the water amount (volume or weight) falling into a small-area aperture within a certain period of time, whereas the MRR essentially utilizes the Doppler frequency of microwave signals. Given that rain gauges and MRR have different measuring methodologies, their respective comparisons with C- and X-band can provide different perspectives to evaluate our radar data.

Thus, we compare the X-band radar data with independent precipitation measurements from the local rain gauge network and MRR, respectively. This comparison aims to quantitatively assess the agreement between the X-band radar measurements and precipitation measurements from other independent instruments, and then we use this agreement to assess the accuracy and reliability of our X-band radar measurements in terms of QPE.

Besides, the outcome of comparisons can be used for the Z_{H} calibration. The radar system consists of many different mechanical or electronic components and each of them might make its contribution to the systematic errors of the entire radar system, which leads to an overall deviation of the Z_{H} magnitude. This deviation is named as Z_{H} *calibration factor* (ΔZ). Usually a weather radar system in operation should be calibrated regularly in an attempt to minimize ΔZ to be within 1 dB for the acceptable error for the QPE. ΔZ can be either positive or negative in principle. The approaches to determine this ΔZ include comparisons with targets of known backscattering cross sections like corner reflectors or spheres suspended from balloons or aircraft, or comparisons with disdrometer measurements (Atlas, 2002; van den Heuvel et al., 2018a). The common approach which has been used widely over decades

is to compare with rain gauge measurements which are easily available in most cases (Wilson, 1970; Brandes, 1975; Ninomiya and Akiyama, 1978; Collier, 1986; Wood et al., 2000). ΔZ is calculated as the average ratio of rain gauge-observed and radar data-estimated precipitation quantities at a number of rain gauges without taking the spatial variation into account. According to the Marshall-Palmer Z-R relation,

$$10^{(Z+\Delta Z)/10} = 200 R_{\mathrm{G}}^{1.6}, \tag{5.1}$$

where Z is the measured radar reflectivity, R_{G} is the precipitation rate measured by rain gauges. Thus,

$$\Delta Z = 10(\log_{10} 200 + 1.6 \log_{10}(R_{\mathrm{G}})) - Z \tag{5.2}$$

A synonym for this procedure is named as the radar-gauge adjustment.

In our case, the X-band radar was calibrated by professionals from the manufacturer before being transported to measuring sites. Right before and during the measuring period, we utilized the solar information to calibrate the potential deviation in the receiver. However, according to past experience and similar to others' radar experiments, those actions were not sufficient, and the chances are that the magnitude of $\Delta Z \neq 0 dB$. Since precipitation measurements from rain gauge network, an MRR and a C-band radar are also available, we compared the Z_{H} measurements with external references to see how much the radar-based precipitation estimates deviated from the external references. The quantitative deviation obtained from the comparison between radar data and the external references can be used to determine ΔZ quantitatively (Eq. 5.2).

5.2.1. Radar-Gauge comparison

The concept of Radar-Gauge (R-G) comparison is introduced after discussing advantages and drawbacks of weather radars and rain gauges. Regarding the data used in R-G comparison, we select the rain gauges, and use different versions of radar datasets processed with different combinations of the radar data QC procedures. Then we describe the procedure which geographically matches up rain gauges and radar gates, and this procedure produces a coincident and col-located R-G dataset. The statistics showing the R-G agreements (correlation and concordance) and for Z_{H} calibration are described, followed by the results of the R-G comparisons performed in terms of three temporal scales.

Pros and cons of rain gauges and weather radars

The rain gauge was the first tool that probed the rain and snow over the centuries before the appearances of remote sensing instruments. It is still one of the fundamental instruments in a standard meteorological or hydrological in-situ observation station. Precipitation measurements from rain gauges have been

widely used across either the hydrological or meteorologic community, for the purpose of weather monitoring, severe weather surveillance and flooding event alerts. The routine use of rain gauges implies their widespread data availability and consistency with historic records. The long history of rain gauges implies the potential to access a long-term record of precipitation for climatology studies. Besides, the rain gauge measurement is intuitive, despite the fact that its working principle evolves with adverts of new technologies and that numerous types of rain gauges have existed up to now. However, the drawbacks of rain gauges are also well-known, one of which is its inability to represent the spatial distribution of precipitation. A rain gauge only measures the precipitation falling into its small valid area, usually around $0.02\,\mathrm{m}^2$, and is unable to tell us precipitation information in the space between any two rain gauges. Accordingly, this way a rain gauge collects the rainfall information is referred as 'point' measurement. Interpolation through the rain gauge measurements at the isolated individual points may be accepted for the large-scale stratiform precipitation which is supposedly more spatially uniform. However, in most cases, precipitation is characterized by high spatial variability, which cannot be resolved by rain gauge measurements from scattered points. Even for a dense rain gauge network, chances are these rain gauges fail to capture the small-scale precipitation systems which just pass through the space between two rain gauges, particularly for the isolated or scattered convective storms. What is worse, the majority of the rain gauge networks in reality are sparse, worsening the spatial representativeness of the rain gauge measurements.

In contrast, a weather radar is able to measure all the precipitation falling into its coverage whose areal extent can be up to on the order of $100\,\mathrm{km}^2$. Unlike the point measurements of rain gauges, the radar provides areal measurements. A single radar can provide a complete description of precipitation over a reasonably large region, which exactly compensates for the drawback of rain gauge measurements. Since both instruments can supplement each other, the national weather services in many countries across the world have already adapted the joint use of rain gauges and ground-based weather radars, in order to achieve a more comprehensive observation of the precipitation spatiotemporal distribution, such as the s Radar-Online-Aneichung (RADOLAN) dataset provided by DWD (Bartels et al., 2004a; Weigl and Winterrath, 2009).

Nevertheless, the radar observation of precipitation also has its demerits. As mentioned, what a radar physically measures is EM signals rather than rain or snow, and the conversion of EM signals to the precipitation information is indirect and undergoes several idealized hypotheses which are not always valid in reality. Deviations from these hypotheses bring about uncertainties and errors to the radar-based precipitation estimation, even under the idealized circumstance that all the radar measurements are accurate without systematic errors. The typical sources of error and uncertainty in estimating the surface rainfall (Austin, 1987) have been reviewed in several papers by the researchers either from the meteorology and hydrology community. In addition to a short summary presented in Tab. 5.2, in my

viewpoint, the two most typical sources of errors are nonlinearity in Z-R relation and uneven sampling volumes (Vivekanandan et al., 2003).

Tab. 5.2.: A variety of errors associated with radar-based precipitation estimation (Legates, 2000)

Regarding reflectivity measurement	
1. Ground clutter contamination	overestimate
2. Anomalous propagation	overestimate
3. Partial beam blockage	underestimate
4. Attenuation during propagation	underestimate
5. Wet radome attenuation	underestimate
6. Incorrect hardware calibration	over/under-estimate
Regarding rainfall estimator	
1. Variation in drop size distribution	over/under-estimate
2. Solid or mixed phase hydrometeors	overestimate
3. Drop falling velocity	over/under-estimate
Regarding below beam effect	
1. horizontal wind drift	over/under-estimate
2. Evaporation of falling drops	overestimate
3. Coalescence below the radar beam	underestimate

In contrast to the aforementioned complexity in using radar data in the precipitation estimation, the rain gauge measurement is straightforward, and easy to understand and interpret, especially for the users without specific training to understand the radar data. Together with other merits of rain gauges just discussed above (the widespread data availability, long-term records, etc.), the precipitation measurements from rain gauges have been routinely regarded as a benchmark, and used as a reference to calibrate other precipitation instruments such as precipitation satellites, passive radiometers, and ground-based weather radars. In an objective and precise sense, each instrument has its own merits and demerits. The true precipitation information exists in nature, but none of these instruments alone is able to probe it in a strict sense, which is limited by the measuring methodology of each instrument.

Introducing R-G comparison

For the weather radar community, especially in the operational weather/hydrology service sectors, there is a longterm convention of using the rain gauge measurements to evaluate and calibrate the radar data. The early work dates back to Zawadzki (1975); Wilson and Brandes (1979). In spite of other available methods for the Z calibration (Williams et al., 2013; van den Heuvel et al., 2018b), the calibration through the comparison between radar data and rain gauge measurements is still widely used. Although we

acknowledge neither the rain gauge nor the weather radar alone can be an idealized instrument, we follow this convention by comparing the precipitation estimates derived from radar data with rain gauge measurements. This procedure is named after the R-G comparison, and the rest of this section focuses on this R-G comparison. To clarify, holding a scrupulous attitude, we refer to the procedure of comparing the radar-based precipitation estimates and rain gauge precipitation measurements as *evaluation* rather than validation, and regard rainfall information from rain gauges as a *reference* rather than the 'truth'.

The radar-based precipitation quantities are calculated through non-linear empirical relations—precipitation estimators (Section 2.3). We calculate the precipitation intensity/rate in unit of $\mathrm{mm\,h^{-1}}$ using the Marshall-Palmer Z-R relation $Z = 200R^{1.6}$ whose non-linearity introduces an issue about intensity resolution (Einfalt et al., 2004). For instance, for light rain with Z at 10 dBZ, the disturbance of 0.5 dBZ causes the deviation of 0.01 $\mathrm{mm\,h^{-1}}$ ($0.154 - 0.143 = 0.011\,\mathrm{mm\,h^{-1}}$ and $0.165 - 0.154 = 0.011\,\mathrm{mm\,h^{-1}}$). Similarly, the deviations caused by disturbance of 0.5 dBZ are on the order of 0.2 $\mathrm{mm\,h^{-1}}$ and 3.5 $\mathrm{mm\,h^{-1}}$ for the moderate (30 dBZ) and heavy (50 dBZ) rain, respectively. Due to the nonlinear relationship between Z and precipitation intensity, the intensity resolution increases significantly when Z changes from low to high intensity. The higher Z is, the less accurate the radar-based precipitation estimate is. It also implies, averaging Z at various intensities introduces a bias, and this bias increases with inhomogeneity of the Z field. Because the R-G comparison requires conversion between Z and R through non-linear reflectivity to rainfall relationship or equation (Z-R) relations, the intensity resolution is a potential source of errors in the R-G comparison.

Tab. 5.3.: Precipitation intensity estimated from the Marshall-Palmer relations

Z (dBZ)	9.5	10	10.5	29.5	30	30.5	49.5	50	50.5
R ($\mathrm{mm\,h^{-1}}$)	0.143	0.154	0.165	2.54	2.73	2.94	45.2	48.6	52.3

The sources of error and uncertainty in the R-G comparison can be classified into three scatologies, unique to the radar, or unique to the rain gauges, or shared by both radars and gauges. Regarding the radar data, besides the intensity resolution discussed above, the sources of errors lie in the radar-based precipitation estimation which is limited by lack of a unique transformation from Z to R, hardware calibration problems, and contamination by ground clutter, partial beam occlusion, or vertical variation of precipitation (Anagnostou et al., 2004). Besides measurements errors (Section 3.2.3), the sampling errors of rain gauges have been discussed by previous literature (Morrissey et al., 1995; Steiner, 1996; Nystuen, 1998; Villarini et al., 2008). Meanwhile, radar measurements are also affected by the sampling errors, both temporal and spatial (Fabry et al., 1994; Villarini et al., 2008; Cristiano et al., 2017). In the R-G comparison, measurements from both radar and gauges are in the same temporal scale, and the R-G comparison highly depends on its temporal resolution of data—the sources of error shared by both datasets. The rain gauge provides the 1-minute precipitation amount (Section 3.2.3) and R estimated from radar

data is instantaneous (Section 2.3). Accumulating these precipitation quantities over the longer time interval can help reduce the random errors in both datasets.

We adopt various approaches to tackle these sources of errors. As shown in Appendix B.3.2, the Marshall-Palmer Z-R relation should be suitable for the precipitation estimation in the area close to Stuttgart during summertime (Appendix B.3.2). The radar data involved in the following R-G comparison are Z_{H} with different combinations of the data QC procedures discussed in Chapter 4. These QC procedures address the data contamination by non-meteorological echoes. To mitigate the beam blockage effect (Section 3.1.3), we constrain the R-G comparison only over the selected rain gauges which are located in the azimuthal directions free of beam blockage. We trust the data from DWD, and don't introduce the data QC for rain gauge mesaurements. To address the errors in terms of the time scale, the R-G comparisons are carried out in three different temporal scales—hourly, daily and the total period.

Selection of rain gauges and versions of radar datasets

We selected rain gauges for the following R-G comparison. From May to October in 2017, there were totally 50 / 82 rain gauges within the 75-km / 100-km range for the X-band radar. Excluding the rain gauges located within southeastern quarter in which the radar did not emit radiation, we have 39 / 65 rain gauges (Fig. 5.11(a)). Then, removing rain gauges within the azimuthal sector which is affected by the partial beam blockage for the radar beam at the 1.5° elevation, we have 28 / 46 rain gauges. Further eliminating the rain gauges which is in proximity to the edge of 75-km radar coverage because the radar signals of fine scans already decay severely beyond 73 km away from the radar, we have 24 / 46 rain gauges. It implies that, there are 22 rain gauges located between the 75 km and 100 km away from the radar. These 22 rain gauges theoretically can be involved in the X-band radar data evaluation, merely for the coarse scan. However, owing to either the range degradation, or higher altitudes caused by the slanted radar beams, or the deteriorating impact of attenuation as the range increases, we expect a weaker agreement in the R-G comparison over these 22 rain gauges located beyond 75 away from the X-band radar. Meanwhile, the magnitude of ΔZ may change depending on whether the R-G comparison is also conducted over the rain gauges within 75 km or 100 km away from the radar.

Recall the utmost objective of this research. We are interested in comparing the fine and coarse scan data in a fair manner. Thus, it is more reasonable to merely consider the 24 rain gauges within the 75-km range of the X-band radar and leave out those 22 rain gauges beyond 75 km away from the radar. In brief, after excluding the rain gauges which are improper in the R-G comparison, and keeping the consistency of R-G comparisons between the fine and coarse scans, we ended up with 24 rain gauges to be used in the following R-G comparison for both fine and coarse scan datasets.

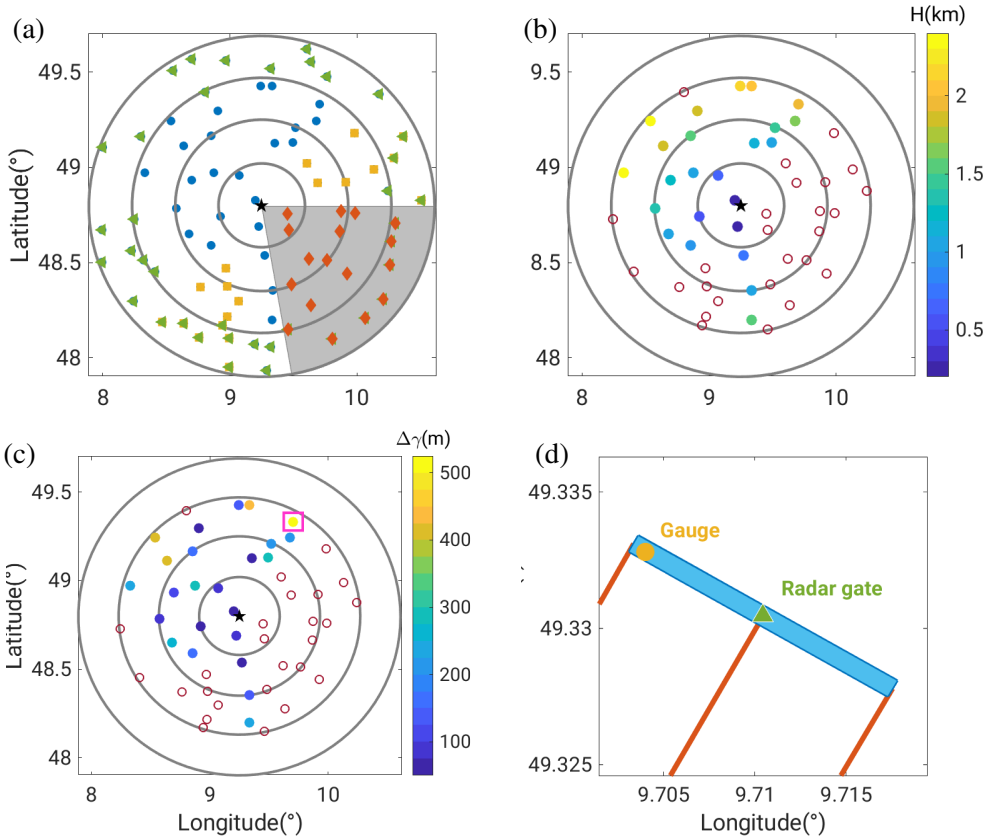

Fig. 5.11.: Information on the rain gauges involved in the R-G comparison between the rain gauges from DWD rain gauge network and the X-band radar in the Stuttgart field experiment, where the black stars indicate the location of the X-band radar, and the gray concentric circles indicate the 25-km, 50-km, 75-km and 100-km range rings. (a) shows the rain gauges within the 100-km range of the X-band radar, the red filled diamond markers indicate the rain gauges within the total beam blockage area, the yellow filled square markers indicate the rain gauges within the partial beam blockage area, the green filled triangle markers indicate the rain gauges beyond the 73-km range, the blue filled round markers are the rain gauges to be selected for the final R-G comparison. (b) shows the height of the match-up radar gates above the ground surface, and (c) shows the distances of rain gauges to the center of the corresponding match-up radar gates, where the unfilled dark red circles in (b) and (c) are the DWD rain gauges excluded due to the either partial or total beam blockage. (d) is obtained by zooming the plot in (c) for a specific rain gauge highlighted by the unfilled square in magenta,

The R-G comparison in this thesis uses different versions of radar data which are processed using different data QC procedures (Chapter 4) or their various combinations. Statistics indicating the correlations and concordance are calculated for each R-G comparison. The role of individual data QC procedure in the precipitation estimation can be illustrated by comparing the magnitude of these statistics. For instance, a R-G comparison uses the X-band radar data without any QC procedures and the other R-G comparison uses the X-band radar data with attenuation correction. The statistics, such CC_{PS}, of both R-G comparisons are compared to each other. If CC_{PS} of the second R-G comparison is higher than that of the first R-G comparison, then the X-band radar data after being applied attenuation correction correlate more with the rain gauge measurements. Because rain gauge measurements are regarded as

the reference, a closer correlation with the rain gauge measurements means R from the radar data after being applied attenuation correction are more accurate and reliable. It substantiates the importance of attenuation correction procedure in improving the data quality of the X-band radar dataset. Similar procedures are carried out for other R-G comparison using other data QC procedures, and their statistics are also compared and evaluated. Thus, through comparing the statistics representing the correlations and concordance between rain gauge and radar measurements, we can assess the effect of different data QC procedures on the R-G comparison, and further assess the role of these QC procedures on the quality of radar-derived precipitation estimation.

In addition to the radar data processed with different combinations of QC procedures, we can also compare the radar data from fine and coarse scans according to the statistics in their respective R-G comparison. It provides an indirect method to compare the fine and coarse scan datasets in terms of their precipitation estimation.

R-G matching-up procedure

A rain gauge provides point measurements in contrast to the radar measurements over a large area. For a better agreement in the R-G comparison, we need to seek the radar measurements measured at the same (or close) time and location as the rain gauge. This procedure is named after the R-G matching-up procedure whose details are shown as follows.

At a certain time point, for a rain gauge, we seek the radar gate geographically the closest to that rain gauge, obtain its Z_{H} (or other polarimetric variable) of that radar gate, and then calculate rainfall rates (R_{radar}) using Z_{H} of that radar gate via radar-based precipitation estimators ($R = R(Z_{\mathrm{H}})$), such as the Marshall-Palmer Z-R relation. Next, integrating these radar-derived rainfall rates (R_{radar}) over a certain period of time (either an hour or 24 hours), we obtain rainfall accumulation (AR_{radar}). The corresponding precipitation accumulation from the rain gauge (AR_{G}) over the same period is also calculated. Dividing both AR_{radar} and AR_{G} by the time interval, we get the mean rainfall rate $\overline{R}_{\mathrm{radar}}$ and $\overline{R}_{\mathrm{G}}$. Then, we use the inverse form of $R = R(Z_{\mathrm{H}})$ to calculate the equivalent mean radar reflectivity $\overline{Z}_{\mathrm{radar}}$ and $\overline{Z}_{\mathrm{G}}$ corresponding to $\overline{R}_{\mathrm{radar}}$ and $\overline{R}_{\mathrm{G}}$. So, we get a pair of AR_{radar} and AR_{G}, and a pair of $\overline{Z}_{\mathrm{radar}}$ and $\overline{Z}_{\mathrm{G}}$. Repeat the foregoing steps for a number of rain gauges. In this way, we obtain the coincident R-G dataset of AR_{G} and the matched-up AR_{radar}, of $\overline{Z}_{\mathrm{radar}}$ and the matched-up $\overline{Z}_{\mathrm{G}}$. The following R-G comparisons are performed in two aspects, between AR_{radar} and AR_{G}, and between $\overline{Z}_{\mathrm{radar}}$ and $\overline{Z}_{\mathrm{G}}$. Through this geographical match-up procedure, each rain gauge is linked to a specific match-up radar gate in the polar coordinate of the radar measurements.

This match-up procedure could be done alternatively by involving several radar gates (such as 3×3 gates along both the radial and azimuthal directions, or all the gates within a $1 \times 1\,\mathrm{km}^2$ area of the rain gauge, rather than merely a single radar gate. However, using the areal means over several

the radar gates implicitly decreases the spatial resolution of the radar data that are involved in the R-G comparison. It contradicts the objective of this study intended to investigate the advantages of the high-resolution radar measurements compared to the normal- or low-resolution radar data. Thus, we only use the 'nearest' radar gate for the following both C- and X-band R-G comparison (also for the radar-MRR comparison in Section 5.2.2).

A deeper insight into the concept of this 'nearest' radar gate is as follows. We suppose the directions of centerlines of radar beams remain static in space, exactly from 0.5° to 359.5° with a 1° interval, although in practice the exact azimuths slightly deviate from 0.5° with a small fraction, up to 0.06°. We regard these deviations as negligible. Since that the radial resolution is fixed, the position of each radar gate is static in space. Given that radar measurements are in polar coordinate, the radar beam is in the shape of a cone, and its projection to the ground surface is shaped as a 1° sector of a circle. The area of a radar gate along a radar beam is shaped as a 1° sector enclosed by two concentric circles (Fig. 5.11(d)). This area becomes larger with the increasing range of the radar gate, up to 9.8×10^4 m^2 and 4.4×10^5 m^2 for the fine and coarse scans respectively. It means a radar gate is not a single point as a rain gauge, but extends over a certain area. When we search for the 'nearest' radar gate to match up a specific rain gauge, we actually seek for an area which covers that rain gauge. Obviously, the size of such an area varies. Conventionally, we regard what the radar measures over a radar gate is the ensemble mean within that sampling volume. In the foregoing match-up procedure, the center of a radar gate is used to represent the location of a radar gate. It implies a physical distance or displacement $\Delta\gamma$ between the center of the match-up radar gate and the rain gauge (Fig. 5.11(d)). This displacement varies with the range of the radar gate if the spatial resolution of radar measurements is unchanged. Among the rain gauges to be compared with the X-band radar, $\Delta\gamma$ exceeds 500 m, and the average $\Delta\gamma$ is 200 m (Fig. 5.11(c)). Among the rain gauges to be compared with the C-band radar, the average $\Delta\gamma$ is 400 m with a maximum of 1 km (not shown). For the C-band data at 500-m resolution, $\Delta\gamma$ is comparable to its radial resolution, while for high-resolution X-band radar data, $\Delta\gamma$ can be a few times as its radial resolution, and should be taken into consideration for the R-G comparison. $\Delta\gamma$ essentially is a reflection of the effect of the radar data's range-dependence on the R-G comparison, and it renders the R-G comparison range-dependent.

Statistics in the R-G comparison

After constructing the paired R-G dataset, the degree of agreement between radar estimates and gauge measurements can be used to evaluate data quality of both data. As mentioned, the sampling methodology of a radar is absolutely different from that of rain gauges. The four possible scenarios are that only the radar, or only the rain gauge, or neither or both are of good quality. The good agreement between radar's and gauge's measurements is impossible if the first two scenarios occur. Since both instruments have different sources of errors and uncertainties, a good R-G agreement is also impossible if neither in-

strument works properly. The good R-G agreement is most likely to occur in case both instruments work correctly and are able to provide measurements of good data quality. In other words, the disagreement is a normal situation, and the agreement is unlikely just a matter of chance. Thus, especially for radar and gauge datasets which are sampled via absolutely different methods, the close agreement between them implicitly indicates good data qualities for both datasets.

The following statistics (Section 3.3.3) are used to quantify this degree of agreement: Pearson correlation coefficient (CC_{PS}), Spearman rank coefficient (CC_{SP}), Lin's concordance correlation coefficient (*CCC*), bias (*B*), normalized bias (*nB*), Root Mean Square Error (RMSE), relative RMSE (*rRMSE*), absolute average difference (AAD), and slope and intercept of least square orthogonal fitting line. Regarding the R-G comparisons, CC_{PS} and CC_{SP} are indicators of linear and non-linear correlations respectively, whereas other statistics measure concordance—the comparableness or equivalence between AR_{G} and $AR_{X\text{-}band}$. Thus, the degree of agreement can be evaluated in two aspects—correlation and concordance. Higher values in CC_{PS}, CC_{SP} and *CCC*, smaller magnitudes in the absolute values of *B* and *nB*, smaller values in RMSE (*rRMSE*), and AAD, the fitting line with its slope closer to 1 and intercept approaching zero, imply a tight concordance and correlation between the rain gauge measurements and radar estimates.

Recall the concepts of these three *CC*s (Section 3.3.3). CC_{PS} is high for the tight linear correlation but low for the non-linear correlation, CC_{SP} is high for either linear and non-linear correlation, and *CCC* is high for the comparable magnitudes of both data. It implies, if the radar data and rain gauge measurements are compared via the same variable, CC_{PS} and CC_{SP} should be high in case of good accord between two datasets. If the comparison is done in terms of two variables, such Z_{H} from radar data, and rainfall rate from the rain gauge measurements, CC_{PS} is definitely low because the rainfall rate is not linearly proportional to Z_{H} (recall the Marshall-Palmer Z-R relation), but CC_{SP} can be high if both data are correlated well nonlinearly. The Z_{H} calibration, such as adding or subtracting a few dBs to Z_{H} before converting to the rainfall rate, does not affect CC_{PS}, but changes *CCC*. Only after the radar data are calibrated properly to reach the comparable magnitude with the rain gauge can *CCC* be high. According to the characteristics of these three *CC*s, for the radar data without Z_{H} calibration, we mainly reply on CC_{PS} to determine the R-G correlation.

As mentioned, the difference between radar estimates and gauge measurements is also used to calibrate the radar data. The accuracy of Z_{H} is usually 1 dB, which roughly corresponds to 18% bias in radar-based rain rate estimation. To align with the minimum interval, we use 0.5 dB in this research. For the X-band radar data, the different pulse durations between fine and coarse scan may correspond to different ΔZ. The results in Section 5.3 have already shown a discrepancy in the calibration factors between the fine and coarse scan data. Thus, we need to calibrate the fine and coarse scans separately, and obtain ΔZ probably which could be equal or unequal between fine and coarse scans.

Since CC_{PS} is immune to the Z_H calibration, we use other statistics to seek the strongest concordance, and then determine the magnitude of ΔZ. Analogous to the concept of the *bias* in statistics defined as the systematic difference between an estimate of and the true value of a parameter, for the R-G comparison, we define the *bias* as the difference between rain gauge measurements and radar-based precipitation estimates (Section 3.3.3), although we acknowledge neither of them provides the true value. Determining ΔZ (Eq. 5.1) implicitly assumes rain gauge measurements as the reference, and the magnitude of radar-based precipitation estimates needs to be adjusted to minimize the difference between radar and gauge measurements. In other words, the Z_H calibration is to make both the rain gauge measurements and the calibrated radar data comparable in magnitude by adding or subtracting a few dBs to Z_H. Such a few dBs are the magnitude of ΔZ. In the R-G comparison on the total period time scale, we use the absolute averaged deviation (AAD), whereas we use the bias for the hourly R-G comparison. AAD on the total period time scale is essentially equivalent to the bias for the hourly R-G comparison.

Indubitably, the magnitudes of AAD, RMSE and bias is the largest for the R-G comparison on the total period time scale, the second largest for the daily R-G comparison, and the least for the hourly R-G comparison, since the precipitation accumulation over the 5-month is definitely larger than the 24-hour accumulation, and also greater than the 1-hour accumulation. For comparing the performance of R-G comparison across these three temporal scales, or comparing the performance of R-G comparison between the fine and coarse scans, we can use rRMSE and *nB*, both of which are dimensionless.

The least square fitting is very sensitive to variables in large magnitudes, but for precipitation measurements, those large precipitation quantities such as *AR* are rare and more vulnerable to random errors. In order to mitigate unfavorable effects of random errors, the comparisons are also conducted in terms of Z_H, and such comparisons are able to reflect the R-G consistency for these small-to-medium precipitation quantities due to the logarithmic scale of Z_H. This is the reason why the R-G comparisons are done separately for *AR* and $\overline{Z}$.

Temporal scales of R-G comparison

The rain gauge provides the 1-minute precipitation amount, from which we can calculate precipitation accumulation over a certain period of time. The following R-G comparisons are conducted on three temporal scales—over the total measuring period, daily and hourly, respectively. It means we need the total precipitation accumulation over the entire measuring period (AR_t), 24-hour precipitation accumulation (AR_d), and 1-hour precipitation accumulation (AR_h), respectively from both the X-band radar and rain gauges. AR_h numerically equals precipitation rate averaged over 1 hour.

How to calculate *AR* sometimes make differences. Occasionally the rain gauge measurements are not available when the instrument malfunctions. What is worse, such a situation often occurs during

heavy rain episodes. If the failure time of a rain gauge is too long, its AR_{G} is less the value it is supposed to be. Using such AR_{G} the R-G comparison inevitably brings errors, so we set up the following criteria that AR_{G} is allowed in the R-G comparison only if the rain gauge measurements are available during the more than 95% of the accumulating time.

Accumulating can reduce the random errors in the measurements, and the sampling spatial uncertainties tend to decrease for increasing accumulation time (Villarini et al., 2008). Thus, the R-G comparison on the basis of the total precipitation should be most trustworthy. AR_{h} depends on which time point is used as the starting point for the 1-hour accumulation, and similarly AR_{d} depends on which time point is used as the starting point for the 1-day accumulation. The choice of starting points occasionally affect the R-G comparison.

Besides the starting time point, the wind drift brings more uncertainties to the R-G comparison on the hourly scale. Radar beams are slanted at a certain angle; in this part of analysis we focus on the radar data in the 1.5° elevation sweep. To perform the radar-gauge comparison, we match-up the rain gauge and radar data geographically to obtain a dataset with coincident dataset from both radar and gauge. For each rain gauge, we need to search a radar gate which is geographically closest to that rain gauge. However, the radar sampling volume along the slanted radar beam is alway at a certain height H_0 above the ground surface. If the slope is fixed, this height depends on the distance of the rain gauge to the radar site. If the radar beam samples the hydrometeors within that radar sampling volume at a time point t_0, it will take a time interval Δt for these ascent hydrometers to reach the ground surface. The length of the time interval depends on the height of the sampling volume and the falling velocity of the hydrometeors. The magnitude of the falling velocity depends on the air vertical motion and sizes of the particles, and the sizes of these particles are affected by the microphysical processes such as coalescence and break-up. The magnitude t_0 sometimes can be as long as 10 minutes. For the R-G comparison on an hourly scale, we have rain gauge measurements from t_0 to t_1, if t_1 is 1 hour later than t_0. For the radar measurement, the hourly accumulation time should start from $t_0 - \Delta t$ instead of t_0. t_0 is changeable and different for each rain gauge and variable for each precipitation event, so it is not easy to determine δt for each paired R-G dataset. It implies the comparison in hourly scale in principle is inconsistent. For hourly accumulation, the situation exists but is much mitigated. Such issue is non-existent for the total period accumulated precipitation.

Regarding the sensitivity of R-G comparison to data QC procedures, since the R-G comparison on the basis of AR_{t} should be most trustworthy, we will discuss six different combinations of data QC procedures, and for each setting of data QC procedure, the comparisons are performed in terms of Z_{H} and AR respectively (Tab. 5.4). We discuss four different combinations of data QC procedures for the R-G comparison on the basis of AR_{d} (Tab. 5.5) and four different combinations of data QC procedures for the R-G comparison on the basis of AR_{h} (Tab. 5.6). As follows, we calculate statistics and present

the 2D-PDF or scatterplots to visualize the comparableness and correlation between the radar and gauge measurements for each combination of data QC procedure as shown in Tabs. 5.4, 5.5 and 5.6.

Tab. 5.4.: Combinations of data quality control procedures for studying sensitivity of the R-G comparisons over the total period to the data QC procedures

Comparison in AR	Comparison in $\overline{Z}$	Spike signal removal	Second-trip echo removal	Non-meteorological echo removal	Attenuation correction	Z_{H} calibration
Figs. 5.12(a) and 5.12(b)	Figs. 5.15(a) and 5.15(b)	N	N	N	N	N
Figs. 5.12(c) and 5.12(d)	Figs. 5.15(c) and 5.15(d)	Y	Y	N	N	N
Figs. 5.13(a) and 5.13(b)	Figs. 5.16(a) and 5.16(b)	Y	Y	Y	N	N
Figs. 5.13(c) and 5.13(d)	Figs. 5.16(c) and 5.16(d)	Y	Y	Y	N	Y
Figs. 5.14(a) and 5.14(b)	Figs. 5.17(a) and 5.17(b)	Y	Y	Y	Y	N
Figs. 5.14(c) and 5.14(d)	Figs. 5.17(c) and 5.17(d)	Y	Y	Y	Y	Y

Tab. 5.5.: Combinations of data quality control procedures for studying sensitivity of daily R-G comparisons to the data QC procedures

Figs. in AR	Figs. in $\overline{Z}$	Spike signal removal	Second-trip echo removal	Non-meteorological echo removal	Attenuation correction	Z_{H} calibration
Figs. 5.18(a) and 5.18(b)		N	N	N	N	N
Figs. 5.18(c) and 5.18(d)		Y	Y	Y	N	N
Figs. 5.18(e) and 5.18(f)		Y	Y	Y	Y	N
Figs. 5.19(a) and 5.19(b)	Figs. 5.19(c) and 5.19(d)	Y	Y	Y	Y	Y

Tab. 5.6.: Combinations of data quality control procedures for studying sensitivity of hourly R-G comparisons to the data QC procedures

Figs. in AR	Figs. in $\overline{Z}$	Spike signal removal	Second-trip echo removal	Non-meteorological echo removal	Attenuation correction	Z_H calibration
Figs. 5.21(a) and 5.21(b)	Figs. 5.21(a) and 5.21(b)	N	N	N	N	N
Figs. 5.21(c) and 5.21(d)	Figs. 5.22(c) and 5.22(d)	Y	Y	Y	Y	N
Figs. 5.21(e) and 5.21(f)	Figs. 5.22(e) and 5.22(f)	Y	Y	Y	Y	Y

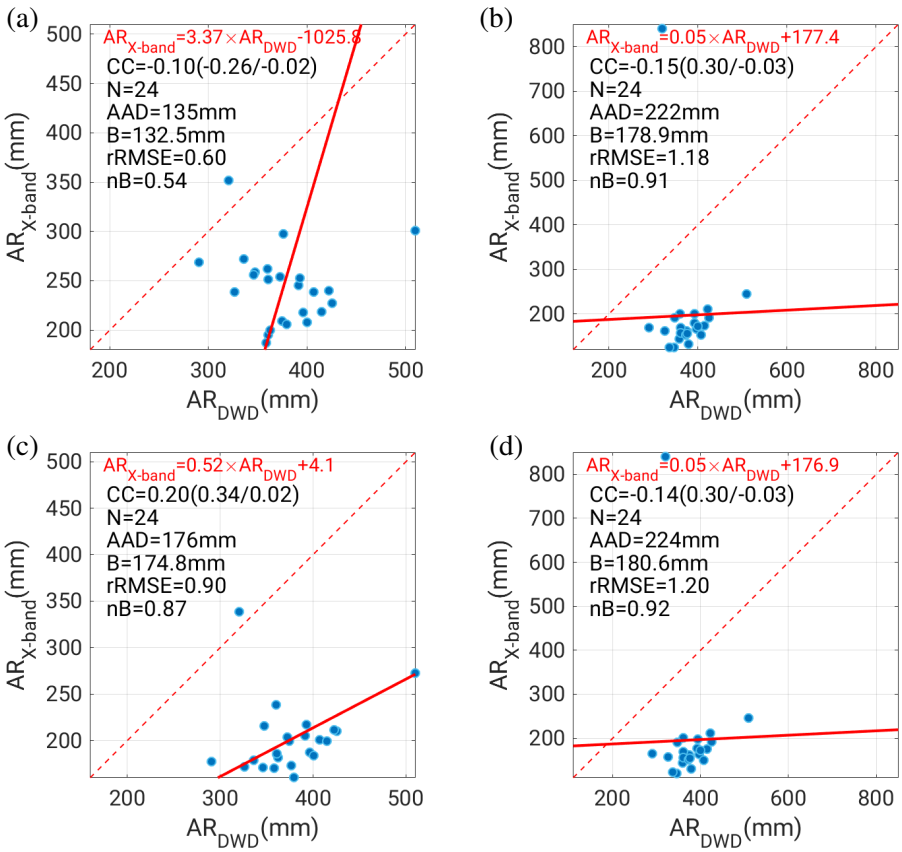

Fig. 5.12.: Scatter diagrams of AR_t between the one measured from DWD rain gauges (AR_{DWD}) and the one estimated from X-band radar data $AR_{X\text{-band}}$ with different combinations of data QC procedures (filtering second-trip echoes, correcting attenuation and Z_H calibration, etc.), where the left/right column is for the fine/coarse scan respectively, (a) and (b) are for the base data without any data QC process, (c) and (d) are for radar data after filtering out spike signals and second-trip echoes, where the solid red lines represent the fitting curve of the orthogonal fitting, and the dashed red lines are diagonal lines

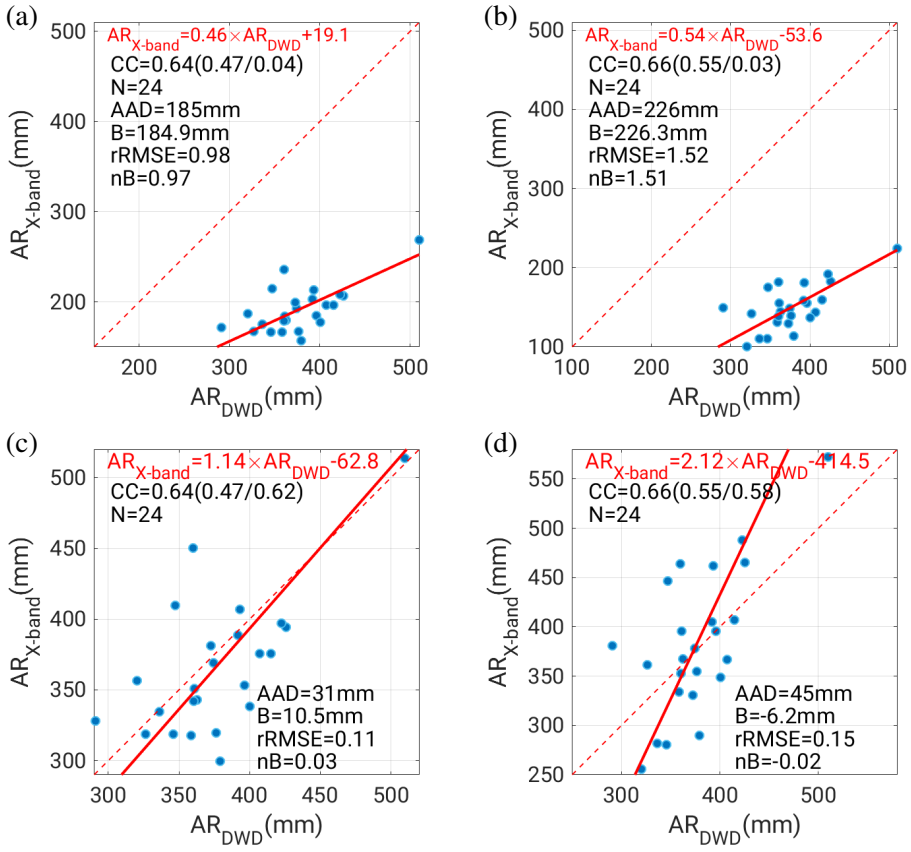

Fig. 5.13.: Similar to Fig. 5.12, but (a) and (b) are for radar data after filtering out spike signals, second-trip echoes and non-meteorological echoes, (c) and (d) are for radar data after filtering out spike signals, second-trip echoes, non-meteorological echoes as well as Z_{H} calibration

Light rain dominates the rainy periods, followed by less frequent moderate rain, and heavy rain is rare. It means, for instantaneous or short-period precipitation quantities such as R and AR_{h}, the amount of data in low values is significant larger than that in large values. It means, the visualization for these instantaneous or short-period precipitation quantities should be different from those for the accumulative precipitation quantities for longer period such as AR_{t} and AR_{d}. For the R-G comparison in terms of AR_{t}, each rain gauge only corresponds to a paired sample (AR_{G} and $AR_{\mathrm{X\text{-}band}}$). Thus 24 rain gauges correspond to 24 pairs of paired R-G samples. Since this number is small, the scatter plot clearly shows the relation between the radar and gauge measurements. For the daily R-G comparison, the number of the paired R-G samples exceeds three thousands. The majority of these paired R-G samples are low in the daily precipitation accumulation, and thus, in the scatter plot, lots of scatterers are clustered about the origin, and are indiscernible along with a bad visual effect. In order to improve the visualization, we switch to the two-dimensional bivariate histogram (Section 3.3) to show the relation in the R-G dataset. The number of samples increases even further for the hourly R-G comparison, so we use the two-dimensional bivariate histogram for the hourly comparison as well.

R-G comparison over the total period

The R-G comparison using the radar data without any data QC procedure brings about extremely low correlation coefficients (CC_{PS}) for both fine and coarse scans (Figs. 5.12(a) and 5.12(b)). After removing the spike signals and second-trip echoes, CC_{PS} for the fine scan data becomes positive, while CC_{PS} for the coarse scan data remains nearly the same (Figs. 5.12(c) and 5.12(d)). Given the fact that spike signals are much more prevalent in the fine scans, and the second-trip echoes exist only in the fine scans, the spike signal and second-trip echo removal procedures improve the fine scan data, but have minimal effect on the coarse scan data. The NMER procedure significantly increases CC_{PS} for both fine and coarse scans, which highlights the negative effect of non-meteorological echoes on the radar data quality and the necessity of eliminating the non-meteorological echoes (Figs. 5.12(c) and 5.13(a))..

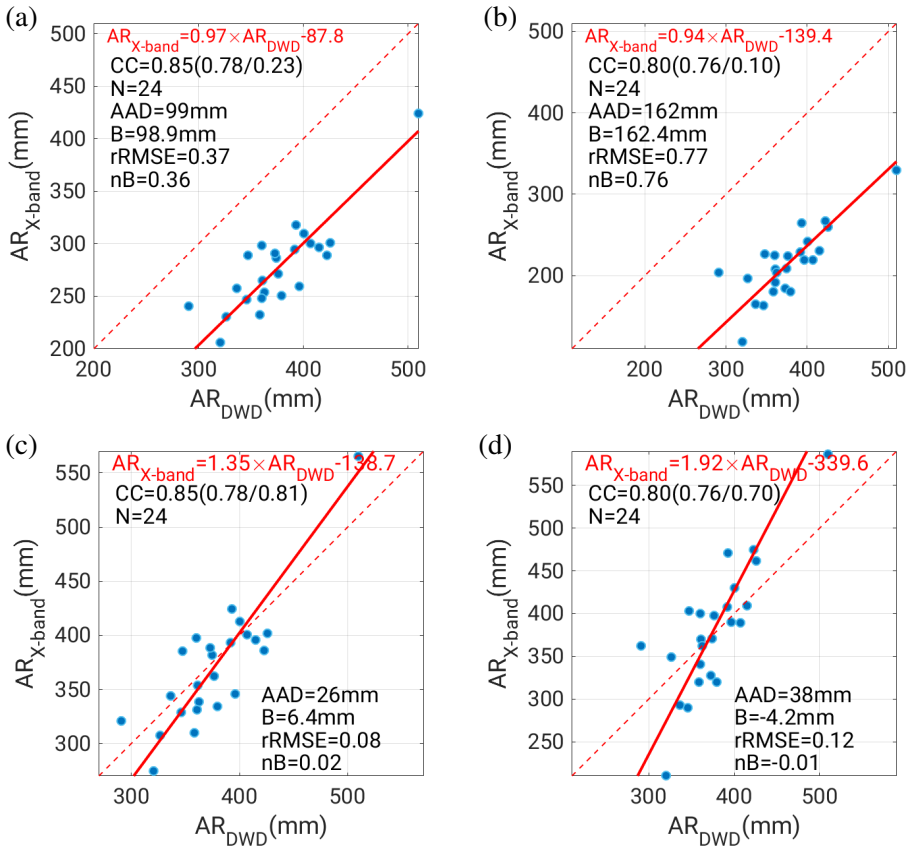

Fig. 5.14.: Similar to Fig. 5.13, but all four panels are for the attenuation corrected radar data

After further removing the non-meteorological echoes, the scatter diagrams exhibit similarity in terms of the positions of scatterers between the fine and coarse scans (Figs. 5.13(a) and 5.13(b)). It implies the comparableness of fine and coarse scan data which is only possible after removing these noises in the radar data (including the spike signals, second-trip and non-meteorological echoes). However, the scatterers are well below the diagonal lines. This underestimation is attributed to severe attenuation.

If the Z_H calibration is done for the radar data without attenuation correction, then ΔZ determined by minimizing AAD values, are 4.5 dB and 6.5 dB, respectively for the fine and coarse scans. As anticipated, the Z_H calibration effectively cuts down (absolute) values of AAD, B, rRMSE and normalize bias (nB), and the scatterers and their associated least square fitting lines become closer to the diagonal lines (Figs. 5.13(c) and 5.13(d)). ΔZ of 4.5 dB and of 6.5 dB are quite large. This is because, without correcting attenuation, these ΔZs include compensations for Z_H magnitudes due to the severe attenuation, and this Z_H calibration actually plays a role in combing attenuation correction and Z_H calibration procedures.

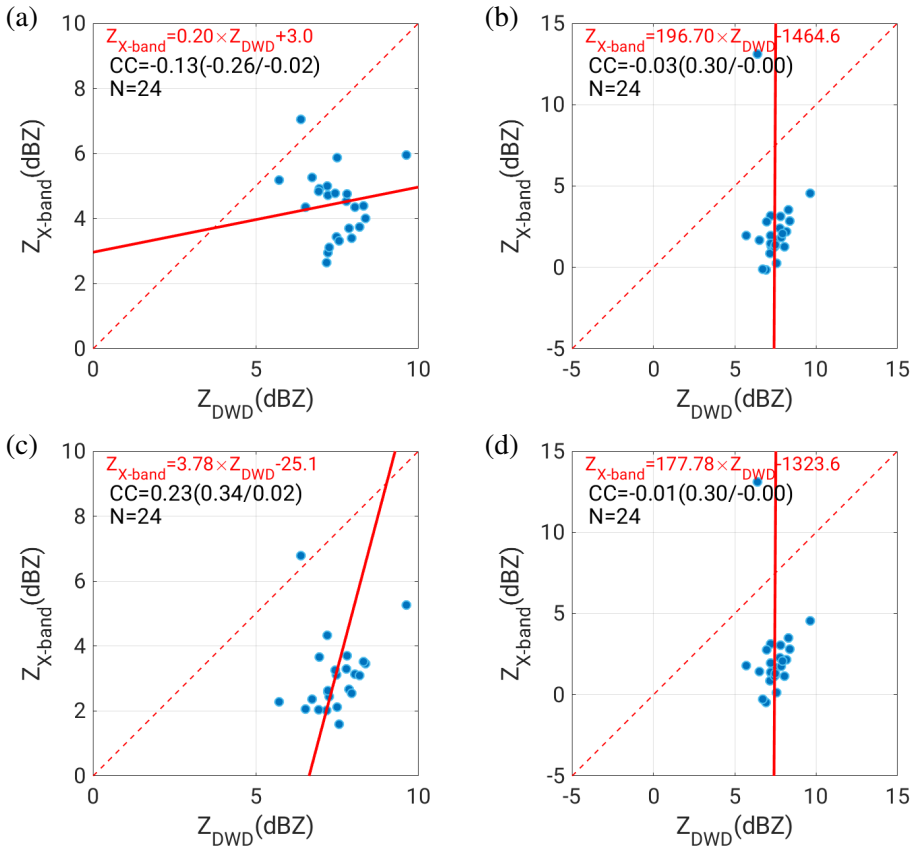

Fig. 5.15.: Same as Fig. 5.12, but in terms of $\overline{Z}_t$ converted from rainfall rate averaged over the entire period

In principle, the attenuation correction should be applied before Z_H calibration. For the radar data processed with attenuation correction and NMER, CC_{PS} is larger than the radar data processed with NMER but without attenuation correction, and the fitting lines for both fine and coarse scans become almost parallel to the diagonal lines, with its slope much closer to 1 (Figs. 5.14(a) and 5.14(b)). Besides CC_{PS} and fitting curves, the remaining other statistics (AAD, bias, etc.) are smaller, indicating that the attenuation correction procedure strengthens the R-G correlation and reduces the difference between the two datasets. However, similar to Fig. 5.13(a), the majority of scatterers are still below the diagonal lines, calling for the Z_H calibration. The attenuation correction has already compensated part of smaller magnitudes in Z_H, but not all of them. It means both fine and coarse scans are truly miscalibrated.

Similarly, ΔZ is determined by minimizing AAD, leading to ΔZ of 2 dB and 4 dB for the fine and coarse scans, respectively.

As mentioned, besides AR, $\overline{Z}$ are also used for the R-G comparison. $\overline{Z}_t$ corresponding to AR_{t} is calculated as follows. AR_{t} is divided by the number of measuring hours leads to the mean precipitation rate of the 5-month measuring period, which can be converted to $\overline{Z}_t$ by means of the inverse form of the Marshall-Palmer relation. Similar to the R-G comparison in terms of AR_{t}, the R-G comparisons in terms of $\overline{Z}_t$ using Z_{H} without data QC exhibit bad correlations between measurements of the radar and rain gauges (Figs. 5.15(a) and 5.15(b)), indicated by the closely clustered scatterers. The subsequent spike signal and second-trip echo removal procedures slightly tighten the R-G correlation for the fine scan data (Figs. 5.15(c) and 5.15(d)), and the additional NMER procedure largely increases CCs (Figs. 5.16(a) and 5.16(b)). Especially for the fine scans, the slope of the fitting curve becomes 1 along with an intercept of 4.7 dB. Adding $\Delta Z = 4.5\,dB$ to the fine scan data, we ended up with the fitting curve with a slope of 1 and an intercept of 0.2 dB (Figs. 5.16(c)). For the coarse scan, with $\Delta Z = 6.5\,dB$, the scatterers move leftward, approaching the diagonal line, although this fitting curve still deviates from the diagonal line (Fig. 5.16(d)).

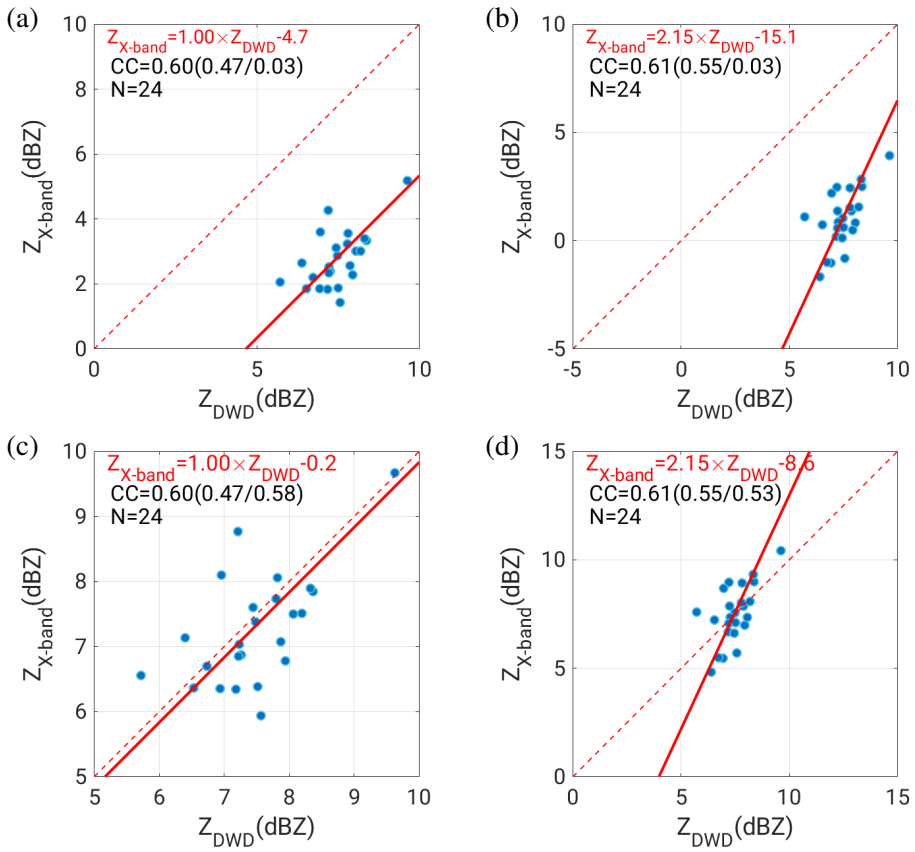

Fig. 5.16.: Same as Fig. 5.13, but in terms of $\overline{Z}_t$ converted from rainfall rate averaged over the entire period

Indicated by the increase in *CC*s, the R-G correlations become even stronger if the attenuation correction is applied, but all the scatterers are still below the diagonal line, indicating the radar data are still clearly underestimated against the rain gauge measurements even after correcting attenuation (Figs. 5.17(a) and 5.17(b)). For the fine scan, the attenuation correction procedure modifies the slope of the fitting curve and shifts the fitting curve from the diagonal line. With $\Delta Z = 2\,dB$ and $\Delta Z = 4\,dB$ for fine and coarse scan data respectively, the R-G scatterers are relocated much closer to the diagonal lines (Figs. 5.17(c) and 5.17(d)).

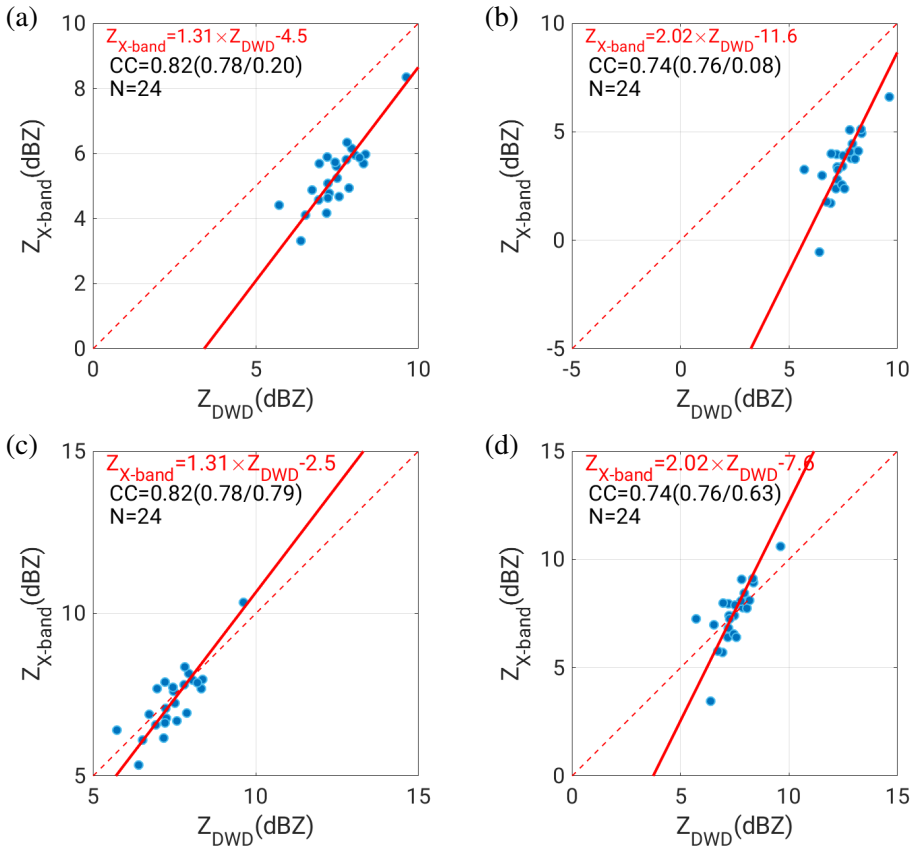

Fig. 5.17.: Similar to Fig. 5.16, but all four panels are for the attenuation-corrected radar data

Tabs. 5.7 summarizes *CC*s and AADs of the foregoing R-G comparisons with all the six combinations of data QC procedures in terms of both *AR* and $\overline{Z}$. As mentioned, CC_{PS} quantifies the linear correlation, and AAD quantifies the difference between radar and gauge measurements in terms of magnitude of *AR*. Adding removals of spike signals and second-trip echoes increases *CC*s slightly but enlarges AAD, so the role of the spike signal removal and second-trip echo removal procedures is to tighten the R-G correlation but both procedures increase differences in the *AR* magnitude (Figs. 5.12(a) vs. 5.12(c)). For both fine and coarse scan data, removing non-meteorological echoes tremendously increases CC_{PS} but also enlarges AAD (Figs. 5.12(c) vs. 5.13(a), or Figs. 5.12(d) vs. 5.13(b)), so the role of non-meteorological echo removal is to further intensify the R-G correlation and NMER has no contribu-

tion towards reducing the difference in the magnitudes of *AR*. The additional attenuation correction leads to increases in both *CC*s and reductions in AAD, which shows the role of attenuation correction in both tightening the R-G correlation and filling up the R-G gap in the *AR* magnitude (Figs. 5.13(a) vs. 5.14(a), or Figs. 5.13(b) vs. 5.14(b)). Applying the Z_H calibration to either attenuation-corrected or uncorrected radar data tremendously reduces AAD, but has no impact on *CC*s. It means the role of the Z_H calibration is to change the *AR* magnitude of radar-derived precipitation estimates, but has no effect on the R-G correlation (Figs. 5.13(a) vs. 5.13(c), or Figs. 5.13(b) vs. 5.13(d) for the radar data without attenuation correction, and Figs. 5.14(a) vs. 5.14(c), or Figs. 5.14(b) vs. 5.14(d) for the attenuation-corrected radar data).

Tab. 5.7.: *CC*s and AAD for the R-G comparisons over the total period using Z_H processed with different combinations of data QC procedures

Scan	Figs. in Z	AAD(mm)	CC_{PS}	CC_{SP}	CCC	Figs. in AR_t	CC_{PS}	CC_{SP}	CCC
Fine	5.12(a)	135	-0.1	-0.26	-0.02	5.15(a)	-0.13	-0.26	-0.02
Coarse	5.12(b)	222	-0.15	0.3	-0.03	5.15(b)	-0.03	0.3	0
Fine	5.12(c)	176	0.2	0.34	0.02	5.15(c)	0.23	0.34	0.02
Coarse	5.12(d)	224	-0.14	0.3	-0.03	5.15(d)	-0.01	0.3	0
Fine	5.13(a)	185	0.64	0.47	0.04	5.16(a)	0.60	0.47	0.03
Coarse	5.13(b)	226	0.66	0.55	0.03	5.16(b)	0.61	0.55	0.03
Fine	5.13(c)	31	0.64	0.47	0.62	5.16(c)	0.60	0.47	0.58
Coarse	5.13(d)	45	0.66	0.55	0.58	5.16(d)	0.61	0.55	0.53
Fine	5.14(a)	99	0.85	0.78	0.23	5.17(a)	0.82	0.78	0.2
Coarse	5.14(b)	162	0.8	0.76	0.1	5.17(b)	0.74	0.76	0.08
Fine	5.14(c)	26	0.85	0.78	0.81	5.17(c)	0.82	0.78	0.79
Coarse	5.14(d)	38	0.8	0.76	0.7	5.17(d)	0.74	0.76	0.63

R-G daily comparison

In terms of AR_d, *CC*s are high for the radar data which have not been processed with any data QC procedures (Figs. 5.18(a) and 5.18(b)). However, similar to the R-G comparison for the entire period, the most R-G paired data are well below diagonal lines, which means that the radar precipitation estimates are severely underestimated in comparison to the rain gauge measurements. After filtering all the noises (spike signals, second-trip and non-meteorological echoes all together), *CC*s increase slightly, and the bias, rRMSE and *nB* all decline more obviously (Figs. 5.18(c) and 5.18(d)). The additional attenuation correction procedure improves the radar data,making them approach the rain gauge measurements, illustrated quantitatively by the reduced AAD, bias, rRMSE, *nB*, as well as the increased *CC*s (particularly *CCC*), and qualitatively by less tilted fitting lines (Figs. 5.18(e) and 5.18(f)).

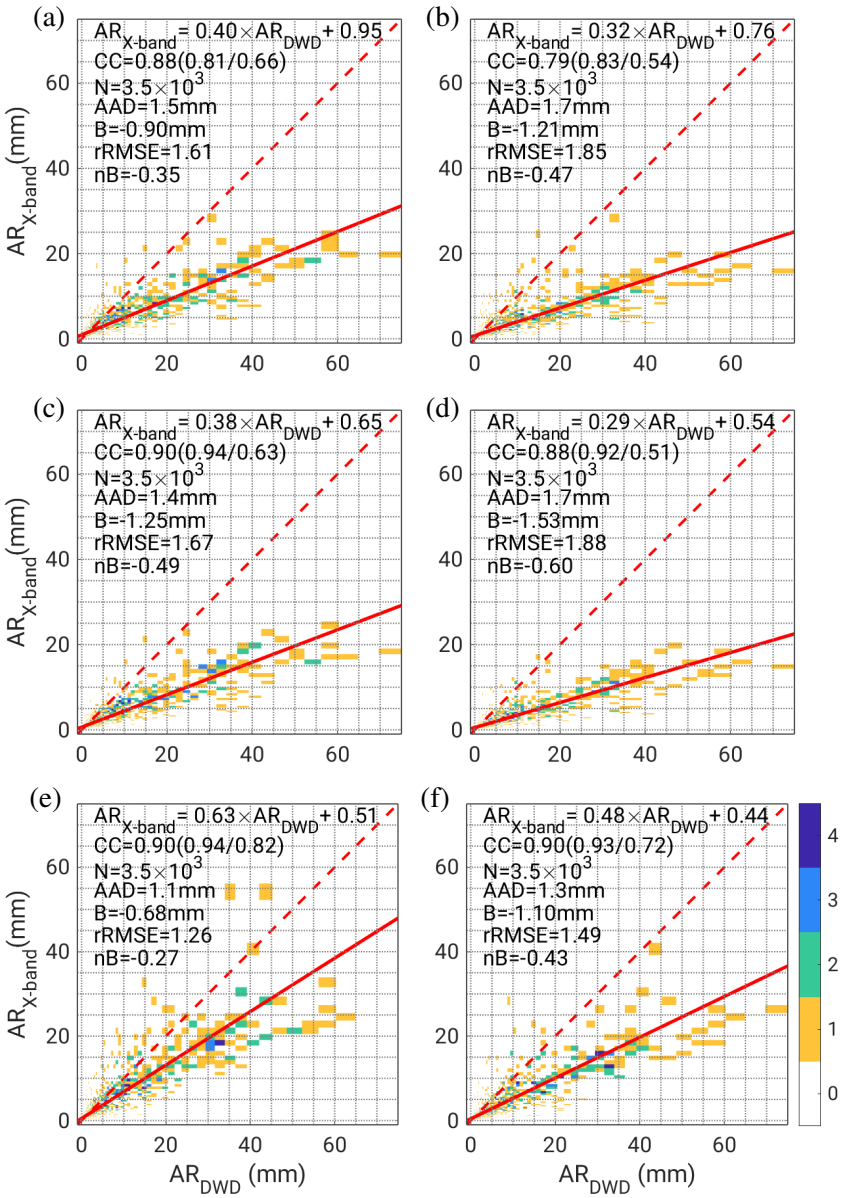

Fig. 5.18.: Two-dimensional bivariate histogram of the absolute occurrence frequency to compare AR_{d} measured from the DWD rain gauge network (AR_{DWD}) and estimated from X-band radar data AR_{X-band} with different combinations of data QC procedures (filtering second-trip echoes, correcting attenuation and Z_{H} calibration, etc.), where (a) and (b) are for the base data without any data quality process, (c) and (d) are for the radar data after filtering noise including spike signals, second-trip echoes and non-meteorological echoes, (e) and (f) are for the data after filtering out the noise and correcting attenuation, and the meaning of red dashed/solid lines, *CC*, *N*, AAD, *B*, rRMSE, and *nB* are the same as Fig. 5.12

The Z_{H} calibration procedure further shifts the R-G paired data back to the diagonal lines, along with reductions in bias, AAD, rRMSE and *nB* (Figs. 5.19(a) and 5.19(b)). From the scatter diagram, we see the scatterers with large *AR* values still deviate from the diagonal line, but they can be distributed in both sides of the diagonal line (Figs. 5.20(a) and 5.20(b)). Comparing Figs. 5.19(a) and 5.20(a) shows pros and cos of scatter diagrams and 2D-histogram respectively. Although AR_{d} cancels

out lots of random errors and uncertainties, for the heavy rain case, we still see large discrepancies between the rain gauge and radar measurements. Several reasons may account for these discrepancies, including the inappropriateness of Marshall-Palmer Z-R relation, the distinct sampling methods between radar and gauges, the incapability of attenuation correction to recover all the signals. Similarly, for the R-G comparison in terms of AR_{d}, the R-G comparison in terms of $\overline{Z}$ converted from daily mean $\overline{R}$ also shows a good agreement between the radar estimates and rain gauge measurements (Figs. 5.19(c) and 5.19(d)).

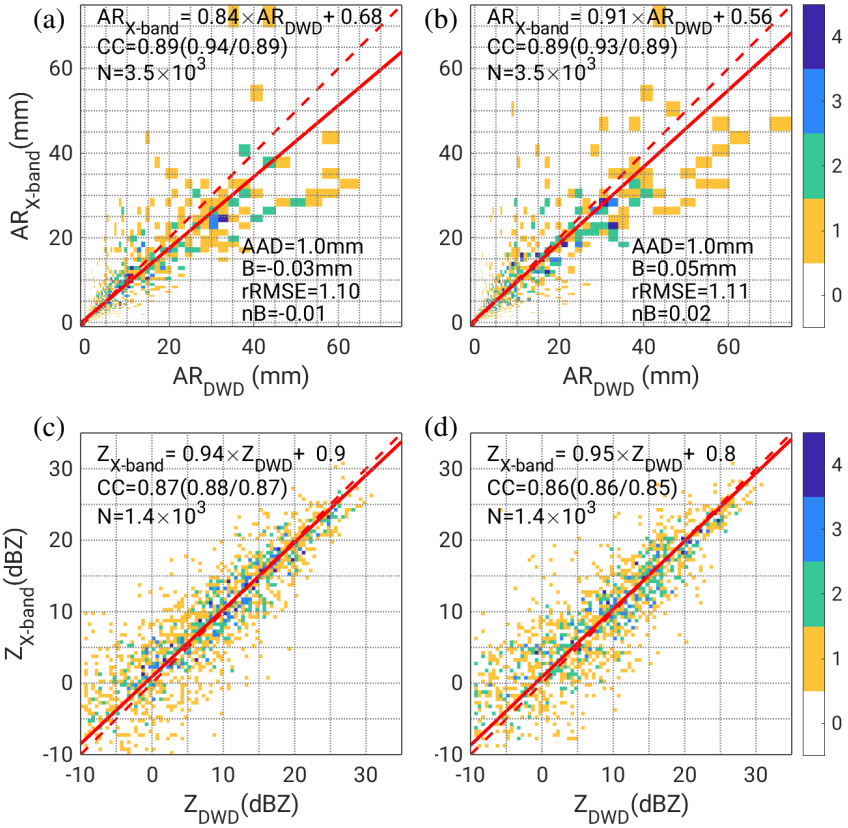

Fig. 5.19.: Two-dimensional bivariate histogram of the absolute occurrence frequency, (a) and (b) of AR_{d} measured from the DWD rain gauge network (AR_{DWD}) and estimated from X-band radar data $AR_{\mathrm{X-band}}$, (c) and (d) of $\overline{Z}$ converted from daily mean rainfall rate ($\overline{R}$), where the solid red lines represent the orthogonal fitting curves and the dashed red lines are diagonal lines

Tab. 5.8 summarizes *CC*s and AAD. In contrast to the R-G comparison over the entire measuring period, *CC*s of the daily R-G comparisons are high, so changes in *CC*s are not apparent. Filtering out the noises, such as spike signals, second-trip and non-meteorological echoes, slightly increases *CC*s, but enlarges biases. The subsequent attenuation correction procedure reduces the magnitudes of biases, but does not alter *CC*s. The role of these data QC procedures in the daily R-G comparison is identical to that in the R-G comparison over the total period. The slope of fitting line also clearly shows the role of

these data QC procedures; removing the noise creates a larger discrepancy in terms of AR_{d} magnitude , while attenuation correction and Z_{H} calibration reduce such a discrepancy.

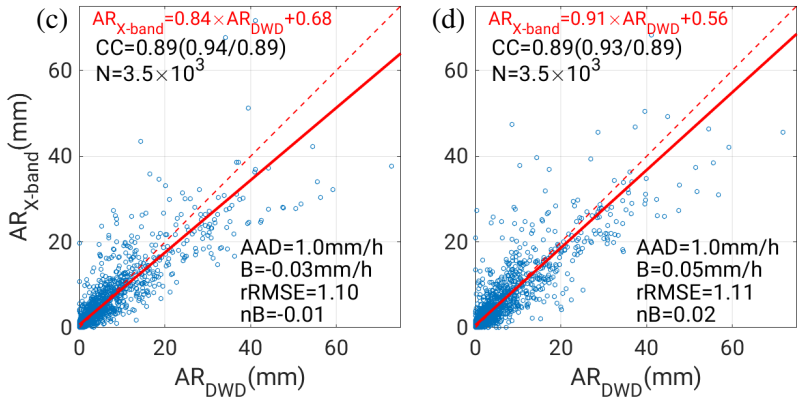

Fig. 5.20.: The same as Figs. 5.19(a) and 5.19(b) but in the form of scatterplot

Tab. 5.8.: *CC*s and bias for the daily R-G comparisons using Z_{H} processed with different combinations of data QC procedures

Scan	Figs.	B(mm)	CC_{PS}	Slope	CCC
Fine	5.18(a)	-0.9	0.88	0.4	0.66
Coarse	5.18(b)	-1.21	0.79	0.32	0.54
Fine	5.18(c)	-1.25	0.9	0.38	0.63
Coarse	5.18(d)	-1.53	0.88	0.29	0.51
Fine	5.18(e)	-0.68	0.90	0.63	0.82
Coarse	5.18(f)	-1.1	0.90	0.48	0.72
Fine	5.19(a)	-0.03	0.89	0.84	0.89
Coarse	5.19(b)	0.05	0.89	0.91	0.89
Fine	5.19(c)	–	0.87	0.94	0.87
Coarse	5.19(c)	–	0.86	0.95	0.85

R-G hourly comparison

When it comes to the hourly R-G comparison, the radar data are obviously underestimated when compared with the rain gauge measurements as well (Figs. 5.21(a) and 5.21(b)), and the combined use of spike signal removal, second-trip and NMER and attenuation correction procedures strengthens the R-G correlation, and reduces the deviation of radar estimates from the reference data—rain gauge measurements (Figs. 5.21(c) and 5.21(d)). Analogous to the R-G comparison on the other two time scales, the following Z_{H} calibration for the hourly R-G comparison also further reduces the difference between the radar estimates and rain gauge measurements, contributing to a pronounced R-G agreement in terms of R magnitude (Figs. 5.21(e) and 5.21(f)). As discussed, the hourly R-G comparison contains far more

scatterers, and the 2D histogram is much more suitable to illustrate the R-G correlation. Note that AR_{h} numerically equals to the mean of all the instantaneous R within that hour, so we use the hourly mean rainfall rate $\overline{R}$ herein.

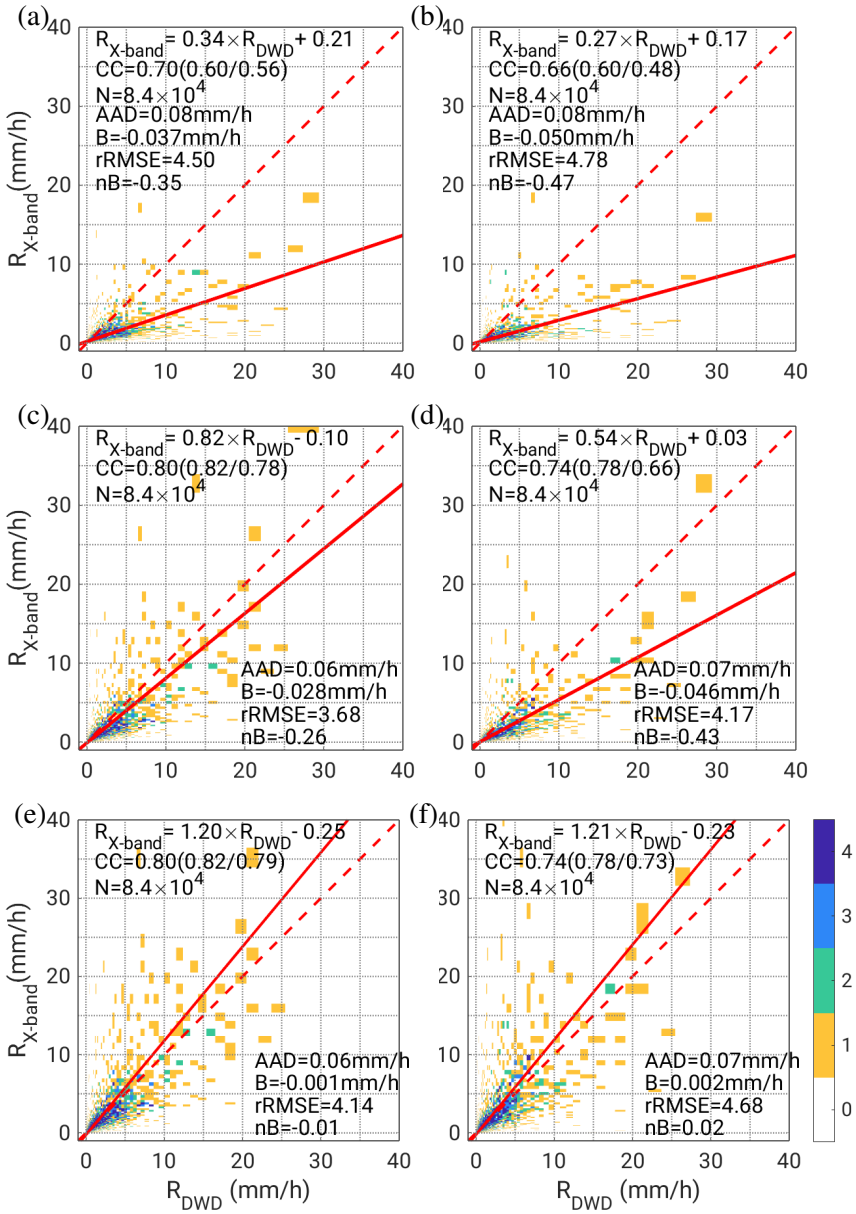

Fig. 5.21.: Similar to Fig. 5.18, but in terms of hourly $\overline{R}$ estimates, where (a) and (b) are for the base data without any external data QC process, (c) and (d) are for radar data with data QC processes (removing noise and attenuation correction) but without Z_{H} calibration, and (e) and (f) are for the radar data after being applied with both data QC processes and Z_{H} calibration

Regarding the equivalent mean $\overline{Z}$ converted from the mean hourly $\overline{R}$, the filtering procedure and attenuation correction increase CCs (Figs. 5.22(c) and 5.22(d)), and the Z_{H} calibration trims deviations of radar estimates from rain gauge measurements (Figs. 5.22(e) and 5.22(f)).

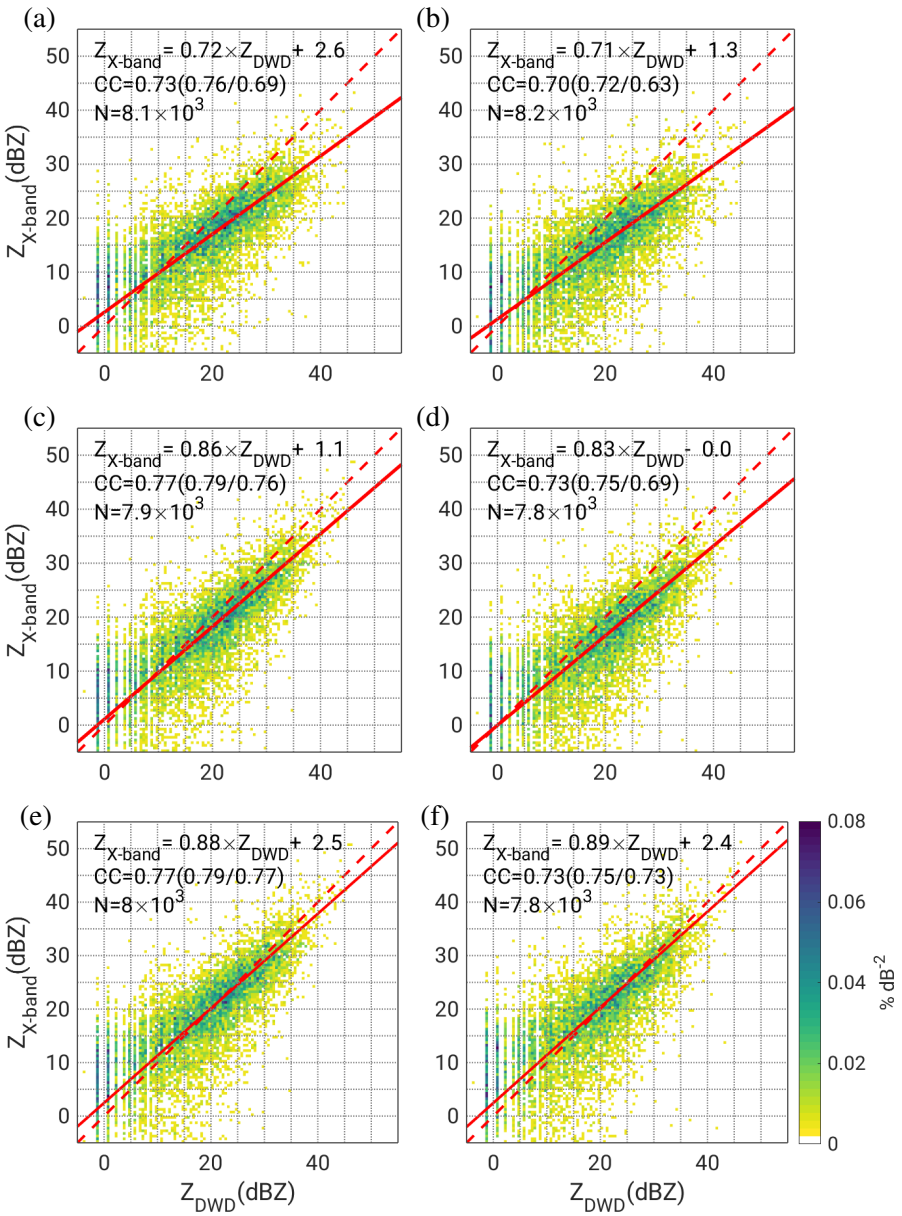

Fig. 5.22.: 2D-PDF to compare the equivalent mean $\overline{Z}$ converted from the hourly $\overline{R}$ retrieved from between the X-band radar data ($R_{\text{X-band}}$) and precipitation measurements from DWD rain gauge network (R_{DWD}), where (a) and (b) are for the radar data without any external data QC procedures, (c) and (d) are for radar data with four data QC procedures (removing three types of noise and attenuation correction) but without Z_{H} calibration, and (e) and (f) are for the radar processed data after being applied with both four data QC procedures and Z_{H} calibration, where *CC*s are CC_{PS}, CC_{SP} and *CCC* from left to right, and *N* represents number of samples or scatterers

Tab. 5.9 summarizes *CC*s and biases for the hourly R-G comparison. Similar to the daily R-G comparison, the data QC procedures except the Z_{H} calibration increase *CC*s, but the main contribution to reduce the absolute of bias is made by the Z_{H} calibration.

From Fig. 5.14, Fig. 5.17, Fig. 5.18, Fig. 5.19, Fig. 5.21 and Fig. 5.22, *CCC*s in the R-G comparison on the basis of the fine scan data are always slightly larger than those of the coarse scan data. It is

not accidental. A possible explanation is that, a rain gauge is closer to its matched radar gate in the fine scans than to its matched radar gate in the coarse scans. It indicates the benefit of using the radar measurements at a higher spatial resolution, which is particularly true for convective storms characterized with large spatial variability.

The foregoing analyses compare the radar and rain gauge measurements, and also perform the absolute Z_H calibration by the radar-gauge adjustment. Literature has proved that the use of the gauge-corrected radar measurements can result in better prediction accuracy than what is achieved with the radar-only or gauge-only input (Vieux et al., 2009), and using radar data combined with rain gauge measurements can even help improve model's predictions (Vonach et al., 2018). Similarly, our results also prove the radar data after the absolute Z_H calibration should be in a higher quality, and the absolute Z_H calibration is a necessary data QC procedure in addition to these data QC procedures presented in Chapter 4.

Tab. 5.9.: *CC*s and bias for the hourly R-G comparisons using Z_H processed with different combinations of data QC procedures

Scan	Figs. in Z	B(mm)	CC_{PS}	CC_{SP}	CCC	Figs. in R	CC_{PS}	CC_{SP}	CCC
Fine	5.21(a)	-0.037	0.7	0.6	0.56	5.21(a)	0.73	0.76	0.69
Coarse	5.21(b)	-0.05	0.66	0.6	0.48	5.21(b)	0.70	0.72	0.63
Fine	5.21(c)	-0.028	0.8	0.82	0.78	5.22(c)	0.77	0.79	0.76
Coarse	5.21(d)	-0.046	0.74	0.78	0.66	5.22(d)	0.73	0.75	0.69
Fine	5.21(e)	-0.001	0.8	0.82	0.79	5.22(e)	0.77	0.79	0.77
Coarse	5.21(f)	-0.002	0.74	0.78	0.73	5.22(f)	0.73	0.75	0.73

5.2.2. Radar-MRR comparison

The antenna of a MRR usually looks up vertically when rain drops fall down approximately along the vertical direction as well. Relying on empirical relations between w_t and raindrops' D, the DSD can be retrieved, and then can be used to calculate Z, R, and LWC(Section 3.2.2).

The MRR owned by the University of Stuttgart is situated within the radar coverage of both C- and X-band radars (Fig. 5.23(a)). The C-band radar is in the northwest of the MRR, while the X-band radar is in the northeast direction. For both the C- and X-band radars, their slanted radar beams at different elevations intersect the vertical radar beams of the MRR at different heights, and we only consider the measurements at these intersection points for the following radar-MRR comparison (Figs. 5.23(c) and 5.23(d)). The C-band radar is located nearly 5 times farther from MRR compared to X-band radar (Fig. 5.23(a)); the sampling volumes are roughly 1.4 km^3 for the intersection between the C-band radar and the MRR, and 0.05 km^3 for intersection between the X-band radar and the MRR, respectively.

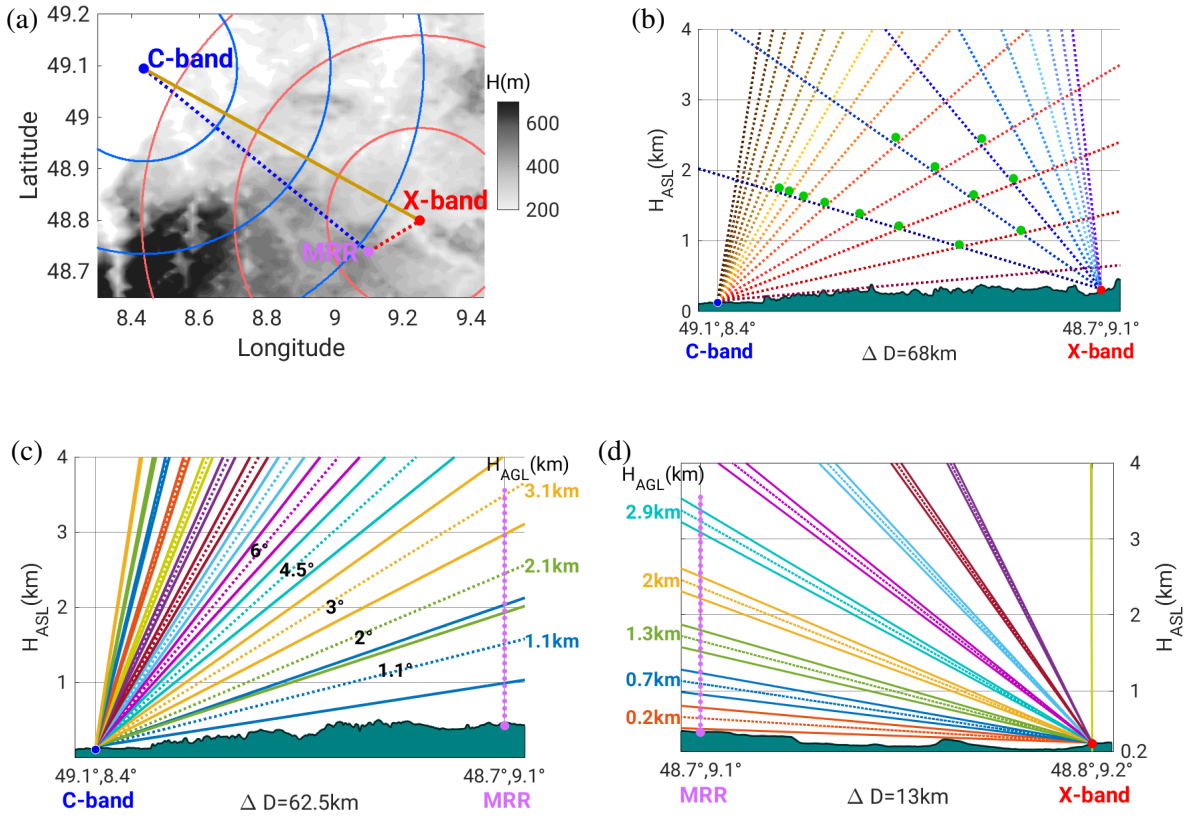

Fig. 5.23.: (a) Top view of the locations of C- and X- band radars and Micro Rain Radar (MRR), where the red and blue concentric circles are the 20-km, 40-km and 60-km range rings; (b) cross section of the intersection of radar beams of the C- and X-band radar along the shortest line (the brown solid line in (a)) between C- and X-band radars, where the green dots in the intersection points represent the radar sampling volumes whose radar data taken into analyses in the Section 5.2.3; (c) cross section of the intersection of the radar beams of the C-band radar and MRR; (d) cross section of the intersection of the radar beams of the X-band radar and MRR, H_{AGL} is the height above the ground surface, H_{ASL} is the height above the mean sea level, ΔD is the distance between the MRR and the radar

Similar to Section 5.2.1, the following radar-MRR comparison is performed on three time scales, instantaneous, hourly and daily, in terms of Z_{H} or $\overline{Z}$ or R or AR. The instantaneous Z_{H} for the X-band radar means the Z_{H} measuremetns from a radar sweep of a volume scan, without any interpolation or integration. The instantaneous R for the X-band radar is calculated from the instantaneous Z_{H} using the Marshall-Palmer Z-R relation. The MRR provides Z_{H} and R in the 1-minute temporal resolution, which is referred as the instantaneous Z_{H} and R. It means that both the MRR and the X-band radar measure Z_{H} instantaneously, and we can directly compare these instantaneous Z_{H} measurements between the radar and the MRR.

These instantaneous Z_{H} measurements are converted to R through the Marshall-Palmer Z-R relation, generating instantaneous precipitation rate (R) in unit of $\mathrm{mm\,h^{-1}}$ for both the X-band radar and MRR for the second form of the radar-MRR comparison. Averaging these instantaneous R within an

hour brings about hourly $\overline{R}$ in unit of $\mathrm{mm\,h^{-1}}$ for both the X-band radar and MRR, and then we can compare the hourly $\overline{R}$ between the X-band radar and the MRR. Convert the hourly $\overline{R}$ to the equivalent mean $\overline{Z}$, and we have the fourth form of the radar-MRR comparison. Further integrating the hourly mean precipitation rate over 24 hours, and we obtain AR_{d} also for both the X-band radar and MRR, and then compare both. Similarly, dividing AR_{d} with number 24 leads to the daily $\overline{R}$ from which the equivalent mean $\overline{Z}$ can be calculated for both the X-band radar and MRR, which allows us to compare the daily precipitation accumulation in the logarithmic scale.

For an intersection point at a single elevation (Fig. 5.23(d)), the role of a single MRR is similar to that of a rain gauge. Unlike the R-G comparison over a rain gauge network consisting a number of rain gauges, for the radar-MRR comparison, AR_{t} is only one pair of data. For rain gauges, since their corresponding match-up radar gates are usually located a few hundreds to a few thousand meters above the rain gauge, there is a time lag between the time point when the radar beam intercepts the precipitation and the time point when the rain gauge detects the precipitation (Mittermaier et al., 2004; Lack and Fox, 2007; Dai et al., 2013). Thus, the R-G comparison on the instantaneous R is improper. In contrast, the temporal resolution of MRR measurements is one minute. The radar beams from the X-band radar and MRR can intersect each other nearly simultaneously without any time gap, so the radar-MRR comparison on the instantaneous time scale is reasonable. The sample size for the instantaneous Z and R data should be very large. Due to the precipitating time in nature less than 2%, the majority of the instantaneous Z and R represent dry conditions, so we use a double-conditional criterion that precipitation quantities of both the radar and MRR should be simultaneously larger than $0.1\ \mathrm{mm\,h^{-1}}$.

The reason for performing the radar-MRR comparisons in terms of both instantaneous Z_{H} and R is that each form of comparison provides information which supplements each other. In nature, heavy precipitation is rare. In other words, the less intense the precipitation is, the more frequent it is. Thus, the majority of Z_{H} values on the logarithmic scale are below 20 dBZ, while the high Z_{H} values take up only a very tiny portion. The calculations for CCs and the least square orthogonal fitting treat the high or low Z_{H} values equally, and thus their results are predominantly determined by low Z_{H} values. Z_{H} in weak intensity is of less interest to the people who are concerned mainly with the precipitation amount, but is a good indicator of data quality of the radar measurements. In contrast, for the variable in terms of R or AR, the data from heavy rain play the main role, and contribute much to the results of CCs and least square fittings. It agrees with concerns of most hydrologists, but the sample size of data in heavy precipitation intensity is quite small. In brief, the radar-MRR comparison using Z_{H} emphasizes the frequent light rain and the overall data quality, whereas the radar-MRR comparison using R represents the infrequent heavy rain and the quality of precipitation estimation. A combination of both Z_{H} and R or AR provides us a more thorough evaluation of the C- and X-band radar data

The previous R-G comparison presents satisfying results, but the radar-MRR comparison is still necessary. Given that only one MRR was available within the X-band radar coverage during the

measuring period, its role is somehow similar to that of only one rain gauge. The radar-MRR comparison cannot evaluate the radar data through a large areal extent, but instead it gives an insight into radar measurements along the vertical direction. In the R-G comparison, we focus on the radar data of the lowest elevation since we are interested in the radar measurements as much as close to the rain gauges installed on the ground surface. In contrast, the MRR measurements can be available through the vertical direction, which allows us to compare the X-band radar data with MRR measurements at different altitudes above the ground (Fig. 5.23(d)). The maximum range of the MRR is 2.9 km, so only the X-band radar beams of the lowest five elevations can physically intersect the vertical radar beams of MRR (Fig. 5.23(c)). Thus, in principle, for the coarse scan, we can compare the measurements of the MRR and the X-band radar at five altitudes up to 2.9 km above the ground. However, aligned with the ultimate objective of this study on the effect of spatial resolution, in order to compare the performance of the radar-MRR comparison between fine and coarse scans, we limit the following radar-MRR comparison to the lowest three elevations in which the radar data of both scans are accessible.

Meanwhile we are also interested in evaluating the X-band radar data along the vertical extent other than at the lowest elevation, for the following reasons. First, we obtained ΔZ via the previous R-G comparison using the X-band radar data at the 1.5° elevation. Theoretically, ΔZ should be invariable within a volume scan regardless of the elevation. We are not sure about whether this invariability is valid in practice for our X-band radar measurements. Thus, the radar-MRR comparison can aid us in checking the consistency of ΔZ within either the fine scan data or the coarse scan data. Second, the solid or mixed-phase of precipitation is more frequent at higher altitudes, and bright bands may be seen in the slanted radar beams at larger elevation angles. The regional freezing level during rainy periods in summer is as high as 2.5 km on average. The X-band radar beams of the lowest three elevations intersect the MRR radar beam below 1.5 km (Fig. 5.23(d)), implying that all the hydrometeors within our consideration theoretically should be in liquid phase. It provides us a chance to assess how the vertical variability of precipitation (primarily liquid phase) affects the evaluation of radar data using external references. Third, the measuring principle of the MRR is absolutely distinct from either weather radars or rain gauges (Section 3.2.2), which may aid us with a more comprehensive estimation of precipitation.

Radar-MRR comparison in instantaneous scale

We start with Z_{H} without any data QC procedure, since Z_{H} can be directly accessed in the both X-band radar and MRR measurements. Regardless of the elevation of radar beams (an indication of the above-ground height of the match-up sampling volumes), no matter for fine or coarse scans (the sample size of the fine scan data is three times as that of the coarse scan data), *CC*s are quite high compared to their counterparts in the previous R-G comparisons (recall Fig. 5.22), and the majority of paired data ($Z_{\text{X-band}}$ and Z_{MRR}) are in proximity to the diagonal lines (Fig. 5.24). *CC*s decrease slightly as the elevation of

paired data increases. As discussed, the high *CC*s show the majority of the X-band radar Z_H data, particularly in low intensity, agree well with the measurements from MRR. The tighter correlation between the X-band radar and MRR rather than the R-G correlation may be due to the fact that both measurements are from the collocated and simultaneous sampling volumes. All the fitting curves are below the diagonal lines, in accord with the positive ΔZ from the previous R-G comparisons. For either the fine or coarse scan data, the fitting curve become closer to the diagonal line (45° inclined) as the elevation of paired data increases. For each elevation, the intercept of the fitting curve for the fine scan is always roughly 1 dB in magnitude less than that for the coarse scan, but both slopes are comparable (for instance, Figs. 5.24(a) and 5.24(b)).

With a combination of several data QC procedures which remove spike signals, second-trip and non-meteorological echoes, and also correct attenuation, the sample size N is reduced by one-third for the 1.5° elevation, and only slightly for the 3.6° and 6.2° elevations (Fig. 5.25). It is because most of non-meteorological echoes and the majority of second-trip echoes occur in the low level of atmosphere, corresponding to the radar measurements at the lowest elevation. The data QC procedures responsible for the removal of second-trip and non-meteorological echoes modify the radar data mainly at the lowest elevation, and the modification of radar data at the other two elevations is caused by mainly attenuation correction and secondarily spike signal filtering (the chance of the latter one is much smaller). *CC*s, regardless of which definition, change little, but the slopes of the fitting curves become further closer to 1, compared to the radar-MRR comparison using the radar measurements without the data QC procedures. Such improvements illustrate the necessity of data QC procedures for the X-band radar data. Except the coarse scan at 1.5° elevation, despite the change in slopes, the intercepts of the fitting curves remain nearly unchanged. It implies that, the attenuation correction tends to increase the magnitude of Z_H, and the increases are reflected in the values of slopes rather than the intercepts (except the coarse scans at 1.5° elevation).

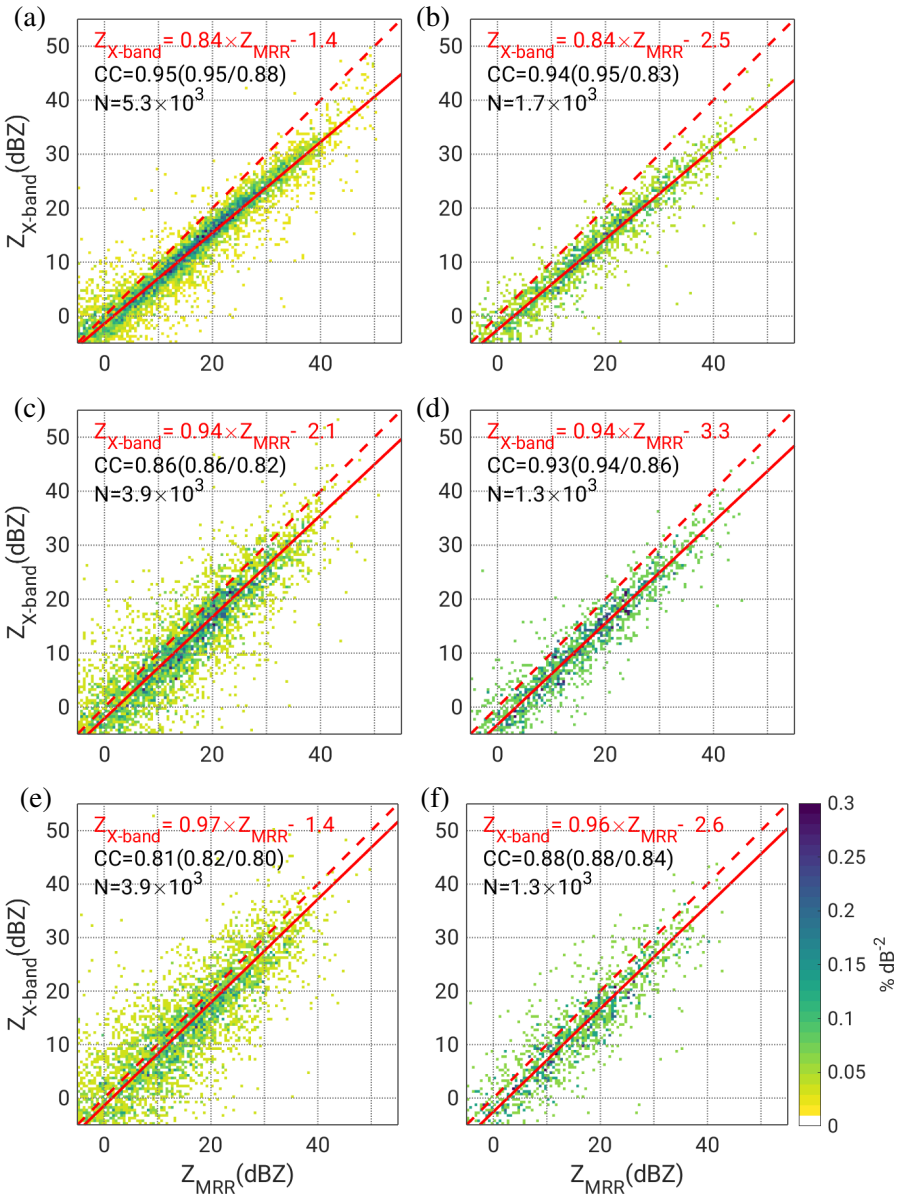

Fig. 5.24.: 2D-PDFs of instantaneous Z_H, where (a) is for the fine scan data at the 1.5° elevation from 23 May 2017 to 16 October 2017, (b) is the same as (a) but for the coarse scan, (c) is for the fine scan data at 3.6° elevation from 6 July 2017 to 16 October 2017, (d) is the same as (c) but for the coarse scan, (e) is for the fine scan data at the 6.2° elevation from 6 July 2017 to 16 October 2017, (f) is the same as (e) but for the coarse scan, *CC*s are CC_{PS}, CC_{SP} and *CCC* from the left to right, *N* is the number of paired data, the red solid lines are the orthogonal fitting curves, and the red dashed lines are the diagonal lines

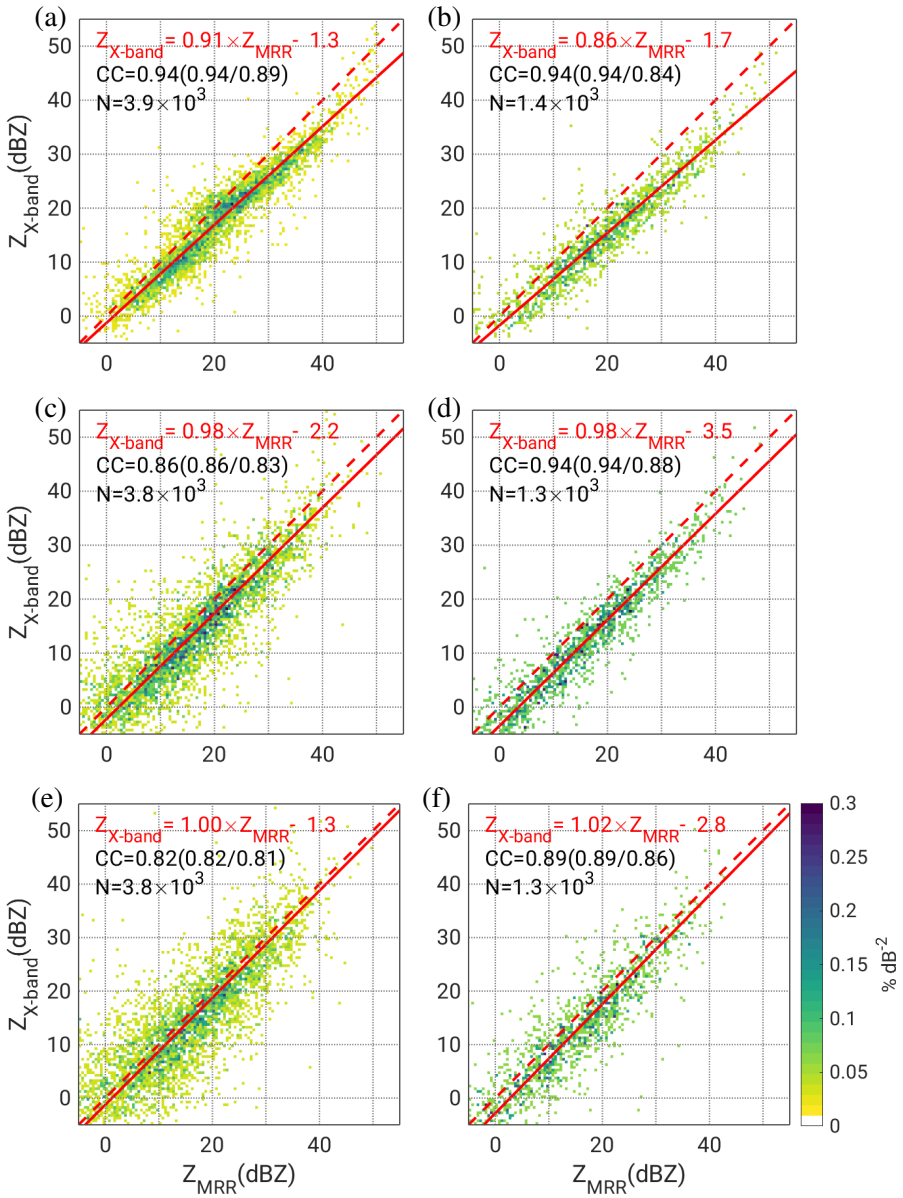

Fig. 5.25.: Same as Fig. 5.24, but in terms of the instantaneous Z_{H} applied with data QC procedures, including filtering spike signals, second-trip and non-meteorological echoes, correcting attenuation, but excluding the Z_{H} calibration

Then we look at the radar-MRR comparison in terms of instantaneous R converted from both the instantaneous Z_{MRR} and $Z_{X\text{-}band}$ measurements without any data QC procedures. $R_{X\text{-}band}$ of the X-band radar is estimated from Z_{H} using the Marshall-Palmer relation, but R_{MRR} is estimated using the other empirical relation specifically for the MRR (Section 3.2.2). For the 1.5° elevation, the linear correlation (inferred from CC_{PS}) between the X-band radar and MRR is stronger than that of the R-G comparison (recall Figs. 5.21(a) and 5.21(b)), but along with larger *AAD* and biases (Figs. 5.26(a) and 5.26(b)). As discussed, such stronger correlation is attributed to the coincident measuring manner in the radar-MRR comparisons. However, when it comes to the 3.6° and 6.2° elevations, CC_{PS} become lower than that of

the 1.5° elevation remarkably for the fine scan data and minimally for the coarse scan data, whereas CC_{SP} is greater than that of the 1.5° elevation, for both fine and coarse scans. It opposes the radar-MRR comparison in terms of Z_{H} where *CC*s of all three definitions decrease with the increasing elevations (recall Fig. 5.26). This contrast may be explained in two aspects. First, as discussed, the radar-MRR comparison in terms of Z weights Z in low intensity, while the radar-MRR comparison in terms of R weights R in large intensity. It means that, at the 3.6° and 6.2° elevations, the X-band radar data agrees linearly with the MRR measurement for the low Z_{H} or in light rain, but not for the high Z_{H} or in moderate-to-heavy rain. Meanwhile, the increasing CC_{PS} indicates, at the 3.6° and 6.2° elevations, the correlation between the X-band radar and MRR measurements inclines to be more non-linear. We may infer it is attributed to major changes in the DSD for hydrometeors at higher altitudes which invalidates the Marshall-Palmer Z-R relation for estimating R from radar measurements at higher altitudes. Thus, we ended with the diminishing CC_{PS} but increasing CC_{SP} for the radar-MRR comparison at the 3.6° and 6.2° elevations.

Besides *CC*s, the majority of scatterers for comparing R_{MRR} and $R_{X\text{-}band}$ fall below the diagonal lines, proving that the radar measurements are underestimated relative to their counterparts of MRR. An exception exists for the fine scan at 6.2° elevation, where the fitting line nearly overlaps the diagonal line, and scatterers are distributed more or less evenly in both sides of the diagonal lines. Other statistics (AAD, bias, rRMSE, *nB*) decrease with the increasing elevations. Such decreases are associated with an shrinkage in the absolute magnitude of R at higher altitudes. The falling raindrops undergo microphysical processes which modify DSD. Recall the definition of Z (Eq. 2.6) and the radar equation (Eq. 2.13). The magnitude of Z is proportional to the sixth power of D and thus is very sensitive to the large rain drops. Assuming the same precipitation intensity through the vertical extent, the precipitation at higher altitudes consist of a larger number of smaller raindrops in contrast to a smaller number of large raindrops at lower levels, so Z_{H} measured by the radar at higher altitudes is smaller, as well as $R_{\text{X-band}}$ estimated at higher altitudes. In brief, the decrease in the bias and AAD is due to an inherent vertical variability of precipitation.

If $R_{\text{X-band}}$ is estimated using Z_{H} data which are processed with all the data QC procedures except the Z_{H} calibration, the scatterers become closer to the diagonal lines, and the fitting curves get closer to the diagonal lines (Fig. 5.27), compared to the scenario without any data QC procedures (recall Fig. 5.26). The underestimation is still obvious for the 1.5° elevation, calling for the Z_{H} calibration. However, for both fine and coarse scan data at the 6.2° elevations, the fitting curves become above the diagonal lines, which means a negative ΔZ. It implies ΔZ are different for the radar data of different elevations.

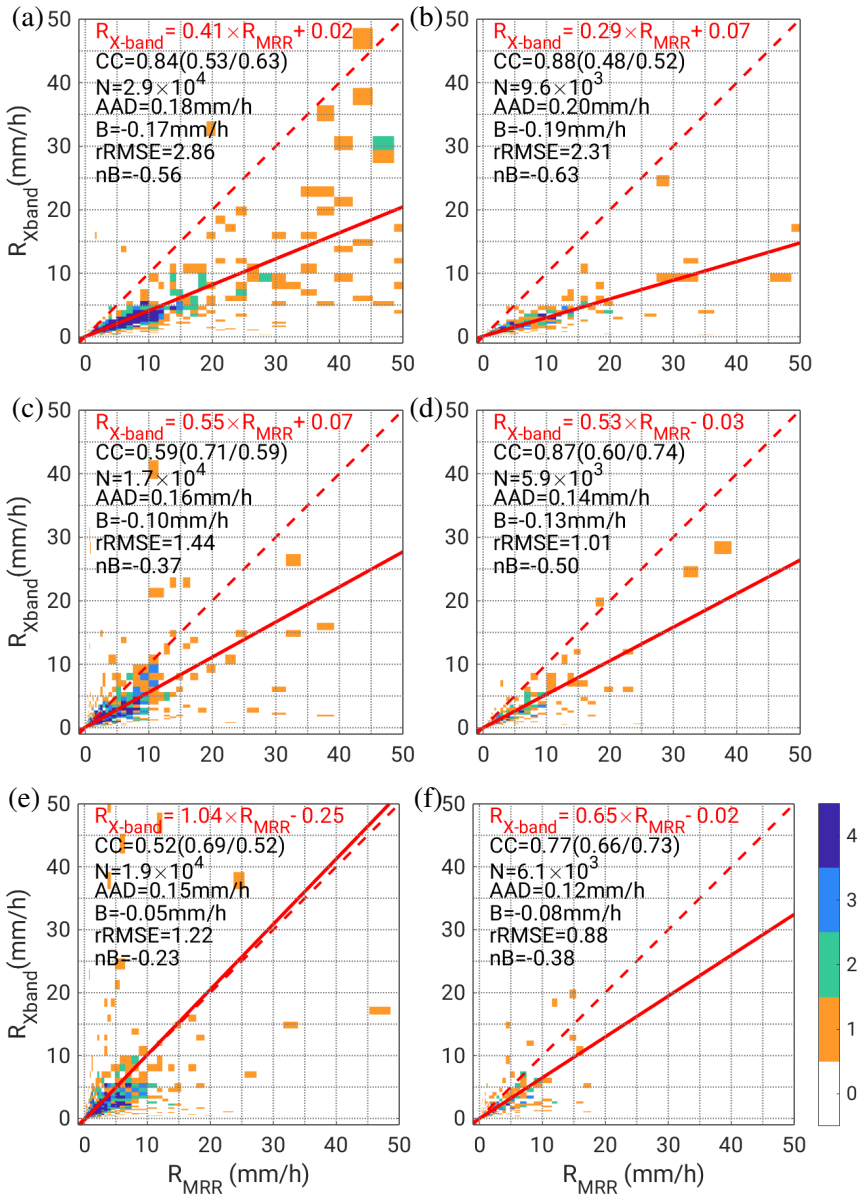

Fig. 5.26.: Similar to Fig. 5.24, but in the form of the absolute occurrence frequency of instantaneous rainfall rate (R) converted from the radar reflectivity (Z_{H}) through the Marshall-Palmer Z-R relation, where CCs from the left to right sides are the Pearson (CC_{PS}), Spearman (CC_{SP}), and Concordance (CCC) correlation coefficients

Besides the fitting curves, the data QC procedures bring a slight reduction on the bias AAD, rRMSE and nB, regardless of the elevations, for both fine scans or coarse scans. Unlike the foregoing R-G comparison, data QC procedures do not change (improve) the radar-MRR comparison significantly. A few reasons may explain it. First the second-trip and non-meteorological echoes primarily prevail at the lowest elevations (Section 4.3 and Section 4.5), and also the spike signal is also quite infrequent at the azimuthal direction of the MRR to the X-band radar (Fig. 4.4). It means, for the 3.6° and 6.2° elevations, the combination of several data QC procedures can be simplified as merely the attenuation correction

procedure. Second, given that the MRR is quite close to the X-band radar (only 10 km), the chance that moderate-to-heavy precipitation occurs at the space between MRR and the X-band radar is much less. Thus, the attenuation correction only modifies Z_H to a minor or moderate extent, so we did not see a tremendous improvement with the application of attenuation correction.

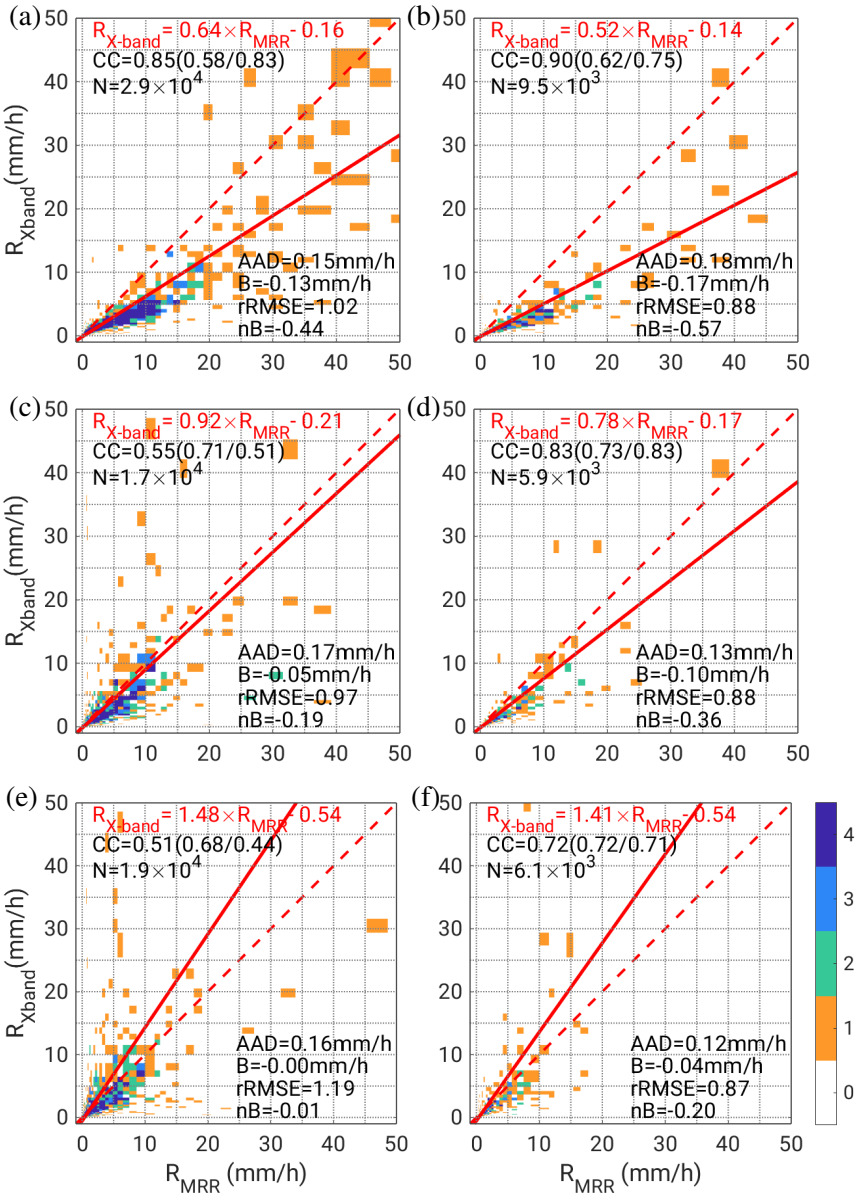

Fig. 5.27.: Same as Fig. 5.26, but in terms of instantaneous rainfall rate (R) estimated from the radar reflectivity (Z_H) applied with data QC procedures, including filtering spike signals, second-trip and non-meteorological echoes, and correcting attenuation

Comparing the statistics from radar data without data QC procedures with the statistics from radar data with data QC procedures shows the combination effect of filtering spike signals, second-trip and non-meteorological echoes, and correcting attenuation increases *CC*s and reduces biases (Tabs. 5.10 and 5.11). Unlike the R-G comparisons, the variation of the radar-MRR comparisons with elevations is

discussed. The difference in CC_{PS}s and biases with elevations shows Z_{H} measurements from the lowest elevation of the X-band radar correlate best with the MRR measurement, but present the largest biases before applying Z_{H} calibration.

Tab. 5.10.: *CC*s and bias for the instantaneous R-G comparisons using Z_{H} processed without data QC procedures

θ_e	Scan	Figs. in Z	B (mm)	CC_{PS}	Slope	CCC	Figs. in R	CC_{PS}	Slope	CCC
1.5°	Fine	5.26(a)	-0.17	0.84	0.41	0.63	5.24(a)	0.95	0.84	0.88
	Coarse	5.26(b)	-0.19	0.88	0.29	0.52	5.24(b)	0.94	0.84	0.83
3.6°	Fine	5.26(c)	-0.1	0.59	0.55	0.59	5.24(c)	0.86	0.94	0.82
	Coarse	5.26(d)	-0.13	0.87	0.53	0.74	5.24(d)	0.93	0.94	0.86
6.2°	Fine	5.26(e)	-0.05	0.52	1.04	0.52	5.24(e)	0.81	0.97	0.80
	Coarse	5.26(f)	-0.08	0.77	0.65	0.73	5.24(f)	0.88	0.96	0.84

Tab. 5.11.: *CC*s and bias for the instantaneous R-G comparisons using Z_{H} processed with data QC procedures

θ_e	Scan	Figs. in Z	B (mm)	CC_{PS}	Slope	CCC	Figs. in R	CC_{PS}	Slope	CCC
1.5°	Fine	5.27(a)	-0.13	0.85	0.64	0.83	5.25(a)	0.94	0.91	0.89
	Coarse	5.27(b)	-0.17	0.90	0.52	0.75	5.25(b)	0.94	0.86	0.84
3.6°	Fine	5.27(c)	-0.05	0.55	0.92	0.51	5.25(c)	0.86	0.98	0.83
	Coarse	5.27(d)	-0.1	0.83	0.78	0.83	5.25(d)	0.94	0.98	0.88
6.2°	Fine	5.27(e)	0	0.51	1.48	0.44	5.25(e)	0.82	1.0	0.81
	Coarse	5.27(f)	-0.04	0.72	1.41	0.71	5.25(f)	0.89	1.02	0.86

Radar-MRR hourly and daily comparison

Here we discuss the precipitation quantities on the hourly and daily scales. To make it short, we only present the results already being applied with data QC procedures except the Z_{H} calibration. Although its sample size of the paired data in terms of AR_{h} is much smaller than that of the instantaneous R, comparisons in terms of both R and AR_{h} share some similarity. For instance, the X-band radar data at the 1.5° elevation are still considerably underestimated in comparison with the coincident MRR measurements, and such underestimation diminishes for the 3.6° and 6.2° elevation with the scatterers closer to the diagonal lines (Fig. 5.28). However, the comparisons on hourly and instantaneous scales are different in other aspects. Since the hourly averaging cancels out the random variation and random errors in the measurements, *CC*s of all three definitions are larger than that using instantaneous R. Meanwhile, these correlations are also larger than their counterparts in the R-G comparison (recall Figs 5.21(f)). Thanks to the sampling strategies of both instruments and high temporal resolution of MRR, we are able to use the collocated and coincident measurements for the radar-MRR comparison, which accounts for this

improved correlation. Because the absolute magnitudes of AR_h and R are different, it is improper to compare AADs or biases directly. We can compare rRMSE and nB instead, and both are smaller on the hourly scale than those of the instantaneous scale.

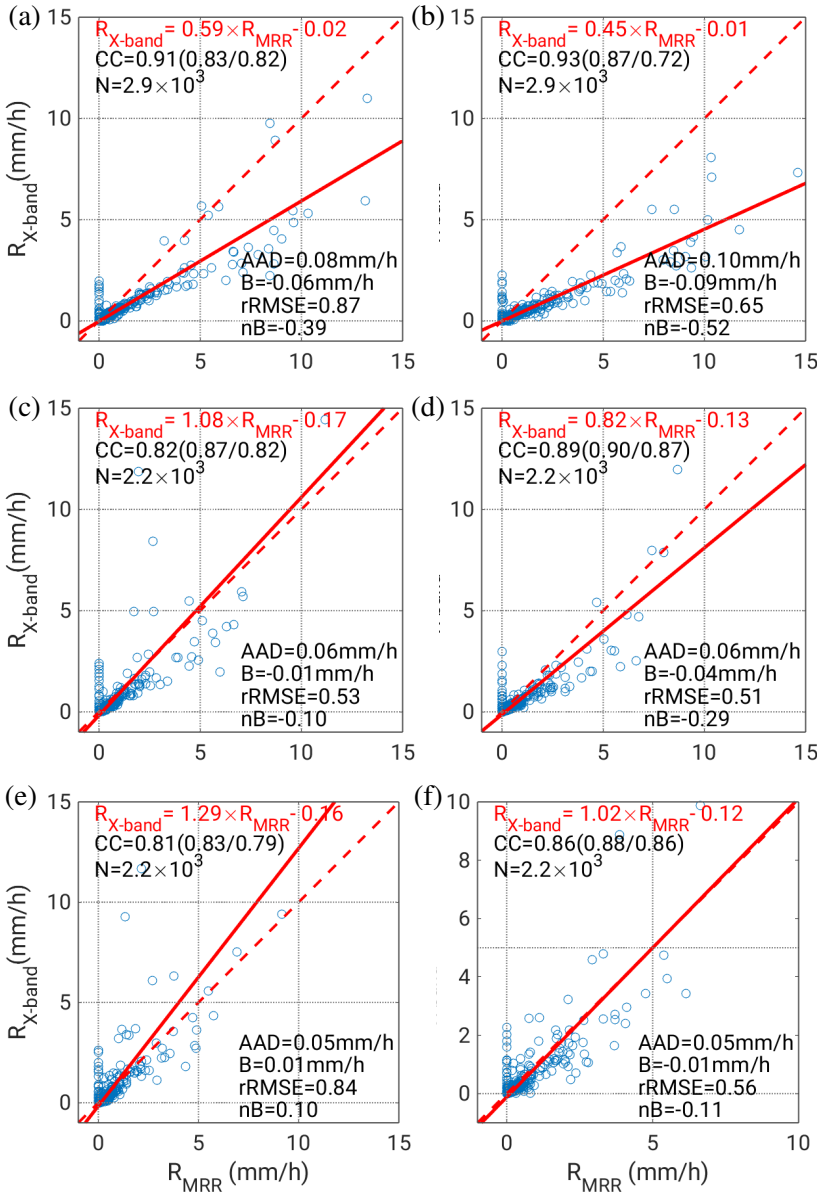

Fig. 5.28.: Scatter diagrams to compare the MRR and X-band radar data in terms of hourly mean rainfall rate calculated from the instantaneous rainfall rate (R) in Fig. 5.27; the meaning of other statistics are the same as Fig. 5.27, and also similar to Fig. 5.27; the radar data are applied with data QC procedures, including filtering spike signals, second-trip and non-meteorological echoes and correcting attenuation, the meaning of dashed red lines and solid red lines and other statistics (*CC*, *N*, AAD, *B*, rRMSE and *nB*) are the same as Fig. 5.26

Correlation between the X-band radar and MRR can be even more easily visualized for the radar-MRR comparison in terms of the equivalent mean $\overline{Z}$ with the data QC procedures. Besides the high *CC*s of all three definitions, all the fitting curves are characterized by the slope close to 45°(Fig. 5.29).

For each single elevation, the intercept of the fine scan is always roughly 1 dB less than that of the coarse scan, which agrees with ΔZ we obtain from the foregoing R-G comparison and ΔZ of fine scan data is always less than that of the coarse scan data. When compared to the radar-MRR comparison in terms of the instantaneous Z_{H}, *CC*s on the basis of the hourly equivalent Z_{H} at the 3.6° and 6.2° elevations are higher.

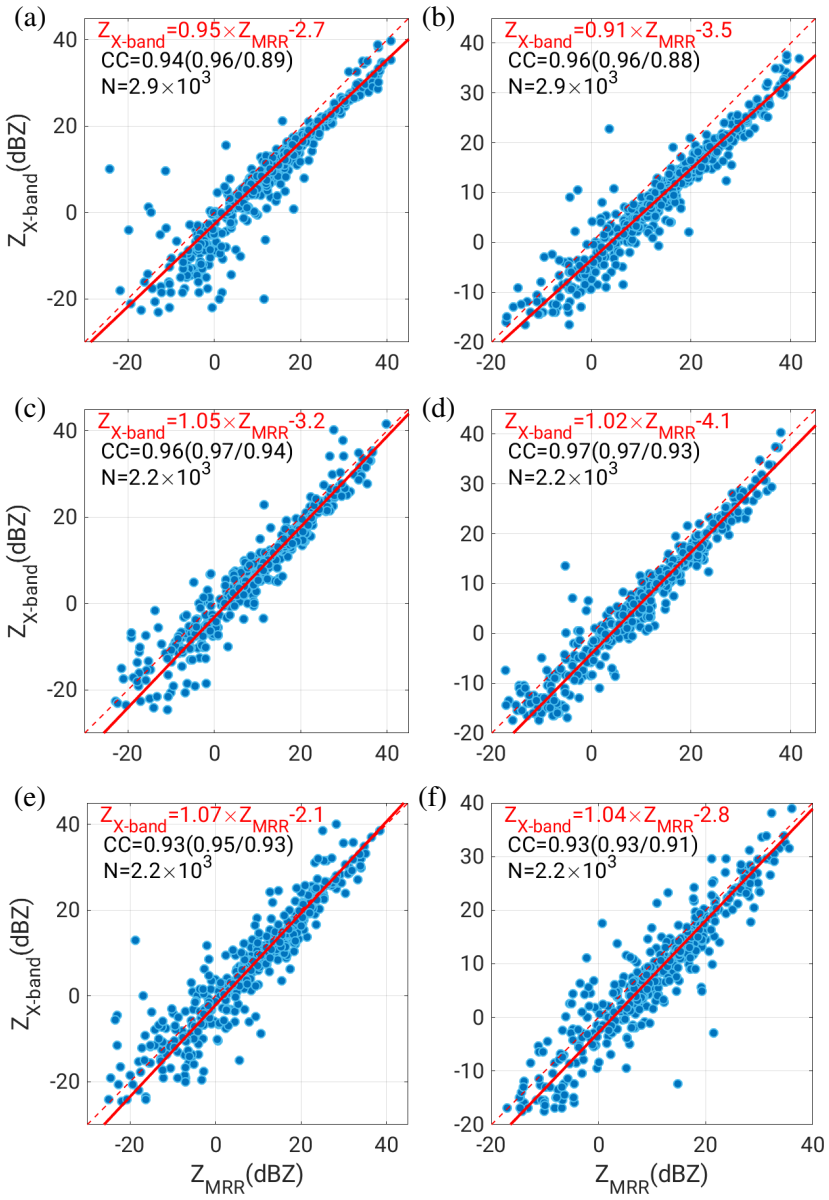

Fig. 5.29.: Same as Fig. 5.28, but in terms of hourly equivalent radar reflectivity (Z_e)

The results of the radar-MRR comparison in terms of AR_{d} resemble the results in terms of AR_{h}, such as the evident underestimations at the 1.5° elevation, and the moderate underestimations for the 3.6° elevation for the coarse scan, illustrated by relative positions of the fitting curve and diagonal lines (Fig. 5.30). However, a few minor differences still exist. With regard to AR_{h} , CC_{SP} decrease

slightly as the elevations increase (recall Fig. 5.28). In contrast, regarding AR_d, both CC_{SP} and CC_{PS} reach their maximum for the radar-MRR comparison at the lowest elevation, in which *CCC* falls to its minimum value. It implies that, the linear correlation between the radar and MRR is the tightest at the 1.5° elevation, but the closeness in terms of the *AR* magnitude is the least at this 1.5° elevation. The least closeness may be attributed to the beam blockage effect along the southwestern azimuthal directions, or is due to the Z_H miscalibration. With the increasing elevations from 1.5° to 6.2°, CC_{SP} decreases slightly and *CCC* increases slightly, and the minimum CC_{PS} occurs in the second lowest elevation.

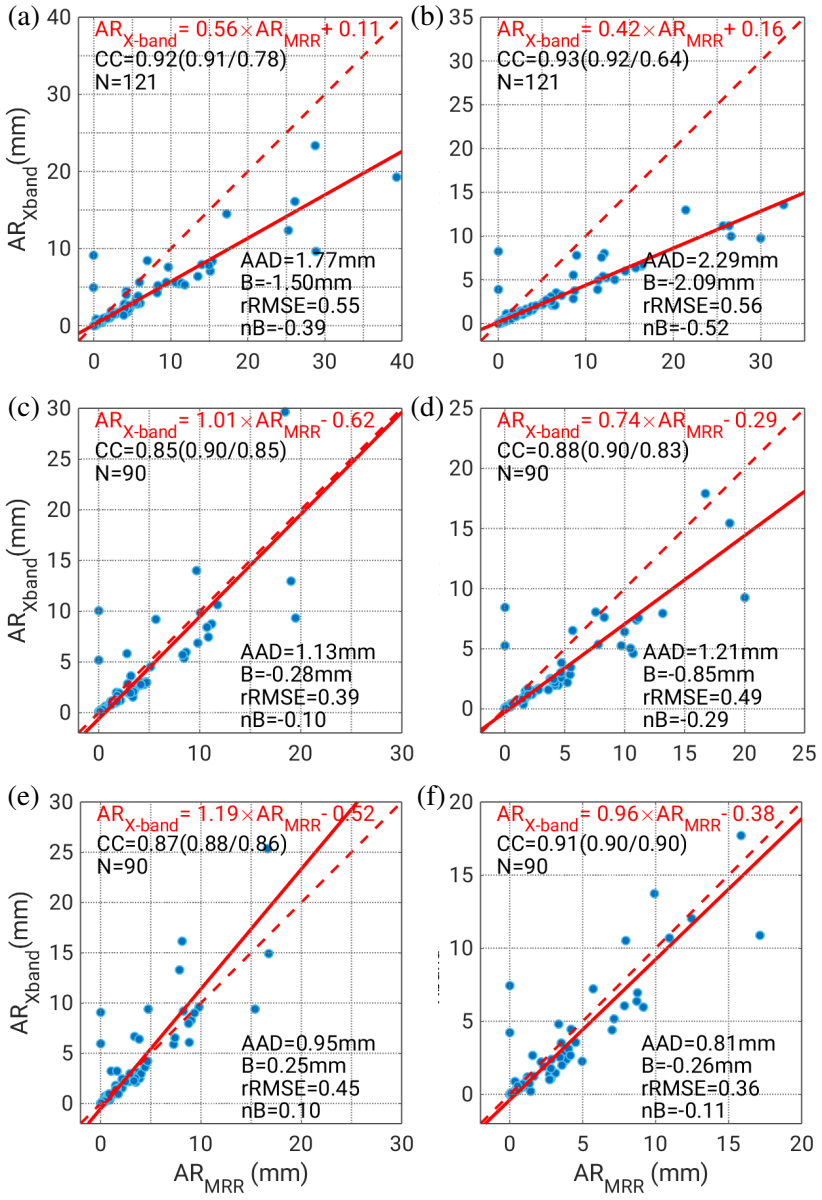

Fig. 5.30.: Similar to Fig. 5.28, but in terms of daily precipitation accumulation (*AR*)

When it comes to the equivalent Z_H converted from the daily average precipitation, the radar-MRR comparison exhibits high *CC*s of all three definitions, and the fitting curves with the slopes ap-

proaching 1 (Fig. 5.31). These *CC*s on daily scale are higher than those on the hourly scale (recall Fig. 5.29). Moreover, the intercepts of all the fitting curves are quite comparable around 3.5 dB, except 2.5 dB for the fine scan at the 1.5° elevation.

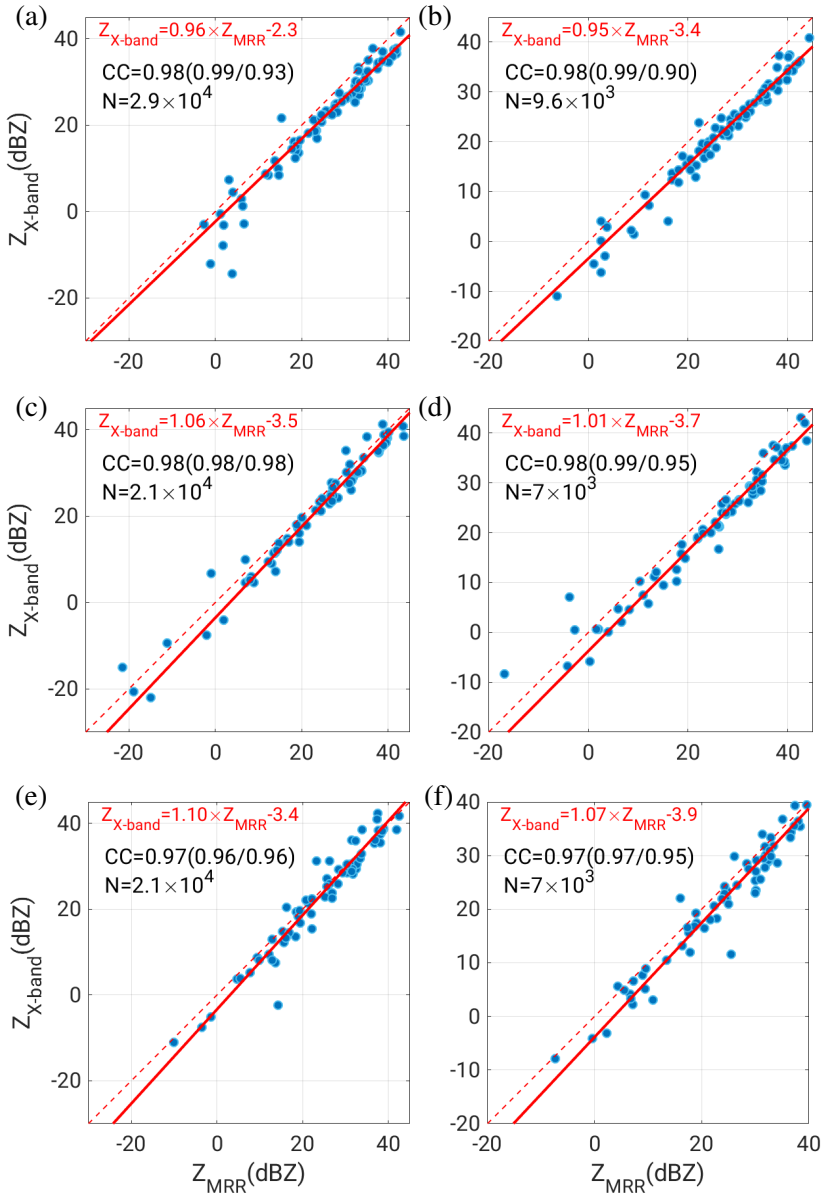

Fig. 5.31.: Same as Fig. 5.30, but for equivalent radar reflectivity Z_e converted from the daily averaged precipitation rate

Regarding the hourly time scale, at the 1.5° elevation, the radar-MRR comparisons (Tab. 5.12 present the larger biases than its counterpart in the R-G comparison (Tab. 5.9), but obviously higher CC_{PS}s before Z_{H} calibration. The beam blockage effect for the 1.5° elevation is the reason for these larger biases, and the biases become much smaller for the other two elevations.

Regarding the daily time scale, at the 1.5°, the radar-MRR comparison 5.13) also presents present the larger biases than its counterpart in the R-G comparison (Tab. 5.8), but obviously higher CC_{PS}s before Z_{H} calibration. Similar to the comparisons on the hourly time scale, absence of the beam blockage effect at the higher elevations reduces the biases.

Tab. 5.12.: *CC*s and biases for the hourly R-G comparisons using Z_{H} processed with different combinations of data QC procedures

θ_e	Scan	Figs. in Z	B (mm)	CC_{PS}	Slope	CCC	Figs. in R	CC_{PS}	Slope	CCC
1.5°	Fine	5.28(a)	-0.06	0.91	0.59	0.82	5.29(a)	0.94	0.95	0.89
	Coarse	5.28(b)	-0.09	0.93	0.45	0.72	5.29(b)	0.96	0.91	0.88
3.6°	Fine	5.28(c)	-0.01	0.82	1.08	0.82	5.29(c)	0.96	1.05	0.94
	Coarse	5.28(d)	-0.04	0.89	0.82	0.87	5.29(d)	0.97	1.02	0.93
6.2°	Fine	5.28(e)	0.01	0.81	1.29	0.79	5.29(e)	0.93	1.07	0.93
	Coarse	5.28(f)	-0.01	0.86	1.02	0.86	5.29(f)	0.93	1.04	0.91

Tab. 5.13.: *CC*s and bias for the daily R-G comparisons using Z_{H} processed with different combinations of data QC procedures

θ_e	Scan	Figs. in Z	B (mm)	CC_{PS}	Slope	CCC	Figs. in R	CC_{PS}	Slope	CCC
1.5°	Fine	5.30(a)	-1.5	0.92	0.56	0.78	5.31(a)	0.98	0.96	0.93
	Coarse	5.30(b)	-2.09	0.93	0.42	0.64	5.31(b)	0.98	0.95	0.9
3.6°	Fine	5.30(c)	-0.28	0.85	1.01	0.85	5.31(c)	0.98	1.06	0.98
	Coarse	5.30(d)	-0.85	0.88	0.74	0.83	5.31(d)	0.98	1.01	0.95
6.2°	Fine	5.30(e)	0.25	0.87	1.19	0.86	5.31(e)	0.97	1.10	0.96
	Coarse	5.30(f)	-0.26	0.91	0.96	0.90	5.31(f)	0.97	1.07	0.95

Analogous to the R-G comparisons in terms of AR_{t} in Section 5.2.1, we also total the precipitation accumulation over the entire period based on the MRR and X-band radar coincident dataset ($AR_{X\text{-}band}$ and AR_{MRR}). Comparing AR_{X-band} and AR_{MRR}, we obtain ΔZ for the data at each elevation for fine and coarse scans, respectively (Tab. 5.14). Unlike the hypothesis we made, according to the radar-MRR comparison, ΔZ_H are not consistent with a volume scan through the sweeps of different elevations. ΔZ are the largest at the lowest elevation (2 or 2.5 dB larger than that of the second lowest elevation). It contradicts our preliminary assumption that ΔZ obtained via the previous R-G comparisons replying on the radar data at the lowest elevation only can also be applicable to the radar data at other elevations. One explanation is the vertical variability in DSD and the associated invalid rainfall estimators (the Marshall-Palmer Z-R relation) at higher altitudes. Another factor is the potential partial beam blockage for the lowest elevation in the azimuthal directions of MRR to the X-bad radar (Fig. 3.2(b)). This partial beam blockage reduces the intensity of radar echoes, calling for a large positive ΔZ_H at the 1.5° elevation.

Tab. 5.14.: Radar reflectivity calibration factors $\Delta Z_H(dB)$ obtained from the X-band radar-MRR comparison

Elevation (°)	Fine (dB)	Coarse (dB)	Fine (atc) (dB)	Coarse (atc) (dB)
1.5°	5.0	6.5	3.5	4.5
3.6°	3.0	4.0	0.5	2.5
6.2°	3.0	3.0	0.5	1.0
R-G: 1.5°	4.5	5.5	2.0	3.0

Besides, according to this radar-MRR comparison, ΔZ_H for the coarse data is larger than that for the fine scan data. For instance, at the 1.5° elevation, ΔZ_H for the coarse scan data is 1 dB greater than that of the fine scan data, no matter whether the attenuation correction is applied or not, which is in good accord with the results from the R-G comparison, although the values of ΔZ_H from the radar-MRR comparison are slightly different from those of the R-G comparison. This difference might be caused by the miscalibration of the MRR instrument, or the effect of partial beam blockage along the azimuthal direction of MRR to the X-band radar.

5.2.3. Comparison between C- and X-band radar data

This section tackles a comparison between the C- and X-band radar measurements—the X-C comparison. The reasons for this additional comparison are as follow. First, unlike the previous R-G or radar-MRR comparisons in which MRR and rain gauges are characterized by completely different measuring principles from weather radars, the C- and X-band radars both adopt a similar measuring principle in general. Second, the previous R-G or radar-MRR comparisons are basically conducted over a limited number of spatially sparsely scattered radar gates, whose effective measuring areas are just a fraction of the total radar coverage area. In contrast, the direct comparison between the C- and X-band radar datasets are conducted over large areas. It involves a significant larger sample, and we expect the results should be more convincing and robust.

We compare C- and X-band radar measurements in three ways using the radar data, i) at direct intersections of the radar beams from C- and X-band radar, ii) of two case studies, iii) over the entire measuring period. The C-X comparison at intersections uses radar data at the original polar coordinate, where X-C comparisons of the other two ways are based on the radar data at the three-dimensional Cartesian coordinate. For the other two ways, since the C- and X-band radars are situated at different sites and have their own volume scans with different elevation angles, for the direct comparison, we need to interpolate both the C- and X-band radar data into the same polar coordinate. Given the radial resolution of C-band radar data is 500 m, the grid size for interpolation is 500 m$\times$500 m$\times$100 m, starting from the 1-km altitude above the radar site.

We don't process external QC procedure to the C-band radar data directly generated by the radar signal processor. To avoid potential data contaminations due to non-meteorological echoes, we omit the C-band radar data below 1 km above the radar site. To keep consistency, the X-band radar data within the 1-km height above the ground surface are also excluded. In this way, most non-meteorological echoes in the X-band radar dataset are already excluded, which eliminates the necessity of spike signal removal, second-trip echo and NMER. Regarding the attenuation in the C-band frequency, the ZPHI or iterative ZPHI attenuation correction (Section 4.6) can be performed to the C-band radar data. However, parameters in the attenuation correction procedure have to be changed if it is applied to the C-band rather than the X-band radar data, since the attenuation correction procedure is based on ϕ_{DP} measurement whose magnitude is frequency-dependent. Thus, the C-band data are without attenuation correction. Attenuation correction is a necessity to the X-band radar data, so the only data QC procedure applied to the X-band radar is the attenuation correction (Section 4.6).

C-X comparison at intersections of radar beams

Intersections of the radar beams of the C- and X-band radars are determined through the geographical matching-up (Fig. 5.23(b)). We exclude intersections above 3 km altitude to avoid contamination from bright-band and solid precipitation, and exclude intersections along the C-band radar beam at the 0.4° elevation to avoid ground clutters. Each single intersection has different distances to both radars, and at the same intersection, V_c along the X-band radar beam is much smaller than that of the C-band radar beam. To avoid the huge difference in the sampling volumes, we also exclude the intersection points whose sampling volume of the C-band radar beams is more than 20 times larger or smaller than the co-located sampling volume of the X-band radar beams. Most intersection points for the fine scans cannot satisfy this criterion, and thus we mainly focus on the comparison between the coarse scan data and the C-band radar data.

For each intersection, we obtain the paired dataset with Z_H from the C- and X-band radars. Since Z_H less than -5 dBZ is unlikely the precipitation echo, if we use -5 dBZ as the threshold to roughly separate precipitation and non-meteorological echoes, the paired data with both Z_H from C- and X-band radar below -5 dBZ occupy roughly 85% for this whole paired dataset, with both Z_H above -5 dBZ occupying 10%. The remaining 5% paired data correspond to the situation in which either Z_H of C-band radar is greater than -5 dBZ or Z_H of coarse scan data is larger than -5 dBZ. It implies, both Z_H measurements from C- and X-band radars agree well with each other about whether echoes are from precipitation or not during most of the time. When we compare the Z_H dataset from the C-band radar with the Z_H dataset from the X-band radar, if one of the radar datasets suffers great data quality issues, it is very likely that both radar datasets disagree with each other. Thus, the agreement does not only indicate a good accord between two datasets, but also implies both radar datasets are in good or at least acceptable data quality.

If we take the paired data with both Z_H greater than -5 dBZ into account only, the C- and X-band radar data (coarse scan) show a close agreement in terms of both Z_H and R over the selected intersections, illustrated by the high *CC*s and the overlap of the fitting lines with the diagonal lines for the comparison in terms of Z_H (Fig. 5.32(a)) and the near-zero bias for the comparison in terms of R (Fig. 5.32(b)). For the X-C comparison in terms of R, the reason for the slightly larger number of scatterers above diagonal lines might be due to the lack of attenuation correction in the C-band radar data.

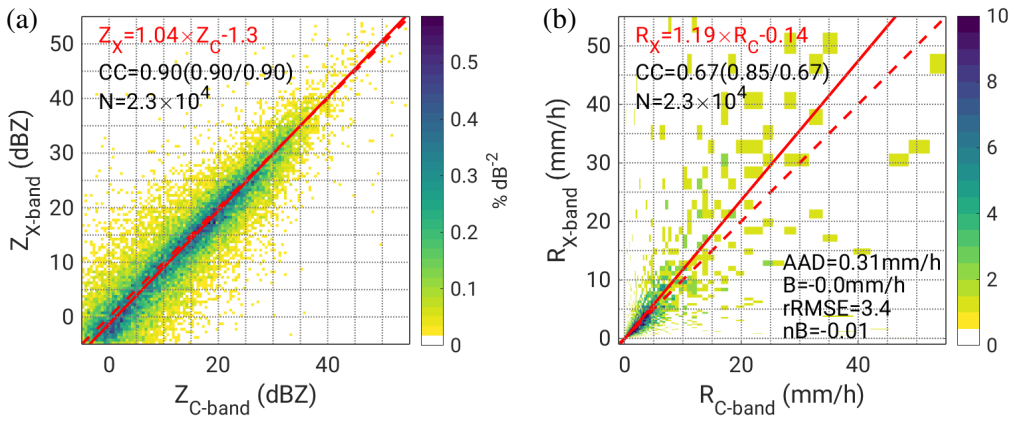

Fig. 5.32.: Comparison between the C- and X-band radar measurements at the intersection points of C- and X-band radar beams, where (a) is 2D-PDF of instantaneous radar reflectivity (Z_H); the meanings of the red lines and statistics are identical to Fig. 5.24, and (b) is the bivariate histogram of the absolute occurrence frequency of instantaneous rainfall rate (R) with orthogonal linear fitting; the meanings of the red lines and statistics are identical to Fig. 5.26

Case studies

We talk about two cases. The first case addresses measured instantaneous Z_H from single volume scans during the 5-minute interval, whereas the second case calculates $\overline{R}$ based on Z_H of multiple volume scans during the 100-minute period. The comparison based on the single volume scans is very likely to be affected by random variation.

The first case consists of several medium-sized convective cells in the southwestern direction of the X-band radar. Take gridded data at the 2.9-km altitude for example. The interpolated fine and coarse scan data after applying the data QC procedures resemble the C-band radar data well spatially (Fig. 5.33). The comparisons in terms of Z_H between both C- and X-band radar dataset, either the fine or coarse scan, present high *CC*s and fitting curves with 45° and small intercepts, for both fine and coarse scan data (Figs. 5.34(a) and 5.34(b)).

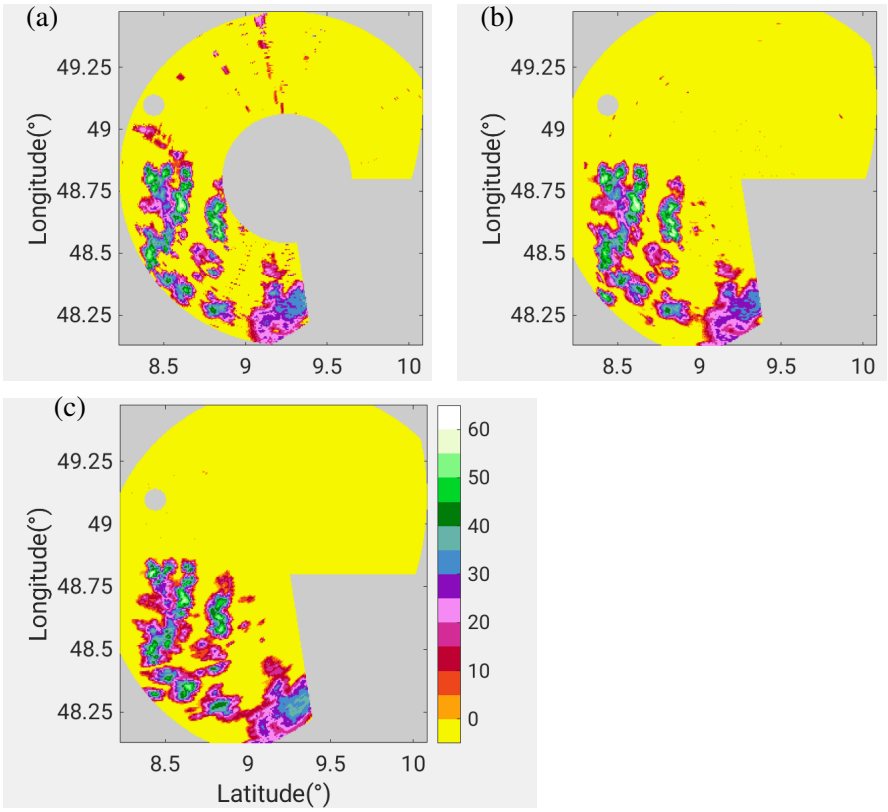

Fig. 5.33.: Interpolated gridded Z_H from (a) a fine scan at 13:23, (b) a coarse scan at 13:24 and a C-band radar scan at 13:25 UTC on 2 June 2017 at an altitude of 2.9 km above the ground surface

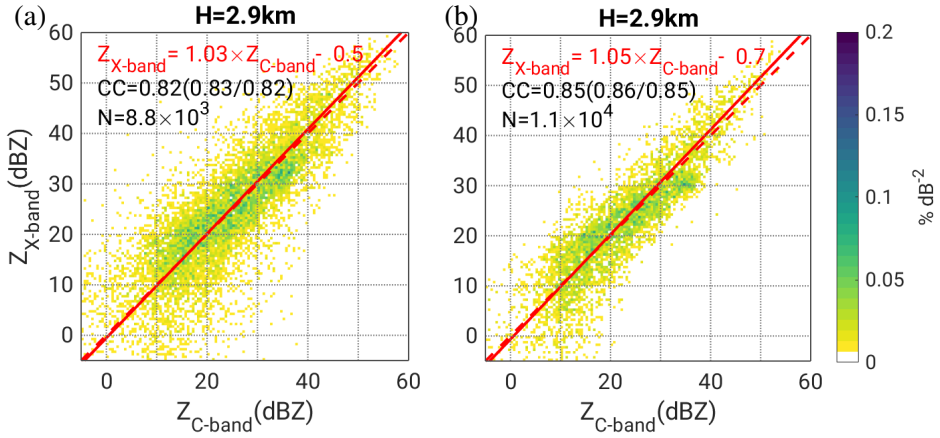

Fig. 5.34.: Comparison of instantaneous Z_H and R between C- and X-band radar dataset for the case of Fig. 5.33, where (a) and (b) are 2D-PDFs in terms of Z_H whose meanings of statistics and red lines are identical to Fig. 5.24

For the second case, also take the gridded data at the 2.9-km altitude for example. The spatial distribution of $\overline{R}$ calculated from the X-band Z_H of either the fine or coarse scans, greatly resemble that of the C-band radar data (Fig. 5.35). The blank circle in the fine scan is attributed to the lack of radar measurements at elevations above 6.2° in the fine scan. Both fine and coarse scan data are highly

correlated with the C-band radar data, and *CC*s of the coarse scans are higher than those of the fine scans (5.36(b)). From the aspect of rainfall rate R, similar to the case study discussed above, the lack of attenuation correction in the C-band radar data renders the precipitation rate estimated from the C-band radar dataset slightly lower than that of either the fine or coarse scan data. For other altitudes, *CC*s in the comparison between the fine scan data and the C-band radar data are lower than their counterpart between the coarse scan data and the C-band radar data. One possible explanation is the aforementioned lack of fine scan data at the higher elevations.

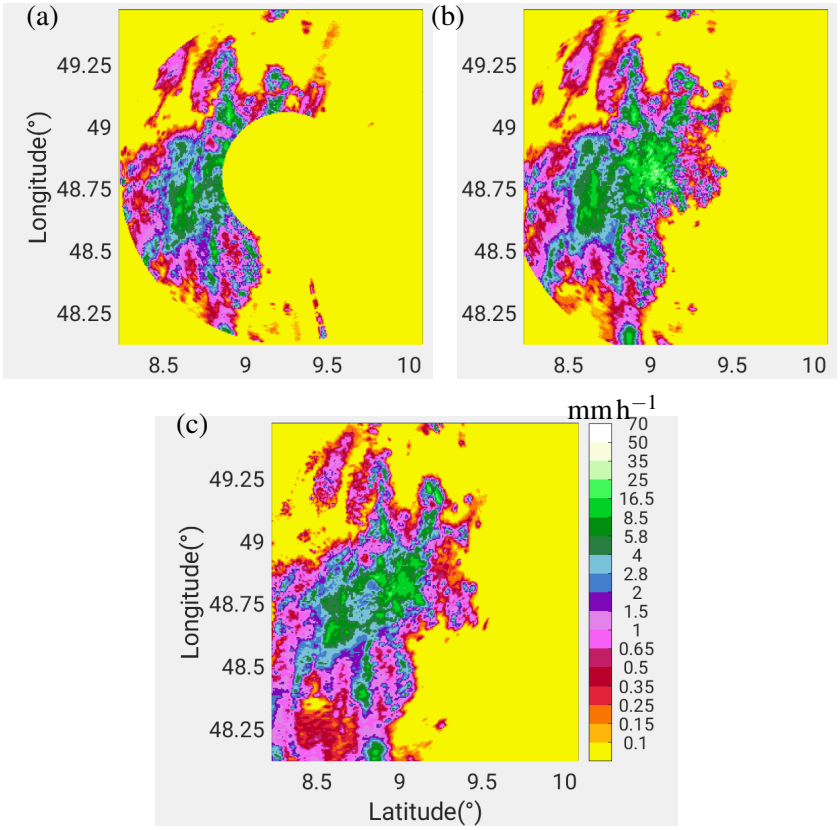

Fig. 5.35.: Interpolated gridded averaged rainfall rate (R) over a 100-minute convective episode from 23:10 UTC on 29 May to 00:49 UTC on 30 May 2017 at an altitude of 2.9 km above the ground surface estimated from radar reflectivity (Z_H) from the fine scan (panel (a)), coarse scan (panel (b)) and C-band (panel (c)) radar data respectively

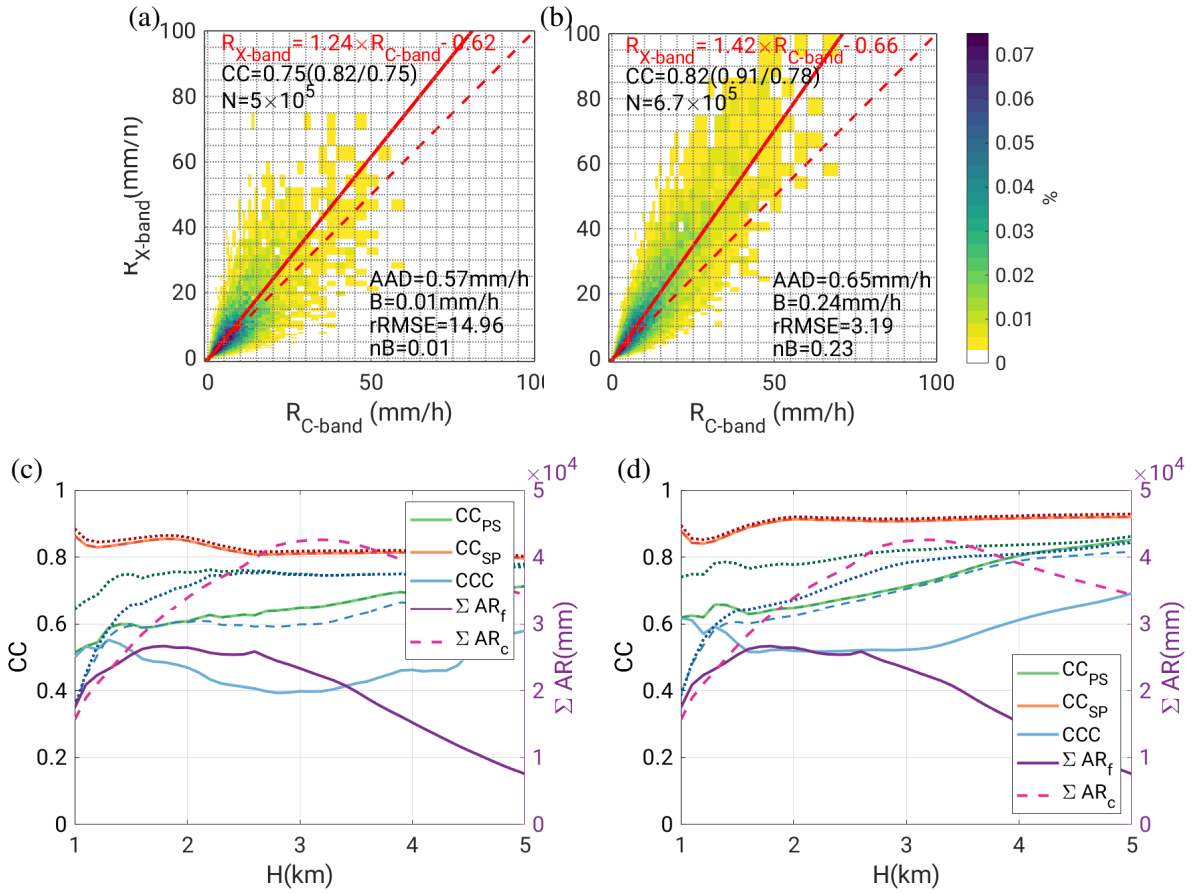

Fig. 5.36.: Similar to Fig. 5.34, but for the case in Fig. 5.35, and the violet solid lines and magenta dashed lines are the summation of 100-minute precipitation accumulation over all the interpolated gridded pixels at a 2.9 km altitude, the left (right) column is for the fine (coarse) scan data

Overall data

In terms of Z_H, the C-X comparison either for the fine or coarse scan shows high *CC*s and fitting curves in 45° inclination (Figs. 5.37(a) and 5.37(b)). Moreover, the intercept of the fitting curve for the fine scan is 1 dB less than that for the coarse scan, exactly agreeing with the calibration factors obtained from the previous R-G comparison. In contrast, in terms of R, the fitting curves are below the diagonal lines (Figs. 5.37(c) and 5.37(d)). One possible explanation is, as opposed to the comparison in terms of Z_H which excludes Z_H below -5 dBZ, the comparison in terms of R takes all the weak echoes in to account. Another possible reason lies in the inappropriateness of the Marshall-Palmer relation at the 1.7 km altitude.

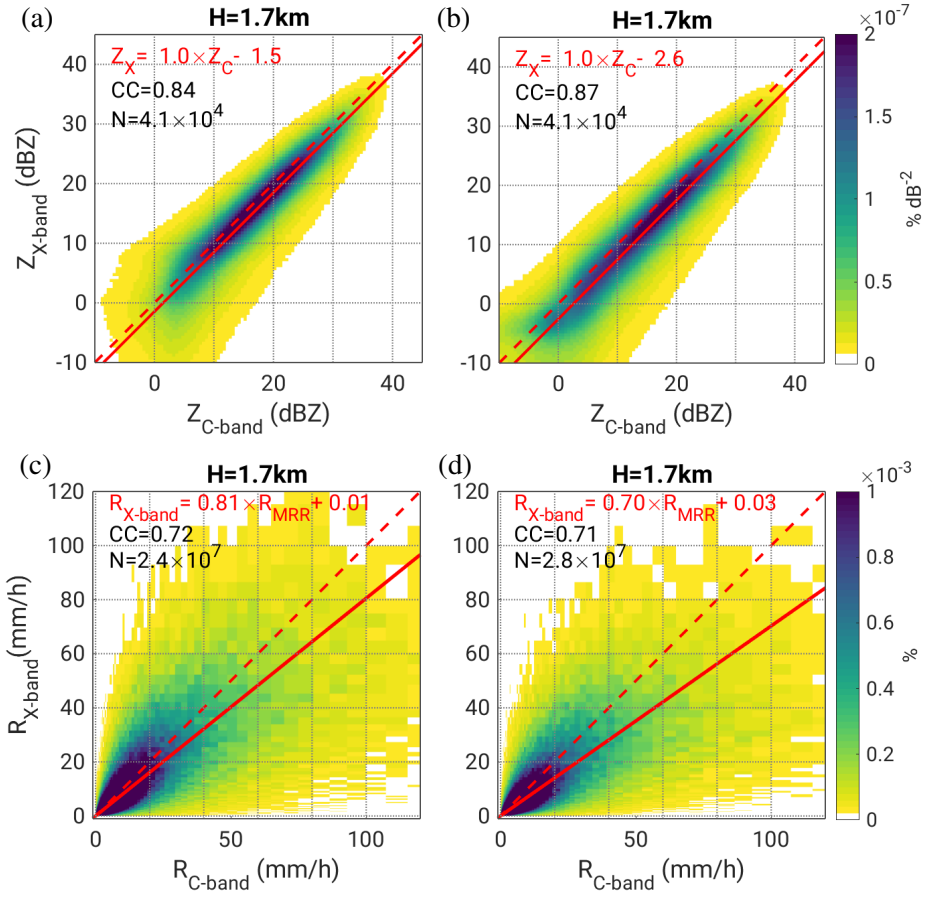

Fig. 5.37.: Comparison between the C- and X-band radar measurements over all the gridded data interpolated into the horizontal surfaces 1.7 km above the radar site, where (a) and (b) are 2D-PDF of instantaneous radar reflectivity (Z_H), the meanings of the red lines and statistics are identical to Fig. 5.24, and (c) and (d) are the bivariate histogram of the relative occurrence frequency of instantaneous rainfall rate (R) with orthogonal linear fitting, the meanings of the red lines and statistics are identical to Fig. 5.26

5.3. Precipitation estimation from fine and coarse scans

In addition to case studies of individual convective storms in Section 5.1, we are interested in the quantitative characteristics of precipitation quantities over longer time intervals, such as AR_t. Aligned with the research objective, we are concerned with what differences are between AR calculated using Z_H from the fine and coarse scan data respectively (AR_f and AR_c). Similar to the foregoing discussion on sensitivity of the R-G comparison to the radar data QC procedures (Section 5.2), we are also concerned with the sensitivity of these differences between AR_f and AR_c to each data QC procedure.

Given the different Δr between the fine and coarse scans, in order to quantify the difference between AR_f and AR_c, we interpolate the fine scan radar data into the same Δr as the coarse scan data and also interpolate the coarse scan data into the same Δr as the fine scan data (Section 3.1.5). The former interpolation is upscaling and the latter one is downscaling. The interpolation is done in terms

of R, which is on the linear scale and is calculated from Z_H using the Marshall-Palmer Z-R relation. We obtain R_{f2c} from the upscaling and R_{c2f} from the downscaling respectively. By integrating R_{f2c} and R_{c2f} over the total measuring period, we obtain AR based on the fine scan data but at the 250-m radial resolution—AR_{f2c} (Fig. 5.38(a)), and AR based on the coarse scan data but at the 75-m radial resolution—AR_{c2f} (Fig. 5.38(b)). After introducing $DAR = AR_{f2c} - AR_c$ or $DAR = AR_f - AR_{c2f}$, we analyze i) spatial distributions of positive or negative DARs, ii) how the magnitude of DARs changes with different data QC procedures. So far we have five data QC procedures available— removal of spike signals (Section 4.2), second-trip (Section 4.3) and non-meteorological echoes (Section 4.5), attenuation correction (Section 4.6) and Z_H calibration (Section 5.2).

Before applying these data QC procedures, AR_{f2c} primarily varies from 150 to 200 mm (Fig. 5.38(a)), in contrast to AR_c which primarily varies from 100 to 150 mm (Fig. 5.38(b)). Despite the loss of weak echoes in fine scans, AR_{f2c} is much larger than AR_c, especially at the farther range beyond 30 km (Fig. 5.38(c)). It means the contribution of the weak echoes to AR is negligible, and there should be other factors accounting for the greater magnitude of AR_{f2c}, and contributions of those factors to AR are much greater than the contribution of weak echoes to AR.

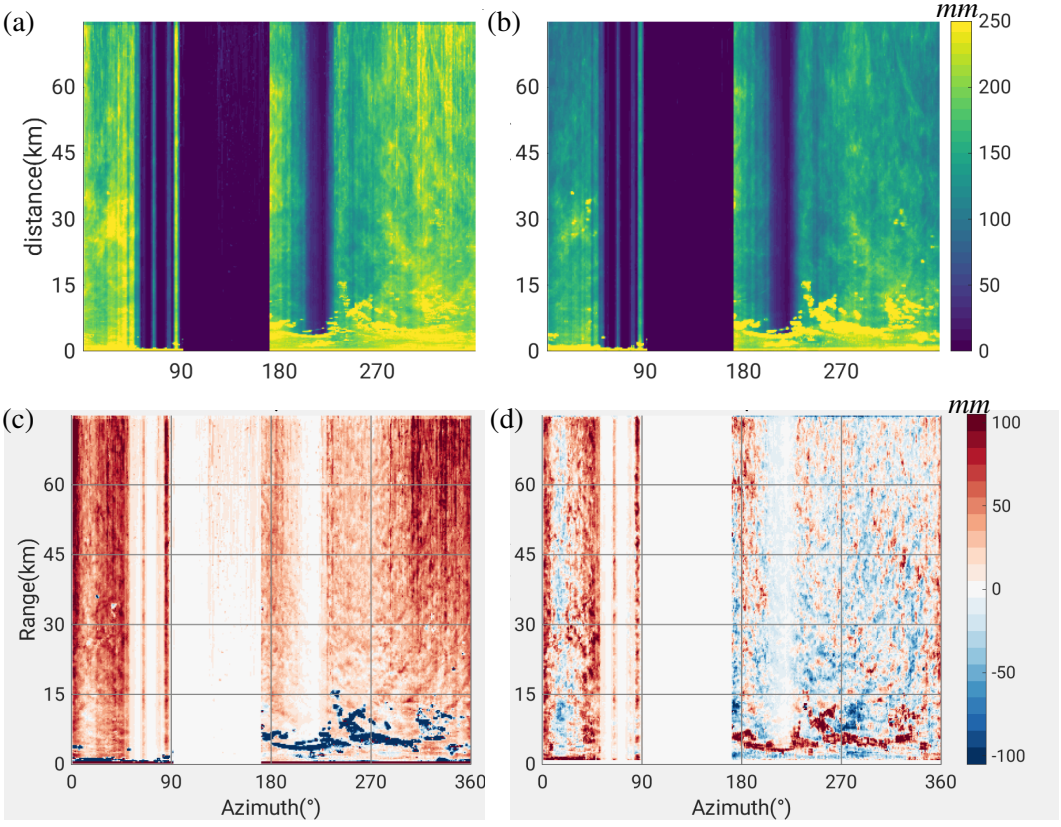

Fig. 5.38.: Azimuth-range sections of AR estimated from the fine (a) and coarse (b) scan data, DAR before (c) and after (d) processing data QC procedures

The radar data contaminated by GCs are usually characterized with high Z_{H}. Since the fine scan data are less subject to the GCs (Section 4.4), the GC gates usually exhibit higher AR_c rather than AR_f, and their locations can be easily discernible by negative *DAR* (Fig. 5.38(c)). Moreover, the absolute magnitude of *DAR* is much less between the azimuths of 180° and 300 degree, and even approaches zero between the azimuths of 200° and 225°(Fig. 5.38(c)). It is due to the partial blockage effect of radar beam caused by the terrain structures near the radar site (Fig.3.2), and this beam blockage effect is more severe between azimuths of 200° and 225°.

In principle, the precipitation amount falling into a certain region during a certain period of time should be unaffected by how instruments observe the precipitation. If both fine and coarse scans measure precipitation in a correct way, accumulating precipitation quantities over a 5-month period surely offsets any instantaneous or localized differences between AR_{f} and AR_{c}, and then *DAR* should be zero. A positive or negative *DAR* conflicts our assumption. The dominance of a positive *DAR* in Fig. 5.38(c) implies potential data quality issues for the base data processed by the radar signal processor only without external data QC procedures. The issues can be relevant to either or both fine and coarse scan data, which confirms the necessity of applying the data QC procedures discussed in Chapter 4.

After applying the all five data QC procedures, the dominance of positive *DAR* disappears, and the positive and negative *DAR* values spatially randomly alternate (Fig. 5.38(d)). Especially for the azimuths between 225° and 360°beyond 15 km away from the radar, the absolute magnitude of *DAR* varies below 30 mm. However, we also notice the obvious positive *DAR* remains between the azimuths from 0° to 7°, and from 35° to 55°, and the magnitude of these spatially continuous *DAR* is reduced after these data QC procedures.

The comparison of *DAR* patterns between before and after data QC procedures (Figs. 5.38(c) and 5.38(d)) proves that data QC procedures generally improve the reliability of the radar-based precipitation estimation. This is an accumulative effect of all the data QC procedures, however, the contribution of one individual step to the final precipitation estimation may be different from that of other steps. As follows, we compare AR_{f2c} with AR_c, both of which are at 250-m radial resolution, with or without one of the data QC procedures—the spike signal removal, the second-trip echo removal, the non-meteorological echoes filtering, the attenuation correction, the Z_{H} calibration—of their combinations to illustrate the effect of each individual data QC procedure on the radar estimation of precipitation (Tab. 5.15).

Tab. 5.15.: Combinations of data QC procedures to show sensitivity of DAR to the data QC procedures

Figs.	Spike signal removal	Second-trip echo removal	Non-meteorological echo removal	Attenuation correction	Z_H calibration
5.39(a), 5.45(a)	N	N	N	N	N
5.39(c)	Y	N	N	N	N
5.39(e)	Y	Y	N	N	N
5.39(b), 5.45(b)	N	N	N	Y	N
5.39(d), 5.45(c)	Y	N	N	Y	N
5.45(d)	N	Y	N	Y	N
5.39(f), 5.45(e)	Y	Y	N	Y	N
5.42(a)	Y	Y	NMER 1	N	N
5.42(c)	Y	Y	NMER 2	N	N
5.42(e)	N	N	MEER 3	N	N
5.42(b)	N	N	NMER 1	Y	N
5.42(d)	Y	N	NMER 2	Y	N
5.42(f), 5.45(f)	Y	Y	NMER 3	Y	N
5.38(d)	Y	Y	NMER 3	Y	Y

Tab. 5.16.: Combinations of data QC procedures to show sensitivity of DDAR to the data QC procedures

Figs.	Spike signal removal	Second-trip echo removal	Non-meteorological echo removal	Attenuation correction	Z_H calibration
Fig.5.40(a)	**N**	N	N	N	N
	Y	N	N	N	N
Fig.5.40(c)	**Y**	**N**	N	N	N
	N	**Y**	N	N	N
Fig.5.40(e)	N	**N**	N	N	N
	N	**Y**	N	N	N
Fig.5.40(b), 5.46(b)	**N**	N	Y	N	N
	Y	N	Y	N	N
Fig.5.40(d), 5.46(d)	**Y**	**N**	Y	N	N
	N	**Y**	Y	N	N
Fig.5.40(f), 5.46(c)	N	**N**	Y	N	N
	N	**Y**	Y	N	N
Fig.5.41(a), 5.46(a)	N	N	N	**N**	N
	N	N	N	**Y**	N
Fig.5.41(b)	Y	N	N	**N**	N
	Y	N	N	**Y**	N
Fig.5.41(c)	N	N	Y	**N**	N
	N	N	Y	**Y**	N
Fig.5.43(a)	Y	N	**NMER 1**	N	N
	Y	N	**NMER 2**	N	N
Fig.5.43(c)	Y	N	**NMER 2**	N	N
	Y	N	**NMER 3**	N	N
Fig.5.43(e)	Y	N	**NMER 1**	N	N
	Y	N	**NMER 3**	N	N
Fig.5.43(b)	Y	N	**NMER 1**	Y	N
	Y	N	**NMER 2**	Y	N
Fig.5.43(d), 5.46(f)	Y	N	**NMER 2**	Y	N
	Y	N	**NMER 3**	Y	N
Fig.5.43(f)	Y	N	**NMER 1**	Y	N
	Y	N	**NMER 3**	Y	N
Fig.5.46(e)	Y	N	**N**	Y	N
	Y	N	**NMER 3**	Y	N

Applying the spike signal removal reduces *DAR* either with or without attenuation correction (Fig. 5.39(c) or Fig. 5.39(d)), and this reduction is consistent with our discussion in Section 4.2 that the spike signals occur much more frequently in the fine scan data than those in the coarse scan data. The spike signals often appear with erratically high Z_H above 45 dBZ, introducing positive anomalies. Thus, this spike signal filtering procedure removes the unwanted data in the fine scans, and corrects the fine scan data to be closer to the coarse scan data, in terms of *AR*.

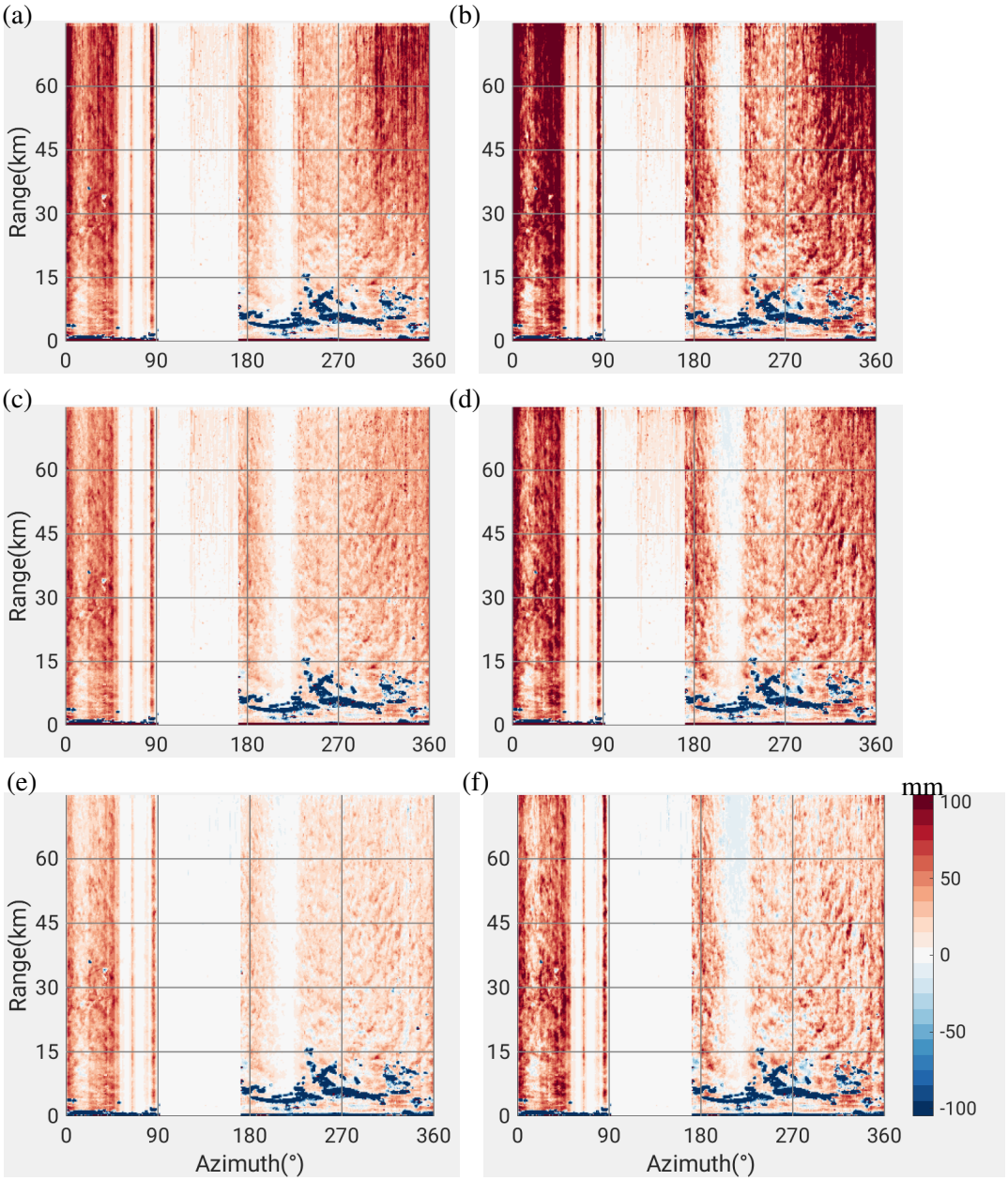

Fig. 5.39.: Azimuth-range section of *DAR*, (a), (c) and (e) are for radar data without attenuation correction, (b), (d) and (f) are for radar data with attenuation correction, (a) and (b) are for radar data without any filtering, (c) and (d) for the radar data after filtering spike signals, and (e) and (f) are for the radar data after filtering the second-trip echoes and the majority of spike signals

Applying the second-trip echo removal also reduces *DAR* (Fig. 5.39(e) or Fig. 5.39(f)). Similar to the spike signal removal above, filtering out the second-trip echoes removes these unwanted "extra" fake precipitation as well. For this X-band radar dataset, the second trip echoes prevail only in the fine scan data. As mentioned in Section.4.3, the second-trip echo filtering adopted in our research also automatically remove the majority of spike echoes, which leads to smaller magnitudes in *DAR* values after applying the second-trip echo removal only than those after filtering spike signals only.

In order to quantitatively compare changes in *DAR* under the conditions of different data QC procedures, we define a term as as *DDAR*, referring to the difference between two *DARs* which use different data QC procedures. For instance, if the scenarios without and with spike filtering are defined as scenario 1 and scenario 2, respectively, then $DDAR_{1,2} = (DAR)_2 - (DAR)_1$ quantitatively presents the magnitude of fake precipitation estimates associated with the spike signals (either Fig. 5.40(a) or Fig. 5.40(b)). Similarly, for instance, if the scenarios without and with second-trip echoes filtering are defined as scenario 1 and scenario 3, respectively, $DDAR_{1,3} = (DAR)_3 - (DAR)_1$ quantitatively presents the magnitude of fake precipitation estimates associated with a combination of the second-trip echoes and the majority of spike signals (either Fig. 5.40(e) or Fig. 5.40(f)). The pure effect of second-trip echoes can be seen by comparing the scenario 2 and scenario 3 (either Fig. 5.40(c) or Fig. 5.40(d)). Obviously, the second-trip echoes account a smaller proportion for the difference between fine and coarse scans, compared to the spike signals, in terms of precipitation accumulation amount, for the data either without attenuation correction (Fig. 5.40(a)) or with attenuation correction (Fig. 5.40(c)). Although the occurrence frequency of the second-trip echoes is much higher than that of the spike signals (Figs. 4.4 and 4.14), the spike signal filtering takes a slightly more important role in correcting the magnitudes of precipitation estimation for the fine scan. The reason is that the majority of second-trip echoes are weak in intensity, and contribute marginally to magntiudes of the rainfall accumulation, whereas a large portion of spike signals is characterized by high Z_{H} along with moderate or heavy "fake" precipitation.

The attenuation correction also influences the magnitude of DARs; differences in *AR* between fine and coarse scan become more remarkable after correcting attenuation (Fig. 5.39). The magnitude of such increased DARs is related to other data QC procedures. For instance, if the radar data without and with attenuation correction are defined as scenario 4 and 5 respectively, $DDAR_{4,5} = (DAR)_5 - (DAR)_4$ quantitatively presents extra difference between fine and coarse scans caused by the attenuation correction procedure (Fig. 5.41). *DDAR* is the largest for the radar data without any filtering, becomes smaller when the spike signals are filtered, and even shrinks when further applying the second-trip echo removal. This gradual shrinkage reflects why the attenuation correction enlarges *DAR*. In practice, we applied the attenuation correction in prior to the spike signal and second-trip echo filtering. Without filtering out noise, the attenuation correction algorithm treats all the noise equally as the precipitation echoes, and the corrected Z_{H} values are also added to these noises, accounting for the larger difference between fine and coarse scan resulting from the attenuation correction.

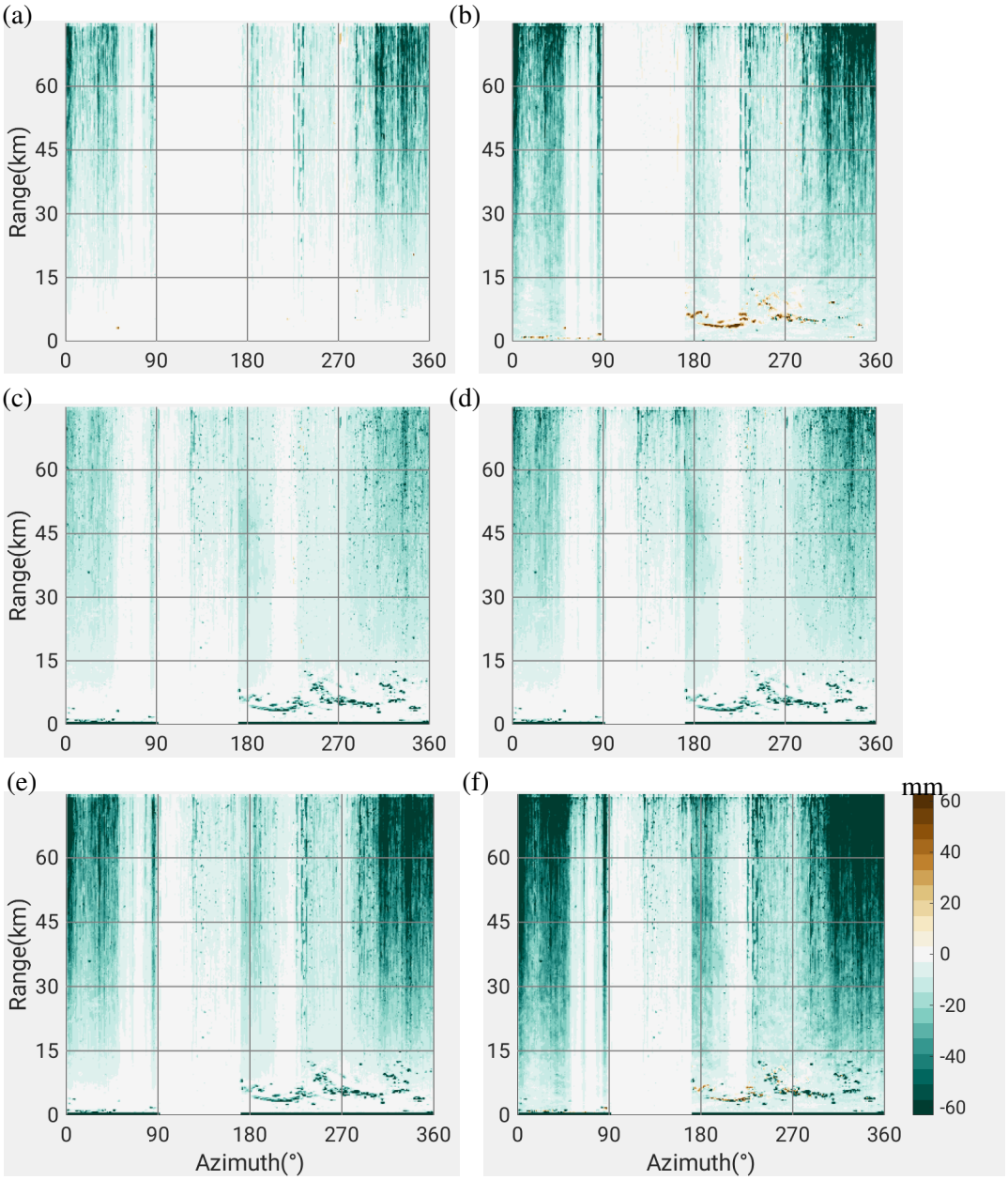

Fig. 5.40.: Azimuth-range section of *DDAR*, (a), (c) and (e) are for the radar data without attenuation correction, (b), (d) and (f) are for the radar data with attenuation correction, (a) and (b) compare *DAR* based on the radar data with and without spike echoes filtering, (c) and (d) compare *DAR* based on the radar data with spike signal removal or with second-trip echo removal, and (e) and (f) compare *DAR* based on the radar data with and without second-trip echoes removal

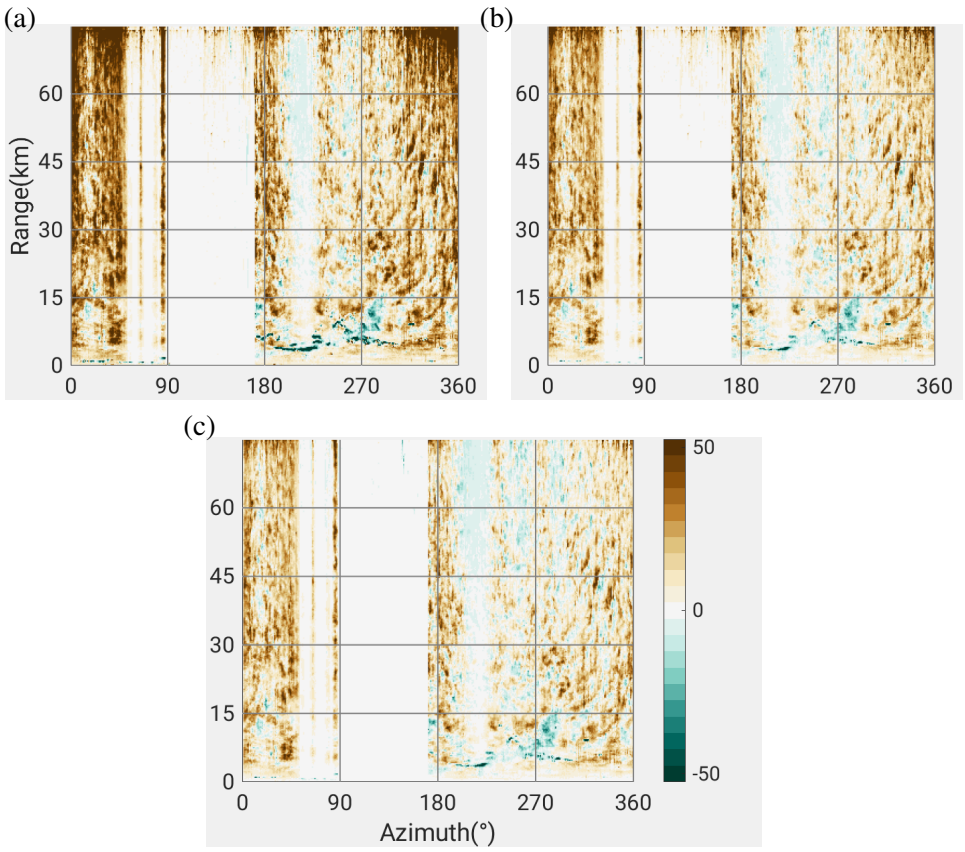

Fig. 5.41.: Azimuth-range section of *DDAR*, the difference between *DAR* using radar data without or with attenuation correction, where (a) compares the radar data without any filtering, (b) is for the radar data with spike echoes removal only, and (c) is for the radar data with second-trip echoes removal

The non-meteorological echoes (including GCs) removal (NMER) can be achieved through three methods: the retrievability of K_{DP} either prior to or after removals of the spike signals and second-trip echoes, or through the fuzzy logic classification based on polarimetric variables and their texture parameters (Section 4.5). The third method presents the largest *DAR* (Fig. 5.42(e)). *DARs* from the first and second methods are quite similar, but both show range dependence — *DAR*s diminish as the radar gates become farther from the radar. Such a range dependence is unexpected and undesirable. Besides, a small number of radar gates contaminated by GCs remain if the first and second NMER approaches are used, while the third NMER method is able to completely remove data contaminated by GCs. Lack of range-dependence and successful removals of GCs imply that the third NMER method is more robust and reasonable than the other two NMER methods.

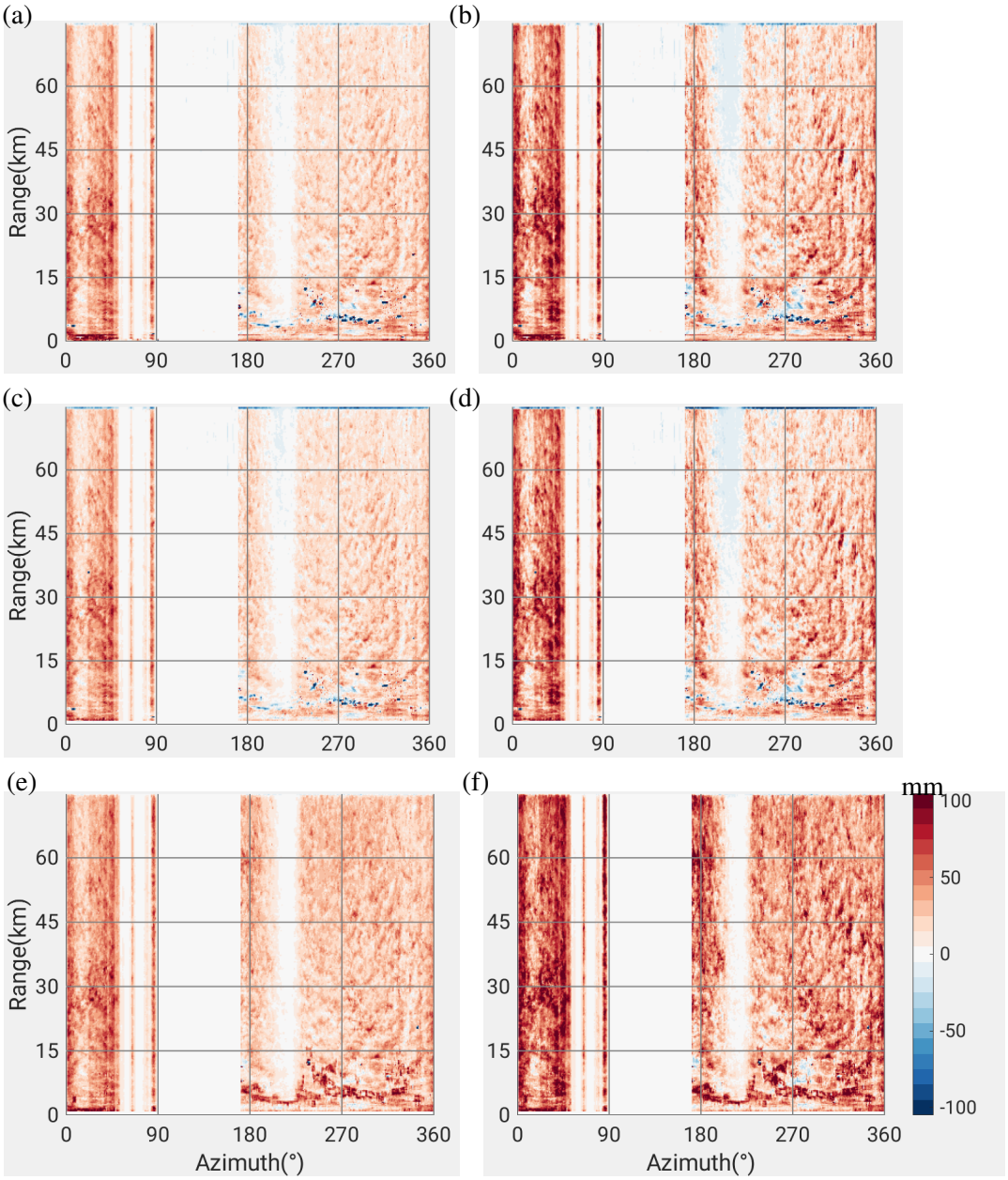

Fig. 5.42.: Azimuth-range section of *DAR*, (a), (b) and (c) are for the radar data without attenuation correction, (b), (d) and (f) are for the radar data after attenuation correction, (a) and (b) are for the radar data applying spike signal and 2nd-trip echo filtering after NMER, (c) and (d) are for the radar data applying spike signal and 2nd-trip echo filtering in prior to NMER, (e) and (f) are for the radar data applying the fuzzy logic polarimetric NMER

The term *DDAR* is defined again in order to quantitatively show the magnitude of *DAR*s with different NMER methods. If the scenario with the first, the second and the third NMER methods are defined as scenarios 6, 7 and 8, respectively, then $DDAR_{6,7} = (DAR)_7 - (DAR)_6$ quantitatively presents the differences in *DAR* caused by using the first or second NMER methods (either Fig. 5.43(a) or Fig. 5.43(b)). Similarly, $DDAR_{7,8} = (DAR)_8 - (DAR)_7$ defines the difference in DAR between us-

ing the first and third NMER methods (Fig. 5.43(c) and 5.43(d)), and $DDAR_{6,8} = (DAR)_8 - (DAR)_6$ defines the difference in DAR between using the first and third NMER methods (Fig. 5.43(e)), and 5.43(f). The first and second NMER methods are nearly identical except a few radar gates in proximity to the GCs, which means that it makes almost no difference whether removing the spike signal and second-trip echoes filtering before or after the NMER. In contrast, *DAR*s of the third NMER method differ greatly from those of other two methods. This third NMER method brings about a more noticeable difference between the fine and coarse scan. As demonstrated in Section 4.5, the fuzzy logic NMER exhibits different performances between the fine and coarse scans, explaining the large magnitude of $DDAR_{6,8} = (DAR)_8 - (DAR)_6$. Since $(DAR)_8$ is not range-dependent but $(DAR)_7$ is range-dependent, $DDAR_{7,8}$ shows the range-dependent pattern (Fig. 5.43(c) and 5.43(d)). Moreover, *DDAR* is greater if the attenuation correction is applied to Z_H. Besides, *DDAR* is positively large around the radar gates located near the GCs in contrast to GC radar gates delineated by negative *DAR* in (Fig. 5.39). Given that *DAR* values are negative over these GCs, the positive $DDAR = (DAR)_8 - (DAR)_6$ means the magnitude of $(DAR)_8$ is less than that of $(DAR)_6$ over these GCs. It means the third NMER method is capable of getting grid of the GCs, while the other two methods are less capable than the third NMER method, which accounts for such distinct *DDAR*s in Fig. 5.43(c).

DAR is still not reduced to zero for the radar data after removing the spike signals, second-trip echoes, non-meteorological echoes and correcting attenuation. Another factor that has not been discussed in Chapter 4 but is also associated with radar data quality is the Z_H calibration. Because of the difference in τ for the fine and coarse scans, Z_H can be miscalibrated differently. ΔZ obtained from Section 5.2 confirms the different calibration factors for both fine and coarse scans. As discussed in Section 5.2, ΔZ are $+2\,dB$ and +3.5 dB for the fine and coarse scans respectively. After taking ΔZ into consideration, *DAR* is minimized (Fig. 5.38(d)) and we ended up with *AR* comparable for the fine and coarse scan data.

The PPI displays are also shown to see the spatial distribution of improvements to the precipitation estimation after the radar data are applied with the data QC procedures (Fig. 5.44). Comparing *DAR* without and with data QC procedures indicates that noise in the radar data, regardless of spike signals or second-trip echoes, tends to obscure the true precipitation information. Only after successfully eliminating the noise can the radar-based precipitation estimation be reliable. However, *AR*s from the fine and coarse scans are still not comparable in two azimuthal sectors in the north and northeast directions. Besides, in the south direction beyond 50 km away from the radar, a moderately positive area prevails. It corresponds to the Black Forest region which is renowned for its high altitude, and consequent ampler precipitation and higher frequency of heavy precipitation compared to other regions. Chances are that DSDs in the Black Forest may differ from those of other regions, and then the Marshall-Palmer Z-R relation is inappropriate, resulting in the deviations in the Z_H-based precipitation estimates.

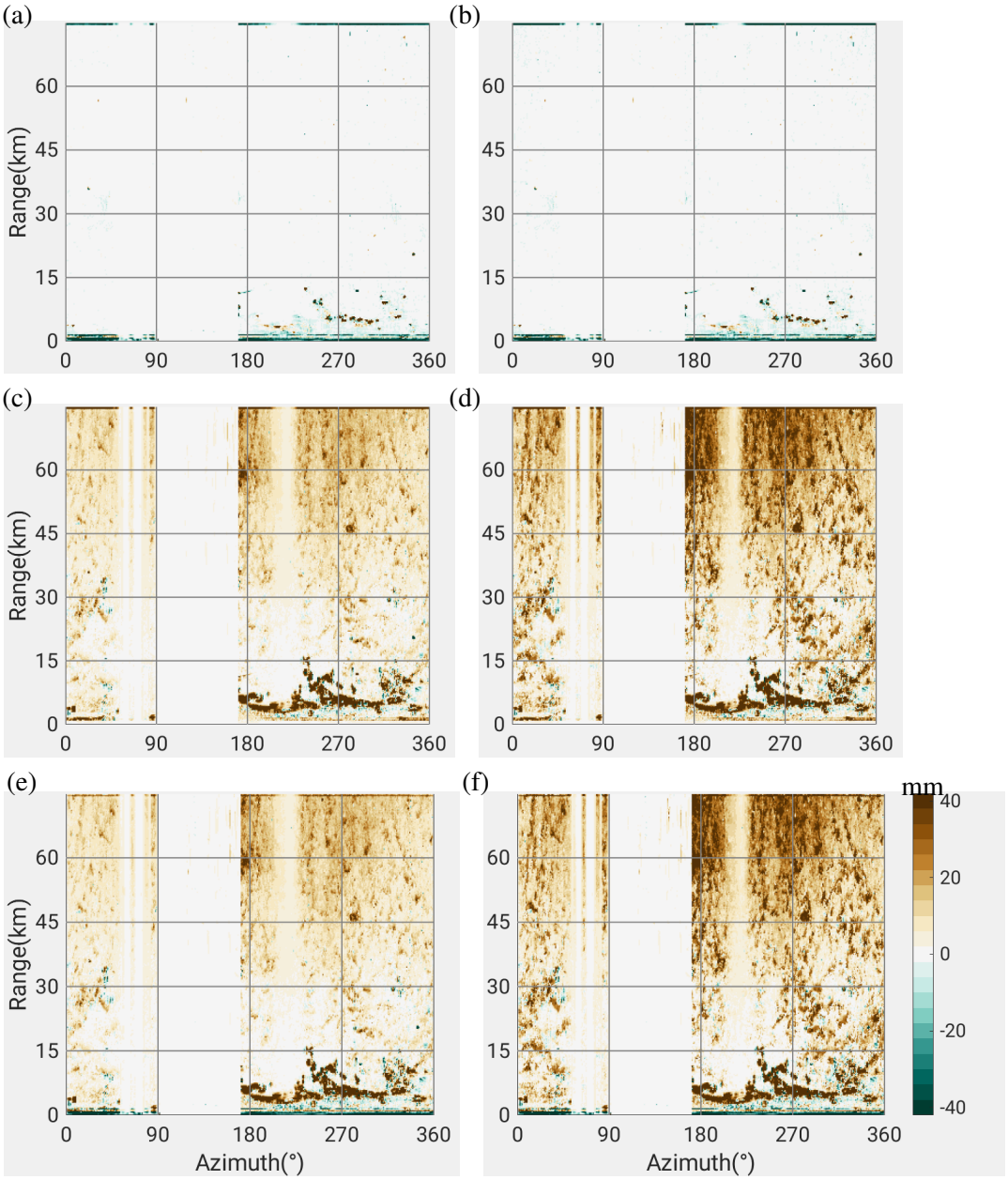

Fig. 5.43.: Azimuth-range section of *DDAR*, (a), (b) and (c) are for the radar data without attenuation correction, (b), (d) and (f) are for the radar data after attenuation correction, (a) and (b) compare the radar data with the NMER methods 1 and 2, (c) and (d) are for the radar data with the NMER methods 2 and 3, (e) and (f) are for the radar data with the NMER methods 1 and 3

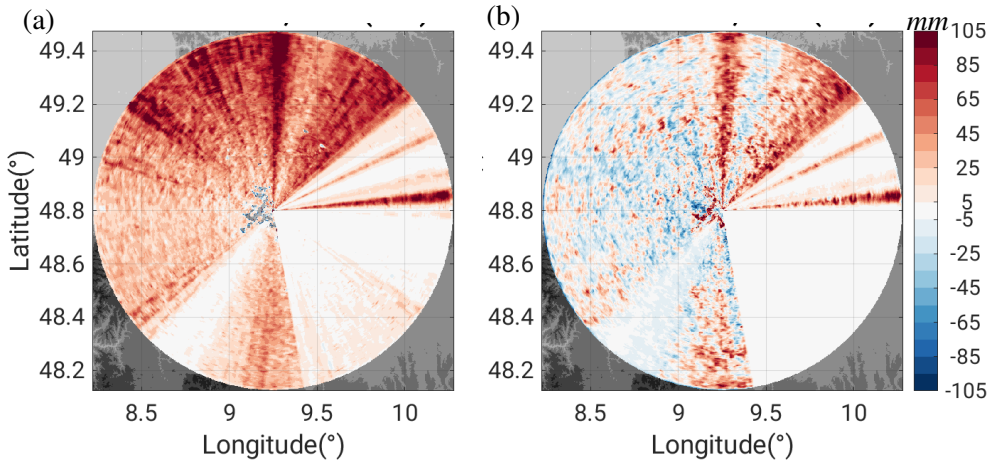

Fig. 5.44.: PPI displays corresponding to (c) and (d) in Fig. 5.38

As mentioned, either the interpolated fine scan data in 250-m radial resolution, or the interpolated coarse scan data at 75-m radial resolution are obtained through the interpolation on the scale of R utilizing the Marshall-Palmer relation. Inversely, we also covert the interpolated R back to Z through the inverse form of the Marshall-Palmer relation, and then obtain data of another two parameters Z_{f2c} and Z_{c2f}.

The 2D-PDF in terms of Z_{H} is used to show the correlation between this "interpolated" radar reflectivity in the fine and coarse scans (Fig. 5.45). Since this 2D-PDF varies with the different data QC procedures and their combinations, in order to illustrate the effect of each data QC procedure on the probability distribution of Z_{H}, the difference between two 2D-PDFs is defined as $\Delta PDF = PDF_2 - PDF_1$, where the subscripts 1 and 2 refer to different data QC scenarios (Fig. 5.46). The positiveness in ΔPDF refers to the higher 2D-PDF in the scenario 2 than that in the scenario 1, vice versa for the negativeness. For instance, the positiveness at Z_{H} between 45 to 50 dBZ means the radar data under the scenario 2 has a larger number of Z_{H} between 45 and 50 dBZ than the scenario 1.

Start with the attenuation correction. Its effect is to expand the 2D-PDF to the right upper corner, since the attenuation correction procedure recovers these "attenuated" weak echoes back to high Z_{H} values, but the slope and intercept of the fitting curve stay the same (Fig. 5.45(a) and 5.45(b)).These added moderate-to-high Z_{H} values are corrected from the low Z_{H} values, with the former corresponding to the positive area in Fig. 5.46(a), and the latter corresponding to the negative area in Fig. 5.46(a). Either the positive or negative area lies symmetrically along the diagonal line, which indicates that the attenuation correction is immune to the difference in Δr between fine and coarse scan data.

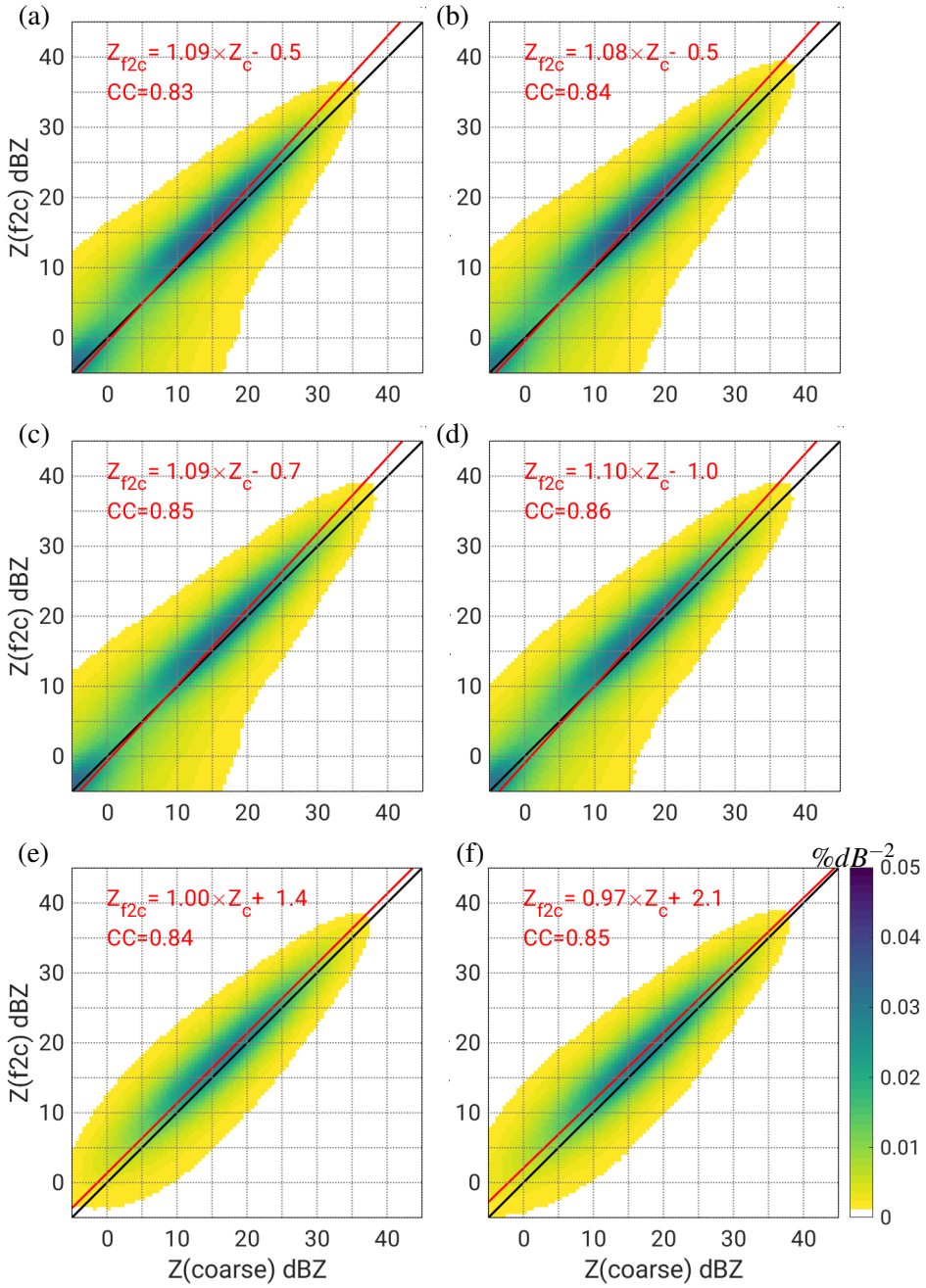

Fig. 5.45.: 2D-PDF of Z_H to compare the interpolated fine and coarse scan data in terms of Z_H, where (a) is for radar data without any data QC procedure, (b) for radar data with attenuation correction, (c) for radar data with attenuation correction and spike signal filtering, (d) for radar data with attenuation correction and second-trip echo removal, (e) for radar data with attenuation correction, spike filter, second-trip echoes removal and NMER using K_{DP}, and (f) for radar data with attenuation correction and NMER using the polarimetric fuzzy logical methods. The black line is the diagonal line, the red line is the fitting curve, *CC* is the Pearson correlation coefficient

Applying the spike signal removal after attenuation correction slightly decreases the intercept of the fitting curve (Fig. 5.45(c)). The negative area, an indicator of the removed Z_H values by the spike signal removal, extends over Z_H values between 10 dBZ and 35 dBZ, and concentrates around the

diagonal line, with its centerline in proximity to, or more accurately, slightly above the diagonal line (Fig. 5.46(b)). It illustrates that spike signals primarily vary around 10 dBZ and 35 dBZ. Meanwhile, this spike signal removal procedure creates a small positive area centered at -5 dBZ, which is caused by the interpolation.

The second-trip echo removal procedure further reduces the intercept of the fitting curves (Fig. 5.45(d)). Recall that our second-trip echo removal algorithm also removes the majority of spike echoes (Section 4.3), a portion of the negative areas above 10 dBZ is identical to the elongate negative area along the diagonal line caused by the removal spike signals already shown in Fig. 5.45(b), and the remaining negative area corresponds to Z_{H} values primarily below 15 dBZ, with a center around 0 dBZ for Z_{f2c} and -12 dBZ for Z_{c} (Fig. 5.46(c)). This clear deviation of this negative area from the diagonal line is exactly in accord to the fact that the second-trip echoes only occur in fine scans. Obviously, only this latter negative area represents the change in Z_{H} associated with the second-trip echoes. Unlike the former negative area which is due to the spike signals and is constrained in proximity to diagonal line, this latter area is more extensive but "diluted" with smaller magnitudes, which means the second-trip echoes are prevalent in our radar data and their Z_{H} magnitudes vary widely but seldom surpass over 20 dBZ (Fig. 5.45(d)).

Adding the NMER procedure, regardless of which NMER method, modifies the shape of the 2D-PDF, such as cutting off its two-sided tailors, and turns the previously negative intercept of fitting lines into positive values, which means Z_{H} values of fine scans are slightly greater than those of coarse scans (either Fig. 5.45(d) or Fig. 5.45(f)). Specifically, the NMER 3 brings the fitting curve with a slope of 1 and an intercept of 1.4 dB (Fig. 5.45(e)). This intercept on the magnitude of 1.4 dB corresponds exactly to ΔZ of 1.5 dB and 3.0 dB for the fine and coarse scans, respectively (to be elaborated in Section 5.2).

According to ΔPDF, Z_{H} values eliminated by this NMER are primarily below 5 dBZ, and occasionally vary from 5 dBZ to 30 dBZ (Fig. 5.46(e)). The former corresponds to a negative area in shape of a slanted oblate oval, whereas the latter corresponds to an elongated area expanding to the right upper corner. The former area is in absolutely dark blue while the latter area is in light color. It means that, the majority of the non-meteorological echoes are characterized by Z_{H} intensity less than than 10 dBZ, corresponding to the non-existence of any precipitation or the presence of light rain. Besides, the former area is roughly symmetric about the diagonal line, but the latter area deviates slightly from the diagonal line at a magnitude of 1–2 dB, which is quite likely to be caused by the different Z_{H} miscalibration between the fine and coarse scan data. It indicates that most of the non-meteorological echoes are comparable between the fine and coarse scan data in terms of Z_{H} intensity if Z_{H} values of both data are calibrated correctly.

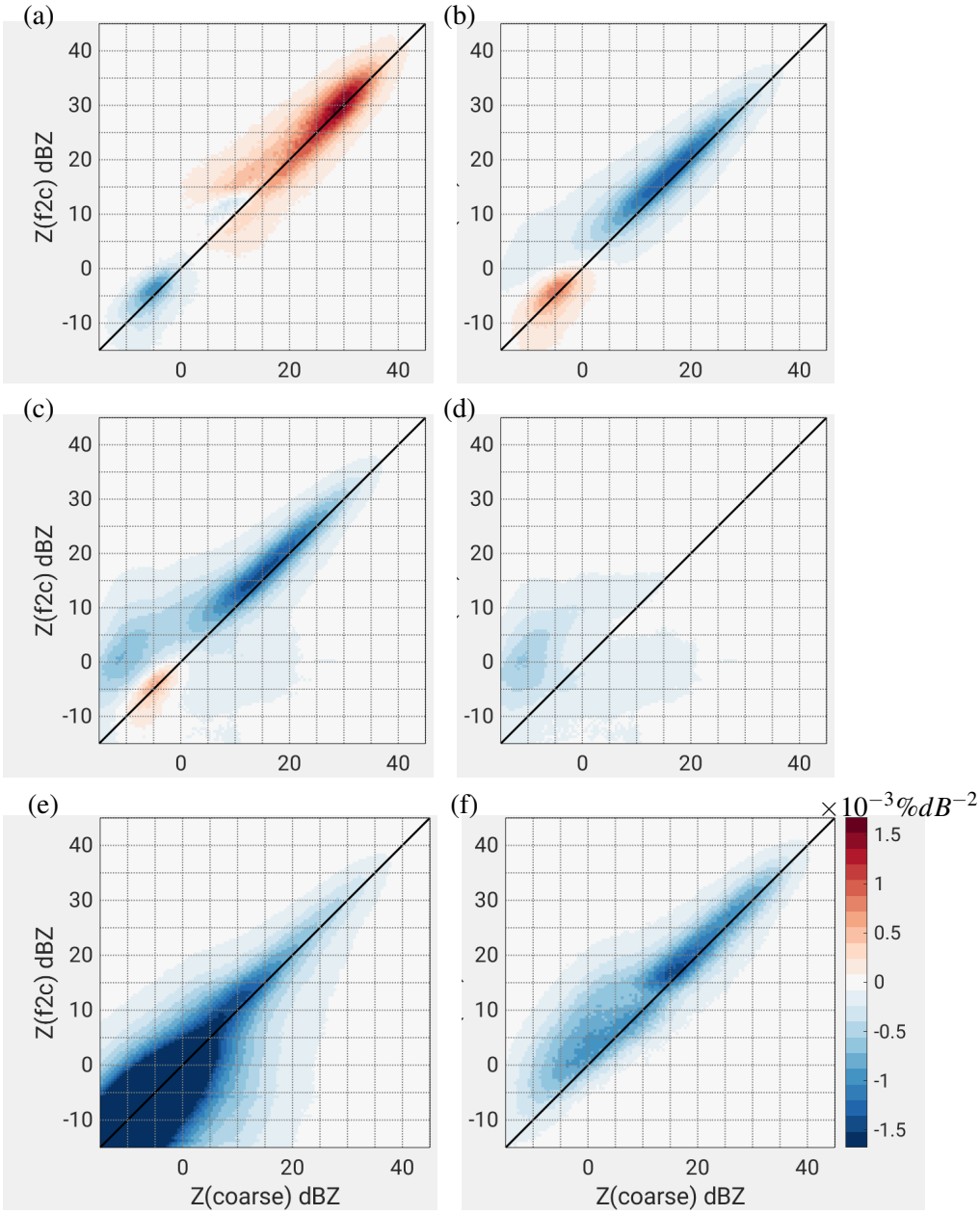

Fig. 5.46.: Difference between two 2D-PDFs of radar reflectivity (Z_H), where (a) compares the 2D-PDFs for radar data between without and with attenuation correction, (b) for radar data between without and with spike signal removal, (c) for radar data between without and with filtering both spike and second-trip echoes, (d) for radar data between without and with second-trip echo removal, (e) for radar data between with or without NMER method 3, (f) for radar data between two different NMER methods, and the black line is the diagonal line

The characteristic of this negative area caused by the non-meteorological echo filtering procedure (Fig. 5.46(e)) differs from that of the other two negative areas caused by the spike signal removal (Fig. 5.46(b)) and the second-trip echo removal (Fig. 5.46(d)). For the spike signal, the negative ΔPDF area lies along the diagonal line, with its maximum centered around 15–20 dBZ and with definite contours, and the negativeness decreases toward both the right upper or the left lower corner. The negative

ΔPDF area with respects to the NMER also lies along the diagonal line, and its negativeness decrease toward the right upper corner, but its left lower corner is far below -15 dB. Taking the 20-25 dBZ square from both Fig. 5.46(c) and 5.46(e), the negativeness caused by the spike signal removal is more than that caused by the NMER procedure. It is the same for other Z_H data greater than 25 dBZ. This comparison implies the number of spike signals larger than 20 dBZ is more than that of non-meteorological echoes, although the overall number of non-meteorological echoes is tremendously greater than that of spike signals.

Unlike the NMER methods 1 and 2 both of which require additional steps to filter spike signals and second-trip echoes, NMER method 3 automatically removes the majority of spike signal and the second-trip echoes along with its non-meteorological echoes, because the polarimetric characteristics of spike signals and second-trip echoes are distinct from the precipitation echoes. When comparing the 2D-PDFs of the NMER methods 2 and 3, we see negative areas which indicate that the NMER method 3 tends to filter out more Z_H than the combination of NMER 2 and spike signal/second-trip echo removals (Fig. 5.46(f)). Be cautious about the magnitude of the darkness in Fig. 5.46(f) is smaller than the rest in Fig. 5.46.

In brief, these data QC procedures only slightly modify CC_{PS} between Z_{f2c} and Z_c, slopes and intercepts of the fitting curves. However, although the change in numerical values is small, we obtain a more reasonable fitting line after processing the radar data with the proper data QC procedures. For the inter-comparison using ΔPDF, the positive and negative areas in ΔPDF present information about how the data QC procedures change the Z_H distribution simultaneously for both fine and coarse scans.

However, the precipitation estimation within the entire chapter is retrieved only based on Z_H through the Marshall-Palmer relation. The empirical single-polarization rainfall estimators are often not valid or proper. No matter which external sources we used to evaluate the X-band radar measurements, the sensitivity of this rainfall estimation to DSD variability is inherent, bringing about unavoidable discrepancies between the radar-based precipitation estimates and the true R. Thus, it is not easy to achieve quantitative agreements between radar data and rain gauge measurements. Thus, polarimetric-tuned rainfall estimators have been proposed (Ryzhkov et al., 1997; Brandes et al., 2003; Bringi et al., 2004) (Section 2.3). Nevertheless, the coefficients in these polarimetric estimators are highly variable depending on the DSD, radar frequency and precipitation type. Determination of proper coefficients and then the subsequent precipitation estimation could be a future work.

5.4. Sub-summary

Recall Fig. 5.1. This chapter focuses on effects of the spatial resolution on the radar-based precipitation estimates by comparing these radar-based precipitation estimates calculated respectively from the fine and coarse scan data.

For case studies of convective storms (Section 5.1), comparisons of radar images from Z_H in three different resolutions show the radar data with higher spatial resolution are more capable of presenting the small-scale Z_H-derived R gradients, depicting spatially highly variable precipitation patterns, and delineating inner structures of convective storms. This is a benefit of radar data at high spatial resolution.

We also compare the X-band radar fine and coarse scan data with external precipitation datasets including the C-band radar, rain gauge measurements and MRR (Section 5.2). Both fine and coarse scan data are processed with different combinations of data QC procedures, so we obtain various versions of fine and coarse scan datasets. Comparing radar data of these versions shows different degrees of agreement. The differences in degree of agreement indicate various roles of data QC procedures on the agreement between the X-band radar data with other precipitation datasets. We quantify the degree of agreement in two aspects—correlation and concordance (comparableness of magnitude), and find the removal of noises including spike signals, second-trip echoes and non-meteorological echoes strengthens the linear correlations, but has no contribution to minimize the difference in magnitudes of precipitation quantities. We also find the attenuation correction can both improve the correlation and concordance, while the Z_H calibration plays the main role in shrinking differences in magnitudes of precipitation quantities. For each combination of data QC procedure, the degree of agreement is also compared between the fine and coarse scans, and the fine scan data show a closer agreement with the external references, proved by the higher correlation coefficient and their least square orthogonal fitting curves. It is regarded as one more benefit of using the radar data at a higher spatial resolution. ΔZ values for the Z_H absolute calibration procedures are also obtained through the R-G comparisons.

The spatial distributions of AR_t (Section 5.3) (Fig. 5.1) are also generated using the fine and coarse scan data which are processed with different data QC procedures. Large discrepancies exist between AR_f and AR_c in terms of the magnitude or the spatial distribution of AR. Analyzing spatial distributions of the difference between AR_f and AR_c for each combination of data QC procedures gives the information about the sensitivity of different data QC procedures on the radar-based precipitation quantities. For instance, we find, although fine scan data tend to miss weak echoes, the presence of spike signals and second-trip echoes of the fine scan brings larger precipitation amount. Although second-trip echoes occur much more frequently than spike signals, their contribution to the "fake" precipitation is much less than their counterpart caused by spike signals. The attenuation correction enlarges differences between AR_f and AR_c, which corresponds to different ΔZ calculated from the aforementioned R-G comparisons between the fine and coarse scans.

To sum up, comparisons about radar-based precipitation quantities in terms of the foregoing three aspects show the differences between fine and coarse scan data, illustrate the sensitivity of these differences to the data QC procedures, and demonstrate effects of the spatial resolution on the radar-based precipitation estimation.

6. Summary

Precipitation information underpins many hydrological and meteorological applications. The weather radar is the only tool which is able to observe precipitation at the temporal resolution of 5-10 minutes and the spatial resolutions at the 1-km resolution. However, the requirement for the spatial resolution of precipitation data can sometimes be even more demanding than this 1-km resolution, due to high spatial heterogeneity of precipitation. For instance, regarding hydrological applications for small urban catchments, we are interested in the precipitation variability unsolved by the 1-km resolution precipitation data which are currently derived from radar measurements provided by the majority of operational radar networks. Observation of this sub-kilometer precipitation variability requires radar measurements to be at the corresponding sub-kilometer spatial resolution. Although radar data at resolutions higher than 1-km scale have been available in some field campaigns using X-band radars, there is no systematic research about what differences are made by changing the radar sampling from a coarser resolution to a finer resolution. Previous studies on effects of spatial resolutions of radar measurements dealt with the statistically generated resolutions instead of the directly measuring spatial resolution, and they focused on errors quantified by precipitation quantities other than the directly measured radar variables. Our aim of this research is to investigate effects (either benefits or drawbacks) of increasing the spatial resolution of radar measurements using radar data with different spatial resolutions which are directly measured and include at least one sub-kilometer resolution. We specifically interpret the effects caused by changing spatial resolutions in two aspects—in terms of radar data quality and radar-derived precipitation estimation. In brief, we investigate effects of spatial resolutions on radar data quality and effects of spatial resolutions on radar-derived precipitation estimation.

This research is based on an X-band radar dataset obtained via a 5-month field campaign in the Stuttgart metropolitan area. An X-band radar was operated in a scan strategy with two quasi-simultaneous scans at two different radial resolutions, 75 m and 250 m for fine and coarse scans, respectively. In terms of the scientific control, the coarse scan data is regarded as the control group and the fine scan data as the experimental group. Regarding our aim, to illustrate effects of the spatial resolution, we compare both fine and coarse scan datasets, in terms of radar data quality and radar-derived precipitation estimates, corresponding to the research objectives proposed in Chapter 1. First, different characteristics of noise between fine and coarse scans indicate differences in radar data quality caused by changing spatial resolution of radar measurements. Second, different degrees of consistency with other precipitation measurements between fine and coarse scans indicate differences in radar-derived precipitation estima-

tion caused by changing spatial resolution of radar measurements. Third, the above differences in radar data quality and in radar-derived precipitation estimation exhibit different degrees of sensitivity to the various data QC procedures.

The comparisons lead to the following data analyses and associated results in 12 different points. The last three points belong to the data analyses regarding the quality of the radar-derived precipitation estimates, and the remaining points are for the data analyses regarding the quality of radar data. It means data analyses of the first 9 points use the level II radar data and correspond to the first research objective, while data analyses of the other 3 points are for the second research objective and use the level III data—precipitation quantities which are estimated based on the radar data. Only the analyses about weak echoes and convective storms are qualitative, and the remaining are all quantitative. Among them, the data analyses concerning spike signals, second-trip echoes and non-meteorological echoes generate their corresponding data quality control procedures customized for this research.

1) **Loss or presence of weak echoes**. The visual inspections over radar images give us a first impression on similarities or dissimilarities between two scan datasets. These quick inspections mainly focus on the spatial distribution and intensity of radar variables. They not only confirm the first difference between fine and coarse scans—the loss of weak echoes in the fine scan which is in accord with the radar theory, but also unfold two types of suspicious echoes that add 'extra' Z_{H} into the fine scan data;

2) **Data contaminations caused by spike signals**. One type of suspicious data, termed as spike signals, is characterized by the unreasonably high and stable u-ϕ_{DP} values, and we used these two characteristics as the criteria to identify these spike signals automatically. Based on the diurnal variation and spatial distribution of these identified spike signals in the entire dataset, we speculate these noises are from the X-band radars on ships along the Necker inland waterway. We also find these spike signals are also present in coarse scan data but at a much lower frequency, which implies the external spike signals affect the fine scan data in a much more intense extent than the coarse scan data. It is the second difference between the fine and coarse scans; the fine scan data are more subjected to external noises. The by-product of this part of data analyses is the spike signal removal procedure applicable for both fine and coarse scan data.

3) **Data contamination caused by second-trip signals**. The other type of suspicious data frequent in the fine scans but not in the coarse scans is the second-trip echo. Given that the maximum range of the radar coverage in the fine scan is identical to its theoretical r_{max}, the second-trip echoes appear frequently in the fine scan in form of extra Z_{H} and ϕ_{DP} magnitudes. In contrast, the maximum range of the radar coverage in the coarse scan is even less than 1/4 of its theoretical r_{max}, the second-trip echoes of the coarse scan seldom reach measurable magnitudes. Thus we can omit them safely. It is the third difference between the fine and coarse scan data—only the fine scan data are affected by the second-trip echoes. The Z_{H} magnitude of a second-trip echo is reduced in comparison to its original Z_{H} magnitude,

while the u-ϕ_{DP} magnitude of a second-trip echo is the same as its original u-ϕ_{DP} magnitude. These 'extra' high u-ϕ_{DP} magnitudes distort the monotonic increasing tendency of u-ϕ_{DP} along the azimuthal direction, leading to the prevalence of erroneous negative K_{DP} retrievals in the fine scan data, which is another illustration of the third difference between the fine and coarse scan data in terms of K_{DP}. Besides, these 'extra' high u-ϕ_{DP} values used in attenuation correction also bring the wrong corrections to Z_H and Z_{DR}, which means the attenuation correction in the fine scan data sometimes can be wrong if the second-trip echoes are not filtered. This negative effect caused by high u-ϕ_{DP} of second-trip echoes in the fine scans is regarded as the third illustration of the third difference between the fine and coarse scan data. Both K_{DP} retrieval and attenuation correction procedures necessitate the removal of second-trip echoes. Given low magnitudes of SQI for most second-trip echoes, SQI is used to identify and filter out the second-trip echoes. The spatiotemporal distribution of all these identified second-trip echoes in the entire dataset further demonstrates the unique characteristics of second-trip echoes distinct from other types of noises. The by-product of this part of data analyses is the second-trip removal procedure solely applicable for the fine scan data.

4) Z_H **data contamination caused by ground clutters**. The ground clutters, identified via their abnormal high frequency of large Z_H, also show different characteristics between the fine and coarse scans in terms of its occurrence frequency, spatial extent and Z_H intensity. The identified ground clutters expand in a much smaller areal extent in the fine scans, and the mean Z_H of these ground clutters is smaller in the fine scan data than their counterpart in the coarse scan data. Both differences imply that the high spatial resolution can help mitigate the contamination of ground clutters in the radar data using Z_H only without further information from Doppler velocity or polarimetric variables. Such a mitigation in the data contamination caused by ground clutters in the fine scan is the fourth difference between the fine and coarse scans. The by-products of this part of data analysis are the ground clutter static maps established for the fine and coarse scan respectively. Unlike the above two points about spike signals and second-trip echoes, this static map is used for identification rather than data correction.

5) **Polarimetric data contamination caused by non-meteorological echoes**. Besides the ground clutters, the radar data are also severely contaminated by insect echoes. During rainy period, three classes of echoes (ground clutters, insect echoes and precipitation echoes) are always present simultaneously and even mixed with each other. In order to distinguish between non-meteorological (consisting of ground clutters and insect echoes) and precipitation echoes, a fuzzy logic classification was developed and this procedure includes establishing membership functions, aggregating memberships from the selected polarimetric discriminators, and assigning echo classes. Membership functions are built based on polarimetric variables and their texture parameters. The fine and coarse scan data exhibit different characteristics in terms of polarimetric variables and their texture parameters, and their associated membership functions; it is the fifth difference between the fine and coarse scan data. These differences in membership functions between the fine and coarse scans lead to different performances of this classifi-

cation procedure depending on whether the fine or coarse scan data are used. The results show that the classification procedure using the coarse scan data has higher chance to misidentify precipitation echoes as non-meteorological echoes than the same procedure using the fine scan data. It means the fine scan data are more efficient in identifying precipitation echoes from ground clutters and insect echoes; it is the second illustration of the fifth difference between fine and coarse scan. This fuzzy logic classification is the by-product of comparisons between fine and coarse scans. The algorithm is physics-based, intuitive, easy to implement and computationally efficient; it only relies on polarimetric variable without referring to any other external information, and is free from Z_{H} constraint to avoid the Z_{H} degradation caused by range dependence and attenuation.

6) **Attenuation correction**. Attenuation correction is a necessary step in the data quality procedure for the X-band frequency, and in this research we use the attenuation correction on the basis of u-ϕ_{DP}. Given u-ϕ_{DP} is a variable integrated over the range and its magnitude is not affected by the radial resolution of radar sampling, the attenuation correction should not be affected by the radial resolution in principle. However, it is not true in case of severe convective storms or for precipitation behind wide-spread stratiform precipitation. If the Z_{H} data are attenuated below the signal noise level and become weak echoes, these Z_{H} data are "overlooked" by fine scans, and we are unable to recover these lost Z_{H} via attenuation correction. In contrast, these weak echoes remain in the coarse scan, and the attenuation correction is able to recover Z_{H} in the coarse scan data. The situation is similar for differential attenuation correction for Z_{DR}. This difference in the attenuation-corrected Z_{H} or Z_{DR} is the sixth difference between the fine and coarse scan, which is essentially linked to the aforementioned first difference. Besides the comparison between fine and coarse scan, our analysis also evaluates the performance of two attenuation correction algorithms—the ZPHI and iterative ZPHI algorithms respectively, and also validates the magnitudes of attenuation-corrected Z_{H} data by comparing their precipitation estimates with the precipitation estimates based on K_{DP} which is immune to the attenuation.

7) **Statistics errors**. To see whether fine and coarse scans differ with respect to characteristics of polarimetric variables, we evaluate our polarimetric dataset via the following three aspects: a) the theoretical statistical errors or accuracy of polarimetric variables using the perturbation method; b) a variety of statistics of polarimetric measurement in light rain; c) the standard deviation of K_{DP} in the convective precipitation systems. Based on the scanning parameters, the theoretical statistical errors of the fine scan data are greater than those of the coarse scan data, but the difference shrinks for the larger ρ_{HV}. It means, for the majority of precipitation echoes, the difference in theoretical statistical errors between fine and coarse scans is much smaller. For the statistics in the light rain, both fine and coarse scan data exhibit good data quality, and these statistics are comparable in magnitude for both scans. The statistics evaluating the quality of K_{DP} for convective storms are also comparable for both scans.

8) **Range dependence**. The range dependence of radar variables, either single-polarization or polarimetric, is discussed for three categories of dataset. They are a dataset including precipitation

echoes merely, a dataset including non-meteorological echoes only and the entire radar data including precipitation and non-meteorological echoes. In terms of the entire radar dataset without applying data QC procedures, within the 30-km range, Z_{DR} and u-ϕ_{DP} of the coarse scan data are in larger magnitudes than those of the fine scan data, whereas ρ_{HV} of the coarse scan data are in smaller magnitudes. In the farther range beyond 30 km away from the radar, K_{DP} of the coarse scan is more concentrated within low values with a narrower distribution, whereas SNR and SQI of the coarse scan data are in larger magnitudes than those of the fine scan data. Besides, the four sets of data—the non-meteorological echoes in fine scans, non-meteorological echoes in coarse scans, precipitation echoes in fine scans and precipitation echoes in coarse scans—all exhibit different characteristics from others in terms of their range dependence; the most dramatic differences are present for Z_H, SNR and SQI. This difference in terms of the range dependence is the seventh difference between the fine and coarse scan data.

9) **Roles of QC procedures**. The aforementioned four data QC procedures are removals of spike signals, second-trip echoes and non-meteorological echoes (ground clutters and insect echoes), and attenuation correction. Given the importance of Z_H, PDFs of Z_H data with various combination of data QC procedures are compared between fine and coarse scan data. This comparison is used to evaluate th effects of these data QC procedures on the Z_H data, and also to assess the difference in such effects between the fine and coarse scan data. Attenuation correction increases the frequency of high Z_H for both scan datasets, while the other three data QC procedures tend to shrink the difference in PDFs of Z_H between the fine and coarse scan data. It implies, in the raw data without external data QC procedures, the differences in PDFs are attributed to several types of noise which exhibit different characteristics in the fine and coarse scan datasets. Applications of data QC procedures remove these noises, thereby reducing the discrepancies between the fine and coarse scan data. For Z_H applied with these four data QC procedures, PDFs of both fine and coarse scan data become closer but are still not identical. If the PDF of coarse scan data is shifted slightly rightwards, equivalent to adding a constant increment of Z_H to the coarse scan, then PDFs of both scans can resemble each other. The existence of this increment of Z_H is due to the different miscalibration for fine and coarse scans regarding the radar system hardware. This difference is irrelevant to the effect of different spatial resolutions, but it is directly related to the magnitude of Z_H-based precipitation estimates (to be discussed below).

After analyzing the level II data and addressing the first research objective from the above discussion, starting from here, we focus on the level III data and address the second research objective.

10) **Convective storm delineation**. The weather radar is well-known for its capability to resolve convective storm structures. For the majority of radar data users, the primitive use of radar data is via quick looks through radar images. In order to see the differences between fine and coarse scans in terms of their presentations of precipitation structures, a series of visual and qualitative inspection of radar images is done for two small-sized intense convective storms. The C-band radar data with the 500-m radial resolution is also involved, serving as the reference at a third radial resolution. Given Z_H is

a good indication of precipitation instantaneous intensity, the contours and Z_H gradients are more smooth and natural for the fine scan data, with a clearer presentation of the storms' internal structure from the radar images than those of the coarse scan. However, we cannot make quantitative investigations for these case studies of convective storms. The reason lies in the time gap between the fine and coarse scans. During this 100-second time gap, the convective precipitation evolves and moves, with the changing storm's internal structures; such a change is even more rapid for the small-size intense convective storms. It implies that, the discrepancy between the fine and coarse scan data is caused by a combination of the effect of radial resolution and evolutions of convective storms. We are unable to distinguish which factor plays the main role in explaining such discrepancies. For other radar variables, the comparison is done between the fine and coarse scan data without the C-band radar data. In the radar images, similar to Z_H, the gradients of other radar variables are smoother for the fine scans, which can assist us in delineating the internal structures of convective storms. This difference, albeit gained from the visual inspection, fits common sense, and meets our expectation before performing any filtering or correction to the radar data. Thus, the eighth difference between the fine and coarse scan is that, the fine scan data are more skillful in presenting a natural and clear configuration of convective storm internal structures.

11) **Evaluation with external references**. To evaluate quality of radar-derived precipitation quantities and to determine calibration factors (Z_H offset) for Z_H measurements, we use three external sources of precipitation measurements as the reference; they are from rain gauge network, MRR and C-band radar. Comparing precipitation quantities estimated respectively from fine and coarse scans to these external precipitation datasets, the agreement between these precipitation quantities and these external datasets can be used to indicate the quality of precipitation quantities estimated using the fine or coarse scan data. Besides, this comparison between radar and gauge measurements (R-G) is a routine for absolute Z_H calibration in operational utilizations of weather radar data. This procedure is also named as radar-gauge adjustment. The comparisons are performed in three temporal scales—the total measuring period, daily and hourly respectively, and based on different fine or coarse scan datasets processed with various combinations of data QC procedures. Results show that, regardless temporal scales and combinations of four data QC procedures (spike signal, second-trip echo removal, non-meteorological echo removal and attenuation correction), the fine scan data exhibit greater correlations with precipitation measurements from rain gauges, proved by the higher correlation coefficient and the least square orthogonal fitting curves which are closer to the one-to-one diagonal line. This stronger agreement with the rain gauge measurements in the fine scan data than the coarse scan data meets our expectation. For geographically matching up rain gauges with the closest radar gates, because of the smaller sampling volumes of the fine scan, the distance of a rain gauge and its matched-up radar gates can be shorter for the radar gates of fine scans than those of coarse scans. It means the precipitation information derived from radar measurements of the fine scan resembles more what is measured by rain gauges whose effective measuring area are quite small. This is the ninth difference between the fine and coarse scan.

Results from R-G comparison also show, among these four data QC procedures, attenuation correction contributes most to a stronger agreement between the radar and rain gauge measurements. It is because the attenuation correction adds the Z_H increment on the order of several dB directly to Z_H value, thereby significantly changing the magnitude of Z_H. The difference in Z_H magnitude after applying all the four data QC procedures is attributed to radar miscalibration. Thus, from the comparison between the radar and gauge measurements, we obtain the calibration factors for the fine and coarse scans respectively as 4.5 dB and 6.5 dB for the Z_H without data QC procedure, and 2 dB and 4 dB for Z_H after applying these four data QC procedures. The similar comparisons were conducted for MRR measurements. Unlike rain gauge measurement, the MRR measurements along the vertical extent allow us to evaluate the Z_H measurements at radar sweeps of other elevations. For the comparison using MRR measurements, correlation coefficients for the coarse scan are higher.

12) **Spatial distribution of precipitation total accumulation**. Given the different spatial resolutions for the fine and coarse scan, we obtain another two Z_H datasets by interpolating the fine scan data as the same resolution as the coarse scan, and interpolating the coarse scan data as the same resolution as the fine scan. Then differences in radar-derived precipitation estimates between the fine and coarse scan data can be directly calculated, referred as DAR. We specifically define DAR as subtracting AR of the coarse scan data from AR of the fine scan data, so the positive values mean precipitation quantities estimated by the fine scan data are greater than those estimated by the coarse scan data, and vice versa. We investigate spatial distributions of the magnitudes of *DAR*s estimated from Z_H with various combinations of data QC procedures. Each combination of data QC procedures corresponds to a distribution map of DAR magnitudes. Before any data QC procedure, DARs are positive over the majority of the entire radar coverage except the negative values over the radar gates severely affected by ground clutters; applying the attenuation correction procedure further enlarges DAR magnitudes; applying the removal of second-trip echoes and spike signals reduces DARs; applying the polarimetric non-meteorological echo removal also slightly enlarges DARs, but turns the initial negative DARs over the radar gates contaminated by ground clutters into positive values; applying the calibration factors to both data further reduces DAR to the minimum level as close to zero as possible, leading to random alternating positive and negative values over the radar coverage. The role of these four data QC procedures is to remove their corresponding types of noise. These changes in the distribution map of magnitudes of different DARs calculated using Z_H with various combinations of these four data QC procedures indicate different roles of these types of noise in the magnitude of radar-based precipitation quantities. These distribution maps directly compare the spatial characteristics of precipitation estimation between fine and coarse scans, and the changes across distribution maps indicate the sensitivity of precipitation estimation to these data QC procedures. The spatial distribution of DARs together with its sensitivity to data QC procedures is the eleventh illustration of differences between the fine and coarse scans.

Tab. 6.1.: A summary of the differences between the fine and coarse scan data

Category	Type	Fine scan	Coarse scan	Outcome
Radar data quality	Weak echo	Reduced amount	Remaining	Identification
	Spike signal	Frequent	Occasional	QC correction
	Second-trip echo	Very frequent	Absent	QC correction
	Ground clutter in Z	Smaller extent, weaker in intensity	Wider extent, stronger in intensity	QC correction
	Non-meteorological echo	Different statistics in terms of polarimetric variables		QC correction
		More efficient in removal	Less efficient in removal	
	Attenuation correction	Correct insufficiently	Correct more	QC correction
	Statistic errors	Greater theoretical error	Less theoretical error	Identification
		Comparable for measured errors		
	Range dependence	Different characteristics		Identification
	Probability distribution	Different responses to quality control procedures		Identification
Radar-based precipitation estimation	Characterizing convection storm	More details, smoother, more nature	Less details, irregular gradients	Identification
	Evaluation with external references	Greater agreements	Worse agreements	QC correction
	Precipitation total accumulation	Different responses to quality control procedures		Identification

The foregoing discussions about the differences (Tab. 6.1) between the fine and coarse scan data correspond to three research objectives proposed in Chapter 1. All the differences from these comparisons, although illustrated in various ways and related to different factors, can be fundamentally attributed to the difference in radial resolutions. For our X-band radar data, using the sub-kilometer high-resolution radar measurements brings about both benefits and drawbacks, but there is no census on whether the benefits are more than the drawback, verse vice. The relative importance of benefits or drawbacks should be considered on a case-by-case basis, and depends on the propose of using the radar data. Our exhaustive discussion can provide practical guidelines for the radar meteorologists when they plan to increase the spatial resolution for their radar measurements.

Associating these foregoing differences to the past research, we can summary originality of this research as follows,

i) Previous studies by other researchers to explore the precipitation sub-kilometer variability unsolved by radar measurements in the spatial resolutions coarser than the 1-km resolution were primarily based on statistical manipulations which essentially utilizes radar data at only one spatial resolution. In contrast, this research involves two independent measurements sampled independently and physically in different spatial resolutions, which gets rid of the need for statistical manipulations and eliminates the associated uncertainties, and thus renders results of this thesis more rigorous and trustworthy.

ii) Previous studies mainly used results from numerical simulations of hydrological models as the criteria to evaluate the quality of radar measurements in different artificial resolutions, but their evaluation criteria are sometimes unstable. In contrast, this study focuses merely on the precipitation estimates which can be easily calculated and are not dependent on the hydrological models.

iii) Some research whose experiments also utilized the small temporal or spatial scale but their datasets were for a very short time (from a few hours or days), and so their results are less convincing and less robust. In contrast, this research is based on a quite large radar dataset from a radar field campaign whose areal coverage expands over $1.5 \times 10^4\,\mathrm{km}^2$ for a 5-month period, strengthening the representativeness and credibility of the results of this research.

Tab. 6.2.: Recommendations for fine and coarse scans in practical radar data applications

Category	Concerns	Fine or coarse
Radar data quality	Inclusion of weak echoes	Coarse
	Complete attenuation correction	Coarse
	Free of second-trip echo contamination	Coarse
	Free of contamination from external signal	Coarse
	Less ground clutter contamination	Fine
	Efficient non-meteorological removal	Fine
Radar-based precipitation estimation	Detailed delineation of convective storm	Fine
	Radar-gauge comparison	Fine
	Detection of light rain/snow	Coarse

We obtain a comprehensive understanding of the effects of spatial resolutions on the radar data quality and the radar-based precipitation estimation. We also have a more concrete knowledge of the benefits and drawbacks brought by using a higher spatial resolution, which can provide guidelines in selecting an appropriate spatial resolution for other radar experiments. In general, the recommendation is flexible. On the basis of data analyses regarding the various differences between fine and coarse scan data in different scenarios, whether the fine scan data are preferred over the coarse scan data or the other way around depends on the propose of radar data applications (Tab. 6.2).

A. Acronyms and Symbols

2D-PDF Two-dimensional probability density function

AAD Averaged absolute deviation

AMSL Above mean sea level

AP Anomalous propagation

ATAR Alternate transmission and alternate reception

ATSR Alternate transmission and simultaneous reception

CCC Concordance correlation coefficient

CCOR Clutter correction ratio

CDF Cumulative Distribution Function

FSE Fractional standard error

DLR German Aerospace Research Establishment

DSD Drop size distribution

DWD German Weather Service

EM Electromagnetic (waves)

FIR Finite impulse response

FLC Fuzzy logic classification

GC Ground Clutter

IC Insect echo

KIT Karlsruhe Institute of Technology

LWC Liquid water content

MDS Minimum detectable signal

MF Membership function

MRR Micro rain radar

NBF Non-uniform beam filling

NEXRAD Next-Generation Radar

NCP Normalized coherent power

NMER Non-meteorological echo removal

NNE North-northeast

NWP Numerical Weather Prediction

OR Orthogonal Regression

PDF Probability Density Function

PPI Plain Position Indicator

PR Precipitation echo

PRF Pulse repetition frequency

PRT Pulse repetition time or T_s

QC Quality control

QPE Quantitative precipitation estimation

QPF Quantitative precipitation forecast

Radar RAdio Detecting And Ranging

RADOLAN S Radar-Online-Aneichung

RMSE Root Mean Square Error

rRMSE Relative Root Mean Square Error

RHI Range-height Indicator

rpm Revolutions per minute

R-G Radar-Gauge

SCWC Self-consistent with Constraint Method

SD Standard devation

SHV Simultaneous transmission/reception

SNR Signal-to-noise ratio

STSR Simultaneous transmission and simultaneous reception

STN Meteorological station with rain gauge

SQI Signal quality index

UTC Universal Time Coordinate

VCP Volume Coverage Pattern

WSR-88D Model number of the current operational weather radar in United States

T-R Transmitter-Receiver

Z-R Reflectivity to rainfall relationship or equation

a Generic coefficient of a power-law relationship

a_{e} Radius of Earth

A Specific attenuation $(dB\,km^{-1})$

A_{DP} Specific differential attenuation $(dB\,km^{-1})$

$\mathbf{A}$ Wave amplitude vector

A_y Wave amplitude vector in y-axis direction

A_z Wave amplitude vector in z-axis direction

AR Precipitation accumulation ——

AR_{G} Precipitation accumulation from rain gauge

AR_{R} Precipitation accumulation from radar data

a Generic exponent of a power-law relationship

B Bias

c Speed of light in a vaccum

c Coarse scan, used in subscript

c_{h} Propagation speed for the horizontally polarized waves

c_i Number of sample in a category

c_{v} Propagation speed for the vertically polarized waves

CC	Correlation coefficient
CC_{PS}	Pearson correlation coefficient
CC_{SP}	Spearman rank correlation coefficient
C_{r}	Radar constant
d_i	Difference between the ranks of two sample
D	Diameter of hydrometeor or scatterer
D_{a}	Diameter of a prabolic refector, or antenna aperture size
D_{m}	Mass/volume-weighted diameter
D_{max}	The maminum diameter of hydrometeors in DSD
$\mathbf{E}$	Electric field
$\vec{E}$	Electric field
$\vec{E}(\vec{r},t)$	Electric field
$\vec{E}(x,t)$	Electric field vector within the y-z plane
E_y	Wave amplitude vector in y-axis direction
E_z	Wave amplitude vector in z-axis direction
f	Fine scan, used in subscript
f	Frequency of wave
f_{D}	Doppler frequency
f_{HH}	Forward-scatter amplitude at horizontal polarization
f_{VV}	Forward-scatter amplitude at vertical polarization
$f()$	Probability density distribution
g	Linear scale antenna gain function
G	Antenna gain function
h	Height of an example sampling volume
h_0	Height of antenna above the ground
H_{AGL}	Height above the ground surface
H_{ASL}	Height above the mean sea level

j	Indices of series
j	Incident wave used in supercript
k	Wavenumber
k_{g}	Coefficient in defining antenna gain
$\hat{k}_{\mathrm{i}}$	Unit vector of the incident wave
$\hat{k}_{\mathrm{s}}$	Unit vector of the scaterred wave
K_{DP}	Coefficient in defining antenna gain
K	Dielectric factor
K_{w}	Dielectric factor of water
L_{DR}	Linear depolarization ratio
L_{m}	Microwave loss
L_{r}	Receiver loss
L_{a}	Atmospheric loss
m	Indices of series
M	Hit per scan, number of signal sample along sample time axis
M_{l}	Number of equivalent independent samples
M_n	The n th moment of DSD
n	Complex refraction index
nB	Normalized bias
N	Number of radar gates, or number of a sample
N_{a}	Antenna rotation speed
N_{r}	Refractivity
N_{t}	Total number concentration
N_0	Number concentration parameter ($mm^{-\mu-1}\,m^{-3}$)
$N(D)$	Drop size distribution
P	Probability of an event
P_0	Supposed power received along radar beam axis

P_l	Actual power received along radar beam axis
P_N	Noise power level
P_r	Intensity of the received power
$\overline{P}_r$	Intensity of the transmitted power
$\mathbf{P}$	Electric polarization
$\vec{P}$	Electric polarization
PIA	Two-way path-integrated attenuation
PIA_DP	Two-way path-integrated differential attenuation
Q	Quantile of a sample
r	Radar range—the distance of a radar pixel to the radar site along the radar beam
r_max	Maximum unambiguous range
$r(m)$	Autocorrelation coefficient
$r\Theta$	Angular resolution in km along the azimuthal direction
R	Precipitation rate ($\mathrm{mm\,h^{-1}}$)
R_0	Signal autocorrelation at lag 0
R_1	Signal autocorrelation at lag 1
s	Distance along the earth's surface between two points
s_hh, s_vv	Backscatter coefficient, or scattering amplitude of the wave scattering for co-polar component
s_hv, s_vh	Backscatter coefficient, or scattering amplitude of the wave scattering for cross-polar component
S_inc	Power flux density intercepted by a particle
S_r	Power flux density at the receiving point
$\vec{S}$	Scattering matrix
t	Time point
T_d	Dwell time
T_s	Pulse repetition time
T_0	Signal autocorrelation at lag 0 from uncorrected data

v_a Unambiguous velocity

v_c Speed of light in a medium except vaccum

v_D Mean Doppler velocity

v_{max} Nyquist velocity

V_c Radar sampling volume

v_r Radial velocity

w_t Terminal fall velocity of falling raindrops

$\hat{x}$ Unit vector along the x-axis direction in a three-dimensional cartesian coordinate

X Predictor

$\hat{y}$ Unit vector along the y-axis direction in a three-dimensional cartesian coordinate

Y Response

$\hat{z}$ Unit vector along the z-axis direction in a three-dimensional cartesian coordinate

Z Radar reflectivity factor

Z_{DR} Differential reflectivity in logarithmic scale (dB)

Z_{dr} Differential reflectivity in linear scale

Z_e Equivalent radar reflectivity factor

Z_{hh} Equivalent radar reflectivity factor at horizontal polarization in linear scale ($mm^6\,m^{-3}$)

Z_H Equivalent radar reflectivity factor at horizontal polarization in logarithmic scale ($mm^6\,m^{-3}$)

Z'_H Equivalent radar reflectivity factor at horizontal polarization in logarithmic scale ($mm^6\,m^{-3}$)

Z_{min} Minimum detectable radar reflectivity

Z_{vv} Equivalent radar reflectivity factor at vertical polarization in linear scale ($mm^6\,m^{-3}$)

Z_V Equivalent radar reflectivity factor at vertical polarization in logarithmic scale ($mm^6\,m^{-3}$)

α Coefficient for attenuation correction, ratio of A_h and K_{DP}

β Coefficient for differential attenuation correction, ratio of A_{DP} and K_{DP}

δ Phase difference

δh	Displacement of a radar sampling volume
δ_0	Backscatter differential phase
Δ	Difference between two precipitation data
Δr	Range spaceing or range interval over which echoes are averaged to make a final range gate
Δt	Time gap
Δx_i	Bin width in histogram or PDF
ΔZ	Z calibration factor
ΔZ_{atc}	Z calibration factor
ΔZ_{DR}	Increament of Z_{DR} for Z_{DR} calibration
$\Delta\Phi$	Phase shift during a radar pulse
ε	Dielectric constant or permittivity
ε_{r}	Relative dielectric constant or relative permittivity
ε_0	Free space permittivity
η	Radar reflectivity
θ_{e}	Elevation angle of radar beam
θ_{beam}	Beamwidth
θ_{min}	Terrain-following minimum elevation
θ_{sfc}	Terrain-following elevation
Θ	Horizontal or azimuth beamwidth, azimuthal resolution in $^\circ$
κ	Width-to-length ratio of a radar gate, ratio of radial resolution to azimuthal resolution
λ	Wavelength
Λ	Distributiion shape parmeter in DSD model (mm^{-1})
μ	Distribution shape parameter in DSD model
μ_{M}	Ratio of M to M_l
μ_{X}	Expectation of sample X
μ_{Y}	Expectation of sample Y
ρ_{HV}	Copolar cross-correlation coefficient

ρ_w	Density of water
σ	Texture parameter of a variable
σ_b	Backscattering cross section
σ_H	Backscattering cross section for horizontal polarization
σ_v	Spectrum width of Doppler velocity distribution
σ_V	Backscattering cross section for vertical polarization
σ_X	Standard deviation of sample X
σ_Y	Standard deviation of sample X
$\sigma(D)$	Single particle scattering cross section
τ	Transmit pulse duration
τ_{decorr}	Decorrelation time
ϕ	Propagation differential phase
ϕ_a	Azimuth angle of a radar beam
ϕ_{hh}	Phase of horizontally polarized wave
ϕ_{vv}	Phase of vertically polarized wave
ϕ_0	System differential phase
ϕ_{01}	Initial phase for y-component of electric field
ϕ_{02}	Initial phase for z-component of electric field
ϕ_0	Initial phase for z-component fo electric field
Ψ_{DP}	Differential phase shift
Φ	Vertical or elevation beamwidth
Φ_{DP}	Differential phase
χ	Electric susceptibility
ω	Angular frequency

B. Appendix

B.1. Auxiliary analyses for X-band radar data

B.1.1. Sensitivity of attenuation correction to spike signals

The attenuation correction procedure is based on u-ϕ_{DP} (Section 4.6), and spike signals are characterized by high u-ϕ_{DP} (Section 4.3). If attenuation correction is applied prior to spike signal filtering, the large u-ϕ_{DP} of spike signals might lead to erroneous Z_{H} after attenuation correction. For example, for the azimuth at 28°, we see a tremendous increase in Z_{H} after attenuation correction—the exponentially increasing green curve within the rightmost shaded area in upper plot in Fig. B.1(b). In contrast, the black curve for the Z_{H} without attenuation correction stays steady around 20 dBZ, corresponding to rainfall rate about 0.5 $\mathrm{mm\,h^{-1}}$. The 'unrealistic' u-ϕ_{DP} of these spike signals used in the attenuation correction procedure bring about the unreasonable radar reflectivity correction ΔZ_{atc}; this large ΔZ_{atc} superimposed with the original Z_{H} before applying attenuation correction (the black curve) leads to Z_{H} up to 60 dBZ. Such high Z_{H} is usually associated with severe convective storms with heavy rain or hail, but obviously the high Z_{H} in this case is noise caused by a improper combination of the spike signals and attenuation correction, and there is no heavy rain. We should filter out this misleading high Z_{H} before using Z_{H} for estimating precipitation rates. It also reveals the necessity of spike signal filtering especially for Z_{H} with attenuation correction.

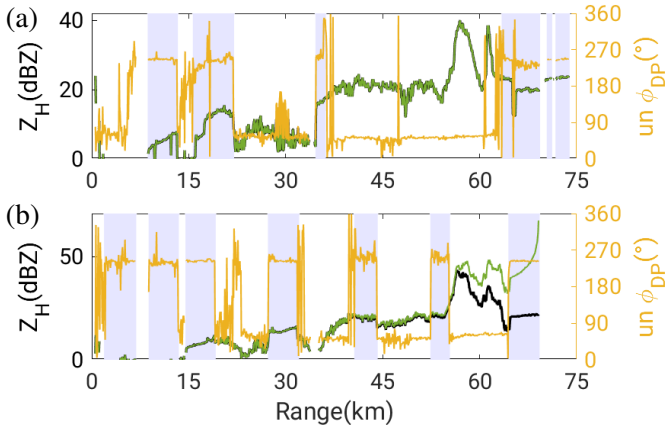

Fig. B.1.: Rays at azimuths of 27° (a) and 28° (b) for the same data as Fig. 4.5, where shaded areas are the radar gates contaminated by the spike signals, the black/green lines are Z_{H} before/after attenuation correction, and the yellow lines are uncorrected differential phase ϕ_{DP}

However, this erroneous ΔZ_{atc} only occurs in a small part of the radar beam; along the same radar beam, for other radar data contaminated by spike signals (other shading areas), Z_H before and after attenuation correction are the same. Besides, for the radar beam of the adjacent azimuth at 27°, the attenuation corrected Z_H is identical to Z_H without attenuation correction for the entire radar beam. It implies, the presence of spike signals does not always lead to the wrongly ΔZ_{atc}, and the attenuation correction procedure is not always affected by spike signals.

Regardless of the impact of spike signals on attenuation correction, all these radar gates identified as being contaminated by spike signals are filtered out by applying the spike signal filtering procedure. It means that whether spike signals removal is applied prior to or after attenuation correction makes nearly no difference to Z_H values.

B.1.2. Sensitivity of attenuation correction to second-trip echo

As shown in Fig.4.9, the second-trip echoes bring "extra" erroneous u-ϕ_{DP} measurements. Given that the attenuation correction procedure relies on the magnitude of u-ϕ_{DP} (Section 4.6) and precedes the second-trip echo filtering in our data QC procedure, we inspect the impact of these 'extra' second-trip echoes in terms of u-ϕ_{DP} on the attenuation correction as follows.

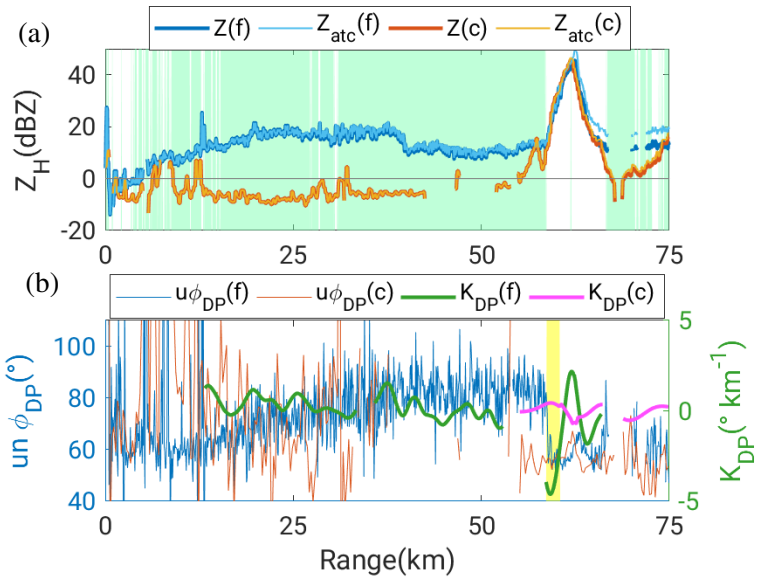

Fig. B.2.: An example ray to illustrate that the existence of second-trip echoes in terms of uncorrected differential phase ϕ_{DP} brings errors to the attenuation correction of the fine scan in the same case at 00:03 UTC 7 July 2017 as Fig. 4.7. The top figure shows the attenuation corrected Z_H (in light blue line) for the fine scan and their corresponding uncorrected Z_H (in dark blue line), and the attenuation-corrected and uncorrected Z_H for the coarse scan (in the overlapping red and orange lines), and the green areas flag the radar gates as being contaminated by second-trip echo; the bottom figure shows the uncorrected differential phase ϕ_{DP} for the fine and coarse scans respectively (in thin blue and red lines respectively), and specific differential phase K_{DP} for fine and coarse scans respectively (in thin green and magenta lines respectively). The yellow area highlights the suspiciously large negative K_{DP} values associated with second-trip echoes

B.1.3. Another type of suspicious echoes

A few radar images in our dataset display echoes with moderate intensity scattered throughout the entire three-dimensional radar coverage during the non-rainy periods (Fig.B.3). Different from other types of echoes (Section 4.5), the spatial distributions of these suspicious echoes can be either radial or circular. I don't know the sources for this type of noise. Fortunately, it only occurred a few times and does not impact the entire dataset too much.

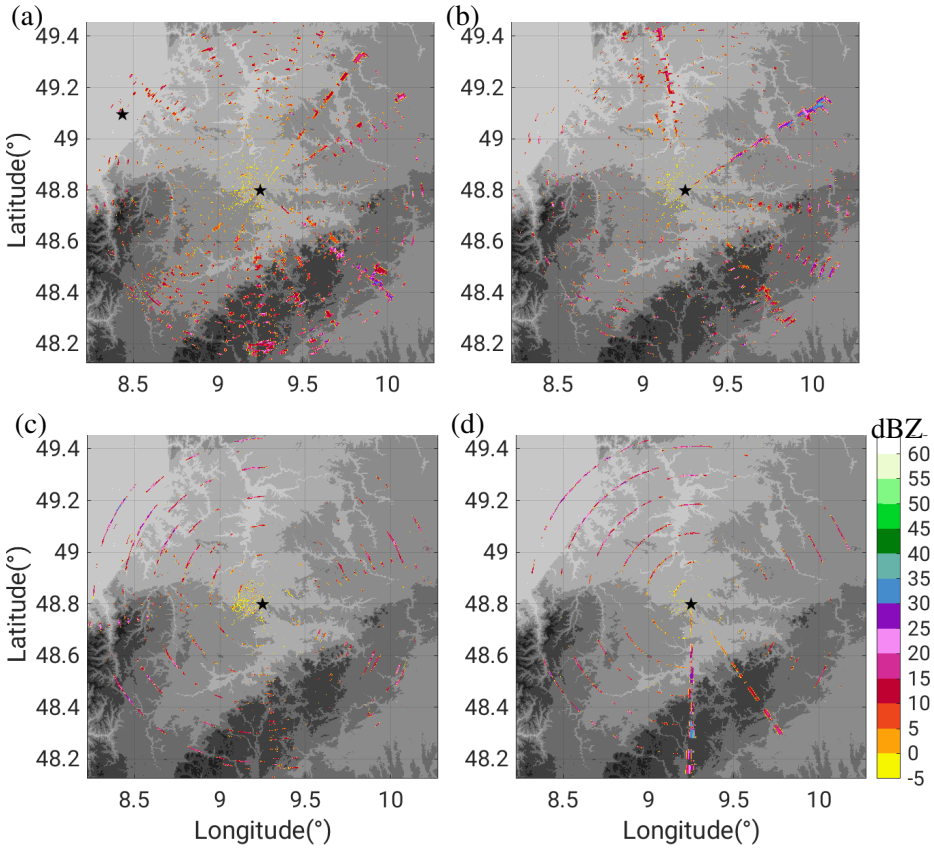

Fig. B.3.: PPI displays of Z_H (a) at 1.5°-elevation at 17:51 UTC on 3 June 2017, (b) at 3.2°-elevation at 17:51 UTC on 3 June 2017, (c) at 1.5°-elevation at 08:03 UTC on 13 June 2017, and (d) at 3.2°-elevation at 08:03 UTC on 13 June 2017

B.1.4. Spatial distribution of polarimetric variables

As a supplementary to Section 4.9.3, this section presents differences in the mean Z_{DR}, ρ_{HV}, SNR and SQI: 1) between the fine scan and coarse scans, and 2) between the data prior to and after the data quality processes, that is, between the raw data and the processed data. These mean values are averaged over all the measurements from 23 May 2021 to 16 October 2021.

For Z_{DR}, the raw Z_{DR} of the coarse scan presents a much larger area of the mean Z_{DR} more than 1.5 dB greater than the mean Z_{DR} of the fine scan (Figs. B.4(a) and B.4(b)). This corresponds to the

conclusion in Section 4.4 that the ground clutters are more prevalent in the coarse scan data. With the data QC procedure, the averaged Z_{DR} grater than 1.5 dB are removed to a large extent. The spatial distribution of the mean Z_{DR} of both scan gets similar to each other. As we know that Z_{DR} is strongly affected by the ground clutters (Section 4.5), such reductions of large positive Z_{DR} in both scans substantiate the non-meteorological echo removal can successfully remove the majority of the ground clutters.

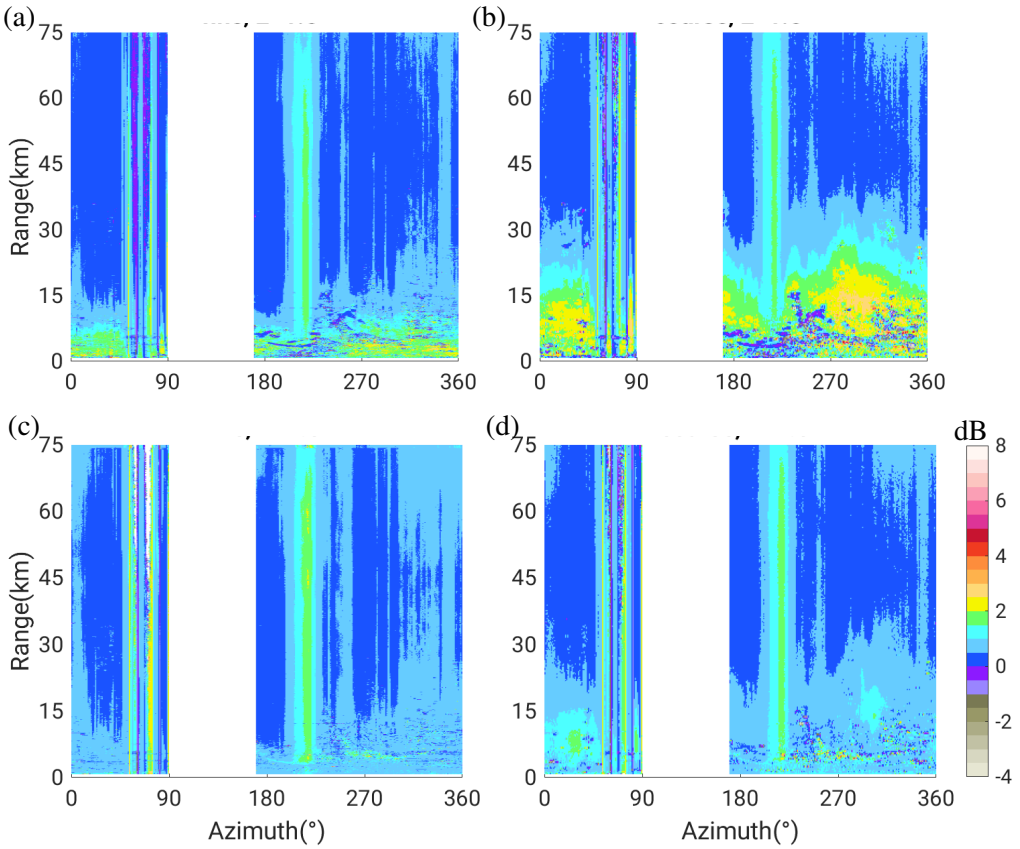

Fig. B.4.: Range-azimuth mapping of Z_{DR}, where (a) is for raw Z_{DR} of fine scans, (b) for raw Z_{DR} of coarse scans, (c) for processed Z_{DR} of fine scans, and (d) for processed Z_{DR} of coarse scans

Prior to radar data QC, the mean ρ_{HV} in fine scans are quite different from that in coarse scans. First, although in both scans the ρ_{HV} measurements smaller than 0.85 dominate in the range closer to the radar site, such an area extends to a farther range for the coarse scan dataset. This again corresponds to a larger amount of non-meteorological echoes in the coarse scan than the fine scan. Second, for the farther range such as 30 km away from the radar, the majority of the mean ρ_{HV} values are above 0.95 for the coarse scan, but the mean ρ_{HV} values between 0.92 and 0.95 prevail in the fine scan. It implies that the fine scans provide ρ_{HV} smaller than its counterpart at the same locations in the coarse scans. As mentioned in Section 4.8 that ρ_{HV} is an indicator of the polarimetric data quality, the difference in spatial distribution of ρ_{HV} implies a worse data quality for the fine scan data.

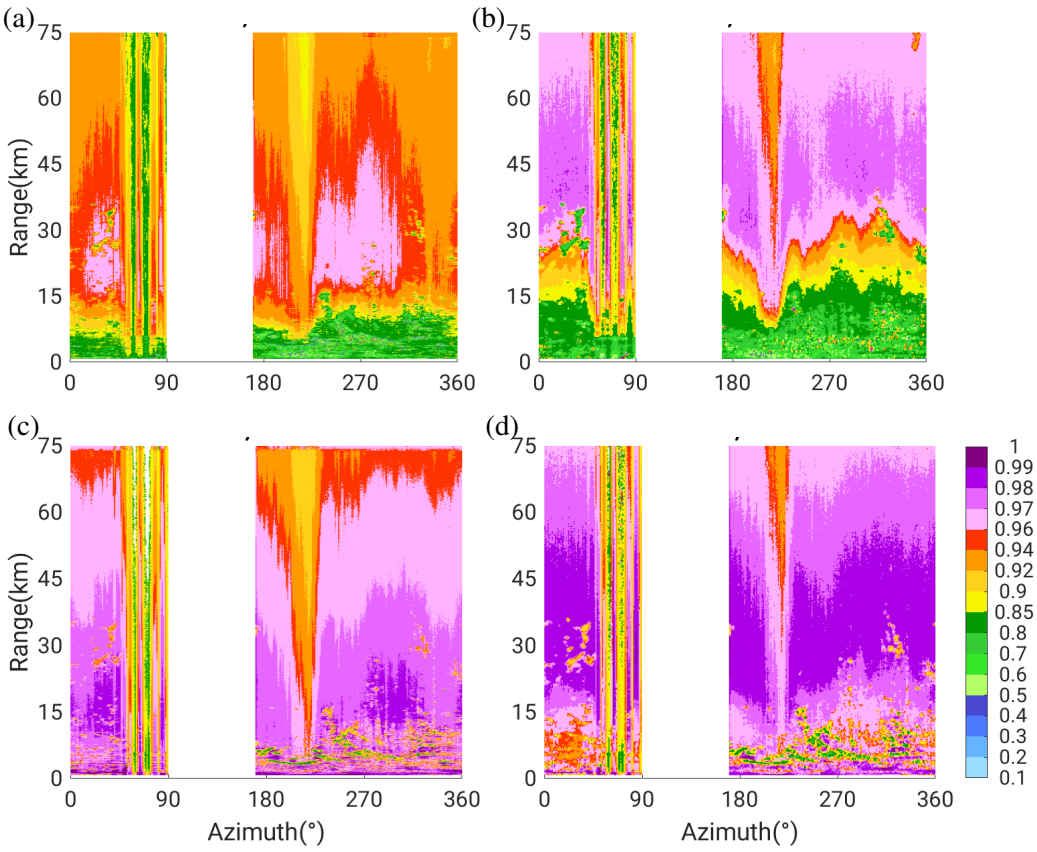

Fig. B.5.: Range-azimuth mapping of ρ_{HV}, (a) for the raw ρ_{HV} of fine scans, (b) for the raw ρ_{HV} of coarse scans, (c) for the processed ρ_{HV} of fine scans, and (d) for the processed ρ_{HV} of coarse scans

The data QC procedure removes the majority of non-meteorological echoes whose ρ_{HV} are low. As a result, the low mean ρ_{HV} measurements within 20 km away in the raw dataset disappear in the processed dataset, and for the rest of the range, the ρ_{HV} values also increase. Moreover, the discrepancies in the ρ_{HV} magnitude between the fine and coarse scans become smaller. In other words, at least for ρ_{HV}, the removal of non-meteorological echoes reduces the difference between the fine and coarse scan data. It implies the non-meteorological echoes are more subject to the spatial resolution than the precipitation echoes.

For SNR, before the data QC, the mean SNR in both datasets are low except the radar gates in proximity to the radar site, and in general the mean SNR in the coarse scan data is slightly larger than its counterpart in the fine scan data. After the data QC process is applied, the mean SNR in the processed dataset increases to at least above 12 dB for the fine scan data, and at least above 15 dB for the coarse scan data. In general, the SNR in fine scan is slightly smaller than that in the coarse scan, which corresponds to loss of weak echoes in the fine scan (Section 4.1.1). Despite the slight discrepancy in the magnitude of SNR between the fine and coarse scans, the data QC procedure discloses the range dependence which is hidden by the presence of non-meteorological echoes for both scans.

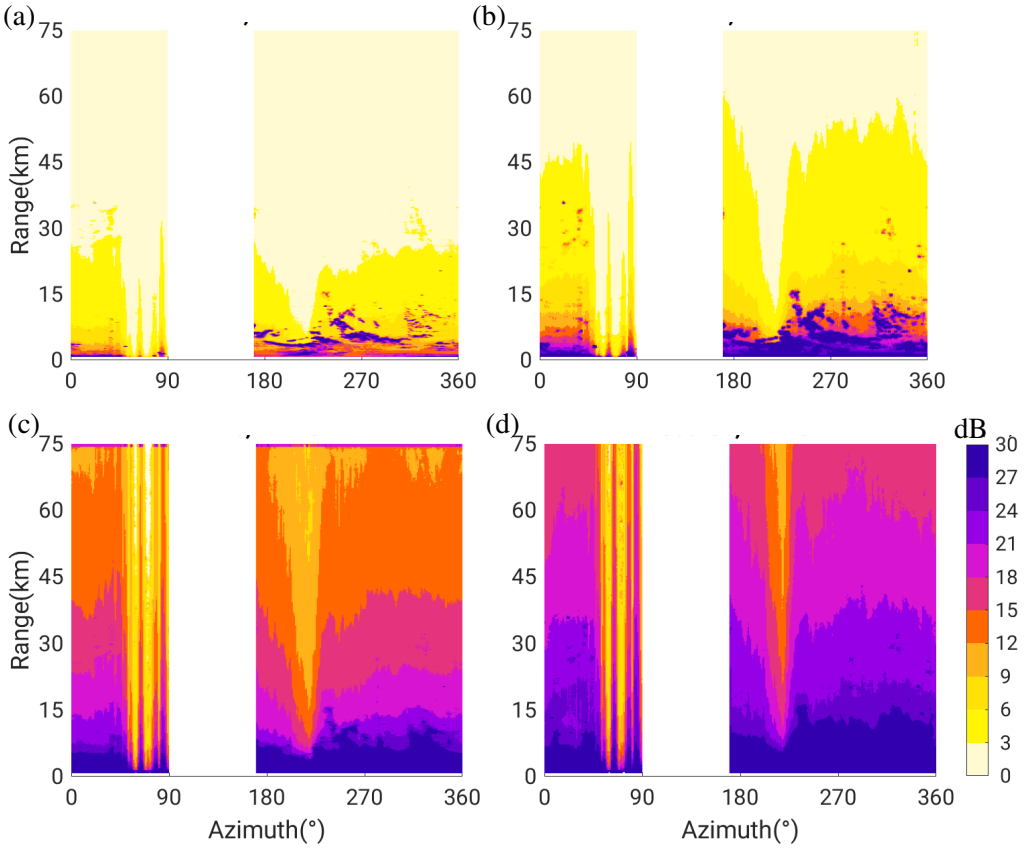

Fig. B.6.: Range-azimuth mapping of SNR, where (a) is for the raw SNR of fine scans, (b) for the raw SNR of coarse scans, (c) for the processed SNR of fine scans, and (d) for the processed SNR of coarse scans

The situation is just the opposite for SQI. Before the data QC, the spatial distributions of SQI in both scans are similar along with the range dependence, although the magnitude of SQI in the fine scans is slightly lower than that in the coarse scans. In contrast, the data QC procedure brings about huge discrepancies between the fine and coarse scans. The overall SQI magnitude in the fine scan significantly increases to at least above 0.8 along with the clear range dependence. For the coarse scan, the overall SQI magnitude also decreases from 0.7 to 0.55, except some abnormal areas between 180° to 225° in azimuth. I cannot explain what cause these abnormal SQI values. Such an obvious discrepancy can be attributed to the second-trip echo removal process which is only applied for the fine scan dataset (Section 4.3).

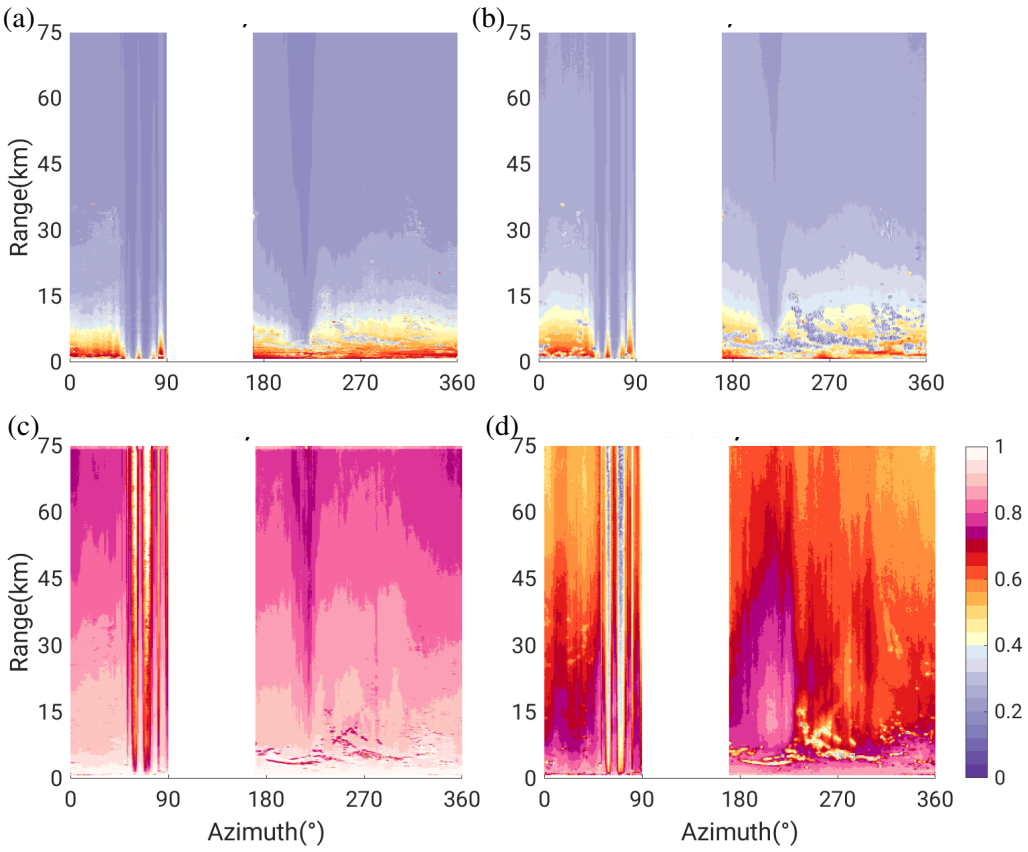

Fig. B.7.: Range-azimuth mapping of signal-to-noise ratio (SQI), where (a) is for the raw SQI of fine scans, (b) for the raw SQI of coarse scans, (c) for the processed SQI of fine scans, and (d) for the processed SQI of coarse scans

B.1.5. C-band radar data consistency check

B.2. Auxiliary analyses for C-band radar data

B.2.1. C-band radar data consistency check

C-band radar data used in this study span from 1998 to 2012, and from 2014 to 2019. Given such long time, we checked the data consistency via Z_{min}over a 20-year period, before evaluating the C-band radar data with the external rainfall measurements (MRR radar or rain gauge network) (Section 5.2).

The buildings and trees have changed over two decades, which means the static GC mapping should be updated regularly. Thus, we also examined the evolution of ground clutter over this 20-year period to establish the static GC map for each summer period (not shown).

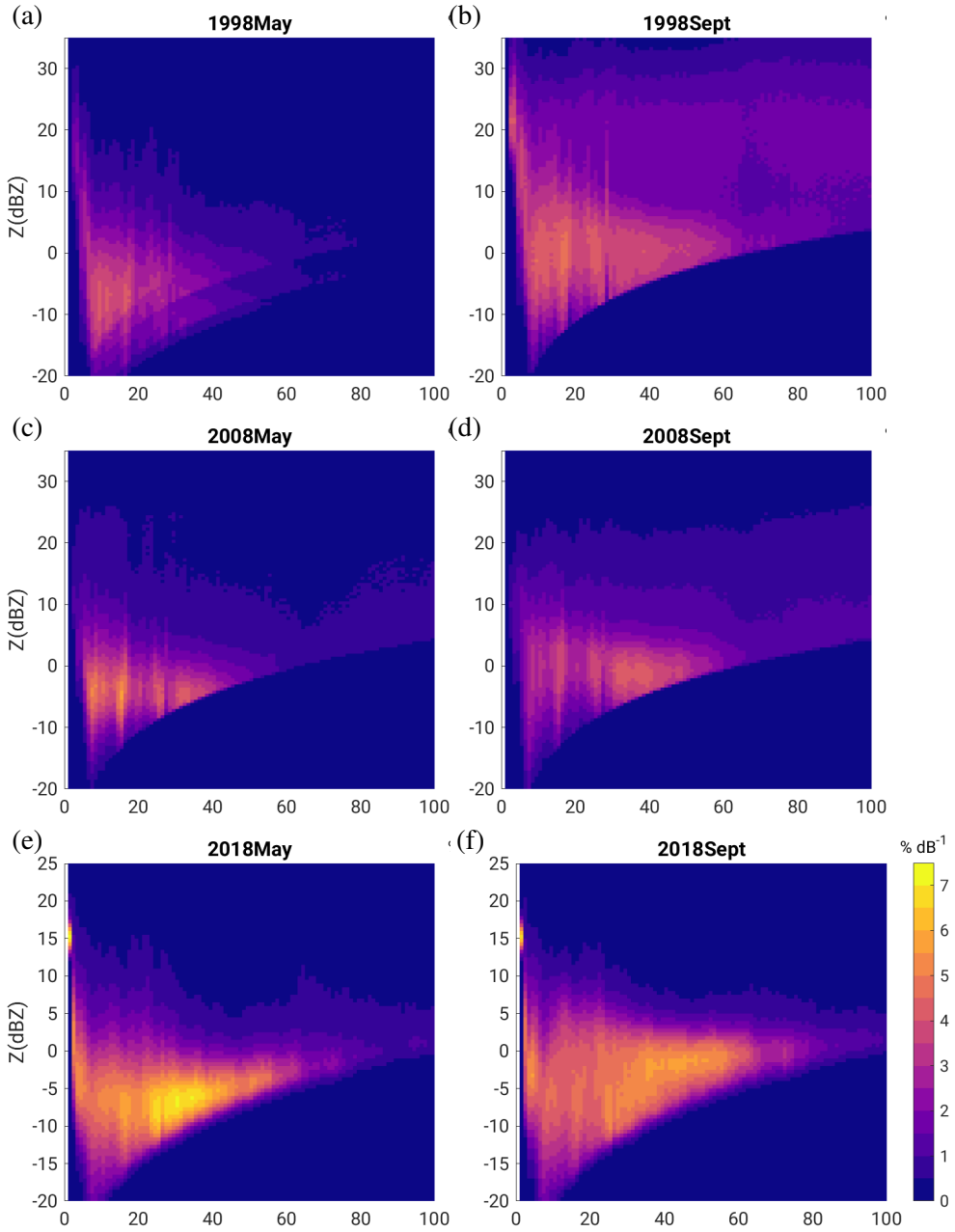

Fig. B.8.: Ray curve of Z_{min}over a month

B.2.2. C-band radar vs DWD

When it comes to using rain gauge measurements to evaluate the C-band radar data, we regard the precipitation accumulation over a month as the minimum unit, and then we have 3-dimensional datasets as follows,

$$A_{i,j,k}, \quad i = 2005, 2006, ..., 2019, j = 5, 6, ..., 9, k = 1, 2, ..., 125 \tag{B.1}$$

where the first index means a year between 2005 and 2019, the second index is for the month (May to September), and the third index represents the indexing of rain gauges sorted by their distances to the C-band radar. Given that the C-band radar data have a much longer time series (over two decades), unlike the foregoing R-G comparison for the X-band radar, the temporal scales we focus on here are monthly, annual and the total period, that is to say, accumulation from every month in each year ($A_{i,j,k}$), 5-month accumulation in each year ($Y_{i,k} = \sum_{j=5}^{9} A_{i,j,k}$), monthly accumulation across over all the years (for May, June, July, August and September separately) ($M_{j,k} = \sum_{i=2005}^{2019} A_{i,j,k}$), and total accumulation including all the five months across all the years ($T_k = \sum_{i=2005}^{2019} \sum_{j=5}^{9} A_{i,j,k}$).

Except the different time scales, the ideas of the R-G comparison using the C-band radar data are akin to the previous discussion on the X-band radar data, in terms of the matching-up procedure, the statistics and so forth. The precipitation estimates derived from the C-band radar data are also matched to rain gauge measurements, and we are ended up with the coincident dataset from the C-band radar data and rain gauge measurements. Only the C-band radar data from the 1.1° elevation are involved (the data at the 0.4° are largely contaminated by the ground clutters and beam blockage effect). Because of the data issue in May 1997 and the lack of measurements in June 2013 (due to the dual-polarization upgrade), we exclude the summers of 1997 and 2013 to assure that the C-band radar dataset used in the R-G comparison is of good data quality. According to the geographical distribution of rain gauges within the 120-km C-band coverage (Fig. 3.1(d)), rain gauges are absent in the southwest sector due to the country border between Germany and France. The number of rain gauges with valid measurements changes over time (see Fig. B.9). The number of the available rain gauges was insufficient before 2005 (Fig. B.17), so the comparison between the C-band radar data and rain gauge measurements is conducted only for 14 summers from 2005 to 2019 except 2013, equivalent to 70 months. For each rain gauge, the comparison is conducted only if at least the 95% of time has valid measurements. The rain gauges whose corresponding 'match-up' radar gates always report abnormally high values induced by the ground clutters or abnormally low values caused by the beam blockage effect are also excluded in the following R-G comparison.

Take precipitation accumulation in July 2017 ($A_{i,j,k}(i = 2017, j = 7, k = 1, 2, ..., 125)$) as an example (Fig. B.10(a)). The one-month precipitation accumulation over July 2017 from both radar data and rain gauge measurements are in accord, illustrated by the CC_{SP} of 0.69, the near 45° slope and the small intercept of the orthogonal regression fitting line, the low AAD, the low rRMSE, and the near-zero normalized bias. Not for July 2017 only, the majority of CC_{SP}s for other single-month accumulations exceed 0.6 (Fig. B.11), and the majority of RMSE values fall below 30 mm.

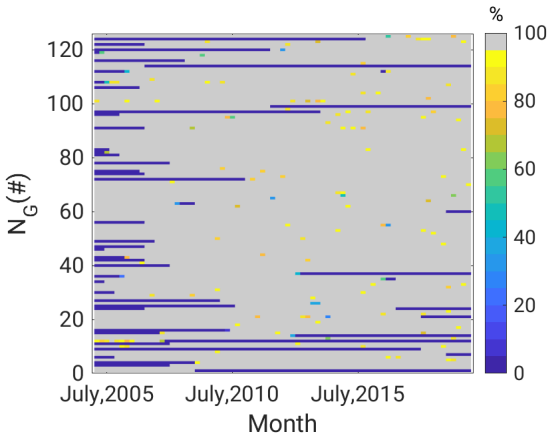

Fig. B.9.: Data availability of precipitation measurements for the rain gauges within C-band 120-km coverage from May to September from 2005 to 2019. N_G means the number of available rain gauges at a month. The color shading represents the percentage of the available rain gauge measurements for each month in each year.

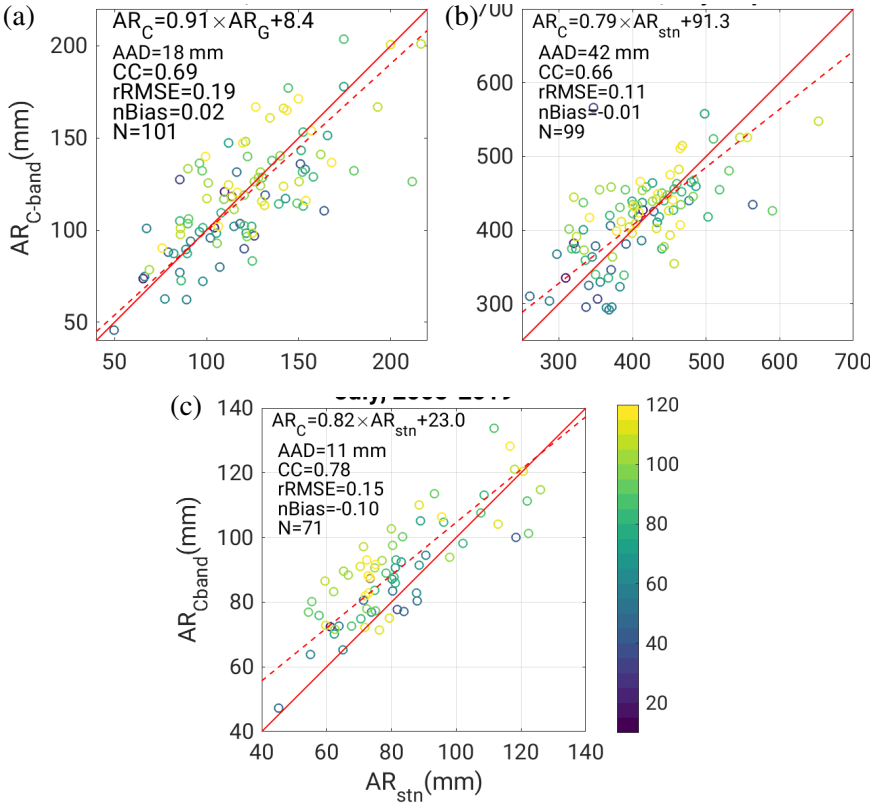

Fig. B.10.: Scatterplot for comparing precipitation accumulation between C-band radar and DWD rain gauge for (a) July 2017, (b) for May to September in 2017 and (c) for all the Julies through 2005-2019. The color of these dots indicate the distance of a rain gauge to the C-band radar; the dashed red line is the orthogonal regression fitting line; the solid red line is the diagonal line of scatterplot; the metrics shown in the left upper corner include the OR fitting equation, AAD, CC_{SPS}, rRMSE, nB and the number of dots in the scatterplot N

Take precipitation accumulation of the summer (May to September) in 2017 ($\sum_{j=5}^{9} A_{i,j,k}(i = 2017, k = 1,2,...,125)$ or $Y_{i,k}(i = 2017, k = 1,2,...,125)$) as the second example (see Fig. B.10(b)). As expected, AAD increases because this second example involves 5-month accumulation; the orthogonal regression fitting line deviates more from the diagonal line, compared to the first example for July 2017. This slight disagreement might be due to the absence of the C-band radar measurements for two rainy days with long-time heavy rain events in September 2017 due to the malfunction of the radar hardware.

Take precipitation accumulated over all Julys from 2005 to 2019 ($\sum_{i=2005}^{2019} A_{i,j,k}(j = 7, k = 1,2,...,125)$ or $M_{j,k}(j = 7, k = 1,2,...,125)$) divided by number of years as the third example (see Fig. B.10(c)). It also illustrates a good accord between radar and rain gauge, similar to the first example.

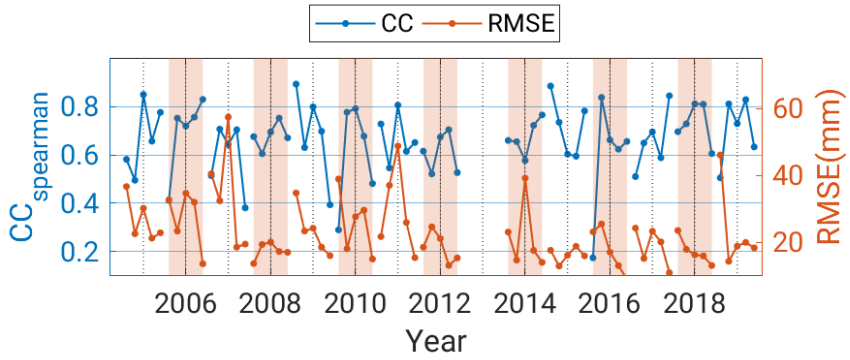

Fig. B.11.: Time series of Spearman CCs and RMSE from the comparison between rain gauges and C-band radar data over the all the 5-month summers from 2005 to 2019 except 2013. The blue line is for Spearman CCs and the red line is for RMSE

Analogous to the first example, if we consider the monthly precipitation accumulation for all the single months (Fig. B.12(a)), the number of the paired data ($AG_{\text{radar}}, AG_{\text{G}}$) exceeds 7000. Analogous to the second example, if we consider all the 5-month accumulation from 2005 to 2017 (Fig. B.12(b)), the number of the paired data exceeds 1000. Analogous to the third example, if we consider the monthly accumulation averaged from 2005 to 2017 for the total five months, the number of the paired data exceeds 350 (Fig. B.12(c)). The comparison based on the larger amount of the paired data is supposed to further ensure the representativeness of our R-G comparison.

Regardless of the temporal scales, the R-G comparison based on the larger size of samples also show good R-G correlations (Fig. B.12). The correlation efficients on all four temporal scales exceed over 0.65. Considering the high variability of precipitation and intrinsic differences in the R-G comparison (Tab. 5.2 and Section 2.3), these *CC*s are high enough to support the correlation between the C-band radar data and the independent measurements from the rain gauge network. Moreover, the orthogonal regression fitting curves have slopes close to a slope of 45°, further demonstrating the resemblance in terms of the absolute magnitude of the precipitation accumulations obtained between the radar and rain gauges. In addition, the relative RMSE decreases with the longer temporal scales, because the random variations tend to cancel out if the integration time becomes longer, and normalized biases are close

to zero, further substantiating the concordance between the radar-based precipitation estimates and rain gauge measurements.

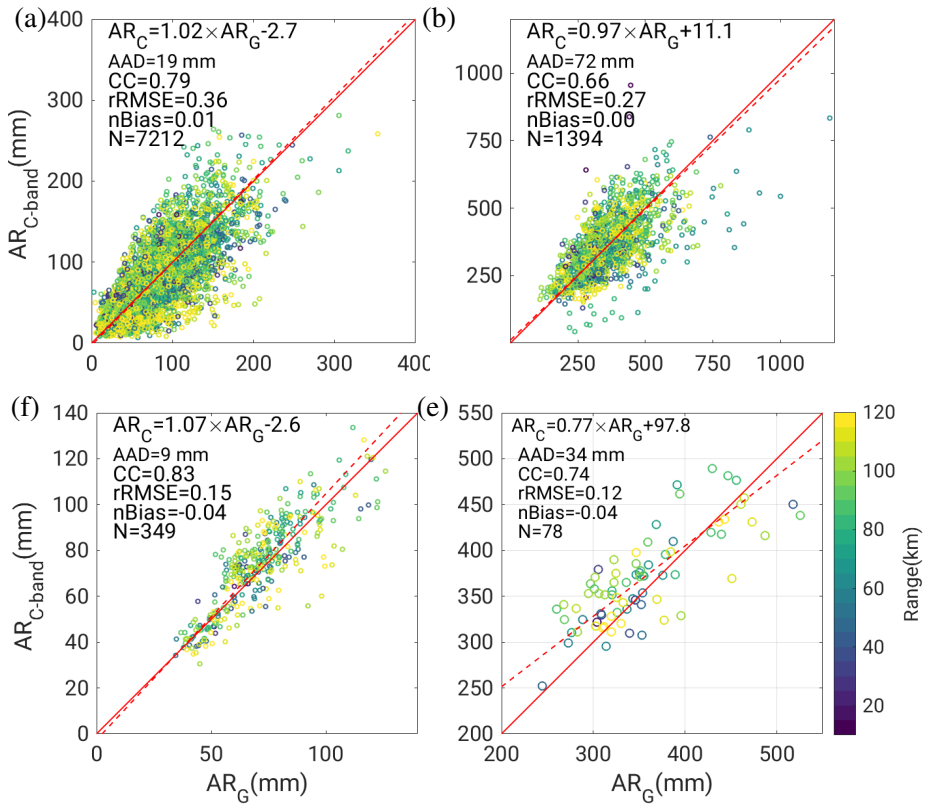

Fig. B.12.: Scatterplot for comparing precipitation accumulation between C-band radar and DWD rain gauge for (a) individual single month accumulation, (b) 5-month accumulation in each year, (c) monthly accumulation for a specific month (May, June, July, August and September individually) averaged across all the years, and (d) 5-month accumulation averaged over all the years. Other features are the same as Fig. B.10

Colors of the dots in Fig. B.12 represents the distances of rain gauges to the C-band radar; these dots distribute randomly along the diagonal line of the scatterplot. If radar data are severely affected by the attenuation issue, the dots representing rain gauges located far from the C-band radar will mainly lie below the diagonal lines. However, it is not the situation as our data show in Fig. B.12(d). Thus, we may implicitly infer that attenuation at the C-band radar doesn't lead to severe underestimation of the precipitation estimates for the long-term accumulation.

If the aforementioned statistics (correlation coefficients, RMSE, etc.) are calculated for each rain gauge individually, we can obtain the geographical distribution of the statistics (Fig. B.13), which allows us to identify some rain gauges whose measurements disagree with the radar data, and to inspect the range-dependence effect or the overshooting effect.

At the 2° elevation, the concordance between rain gauge measurements and radar estimates deteriorates as the rain gauges are situated farther from the C-band radar, shown by the CC_{SPS} decreas-

ing from 0.8 to below 0.5 (Fig. B.13(b)). Besides, through the mapping of the mean field bias between radar and gauge (Smith and Krajewski, 1991), we can find the radar overestimates the rain gauge measurements for rain gauges near the C-band radar, and this overestimation gradually mitigates with the further increasing range and reverses into an underestimation starting from the distance around 80 km; this underestimation becomes more apparent with the further increasing range, and the magnitude of this underestimation for the rain gauges beyond the 100-km distance away from the radar is much larger than the magnitude of overestimation for the rain gauge in proximity to the radar (Fig. B.13(d)).

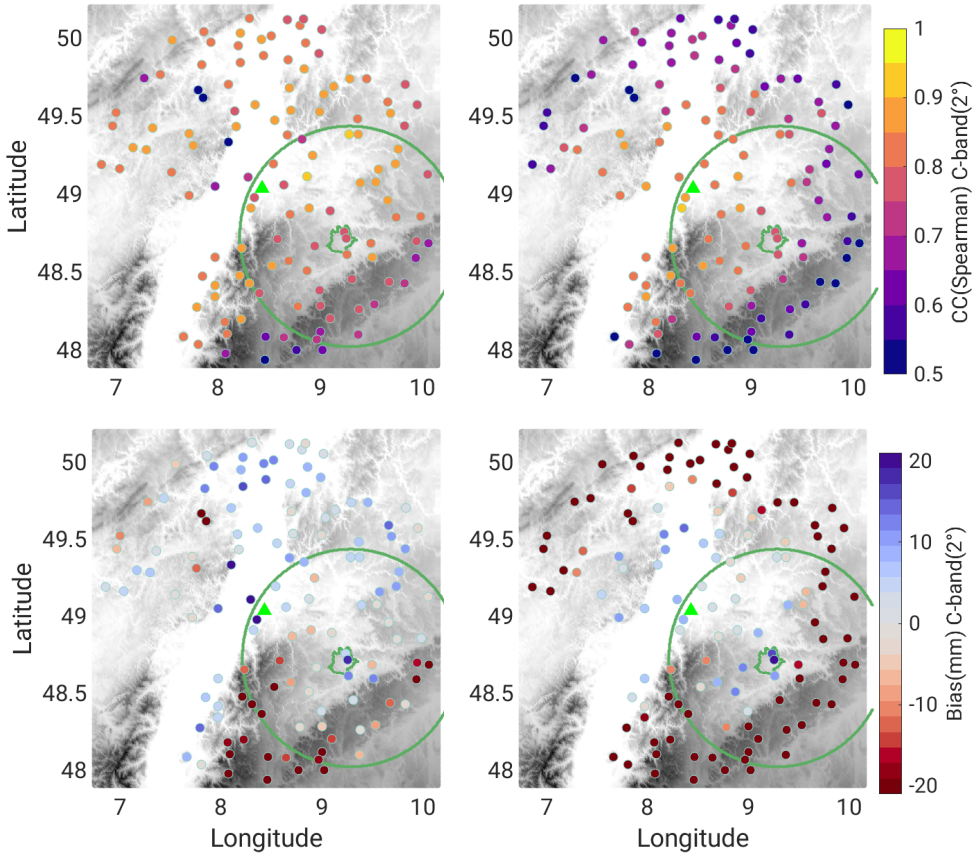

Fig. B.13.: Mapping statistics (such as CC and bias) of each rain gauge for comparison between the C-band radar and DWD rain gauge measurement for summertime 1998–2019 at the 2nd and 3rd elevations. The color shading shows the magnitude of CC_{SPS} and bias ($B = AR_{\text{C-band}} - AR_{\mathrm{G}}$ as defined in 3.3.3); the cool color in (c) and (d) implies that radar data overestimate the rain gauge measurements, vice verse for the warm color; the green triangle in the center indicates the location of the C-band radar, the green irregular closed curve in the southeast direction of the C-band radar shows the boundary of the Stuttgart city; the large green circle confines the 75-km coverage of the X-band radar

This reason for this change in bias is as follows. Along a radar beam of the 2° elevation, the radar gates 80 km away from the radar reach 3.3 km in height, as high as the averaged freezing level in this region (Section 3.1.4). It means what the radar observes is likely to be solid hydrometeors (ice crystals, snowflakes, etc.) or be a mixture of liquid and solid precipitation. The physical characteristics of the solid hydrometers differ markedly from those of the liquid hydrometeors in terms of their size, shape,

density and particularly ε. The dielectric factor K used in the radar equation (Eq. 2.13) is calculated from ε, with a high value of 0.93 for liquid hydrometers but a low value of 0.176 for solid hydrometers. These differences in physical properties inevitably lead to the differences in the radar's observations of solid, liquid, or the mixture phase precipitation, which demands a different precipitation estimator such as a relation linking radar reflectivity and snow (Z-S relation) instead of the Z-R relation used previously. In our case, it is impossible to observe the solid precipitation (snow or graupel) near the ground surface during the summertime in the southern Germany, which implies that what rain gauges measure should always be liquid precipitation except occasional hail. Using the aforementioned Z-R relation radar reflectivity without distinguishing between liquid and solid hydrometers leads to incorrect estimations of precipitation.

In principle, we expect the R-G discord for the radar gates at a certain height (around the freezing level) above the surface, as the case of the 2° elevation radar beam beyond 3.3 km. This effect caused by the curvature of earth and the slanting radar beam is named as *overshooting*. That accounts for why people prefer radar data from low elevations when they estimate the precipitation near the ground surface. A tradeoff exists between avoiding overshooting and avoiding the ground clutter contamination when selecting the proper elevations. In the other words, for the high elevation, we may only rely on the data from the radar gates below freezing levels for the purpose of comparison between the radar data and rain gauge measurement if the classic Z-R relation is used.

Contradicting to the 2° elevation, the R-G comparisons at the 1.1° elevation over the majority of the rain gauges exhibit high CC_{SPS} exceeding 0.75 and small biases with the absolute magnitude less than 20 mm, even for the rain gauges beyond 100km far away from the C-band radar. This accord between two datasets suggests that, for R-G comparison at the 1.1° elevation, the range effect is minimal.

A short discussion follows about the noticeable biases in the R-G comparison for a few rain gauges in Fig. B.13(c). The large negative or positive biases are mainly owing to the topography (Fig. B.14(a)). For instance, a radar gate along the azimuth of 324° close to the 40-km range ring reports a large positive bias whereas two radar gates along the similar azimuthal direction near the 80-km range ring report negative biases. This positive bias is due to the ground clutter where an elevated terrain height (maybe a hill) (the beam blockage in the northwest direction of the C-band radar starts roughly at the 40-km ring as well, as shown in Fig. B.14(b))) acts as a strong 'reflector' which causes high Z_{H} at a much higher frequently. Meanwhile this reflector also reduces the radiation arriving at the farther radar gates behind the reflector, resulting in the reduced radar reflectivity, which further leads to negative biases. Besides a few radar beams in the northwestern direction, the terrain-induced beam blockage is more obvious in the southern directions of the C-band radar (Fig. B.14(b)); the rain gauges located 'behind' the elevated terrain height (Black Forest and Swabian Alps) show an underestimation on the order of magnitude about 30 mm in terms of R-G comparisons of the monthly precipitation accumulation. Although all

these radar gates are affected by the underestimation, the radar gates farther from the radar have a lower CC_{SP} illustrated by the smaller size of the circles.

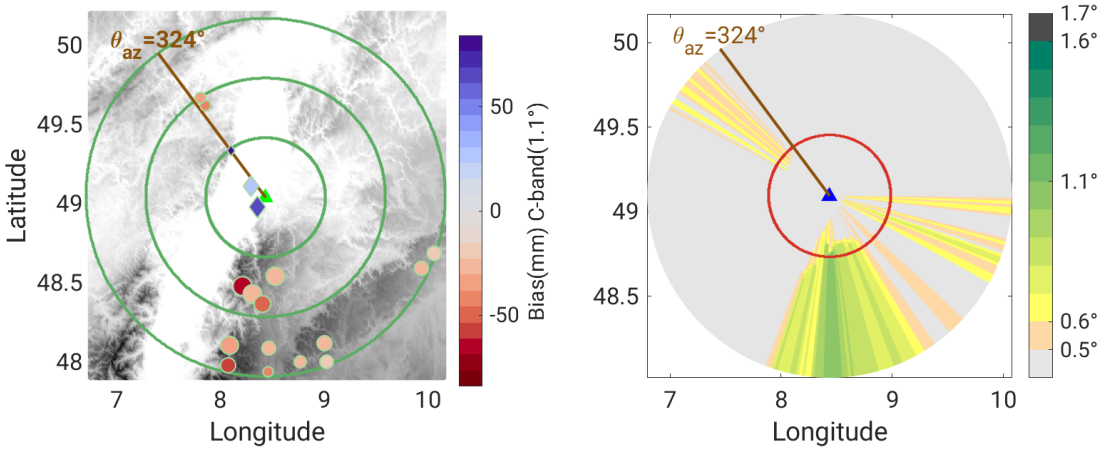

Fig. B.14.: (a) Mapping of the statistics over rain gauges which show significant overestimation or underestimation in Fig. B.13(c). The size of marker is linearly proportional to its CC_{SP}; the diamond marks in cool colors indicate the overestimation of radar data; the circular marks in warm colors indicate the underestimation of radar data; three large green concentric circles represent 40-, 80- and 120-km range rings of the C-band radar coverage. (b) The terrain-permitting minimum elevation for the 1.1° elevation sweep of the C-band radar. The blue triangle indicates the location of the C-band radar; the red circle is the 40-km range ring

In short, the range effect and overshooting influence the accuracy of the radar-derived precipitation estimates at the 2° elevation but not that much for the 1.1° elevation. Besides a few radar gates affected by the topography, the majority of the 'match-up' radar gates at the 1.1° show clear concordance with the rain gauge measurements from their corresponding rain gauges. Interestingly, the attenuation at the C-band radar is not as severe as that in the X-band radar (Section 4.6 and Section 5.2.1).

The long-term record data from the C-band radar and rain gauges allow us to have a quick look on the dryness or wetness of the summers in the two decades (Fig. B.15(a)). August 2006, and July 2014 show the simultaneous and concordant monthly precipitation accumulation maximums from radar estimation and rain gauge measurements, illustrated by peaks in the time series of monthly precipitation accumulation averaged over all the R-G pairs. It is the same for the precipitation minimums in July 2015 and September 2016. In this way, we can easily identify the climatologically 'dry' and 'wet' months or 'dry' and 'wet' summers. However, keep in mind that this annual variation of summer precipitation is based on the geographically scattered samples—roughly 100 rain gauges and their match-up corresponding radar gates. Although the rain gauges are distributed randomly and more or less evenly, the total number is limited. Meanwhile, this time series easily show clear overestimations from May-July in 2007 and from June to August in 2011, and a clear underestimation in 2013.

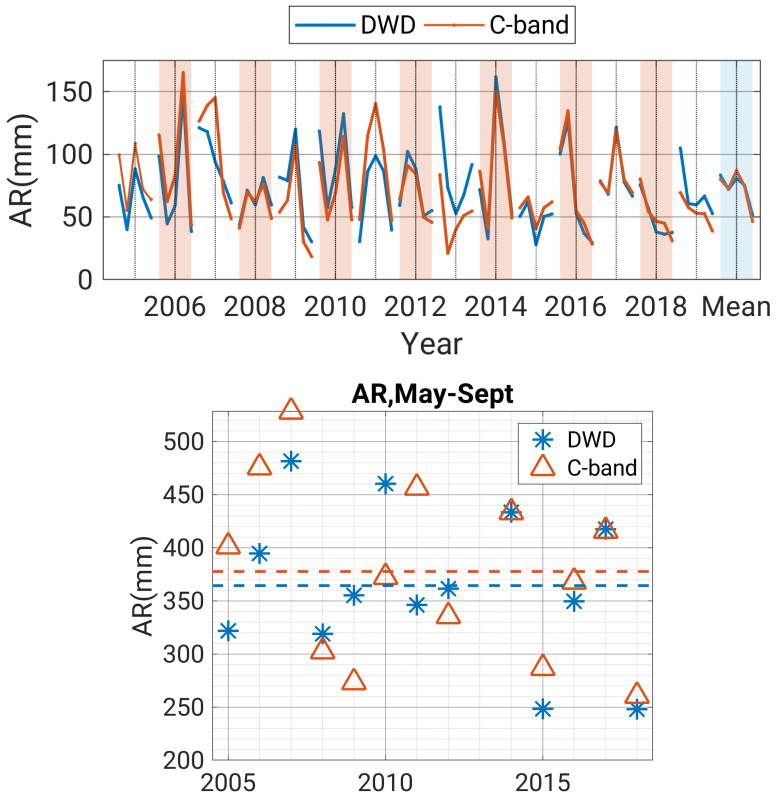

Fig. B.15.: Time series of R-G comparison of yearly/monthly precipitation accumulations from 2005 to 2019. The dashed lines in (b) are the 5-month precipitation accumulations averaged from summer 2005 to 2019 except 2013

B.2.3. C-band radar vs MRR

The C-band radar is located around 60 km away from the MRR site, and radar beams of the C-band radar at 1.1°, 2.0° and 3.0° intersect the MRR radar beam (the lowest elevation of C-band radar is excluded) at the altitudes of 1.1 km, 2.1 km and 3.1 km (Fig. 5.23(c)). However, the last intersection reaches the maximum range of the MRR, in which the MRR measurements may be not that reliable. Thus, we primary focus on the radar-MRR comparison for the C-band radar sweeps at 1.1° and 2.0° elevations, and ignore the radar sweeps at 3° elevation.

The C-band radar and MRR match-up procedure is identical to that for matching up the X-band radar and MRR. Since no data control quality procedures were applied to the C-band radar, we exclude the discussion of the effect of data control quality on the radar-MRR comparison. On the other hand, given that the C-band radar data do not undergo any data QC, we also exclude Z_H below a certain threshold (0 dBZ), to avoid these weak echoes which are most likely from non-meteorological targets and have little weights in precipitation estimation, and thus are of no interest in this study. To make it

short and avoid duplication, unlike the X-band radar-MRR comparison going through three time scales, we only consider the C-band radar-MRR comparison in the instantaneous time scale.

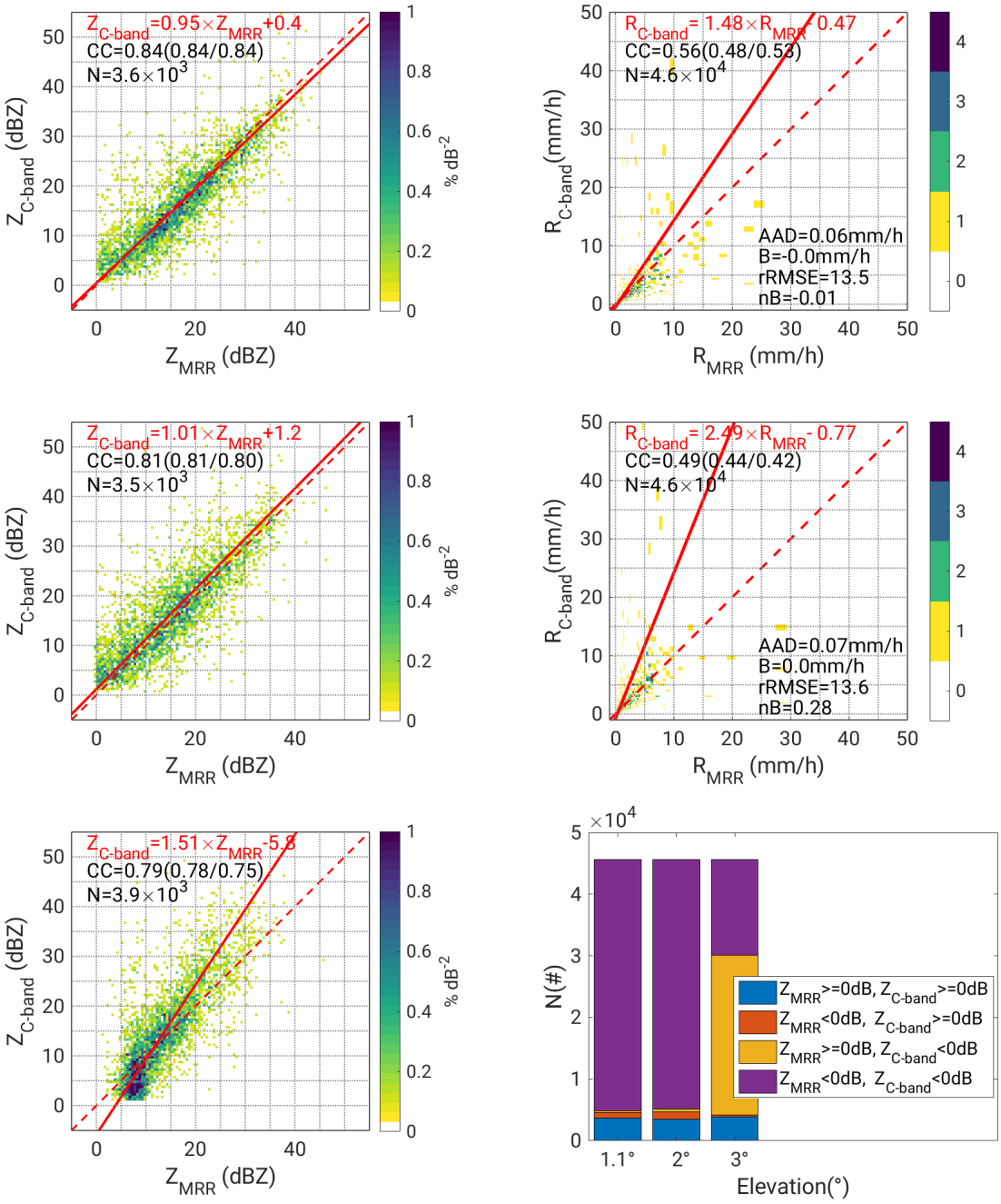

Fig. B.16.: 2D-PDF with orthogonal linear fitting lines to compare the C-band radar and MRR measurements, where (a), (c) and (e) are in terms of radar reflectivity Z_H for the radar data of the elevation of 1.1°, 2.0°, and 3.0°, respectively, (b) and (d) are in terms of precipitation rate for the 1.1° and 2.0° elevations, the dashed red line is the diagonal line, and the solid red line is the orthogonal fitting line, and (d) shows the number of the paired radar data ($Z_{\text{C-band}}$ and Z_{MRR}) under different scenarios

Z_H data from intersection points of the C-band radar and MRR at heights of 1.1 km and 2.1 km show consistent concordances—illustrated by the closeness of fitting lines to the diagonal lines—and correlation, illustrated by high correlation coefficients (Fig. B.16(a) and B.16(c)). In contrast, for the intersection point at 3.1 km high, the fitting curve deviates substantially from the diagonal lines and a large number of scatterers cluster whose MRR Z_H values fall between 5 and 10 dBZ (Fig. B.16(e)). Given that the radar-MRR comparison for the C-band radar only considers Z_H above 0 dBZ, we notice that, for the elevations of 1.1° and 2.0°, $Z_{\text{C-band}}$ and Z_{MRR} shows consistence in being above or below the threshold simultaneously, but not for the elevation of 3.0° (Fig. B.16(f)). Both the deviation of the fitting curve and disagreement on being below or above 0 dBZ reconfirms that Z_H from the last radar gate are in bad quality, probably due to the loss of signals, improper attenuation correction or inappropriate use of the empirical relations between falling velocity of raindrops and drop size, and so the comparison for the elevation of 3.0° might be excluded. Besides, the correlation coefficients decrease slightly as the elevation increases, but they are high enough to illustrate the correlation between the radar and MRR measurements, even for the elevation of 3.0°. It implies, the different magnitudes of both data do not affect the values of *CC*. In brief, Z_H from MRR and C-band radar ($Z_{\text{C-band}}$ and Z_{MRR}) agree quite well with each other.

B.3. Auxiliary analyses for other data

B.3.1. Precipitation climatology based on 20-year rain gauge network dataset

We first examine the annual variation of the total 5-month summer precipitation accumulation for the rain gauges within the area of study. The entire dataset includes the rain gauge measurements over the past two decades,and the measurements within one year is regarded as a subset. For each year, each rain gauge, if its operation time is long enough (exceeding 97%), reports its 5-month precipitation accumulation (AR_G). Thus, the sub-dataset for a year contains N AR_G (N is the number of rain gauges in a year). On the basis of the inter-quartile range (IQR) and median in each sub-dataset, the summers 2003, 2015, and 2018 are identified as the 'dry' summers, the summers 2000, 2002 and 2007 are considered as the 'wet' summers, and the summers 1999, 2004, 2012 and 2016 are regarded to be in a close resemblance with the 'mean' status (Fig. B.17). The summer 2017, when we conducted our X-band radar field experiment in Stuttgart, is identified as a moderately wet summer.

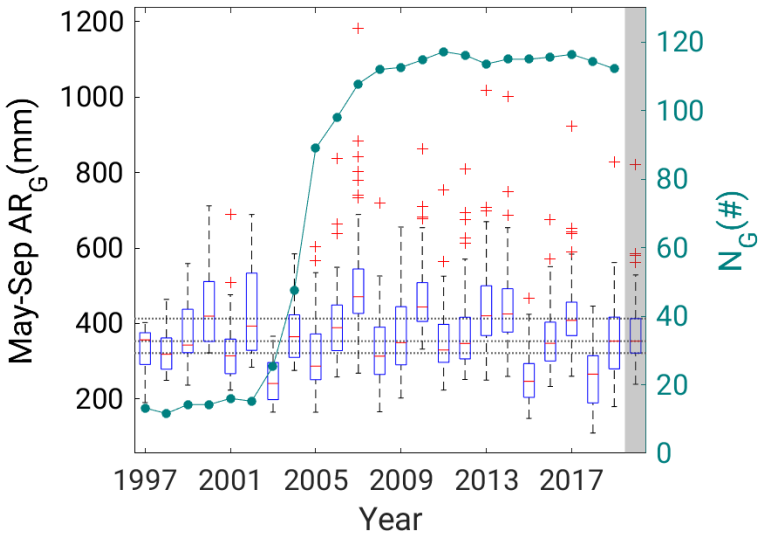

Fig. B.17.: Boxplot of the 5-month summer precipitation accumulation over the rain gauge network (on the left axis) and the number of available rain gauges within the C-band radar coverage (on the right axis), where the rightmost box represents the 'mean' box averaged from 1997 to 2019, the short horizontal red lines within the boxes are median, the upper and lower sides of the boxes represent the first and third quartiles ($Q1$ and $Q4$), equivalently the 0.25 and 0.75 quantiles ($Q_{0.25}$ and $Q_{0.75}$) (the length of the box represents the inter-quartile range (IQR $= Q3 - Q1$)), the whiskers extending upward from the upper sides of the boxes represent the range from $Q3$ to $Q3 + 1.5 \times$ IQR, the whiskers extending downward from the lower sides of the boxes represent the range from $Q1$ to $Q1 - 1.5 \times$ IQR, the 'plus sign' markers represent the outliers whose values are less than $Q1 - 1.5 \times$ IQR or greater than $Q3 + 1.5 \times$ IQR, three gray horizontal dashed lines correspond to $Q1$, median and $Q3$ of the 'mean' box

The length of boxes in the box diagram (Fig. B.17) represents the variability of the rainfall accumulations among the rain gauges within the C-band radar coverage in a summer. The wet summer 2002, in spite of less than 20 available rain gauges, is associated with the box with the largest vertical dimension, which implies that the precipitation in summer 2002 should be highly uneven within the area. This large spatial variation in summer 2002 can be further confirmed via the comparison between the boxes of 2001 and 2002. Since the rain gauge networks in summers 2001 and 2002 were nearly identical, the much shorter length of box for summer 2001 further confirms its relative small spatial variation.

Similarly, the relative short vertical dimension of the box for the summer 2017 implies that the precipitation of 2017 spatially distributed more homogeneously compared to other years. Combined with the apparent wetness of 2017, the precipitation in summer 2017 simultaneously satisfies two favorable criteria—enough precipitation amount and its (relatively) even spatial distribution; these two characteristics strengthen the reliability of targeting the summer 2017 as the measuring period of our X-band radar field experiment–a specifically detailed investigation (to be honest we did not and also was unable to predict the precipitation of 2017 before our campaign; it is just our luck).

Most of the red lines representing the medians are located below the center of the boxes (Fig. B.17); these right-skewed boxes indicate right-skewness of the probability density distribution, a larger variation among the precipitation measurements above the medians combined with a smaller variation among the precipitation measurement below the medians. The outliers appear only above the boxes, which means the prevalence of the positive anomalies and the absence of the negative anomalies. The extremely high values for some rain gauges are very likely due to a few convective precipitation events with heavy precipitation amounts passing over some random rain gauges, resulting in outliers above the upper whiskers. In 2017, a few outliers above the boxes imply the convective systems may have been more active in 2007, which indirectly implies a sufficient number of extremely convective storms for our specific study on convective precipitation.

B.3.2. MRR data evaluation with a rain gauge

Before comparing MRR with radar data and evaluating radar data with MRR (Section 5.2), we assessed the MRR data with its collocated rain gauge. These data used in the assessment were from the entire measuring period for the X-band experiment period.

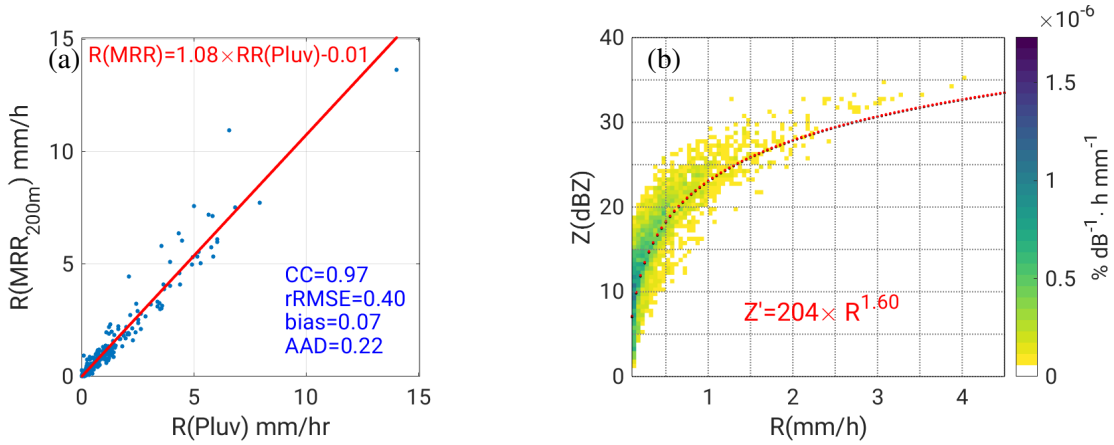

Fig. B.18.: (a) Scatterplot between rainfall rate measured by Pluvios rain gauge and rainfall rate measured by MRR, and (b) 2D-PDF between rainfall rate and Z_H both measured by MRR

The effective measure areas (projected on the ground surface) are on the order of cm^2 for a rain gauge, of m^2 for a vertical-pointing radar, and of km^2 for a volume scan radar, respectively. The sampling manner of a vertical-pointing scan mode is closer to the rain gauge, compared to a volumetric scan mode, in terms of the magnitude of the area. It implies that what a vertical-pointing scanning mode observes should be statistically closer to what a rain gauge measures, and thus we give credence to the agreement between precipitation estimates derived from a vertical-pointing MRR and precipitation measurements provided by the rain gauge 'Pluvios'.

For the Z-R relation ($Z = aR^b$), on the basis of our datasets, the non-linear fitting procedure determines the value for a about 200 and for b about 1.6, making our Z-R relation nearly identical to the classic Marshall-Palmer relation. In other words, the classic Marshall-Palmer relation is applicable to the precipitation in the area of investigation.

B.3.3. Freezing layer height

To estimate the freezing level height, we use the air temperature vertical profile calculated using the radiosonde data from a radiosonde site in Stuttgart airport at 48.83°N and 9.2°E at an altitude of 321 m above the sea level. The data were accessed from the University of Wyoming (Oolman, 2017; Durre and Yin, 2008). Since we are interested in precipitation, the freezing level heights during the rainy periods are also particularly sorted out. For the entire measuring period of our X-band radar experiment, the freezing on average was around 3.2 km during the rainy period and 3.5 km including rainy and non-rainy period (Fig. B.19)

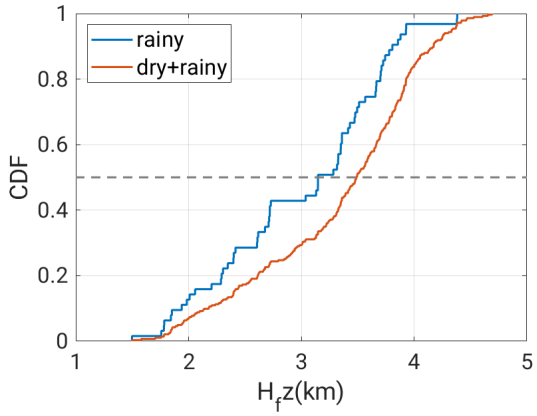

Fig. B.19.: The CDF of the freezing level height from radiosonde data during the entire period and the rainy period

C. List of Figures

D. List of Tables

E. Acknowledgments

I would like to give my special gratitudes to the following people/organizations:

- my supervisors without whom I would not have been able to complete this research—Prof. Christoph Kottmeier, Dr. Norbert Kalthoff and Dr. Jan Handwerker;
- my colleagues in Department Troposphere Research in Institute of Meteorology and Climate Research (IMK-TRO), especially members in the research group Land Surface and Boundary Layer;
- the Graduate School of the Center for Climate and Environment (GRACE), and Karlsruhe House of Young Scientists (KHYS) that provided financial supports for several workshops, summer schools and seminars I attended;
- my family in China and my friends (H.X, S.W, J.G)

F. Bibliography

Al-Sakka, H., A.-A. Boumahmoud, B. Fradon, S. J. Frasier, and P. Tabary, 2013: A new fuzzy logic hydrometeor classification scheme applied to the French X-, C-, and S-band polarimetric radars. *Journal of applied meteorology and climatology*, **52 (10)**, 2328–2344.

Anagnostou, E. N., M. N. Anagnostou, W. F. Krajewski, A. Kruger, and B. J. Miriovsky, 2004: High-resolution rainfall estimation from X-band polarimetric radar measurements. *Journal of Hydrometeorology*, **5 (1)**, 110–128.

Anagnostou, M. N., J. Kalogiros, E. N. Anagnostou, and A. Papadopoulos, 2009: Experimental results on rainfall estimation in complex terrain with a mobile X-band polarimetric weather radar. *Atmospheric Research*, **94 (4)**, 579–595.

Andsager, K., K. V. Beard, and N. F. Laird, 1999: Laboratory measurements of axis ratios for large raindrops. *Journal of the Atmospheric Sciences*, **56 (15)**, 2673–2683.

Arnbjerg-Nielsen, K., P. Willems, J. Olsson, S. Beecham, A. Pathirana, I. Bülow Gregersen, H. Madsen, and V.-T.-V. Nguyen, 2013: Impacts of climate change on rainfall extremes and urban drainage systems: a review. *Water Science and Technology*, **68 (1)**, 16–28.

Asai, T., M. Yoshizaki, and K. Ishikawa, 1977: Some results on an objective analysis for tracking radar echoes of convective clouds. *Journal of the Meteorological Society of Japan. Ser. II*, **55 (5)**, 553–558.

Atlas, D., 1964: Advances in radar meteorology. *Advances in geophysics*, Elsevier, Vol. 10, 317–478.

———, 2002: Radar calibration: Some simple approaches. *Bulletin of the American Meteorological Society*, **83 (9)**, 1313–1316.

Atlas, D. and H. C. Banks, 1951: The interpretation of microwave reflections from rainfall. *Journal of Meteorology*, **8 (5)**, 271–282.

Atlas, D., M. Kerker, and W. Hitschfeld, 1953: Scattering and attenuation by non-spherical atmospheric particles. *Journal of Atmospheric and Terrestrial Physics*, **3 (2)**, 108–119.

Austin, P. M., 1987: Relation between measured radar reflectivity and surface rainfall. *Monthly Weather Review*, **115 (5)**, 1053–1070.

Aydin, K., Y. Zhao, and T. A. Seliga, 1989: Rain-induced attenuation effects on C-band dual-polarization meteorological radars. *IEEE transactions on geoscience and remote sensing*, **27 (1)**, 57–66.

Balakrishnan, N. and D. Zrnic, 1990: Use of polarization to characterize precipitation and discriminate large hail. *Journal of the atmospheric sciences*, **47 (13)**, 1525–1540.

Balanis, C. A., 2016: *Antenna Theory: Analysis and Design*. 4th ed., John wiley & sons, 1073 pp.

Barge, B. and G. Isaac, 1973: The shape of alberta hailstones. *J. Rech. Atmos*, **7 (1)**, 11–20.

Barredo, J. I., 2007: Major flood disasters in Europe: 1950–2005. *Natural Hazards*, **42 (1)**, 125–148.

Bartels, H., E. Weigl, T. Reich, P. Lang, A. Wagner, O. Kohler, and N. Gerlach, 2004a: MeteoSolutions GmbH: Projekt RADOLAN–Routineverfahren zur Online-Aneichung der Radarniederschlagsdaten mit Hilfe von automatischen Bodenniederschlagsstationen (Ombrometer). *Deutscher Wetterdienst, Offenbach*.

———, 2004b: Routineverfahren zur Online-Aneichung der Radarniederschlagsdaten mit Hilfe von automatischen Bodenniederschlagsstationen (Routine procedure for online accumulation of radar precipitation data using automatic ground precipitation stations.). *Abschlussbericht, Selbstverlag, Deutscher Wetterdienst Offenbach*.

Battan, L. J., 1973: *Radar Observation of the Atmosphere*. The University of Chicago Press, 324 pp.

Beard, K. V. and C. Chuang, 1987: A new model for the equilibrium shape of raindrops. *Journal of the Atmospheric sciences*, **44 (11)**, 1509–1524.

Beasley, E. W., 1966: Effect of surface reflections on rain cancellation in radars using circular polarization. *Proceedings of the IEEE*, **54 (12)**, 2000–2001.

Bech, J., B. Codina, J. Lorente, and D. Bebbington, 2003: The sensitivity of single polarization weather radar beam blockage correction to variability in the vertical refractivity gradient. *Journal of Atmospheric and Oceanic Technology*, **20 (6)**, 845–855.

Bechini, R. and V. Chandrasekar, 2015: A semisupervised robust hydrometeor classification method for dual-polarization radar applications. *Journal of Atmospheric and Oceanic Technology*, **32 (1)**, 22–47.

Bell, M. M., W.-C. Lee, C. A. Wolff, and H. Cai, 2013: A Solo-based automated quality control algorithm for airborne tail Doppler radar data. *Journal of applied meteorology and climatology*, **52 (11)**, 2509–2528.

Bentley, M. L., W. S. Ashley, and J. A. Stallins, 2010: Climatological radar delineation of urban convection for Atlanta, Georgia. *International Journal of Climatology*, **30 (11)**, 1589–1594.

Berens, P. et al., 2009: CircStat: a MATLAB toolbox for circular statistics. *J Stat Softw*, **31 (10)**, 1–21.

Berne, A., G. Delrieu, J.-D. Creutin, and C. Obled, 2004: Temporal and spatial resolution of rainfall measurements required for urban hydrology. *Journal of Hydrology*, **299 (3-4)**, 166–179.

Besic, N., J. Figueras i Ventura, J. Grazioli, M. Gabella, U. Germann, and A. Berne, 2016: Hydrometeor classification through statistical clustering of polarimetric radar measurements: A semi-supervised approach. *Atmospheric Measurement Techniques*, **9 (9)**, 4425–4445.

Bohren, C. F. and D. R. Huffman, 1983: *Absorption and Scattering of Light by Small Particles*. John Wiley & Sons, 544 pp.

Bornstein, R. and Q. Lin, 2000: Urban heat islands and summertime convective thunderstorms in Atlanta: Three case studies. *Atmospheric Environment*, **34 (3)**, 507–516.

Borowska, L., D. Zrnić, A. Ryzhkov, P. Zhang, and C. Simmer, 2011: Polarimetric estimates of a 1-month accumulation of light rain with a 3-cm wavelength radar. *Journal of Hydrometeorology*, **12 (5)**, 1024–1039.

Brandes, E. A., 1975: Optimizing rainfall estimates with the aid of radar. *Journal of Applied Meteorology and Climatology*, **14 (7)**, 1339–1345.

Brandes, E. A., J. Vivekanandan, and J. W. Wilson, 1999: A comparison of radar reflectivity estimates of rainfall from collocated radars. *Journal of Atmospheric and Oceanic Technology*, **16 (9)**, 1264–1272.

Brandes, E. A., G. Zhang, and J. Vivekanandan, 2002: Experiments in rainfall estimation with a polarimetric radar in a subtropical environment. *Journal of Applied Meteorology*, **41 (6)**, 674–685.

———, 2003: An evaluation of a drop distribution–based polarimetric radar rainfall estimator. *Journal of Applied Meteorology*, **42 (5)**, 652–660.

Bringi, V., V. Chandrasekar, N. Balakrishnan, and D. Zrnić, 1990: An examination of propagation effects in rainfall on radar measurements at microwave frequencies. *Journal of Atmospheric and Oceanic Technology*, **7 (6)**, 829–840.

Bringi, V., V. Chandrasekar, P. Meischner, J. Hubbert, and Y. Golestani, 1991: Polarimetric radar signatures of precipitation at S and C-bands. *IEE Proceedings F (Radar and Signal Processing)*, IET, Vol. 138, 109–119.

Bringi, V. and A. Hendry, 1990: Technology of polarization diversity radars for meteorology. *Radar in Meteorology*, Springer, 153–190.

Bringi, V., T. Tang, and V. Chandrasekar, 2004: Evaluation of a new polarimetrically based Z–R relation. *Journal of Atmospheric and Oceanic Technology*, **21 (4)**, 612–623.

Bringi, V. and D. Zrnic, 2019: Polarization weather radar development from 1970–1995: Personal reflections. *Atmosphere*, **10 (11)**, 714.

Bringi, V. N. and V. Chandrasekar, 2001: *Polarimetric Doppler Weather Radar: Principles and Applications*. Cambridge university press, 664 pp.

Bringi, V. N., T. Keenan, and V. Chandrasekar, 2001: Correcting C-band radar reflectivity and differential reflectivity data for rain attenuation: A self-consistent method with constraints. *IEEE Transactions on Geoscience and Remote Sensing*, **39 (9)**, 1906–1915.

Browne, I. C. and N. Robinson, 1952: Cross-polarization of the radar melting-band. *Nature*, **170 (4338)**, 1078–1079.

Cao, Q., G. Zhang, E. Brandes, T. Schuur, A. Ryzhkov, and K. Ikeda, 2008: Analysis of video disdrometer and polarimetric radar data to characterize rain microphysics in Oklahoma. *Journal of Applied Meteorology and Climatology*, **47 (8)**, 2238–2255.

Cao, Q., G. Zhang, R. D. Palmer, and L. Lei, 2011: Detection and mitigation of second-trip echo in polarimetric weather radar employing random phase coding. *IEEE transactions on geoscience and remote sensing*, **50 (4)**, 1240–1253.

Capozzi, V., E. Picciotti, V. Mazzarella, F. S. Marzano, and G. Budillon, 2018: Fuzzy-logic detection and probability of hail exploiting short-range X-band weather radar. *Atmospheric Research*, **201**, 17–33.

Carey, L. D., S. A. Rutledge, D. A. Ahijevych, and T. D. Keenan, 2000: Correcting propagation effects in C-band polarimetric radar observations of tropical convection using differential propagation phase. *Journal of Applied Meteorology*, **39 (9)**, 1405–1433.

Chandrasekar, V., R. Keränen, S. Lim, and D. Moisseev, 2013: Recent advances in classification of observations from dual polarization weather radars. *Atmospheric Research*, **119**, 97–111.

Chandrasekar, V., Y. Wang, and H. Chen, 2012: The CASA quantitative precipitation estimation system: A five year validation study. *Natural Hazards and Earth System Sciences*, **12 (9)**, 2811–2820.

Collier, C., 1986: Accuracy of rainfall estimates by radar, Part I: Calibration by telemetering raingauges. *Journal of Hydrology*, **83 (3-4)**, 207–223.

Cordesses, R., J. Fournet-Fayard, D. Ramond, and P. Amayenc, 1983: ANATOL- A S-band differential reflectivity radar for meteorological studies. *Conference on Radar Meteorology, 21 st, Edmonton, Alberta, Canada*, American Meteorological Society, 358–361.

Cristiano, E., M.-C. t. Veldhuis, and N. v. d. Giesen, 2017: Spatial and temporal variability of rainfall and their effects on hydrological response in urban areas–a review. *Hydrology and Earth System Sciences*, **21 (7)**, 3859–3878.

Crum, T. D., R. L. Alberty, and D. W. Burgess, 1993: Recording, archiving, and using WSR-88D data. *Bulletin of the American Meteorological Society*, **74 (4)**, 645–654.

Dabberdt, W. F., J. Hales, S. Zubrick, A. Crook, W. Krajewski, J. C. Doran, C. Mueller, C. King, R. N. Keener, R. Bornstein, et al., 2000: Forecast issues in the urban zone: Report of the 10th Prospectus Development Team of the US Weather Research Program. *Bulletin of the American Meteorological Society*, **81 (9)**, 2047–2064.

Dai, Q., D. Han, M. A. Rico-Ramirez, and T. Islam, 2013: The impact of raindrop drift in a three-dimensional wind field on a radar–gauge rainfall comparison. *International journal of remote sensing*, **34 (21)**, 7739–7760.

Davini, P., R. Bechini, R. Cremonini, and C. Cassardo, 2012: Radar-based analysis of convective storms over northwestern Italy. *Atmosphere*, **3 (1)**, 33–58.

Delrieu, G., H. Andrieu, and J. D. Creutin, 2000: Quantification of path-integrated attenuation for X-and C-band weather radar systems operating in Mediterranean heavy rainfall. *Journal of Applied Meteorology*, **39 (6)**, 840–850.

Delrieu, G., J. D. Creutin, and H. Andrieu, 1995: Simulation of radar mountain returns using a digitized terrain model. *Journal of Atmospheric and Oceanic Technology*, **12 (5)**, 1038–1049.

Diederich, M., A. Ryzhkov, C. Simmer, P. Zhang, and S. Trömel, 2015: Use of specific attenuation for rainfall measurement at X-band radar wavelengths. Part II: Rainfall estimates and comparison with rain gauges. *Journal of Hydrometeorology*, **16 (2)**, 503–516.

Dolan, B. and S. A. Rutledge, 2009: A theory-based hydrometeor identification algorithm for X-band polarimetric radars. *Journal of Atmospheric and Oceanic Technology*, **26 (10)**, 2071–2088.

Douben, K.-J., 2006: Characteristics of river floods and flooding: a global overview 1985–2003. *Irrigation and Drainage: The journal of the International Commission on Irrigation and Drainage*, **55 (S1)**, S9–S21.

Doviak, R., V. Bringi, A. Ryzhkov, A. Zahrai, and D. Zrnić, 2000: Considerations for polarimetric upgrades to operational WSR-88D radars. *Journal of Atmospheric and Oceanic Technology*, **17 (3)**, 257–278.

Doviak, R., D. Sirmans, D. ZRNIC, and G. WALKER, 1977: Resolution of pulse-Doppler radar range and velocity ambiguities in severe storms. *Conference on Radar Meteorology, 17 th, Seattle, Wash*, 15–22.

Doviak, R. J. et al., 1993: *Doppler Radar and Weather Observations*. 2d ed., Dover Publisher, 562 pp.

Dufton, D. and C. Collier, 2015: Fuzzy logic filtering of radar reflectivity to remove non-meteorological echoes using dual polarization radar moments. *Atmospheric Measurement Techniques*, **8 (10)**, 3985–4000.

Durre, I. and X. Yin, 2008: Enhanced radiosonde data for studies of vertical structure. *Bulletin of the American Meteorological Society*, **89 (9)**, 1257–1262.

DWD Climate Data Center (CDC), 2019: 1-minute station observation of precipitation amount in mm for germany. Accessed 25 June 2019.

Einfalt, T., K. Arnbjerg-Nielsen, C. Golz, N.-E. Jensen, M. Quirmbach, G. Vaes, and B. Vieux, 2004: Towards a roadmap for use of radar rainfall data in urban drainage. *Journal of Hydrology*, **299 (3-4)**, 186–202.

Emmanuel, I., H. Andrieu, E. Leblois, and B. Flahaut, 2012: Temporal and spatial variability of rainfall at the urban hydrological scale. *Journal of hydrology*, **430**, 162–172.

ETSI, 2016: Navigation radar used oninland waterways;Harmonised Standard covering the essential requirements of article 3.2 of Directive 2014/53/EU. URL `https://www.etsi.org/deliver/etsi_en/302100_302199/302194/02.01.01_30/en_302194v020101v.pdf`.

Fabry, F., 2015: *Radar Meteorology: Principles and Practice*. Cambridge University Press, 256 pp.

Fabry, F., G. Austin, and D. Tees, 1992: The accuracy of rainfall estimates by radar as a function of range. *Quarterly Journal of the Royal Meteorological Society*, **118 (505)**, 435–453.

Fabry, F., A. Bellon, M. R. Duncan, and G. L. Austin, 1994: High resolution rainfall measurements by radar for very small basins: the sampling problem reexamined. *Journal of Hydrology*, **161 (1-4)**, 415–428.

Feng, L., H. Xiao, G. Wen, Z. Li, Y. Sun, Q. Tang, and Y. Liu, 2016: Rain attenuation correction of reflectivity for X-band dual-polarization radar. *Atmosphere*, **7 (12)**, 164.

Fiener, P. and K. Auerswald, 2009: Spatial variability of rainfall on a sub-kilometre scale. *Earth Surface Processes and Landforms*, **34 (6)**, 848–859.

Frech, M., 2013: Monitoring the data quality oft he new polarimetric weather radar network of the German Meteorological Service, extended abstract 9B. 3. *AMS Radar conference*.

French, M. M., D. W. Burgess, E. R. Mansell, and L. J. Wicker, 2015: Bulk hook echo raindrop sizes retrieved using mobile, polarimetric Doppler radar observations. *Journal of Applied Meteorology and Climatology*, **54 (2)**, 423–450.

Fridlind, A. M., M. v. Lier-Walqui, S. Collis, S. E. Giangrande, R. C. Jackson, X. Li, T. Matsui, R. Orville, M. H. Picel, D. Rosenfeld, et al., 2019: Use of polarimetric radar measurements to constrain simulated convective cell evolution: a pilot study with Lagrangian tracking. *Atmospheric Measurement Techniques*, **12 (6)**, 2979–3000.

Friedrich, K., M. Hagen, and T. Einfalt, 2006: A quality control concept for radar reflectivity, polarimetric parameters, and Doppler velocity. *Journal of Atmospheric and Oceanic Technology*, **23 (7)**, 865–887.

Giangrande, S. E., S. Collis, A. K. Theisen, and A. Tokay, 2014: Precipitation estimation from the ARM distributed radar network during the MC3E campaign. *Journal of Applied Meteorology and Climatology*, **53 (9)**, 2130–2147.

Giangrande, S. E., R. McGraw, and L. Lei, 2013: An application of linear programming to polarimetric radar differential phase processing. *Journal of Atmospheric and Oceanic Technology*, **30 (8)**, 1716–1729.

Gires, A., C. Onof, C. Maksimovic, D. Schertzer, I. Tchiguirinskaia, and N. Simoes, 2012: Quantifying the impact of small scale unmeasured rainfall variability on urban runoff through multifractal downscaling: A case study. *Journal of Hydrology*, **442**, 117–128.

Giuli, D., 1986: Polarization diversity in radars. *Proceedings of the IEEE*, **74 (2)**, 245–269.

Giuli, D., M. Gherardelli, A. Freni, T. Seliga, and K. Aydin, 1991: Rainfall and clutter discrimination by means of dual-linear polarization radar measurements. *Journal of Atmospheric and Oceanic Technology*, **8 (6)**, 777–789.

Goodman, J. W., 2015: *Statistical Optics*. John Wiley & Sons, 544 pp.

Gorgucci, E., V. Chandrasekar, and L. Baldini, 2006: Correction of X-band radar observation for propagation effects based on the self-consistency principle. *Journal of Atmospheric and Oceanic Technology*, **23 (12)**, 1668–1681.

Gorgucci, E., V. Chandrasekar, V. Bringi, and G. Scarchilli, 2002: Estimation of raindrop size distribution parameters from polarimetric radar measurements. *Journal of the Atmospheric Sciences*, **59 (15)**, 2373–2384.

Gorgucci, E., G. Scarchilli, and V. Chandrasekar, 1999a: A procedure to calibrate multiparameter weather radar using properties of the rain medium. *IEEE Transactions on Geoscience and Remote Sensing*, **37 (1)**, 269–276.

———, 1999b: Specific differential phase estimation in the presence of nonuniform rainfall medium along the path. *Journal of Atmospheric and Oceanic Technology*, **16 (11)**, 1690–1697.

Gourley, J. J., P. Tabary, and J. Parent du Chatelet, 2007: A fuzzy logic algorithm for the separation of precipitating from nonprecipitating echoes using polarimetric radar observations. *Journal of Atmospheric and Oceanic Technology*, **24 (8)**, 1439–1451.

Grazioli, J., D. Tuia, and A. Berne, 2015: Hydrometeor classification from polarimetric radar measurements: a clustering approach. *Atmospheric Measurement Techniques*, **8 (1)**, 149–170.

Green, A., 1975: An approximation for the shapes of large raindrops. *Journal of Applied Meteorology and Climatology*, **14 (8)**, 1578–1583.

Gu, J.-Y., A. Ryzhkov, P. Zhang, P. Neilley, M. Knight, B. Wolf, and D.-I. Lee, 2011: Polarimetric attenuation correction in heavy rain at C band. *Journal of Applied Meteorology and Climatology*, **50 (1)**, 39–58.

Gunn, K. L. S. and T. W. R. East, 1954: The microwave properties of precipitation particles. *Quarterly Journal of the Royal Meteorological Society*, **80 (346)**, 522–545.

Habib, E., G. Lee, D. Kim, and G. J. Ciach, 2010: Ground based direct measurement. *Rainfall: State of the Science; Testik, FY, Mekonnen, G., Eds*, 61–77.

Hall, M., S. Cherry, J. Goddard, and G. Kennedy, 1980: Rain drop sizes and rainfall rate measured by dual-polarization radar. *Nature*, **285 (5762)**, 195–198.

Han, D., I. D. Cluckie, R. J. Griffith, and G. L. Austin, 2000: Using weather radars to measure rainfall in urban catchments. *Journal of Urban Technology*, **7 (1)**, 85–102.

Handwerker, J., 2002: Cell tracking with TRACE3D—A new algorithm. *Atmospheric Research*, **61 (1)**, 15–34.

Helmert, K., P. Tracksdorf, J. Steinert, M. Werner, M. Frech, N. Rathmann, T. Hengstebeck, M. Mott, S. Schumann, and T. Mammen, 2014: Dwds new radar network and post-processing algorithm chain. *Proc. Eighth European Conf. on Radar in Meteorology and Hydrology (ERAD 2014), Garmisch-Partenkirchen, Germany, DWD and DLR*, Vol. 4.

Hendry, A. and G. McCormick, 1971: Polarization properties of precipitation scattering. *Bull. Radio Elec. Eng. Die., Nat. Res. Counc. Can.*, **21**, 9–20.

Hitschfeld, W. and J. Bordan, 1954: Errors inherent in the radar measurement of rainfall at attenuating wavelengths. *Journal of Meteorology*, **11 (1)**, 58–67.

Holleman, I., L. Delobbe, and A. Zgonc, 2008: Update on the European weather radar network (OPERA). *Proc. 5th Eur. Conf. on radar in meteorology and hydrology, Helsinki, Finland, 30 June–4 July 2008*, Citeseer.

Homeyer, C. R. and M. R. Kumjian, 2015: Microphysical characteristics of overshooting convection from polarimetric radar observations. *Journal of the Atmospheric Sciences*, **72 (2)**, 870–891.

Houze Jr, R. A., S. A. Rutledge, M. Biggerstaff, and B. Smull, 1989: Interpretation of Doppler weather radar displays of midlatitude mesoscale convective systems. *Bulletin of the American Meteorological Society*, **70 (6)**, 608–619.

Hu, J., D. Rosenfeld, D. Zrnic, E. Williams, P. Zhang, J. C. Snyder, A. Ryzhkov, E. Hashimshoni, R. Zhang, and R. Weitz, 2019: Tracking and characterization of convective cells through their maturation into stratiform storm elements using polarimetric radar and lightning detection. *Atmospheric Research*, **226**, 192–207.

Huang, G.-J., V. Bringi, and M. Thurai, 2008: Orientation angle distributions of drops after an 80-m fall using a 2D video disdrometer. *Journal of Atmospheric and Oceanic Technology*, **25 (9)**, 1717–1723.

Huang, H., G. Zhang, K. Zhao, and S. E. Giangrande, 2016: A hybrid method to estimate specific differential phase and rainfall with linear programming and physics constraints. *IEEE Transactions on Geoscience and Remote Sensing*, **55 (1)**, 96–111.

Hubbert, J. and V. Bringi, 1995: An iterative filtering technique for the analysis of copolar differential phase and dual-frequency radar measurements. *Journal of Atmospheric and Oceanic Technology*, **12 (3)**, 643–648.

Hubbert, J., V. Bringi, L. Carey, and S. Bolen, 1998: CSU-CHILL polarimetric radar measurements from a severe hail storm in eastern Colorado. *Journal of Applied Meteorology*, **37 (8)**, 749–775.

Hubbert, J., S. Ellis, M. Dixon, and G. Meymaris, 2010: Modeling, error analysis, and evaluation of dual-polarization variables obtained from simultaneous horizontal and vertical polarization transmit radar. Part I: Modeling and antenna errors. *Journal of Atmospheric and Oceanic Technology*, **27 (10)**, 1583–1598.

Hubbert, J., F. Pratte, M. Dixon, and R. Rilling, 2008: The uncertainty of Zdr calibration. *Proc. Fifth European Conf. on Radar in Meteorology and Hydrology*.

Hulst, H. C. and H. C. van de Hulst, 1981: *Light Scattering by Small Particles*. Courier Corporation.

Humphries, R., 1974: Depolarization effects at 3 GHz due to precipitation Sci. *Rep. MW-82. Stormy Weather Group, McGill University, Montreal*.

Hunter, I., 1954: Polarization of radar echoes from meteorological precipitation. *Nature*, **173 (4395)**, 165–166.

Husson, D. and Y. Pointin, 1989: Quantitative estimation of the hailfall intensity with a dual polarization radar and a hailpad network. *24th conference on Radar Meteorology, 24th, Tallahassee, FL, USA*, American Meteorological Society, 318–321.

Huuskonen, A., L. Delobbe, B. Urban, and A. Huuskonen, 2012: EUMETNET OPERA: Achievements of OPERA-3 and challenges ahead. *Proceedings of ERAD 2012*, 25–29.

i Ventura, J. F., M. Schneebeli, A. Leuenberger, M. Gabella, J. Grazioli, T. H. Raupach, D. Wolfensberger, P. Graf, H. Wernli, A. Berne, and U. Germann, 2015: The PARADISO campaign: Description and first results. *Proc. 37th Conf. Radar Meteorol.*

Illingworth, A. J. and D. Zrnic, 1995: Workshop on weather radar polarimetry for research and operational applications. *Bulletin of the American Meteorological Society*, **76 (4)**, 555–558.

Jacobi, S. and M. Heistermann, 2016: Benchmarking attenuation correction procedures for six years of single-polarized C-band weather radar observations in South-West Germany. *Geomatics, Natural Hazards and Risk*, **7 (6)**, 1785–1799.

Jaidan, N., L. El Amraoui, J.-L. Attié, P. Ricaud, and F. Dulac, 2018: Future changes in surface ozone over the Mediterranean Basin in the framework of the Chemistry-Aerosol Mediterranean Experiment (ChArMEx). *Atmospheric Chemistry & Physics*, **18 (13)**.

Jameson, A., 1985: Microphysical interpretation of multiparameter radar measurements in rain. Part III: Interpretation and measurement of propagation differential phase shift between orthogonal linear polarizations. *Journal of the Atmospheric Sciences*, **42 (6)**, 607–614.

———, 1991: A comparison of microwave techniques for measuring rainfall. *Journal of Applied Meteorology*, **30 (1)**, 32–54.

———, 1992: The effect of temperature on attenuation-correction schemes in rain using polarization propagation differential phase shift. *Journal of Applied Meteorology*, **31 (9)**, 1106–1118.

Jameson, A. and E. Mueller, 1985: Estimation of propagation-differential phase shift from sequential orthogonal linear polarization radar measurements. *Journal of Atmospheric and Oceanic Technology*, **2 (2)**, 133–137.

Jang, J.-S., 1993: Anfis: adaptive-network-based fuzzy inference system. *IEEE transactions on systems, man, and cybernetics*, **23 (3)**, 665–685.

Jensen, N. and L. Pedersen, 2005: Spatial variability of rainfall: Variations within a single radar pixel. *Atmospheric Research*, **77 (1-4)**, 269–277.

Joe, P. and P. May, 2003: Correction of dual PRF velocity errors for operational Doppler weather radars. *Journal of Atmospheric and Oceanic Technology*, **20 (4)**, 429–442.

Jongman, B., S. Hochrainer-Stigler, L. Feyen, J. C. Aerts, R. Mechler, W. W. Botzen, L. M. Bouwer, G. Pflug, R. Rojas, and P. J. Ward, 2014: Increasing stress on disaster-risk finance due to large floods. *Nature Climate Change*, **4 (4)**, 264–268.

Jordan, P., A. Seed, and G. Austin, 2000: Sampling errors in radar estimates of rainfall. *Journal of Geophysical Research: Atmospheres*, **105 (D2)**, 2247–2257.

Keenan, T., K. Glasson, F. Cummings, T. Bird, J. Keeler, and J. Lutz, 1998: The BMRC/NCAR C-band polarimetric (C-Pol) radar system. *Journal of Atmospheric and Oceanic Technology*, **15 (4)**, 871–886.

Kennedy, P. C., S. A. Rutledge, W. A. Petersen, and V. Bringi, 2001: Polarimetric radar observations of hail formation. *Journal of Applied Meteorology*, **40 (8)**, 1347–1366.

Kidd, C., A. Becker, G. J. Huffman, C. L. Muller, P. Joe, G. Skofronick-Jackson, and D. B. Kirschbaum, 2017: So, how much of the Earth's surface is covered by rain gauges? *Bulletin of the American Meteorological Society*, **98 (1)**, 69–78.

Klazura, G. E. and D. A. Imy, 1993: A description of the initial set of analysis products available from the NEXRAD WSR-88D system. *Bulletin of the American Meteorological Society*, **74 (7)**, 1293–1312.

Koffi, A., M. Gosset, E.-P. Zahiri, A. Ochou, M. Kacou, F. Cazenave, and P. Assamoi, 2014: Evaluation of X-band polarimetric radar estimation of rainfall and rain drop size distribution parameters in West Africa. *Atmospheric research*, **143**, 438–461.

Kostinski, A. B., 1994: Fluctuations of differential phase and radar measurements of precipitation. *Journal of Applied Meteorology*, **33 (10)**, 1176–1181.

Kouketsu, T. and H. Uyeda, 2010: Validation of hydrometeor classification method for X-band polarimetric radar—Comparison with ground observation of solid hydrometeor. *Proc. Sixth European Conf. on Radar in Meteorology and Hydrology*.

Krämer, S. and H. Verworn, 2008: Improved C-band radar data processing for real time control of urban drainage systems. *Proceedings of the 11th International Conference on Urban Drainage*, IWA Publ. London, Vol. 110.

Krause, J. M., 2016: A simple algorithm to discriminate between meteorological and nonmeteorological radar echoes. *Journal of Atmospheric and Oceanic Technology*, **33 (9)**, 1875–1885.

Kron, W., M. Steuer, P. Löw, and A. Wirtz, 2012: How to deal properly with a natural catastrophe database—analysis of flood losses. *Natural Hazards and Earth System Sciences*, **12 (3)**, 535–550.

Kumjian, M. R., 2013: Principles and Applications of Dual-Polarization Weather Radar. Part I: Description of the Polarimetric Radar Variables. *Journal of Operational Meteorology*, **1**.

———, 2018: Weather radars. *Remote Sensing of Clouds and Precipitation*, Springer, 15–63.

Kumjian, M. R., A. P. Khain, N. Benmoshe, E. Ilotoviz, A. V. Ryzhkov, and V. T. Phillips, 2014: The anatomy and physics of Z DR columns: Investigating a polarimetric radar signature with a spectral bin microphysical model. *Journal of Applied Meteorology and Climatology*, **53 (7)**, 1820–1843.

Kyznarová, H. and P. Novák, 2009: CELLTRACK—Convective cell tracking algorithm and its use for deriving life cycle characteristics. *Atmospheric research*, **93 (1-3)**, 317–327.

Lack, S. A. and N. I. Fox, 2007: An examination of the effect of wind-drift on radar-derived surface rainfall estimations. *Atmospheric research*, **85 (2)**, 217–229.

Lakshmanan, V., C. Karstens, J. Krause, K. Elmore, A. Ryzhkov, and S. Berkseth, 2015: Which polarimetric variables are important for weather/no-weather discrimination? *Journal of Atmospheric and Oceanic Technology*, **32 (6)**, 1209–1223.

LAMBRECHT, 2021: rain[e]H3 Weighing precipitation sensor. URL {`https://www.lambrecht.net/en/products/precipitation/weighing-precipitation-sensor-rain-e-h3`}.

Le Bouar, E., J. Testud, and T. D. Keenan, 2001: Validation of the rain profiling algorithm "ZPHI" from the C-band polarimetric weather radar in Darwin. *Journal of Atmospheric and Oceanic Technology*, **18 (11)**, 1819–1837.

Legates, D. R., 2000: Real-time calibration of radar precipitation estimates. *The Professional Geographer*, **52 (2)**, 235–246.

Leonardi, R., G. Scarchilli, E. Gorgucci, and C. Goretti, 1984: Polar 55C-A C-band advanced meteorological radar developed for CNR, Italy. *Conference on Radar Meteorology, 22nd, Zurich, Switzerland*, American Meteorological Society, 238–243.

Lim, S. and V. Chandrasekar, 2011: Identification of rain/ice mixture from dual polarization weather radar. *2011 IEEE International Geoscience and Remote Sensing Symposium*, IEEE, 2353–2356.

Lin, L. I.-K., 1989: A concordance correlation coefficient to evaluate reproducibility. *Biometrics*, **45 (1)**, 255–268.

Liu, H. and V. Chandrasekar, 2000: Classification of hydrometeors based on polarimetric radar measurements: Development of fuzzy logic and neuro-fuzzy systems, and in situ verification. *Journal of Atmospheric and Oceanic Technology*, **17 (2)**, 140–164.

Maesaka, T., K. Iwanami, and M. Maki, 2012: Non-negative KDP estimation by monotone increasing Φ DP assumption below melting layer. *Extended Abstracts, Seventh European Conf. on Radar in Meteorology and Hydrology*.

Maier, R., G. Krebs, M. Pichler, D. Muschalla, and G. Gruber, 2020: Spatial rainfall variability in urban environments—high-density precipitation measurements on a city-scale. *Water*, **12 (4)**, 1157.

Maki, M., S.-G. Park, and V. Bringi, 2005: Effect of natural variations in rain drop size distributions on rain rate estimators of 3 cm wavelength polarimetric radar. *Journal of the Meteorological Society of Japan. Ser. II*, **83 (5)**, 871–893.

Marks, D. A., D. B. Wolff, L. D. Carey, and A. Tokay, 2011: Quality control and calibration of the dual-polarization radar at Kwajalein, RMI. *Journal of Atmospheric and Oceanic Technology*, **28 (2)**, 181–196.

Marshall, J. S. and W. M. K. Palmer, 1948: The distribution of raindrops with size. *Journal of meteorology*, **5 (4)**, 165–166.

Martner, B. E., S. E. Yuter, A. B. White, S. Y. Matrosov, D. E. Kingsmill, and F. M. Ralph, 2008: Raindrop size distributions and rain characteristics in California coastal rainfall for periods with and without a radar bright band. *Journal of Hydrometeorology*, **9 (3)**, 408–425.

Marzano, F., D. Scaranari, M. Celano, P. Alberoni, G. Vulpiani, and M. Montopoli, 2006: Hydrometeor classification from dual-polarized weather radar: extending fuzzy logic from S-band to C-band data. *Adances in Geosciences*, 109–114, URL `https://hal.archives-ouvertes.fr/file/index/docid/296848/filename/adgeo-7-109-2006.pdf`.

Marzano, F. S., D. Scaranari, M. Montopoli, and G. Vulpiani, 2007: Supervised classification and estimation of hydrometeors from C-band dual-polarized radars: A Bayesian approach. *IEEE transactions on Geoscience and Remote Sensing*, **46 (1)**, 85–98.

Marzoug, M. and P. Amayenc, 1994: A Class of Single-and Dual-Frequency Algorithms for Rain-Rate Profiling from a Spaceborne Radar. Pad I: Principle and Tests from Numerical Simulations. *Journal of Atmospheric and Oceanic Technology*, **11 (6)**, 1480–1506.

Matrosov, S. Y., 2010: Evaluating polarimetric X-band radar rainfall estimators during HMT. *Journal of Atmospheric and Oceanic Technology*, **27 (1)**, 122–134.

Matrosov, S. Y., R. Cifelli, and D. Gochis, 2013: Measurements of heavy convective rainfall in the presence of hail in flood-prone areas using an X-band polarimetric radar. *Journal of applied meteorology and climatology*, **52 (2)**, 395–407.

Matrosov, S. Y., R. Cifelli, P. C. Kennedy, S. W. Nesbitt, S. A. Rutledge, V. Bringi, and B. E. Martner, 2006: A comparative study of rainfall retrievals based on specific differential phase shifts at X-and S-band radar frequencies. *Journal of Atmospheric and Oceanic Technology*, **23 (7)**, 952–963.

Matrosov, S. Y., K. A. Clark, B. E. Martner, and A. Tokay, 2002: X-band polarimetric radar measurements of rainfall. *Journal of Applied Meteorology*, **41 (9)**, 941–952.

Matrosov, S. Y., D. E. Kingsmill, B. E. Martner, and F. M. Ralph, 2005: The utility of X-band polarimetric radar for quantitative estimates of rainfall parameters. *Journal of hydrometeorology*, **6 (3)**, 248–262.

McBride, G., 2005: A proposal for strength-of-agreement criteria for lin's concordance correlation coefficient. *NIWA client report: HAM2005-062*, **62**.

McCormick, G. and A. Hendry, 1979a: Radar measurement of precipitation-related depolarization in thunderstorms. *IEEE Transactions on Geoscience Electronics*, **17 (4)**, 142–150.

———, 1979b: Techniques for the determination of the polarization properties of precipitation. *Radio Science*, **14 (6)**, 1027–1040.

Meischner, P., V. Bringi, D. Heimann, and H. Höller, 1991: A squall line in southern Germany: Kinematics and precipitation formation as deduced by advanced polarimetric and Doppler radar measurements. *Monthly weather review*, **119 (3)**, 678–701.

Melnikov, V. M. and D. Zrnic, 2004: Simultaneous transmission mode for the polarimetric WSR-88D: Statistical biases and standard deviations of polarimetric variables.

Melnikov, V. M. and D. S. Zrnić, 2007: Autocorrelation and cross-correlation estimators of polarimetric variables. *Journal of Atmospheric and Oceanic Technology*, **24 (8)**, 1337–1350.

Meneghini, R. and K. Nakamura, 1990: Range profiling of the rain rate by an airborne weather radar. *Remote Sensing of Environment*, **31 (3)**, 193–209.

Metcalf, J. I. and R. G. Humphries, 1981: Workshop on Polarization Techniques in Radar Meteorology. *Bulletin of the American Meteorological Society*, **62 (3)**, 416–417.

METEK GmbH, 2014: Micro Rain Radar MRR-2. URL {`https://metek.de/wp-content/uploads/2014/05/Datasheet_MRR-2.pdf`}, accessed 6 July 2020.

Mittermaier, M. P., R. J. Hogan, and A. J. Illingworth, 2004: Using mesoscale model winds for correcting wind-drift errors in radar estimates of surface rainfall. *Quarterly Journal of the Royal Meteorological Society: A journal of the atmospheric sciences, applied meteorology and physical oceanography*, **130 (601)**, 2105–2123.

Montopoli, M. and F. S. Marzano, 2011: Meteorological Radar Systems. *Integrated Ground-Based Observing Systems*, Springer, 33–57.

Moore, R. J., A. E. Jones, D. A. Jones, K. B. Black, and V. A. Bell, 2004: Weather radar for flood forecasting: some UK experiences. *Sixth International Symposium on Hydrological Applications of Weather Radar*, Citeseer, 2–4.

Morrissey, M. L., J. A. Maliekal, J. S. Greene, and J. Wang, 1995: The uncertainty of simple spatial averages using rain gauge networks. *Water Resources Research*, **31 (8)**, 2011–2017.

M.Thurai, R., 2007: *Dual-Polarization Weather Radar Handbook*. Selex-Si Gematronik.

Mueller, E., 1984: Calculation procedures for differential propagation phase shift((for meteorological radar)). *Conference on Radar Meteorology, 22 nd, Zurich, Switzerland*, 397–399.

Nations, U., 2019: World population prospects 2019: highlights. *Department of Economic and Social Affairs, Population Division*.

Niemczynowicz, J., 1991: On storm movement and its applications. *Atmospheric Research*, **27 (1-3)**, 109–127.

Niemi, T. J., L. Warsta, M. Taka, B. Hickman, S. Pulkkinen, G. Krebs, D. N. Moisseev, H. Koivusalo, and T. Kokkonen, 2017: Applicability of open rainfall data to event-scale urban rainfall-runoff modelling. *Journal of hydrology*, **547**, 143–155.

Ninomiya, K. and T. Akiyama, 1978: Objective analysis of heavy rainfalls based on radar and gauge measurements. *Journal of the Meteorological Society of Japan. Ser. II*, **56 (3)**, 206–210.

Nystuen, J. A., 1998: Temporal sampling requirements for automatic rain gauges. *Journal of Atmospheric and Oceanic Technology*, **15 (6)**, 1253–1260.

Ochoa-Rodriguez, S., L.-P. Wang, A. Gires, R. D. Pina, R. Reinoso-Rondinel, G. Bruni, A. Ichiba, S. Gaitan, E. Cristiano, J. van Assel, et al., 2015: Impact of spatial and temporal resolution of rainfall inputs on urban hydrodynamic modelling outputs: A multi-catchment investigation. *Journal of Hydrology*, **531**, 389–407.

Offutt, W., 1955: A review of circular polarization as a means of precipitation clutter suppression and examples. *Proc. National Electronics Conference, Chicago*, Vol. 2, 94–100.

Oolman, L., 2017: University of Wyoming Department of Atmospheric Science, weather data upper air sounding. URL `http://weather.uwyo.edu/upperair/sounding.html`.

Otto, T. and H. W. Russchenberg, 2011: Estimation of specific differential phase and differential backscatter phase from polarimetric weather radar measurements of rain. *IEEE Geoscience and Remote Sensing Letters*, **8 (5)**, 988–992.

Park, H. S., A. Ryzhkov, D. Zrnić, and K.-E. Kim, 2009: The hydrometeor classification algorithm for the polarimetric WSR-88D: Description and application to an MCS. *Weather and forecasting*, **24 (3)**, 730–748.

Park, S., M. Maki, K. Iwanami, V. Bringi, and V. Chandrasekar, 2005: Correction of radar reflectivity and differential reflectivity for rain attenuation at X band. Part II: Evaluation and application. *Journal of Atmospheric and Oceanic Technology*, **22 (11)**, 1633–1655.

Paschalis, A., P. Molnar, S. Fatichi, and P. Burlando, 2013: A stochastic model for high-resolution space-time precipitation simulation. *Water Resources Research*, **49 (12)**, 8400–8417.

Paz, I., B. Willinger, A. Gires, A. Ichiba, L. Monier, C. Zobrist, B. Tisserand, I. Tchiguirinskaia, and D. Schertzer, 2018: Multifractal comparison of reflectivity and polarimetric rainfall data from C-and X-band radars and respective hydrological responses of a complex catchment model. *Water*, **10 (3)**, 269.

Pazmany, A. L., J. B. Mead, H. B. Bluestein, J. C. Snyder, and J. B. Houser, 2013: A mobile rapid-scanning X-band polarimetric (RaXPol) Doppler radar system. *Journal of Atmospheric and Oceanic Technology*, **30 (7)**, 1398–1413.

PC, S., T. Nakatani, and R. Misumi, 2019: The role of the spatial distribution of radar rainfall on hydrological modeling for an urbanized river basin in Japan. *Water*, **11 (8)**, 1703.

Peleg, N., M. Ben-Asher, and E. Morin, 2013: Radar subpixel-scale rainfall variability and uncertainty: lessons learned from observations of a dense rain-gauge network. *Hydrology and Earth System Sciences*, **17 (6)**, 2195–2208.

Peters, G., B. Fischer, and T. Andersson, 2002: Rain observations with a vertically looking Micro Rain Radar (MRR). *Boreal environment research*, **7 (4)**, 353–362.

Piccolo, F. and G. Chirico, 2005: Sampling errors in rainfall measurements by weather radar. *Advances in Geosciences*, **2**, 151–155.

Prein, A. F., C. Liu, K. Ikeda, S. B. Trier, R. M. Rasmussen, G. J. Holland, and M. P. Clark, 2017: Increased rainfall volume from future convective storms in the US. *Nature Climate Change*, **7 (12)**, 880–884.

Proakis, J. G. and D. G. Manolakis, 1988: *Introduction to Digital Signal Processing*. New York: Macmillan, 944 pp.

Probert-Jones, J., 1962: The radar equation in meteorology. *Quarterly Journal of the Royal Meteorological Society*, **88 (378)**, 485–495.

Pruppacher, H. R. and K. Beard, 1970: A wind tunnel investigation of the internal circulation and shape of water drops falling at terminal velocity in air. *Quarterly Journal of the Royal Meteorological Society*, **96 (408)**, 247–256.

Pruppacher, H. R. and J. D. Klett, 2011: *Microphysics of Clouds and Precipitation*. Springer, Dordrecht, 954 pp.

Pruppacher, H. R. and R. Pitter, 1971: A semi-empirical determination of the shape of cloud and rain drops. *Journal of the atmospheric sciences*, **28 (1)**, 86–94.

Rauber, R. M. and S. W. Nesbitt, 2018: *Radar Meteorology: A First Course*. John Wiley & Sons, 488 pp.

Rico-Ramirez, M., I. Cluckie, G. Shepherd, and A. Pallot, 2007: A high-resolution radar experiment on the island of Jersey. *Meteorological Applications: A journal of forecasting, practical applications, training techniques and modelling*, **14 (2)**, 117–129.

Rico-Ramirez, M., S. Liguori, and A. Schellart, 2015: Quantifying radar-rainfall uncertainties in urban drainage flow modelling. *Journal of hydrology*, **528**, 17–28.

Rosenfeld, D., 1987: Objective method for analysis and tracking of convective cells as seen by radar. *Journal of Atmospheric and Oceanic Technology*, **4 (3)**, 422–434.

Rosenfeld, D. and C. W. Ulbrich, 2003: Cloud microphysical properties, processes, and rainfall estimation opportunities. *Radar and Atmospheric Science: A Collection of Essays in Honor of David Atlas*, Springer, 237–258.

Rossa, A., K. Liechti, M. Zappa, M. Bruen, U. Germann, G. Haase, C. Keil, and P. Krahe, 2011: The COST 731 Action: A review on uncertainty propagation in advanced hydro-meteorological forecast systems. *Atmospheric Research*, **100 (2-3)**, 150–167.

Ryde, J., 1946: The attenuation and radar echoes produced at centimeter wavelengths by various meteorological phenomena. *Meteorological Factors in Radio Wave Propagation, London*, 169–189.

Ryzhkov, A., M. Diederich, P. Zhang, and C. Simmer, 2014: Potential utilization of specific attenuation for rainfall estimation, mitigation of partial beam blockage, and radar networking. *Journal of Atmospheric and Oceanic Technology*, **31 (3)**, 599–619.

Ryzhkov, A., M. Pinsky, A. Pokrovsky, and A. Khain, 2011: Polarimetric radar observation operator for a cloud model with spectral microphysics. *Journal of Applied Meteorology and Climatology*, **50 (4)**, 873–894.

Ryzhkov, A., V. Zhuravlyov, and N. Rybakova, 1994: Preliminary results of X-band polarization radar studies of clouds and precipitation. *Journal of Atmospheric and Oceanic Technology*, **11 (1)**, 132–139.

Ryzhkov, A. and D. Zrnić, 1994: Precipitation observed in Oklahoma mesoscale convective systems with a polarimetric radar. *Journal of Applied Meteorology and Climatology*, **33 (4)**, 455–464.

Ryzhkov, A. and D. Zrnic, 1995: Precipitation and attenuation measurements at a 10-cm wavelength. *Journal of Applied Meteorology*, **34 (10)**, 2121–2134.

Ryzhkov, A. and D. Zrnić, 1996: Assessment of rainfall measurement that uses specific differential phase. *Journal of applied meteorology*, **35 (11)**, 2080–2090.

Ryzhkov, A. and D. Zrnic, 1998a: Beamwidth effects on the differential phase measurements of rain. *Journal of Atmospheric and Oceanic Technology*, **15 (3)**, 624–634.

Ryzhkov, A., D. Zrnić, and D. Atlas, 1997: Polarimetrically tuned R (Z) relations and comparison of radar rainfall methods. *Journal of Applied Meteorology*, **36 (4)**, 340–349.

Ryzhkov, A. V., 2007: The impact of beam broadening on the quality of radar polarimetric data. *Journal of Atmospheric and Oceanic Technology*, **24 (5)**, 729–744.

Ryzhkov, A. V., T. J. Schuur, D. W. Burgess, P. L. Heinselman, S. E. Giangrande, and D. S. Zrnic, 2005: The Joint Polarization Experiment: Polarimetric rainfall measurements and hydrometeor classification. *Bulletin of the American Meteorological Society*, **86 (6)**, 809–824.

Ryzhkov, A. V. and D. S. Zrnic, 1998b: Polarimetric rainfall estimation in the presence of anomalous propagation. *Journal of Atmospheric and Oceanic Technology*, **15 (6)**, 1320–1330.

Ryzhkov, A. V. and D. S. Zrnić, 2007: Depolarization in ice crystals and its effect on radar polarimetric measurements. *Journal of atmospheric and oceanic technology*, **24 (7)**, 1256–1267.

———, 2019: *Radar Polarimetry for Weather Observations*. Springer, 486 pp.

Sachidananda, M. and D. Zrnic', 1985: Zdr measurement considerations for a fast scan capability radar. *Radio Science*, **20 (4)**, 907–922.

Sachidananda, M. and D. Zrnić, 1986: Differential propagation phase shift and rainfall rate estimation. *Radio science*, **21 (2)**, 235–247.

———, 1987: Rain rate estimates from differential polarization measurements. *Journal of Atmospheric and Oceanic Technology*, **4 (4)**, 588–598.

Saltikoff, E. and L. Nevvonen, 2011: First experiences of the operational use of a dual-polarisation weather radar in Finland. *Meteorologische Zeitschrift*, **20 (3)**, 323–333.

Salvadore, E., J. Bronders, and O. Batelaan, 2015: Hydrological modelling of urbanized catchments: A review and future directions. *Journal of Hydrology*, **529**, 62–81.

Sauvageot, H., 1992: *Radar Meteorology*. Artech House Publishers, 366 pp.

Schellart, A., S. Liguori, S. Krämer, A. Saul, and M. A. Rico-Ramirez, 2014: Comparing quantitative precipitation forecast methods for prediction of sewer flows in a small urban area. *Hydrological Sciences Journal*, **59 (7)**, 1418–1436.

Schellart, A., W. Shepherd, and A. Saul, 2012: Influence of rainfall estimation error and spatial variability on sewer flow prediction at a small urban scale. *Advances in Water Resources*, **45**, 65–75.

Scherer, D., F. Ament, S. Emeis, U. Fehrenbach, B. Leitl, K. Scherber, C. Schneider, and U. Vogt, 2019: Three-dimensional observation of atmospheric processes in cities. *Meteorol Z*, **28 (2)**, 121–138.

Schilling, W., 1991: Rainfall data for urban hydrology: what do we need? *Atmospheric Research*, **27 (1-3)**, 5–21.

Schroth, A. C., M. S. Chandra, and P. F. Mesichner, 1988: A C-band coherent polarimetric radar for propagation and cloud physics research. *Journal of Atmospheric and Oceanic Technology*, **5 (6)**, 803–822.

Schuur, T., A. Ryzhkov, P. Heinselman, D. Zrnic, D. Burgess, and K. Scharfenberg, 2003: Observations and classification of echoes with the polarimetric WSR-88D radar. *Report of the National Severe Storms Laboratory, Norman, OK*, **73069**, 46.

Schuur, T. J., H.-S. Park, A. V. Ryzhkov, and H. D. Reeves, 2012: Classification of precipitation types during transitional winter weather using the RUC model and polarimetric radar retrievals. *Journal of applied meteorology and climatology*, **51 (4)**, 763–779.

Selex-SI, 2012: *Instruction Manuel Rainbow5 products and algorithms*. Selex system integration GmbH.

SELEX, System Integration GmbH, 2015: *GDRX signal Processing User Manual*. 4th ed.

Seliga, T. and V. Bringi, 1978: Differential reflectivity and differential phase shift: Applications in radar meteorology. *Radio Science*, **13 (2)**, 271–275.

Seliga, T. A. and V. Bringi, 1976: Potential use of radar differential reflectivity measurements at orthogonal polarizations for measuring precipitation. *Journal of Applied Meteorology*, **15 (1)**, 69–76.

Sénési, S., P. Bougeault, J.-L. Chèze, P. Cosentino, and R.-M. Thepenier, 1996: The Vaison-La-Romaine flash flood: Mesoscale analysis and predictability issues. *Weather and Forecasting*, **11 (4)**, 417–442.

Seneviratne, S., N. Nicholls, D. Easterling, C. Goodess, S. Kanae, J. Kossin, Y. Luo, J. Marengo, K. McInnes, M. Rahimi, et al., 2012: Changes in climate extremes and their impacts on the natural physical environment. *Managing the risks of extreme events and disasters to advance climate change adaptation: special report of the intergovernmental panel on climate change*, Field, C. B., V. Barros, T. F. Stocker, and Q. Dahe, Eds., Cambridge University Pres, 109–230.

Sharif, H. O., D. Yates, R. Roberts, and C. Mueller, 2006: The use of an automated nowcasting system to forecast flash floods in an urban watershed. *Journal of Hydrometeorology*, **7 (1)**, 190–202.

Shucksmith, P., L. Sutherland-Stacey, and G. Austin, 2011: The spatial and temporal sampling errors inherent in low resolution radar estimates of rainfall. *Meteorological Applications*, **18 (3)**, 354–360.

Shupiatskii, A., 1959: Radiolokatsionnoe rasseianie nesfericheskimi chastitsami, radar scattering by non-spherical particles. *Tsentral'naia Aerologicheskaia Observatoriia, Trudy*, **(30)**, 39–52.

Shupiatskii, A. and S. Morgunov, 1968: *The Application of Polarization Methods to Radar Studies of Clouds and Precipitation*, Vol. 68. Air Force Cambridge Research Laboratories, Office of Aerospace Research ....

Sirmans, D., D. Zrnic, and B. Bumgarner, 1976: Extension of maximum unambiguous Doppler velocity by use of two sampling rates. *Conference on Radar Meteorology, 17 th, Seattle, Wash*, 23–28.

Smith, J. A., M. L. Baeck, K. L. Meierdiercks, A. J. Miller, and W. F. Krajewski, 2007: Radar rainfall estimation for flash flood forecasting in small urban watersheds. *Advances in Water Resources*, **30 (10)**, 2087–2097.

Smith, J. A. and W. F. Krajewski, 1991: Estimation of the mean field bias of radar rainfall estimates. *Journal of Applied Meteorology*, **30 (4)**, 397–412.

Smith, P. L., 1986: On the sensitivity of weather radars. *Journal of Atmospheric and Oceanic Technology*, **3 (4)**, 704–713.

Snyder, J. C., H. B. Bluestein, G. Zhang, and S. J. Frasier, 2010: Attenuation correction and hydrometeor classification of high-resolution, X-band, dual-polarized mobile radar measurements in severe convective storms. *Journal of Atmospheric and Oceanic Technology*, **27 (12)**, 1979–2001.

Spearman, C., 2010: The proof and measurement of association between two things. *International journal of epidemiology*, **39 (5)**, 1137–1150.

Spiegelman, D., 2010: Commentary: Some remarks on the seminal 1904 paper of Charles Spearman 'The proof and measurement of association between two things'. *International journal of epidemiology*, **39 (5)**, 1156–1159.

Steichen, T. J. and N. J. Cox, 2002: A note on the concordance correlation coefficient. *The Stata Journal*, **2 (2)**, 183–189.

Steiner, M., 1996: Uncertainty of estimates of monthly areal rainfall for temporally sparse remote observations. *Water Resources Research*, **32 (2)**, 373–388.

Straka, J. M., D. S. Zrnić, and A. V. Ryzhkov, 2000: Bulk hydrometeor classification and quantification using polarimetric radar data: Synthesis of relations. *Journal of Applied Meteorology*, **39 (8)**, 1341–1372.

Tabary, P., A.-A. Boumahmoud, H. Andrieu, R. J. Thompson, A. J. Illingworth, E. Le Bouar, and J. Testud, 2011: Evaluation of two "integrated" polarimetric Quantitative Precipitation Estimation (QPE) algorithms at C-band. *Journal of Hydrology*, **405 (3-4)**, 248–260.

Testud, J., E. Le Bouar, E. Obligis, and M. Ali-Mehenni, 2000: The rain profiling algorithm applied to polarimetric weather radar. *Journal of Atmospheric and Oceanic Technology*, **17 (3)**, 332–356.

Thompson, E. J., S. A. Rutledge, B. Dolan, V. Chandrasekar, and B. L. Cheong, 2014: A dual-polarization radar hydrometeor classification algorithm for winter precipitation. *Journal of Atmospheric and Oceanic Technology*, **31 (7)**, 1457–1481.

Thorndahl, S., T. Einfalt, P. Willems, J. E. Nielsen, M.-C. ten Veldhuis, K. Arnbjerg-Nielsen, M. R. Rasmussen, and P. Molnar, 2017: Weather radar rainfall data in urban hydrology. *Hydrology and Earth System Sciences*, **21 (3)**, 1359–1380.

Thorndahl, S., J. A. Smith, M. L. Baeck, and W. F. Krajewski, 2014: Analyses of the temporal and spatial structures of heavy rainfall from a catalog of high-resolution radar rainfall fields. *Atmospheric research*, **144**, 111–125.

Tilford, K., N. Fox, and C. Collier, 2002: Application of weather radar data for urban hydrology. *Meteorological Applications: A journal of forecasting, practical applications, training techniques and modelling*, **9 (1)**, 95–104.

Torres, S. M., Y. F. Dubel, and D. S. Zrnić, 2004: Design, implementation, and demonstration of a staggered PRT algorithm for the WSR-88D. *Journal of Atmospheric and Oceanic Technology*, **21 (9)**, 1389–1399.

Trömel, S., M. R. Kumjian, A. V. Ryzhkov, C. Simmer, and M. Diederich, 2013: Backscatter differential phase—Estimation and variability. *Journal of applied meteorology and climatology*, **52 (11)**, 2529–2548.

Twomey, S., 1953: On the measurement of precipitation intensity by radar. *Journal of Meteorology*, **10 (1)**, 66–67.

Ulbrich, C. W., 1983: Natural variations in the analytical form of the raindrop size distribution. *Journal of climate and applied meteorology*, **22 (10)**, 1764–1775.

Upton, G. and A. Rahimi, 2003: On-line detection of errors in tipping-bucket raingauges. *Journal of Hydrology*, **278 (1-4)**, 197–212.

van den Heuvel, F., M. Gabella, M. Schneebeli, S. Joos, J. Figueras i Ventura, J. Grazioli, P. Speirs, A. Leuenberger, and A. Berne, 2018a: Sphere calibration of two co-located polarimetric x-band radars. *TECO - Technical Conference on Meteorological and Environmental Instruments and Methods of Observatio*.

van den Heuvel, F., M. Gabella, M. Schneebeli, et al., 2018b: Sphere calibration of two co-located polarimetric X-band radars. *TECO - Technical Conference on Meteorological and Environmental Instruments and Methods of Observation*.

Vannitsem, S., J. B. Bremnes, J. Demaeyer, G. R. Evans, J. Flowerdew, S. Hemri, S. Lerch, N. Roberts, S. Theis, A. Atencia, et al., 2021: Statistical Postprocessing for Weather Forecasts: Review, Challenges, and Avenues in a Big Data World. *Bulletin of the American Meteorological Society*, **102 (3)**, E681–E699.

Vasiloff, S. V., K. W. Howard, and J. Zhang, 2009: Difficulties with correcting radar rainfall estimates based on rain gauge data: A case study of severe weather in Montana on 16–17 June 2007. *Weather and forecasting*, **24 (5)**, 1334–1344.

Vieux, B. E., J.-H. Park, and B. Kang, 2009: Distributed hydrologic prediction: Sensitivity to accuracy of initial soil moisture conditions and radar rainfall input. *Journal of Hydrologic Engineering*, **14 (7)**, 671–689.

Villarini, G., P. V. Mandapaka, W. F. Krajewski, and R. J. Moore, 2008: Rainfall and sampling uncertainties: A rain gauge perspective. *Journal of Geophysical Research: Atmospheres*, **113 (D11)**.

Vivekanandan, J., G. Zhang, S. M. Ellis, D. Rajopadhyaya, and S. K. Avery, 2003: Radar reflectivity calibration using differential propagation phase measurement. *Radio Science*, **38 (3)**.

Vonach, T., T. Einfalt, W. Rauch, and M. Kleidorfer, 2018: Rain gauge vs. radar measurements-modelling an extreme rain event with high spatial variability. *International Conference on Urban Drainage Modelling*, Springer, 413–418.

Vulpiani, G., L. Baldini, and N. Roberto, 2015: Characterization of Mediterranean hail-bearing storms using an operational polarimetric X-band radar. *Atmospheric Measurement Techniques*, **8 (11)**, 4681–4698.

Vulpiani, G., P. Tabary, J. Parent du Chatelet, and F. S. Marzano, 2008: Comparison of advanced radar polarimetric techniques for operational attenuation correction at C band. *Journal of Atmospheric and Oceanic Technology*, **25 (7)**, 1118–1135.

Wang, Y. and V. Chandrasekar, 2009: Algorithm for estimation of the specific differential phase. *Journal of Atmospheric and Oceanic Technology*, **26 (12)**, 2565–2578.

Wang, Y., V. Chandrasekar, and V. Bringi, 2006: Characterization and evaluation of hybrid polarization observation of precipitation. *Journal of Atmospheric and Oceanic Technology*, **23 (4)**, 552–572.

Waterman, P., 1965: Matrix formulation of electromagnetic scattering. *Proceedings of the IEEE*, **53 (8)**, 805–812.

Weigl, E. and T. Winterrath, 2009: Radargestützte Niederschlagsanalyse und–vorhersage (RADOLAN, RADVOR-OP). *promet*, **35**, 78–86.

Wen, G., A. Protat, P. T. May, X. Wang, and W. Moran, 2015: A cluster-based method for hydrometeor classification using polarimetric variables. Part I: Interpretation and analysis. *Journal of Atmospheric and Oceanic Technology*, **32 (7)**, 1320–1340.

Werner, M., 2014: A new radar data post-processing quality control workflow for the DWD weather radar network. *Proc. 8th Europ. Conf. On Radar in Meteor. and Hydrol., Garmisch-Partenkirchen, Germany*.

White, W., 1954: Circular polarization cuts rain clutter. *Electronics*, **27**, 158–160.

Wilks, D. S., 2006: *Statistical Methods in the Atmospheric Sciences (2nd Edition)*, Vol. 91. Academic press, 627 pp.

Williams, E., K. Hood, D. Smalley, M. Donovan, V. Melnikov, D. Forsyth, D. Zrnic, D. Burgess, M. Douglas, J. Sandifer, et al., 2013: End-to-end calibration of NEXRAD differential reflectivity with metal spheres. *Proc. 36th Conf. Radar Meteorol*.

Wilson, J. W., 1970: Integration of radar and raingage data for improved rainfall measurement. *Journal of Applied Meteorology and Climatology*, **9 (3)**, 489–497.

Wilson, J. W. and E. A. Brandes, 1979: Radar measurement of rainfall—A summary. *Bulletin of the American Meteorological Society*, **60 (9)**, 1048–1060.

Wolf, C., 2021: Dwell time and hits per scan. URL {`https://www.radartutorial.eu/01.basics/Dwell%20Time%20and%20Hits%20per%20Scan.en.html`}, accessed 12 Dec 2020.

Wood, S., D. Jones, and R. Moore, 2000: Static and dynamic calibration of radar data for hydrological use. *Hydrology and Earth System Sciences*, **4 (4)**, 545–554.

Wright, D. B., J. A. Smith, G. Villarini, and M. L. Baeck, 2014: Long-term high-resolution radar rainfall fields for urban hydrology. *JAWRA Journal of the American Water Resources Association*, **50 (3)**, 713–734.

Wurman, J. and K. Kosiba, 2013: Finescale radar observations of tornado and mesocyclone structures. *Weather and Forecasting*, **28 (5)**, 1157–1174.

Yuan, J. et al., 1994: Hydrological modelling with weather radar data in urban drainage systems. Ph.D. thesis, University of Salford, UK.

Zar, J. H., 2007: *Biostatistical Analysis (5th Edition)*. Prentice-Hall, Inc., USA, 960 pp.

Zawadzki, I., 1975: On radar-raingage comparison. *Journal of Applied Meteorology*, **14 (8)**, 1430–1436.

Zhang, G., 2016: *Weather Radar Polarimetry*. 1st ed., CRC Press, Inc., 322 pp.

Zhang, G., V. N. Mahale, B. J. Putnam, Y. Qi, Q. Cao, A. D. Byrd, P. Bukovcic, D. S. Zrnic, J. Gao, M. Xue, et al., 2019: Current status and future challenges of weather radar polarimetry: Bridging the gap between radar meteorology/hydrology/engineering and numerical weather prediction. *Advances in Atmospheric Sciences*, **36 (6)**, 571–588.

Zhang, J., Y. Qi, K. Howard, C. Langston, and B. Kaney, 2011: Radar quality index (RQI)—A combined measure of beam blockage and VPR effects in a national network. *IAHS Publ*, **351**, 388–393.

Zheng, Y., J. Handwerker, and N. Kathoff, 2019: Summer precipitation climatology from 20-Year C-Band radar dataset. *AMS Radar conference*.

Zrinc, D. and P. Mahapatra, 1985: Two methods of ambiguity resolution in pulse Doppler weather radars. *IEEE Transactions on Aerospace and Electronic Systems*, **21 (4)**, 470–483.

Zrnić, D. and A. Ryzhkov, 1996: Advantages of rain measurements using specific differential phase. *Journal of Atmospheric and Oceanic Technology*, **13 (2)**, 454–464.

Zrnić, D. S., 1991: Complete polarimetric and Doppler measurements with a single receiver radar. *Journal of Atmospheric and Oceanic Technology*, **8 (1)**, 159–165.

———, 1996: Weather radar polarimetry—Trends toward operational applications. *Bulletin of the American Meteorological Society*, **77 (7)**, 1529–1534.

Zrnić, D. S., A. Ryzhkov, J. Straka, Y. Liu, and J. Vivekanandan, 2001: Testing a procedure for automatic classification of hydrometeor types. *Journal of Atmospheric and Oceanic Technology*, **18 (6)**, 892–913.

Zrnic, D. S. and A. V. Ryzhkov, 1999: Polarimetry for weather surveillance radars. *Bulletin of the American Meteorological Society*, **80 (3)**, 389–406.